



Universidade do Minho
Escola de Engenharia

Nicoletta Bianchini
Evaluation of the seismic response of masonry cross vaults
through shaking table tests and numerical analysis

Nicoletta Bianchini

Evaluation of the seismic response of masonry
cross vaults through shaking table tests and
numerical analysis



Universidade do Minho
Escola de Engenharia

Nicoletta Bianchini

Evaluation of the seismic response of masonry
cross vaults through shaking table tests and
numerical analysis

Doctoral Thesis
Civil Engineering

Work concluded under the supervision of:
Professor Paulo B. Lourenço
Doctor Nuno Mendes

May 2023

DIREITOS DE AUTOR E CONDIÇÕES DE UTILIZAÇÃO DO TRABALHO POR TERCEIROS

Este é um trabalho académico que pode ser utilizado por terceiros desde que respeitadas as regras e boas práticas internacionalmente aceites, no que concerne aos direitos de autor e direitos conexos.

Assim, o presente trabalho pode ser utilizado nos termos previstos na licença abaixo indicada.

Caso o utilizador necessite de permissão para poder fazer um uso do trabalho em condições não previstas no licenciamento indicado, deverá contactar o autor, através do RepositóriUM da Universidade do Minho.

Licença concedida aos utilizadores deste trabalho



Atribuição-NãoComercial-Compartilhalgal
CC BY-NC-SA

<https://creativecommons.org/licenses/by-nc-sa/4.0/>

Acknowledgements

This intense journey around the marvellous world of masonry cross vaults is coming to an end thank to many people who helped me during these four years. My first thought is to my supervisor – Dr. Nuno Mendes – to whom just expressing my gratitude does not seem enough after all the support he gave to this work. He has been constantly encouraging, believing in me and in the importance of the project from day one. Also, I would like to express my gratitude to my supervisor Prof. Paulo B. Lourenço for giving me this opportunity, for providing to me all the necessary resources to undertake this research, and for sharing experience, interest and valuable discussions which brought relevant developments to the research.

Thanks to Prof. Calderini, who inspired this research work, and to Michela Rossi and Angelo Gaetani who shared with me their knowledge on vaults, transmitting their passion about the topic through creative discussions. I would like to thank Dr. Paulo Candeias for his incredible job to pursue a successful experimental campaign. Thanks also to JAMOSIL company (Antonio Bernardo, Fernando and Horacio) for building the full-scale vault following the ancient rules. It has been a funny jump in the past. My thank goes to the assistants and technicians of the LNEC and LEST (UMinho) Laboratory (Ana Marques, Antonio Correia, Antonio Costa, Aurelio Artur, Carlos, Felipe, Luciano, Susana) for their assistance in the laboratory. To Dr. Rui Silva who helped me to apply the grout injections. Thanks to Antonetta and Carla who shared the intense days of the shaking table tests with me in Lisbon, making the memories even sweeter and funnier. Kerakoll S.p.A., CENOL, OMYA companies are also kindly acknowledged for cofunding the research and providing the materials for the experimental campaign on the full-scale vault; in particular, Davide Campanini, José Dobón and Giorgia Martinelli. I would like to extend my gratitude to Dr. José Viera de Lemos, Dr. Anjali Mehrotra and Dr. Bora Pulatsu who have contributed to the development of this investigation giving insights and for learning DEM approach and 3DEC software.

My gratitude to the Portuguese Foundation for Science and Technology (FCT) for the financial support through the grant agreements SFRH/BD/136831/2018 and COVID/BD/153210/2023.

Thanks to my brothers-in-crime Antonio A., Antonio R., and Jacopo who since SAHC have been following my ups and downs and they are the best company I could find on the way. To Abide, Alberto, Beatrice, Chandan, Giorgos, Georgious, Eduarda, Elesban, Fabio, Francesco, Francisco, Leidy, Lidia, Pia, Meera, Pilar, Telma, Rafael and Xinyu, for making this journey funny and enjoyable. Thank to my Genoese friends and family for their care and motivation. Lastly, I would like to dedicate this work to my nonna Carla and to Claudio for being a never-ending source of love.

STATEMENT OF INTEGRITY

I hereby declare having conducted this academic work with integrity. I confirm that I have not used plagiarism or any form of undue use of information or falsification of results along the process leading to its elaboration.

I further declare that I have fully acknowledged the Code of Ethical Conduct of the University of Minho.

Avaliação da resposta sísmica de abóbadas de aresta de alvenaria através de ensaios em mesa sísmica e da análise numérica

Resumo: As abóbadas de aresta de alvenaria representam elementos estruturais que continuam a surpreender os observadores, porém a investigação sobre este tópico ainda é limitada. Sendo vulneráveis aos sismos, a sua salvaguarda é crucial, uma vez que podem causar vítimas e perdas significativas. Esta tese tem por objetivo estudar o comportamento sísmico de abóbadas de aresta submetidas à ação de corte e avaliar a eficiência de uma técnica de reforço através de ensaios sísmicos e da análise numérica. O programa experimental incluiu uma abóbada à escala reduzida, impressa em 3D, com juntas secas e uma abóbada à escala real com juntas de argamassa e tijolos maciços, reparada com injeções e reforçada com reboco armado. A resposta experimental da abóbada reduzida foi analisada em termos de mecanismo de colapso, capacidade sísmica e deslocamentos relativos, e forneceu dados para calibrar os modelos numéricos tridimensionais, nomeadamente o micromodelo de elementos finitos (MEF) e o modelo de elementos discretos (MED), e para realizar análises dinâmicas não lineares. Verificou-se que a calibração da rigidez das juntas, efetuada com base nas propriedades modais, se revelou decisiva para os modelos numéricos. Observou-se ainda que a influência do amortecimento não é relevante para elementos com junta seca. O MEF mostrou ser preciso. No entanto o MED reproduziu melhor o dano e o instante em que este ocorreu. O estudo sobre a influência de diferentes sismos com recurso ao MED, permitiu verificar que o colapso apresenta valores semelhantes da velocidade de pico da ação sísmica, apresentando-se como um parâmetro estável para a avaliação sísmica abóbadas. Na escala real, a abóbada reforçada apresentou uma redução do indicador de dano de 20% relativamente à abóbada não reforçada, para a mesma ação sísmica. Para a mesma amplitude, a abóbada reforçada apresentou apenas fissuras ligeiras, contrariamente ao dano severo da abóbada não reforçada. O reboco armado melhorou o desempenho da abóbada, aumentando a sua capacidade, e resultando eficaz para a redução da vulnerabilidade sísmica das abóbadas. Do ponto de vista numérico, avaliou-se a simulação do mecanismo de colapso e a evolução do dano, que apresentam uma boa correspondência em termos de extensões principais (MEF) e abertura e fecho das juntas (MED). Os deslocamento relativos obtidos através do MEF e do MED são conservadores em comparação com resultados dos ensaios em mesa sísmica. O MED com o critério de rotura clássico de Mohr-Coulomb apresentou maior dificuldade em replicar os deslocamentos últimos e o comportamento histerético do que o comportamento material combinado de Mohr-Coulomb com corte, esmagamento e fendilhação, o qual melhorou os resultados em termos de deslocamento e capacidade. Demonstrou-se que o MEF é preciso o suficiente para o estudo do comportamento dinâmico não linear de abóbadas não reforçadas e não reforçadas e reforçadas, no entanto exige um elevado esforço computacional.

Palavras-chave: abóbadas de aresta; análise não linear; ensaios em mesa sísmica; MED; MEF.

Evaluation of the seismic response of masonry cross vaults through shaking table tests and numerical analysis

Abstract: Masonry cross vaults are structural elements that still amaze observers, but the research on this topic is still narrow. Being vulnerable to seismic events, their safety is crucial because they may cause casualties and significant losses. This thesis provides insight into the seismic behaviour of cross vaults subjected to in-plane shear action and evaluates the efficiency of a strengthening technique using laboratory tests and numerical analysis. The experimental program involved a 3D printed reduced-scale vault with dry joints and a full-scale vault built with mortar joints and solid bricks. The latter was repaired with grout injections and strengthened with textile-reinforced mortar (TRM).

The experimental response of the reduced-scale vault was analysed in terms of collapse mechanism, seismic capacity, and drift values, and provided data to calibrate three-dimensional numerical models, namely a micro-modelling finite element model (FEM) and a discrete element model (DEM), and to perform non-linear time history analyses. The calibration of the stiffness of the joints, based on modal properties, resulted to be crucial for the performance of the models. It was also found that damping is not relevant while dealing with dry joint specimens. FEM model showed to be accurate. However, DEM model better reproduced the damage and time occurrence. Studying the influence of different ground motions on the DEM model of the reduced vault, similar peak ground velocities were found at the collapse, indicating a stable parameter for the seismic assessment of vaults.

Concerning the full-scale vault, the strengthened vault presented a reduction of damage indicator of about 20%, compared with the unstrengthened one, for the same seismic action. For the same amplitude, the strengthened vault presented only light cracks, compared to the severe damage of the unstrengthened. TRM enhanced the performance of the vault, providing further capacity and resulting to be an effective solution for reducing the seismic vulnerability of cross vaults. From the numerical point of view, the simulation of the collapse mechanism and damage evolution were assessed, matching in terms of principal strains (FEM), and opening and closing of the joints (DEM). The drifts obtained for both FEM and DEM numerical models are conservative in comparison with the shaking table tests. DEM model with classic Mohr-Coulomb criterion presented more difficulties in replicating the ultimate displacements and the hysteretic behaviour than the combined material behaviour of Mohr-Coulomb with shear, crushing and cracking, which enhanced the results in terms of displacement and capacity. It was demonstrated that FEM model is enough accurate for the study of the non-linear dynamic behaviour of unstrengthened and strengthened masonry vaults but requiring a high computational effort.

Keywords: cross vaults; DEM; FEM; non-linear dynamic analysis; shaking table tests.

Table of contents

Acknowledgements	iii
Resumo	v
Abstract	vi
Table of contents	vii
List of figures	xi
List of tables	xxi
List of symbols	xxvii
Abbreviations	xxvii
Latin symbols	xxix
Greek symbols	xxx
Subscripts	xxx
1. Introduction	1
1.1 Motivation	1
1.2 Masonry cross vaults along the times	3
1.2.1 Definitions	3
1.2.2 Historical development	4
1.2.3 Constructive techniques: materials and strategies	7
1.3 Static and seismic behaviour of masonry groin vaults	8
1.4 Strengthening techniques/anti-seismic devices	13
1.4.1 Traditional techniques	14
1.4.2 Modern techniques	17
1.5 Main and complementary objectives	19
1.6 Outline of the thesis	20
2. State of the art on masonry cross vaults	25
2.1 Introduction	25
2.2 Literature review: experimental investigations	25
2.2.1 Scale factor definitions	25
2.2.2 Reduced-scale groin vaults	27
2.2.3 Full-scale vaults campaigns	32
2.2.4 Final remarks on experimental investigations	33

2.3	Literature review: analytical and numerical investigations	33
2.3.1	Limit analysis	34
2.3.2	Membrane theory	38
2.3.3	Finite element method (FEM).....	38
2.3.4	Discrete element method (DEM)	42
2.3.5	Discrete macro element method (DMEM)	43
2.3.6	Final remarks on analytical and numerical investigations	44
3.	Reduced-scale vault: shaking table tests	47
3.1	Introduction	47
3.2	Description of the reduced-scale groin vault	47
3.2.1	Geometrical aspects and materials.....	47
3.2.2	Setup testing.....	51
3.3	Preliminary experimental campaigns.....	53
3.3.1	Monotonic quasi-static tests: in-plane shear tests	53
3.3.2	Monotonic quasi-static tests: tilting plane tests	54
3.4	Shaking table tests	55
3.4.1	Dynamic identification tests.....	55
3.4.2	Seismic tests: inputs and damage indicators	57
3.4.3	Seismic tests: crack patterns and quantitative results.....	61
3.5	Final remarks	70
4.	Reduced-scale vault: numerical modelling	71
4.1	Introduction	71
4.2	Preparation of the numerical models	71
4.2.1	Discrete element model	72
4.2.2	Finite element model.....	75
4.2.3	Material properties and calibration	76
4.2.4	Static non-linear analysis using the FEM model: in-plane shear tests	78
4.2.5	Static non-linear analysis using FEM model: tilting table.....	82
4.3	Dynamic non-linear analysis using FEM and DEM models	83
4.3.1	Analyses characteristics	83
4.3.2	Damping discussion	84
4.3.3	Results	87

4.4	Parametric analysis	90
4.4.1	Selection of ground motions	90
4.4.2	Results	94
4.5	Final remarks	96
5.	Full-scale vault: design, construction and test setup	99
5.1	Introduction	99
5.2	Full-scale vault: from the design to the construction of an ancient vault	99
5.2.1	Setup definition and boundary conditions.....	100
5.2.2	Construction of the specimen and application of the strengthening	104
5.3	Experimental characterization of materials	113
5.4	Testing setup	123
5.5	Final remarks.....	126
6.	Full-scale vault: shaking table tests.....	127
6.1	Introduction	127
6.2	Input signals and tests sequences	127
6.3	Modal properties of the unstrengthened specimen	132
6.4	Seismic results of the unstrengthened test specimen	134
6.4.1	Crack pattern	135
6.4.2	Deformation profiles and displacement field	139
6.4.3	Hysteretic response	142
6.5	Modal properties of the strengthened specimen	145
6.6	Seismic results of the strengthened test specimen	148
6.6.1	Crack pattern	148
6.6.2	Deformation profiles and displacement field	150
6.6.3	Hysteretic response	152
6.7	Comparisons of the results: unstrengthened vs strengthened specimen	153
6.8	Final remarks.....	159
7.	Full-scale vault: numerical modelling.....	163
7.1	Introduction	163
7.2	Preparation of the numerical models	164
7.2.1	Finite element models: FEM-UNS and FEM-SM.....	164
7.2.2	Discrete element model: DEM-UNS	169

- 7.3 Model updating 172
 - 7.3.1 Finite element model: FEM–UNS and FEM–SM 173
 - 7.3.2 Discrete element model: DEM–UNS 175
- 7.4 Non-linear dynamic analysis 177
 - 7.4.1 Analysis characteristics 178
 - 7.4.2 Non-linear dynamic analysis of the unstrengthened models: DEM–UNS and FEM–UNS..... 179
 - 7.4.3 Non-linear dynamic analysis for the strengthened model: FEM–SM 187
- 7.5 Final remarks 192
- 8. Conclusions 195**
 - 8.1 Research outline 195
 - 8.2 Conclusions from the study on the reduced-scale vault..... 196
 - 8.3 Conclusions from the study on the full-scale vault 197
 - 8.4 Future works 199
- 1. Annex – Works carried out on masonry cross vaults 203**
- 2. Annex – Reduced-scale vault: shaking table tests results 215**
- 3. Annex – Full-scale vault: technical drawings 255**
- 4. Annex – Literature review on historic mortars 261**
- 5. Annex – Full-scale vault: shaking table tests results 265**
- References 297**

List of figures

Figure 1-1. Documents published from 1960 to 2018 in Scopus considering: (a) 9 categories, (b) 5 categories (Bertolesi <i>et al.</i> , 2019).....	2
Figure 1-2. Cross vault architecture: (a) groin vault, (b) rib vault (Millais, 2005).	3
Figure 1-3. Geometry and glossary of a generic groin vault based on Musso (2002).	4
Figure 1-4. Remarkable examples of cross vaults throughout history.	6
Figure 1-5. Historical timeline of cross vaults' evolution.	7
Figure 1-6. Most common arrangements for masonry cross vaults: (a) parallel, (b) perpendicular, (c) mixed, (d) conical, (e) radial (Raimondi, 2013; Boni, Ferretti and Lenticchia, 2021).	8
Figure 1-7. Volumes of three vaults for an equal module of 5×5 m ² (Cangi, 2012).	9
Figure 1-8. In plane-shear mechanism: (a) plan view of single nave church, (b) plan view and transverse section of three-naves church, (c) plan view of a cloister in a palace (Rossi, 2015).	9
Figure 1-9. Typical crack failure in the masonry cross vaults in 3D axonometric view, elevation, and plan.....	10
Figure 1-10. Damage on cross vault after Umbria-Marche earthquake: (a) <i>in-situ</i> picture of the collapsed vault of the transept in the Basilica of St. Francis of Assisi (Galassi, 2008), (b) plan view of the collapsed parts.	11
Figure 1-11. Damage on cross vaults after L'Aquila earthquake associated with shear behaviour: (a) Palazzo Franco Fiore in 1993, (b) damaged cross vault at the last floor level of Palazzo Franco Fiore, (c) damaged cross vault in Palazzo Galeota (Poggio Picenze). In red, cracks associated with shear behaviour; in yellow, the Sabouret's crack and central hinge crack.	12
Figure 1-12. Damage on cross vaults after Emilia earthquake associated with shear behaviour: (a) undamaged view of the Town Hall in Novi di Modena, (b) shear failure of the masonry panels, (c) shear failure of the masonry cross vaults (Occhiuzzi <i>et al.</i> , 2012).	12
Figure 1-13. Damage on cross vaults after Central Italy earthquake associated with shear behaviour: (a) central cloister of <i>La Castellina</i> Museum (Norcia, Umbria), (b) details of the cracks in the cloister at the ground floor level, (c) cross vault at the first-floor level.	13
Figure 1-14. Ties applications: (a) steel ties in the cloister of Complesso dei Tolentini, Venice (Italy), (b) wooden ties / struts in Santa Maria dei Frari Church, Venice (Italy) (Bussi, 2011).	14

Figure 1-15. Traditional strengthening techniques: (a) ties, (b) diagonal extrados ties, (c) application of diagonal extrados ties in Uffizi’s Museum (Florence). Photo credits: <http://www.nuoviuffizi.it/> 15

Figure 1-16. Traditional strengthening techniques: (a) filling (in yellow) - spandrel walls (in red), (b) *scuci-cuci* (local rebuilding), (c) *sottarco* (vaulted shell or arch) from the intrados, (d) external buttress (in red), (e) reinforced concrete hoods. Pictures updated by Cangì (2009) 16

Figure 1-17. Different locations of application of FRP strips for vault strengthening. Updated from Foster *et al.* (2006) 17

Figure 1-18. FRP’s application on the Assisi Town Hall cross vaults: (a) scheme of the strengthening (Borri, Corradi and Vignoli, 2001), (b) and (c) *in-situ* picture taken in 2017 by the author... 18

Figure 1-19. Extrados and intrados disposition of TRM on masonry cross vault (Kerakoll guidelines)... 19

Figure 1-20. Flowchart of the thesis outline. 22

Figure 2-1. Reduced-scale experimental campaigns: (a) Mark *et al.* (1973), (b) Briccoli Bati *et al.* (2002), (c) Theodossopoulos *et al.* (2002). 28

Figure 2-2. Miltiadou-Fezan (2008)’s experimental campaign: (a) location of the selected area in the monastery of Dafni, (b) specimen on the shaking table. 28

Figure 2-3. Williams *et al.* (2012) experimental campaign: (a) cross vault dimensions, (b) specimen before testing, (c) groin vault cracked by lateral spreading. 29

Figure 2-4. De Matteis *et al.* (2010)’s experimental campaign: (a) illustration of the positioning on the shaking table, (b) photographs of the details of the main damage. 29

Figure 2-5. Rossi *et al.* (2015; 2016; 2017b)’s experimental campaign: (a) the 1:5 scale specimen, (b) in-plane shear test setup (c) tilting tests with the tilting plane (α is the angle of rotation and Φ is the angle between the axis of rotation of the tilting plane and the axes of symmetry of the vault) 30

Figure 2-6. Fagone *et al.* (2016)’s experimental campaign: (a) unstrengthened specimen, (b) strengthened specimen with CFRP continuous sheet at the extrados..... 30

Figure 2-7. Reduced-scale experimental campaigns: (a) Rossi *et al.* (2017a), (b) Carfagnini *et al.* (2018), (c) Foti *et al.* (2018). 31

Figure 2-8. Silvestri *et al.* (2021)’s experimental campaign: (a) typical blocks, (b) specimen on the shaking table. 32

Figure 2-9. Full-scale experimental campaigns: (a) Faccio *et al.* (1999), (b) Rossi *et al.* (2020) specimen. 32

Figure 2-10. Torres <i>et al.</i> (2019)'s specimen: (a) timber vault model, (b) detail of the thickness section.	33
Figure 2-11. Graphical representation of limit analysis theorems (Mendes, 2015).	35
Figure 2-12. A homogenization procedure for a curved masonry shell (Kurrer, 2008; Milani, Milani and Tralli, 2008).	36
Figure 2-13. Kinematic limit analysis applications on groin vaults: (a) Milani <i>et al.</i> 's (2008), (b) Chiozzi <i>et al.</i> (2017a), (c) Grillanda <i>et al.</i> (2020).	36
Figure 2-14. Static limit analysis applications on groin vaults: (a) Block and Ochsendorf (2002), (b) Marmo and Rosati (2017), (c) Milani (2022).	38
Figure 2-15. Membrane theory in the vault's web: (a) membrane stresses, (b) membrane forces (Como, 2017).	38
Figure 2-16. Modelling strategies for masonry structures. Adapted from Lourenço (2002).	39
Figure 2-17. FEM macro models of the groin vault tested by Faccio <i>et al.</i> (1999): (a) damage contours for the deformed configuration by Creazza <i>et al.</i> (2002), (b) deformed shapes at peak Milani and Tralli (2012), (c) Sabouret cracks (in red) on the vault studied by Holzer (2011, 2013).	41
Figure 2-18. FEM micro models of the groin vault tested by Rossi <i>et al.</i> (2016): (a) Milani <i>et al.</i> (2016), (b) Alforno <i>et al.</i> (2020, 2021), (c) Gaetani <i>et al.</i> (2021).	41
Figure 2-19. DEM models of the cross vault: (a) Van Mele <i>et al.</i> (2012), (b) Lengyel and Bagi (2015), (c) Fang <i>et al.</i> (2018), (d) Masi (2020).	43
Figure 2-20. Macro-element method and models: a) interface element, b) four-node element with diagonal spring and interfaces links, c) DMEM model of a cross vault (Caliò, Cannizzaro and Marletta, 2010).	44
Figure 3-1. Details of the blocks of the specimen: (a) the standard blocks with the steel core, (b) an example of a diagonal block without the steel core (Rossi, Calderini and Lagomarsino, 2016).	48
Figure 3-2. Geometry of the reduced-scale vault: (a) stereotomy, (b) details of the diagonal blocks (Rossi, Calderini and Lagomarsino, 2016).	48
Figure 3-3. Reduced-scale vault assembly: (a) details of the construction on the plywood scaffolding, (b) at the end of the construction with the thin steel plates.	49
Figure 3-4. Experimental setup designed by Rossi <i>et al.</i> (2016): (a) movable frame to apply displacements, (b) details of the bottom face of the steel plates.	52

Figure 3-5. Experimental setup of the reduced-scale vault: (a) adopted instrumentation in the shake table tests (top view), (b) shake table plan with the location of the specimen (highlighted in red). 53

Figure 3-6. In plane-shear quasi-static tests from Rossi *et al.* (2016): (a) tests setup, (b) force-displacement curve (four tests are shown with similar conditions). 54

Figure 3-7. Tilting table tests from Rossi *et al.* (2016): (a) tilting angle β , (b) rotation Φ around its orthogonal axis, (c) tilting plane tests results. 55

Figure 3-8. Input signals of the dynamic identification tests along X (transverse) direction, Y (longitudinal) direction and Z (vertical) direction 56

Figure 3-9. Frequencies decrease trend as a function of the increasing amplitude of the signal of the dynamic identification tests. 57

Figure 3-10. Elastic response spectrum of the selected input signals and comparison with the 475-year return period design spectrum for Emilia (Mirandola municipality) according to NTC2018. .. 58

Figure 3-11. Scaled time histories of ground motions (Emilia and artificial) at the amplitude equal to 100% for the reduced specimen: (a) accelerations, (b) velocities and (c) displacements. 59

Figure 3-12. Evolution of the damage indicator as a function of the amplitude of the seismic action expressed in terms of (a) PGA, (b) PGV, (c) PGD. 61

Figure 3-13. Damage progression during the intense phase of the Emilia seismic input 75% and of the artificial input (200%) (5 frames/s). (Left side: fixed supports p_1-p_2 ; right side: movable supports p_3-p_4). The main hinges are in red circles. 62

Figure 3-14. In-plane shear mechanism: pictures of the tests (white circles indicate the location of the hinges at the intrados, back circles at the extrados). 64

Figure 3-15. Displacement, acceleration and acceleration-displacement response spectra for the signals measured at the shaking table for the two inputs: Emilia (red) and artificial input (black). 65

Figure 3-16. Hysteretic behaviour of the top arch control point (OC_{2y}) for different stages of testing: (a) Emilia 35% vs artificial EQ 50% and (b) Emilia EQ 75% vs artificial EQ 200% (at the collapse). 67

Figure 3-17. Experimental capacity curve, in terms of horizontal inertial coefficient and displacement measured by OC_{2y} 68

Figure 3-18. Peak and RMS acceleration of the response for the reduced-scale vault in the longitudinal direction: (a) Emilia earthquake, (b) artificial input. 69

Figure 4-1. DEM model in Rhinoceros environment. 73

Figure 4-2. Blocks assumed in the DEM model: (a) rigid polyhedral block; (b) deformable block with tetrahedral element mesh (Lemos, 2021a).....	73
Figure 4-3. Contacts behaviour in DEM model: (a) normal direction, (b) tangential direction.	75
Figure 4-4. Elements adopted in the FEM model: (a) TE12L tetrahedral elements, (b) L6TRU enhanced truss element, (c) T18IF triangular interface element (topology and displacements) (DIANA 10.4, 2019b).....	75
Figure 4-5. Constitutive laws used in the FEM model: (a) linear elasticity for the blocks, (b) Mohr-Coulomb criterion for the interfaces.....	76
Figure 4-6. FEM model in the DIANA environment (finite element mesh not shown).	76
Figure 4-7. Details of the diagonals in the numerical models: (a) Milani <i>et al.</i> (2016), (b) Alforno <i>et al.</i> (2020), (c) Gaetani <i>et al.</i> (2021), (d) FEM model developed in this work.	79
Figure 4-8. Capacity curves for the quasi-static tests: numerical results in comparison with the experimental results obtained from Rossi <i>et al.</i> (2016).	80
Figure 4-9. Experimental and numerical deformed shapes of the in-plane shear mechanism: (a) Rossi <i>et al.</i> (2016), (b) Milani <i>et al.</i> (2016), (c) Alforno <i>et al.</i> (2020), (d) Gaetani <i>et al.</i> (2021), (e) FEM model.....	81
Figure 4-10. Horizontal load multiplier as a function of the direction of the seismic action.	82
Figure 4-11. Viscous damping graph of the numerical models.	85
Figure 4-12. Comparison of the time histories of displacements and accelerations between the shaking table tests and the FEM model results with (W/) and without (W/O) the contribution of the Rayleigh damping.	87
Figure 4-13. FEM and DEM deformed shapes, compared with the experimental results at the end of artificial earthquake for 125% and 150% amplitudes.	88
Figure 4-14. Damage propagation on the vault in comparison between shaking table tests and time history analysis for the DEM model.	89
Figure 4-15. Bell distribution example with the lower, medium, and upper range limits of input.	92
Figure 4-16. Time histories of accelerations, velocities and displacements of the impulsive earthquakes (range A): (a) Helena Montana – ID1, (b) Central Italy – ID 36.....	93
Figure 4-17. Time histories of accelerations, velocities and displacements of the regular earthquakes (range B): (a) Parkfield – ID 9, (b) Mexico Chiapas - ID 40.....	93
Figure 4-18. Time histories of accelerations, velocities, and displacements of the oscillatory earthquakes (range C): (a) San Fernando – ID 11, (b) Northridge – ID 27.	94

Figure 4-19. Deformed shapes of the DEM simulations before the collapse for the selected earthquakes. 96

Figure 5-1. Full-scale geometrical model defined for this work in AutoCAD 3D environment. Main dimensions in m. 100

Figure 5-2. Virtual location of the specimen in an ideal three-nave church. 101

Figure 5-3. Boundary conditions details: (a) steel connectors inside the fixed piers, (b) wheels above the steel surface and anchored to the ground before the tests, (c) steel cables with rod ends and load cells in place. 105

Figure 5-4. Centring of the full-scale vault: (a) *centinatura*, (b) slats system of the *manto*, (c) drum of the *manto*. 106

Figure 5-5. Boundary conditions of the model and its centring before the construction. 107

Figure 5-6. Design of the cuts of the diagonals: (a) scheme of the webs, (b) sequence of cuts (adapted from Cangì, 2016), (c) disposition along the diagonal from the intrados (adapted from Cangì, 2016), (d) explanatory timber and bricks samples. 108

Figure 5-7. Construction sequence of the unstrengthened specimen. 109

Figure 5-8. Closing the key of the vault: (a) disposition of the bricks with their misalignments, (b) filling the joints. 110

Figure 5-9. Transportation and dismantlement operations: (a) specimen before reaching the shaking table, (b) system of ropes for making the *manto* glide outside. 110

Figure 5-10. Cracks after transportation and dismantlement: (a) details of the cracks before the injection, (b) injected cracks. 111

Figure 5-11. 3D photogrammetric model of the unstrengthened specimen. 111

Figure 5-12. Application of the TRM strengthening system: (a) injecting fluid mortar *GeoCalce Antisismico FL* in the cracks, (b) detail of the *Geosteel grid 200* embedded in *GeoCalce Antisismico F* mortar, (c) application process, (d) detail of the corners close to the infill with *Geosteel grid 600*, (e) injecting the fluid mortar *GeoCalce Antisismico FL* mortar, (f) final appearance of the strengthened specimen (SM). 112

Figure 5-13. Compression tests on the bricks according to EN 772-1 (2011): (a) prism at the beginning of the test, (b) failure mode, (c) stress-strain curves. 114

Figure 5-14. Evolution of values of compressive strengths: (a) different blended mortars, (b) M_C and M_{C-lab} curves. 117

Figure 5-15. Evolution of values of flexural and compressive strength at 7 th , 14 th , 28 th day and 56 th , 190 th and 260 th days of age for the joints of the full-scale vault.	118
Figure 5-16. Axial compression tests: (a) setup of wallets (front and back face), (b) undamaged and damaged AC ₂	119
Figure 5-17. Axial compression tests: (a) Stress-strain curves of the masonry wallets (b) Stress-strain curves of the bricks, masonry wallets and mortar cubes.	120
Figure 5-18. Diagonal compression tests: (a) Dimensions of DC _i in mm; (b) setup of wallets: front face; (c) undamaged and damaged wallet before and after the tests; (d) stress-strain curves.	121
Figure 5-19. Triplet shear tests: (a) test scheme and setup of the triplets, (b) undamaged and damaged wallet before and after the tests.	122
Figure 5-20. Testing setup per elevation. Valid for the unstrengthened and strengthened specimen..	124
Figure 5-21. Setup of the unstrengthened model (UNS).	125
Figure 5-22. Setup of the strengthened model (SM).	125
Figure 6-1. Time histories of the target input signals of recorded AQA earthquake: accelerations, velocities and displacements.	129
Figure 6-2. Response spectra of recorded AQA earthquake: spectral acceleration, velocity, and displacement.	129
Figure 6-3. Filter effects and results: (a) gain of Butterworth low-pass filter with cut off $\omega_0 = 1$ vs Fourier filter (example for a high pass filter), (b) principal strains for the preliminary FEM model with AQA 100%.	130
Figure 6-4. Input signals of the dynamic identification tests: (a) North-South (longitudinal) direction, (b) East-West (transverse) direction.	130
Figure 6-5. Mode shapes of the unstrengthened specimen: (a) first global longitudinal mode obtained from the DIT-0-UNS-Y test, (b) second global transverse mode obtained from the DIT-0-UNS-X, (c) third global vertical mode obtained from the DIT-0-UNS-X.	133
Figure 6-6. Crack patterns of the extrados for the unstrengthened specimen at the end of ST-UNS-25%,50%,75%.	136
Figure 6-7. Details of the damage for the unstrengthened specimen after ST-UNS-75%, for (a) to (e) views.	137
Figure 6-8. Evolution of cracks at the extrados appreciated by VC ₅ during ST-UNS-75 with estimated time occurrence.	138

Figure 6-9. In-plane deformation profiles per each seismic test carried on the unstrengthened specimen when $OC_{2,4}$ measure their maximum displacements at $t \approx 4.31$ s. Deformation factor:10. 140

Figure 6-10. In-plane deformation profiles of the ST-UNS-75% for $OC_{1,2,3,4}$ at two instants. Deformation factor: 10..... 141

Figure 6-11. The visible hinge on the North arch during ST-UNS-75% at $t \approx 6.41$ s..... 142

Figure 6-12. Colourmap of accelerations of each measured point along North-South direction when Acc_2 reaches its peak for $t = 2.45$ s during ST-UNS-75%. 143

Figure 6-13. Influence area for each considered accelerometer. 144

Figure 6-14. Envelope response curves of the unstrengthened specimen considering four optical cameras for each seismic test in the North-South direction: (a) OC_1 , (b) OC_2 , (c) OC_3 , (d) OC_4 145

Figure 6-15. Natural vibration modes of the strengthened test specimen obtained from the DIT-0-SM-Y: (a) first global longitudinal mode, (b) second global transverse mode. 147

Figure 6-16. Crack patterns at the shell extrados at the end of each shaking table test for the strengthened specimen..... 149

Figure 6-17. Details of the damage for the strengthened specimen after ST-SM-150%, for (a) to (e) views. 150

Figure 6-18. In-plane deformation profiles of the strengthened configuration per each sequence when all the optical cameras measure the maximum displacements. Deformation factor:10..... 151

Figure 6-19. Detail of the opening of the joints at the South-West corner during ST-SM-150%. 152

Figure 6-20. Envelope response curves of the strengthened specimen considering four control points for each seismic test in the North-South direction: (a) OC_1 , (b) OC_2 , (c) OC_3 , (d) OC_4 153

Figure 6-21. Damage indicator using mode 1 versus: (a) peak ground accelerations, (b) peak ground velocity and (c) peak ground displacements for both UNS and SM configurations. 154

Figure 6-22. Comparison of crack pattern of extrados for UNS and SM configurations: (a) ST-50%, (b) ST-75%. 155

Figure 6-23. Comparison of crack patterns for the last seismic tests performed on the unstrengthened and strengthened configurations: UNS-75% vs SM-150%. 156

Figure 6-24. In-plane deformation profiles for the last seismic tests: (a) ST-UNS-75% vs ST-SM-150%, (b) ST-UNS-75% vs ST-SM-75%. Deformation factor: 10. 157

Figure 6-25. Envelope response curves in comparison of the UNS and SM considering four control points: (a) OC_1 , (b) OC_2 , (c) OC_3 , (d) OC_4	158
Figure 6-26. Experimental capacity curve, in terms of horizontal inertial coefficient and displacement at the key of the vault (OC_1).....	159
Figure 7-1. FEM–UNS macro-model of the full-scale vault in DIANA environment: (a) geometry, (b) mesh of the model.....	165
Figure 7-2. Constitutive laws used in the FEM–UNS and FEM–SM models: (a) non-linear hysteretic behaviour of masonry elements, (b) linear elasticity diagram for steel elements, (c) Mohr–Coulomb criterion for sliding interface.	167
Figure 7-3. Strengthened FEM–SM macro model of the full-scale vault in DIANA 10.5 (2022) environment: (a) shell element for the GEOCALCE F though CQ40S, (b) embedded grid to simulate Geosteel grid 200.	167
Figure 7-4. Grout injections modelled in the strengthened FEM–SM model in DIANA 10.5 (2022): (a) damaged intrados at the end of the ST–UNS–75%, (b) solid elements to simulate injections (intrados and North elevation).	168
Figure 7-5. Geometry of the DEM model in 3DEC 7.0 environment.....	170
Figure 7-6. List of joints contact of the DEM model in 3DEC 7.0 environment.....	170
Figure 7-7. Contacts behaviour in the DEM model: (a) elastic joint model between brick-steel, shaking table-brick, shaking table-steel and steel-steel, (b) Mohr–Coulomb criterion between brick-brick in the normal direction, (c) Mohr–Coulomb criterion between brick-brick in the tangential direction.....	171
Figure 7-8. Failure surface implemented for Mohr–Coulomb (MC) and combined material behaviour of Mohr–Coulomb (MC–CM). Adapted by Pulatsu (2023)..	172
Figure 7-9. Mode shapes of the first modes of the specimens (UNS and SM) and numerical models: (a) DIT–0–UNS–Y test, (b) first mode obtained from eigenvalue analysis for FEM–UNS model, (c) DIT–0–SM–Y test; (d) first mode obtained from eigenvalue analysis for FEM–SM model. ..	174
Figure 7-10. Velocity time history adopted in the dynamic identification for the calibration of DEM–UNS model.....	175
Figure 7-11. Comparison of Frequency Response Functions obtained from the numerical modelling and the dynamic identification tests. (DIT–0–UNS–Y, red dashed line) and the numerical model (DEM–UNS, black solid line).	175

Figure 7-12. DEM calibration: (a) MAC matrix, (b) first mode shape between DIT and DEM-UNS model performing vibration analysis..... 177

Figure 7-13. Viscous damping graph of the numerical models. 179

Figure 7-14. Evolution of cracks at the extrados: (a) ST-UNS-75, (b) deformed shapes of DEM-UNS model (deformation factor: 100), (c) strains distribution in FEM-UNS model..... 181

Figure 7-15. Comparison of the displacement profiles between experiments and numerical responses. 182

Figure 7-16. RMSDs in the longitudinal direction: (a) OC₁, OC₃, OC₄, (b) OC₂..... 184

Figure 7-17. Experimental and numerical envelope response curves (FEM, DEM with MC and DEM with MC-CM) of the unstrengthened specimen considering OC₁ for ST-UNS-75%. 185

Figure 7-18. Failure at the level of the collapse on groin vaults: (a) deformed shapes of DEM-UNS model for 100% of the input, (b) seismic damage at the intrados of the groin vault in Sant'Andrea church (Sigillo) after Central-Italy earthquake 2016, (c) seismic damage on the vault of Town Hall of Novi di Modena after Emilia earthquake 2012. 187

Figure 7-19. Damage map for: (a) ST-SM-150%, (b) principal strains distribution in FEM-SM model. 189

Figure 7-20. In-plane deformation profiles of the strengthened configuration for the ST-SM-150% when all the optical cameras measure the maximum displacements. Deformation factor: 10. 190

Figure 7-21. Experimental and numerical envelope response curves of the strengthened specimen for ST-SM-150% considering the optical camera OC₁. 191

List of tables

Table 2-1. Scale factors N according to Cauchy and Cauchy-Froude similitude laws (Carvalho, 1998; Mendes, 2012).....	26
Table 3-1. Sequence and description of the shaking table tests with the reduction of the frequencies for both types of inputs.	60
Table 3-2. Incremental dynamic testing sequence with the respective peak ground acceleration (PGA), peak ground velocity (PGV) and peak ground displacement (PGD).....	64
Table 3-3. Test results at the collapse for Emilia and artificial input in comparison with the quasi-static tests (Rossi, Calderini, and Lagomarsino 2016).....	66
Table 4-1. Differences and similarities related to the material properties of the numerical investigations.	78
Table 4-2. Linear elastic properties of the blocks and mechanical properties of the interface elements. *Estimated through eigenvalue analysis. **Estimated through quasi-static analysis.	83
Table 4-3. Quantitative comparison between experimental and numerical results for 125% and 150% seismic amplitudes. * Relative displacements determined using the LVDT ₁	90
Table 4-4. List of the considered natural recorded earthquakes.	91
Table 4-5. List of the recorded ground motions selected for the sensitivity study and their time histories.	92
Table 4-6. Selected ground motion parameters for the non-linear time history analyses with the main results at the collapse of the DEM model.....	94
Table 5-1. Nomenclature and location of the different components of the full-scale specimen. Masonry elements are highlighted in red and steel elements are highlighted in blue.	102
Table 5-2. Principal modes of vibration of the numerical model and their frequencies.	103
Table 5-3. Characteristics of the bricks: mean values based on six prismatic samples (σ : standard deviation; CoV: coefficient of variation).	115
Table 5-4. Characteristics of the mortar provided by Kerakoll and OMYA.....	116
Table 5-5. Mortars proportioning by volume and by weight, water ratio and flow measured according to EN 1015-3.	116
Table 5-6. Material properties of the <i>GeoCalce Antisismico F</i> and <i>GeoCalce Antisismico FL</i> mortars, collected during the application of the strengthening technique at different ages.	119
Table 5-7. Summary of the material characterisation tests on the masonry wallets.....	122

Table 6-1. List of tests carried out on the unstrengthened specimen: dynamic identification tests (DIT) and seismic tests (ST). *Performed with the instrumented hammer.....	131
Table 6-2. List of tests carried out on the strengthened specimen: dynamic identification tests (DIT) and seismic tests (ST).	132
Table 6-3. Natural vibration frequencies of the unstrengthened test specimen when excited along the longitudinal and transverse directions. *Performed with the instrumented hammer.	133
Table 6-4. Decrease of frequencies and modal assurance criterion (MAC) for the first three global modes obtained from the DIT_i -UNS-Y and DIT_i -UNS-X tests.	134
Table 6-5. Summary of the absolute maximum displacements measured by $OC_{1,2,3,4}$ for each test of the unstrengthened specimen.	141
Table 6-6. First two natural vibration frequencies and MAC values of the strengthened specimen when excited in the longitudinal and transverse directions.	147
Table 6-7. Summary of the absolute maximum displacements measured by $OC_{1,2,3,4}$ for each test and the strengthened specimen.	151
Table 7-1. Element types of the numerical FEM-UNS and FEM-SM models built in DIANA 10.5 (2022).	165
Table 7-2. Mechanical properties for the TRM system adopted in the numerical FEM-SM (DIANA 10.5, 2022).	168
Table 7-3. Final properties after the calibration for FEM-UNS and FEM-SM models. *Calibrated properties.	174
Table 7-4. Final properties of joints after the calibration for DEM-UNS model. *Calibrated properties.	176
Table 7-5. List of analyses carried out on the unstrengthened and strengthened numerical models. .	178
Table 7-6. Peak values and root mean square of displacements (RMSD) and average errors between the results measured by $OC_{1,2,3,4}$ for each seismic test of the unstrengthened specimen and obtained by DEM-UNS and FEM-UNS models.	183
Table 7-7. Peak values and root mean square (RMSD) of displacements and average errors obtained from $OC_{1,2,3,4}$ of the ST-SM-150% and the FEM-SM model.....	190
Table A1-1. Experimental works carried out in masonry vaults, from the 1970s until the most recent works	204
Table A1-2. Numerical works carried out in masonry vaults	207

Table A2-3. List of shaking table tests on the reduced-scale vault.....	216
Table A2-4. Emilia earthquake 10%: input data and time histories.....	217
Table A2-5. Emilia earthquake 10%: response time histories.....	218
Table A2-6. Emilia earthquake 25%: input data and time histories.....	219
Table A2-7. Emilia earthquake 25%: response time histories.....	220
Table A2-8. Emilia earthquake 50%: input data and time histories.....	221
Table A2-9. Emilia earthquake 50%: response time histories.....	222
Table A2-10. Emilia earthquake 50%: collapse mechanism.....	223
Table A2-11. Emilia earthquake 75%: input data and time histories	224
Table A2-12. Emilia earthquake 75%: response time histories.....	225
Table A2-13. Emilia earthquake 75%: collapse mechanism.....	226
Table A2-14. Emilia earthquake 55%: input data and time histories	227
Table A2-15. Emilia earthquake 55%: response time histories.....	228
Table A2-16. Emilia earthquake 55%: collapse mechanism.....	229
Table A2-17. Emilia earthquake after shock-25%: input data and time histories	230
Table A2-18. Emilia earthquake after shock-25%: response time histories	231
Table A2-19. Emilia earthquake after shock-25%: collapse mechanism	232
Table A2-20. Emilia earthquake after shock-35%: input data and time histories	233
Table A2-21. Emilia earthquake after shock-35%: response time histories	234
Table A2-22. Emilia earthquake after shock-35%: collapse mechanism	235
Table A2-23. Artificial earthquake 10%: input data and time histories.....	236
Table A2-24. Artificial earthquake 10%: response time histories	237
Table A2-25. Artificial earthquake 25%: input data and time histories.....	238
Table A2-26. Artificial earthquake 25%: response time histories	239
Table A2-27. Artificial earthquake 50%: input data and time histories.....	240
Table A2-28. Artificial earthquake 50%: response time histories	241
Table A2-29. Artificial earthquake 75%: input data and time histories.....	242
Table A2-30. Artificial earthquake 75%: response time histories	243
Table A2-31. Artificial earthquake 100%: input data and time histories.....	244
Table A2-32. Artificial earthquake 100%: response time histories	245
Table A2-33. Artificial earthquake 125%: input data and time histories.....	246
Table A2-34. Artificial earthquake 125%: response time histories	247

Table A2-35. Artificial earthquake 125%: collapse mechanism	248
Table A2-36. Artificial earthquake 150%: input data and time histories.....	249
Table A2-37. Artificial earthquake 150%: response time histories	250
Table A2-38. Artificial earthquake 150%: collapse mechanism	251
Table A2-39. Artificial earthquake 200%: input data and time histories.....	252
Table A2-40. Artificial earthquake 200%: response time histories	253
Table A2-41. Artificial earthquake 200%: collapse mechanism	254
Table A4-1. Historic mortars characteristics from the late XIX century until the most recent works, in situ and in laboratory tested.....	262
Table A5-1. List of shaking table tests on the full-scale vault.	266
Table A5-2. ST-UNS-10%: input data and time histories	267
Table A5-3. ST-UNS-10%: acceleration response	268
Table A5-4. ST-UNS-10%: displacements and force response	269
Table A5-5. ST-UNS-25%: input data and time histories	270
Table A5-6. ST-UNS-25%: acceleration response	271
Table A5-7. ST-UNS-25%: displacements and force response	272
Table A5-8. ST-UNS-50%: input data and time histories	273
Table A5-9. ST-UNS-50%: acceleration response	274
Table A5-10. ST-UNS-50%: displacements and force response	275
Table A5-11. ST-UNS-75%: input data and time histories	276
Table A5-12. ST-UNS-75%: acceleration response	277
Table A5-13. ST-UNS-75%: displacements and force response	278
Table A5-14. ST-SM-25%: input data and time histories.....	279
Table A5-15. ST-SM-25%: acceleration response	280
Table A5-16. ST-SM-25%: displacements and force response	281
Table A5-17. ST-SM-50%: input data and time histories.....	282
Table A5-18. ST-SM-50%: acceleration response	283
Table A5-19. ST-SM-50%: displacements and force response	284
Table A5-20. ST-SM-75%: input data and time histories.....	285
Table A5-21. ST-SM-75%: acceleration response	286
Table A5-22. ST-SM-75%: displacements and force response	287
Table A5-23. ST-SM-100%: input data and time histories.....	288

Table A5-24. ST-SM-100%: acceleration response	289
Table A5-25. ST-SM-100%: displacements and force response	290
Table A5-26. ST-SM-125%: input data and time histories	291
Table A5-27. ST-SM-125%: acceleration response	292
Table A5-28. ST-SM-125%: displacements and force response	293
Table A5-29. ST-SM-150%: input data and time histories	294
Table A5-30. ST-SM-150%: acceleration response	295
Table A5-31. ST-SM-150%: displacements and force response	296

This page has been intentionally left blank

List of symbols

Abbreviations

Acc.	Piezoelectric accelerometer
AQA	L'Aquila earthquake
BSF	Base shear forces
CLT	Central limit theorem
CoV	Coefficient of variation
cw	Crack width
DOF	Degrees of freedom
DEM	Discrete element model
DIT	Dynamic identification tests
DM	<i>Decreto ministeriale</i> (Ministerial Decree)
DMEM	Discrete macro element model
EN	European standard/norm
EQ	Earthquake
EW	East-West
FEM	Finite element model
FRP	Fibre-reinforced polymers
GU	<i>Gazzetta Ufficiale</i> (Official Gazette)
IDA	Incremental dynamic analysis
IE _s	Specific input energy
IP	Impulsivity index
LC	Load cells
LD _v	Development length of a velocity
LNEC	Laboratório Nacional de Engenharia Civil
LVDT	Linear variable differential transformer
MAC	Modal assurance criterion
MC	Mohr-Coulomb model (classic formulation)
MC–CM	Combined material behaviour Mohr-Coulomb with shear, crushing and cracking
NE	North-East
NHL	Natural hydraulic lime

NLDA	Non-linear dynamic analysis
NS	North-South
NURBS	Non-uniform rational B-spline
NW	North-West
OC	Optical camera
PGA	Peak ground acceleration
PGD	Peak ground displacement
PGV	Peak ground velocity
REV	Representative element of volume
RMS	Root mean square
SE	South-East
SERA	Seismology and Earthquake Engineering Research Infrastructure Alliance for Europe
SM	Strengthened test specimen (full-scale vault)
SW	South-West
ST	Seismic tests
t_d	Effective duration of the earthquake
t/R	Thickness-to-radius ratio
TNM	Thrust network method
TRM	Textile-reinforced mortar
UL	Updated Lagrange formulation
UNS	Unstrengthened test specimen (full-scale vault)
VC	Video camera
W/B	Water-binder ratio
WE	West–East
W/	With
W/O	Without

Latin symbols

Symbol	Units	Description
A	m ²	Area
<i>c</i>	MPa or KN/m ²	cohesion
<i>d_n</i>	-	Damage indicator
E	MPa or GPa	Young's modulus
<i>f</i> ₀	Hz	First natural frequency
<i>f</i> _{<i>b</i>}	MPa	Flexural strength
<i>f</i> _{<i>c</i>}	MPa	Compressive strength
<i>f</i> _{<i>i</i>}	Hz	Frequency <i>i</i> th
<i>f</i> _{<i>t</i>}	MPa	Tensile strength
<i>f</i> _{<i>y</i>}	MPa	Yield strength
g	m/s ²	Gravity acceleration
<i>G</i> _{<i>c</i>}	KN/m	Fracture energy in compression
<i>G</i> _{<i>f</i>} ^I	KN/m	Fracture energy in tension
<i>G</i> _{<i>f</i>} ^{II}	KN/m	Fracture energy in shear
h	m	Height
<i>K</i> _{bond}	MPa/mm	Bond stiffness of grout
<i>K</i> _{<i>n</i>}	MPa/mm	Normal stiffness
<i>K</i> _{<i>s</i>}	MPa/mm	Tangential stiffness
L, <i>l</i>	m	Length
<i>M</i> _{<i>w</i>}	Richter scale	Moment magnitude
<i>s</i> _{bond}	MPa/mm	Bond strength of grout
<i>t</i>	m	Thickness
<i>t</i>	s	Time
T	s	Period
<i>v</i>	m/s	Velocity
V	m ³	Volume
<i>w</i>	m	Width

Greek symbols

Symbol	Units	Description
α	Deg °	Angle of rotation
β	Deg °	Inclination angle
ε	-	Strain
$\bar{\varepsilon}$	[-]	Standard error
θ	Deg °	Friction angle
λ		Generic horizontal load multiplier
λ_U		Upper bound load multiplier
λ_L	[-]	Lower bound load multiplier
λ_F		Final load factor
μ	[-]	Friction coefficient
$\bar{\mu}$	[various]	Mean value of a parameter
ξ	[-]	Damping ratio
ρ	kg/m ³	Specific mass
σ	[various]	Standard deviation
φ_i	[-]	Mode shape i^{th}
Φ	Deg °	Rotation angle around the axes of symmetry of the vault
ψ	Deg °	Dilatancy angle

Subscripts

Symbol	Description
diag	Diagonals
EXP	Experimental
st.blocks	Standard blocks

This page has been intentionally left blank

This page has been intentionally left blank

1. Introduction

1.1 Motivation

Widely spread among monumental buildings, masonry cross vaults are some of the most vulnerable horizontal structural elements and their seismic assessment is an important topic that deserves attention and care by the research community. The observation of damage caused by past seismic events demonstrates the high vulnerability of historic masonry vaults, which suffer due to several types of mechanisms that are activated during the dynamic action. These mechanisms, which involve horizontal structural elements, like vaults, are dangerous, complex and play a central role to define the seismic performance of monumental buildings, like churches and palaces.

Researchers and professionals face several open issues when dealing with masonry cross vaults. Many authors highlight the difficulties of analysing existing vaults because they are very often damaged due to the interaction with adjacent structural elements or with the counteraction system (such as flying buttresses or foundations). Moreover, the geometric parameters of vaults (thickness, dimension of the units, pattern, etc.) are characterised by a high dispersion, which rarely leads to easy and fast structural comparisons between apparently similar vaults (Bertolesi *et al.*, 2019). In support of this context, also the Italian national code (Ministero delle Infrastrutture e Trasporti, 2018a) states that the masonry vaults are barely considered able to act as floor diaphragms, due to the high level of uncertainties about their capacity to transfer seismic actions to the lateral walls. This makes the topic interesting both for academic and professional purposes and widely necessary, since, to date, only few researchers have been investigating it (Bertolesi *et al.*, 2019). From Figure 1-1 it is possible to notice that less than 40 scientific papers deal with masonry cross vaults from 1960 to 2018 and, in the last four years (from 2019 to 2023), scientific papers on the topic only represent fewer than 1% of the publications on masonry structures.

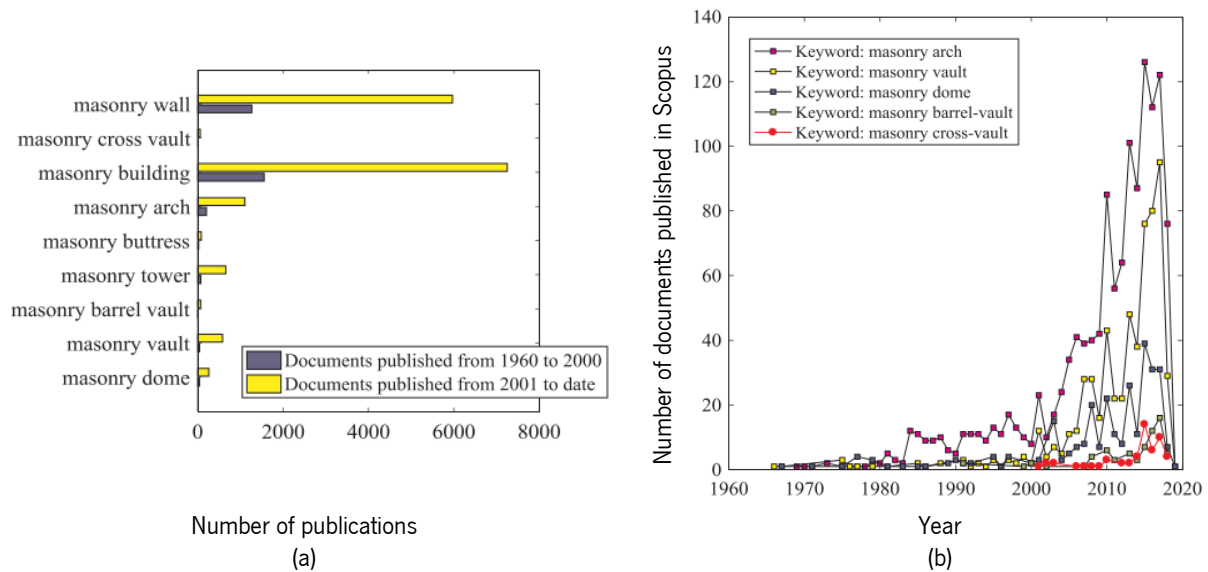


Figure 1-1. Documents published from 1960 to 2018 in Scopus considering: (a) 9 categories, (b) 5 categories (Bertolesi *et al.*, 2019).

This work wants to overcome this research gap by deepening the dynamic aspect of the response of cross vaults subjected to the in-plane shear mechanism, representing the natural evolution of two previous works, namely Rossi (2015) and Gaetani's (2016; 2017) works. Gaetani's work (2016; 2017), performed at the University of Rome and the University of Minho, includes a phased study based on a wide literature review about the historic approaches and construction techniques, and numerical parametric analyses and experimental activities on reduced test specimens. Rossi's research (2015), performed at the University of Genova, presents the experimental investigation of cross vaults, subject to static actions, using a reduced-scale test specimen (1:5) made of 3D printed units in a polymeric material. The same test specimen (Rossi, 2015) is the subject of the first part of this thesis. Later, the study of a full-scale cross vault test specimen with mortar joints is also performed, to overcome the limitation of the reduced-scale vault. These specimens replicate the geometry and boundary conditions of a three-naves church under seismic load.

The main goal of this research is to understand the response of the two specimens under in-plane shear distortion from the experimental and numerical point of view, also evaluating the efficiency of an innovative strengthening technique, namely TRM (textile-reinforced mortar). The in-plane shear mechanism is recurrent in masonry cross vaults of monumental buildings causing severe damage, which compromises the safety of people and the safeguarding of heritage structures.

This research was also part of the European project SERA "Seismology and Earthquake Engineering Research Infrastructure Alliance for Europe" (EUCENTRE, 2017; 2020), responding to the priorities

identified in the call INFRAIA-01-2016-2017 Research Infrastructure for Earthquake Hazard, funded by the European Commission within Horizon 2020 agreement.

1.2 Masonry cross vaults along the times

1.2.1 Definitions

Masonry cross vaults are composed of the intersection at right angles of two barrel vaults (simple or pointed) with the same rise (Gaetani *et al.*, 2016) and the solid material is the net junction of the barrel vaults, whereas their arches can be rounded or pointed. Within this definition, several configurations may be distinguished due to the large variety in terms of geometry, architectural aspects, and construction techniques, but the two main types are respectively groin vaults and rib vaults (Figure 1-2).

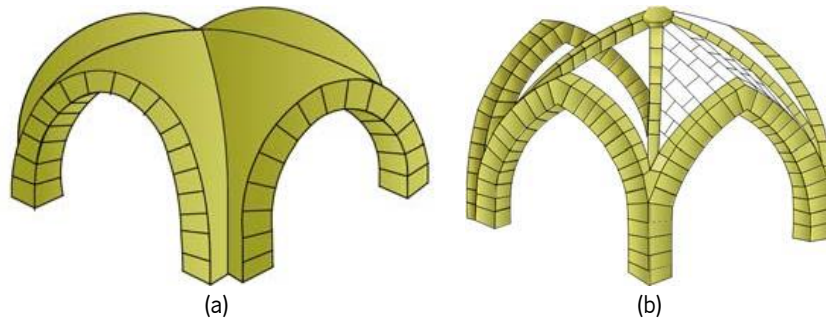


Figure 1-2. Cross vault architecture: (a) groin vault, (b) rib vault (Millais, 2005).

The groin vaults (Figure 1-2a) are the architectural evolution of the barrel vaults, widely spread during Ancient Roman times. The term groin indicates the solid parts between the intersection of the two barrel vaults, also generally known as diagonals. In the case of rib vaults, which are also commonly present in historical buildings, the intersection is composed of the ribs, which are usually an important structural part of the system (Figure 1-2b). Both cases allow to transfer the self-weight of the vault to the four corner pillars, removing the structural bearing behaviour from the lateral walls (Gaetani, 2016). Rib vaults are out of the scope of this research and only groin vaults will be investigated. For the sake of clarity, terminology and glossary related to groin vaults are provided in Figure 1-3 (Musso, 2002).

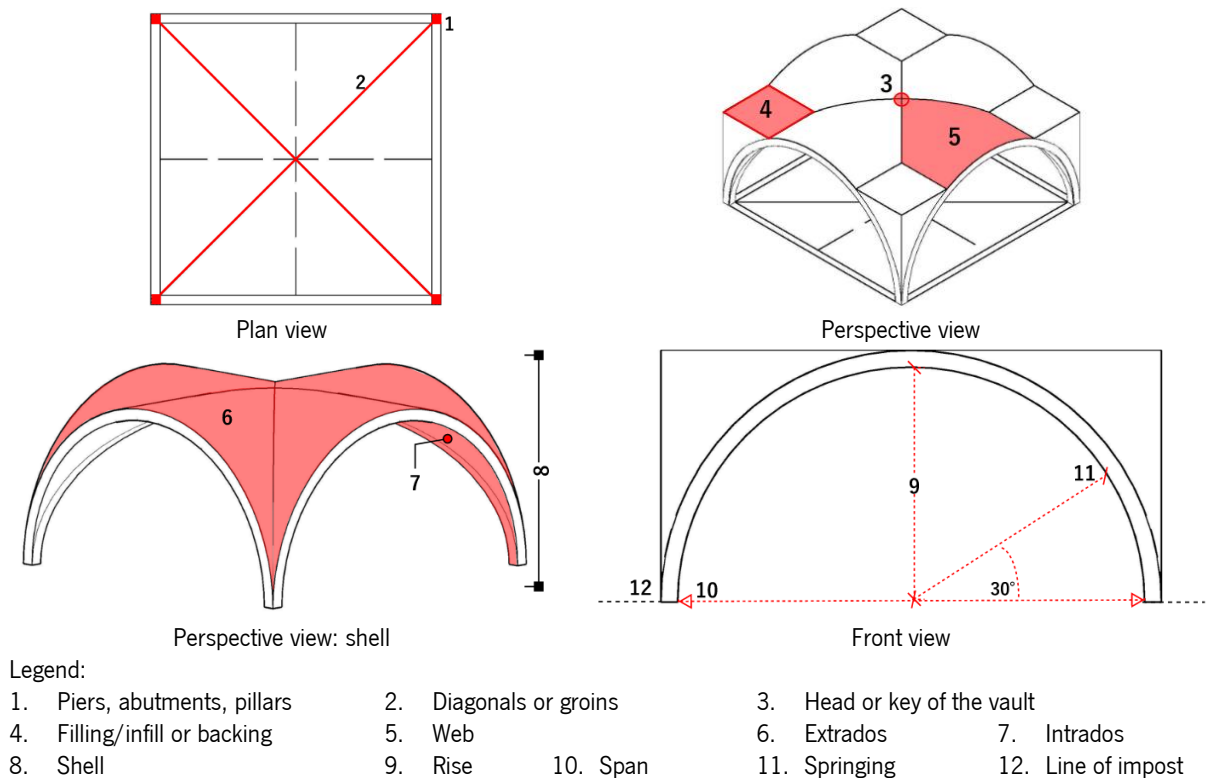


Figure 1-3. Geometry and glossary of a generic groin vault based on Musso (2002).

As it is possible to notice, the piers are the unique supports of the vault, the key identifies the voussoir at the maximum height or rise, the extrados is the exterior surface of the vault, very often not accessible or not visible, while the intrados is most of the times visible and often painted or decorated with frescoes. The volume defined between the extrados and intrados is called the shell of the vault and it is composed of four webs. The filling can be made of the same material as the shell or of core material and it is located along the directrix of each pier for directing the thrusts towards their base. The groin represents the plane of intersection between the two barrel vaults, whereas the impost represents the plane where the curvature of the vault begins. Having only four punctual supports means that the lateral walls are unloaded and they can host larger openings or open corridors that can be adopted to enlighten the interior space of the building or allow the passage, respectively (Borri and Bussi, 2011). The use of masonry cross vaults is typical of medieval churches, cloisters or porticos.

1.2.2 Historical development

The construction of the groin vaults has a long history whose beginning belongs to the development of Roman Architecture from Etruscan traditions (Lescher, 1911). Generally, Romans utilise cross vaults for covering square areas. When there is the need to cover rectangular spaces, those areas are first subdivided into squares and then, covered with smaller squared groin vaults. The Caracalla's Bath (212-217 A.D.) showed the presence of three enormous groin vaults ($\sim 7 \times 8$ m each in plan), made of

bricks and concrete, standing on eight piers. The vaults of the Thermae of Diocletian, in Rome, (A.D. 302) were standing from high columns and, centuries later, they have been converted by Michelangelo for covering the vestibule of the Church of St. Maria degli Angeli, (27.5 m high). Basilica of Maxentius, (A.D. 307) consisted of a Roman concrete structure with three large naves. The central one, the highest and widest of the three, was covered with three cross vaults spanning more than 20 m (Heyman, 1995a). These groin vaults collapsed during the Middle Ages, but they are known as the largest in the Roman Empire. Despite a lack of information regarding the exact configuration of those cross vaults, with the new developments of 3D digital photogrammetry, the thickness of the vault is estimated to be 1/15 of the largest vaulted span (Albuerne and Williams, 2017).

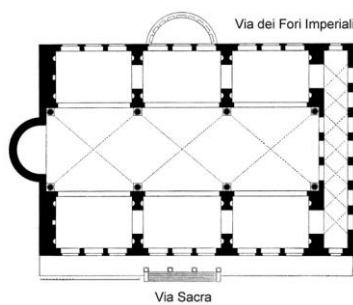
Cross vaults know their golden period during the Middle Ages, when they become a symbol of aesthetic quality (Como, 2017). The need of adopting masonry cross vaults, mainly in religious buildings, is due to the requisite of covering the larger width of the naves due to the increase of believers. Very often, cross vaults are covered with frescoes and paintings, representing scenes of the Bible (such as the vault painted by Giotto and Cimabue in Assisi). Since the groins are difficult to cut, the Romanesque builders decide to start the construction of the vaults from the ribs, erecting, therefore, self-bearing masonry diagonal arches at the first step and then the internal surfaces. In this way, groin vaults turn into rib vaults (Heyman, 1995a).

After the Middle Ages, the decline of groin and rib vaults starts, due to the change in aesthetics and construction needs, which begin with the Renaissance. Furthermore, the Lisbon earthquake and fire (1755) highlights a new problem related to all the structural elements of the monuments, also including the vaulted structures - they are identified as a vulnerable element that requires to be ruled by codes or guidelines. In fact, in the Portuguese system, for a long period, vaults could only be adopted at the ground level, while at the higher levels of the building, only timber floors are implemented. The main aim of this choice is the realisation of fire compartmentation of the building, a perimetral continuous masonry (Borri and Bussi, 2011), avoiding vaulted structures at the higher level of the buildings. In Europe, guidelines vary from one country to another. For example, the Instructions for Engineers, commissioned in the South Calabria region (Italy) after the 1783 earthquake, is considered the first European written code for regulating earthquake-resistant constructions (Ruggieri, 2016). The code states that the execution of vault structures could be possible only at the basement level, in line with the Portuguese system, while it has been completely forbidden for churches. After the Messina earthquake (1908), masonry vaults completely cease to be built, due to article 7 of GU n.225 del 27-9-1906 (*Ministero delle Infrastrutture e Trasporti*, 1906) and articles 10 and 16 GU n.95 del 22-4-1909

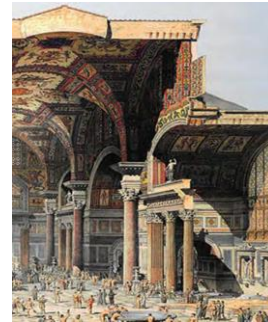
(*Ministero delle Infrastrutture e Trasporti*, 1909) that forbid their construction over the ground level of the buildings and in the staircases. In parallel, cracked or damaged existing vaults have to be demolished and substituted by flat diaphragm floors. Only with the Italian regulation DM 20/11/1987 (*Ministero delle Infrastrutture e Trasporti*, 1987), the construction of vaults is reintroduced, with specific precautions, namely assuring the confinement of the vault within the box masonry system of the walls and assuring the complete absorption of horizontal thrusts, properly distributed along the lateral walls. Regarding contemporary times, the introduction of reinforced concrete and polymeric materials concurs to spread again the use of groin vaults in architecture using the advantages of new technologies and materials. A remarkable example is represented by the reinforced concrete shells of the Air Terminal, St. Louis, by Architect Yamasaki (1954) (Melaragno, 1991). Figure 1-4 and Figure 1-5 show the examples cited in this Section and the historical timeline of the cross vaults from their birth to nowadays.



Terme Caracalla
(A.D. 212-217)



Basilica of Maxentius
(A.D. 307)



Diocletian's Baths
(Roman Age A.D. 302)



St. Maria degli Angeli
(Renaissance period)



Basilica inferiore di
San Francesco d'Assisi (1334)



Air Terminal,
St. Louis (1954)

Figure 1-4. Remarkable examples of cross vaults throughout history.

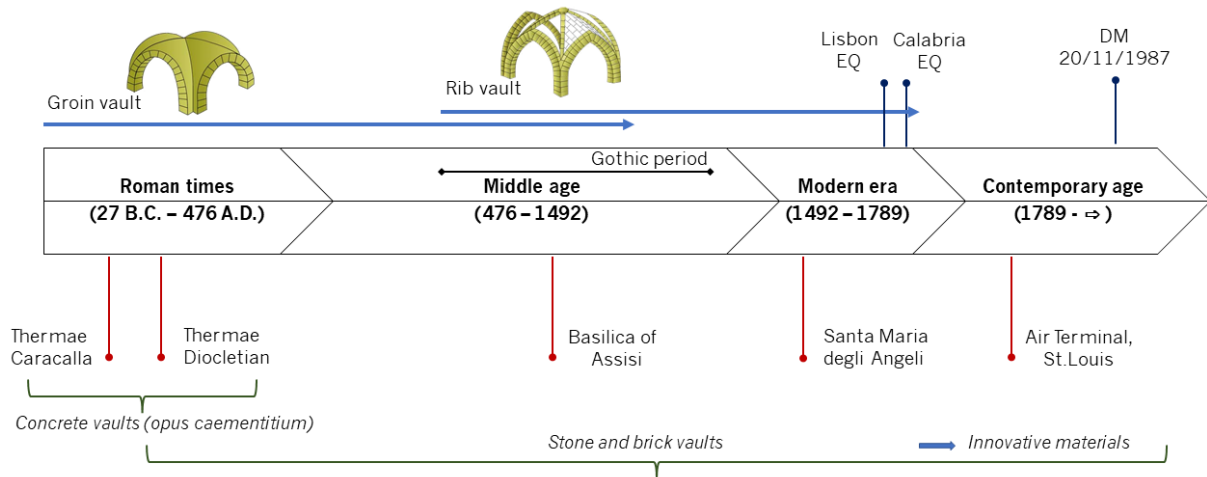


Figure 1-5. Historical timeline of cross vaults' evolution.

1.2.3 Constructive techniques: materials and strategies

Historical research allows gathering data and observing statistical recurrences, which let outline a description of the constructive techniques (Pittaluga, 2002; Foraboschi, 2016), despite the variety of the topic. Over the centuries, the constructive techniques of the groin vaults have been improved, namely their structure, geometry, shapes, dimensions and details until reaching a high level of mastery (Borri and Bussi, 2011). This thesis deepens the study of brick groin vaults (also called *medium vaults* by Rondelet), which are generally widespread among European medieval religious buildings (Borri and Bussi, 2011).

Rondelet's treatise "*Traité théorique et pratique de l'art de bâtir*" (1802), states that clay brick represents the most adaptable type of unit that can be utilised for every kind of vaulted structure, even if other solutions could be more suitable due to the abundance of natural stone in a specific location. Bricks are promoted by the easiness of placing them and their workability (Breyman, 1885). Another reason that encourages the promotion of bricks is the ease of creating connections with other parts of the structure, recreating horizontality and regularity along the height of the structure (Pittaluga, 2002). At the same time, along the diagonals, there is a need to carefully cut the units following stereometric rules, to ensure a high quality of interlocking between the adjacent webs (Cangi, 2011, 2012).

The thickness of the brick vaults at the key is assumed to be equal to $1/30$ of the span, as described by the Treatise of Leon Battista Alberti (1485). If a square cross vault has a span of 3.5 m, its thickness is estimated to be equal to 12 cm. However, various geometric surveys have found that the thickness of bricks exhibits significant variation depending on local construction techniques. The thickness of the mortar joints is characterised by a significant dispersion also. On average, depending on the type of

mortar selected, the joints may vary from 0.5 to 2 cm. Rondelet (1802) states that a well-executed and uniform mortar joint can significantly enhance the structural behaviour of any kind of vault.

The relevance of the filling as static stabilizer is undeniable. However, the correct amount of core material above the corners is more arguable. The treatise of Hernán Ruiz, the Young, (Navascués Palacio, 1974) states, in 1560, that the ideal height of this element is recommended to be until the half of the height of the rise of the vault (Gaetani, 2016). Another important aspect is the disposition of the units along the shell of the vault, also known as stereotomy, arrangement or bond. In the case of masonry brick vaults, stereotomy exhibits significant variability, as described in Figure 1-6 (Raimondi, 2013).

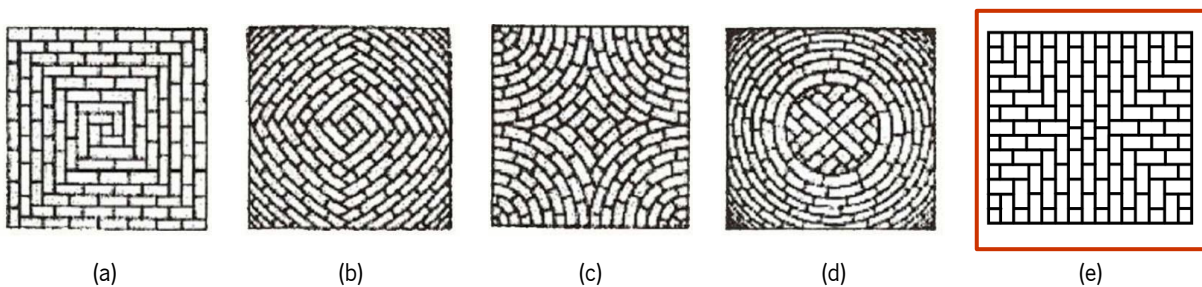


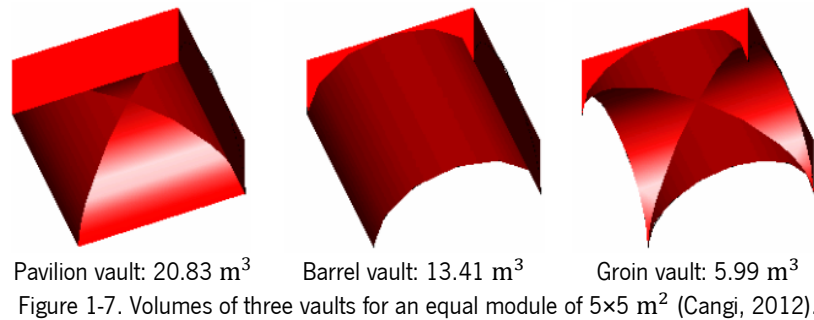
Figure 1-6. Most common arrangements for masonry cross vaults: (a) parallel, (b) perpendicular, (c) mixed, (d) conical, (e) radial (Raimondi, 2013; Boni, Ferretti and Lenticchia, 2021).

The selected arrangement for this research is the so-called “radial arrangement”. It directly transfers the thrusts to the supports, and it is characteristic of medium and large vaults (Figure 1-6e). This configuration requires a temporary timber structure, called *centina* to build the shell.

1.3 Static and seismic behaviour of masonry groin vaults

Groin vaults exhibit advantages that make them more desirable than other double curvature masonry elements. The structural stability is based on two conditions that ensure equilibrium: the internal stability of the vault and the global stability. The internal stability involves a generic thrust line that balances live and dead loads when it is contained within the profile of each section of the vault. The second condition relates to the capability of the bearing elements (the piers and counteracting buttresses) to accommodate the horizontal thrusts generated by the vault (De Matteis, Cacace and Rouhi, 2019). The groin vault distinguishes from other types of vaults because it simplifies the transmission of the lateral thrusts in punctual locations (Breymann, 1885). Another advantage is the reduced amount of material required for achieving the same plan dimensions. For example, when covering the same bay, pavilion vaults are the heaviest, followed by barrel vaults, while groin vaults are

the lightest (Cangi, 2012), weighing approximately three times less than pavilion vaults (Figure 1-7). Additional benefits include the ease and flexibility of illuminating the interior and the aesthetic aspects.



Besides the favourable behaviour under vertical static loads and the positive response in terms of stability, it was found that the in-plane horizontal shear behaviour causes a damage mechanism that is recurrently observed during post-earthquake surveys in churches and palaces. This type of mechanism is relatively unexplored, but it is particularly common in single-nave churches (Figure 1-8a) or three-nave churches (Figure 1-8b). The main reason for damage is the significant difference in stiffness between the nave and the façade and/or transept, which is also found in palaces (Figure 1-8c) featuring laterally constrained cloisters, porches, or loggias (Giovanetti, 2000; Rossi, 2015).

The recurrence of shear cracking is attributed to the lower stiffness of the central nave's colonnade compared to the external walls. This difference in stiffness can result in differential displacements along the longitudinal direction, leading to the development of a shear damage mechanism in the horizontal structural elements (Figure 1-8b) (Bianchini *et al.*, 2019). This failure is mainly identified by typical diagonal cracks that occur along the groins of the vault, both at the intrados and extrados. Figure 1-8b anticipates and introduces the configuration studied in this work - a central bay located in the lateral nave of a three-nave church under simple shear.

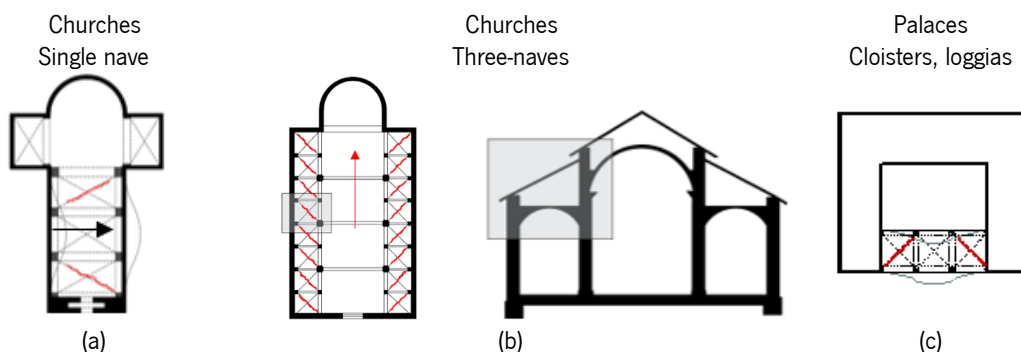


Figure 1-8. In plane-shear mechanism: (a) plan view of single nave church, (b) plan view and transverse section of three-naves church, (c) plan view of a cloister in a palace (Rossi, 2015).

This type of mechanism has been recognised during post-earthquakes surveys, primarily in the Italian territory. In fact, the Italian peninsula is prone to moderate and strong earthquakes, and since the

Umbria-Marche 1997 earthquake, numerous researchers and engineers have been assessing the bearing capacity of residential and monumental buildings following each major shock, starting from the villages closest to the epicentre. These professionals adhere to a precise format for collecting damage information. In particular, churches, palaces, and all monumental buildings follow a damage evaluation format, which is ruled by the Guidelines Modello A-DC PCM-DPC MiBAC (2006) (Civerra, Lemme and Cifani, 2007). This procedure is based on many *in-situ* observations of damage caused by earthquakes experienced by these types of buildings, identifying recurrent failure mechanisms. The form for churches presents twenty-eight failure mechanisms, while the form for palaces includes twenty-two mechanisms. Among them, ten are specifically related to vault failures in different areas of the monuments. These failure mechanisms are triggered by various causes, which can act individually or in combination on the vaults, leading to different crack patterns. Since compound mechanisms may occur during experimental campaigns or numerical simulations, for the sake of completeness a brief description of the more frequent causes and expected crack patterns on groin vaults is presented in Figure 1-9.

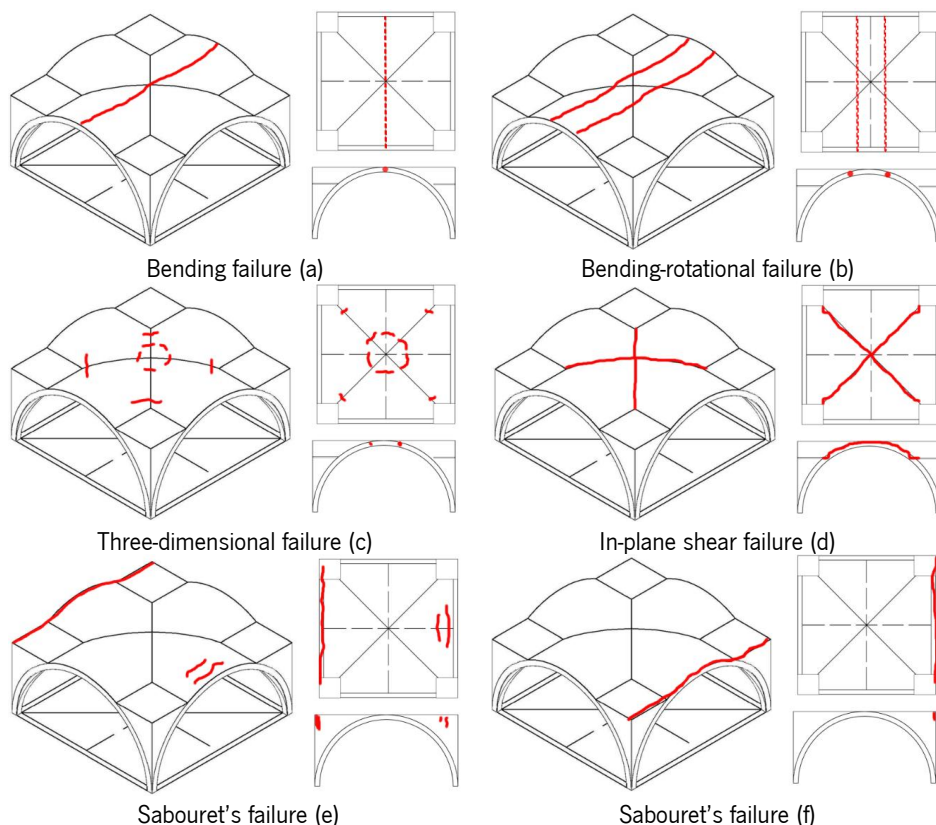


Figure 1-9. Typical crack failure in the masonry cross vaults in 3D axonometric view, elevation, and plan.

Figure 1-9a illustrates the typical bending failure, characterised by a longitudinal crack along the key of the vault, which can also affect a sequence of vaults through the different bays. In general, this type of failure is caused by an increase in vertical loads and simultaneous movement of the vaults' supports.

Similar to the first case, Figure 1-9b outlines a roto-bending failure where, at the key of the vault, a voussoir is cracked and simultaneously the rotation of the supports occurs, causing the creation of four hinges and an increase of the horizontal lateral thrust. Figure 1-9c presents the creation of four hinges, as per the roto-bending failure, but in this type of failure two of the hinges appear at the level of the springings, resulting in a three-dimensional failure due to high punctual loads.

Figure 1-9d depicts in-plane shear failure, characterised by diagonal cracks along the groins. Shear cracks may occur in all the development of the vault, with the severity of the damage typically being more pronounced at the key level and diminishing close to the corners. In some cases, foundation settlements can lead to a similar shear failure mechanism, mainly if the support presents a roto-translational motion along the vertical axis of the piers. Figure 1-9e and f show parallel cracks, mainly external, which are also called *Sabouret's cracks*. They clearly identify the portion of the vault that independently acts as an arch. The cracks are caused by eccentric loads applied to the shell of the vault and are also associated with the separation between the shell and the lateral walls.

To support the need of the research and the features of the in-plane shear collapse mechanism registered during seismic shocks, some *in-situ* pictures are provided. These images have been taken following some of the strongest earthquakes recorded on the Italian territory in the past 25 years. During the Umbria-Marche 1997 earthquake, the two-brick masonry cross vaults of the Basilica of St. Francis of Assisi (1253), frescoed by Giotto and Cimabue, collapsed (Figure 1-10), resulting in casualties. Their failure was linked to shear mechanism and to the excessive volume of non-cohesive infill, which exerted excessive pressures on the shells, causing a reduction in their curvatures (Croci, 1997).

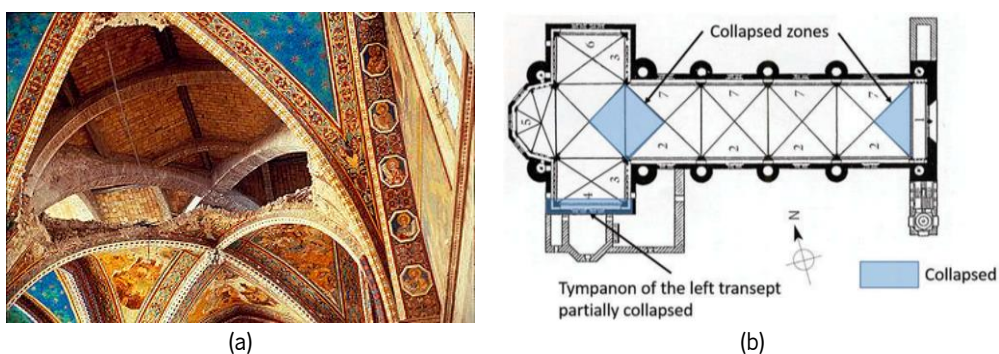


Figure 1-10. Damage on cross vault after Umbria-Marche earthquake: (a) *in-situ* picture of the collapsed vault of the transept in the Basilica of St. Francis of Assisi (Galassi, 2008), (b) plan view of the collapsed parts.

The level of damage registered during the L'Aquila earthquake, on 6th April 2009, confirmed the high seismic vulnerability of historical buildings. About 80% of the monumental built heritage was destroyed or severely damaged, about 240 historical buildings are struck by the sequence of shocks, and among

those buildings, 170 churches partially collapsed (Brandonisio *et al.*, 2013). Figure 1-11 shows two damaged vaults, namely one located in the historical centre of L'Aquila (Figure 1-11a,b), and the other (Figure 1-11c) in the small village of Poggio Picenze, approximately 12 km away from the epicentre. In both cases, shear damage is evident along the vaults of a cloister located at an elevated level of the building. As expected, the evidence demonstrated that higher-positioned vaults experience more severe damage.

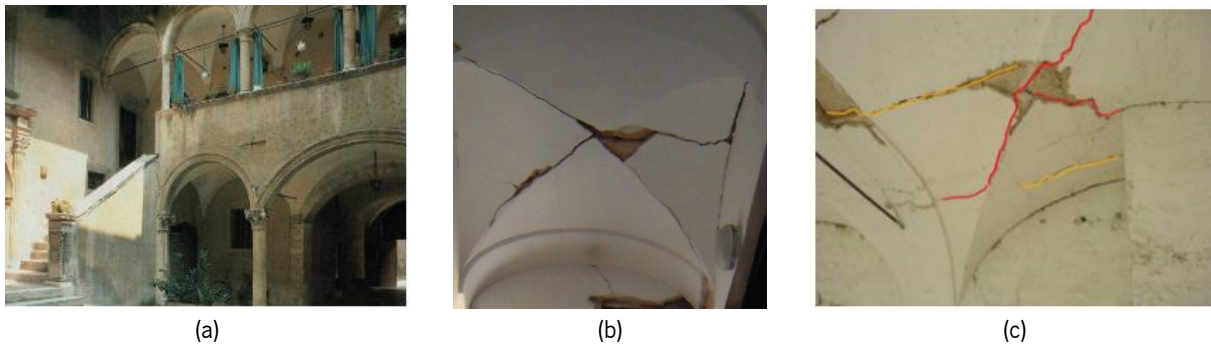


Figure 1-11. Damage on cross vaults after L'Aquila earthquake associated with shear behaviour: (a) Palazzo Franco Fiore in 1993, (b) damaged cross vault at the last floor level of Palazzo Franco Fiore, (c) damaged cross vault in Palazzo Galeota (Poggio Picenze). In red, cracks associated with shear behaviour; in yellow, the Sabouret's crack and central hinge crack.

During Emilia's earthquake (2012), the Town Hall in Novi di Modena (Italy), which is composed of a portico with five bays covered by cross vaults with a rectangular plan, showed the typical shear failure of the masonry panels and vaults (Figure 1-12). The in-plane shear failure observed is most likely due to the high stiffness of the back part of the structure, while the portico is constrained only from the side, opposite to the columns.



Figure 1-12. Damage on cross vaults after Emilia earthquake associated with shear behaviour: (a) undamaged view of the Town Hall in Novi di Modena, (b) shear failure of the masonry panels, (c) shear failure of the masonry cross vaults (Occhiuzzi *et al.*, 2012).

Central Italy earthquake series 2016-2017 is extremely important from a research point of view, because it is one of the first seismic events that occurred in the same area that was affected by a previous earthquake, namely Umbria-Marche 1997. This provides an opportunity to study several cases of retrofitting after 20 years of service. For example, Figure 1-13 shows the case of Museum La

Castellina in Norcia, located near the epicentre. In-plane shear behaviour characterised by diagonal cracks is recognisable either at the ground floor (Figure 1-13b) and in the vault located at the upper floor (Figure 1-13c). Another aspect to notice is that the two ties, located at the ground floor, help the complex of the museum to behave according to a box behaviour, while at the higher levels, the ties are lacking, and differential movements are likely to occur.

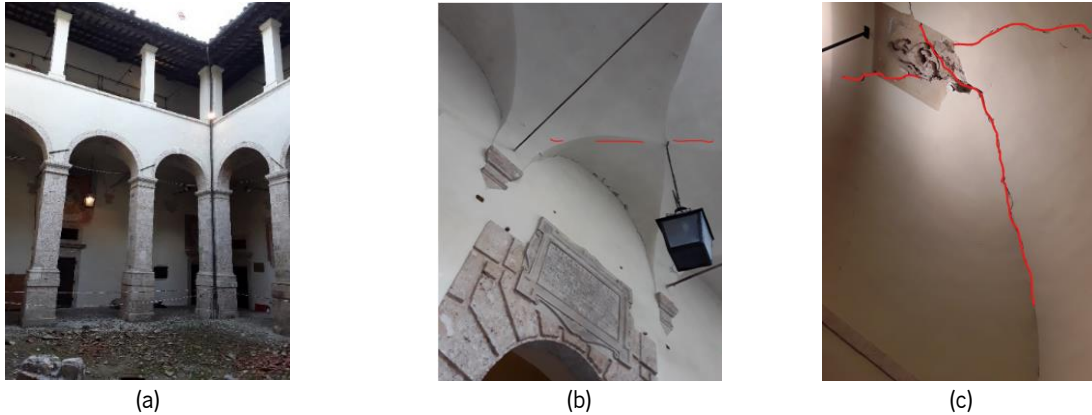


Figure 1-13. Damage on cross vaults after Central Italy earthquake associated with shear behaviour: (a) central cloister of *La Castellina* Museum (Norcia, Umbria), (b) details of the cracks in the cloister at the ground floor level, (c) cross vault at the first-floor level.

Summarising the evidence of the seismic events, it is possible to point out some remarkable aspects, which are at the base of this thesis and reported by Michiels (2018):

- groin vaults are highly exposed to the seismicity of the Italian territory.
- in-plane shear failure is commonly observed in vaults and is caused by the relatively thin thickness of the element and their weaknesses caused by imperfect connections between diagonals and webs.
- vaults are often supported by slender and deformable columns, making them highly vulnerable to large movements. The presence of infill only partially mitigates this vulnerability. Therefore, if the supports of vaults move or fail altogether, the vaults are prone to cracking or collapse.
- understanding the ultimate seismic capacity of vaults and their collapse mechanisms is crucial for the structural analysis and for the design of the strengthening interventions.

1.4 Strengthening techniques/anti-seismic devices

Strengthening means upgrading the structure performance of the vault that decreased due to an external cause (*e.g.* seismic action) (ISO 13822, 2009). Strengthening methods of vaults operate for different purposes: (a) reducing the thrust on abutments, intervening on the seismic demand, (b) intervening when the failure mode of the vault is under modification. According to Cescatti *et al.* (2018),

those purposes aim at reducing the loads and increasing the vault capacity or changing the failure mode.

Despite the large distribution of vaults, there are only a few standards and guidelines that address strengthening measures. For example, ISCARSAH guidelines (2003) for masonry arches and vaults recommend various repair measures, including the installation of tie-rods, the construction of buttresses, and other measures aimed at correcting load distribution. The Italian *Circolare Esplicativa Norme tecniche per le costruzioni* (2018a) suggests several strengthening techniques, ranging from the commonly used and well-studied methods to the least common and investigated ones. A brief description of the main historical techniques used to counteract the seismic actions is reported here.

1.4.1 Traditional techniques

The use of ties, or in general horizontal connecting elements, is one of the first strengthening techniques ever implemented. Horizontal connecting elements, like ties are provided to connect wall-to-wall, wall-to-column or column-to-column systems, on those vaults that may stand above. Typically, ties are inserted below the springing height, usually at the level of the impost, where the thrusts are usually higher. By doing so, during earthquakes, vaults act more as a horizontal diaphragm, which distributes the seismic inertia forces among structural bearing elements (piers or walls) in proportion to their stiffness. Because of this, ties have been used for both ordinary and monumental buildings, as a tool to enhance stability and withstand seismic events. Ties improve the stability of the vault under dead loads, avoiding bending cracks due to movements of the supports, and they enhance the structure to behave as a box. Nevertheless, ties' application influences aesthetics, which can lead to the abandonment of their adoption or to their installation at the level of the extrados, whose utility may be less efficient. Nowadays, ties are primarily made of steel (Figure 1-14a), but in the past, timber ties were also used (sometimes also as struts) (Figure 1-14b).



Figure 1-14. Ties applications: (a) steel ties in the cloister of Complesso dei Tolentini, Venice (Italy), (b) wooden ties / struts in Santa Maria dei Frari Church, Venice (Italy) (Bussi, 2011).

More recently, to overcome the aesthetical impact of ties located at the intrados, a more complex system has been implemented. Diagonal bars are placed at the extrados, acting as a bracing floor system that helps distribute loads and reduce concentrated stresses on the vault. This technique is extensively used to strengthen the cross vaults of the Uffizi Gallery, to accommodate an increase of loads associated with the expansion of the museum, as shown in Figure 1-15.

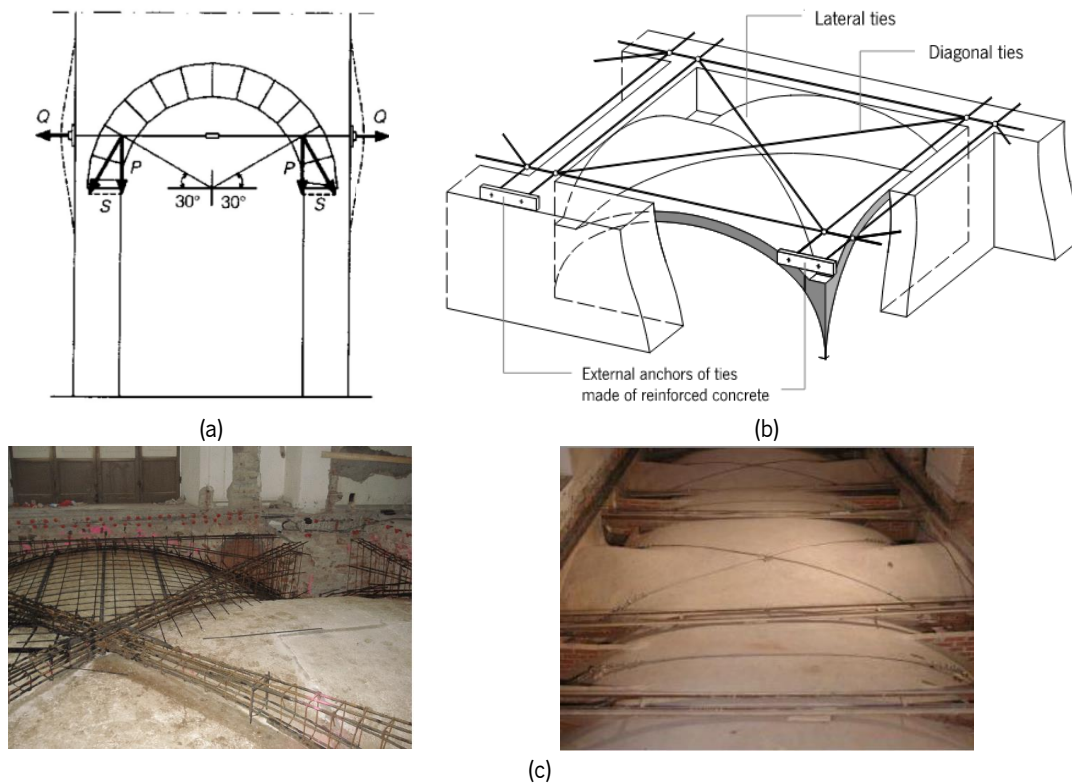


Figure 1-15. Traditional strengthening techniques: (a) ties, (b) diagonal extrados ties, (c) application of diagonal extrados ties in Uffizi's Museum (Florence). Photo credits: <http://www.nuoviuffizi.it/>

The insertion of filling and spandrel walls along the external surface of the vault can also be considered a common strengthening technique (Figure 1-16a). These two ways work mainly to counteract static loads, increasing the effective thickness of the vault close to the corners. However, while spandrel walls contribute to enhancing the transverse stiffness of the vault, acting as an anti-seismic device, the filling is a weight which transfers the thrusts of the vaults to the abutments and reduces the vault span. If a vault is already severely cracked, there are two main ways of repair and strengthening. The first is the use of local rebuilding technique commonly known as *scuci-cuci* (local rebuilding), which consists in removing damaged/detached material and closing the crack with the addition of compatible material (Figure 1-16b). Alternatively, it is possible to increase the thickness of the vault by adding extra solid bricks from the intrados. This method is known as *sottarco* – a vaulted shell or arch underneath the intrados of the existing vault (Figure 1-16c). This latter strategy was widely encouraged after the Irpinia

earthquake (1980), since this technique is introduced by the Italian Code “*Normativa per le riparazioni ed il rafforzamento degli edifici danneggiati dal sisma nelle regioni Basilicata, Campania e Puglia*” (Ministero delle Infrastrutture e Trasporti, 1981), which specified the adoption of an additional concrete shell layer.

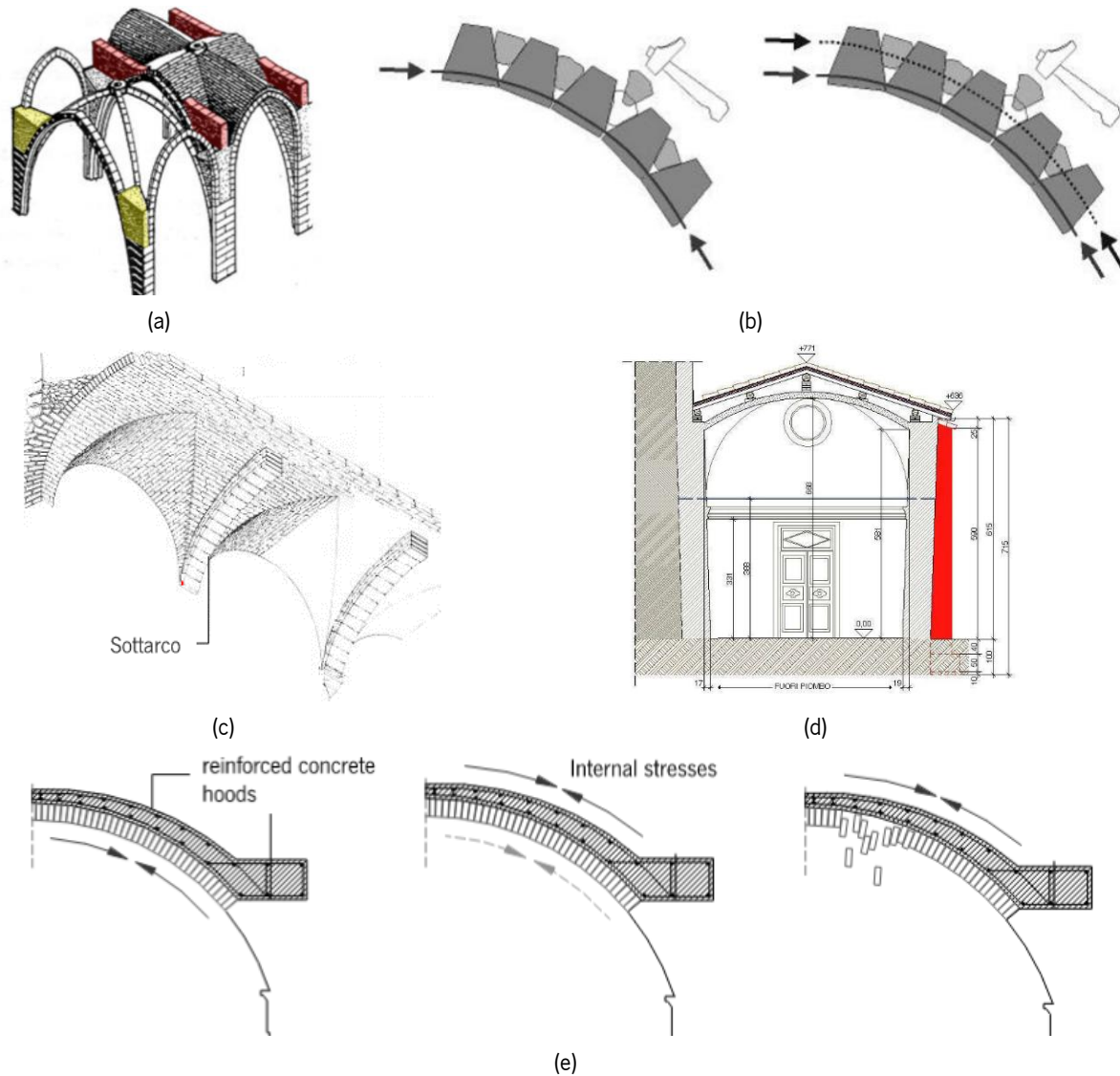


Figure 1-16. Traditional strengthening techniques: (a) filling (in yellow) - spandrel walls (in red), (b) *scuci-cuci* (local rebuilding), (c) *sottarco* (vaulted shell or arch) from the intrados, (d) external buttress (in red), (e) reinforced concrete hoods.

Pictures updated by Cangi (2009)

External buttresses enhance the static capacity of the vaults (Figure 1-16d). Buttresses improve also the dynamic capacity to counteract horizontal forces and deformations, mainly because of their geometry and weight. In the recent past, it was possible to find the use of reinforced concrete hoods (Figure 1-16e) above the extrados of existing vaults in the Italian territory. However, they are an invasive strengthening technique because of the relevant increase of compression due to the rise of mass on the

vault. Their adoption has been firstly discouraged and then, more recently, forbidden for monumental buildings (Ministero delle Infrastrutture e Trasporti, 2018a).

1.4.2 Modern techniques

Modern strengthening techniques utilising composite materials, more compatible with the aesthetics and structural needs, are now available (Zampieri *et al.*, 2018). Composite materials may be preferable because of their limited invasiveness, especially if applied at the extrados. They do not significantly increase the mass of the structure or the stiffness of the vault. Composite materials effectively improve the seismic performance, to the extent that their applications are encouraged by several guidelines, such as the Italian “Guide for the design and construction of externally bonded fibre-reinforced polymers (FRP) systems for strengthening existing structures” (CNR-DT 200 R1, 2013). This guide supports the design and construction of external bonded FRP systems, within the framework of the Italian regulations (2018a), giving preliminary guidance for the strengthening of vaults and domes. Nevertheless, there are important concerns about the reversibility, durability, fire protection and efficiency of these systems when applied in weak historic substrates, that limits the use of externally bonded FRP systems in monumental buildings in Europe.

Strengthening through composite materials involves the application of FRP composites in the form of strips or sheets. In the first case, the strips are usually located at the extrados along the diagonals or the key of the vault (Figure 1-17), while the sheets are generally spread along the entire external surface of the vault (Foster *et al.*, 2006). In the field, the implementation of composite materials on arches is widely investigated and, over time, it has been gradually extended to vaulted systems, starting with barrel vaults. One exception, which deals with groin vaults, is represented by Szolomicki *et al.* (2014), who introduced the basis of analytical and numerical models of FRP on double-curved vaults. Later, Briccoli Bati *et al.* (2002) carried out an intensive experimental investigation about the use of glass fibres strips on a groin vault model (scale 1:3), with lower rise and straight arrangement of the bricks assembled with 5 mm thickness of mortar (Briccoli Bati *et al.*, 2002).

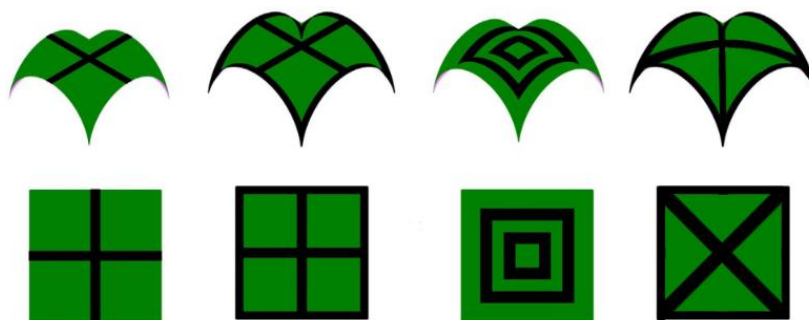


Figure 1-17. Different locations of application of FRP strips for vault strengthening. Updated from Foster *et al.* (2006)

From a practical point of view, the seismic strengthening of the vault of the Town Hall of Assisi is one of the most renowned interventions (Figure 1-18), dated from 2001, after being damaged by Umbria-Marche earthquake in 1997 and resisting to the last seismic event (Central Italy earthquake 2016-2017).

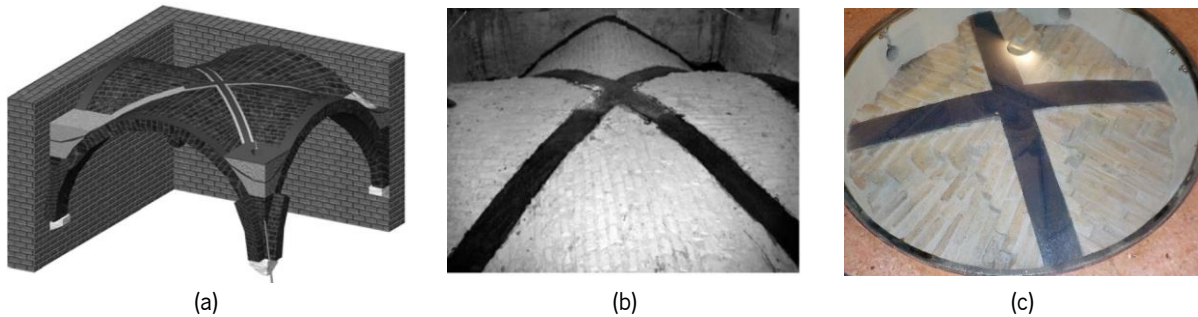


Figure 1-18. FRP's application on the Assisi Town Hall cross vaults: (a) scheme of the strengthening (Borri, Corradi and Vignoli, 2001), (b) and (c) *in-situ* picture taken in 2017 by the author.

An evolution of the fibre-reinforced polymers for masonry structures is represented by the textile-reinforced mortar (TRM), which may be placed at the extrados or intrados of the shell of the vaults. In this strengthening technique, the high-strength fibres (made of steel, basalt, etc) are embedded into an inorganic matrix, and assembled with an appropriate mortar, offering compatibility with substrates. This system presents advantages compared to FRP, namely moisture permeability, durability, compatibility with the masonry surfaces and fire protection (Carozzi *et al.*, 2018).

Several applications of TRM in masonry structures are present in literature (Garmendia *et al.*, 2011; Ramaglia *et al.*, 2017; De Santis, De Felice and Roscini, 2019). These applications serve different purposes, namely the strengthening of in-plane bending and shear capacity of masonry piers and spandrels, enhancement of out-of-plane bending capacity of masonry piers and spandrels, enhancing the axial capacity of masonry columns, and retrofitting interventions to increase the load carrying capacity of masonry arches. However, despite being included in the catalogues of manufacturers of materials for building applications (Figure 1-19), TRM applications on masonry cross vaults have been rarely studied to date.



Figure 1-19. Extrados and intrados disposition of TRM on masonry cross vault (Kerakoll guidelines).

1.5 Main and complementary objectives

The two ultimate goals of this doctoral research are the following:

- to better understand and characterise the in-plane shear behaviour of masonry cross vaults, without and with strengthening, by means of shake table tests on both full-scale and reduced-scale models.
- to assess the capability of different modelling approaches to simulate the seismic response of masonry cross vaults, based on the experimental campaigns.

Beyond these two main goals, this research work involves complementary objectives, and for each of them, the respective motivation is also presented next:

- A. Improving the knowledge on the dynamic and seismic response of masonry cross vaults, in terms of collapse mechanisms, strength, and displacement capacity.

Motivation: Masonry cross vaults are widespread in historic masonry buildings and are often decorated with frescos, wooden carvings, and paintings. Because of their vulnerability, damage and/or collapse of vaults may produce unrecoverable cultural losses, injuries to occupants, and even casualties. Only a few experimental studies concerning their dynamic behaviour are available in the literature. A new set of experimental results may overcome this gap and provide important outputs about the capacity of vaults at both reduced and full-scale levels.

B. Evaluating the role of the seismic input on the response of masonry vaults.

Motivation: Seismic inputs may vary significantly based on their ground motion contents. The response of non-linear structures, such as cross vaults, can be strongly influenced by the type of seismic input. Through numerical analyses, a deeper understanding of the role of different seismic inputs in the response of vaults can be achieved.

C. Assessing the effectiveness of an innovative strengthening technique for masonry cross vaults.

Motivation: When a vault is judged to be unsafe or has been damaged by an earthquake, its repair and strengthening are often considered to safeguard the vault itself. However, few information regarding the improvement of the capacity after the repair and the application of the strengthening techniques is available. Within this lack of knowledge, one of the objectives of this research is to assess the seismic performance of the textile-reinforced mortar (TRM) strengthening technique on full-scale masonry groin vaults.

D. Assessing the reliability of quasi-static tests and shaking table tests on scaled dry joints mock-ups in predicting the dynamic behaviour of real masonry vaults.

Motivation: Quasi-static tests on masonry vaults are easier to perform and more cost-effective than shaking table tests. However, the performance and reliability of the quasi-static tests for the evaluation of the seismic behaviour of vaults should be assessed by comparing their response with the shaking table tests, performed on the same specimen.

E. Assessing the reliability of finite element models (FEM) and discrete element models (DEM) in forecasting the seismic behaviour of reduced-scale and full-scale masonry cross vaults.

Motivation: FEM and DEM models are effective and cost-efficient tools to simulate the seismic behaviour of masonry structures. Several modelling approaches and procedures are proposed in the literature, but their reliability for 3D curved masonry structures, specifically at reduced-scale and full-scale levels and for dynamic loads, has rarely been assessed.

1.6 Outline of the thesis

This work is presented throughout the eight chapters of the document, including the present Introduction, as represented by the flowchart of Figure 1-20.

Chapter 1 introduces the work, covering nomenclature, a brief historical evolution of masonry cross vaults, recurrent seismic damage, objectives, and motivation.

Chapter 2 is devoted to a review of the existing literature and the current state of knowledge about the topics included in this thesis. The literature review primarily focuses on the most relevant aspects of experimental campaigns, both at the reduced-scale and full-scale. Additionally, special emphasis is placed on the different numerical approaches and formulations available for groin vaults.

Chapter 3 presents the experimental campaigns conducted on the reduced-scale vault. This experimental investigation is primarily focused on the in-plane shear response of the small specimen considering and analysing the results of three types of tests, namely quasi-static tests (Rossi, Calderini and Lagomarsino, 2016), dynamic identification tests and shaking table tests. Another aspect emphasised in this Chapter is the variability of the specimen's response to two different inputs, namely one recorded during the Emilia Earthquake 2012 and one artificial accelerogram. First, a description of the specimen and the setup is provided. Then, the main outcomes are discussed in terms of displacement capacity, damage indicators, and collapse mechanism. These experimental results serve as the basis and validation data for subsequent simulations presented in Chapter 4.

Chapter 4 focuses on the numerical analysis of the reduced-scale specimen, performed according to finite element modelling (micro-modelling strategy) and discrete element modelling approaches. First, finite element model and discrete element model are described and calibrated in detail following an iterative fitting procedure. A Mohr-Coulomb constitutive law has been adopted in both numerical models. Afterwards, a series of numerical simulations is presented. In particular, non-linear static and non-linear time history analyses are performed, replicating the experimental campaigns described in Chapter 3. Discrete element analyses are extended to investigate the role of the input in the collapse of vaults. In this context, three sets of ground motions are selected based on statistical observations.

Chapter 5 presents the design of the experimental campaign, which considers the full-scale vault subjected to in-plane shear behaviour. This has been carried out considering traditional construction techniques, ancient rules and thumbs rules, supported by preliminary numerical analysis using a finite macro element model. Thus, the characterisation of the units, mortar and wallets is done by performing a complete set of material tests. Then, the setup of the experimental campaign is presented for both unstrengthened and strengthened vault configurations.

Chapter 6 presents shaking table tests on the full-scale vault, both without and with the application of TRM at the extrados. This experimental investigation is mainly focused on the in-plane shear response of the vault when L'Aquila earthquake 2009 is applied in increasing steps of amplitude at the base of the specimen from the shaking table. Dynamic identification tests are used to control the stability of the in-plane shear associated with the first mode shape of the specimen. The main outcomes of the

specimen are commented in terms of displacement capacity, damage, hysteretic curves, and damage indicators for both the unstrengthened and strengthened specimens. Similar to Chapter 3, these experimental results are employed as the basis and validation data for subsequent simulations presented in Chapter 7.

Chapter 7 presents the simulations of seismic tests described in Chapter 6. Firstly, FEM (macro-modelling approach) model and DEM model are calibrated to match the modal properties obtained by the dynamic identification tests of the unstrengthened configuration. The results of DEM have been improved considering a Moh-Coulomb relation as well as a combined material behaviour of Moh-Coulomb with shear, crushing and cracking. The strengthening solution has only been simulated in the finite element model and for the highest amplitude of action. The results are presented in terms of damage distributions, displacement capacity and hysteretic curves for all the modelling approaches.

Chapter 8 summarizes the main conclusions of the research conducted in this thesis. Additionally, suggestions and proposals for future works are provided.

The thesis also includes a series of Annexes that provide supplementary information to support the main concepts and results of this thesis.

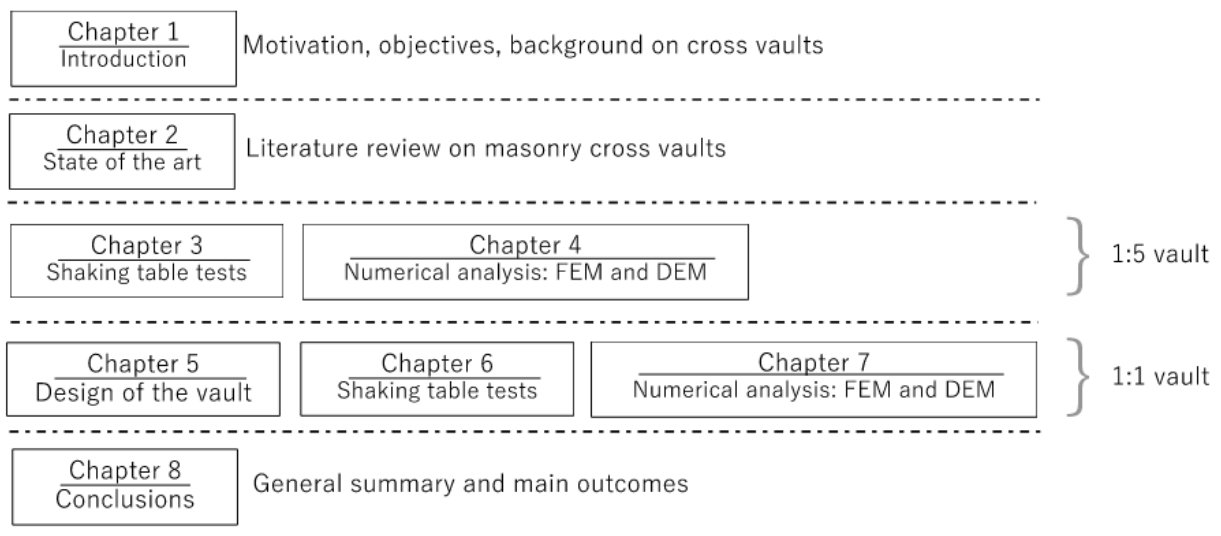


Figure 1-20. Flowchart of the thesis outline.

2. State of the art on masonry cross vaults

2.1 Introduction

After preliminary information on masonry cross vaults gathered in Chapter 1, the scope of Chapter 2 is to present an overview on the main approaches whose knowledge is necessary to drive this research. Indeed, while Chapter 1 introduces preparatory definitions for this thesis, Chapter 2 reports the main tools and strategies, namely experimental works, contemporary and advanced structural analysis methods used for masonry cross vaults and numerical modelling approaches. Regarding the ancient historical rules of thumbs, the reader is referred to Gaetani (2016).

The tools and strategies discussed next represent decisive tools for the assessment of the behaviour of all types of vaulted structures. However, in this framework, only groin vaults are deepened. Therefore, the most relevant experimental and numerical investigations (both for reduced-scale and full-scale cross vaults) are presented and discussed, highlighting assumptions, limitations and applications. The main contributions are summarised in Annex 1.

2.2 Literature review: experimental investigations

Experimental tests are of paramount importance for improving the current comprehension of cross vaults behaviour and for validating existing numerical models. Experiments involving seismic scenarios on full-scale vaults are, at present, partial and limited in number. The reason lies on the fact that full-scale experiments present difficulties, mainly due to the nature of the loading action, and cost and time demand. On the other hand, experiments at reduced-scale offer greater flexibility and convenience, and lower cost and risk associated with the safety of the testing facility and of the personnel. As appropriate scaling laws for the response of masonry structures under seismic excitations are needed before performing such tests, both full-scale and reduced-scale specimens are important for improving knowledge on vaulted structures.

In this paragraph, the scaling laws and a brief overview on both types of experiments (reduced-scale and full-scale) are presented in chronological order.

2.2.1 Scale factor definitions

The design of reduced-scale tests requires appropriate scaling laws in order to guarantee the similarity between a prototype (full-scale structure) and its scaled replica. Reduced-scale specimens require a

specific fabrication and instrumentation to respect the similitude laws based on dimensional analysis. The laws of similitude force the equivalence between objects or phenomena, meaning that scale is not only related to the geometry of the models, but also to other aspects, such as the stress-strain relationship of the materials, the mass and gravity forces, the initial conditions and the boundary conditions (Carvalho, 1998).

Cauchy and Cauchy-Froude similitude laws address the similitude between the mass and gravity forces. Cauchy's law is proper for phenomena in which the restoring forces are derived from the stress-strain constitutive relationships and the elastic restoring forces (Equation 2-1), while Cauchy-Froude's law is adequate for phenomena in which the gravity forces are important, being the Froude number (Equation 2-2) the ratio between inertia forces and gravity forces (Lourenço *et al.*, 2016).

$$\text{Cauchy number} = \frac{\frac{\rho L^3 v^2}{L}}{EL^2} = \frac{\rho v^2}{E} \quad \text{Equation 2-1}$$

$$\text{Froude number} = \frac{\frac{\rho L^3 v^2}{L}}{\rho L^3 g} = \frac{v^2}{Lg} \quad \text{Equation 2-2}$$

The equality in Cauchy and Froude's numbers ensures that restoring, inertial and gravity forces are correctly scaled.

Table 2-1 presents the scale factor ratio N (prototype-full-scale/model-reduced-scale) for each parameter according to Cauchy and Cauchy-Froude similitude laws.

Table 2-1. Scale factors N according to Cauchy and Cauchy-Froude similitude laws (Carvalho, 1998; Mendes, 2012).

Parameter	Cauchy	Cauchy and Froude
Length (L)	N	N
Modulus of elasticity (E)	1	1
Specific mass (ρ)	1	N^{-1}
Area (A)	N^2	N^2
Volume (V)	N^3	N^3
Displacement (d)	N	N
Velocity (v)	1	$N^{1/2}$
Acceleration (a)	N^{-1}	1
Mass (s)	N^3	N^3
Weight (W)	N^3	N^2
Force (F)	N^2	N^2
Moment (M)	N^3	N^3
Stress (s)	1	1
Strain (e)	1	1
Time (t)	N	$N^{1/2}$
Frequency (f)	N^{-1}	$N^{-1/2}$

The main issue is to select the similitude law that better represents the prototype, respecting all the physical and geometrical variables that are selected as indicators for scaling. Hence, the complete similarity is desirable, but usually, it is precluded. Because of this, some variables become more relevant than others, bearing in mind the final purpose of the experimental and numerical campaign.

Noteworthy, in the case of shaking table tests, when dynamic actions are involved, the fulfilment of similitude laws should be required not only in terms of geometrical and physical parameters but also in terms of input actions, which is even harder to satisfy. It is clear that the geometric similitude is achieved by a direct application of the geometric scale factor, however, other conditions are more laborious to be fulfilled, especially when composite blocks replace masonry units.

Experimental campaigns on reduced-scale and full-scale cross vaults are proposed in Section 2.2.2 and Section 2.2.3, showing features, limitations and characteristics that make those specific campaigns important in the state of the art of this research.

2.2.2 Reduced-scale groin vaults

Mark *et al.* (1973)'s work is considered the first wide experimental campaign on vaults, since they declare that, before this work, cross vaults were not fully examined from the experimental point of view. Two bays of the choir vaulting of Cologne Cathedral, belonging to the German Gothic style are replicated (Figure 2-1a). They apply a photo-elastic technique to recreate the 1:50 scaled cross groin vaults specimen made of cast epoxy. This is also considered the first contribution which validates the experimental observations by means of a FEM model (created in SAP software) made of shell elements. This remarkable investigation indicates, both experimentally and numerically, that the major in-plane vault forces are directed to its supports; as it was remarked by several architectural historians, including Abraham (1934).

Briccoli Bati *et al.* (2002) reproduce a 1:3 groin vault, according to the historical guidelines reported in Giovanetti (2000), made of bricks (Figure 2-1b). The plan dimensions are 1.0 m × 1.84 m with a rise of 87 cm and a thickness of 5.2 cm. The joints thickness is set at the constant value of 0.5 cm. Several load conditions (*e.g.* symmetric, asymmetric and settlement of the supports) are investigated. Furthermore, two strengthening techniques are also evaluated, namely the application of ties and the strengthening with glass fibre-reinforced polymer (GFRP) strips. The main outcome is that the increase of admissible loads with the GFRP application is significant, but their durability is debatable.

Theodossopoulos *et al.* (2002) study a 1:4 scale cross vault made of wood, a replica of a portion of the collapsed Abbey Church of Holyrood in Edinburgh, Scotland (Figure 2-1c). In this work, a wide

displacement of the abutments is observed until the failure of the specimen. A finite element model, built in Abaqus software, is used to compare the numerical results with the experimental damage pattern, showing remarkable matching. This work highlights how the stability of the bearing piers and the abutments is of primary importance, supported by quantitative data.

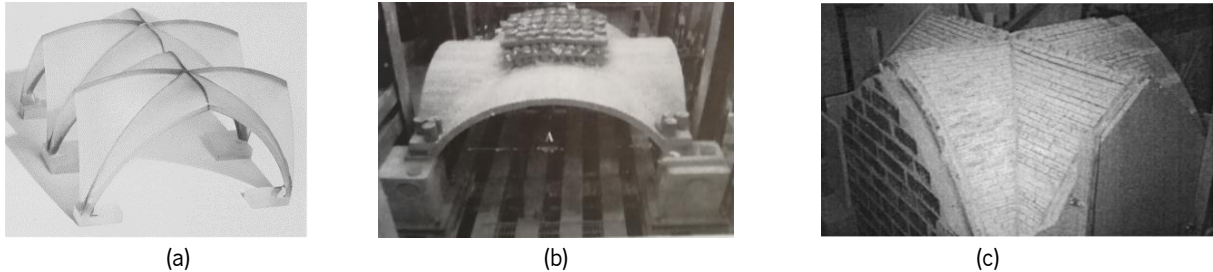


Figure 2-1. Reduced-scale experimental campaigns: (a) Mark *et al.* (1973), (b) Briccoli Bati *et al.* (2002), (c) Theodossopoulos *et al.* (2002).

The first test of a groin vault tested on a seismic simulator is reported by Miltiadou-Fezan (2008). The portion of the Katholikon of the Byzantine monastery of Dafni, Greece, (Figure 2-2) is replicated, considering two walls covered by a groin vault of about 2.5 m × 2.5 m in plan (Figure 2-2b) and 0.20 m of thickness (no scale, the model was made to fit on the shaking table dimensions). This monastery is of interest because it belongs to the world heritage list of UNESCO, damaged by the Athens 1999 earthquake. Besides the relevance of the tests, only qualitative data are available because Miltiadou-Fezan (2008) focused more on the global performance of the monastery (through a FEM model) and the evaluation of the grout injections efficiency, which enhances the seismic behaviour of the structure, at the expenses of the compatibility with the original materials.

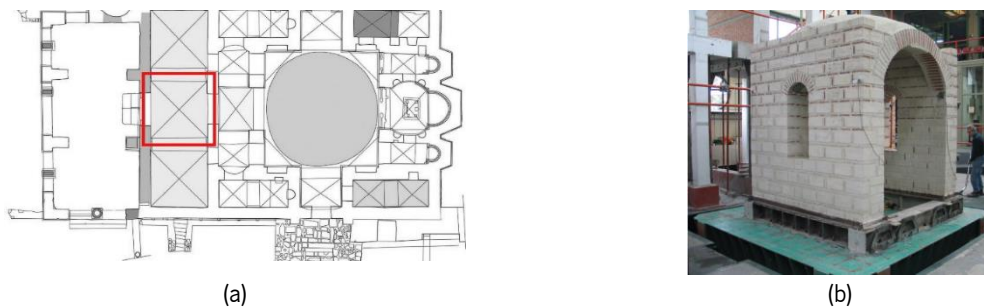


Figure 2-2. Miltiadou-Fezan (2008)'s experimental campaign: (a) location of the selected area in the monastery of Dafni, (b) specimen on the shaking table.

Williams *et al.* (2012) replicate the vaults of the Basilica of Maxentius, Rome, Italy, (Figure 1-4) at 1:25 reduced-scale (Figure 2-3a). The specimen is made of modelling plaster and fine sand, then subjected to unidirectional horizontal base shaking by a series of sinusoidal pulses of varying amplitude and frequency (Figure 2-3b). This experimental campaign is at an early stage of the topic, however, it

already highlighted that under lateral shaking, when the supports slide laterally, the vault develops hinges near the top of each web and evident bending cracks (Figure 2-3c), as observed in Figure 1-9a.

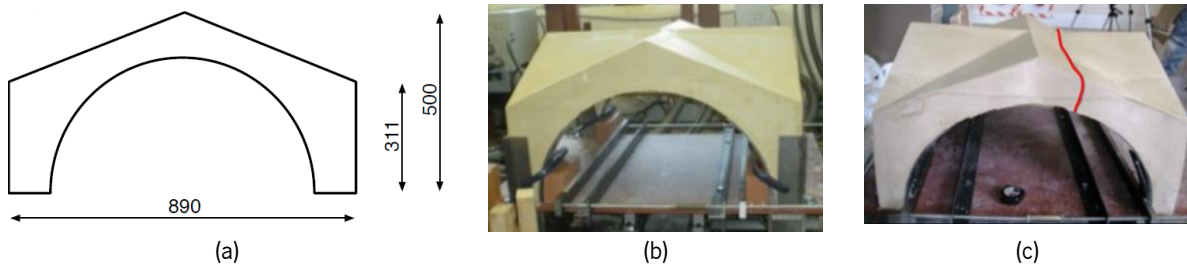


Figure 2-3. Williams *et al.* (2012) experimental campaign: (a) cross vault dimensions, (b) specimen before testing, (c) groin vault cracked by lateral spreading.

The case of the gothic Santa Maria Church of Fossanova in Priverno, Italy, studied by De Matteis and Mazzolani (2010), is remarkable because is widely investigated from different points of view: *in situ* inspections and laboratory tests (such as dynamic identification tests, shaking table tests and numerical simulations (Figure 2-4). De Matteis *et al.* (2010)'s specimen replicates the central part of the Fossanova Church, including three consecutive bays at 1:5.5 scale. Due to the scale factor, equivalent materials and reduced strengths are used, in order to maintain the same equivalent weight and to respect the scale similitude laws (Krstevska *et al.*, 2017). Calitri earthquake (1980), also known as Irpinia earthquake, is the selected seismic input, applied along the transverse direction of the church. The specimen has reached a maximum of 0.14 g and, then, it has been strengthened by an expansive aluminium-cement mortar and tested again until reaching the maximum value of 0.4 g.



Figure 2-4. De Matteis *et al.* (2010)'s experimental campaign: (a) illustration of the positioning on the shaking table, (b) photographs of the details of the main damage.

As mentioned in Chapter 1, Rossi *et al.* (2015; 2016; 2017b) represents the main reference and starting point for this research work. Quasi-static tests and their corresponding numerical simulations are performed using a 1:5 scale groin vault specimen made of 3D printed plastic blocks (Figure 2-5a). The quasi-static experiments involved namely in-plane shear tests (Figure 2-5b) and the tilting table tests (Figure 2-5c). The purpose was to study the behaviour of the vault subjected to horizontal forces

proportional to its mass (in-plane shear tests) and an incremental horizontal differential displacement between two couples of opposite abutments (tilting table tests). As main conclusion, the maximum reference value for the ultimate drift of the specimen is about 4% of the span.

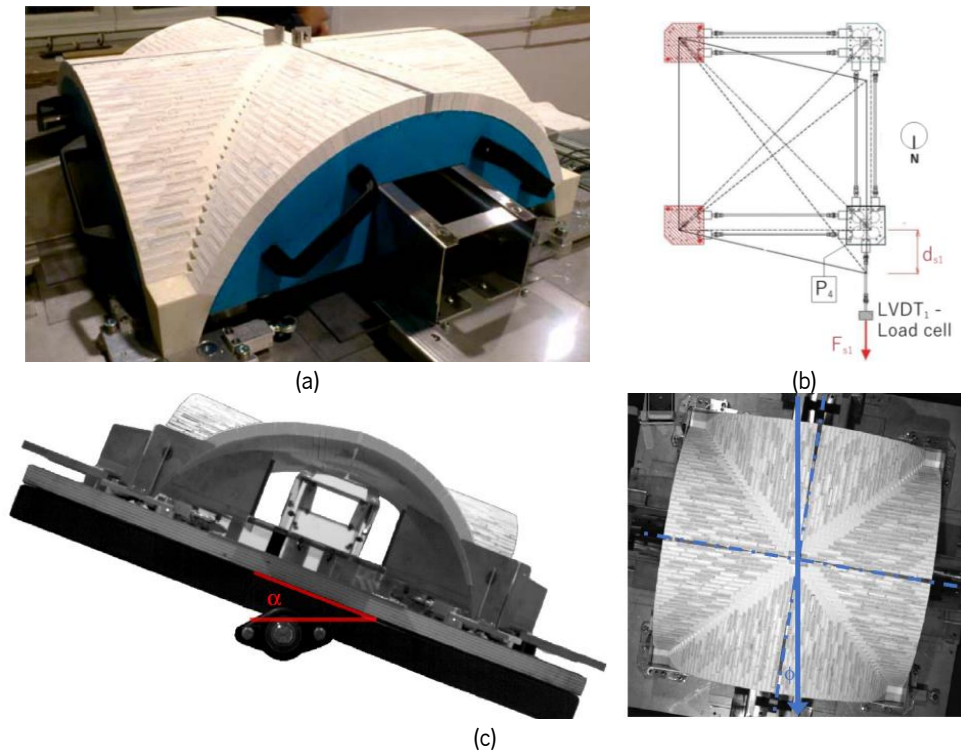


Figure 2-5. Rossi *et al.* (2015; 2016; 2017b)'s experimental campaign: (a) the 1:5 scale specimen, (b) in-plane shear test setup (c) tilting tests with the tilting plane (α is the angle of rotation and Φ is the angle between the axis of rotation of the tilting plane and the axes of symmetry of the vault)

Fagone *et al.* (2016), using a 1:5 scale model made of *Alberese* stones, reproduced the cross vault of St. John Hospital in Jerusalem, Israel, to evaluate the efficiency of continuous carbon fibre reinforced polymer (CFRP) sheets applied at the extrados (Figure 2-6). The experimental results showed that the strengthening system, in comparison with the unstrengthened configuration, is able to increase the collapse load of the vault, without substantial variation of the initial stiffness. The capacity increased of about 45% with the application of the strengthening.



Figure 2-6. Fagone *et al.* (2016)'s experimental campaign: (a) unstrengthened specimen, (b) strengthened specimen with CFRP continuous sheet at the extrados.

Another unreinforced 3D printed groin vault is studied at the Block Research Group's laboratory in ETH Zurich, Switzerland, and introduced by Rossi *et al.* (2017a). This study is based on a 3D printing strategy, which uses force-sensitive robotic arms as testing devices combined with an optical measuring system (Figure 2-7a). The results are read through a point cloud environment as a map of the deviation of all the individual blocks of the model. Loading and support settlement tests are performed and for what concerns the most relevant outcomes, the flexibility of the experimental setup was pointed out. It can reproduce displacement functions, controlled by the robotic arms.

Similarly to the work of Theodossopolus (2002), Carfagnini *et al.* (2018) reproduce the surviving south aisle vault of the Holyrood Abbey, to perform shear displacement tests (Figure 2-7b) at the 1:4 scale. The replica is composed of timber blocks and lime mortar. The initial cracks, orthogonal to the diagonals, show that failure happens at 2.7% opening of the longitudinal span, in agreement with other similar cases available in the literature.

Foti *et al.* (2018) examine a large model, with 1 m × 1 m and 0.07 m of thickness, composed by 195 blocks and dry assembled (Figure 2-7c). Three different loading conditions (vertical, diagonal, and horizontal displacement of the support) lead to the partial collapse of the vault (sliding of the blocks). A discrete element numerical model of the vault was done for comparison purposes with the specimen vault, using rigid blocks.

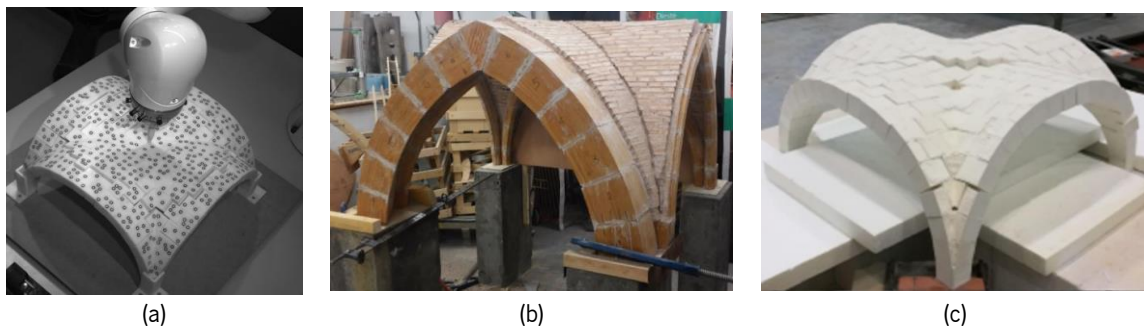


Figure 2-7. Reduced-scale experimental campaigns: (a) Rossi *et al.* (2017a), (b) Carfagnini *et al.* (2018), (c) Foti *et al.* (2018).

Lastly, Silvestri *et al.* (2021)'s work, also inserted in the SERA projects funding (see Chapter 1), consists of a specimen made of 3D printed plastic skin to provide stiffness and strength, filled with mortar and dry joints (Figure 2-8). Both sinusoidal and earthquake motions are imposed in one horizontal direction, with progressively increasing amplitude and different frequencies, up to collapse. This work investigates the effect of different boundary conditions, both at the base of the vault and laterally.

Besides the fact that stress similitude is not preserved (*e.g.* the elastic moduli of the materials are not faithfully scaled), some important outcomes arise: (i) dynamic amplification of the vault model is mainly

influenced by the lateral confinement level - stronger confinement means larger amplification factor; (ii) the seismic response of the vault depends, as expected, on the critical frequency bandwidth of the earthquake input.

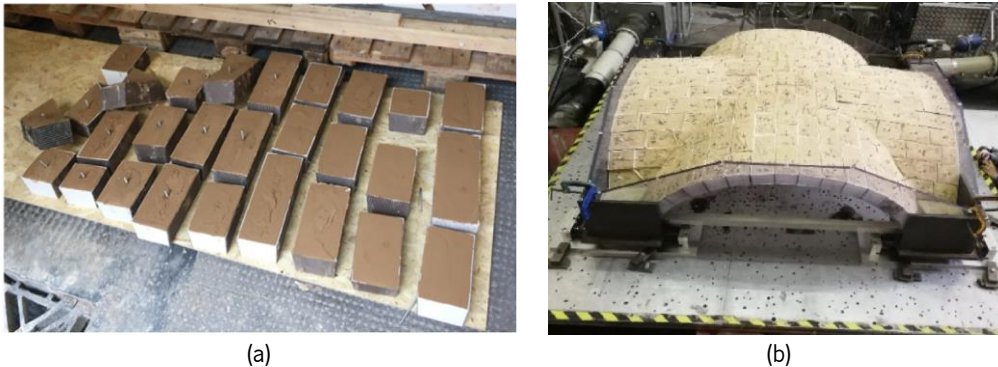


Figure 2-8. Silvestri *et al.* (2021)'s experimental campaign: (a) typical blocks, (b) specimen on the shaking table.

2.2.3 Full-scale vaults campaigns

For what concerns full-scale models, only three cases seem to be available in the literature. The first work corresponds to the experimental tests performed by the research group of the University of Venice in 1999. Di Marco, Faccio and Foraboschi's contribution (Figure 2-9a) consists of a lower-rise groin vault, with a thickness of 12.5 cm, tested with a distributed asymmetric increasing load (Creazza, Meroi and Saetta, 2002). The same model is tested again by Faccio *et al.* (1999), representing the starting point for several numerical simulations (*e.g.* Creazza *et al.* (2002) and Milani *et al.* (2008)).

Rossi *et al.* (2020) present another experimental application of a case study, namely one of the ten cross vaults of the Mosque of Dey (17th century) in Algiers, Algeria, tested on a shaking table in ENEA laboratory (Rome). The specimen is one brick layer in thickness and its dimensions are 0.35 m \times 0.36 m square plan, with a total height of 5.65 m, subjected to one directional seismic input. Similarly to this work, the in-plane shear failure is the objective of the Rossi *et al.* (2020)'s study. However, the vault has collapsed at 0.4 g due to the activation of an out-of-plane mechanism that leads to the development of the typical four-hinge mechanism (see Figure 2-9b).

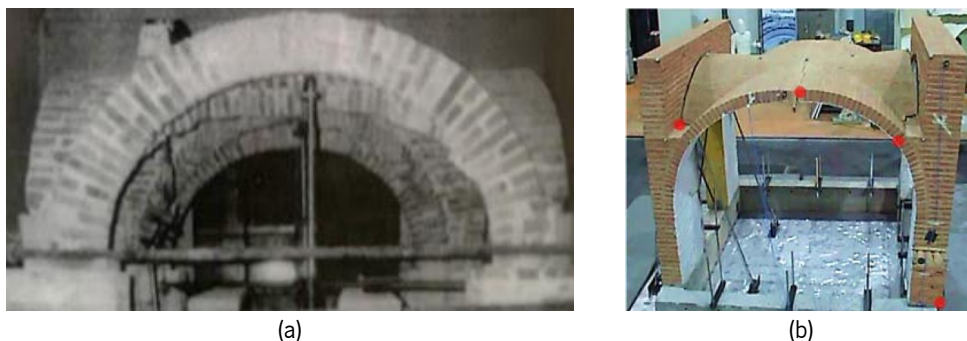


Figure 2-9. Full-scale experimental campaigns: (a) Faccio *et al.* (1999), (b) Rossi *et al.* (2020) specimen.

Lastly, at the Universitat Politècnica de València, Torres *et al.* (2019) examine a full-scale masonry cross vault (4.3 m × 3.6 m) subjected to a series of cyclic settlements on one of its supports (Figure 2-10a). This specimen is the replica of a groin vault of the church of San Lorenzo de Castell de Cabres (Castellon, Spain). Torres *et al.* (2019) demonstrate that settlements, due to the surroundings where the structure is placed, can play a critical role, leading to the collapse. This work represents the most recent full-scale model of a cross vault in the technical literature. Nevertheless, this investigation deals again with the study of static approaches for the vertical settlement at the supports. On the other hand, its comparison with future full-scale experimental models will be complex, since this case is a timbered vault composed of seven layers of flat bricks (Figure 2-10b).



Figure 2-10. Torres *et al.* (2019)'s specimen: (a) timbered vault model, (b) detail of the thickness section.

2.2.4 Final remarks on experimental investigations

Considering all the contributions on tests on reduced-scale and full-scale vaults, fully reported in Annex 1, the following conclusions are drawn from the literature review on experimental campaigns:

- most of the tests deal with reduced-scale specimens, which require a proper scale factor to respect the similitude laws.
- often composite materials simplify the construction and assembly of the specimens, but due to the similitude laws, their total mass is rarely representative of real masonry vaults.
- only few full-scale tests are available, and they deal mainly with the static behaviour of the vault (*e.g.* settlements). The unique example of shaking table test, at full-scale level, showcases an out-of-plane failure of the vault, unlikely to occur in real scenarios.
- only a few evaluations of strengthening techniques with dynamic actions are available and textile-reinforced mortar (TRM) application was never studied.

2.3 Literature review: analytical and numerical investigations

Modern methods and computational tools are available for the assessment of the mechanical behaviour of historical vaults. Modern methods resort to different theories or approaches, including different levels

of complexity, different availability for the practitioner, different time requirements and different costs. These methods, which vary from simplified methodologies (*e.g.* limit analysis) to refined numerical models (*e.g.* discrete element models), are introduced in this Section, focusing on the most important tools for the understanding and development of this work. Historical methods are out of scope and the reader is referred to Gaetani (2016).

2.3.1 Limit analysis

Limit analysis is the first method that bridges over the historical methods to reach the development of modern applications. Born from the observation of the plasticity of steel members, limit analysis plays a remarkable role for obtaining quick and reliable information regarding the ultimate state of structural elements. Heyman is the first researcher to apply limit analysis, not only for elements made of steel but also for masonry structures, using three relevant well-known hypotheses: infinite compressive strength, zero tensile strength and no sliding failure (Heyman, 1995b). These three hypotheses allow the use of the three limit analysis theorems, here outlined and summarised (Figure 2-11).

Kinematic theorem (upper bound theorem)

If a kinematically admissible mechanism can be found, for which the work developed by external forces is positive or zero, then the structure will collapse. The load multiplier λ_U determined by this approach is an upper-bound to the actual one (Heyman, 1982), which means that the load obtained for any kinematic mechanism is greater or equal to the true collapse load. Again, this theorem is widely applicable for arches or other 1D structures (Tralli, Alessandri and Milani, 2014).

Static theorem (safe theorem or lower-bound)

Heyman (1982) affirms that “*a masonry arch/vault is stable if at least one of the infinite admissible equilibrated thrust lines falls entirely into the thickness of the element*”. In other words, if the load λ_L for which the stress state satisfies the equilibrium and yield condition can be found, then it is smaller or equal to the true value of the collapse. The concept means that the structure is safe, *i.e.*, the collapse will not occur, and this is because an admissible state of equilibrium can be found. Thus, the thrust line can be determined, in equilibrium with the external loads, falling within the cross-section at the base of the structure. Thrust line analysis is a useful tool to explain and examine the stability of mono-dimensional structures, like arches or barrel vaults (Tralli, Alessandri and Milani, 2014).

Uniqueness theorem

This theorem states that if equilibrium, mechanism and yield are satisfied, then the load factor obtained from the static and kinematic approach is the same (λ_F).

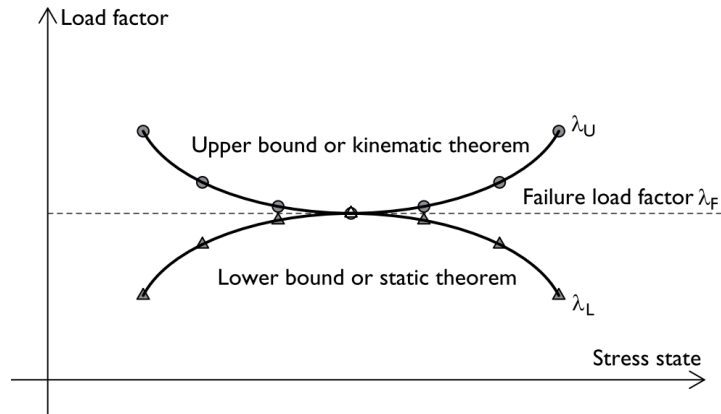


Figure 2-11. Graphical representation of limit analysis theorems (Mendes, 2015).

Although limit analysis methods provide a rapid solution for vaulted structures, they present also limitations for assessment. Huerta (2001) first highlights that masonry vaults studies need to take into account also the heterogeneity of the material and, in addition, limit analysis only provides the maximum capacity without giving information on the load history (Roca, Lourenço and Gaetani, 2019). Thus, in the last decades, it is possible to find more appropriate methods, which consist of the natural evolution of classic limit analysis, able to better represent masonry structures.

Modern methods based on the upper bound theorem

Typically, the kinematic limit analysis is carried out, assuming the failure mechanisms, and then applying the principle of virtual work to determine the corresponding collapse multipliers λ_U . Kinematic limit analyses are particularly simple for existing buildings like churches because the failure mechanisms are directly derived from the observations done in post-earthquake surveys.

In the last 25 years, Milani *et al.* (2008, 2009) have improved the application of limit analysis, which can be denominated as non-uniform rational B-spline (NURBS) limit analysis, which uses models based on the Finite Element Method (FEM) with a rough mesh. This consists in an advanced kinematic limit analysis which considers the homogenization of the material. A 3D kinematic FE limit analysis procedure where classic homogenization theory may be adapted to masonry vaults. Figure 2-12a represents the classic rigorous elementary cell identification for a plane wall, while Figure 2-12b reports the Heuristic identification of the elementary cell for a double curvature masonry shell (Kurrer, 2008). In the limit analysis proposed by Milani *et al.*'s (2008), a rigid infinitely resistant six-noded triangular curved elements is adopted, where the plastic dissipation is concentrated along the edges of adjoining elements that may occur for in plane, bending moment, torsions and out of plane actions. It is based on rigid perfectly plastic material with associated flow law, where the dilatancy angle is equal to the friction angle. Thanks to the duality of the formulation, the upper bound collapse may be defined as well as the

strength domain, following the FE homogenization procedure. In this case, the masonry strength domain at each homogenised interface between contiguous triangular elements is evaluated by resorting to a suitable upper-bound FE homogenization procedure.

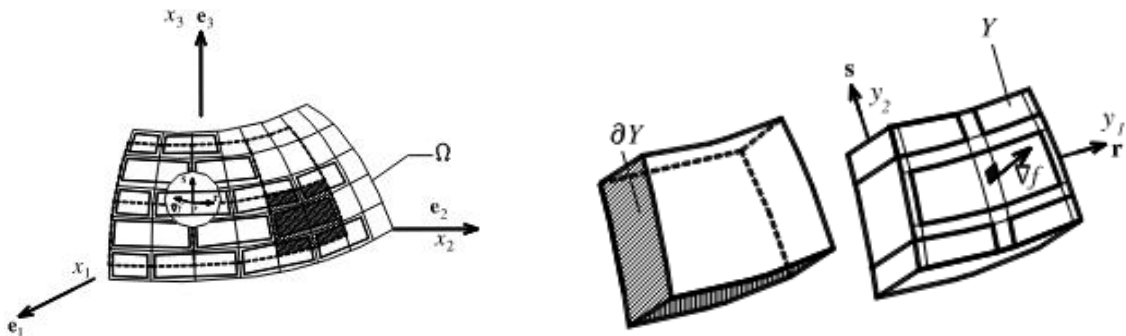


Figure 2-12. A homogenization procedure for a curved masonry shell (Kurrer, 2008; Milani, Milani and Tralli, 2008).

A further step forward is represented by a new Genetic Algorithm NURBS-based approach for masonry vaults, again based on an upper bound formulation (Chiozzi, Milani and Tralli, 2017b, 2017a; Grillanda *et al.*, 2019). The difference consists in the fact that each element of the mesh is a NURBS surface itself, considered as a rigid body in which the geometry is described as a parametric surface. A fast and reliable automatised kinematic limit analysis approach has been developed, able to accurately predict the actual behaviour of vaulted structures, roughly discretised by few rigid infinitely resistant NURBS elements, subjected to horizontal static loads (Grillanda *et al.*, 2019). This improvement allows to discretise the model by using very few elements to maximise accuracy and computational efforts, dependent on the choice of parametrization of the user.

As displayed in Figure 2-13, Milani *et al.*'s (2008), Chiozzi *et al.* (2017a) and Grillanda *et al.* (2020) validate their approach with respect to the cross vault tested by Faccio *et al.* (1999).

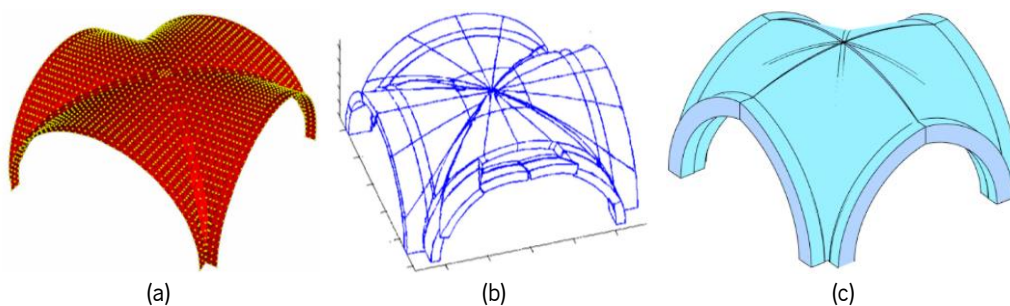


Figure 2-13. Kinematic limit analysis applications on groin vaults: (a) Milani *et al.*'s (2008), (b) Chiozzi *et al.* (2017a), (c) Grillanda *et al.* (2020).

Modern methods based on the lower bound theorem

Among the modern applications of limit analysis, the Thrust network method (TNM) is a methodology for the study of the stability of the vaults that utilises a discrete network of graphic thrusts in equilibrium with the vertical and gravitational loads based on Heyman's safe theorem (lower bound). It considers

compressive forces acting within the structure in equilibrium with the external loads. Using TNM, the model itself is not composed of the volume of the structure, but it is represented by the network of forces that compose it. Therefore, it comprises N_n nodes and N_b branches, where the n_{th} node contains the information regarding the three-dimensional location of the boundaries of the branches, while the branches stand for the direction of the thrust forces. The limitations of the TNM are mainly related to materials unable to withstand tensile stresses and are frequently associated with over-conservative predictions of the collapse multipliers. Block *et al.* (2002; 2014)'s work is the main reference for the application of the TNM for modelling masonry vaults, including cross vaults (Figure 2-14a).

Marmo and Rosati (2017) introduce a reformulation of the TNM, aiming at combining both vertical and horizontal loads to depict also seismic considerations from the application of this method (Figure 2-14b). Similarly, Andreu *et al.* (2007) introduce a TNM method based on the funicular network adopting optimization criteria.

These methods are included in the group of the standard limit analysis based on rigid-perfectly plastic material with associated flow law. This means that the dilatancy angle (where the tangent is the ratio between normal and tangent displacement at the joint level) is considered equal to the friction angle, while, from the experimental campaigns, the dilatancy angle should be set equal to null (Angelillo, Lourenço and Milani, 2014). Therefore, TNM reveals its best features only in cases where volume generation in the failure process is not important.

As for the kinematic method, a limitation of this approach is that the definition of the network connectivity and branch spacing is subjected to the decision of the users, rather than by a membrane distribution of the loads. However, TNM is still widely considered as a good approach, since it is independent of constitutive data and supports settlements, being therefore easily performed in the practice.

Recently, a new Lower Bound (LB) plate and shell limit analysis Finite Element (FE) model is developed by Milani (2022) for the analysis of the collapse of masonry double curvature structures, where masonry can be modelled both by means of a classic no-tension material and with an orthotropic behaviour with small but non-zero strength in tension.

As in Milani *et al.*'s (2008), a discretization of a masonry vault into infinitely resistant hexahedron elements joined by quadrilateral interfaces, where all plastic dissipation occurs is assumed (Figure 2-14c). At the level of the interfaces, the flexural behaviour is ruled by the interaction between bending

moment and membrane axial load, whereas the shear and torsional behaviour are modelled through an in-plane tangential force, the out-of-plane shear and a plate torque.

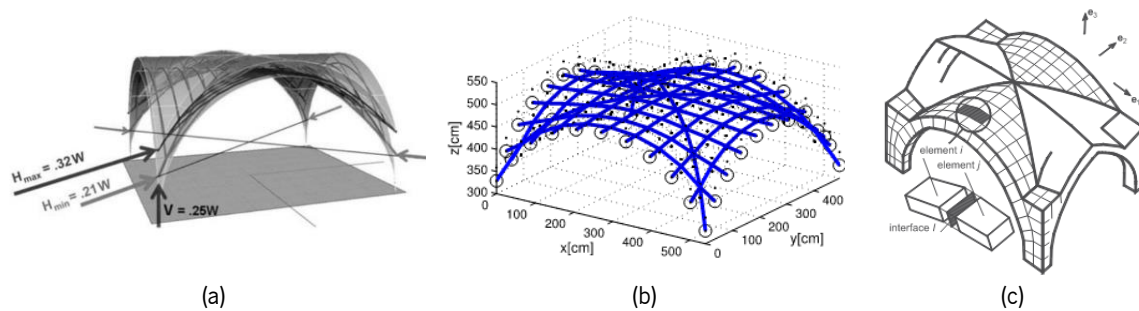


Figure 2-14. Static limit analysis applications on groin vaults: (a) Block and Ochsendorf (2002), (b) Marmo and Rosati (2017), (c) Milani (2022).

2.3.2 Membrane theory

Tomasoni (2008), Fraternali (2010) and Como (2017) introduce a membrane theory in order to also consider 3D effects. The membrane forces interplay among the actions transmitted by the webs to the diagonals ribs and they define the global equilibrium of the cross vault (Como, 2017). From Figure 2-15 is possible to see that the lateral arches transmit the force distribution to the vault's side edges. Considering tensile forces is a necessary condition for the membrane state of stress in the vault. Cracking or detachments are thus inevitable, and the masonry vault must reach a new internal equilibrium. On the other hand, Fraternali (2010) proposes a 3D extension of the membrane network of forces that considers a stress state function, based on discretised Airy stress functions, similar to the TNM. Membrane theory discards singularities in the boundary conditions and loading, discontinuities (*e.g.* cracks or openings) in the discretised equilibrium surfaces and takes into account only the dead loads.

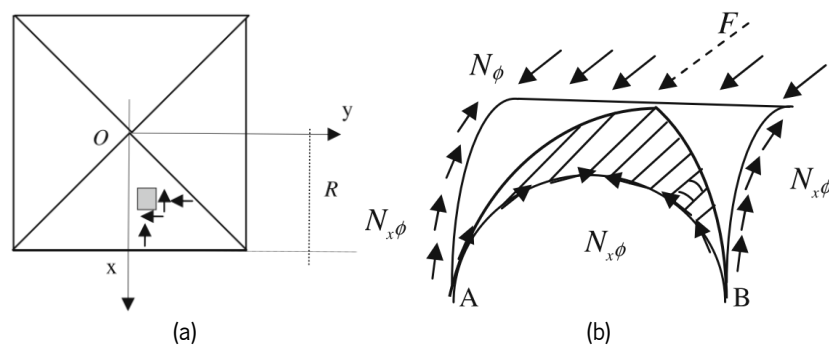


Figure 2-15. Membrane theory in the vault's web: (a) membrane stresses, (b) membrane forces (Como, 2017).

2.3.3 Finite element method (FEM)

In the last decades, the Finite Element Method (FEM) has become the most used and versatile method of structural analysis, because it uses the continuum theory, and it allows obtaining an accurate

representation of a structure. Contrarily to the limit analysis, which depicts only the maximum load capacity of the vault, FEM permits the evaluation of the development of damage during the analysis and it considers the combination of various parameters, in terms of material properties, modelling elements, non-linear and linear analysis and loading conditions. In every point of the structure and at every step of the load, relations between stress and strain are described thanks to complex constitutive laws (Lourenço, 1996), allowing an extensive range of possibilities to describe, among others, masonry structures (Roca *et al.*, 2010), among those, vaults. A general masonry sample composed of units and both head and bed joints can be represented by two main approaches based on FEM, namely micro-modelling or macro-modelling approach (Figure 2-16).

Micro-modelling approach provides a better comprehension of the local behaviour of a selected portion, while macro-modelling is more adaptable for large structural members or full structures. Micro-modelling approach can be divided into two principal categories: the so-called detailed micro-modelling and the simplified micro-modelling. In the first case, a continuum finite element represents units and mortar, while discontinuous elements simulate the interfaces between them (interface elements). In the second case, the size of the units is increased to model both units and mortar material by continuum elements. The behaviour of the joints and interfaces is represented by discontinuous elements.

On the other hand, in the macro-modelling, units, mortar and interfaces are represented together as a continuum through homogenization techniques, which permit to derive the global behaviour of masonry from the constitutive material laws.

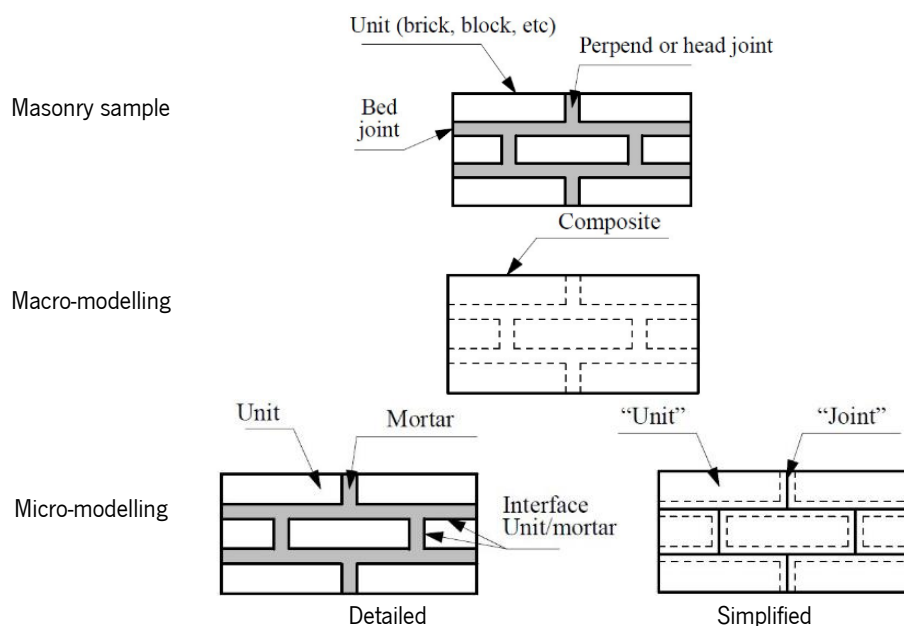


Figure 2-16. Modelling strategies for masonry structures. Adapted from Lourenço (2002).

From the literature (Lourenço, 1996, 2002; Roca *et al.*, 2010), it emerges that accuracy and easiness are indicators that lead to the choice of the type of modelling, based on the needs and the applications, without forgetting the computational facilities. Some examples of FEM applications on cross vaults are next reported.

Macro-modelling

The study of Creazza *et al.* (2002) on a masonry cross vault (Figure 2-17a) follows the macro-modelling approach, where homogenised mechanical properties are calibrated based on experimental tests (Faccio, Foraboschi and Siviero, 1999). Creazza *et al.* (2002) perform displacement control analysis, fixing vertically the model and placing horizontal springs to simulate the boundary conditions. The results show good consistency with the failure mode and maximum capacity, but poor comparison with the expected displacements domain.

Milani and Tralli (2012) propose a two-step model based on the idea of considering masonry elements as a structure, composed of a periodic substructure called “representative element of volume” (REV). REV is composed of a central brick linked to its six neighbours through zero-thickness joints and it changes according to the type of masonry vault considered. In the first step, each brick is meshed by six nodes wedge elements, considering rigid-infinitely resistant, with non-linear elastoplastic and softening interfaces. In the second step of the model, at macro-modelling level, FE non-linear analysis is performed. This approach reduces the computational efforts of the micro-modelling and at the same time improves the inaccurate schematization of the macro-modelling. Furthermore, Holzer (2011, 2013) developed a simplified FEM approach that incorporated an incremental loading analysis. Also, Milani and Tralli (2012) and Holzer (2011, 2013) validate their approaches by using the experimental campaign carried out by Faccio *et al.* (1999) (see Figure 2-17b,c).

Nowadays several FEM models with macro modelling approaches are available in the literature. For example, Milani *et al.* (2019) introduced the 3D advanced non-linear modelling strategies for the evaluation of the cross vault of St. John Hospital in Jerusalem, tested by Fagone *et al.* (2016). A FEM model is prepared in Abaqus, where masonry is modelled using a concrete damage plasticity material, a rigid element and springs approach, which is compared with a model where an upper bond limit analysis with NURBS elements is implemented (Milani *et al.*, 2019).

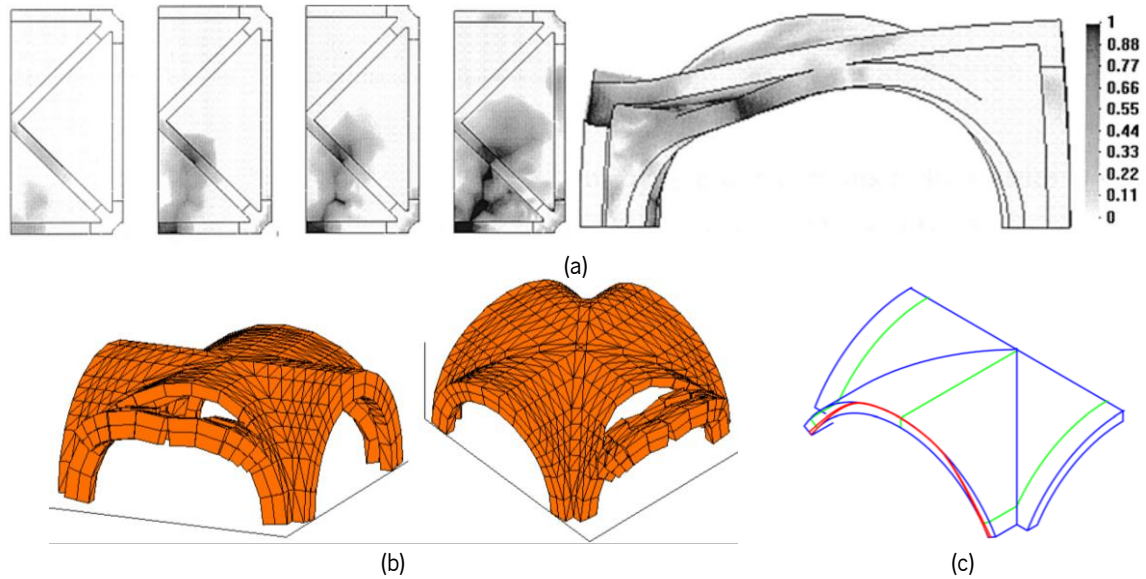


Figure 2-17. FEM macro models of the groin vault tested by Faccio *et al.* (1999): (a) damage contours for the deformed configuration by Creazza *et al.* (2002), (b) deformed shapes at peak Milani and Tralli (2012), (c) Sabouret cracks (in red) on the vault studied by Holzer (2011, 2013).

Micro-modelling

When masonry double-curved elements are contemplated, the simulation of the actual crack propagation is not always accurate using macro-modelling (Tralli, Alessandri and Milani, 2014), and the micro-modelling approach may overcome this issue. Specific attention is given to the works carried out by Milani *et al.* (2016), Alforno *et al.* (2020, 2021) and Gaetani *et al.* (2021), because they validate their finite element models with micro-modelling strategy through the experimental campaign performed by Rossi *et al.* (2016), on the groin reduced-scale vault, 3D printed, with dry joints.

Milani *et al.* (2016) simulate the small blocks using rigid-infinitely resistant 3D elements (parallelepipeds, tetrahedrons and wedges) connected by elastoplastic interfaces with softening. Alforno *et al.* (2020, 2021) use Abaqus software, adopting a built-in friction interface model, while Gaetani *et al.* (2021) concentrate the only source of physical non-linearities on the interfaces. Only the non-linear static analyses are performed by the previous authors.

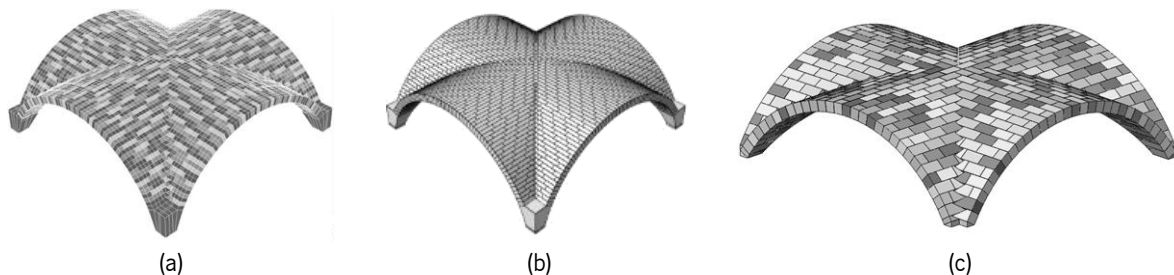


Figure 2-18. FEM micro models of the groin vault tested by Rossi *et al.* (2016): (a) Milani *et al.* (2016), (b) Alforno *et al.* (2020, 2021), (c) Gaetani *et al.* (2021).

As already anticipated in Chapter 1, Rossi *et al.* (2016) 's specimen is also the object of this thesis. Thus, more details are given in Chapter 4.

2.3.4 Discrete element method (DEM)

In discrete element method (DEM), the material is observed as an assembly of distinct masonry units, rigid or deformable which interact along their boundaries (interfaces) behaving according to frictional behaviour (Lemos, 2007; Giresini *et al.*, 2014). This ensures a precise simulation of the separation between blocks, including the sliding at the joints. Although this formulation started being used in the field of rock mechanics (Cundall and Strack, 1979, 1980; Cundall and Hart, 1992), it has been also used for modelling masonry structures (Pulatsu, 2015; Lemos and Campos Costa, 2017), because it is able to simulate accurately the non-linear behaviour of the material.

Indeed, DEM captures the displacement caused by separation or sliding at the joints, replicating the mechanical interaction between the blocks of the structure and depicting the structural response for large displacements (Máca and Oliveira, 2017). In other words, DEM can reproduce the complete split between blocks and the corresponding changes on the contact surface and structural geometry. Those features make DEM a valuable numerical tool in particular for masonry vaults (Pulatsu, 2015), overcoming the conservative assumptions imposed by limit analysis. DEM properly simulates the progression of the failure due to the propagation of cracks and the deformation between each block.

The main characteristics of DEM models are the following (Lemos, 2007):

- blocks can be deformable or rigid and the deformation is concentrated at the joints;
- each block is discretised independently from its neighbours and their interaction is represented by points in the joints or edge-to-edge contacts;
- DEM models allow the complete separation between blocks;
- time-stepping algorithms are used to solve quasi-static problems.

Several static applications on cross or groin vaults are available in the literature (Van Mele *et al.*, 2012; Foti, 2015; Lengyel and Bagi, 2015; Mcinerney and Dejong, 2015; Lengyel, 2017; Fang *et al.*, 2018; Lengyel and Németh, 2018), but dynamic analyses are not common.

Van Mele *et al.* (2012) adopt a DEM code (3DEC) for studying the collapse of a 3D printed groin vault scale model due to large support settlements (Figure 2-19a). Lengyel and Bagi (Lengyel and Bagi, 2015) work consists of one of the few cases in which both DEM and FEM simulations are performed and compared (Figure 2-19b).

To support the enhancement of the results using DEM at the place of TNM, Fang *et al.* (2018) describe the stability of vaults under varying geometric parameters and then determine the minimum thickness, for which the structure is stable, together with the observed collapse mechanism for unstable structures (Figure 2-19c). An interesting outcome by Fang *et al.* (2018) is that, in the groin vault, some dependency on friction angle for stability is shown for thickness-to-radius ratio (t/R) values between 0.13 and 0.20. In this case, the friction angle of 43° is well above the minimum friction angle between stability and instability. Above $t/R = 0.20$, a groin vault with any joint friction angle over 20° is likely to exhibit stability. Remarkable is also the recent contribution of Masi (2020). For the first time, blast dynamic analysis is performed on a cross vault (Figure 2-19d). Physical models confirm the displacement capacity of the model and the collapse failure numerically obtained, giving confidence to the method.

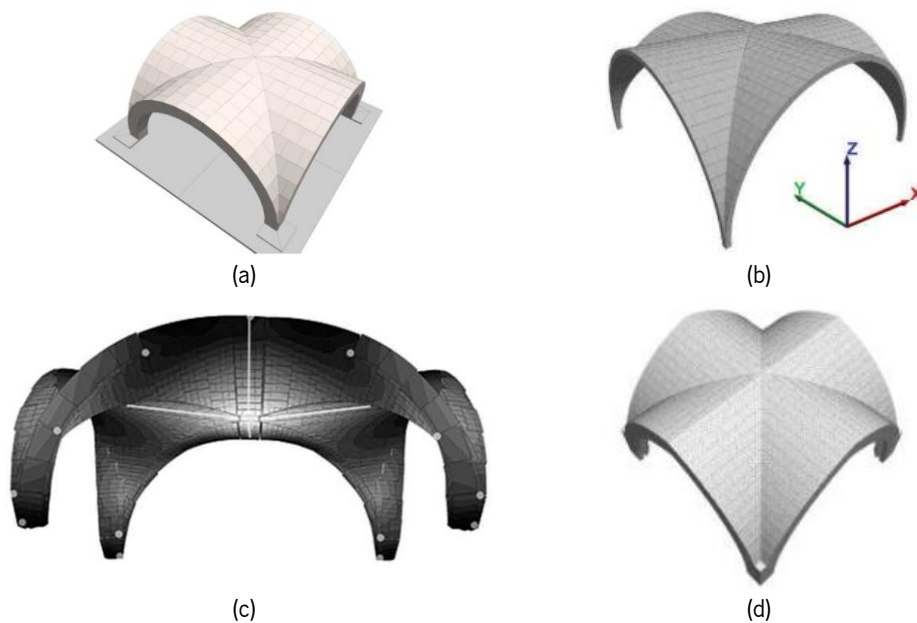


Figure 2-19. DEM models of the cross vault: (a) Van Mele *et al.* (2012), (b) Lengyel and Bagi (2015), (c) Fang *et al.* (2018), (d) Masi (2020).

2.3.5 Discrete macro element method (DMEM)

Lastly, the discrete macro element (DMEM) approach is another modern method where large blocks describe entire portions of the structure, reducing in this way the number of degree of freedom (NDOF) and the computational effort (Pantò *et al.*, 2016). Calìo (2010) and Cannizzaro (2011) introduce a specific non-linear macro-element for curved geometry masonry elements and, therefore, applicable to vaulted structures. This modelling technique expects rigid side elements with diagonal springs (Figure 2-20a), in order to consider the in-plane deformation, while the interaction between themselves is ruled by non-linear links placed orthogonally or parallelly to the interfaces (Figure 2-20b). The number of links

is decided by the user: a high number of links involves high computational effort, but the NDOF remains constant. Caliò (2010) and Cannizzaro (2011) replicate through DMEM method Faccio *et al.* (1999)'s tests (Figure 2-20c), adopting link stiffness calibrated through homogenised mechanical properties. A well matching for the ultimate load is obtained, at the expense of showing larger displacements.

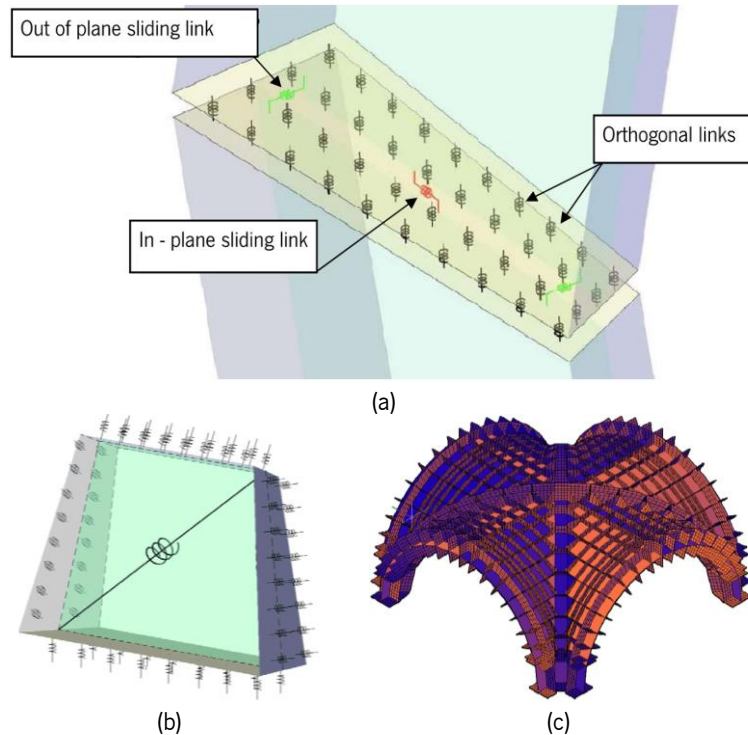


Figure 2-20. Macro-element method and models: a) interface element, b) four-node element with diagonal spring and interfaces links, c) DMEM model of a cross vault (Caliò, Cannizzaro and Marletta, 2010).

2.3.6 Final remarks on analytical and numerical investigations

For the complete list of all the numerical contributions on vaults, the reader is referred to Annex 1 of this document. To summarise, the following conclusions are drawn from the literature review on numerical modern methods:

- despite the extensive use of cross vaults in the built cultural heritage and the already performed numerical investigations with different approaches, predicting their structural behaviour is still a challenging task (Bertolesi *et al.*, 2019).
- geometrical and mechanical features influence the vault failure and they are fundamental for an accurate seismic assessment, without discarding the different characteristics of the seismic input.
- various methodologies have been developed and used to analyse the stability of masonry cross vaults, both in the local and global context of the structure, but only a few approaches have been utilised to study their dynamic behaviour, which is the focus of this doctoral thesis.

- limit analysis is an interesting and fast method to estimate the maximum load factor that vaults may stand. The kinematic limit analysis is the tool considered by national codes (such as Italian code (2018b)), as it provides a quick evaluation of the ultimate resistance of portions of structures subjected to horizontal loads. However, it is likely to overestimate the predicted load-carrying capacity. On the other hand, static limit analysis is interesting from a theoretical point of view but limited to materials unable to withstand tensile stresses, frequently associated with over-conservative predictions of the collapse multipliers.
- membrane theory is suitable for masonry vaults under dead loads, no horizontal actions and no cracks and/or point loads. A membrane analysis generates a safe lower-bound force system on the collapse load.
- macro FEM models are more accurate for the seismic assessment, and able to depict strains and stress per each loading step. However, FEM is computationally more demanding and collapse mechanisms are not always clear during the interpretation of the results. Micro-modelling approach provides realistic and detailed information on small portions loaded up to collapse, but it is challenging to adopt micro-modelling for large-scale structures or in all those cases where the actual masonry texture is difficult to identify, especially along the thickness.
- DMEM is another interesting method where any kind of analysis (except cyclic analyses) is used to investigate curved geometry masonry construction by means of non-linear macro-elements. However, DMEM's accuracy is strongly influenced by the mesh discretization.
- being represented by elements and contacts with friction and cohesion, DEM is particularly indicated for modelling masonry ancient structures. DEM can correctly depict the failure mechanism, while quantitative damage indicators (such as strains, or crack width) are not estimated. DEM requires considerable computational effort even in the analysis of relatively small examples, because, also static loads are applied by imposing a slow velocity ramp at the base of the structure, but on average lower time of analysis are found in comparison with FEM models due to the explicit solution solver (if the number of blocks is moderate).

This page has been intentionally left blank

3. Reduced-scale vault: shaking table tests

3.1 Introduction

Within the context of experimental campaigns, there are no equivalent methods which can represent the seismic behaviour of the structure as successfully as shaking table tests - the most adequate type of test to study the seismic behaviour of structures in the laboratory. Hence, with the aim of better understanding the seismic response of vaulted structures, the present chapter deals with the analysis of the seismic behaviour of a reduced-scale groin vault assembled by dry joint 3D printed voussoirs through shaking table tests. The tests have been carried out in the Laboratory of Civil Engineering (LNEC) in Lisbon (Portugal) using a three-axial platform. Dry joint specimens allow to easily perform several tests, without changing the initial conditions and without damaging the specimen itself. In addition, being the contribution provided by the strength of the joints neglected, their assessment can lead to a conservative response.

This Chapter describes the geometry, materials and setup of this specific specimen, which is tested by imposing the excitation along the longitudinal direction, which can cause the in-plane shear failure of the vault webs. The study has a twofold goal: first, it gives insight into the capacity of the vault undergoing different seismic excitations, namely a ground motion recorded in Mirandola (Italy) during Emilia Romagna's earthquake in 2012 and one artificial code-based earthquake for the same location (Mirandola); secondly, it provides information for validating numerical models based on rigid-infinately resistant voussoirs and friction interfaces elements.

3.2 Description of the reduced-scale groin vault

3.2.1 Geometrical aspects and materials

The specimen consists of a reduced-scale (1:5) 3D printed vault made of plastic blocks with dry joints, already tested under static conditions by Rossi *et al.* (2016), as anticipated in Chapter 2. Rossi *et al.* (2016)'s results are recapped in subsection 3.3 because they are fundamental for the calibration of the numerical models. This specimen is derived from the intersection of two semi-circular barrel vaults, generating a squared base groin vault, with a net span of 0.625 m and a rise of 0.225 m. The groin vault is composed of 1132 blocks: 880 made of plastic with a steel core (Figure 3-1a) and 232 made fully of plastic only located along the diagonals of the specimen (Figure 3-1b). The shape of the blocks

is slightly trapezoidal to compensate for the absence of mortar between them (Figure 3-1a), while the elements located along the diagonals (Figure 3-1b) present three different not-planar surfaces to reproduce the correct closing surfaces between the adjacent webs, improving the cohesion, and to replicate as closely as possible the shape of real intersecting blocks.

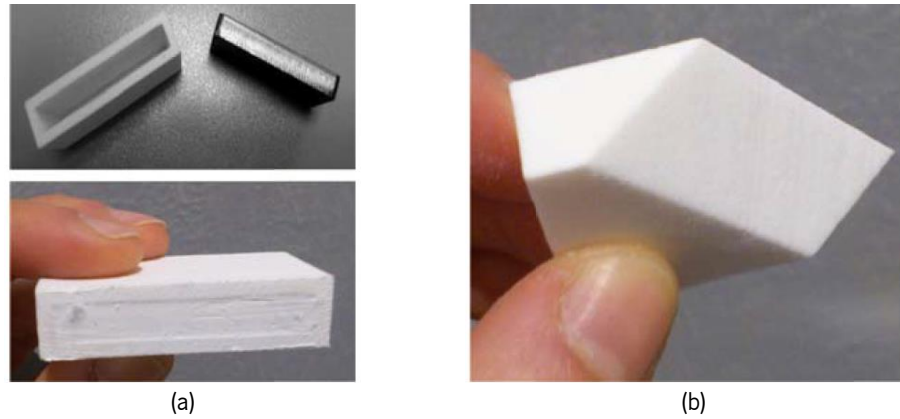


Figure 3-1. Details of the blocks of the specimen: (a) the standard blocks with the steel core, (b) an example of a diagonal block without the steel core (Rossi, Calderini and Lagomarsino, 2016).

The standard blocks' dimensions (red blocks in Figure 3-2) are designed by scaling per 5 the typical dimensions of full-scale clay bricks, namely $0.06 \times 0.12 \times 0.24 \text{ m}^3$ (respectively width, thickness, and length). The scaled block thickness t_b is approximately 0.012 m and it is constant along the shell. The width w_b is 0.024 m, and the length l_b is variable. In particular, l_b along the edges varies from 0.014 m to 0.050 m, while all the other standard red blocks are 0.048 m long (see blocks characterised by different colours in Figure 3-2a). This allows to guarantee the offset of the joints, which is equal to $\frac{1}{4}$ of the length of the standard blocks and to maintain a good interlocking of the bond. Each block is also identified by a numeric code to easily rebuild the specimen after each test. The blocks' stereotomy is radially arranged. This bond configuration directly transfers the thrusts to the supports and it is a typical characteristic of medium and large vaults in historic buildings.

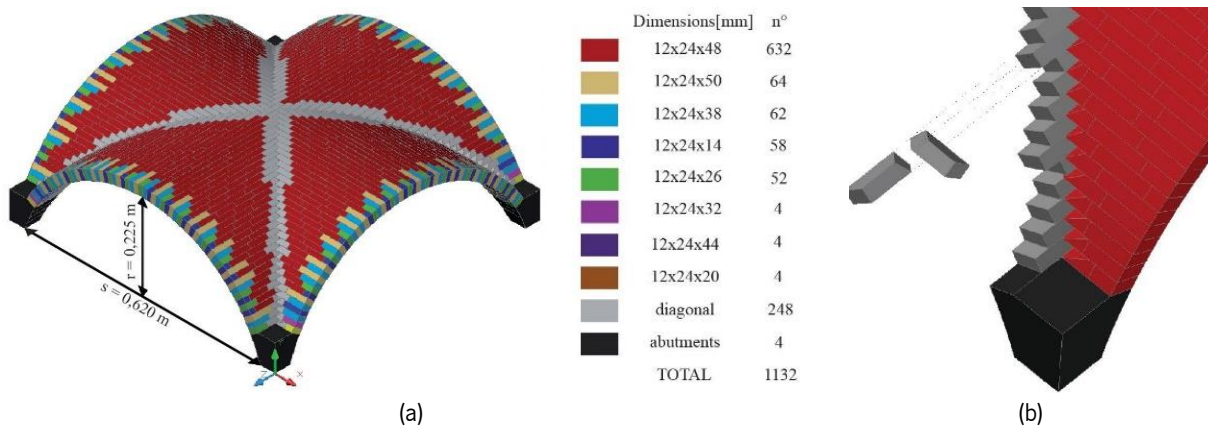


Figure 3-2. Geometry of the reduced-scale vault: (a) stereotomy, (b) details of the diagonal blocks (Rossi, Calderini and Lagomarsino, 2016).

The blocks have been 3D printed with the selective laser sintering (SLS) technology, which allows generating small-scale models by a numerically controlled machine, starting from a 3D digital model, with high geometrical accuracy (± 0.1 mm) and a reasonably short time of production. Indeed, the time of production is estimated between 4–5 hours for the blocks of the shell, and 2 hours for the supports, counting a total duration of about 6–7 hours.

The adopted plastic material is a composite of zp150 powder and zb61 clear binder, printed with a ZPrinter 650. For the sake of clarity, this composite is made of vinyl polymer and carbohydrate plastic powder, bonded with a solution of humectant and water. After production, the blocks have been impregnated with Z-bond 101 for improving strength, adhesion, and durability. This technique ensures good stiffness and friction that allows taking into account rigid block assumption and permits the repeatability of the tests by minimizing the damage. Indeed, the choice of adopting this particular material and technology is led by the need of performing several tests with different configurations without causing damage to the units.

Due to the accumulation of errors in the 3D printing of the blocks, very thin steel plates have been designed and placed at the key of the vault so that the shell can be perfectly closed (Figure 3-3b). The thickness of these small plates varies from 3 mm (at the outer edges) to less than 1 mm (at the centre of the vault), while their length is fixed (48 mm).

The radial bond needs a temporary structure for the construction of the shells, also at this reduced-scale level. Therefore, a scaffolding made of plywood has been designed (Figure 3-3a), which is composed of four wooden pieces corresponding to the four vault webs. Once the specimen is built, the scaffolding is removed by letting the pieces slide on properly inclined aluminium rails, visible in Figure 3-3.

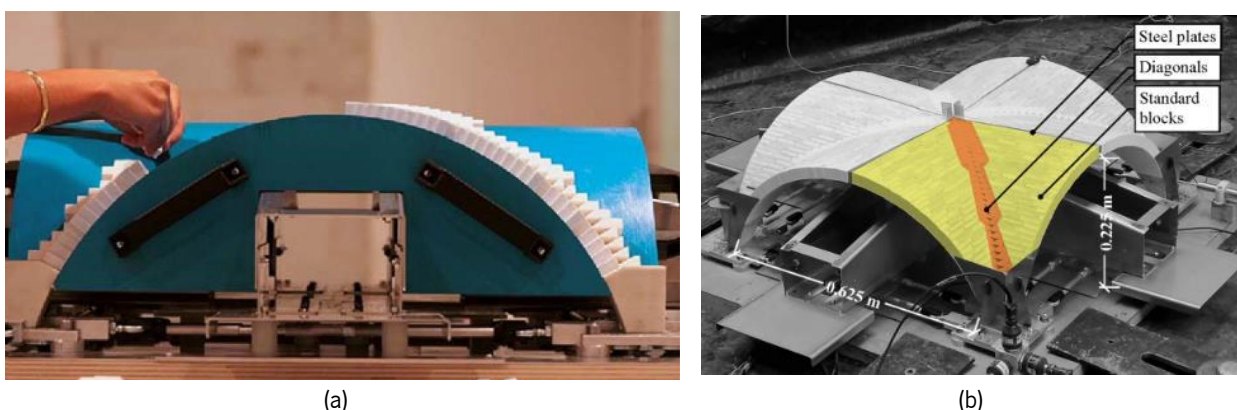


Figure 3-3. Reduced-scale vault assembly: (a) details of the construction on the plywood scaffolding, (b) at the end of the construction with the thin steel plates.

Care and attention are required to remove the scaffolding, in order to avoid undesirable configurations, instabilities and slacks in the assembly. This aspect is important to ensure the repeatability of the tests since defects in the construction process and dismantling could compromise the results and their comparisons. In this sense, after each trial, the vertical drop of the key of the vault is measured through a plumb line while removing the scaffolding, which measures on average 15 mm.

As anticipated, the weight of the standard blocks and of the blocks along the outer edges is increased by inserting a steel core inside each block (Figure 3-1a). This is done to increase the axial compressive stress of the shell of the vault, improving its stability. The reason is driven by the low value of density of the composite material (zp150 powder and zb61 clear binder) that may compromise the success of the experimental campaign. In this way, the density of the standard blocks (yellow blocks in Figure 3-3b) is increased at the value of $\rho_{\text{St.blocks}} = 2.70 \pm 0.05 \text{ g/cm}^3$. Because of their irregular shape and tiny volume, which could not host a steel core inside, the blocks of the diagonals (orange blocks in Figure 3-3b) maintain the original density of the material, which is equal to $\rho_{\text{diag}} = 0.55 \pm 0.02 \text{ g/cm}^3$. Both densities were determined using an electronic high precision scale and knowing the volume of each block. The disposition of the densities along the specimen is symmetric along the diagonals for all four webs. The final weight of the specimen is about 35.6 kg, while the whole structure is about 43 kg, considering the rigid base at the bottom of the specimen. Young's modulus of the masonry assembly composed of standard blocks and dry joints is measured by compression tests on pillars constituted of six standard blocks. Its mean value ($E_m = 123 \text{ MPa}$) is a homogeneous value representative of the masonry of the shell of the vault, even if highly dependent on the normal stress level at the joints. The mean friction coefficient μ between blocks is equal to 0.56, corresponding to the friction angle of $29.60^\circ \pm 2.50^\circ$, determined by testing 12 samples of standard blocks on the tilting table. The assumed values of the density and Young's modulus of all the steel elements (plates at the key of the vault and steel corners to confine the shell) are equal to $\rho_{\text{Steel}} = 7800.0 \text{ kg/m}^3$ and $E_{\text{Steel}} = 210 \times 10^3 \text{ MPa}$, respectively.

The geometry of the vault, the choice of the radial orientation, and the definition of the cuts along the diagonals are guided by the rules of thumb gathered from Rodrigo Gil de Hontañón (cited in Sanabria (Sanabria, 1982)), Formenti (1893), Heyman (1982), Heyman (1995a), Huerta (2004), Cangi (2012), Como (2017), Giovanetti (2000). The specimen aims at representing a full-scale cross-section of a central bay located in a lateral nave of a three-nave church, derived from the intersection of two semi-circular barrel vaults with low rise - a generic monumental church (Figure 1-8b) commonly found in Central Italy, generated by a squared base groin vault with a net span of 3.125 m and 1.125 m rise at

full-scale. Referring to ancient treatises (Heyman, 1995a), masonry cross vault's behaviour is mainly linked to the geometry of the system, namely size and shape, and less depending on mechanical properties. Hence, even if this vault includes different types of materials and the scale reduction factor equal to 5 is considerable, it is still able to represent the main features of masonry groin vaults.

The choice of using a dry joint specimen is also an important aspect. Dry joints specimens may represent not only real dry joint masonry structures but also ancient mortar joint structures whose mortared joints suffered decay during the time, decreasing their already low tensile strength (Lourenço and Ramos, 2004; Pulatsu *et al.*, 2019). A dry joint specimen also allows to easily perform several tests, without significantly changing the initial conditions. Several authors refer that the stiffness of the joints does not have a significant contribution to the response at the collapse of vaults, even if this is only valid for static loading (Giamundo *et al.*, 2014; Sarhosis, Garrity and Sheng, 2015). Moreover, ignoring the contribution provided by the strength of the joints can lead to a conservative response.

3.2.2 Setup testing

The setup was carefully designed, aiming at obtaining the relevant outputs associated with the shear failure of the specimen, with similar conditions to real prototypes (see Figure 1-8). In order to simulate the particular boundary conditions that cause an in-plane shear response of the vault, the special testing device adopted by Rossi *et al.* (2016) was also used. It consists of a frame composed of four steel squared plates, linked to each other by the use of 8 aluminium bars, coupled and hinged at both ends with uni-ball joints. The cross-section of the aluminium bars is hollow with internal and external radii of 8 and 10 mm, respectively. In this way, the distance between the abutments is maintained constant and their rotation along the vertical axis is prevented. Moreover, the abutments of the vault are rigidly fixed on the top of four steel squared plates through a hexagonal bar by interlocking (Figure 3-4a). As shown in Figure 3-4b-c, the abutments (or piers) p_1 and p_2 have been anchored using four bolts each, to connect the corresponding steel plates to the flat aluminium surfaces through the threaded holes (Figure 3-4b), while p_3 and p_4 are left free to move on the flat aluminium surface above four spheres each (Figure 3-4c). As discussed in Rossi *et al.* (2016), boundary conditions are a drawback of the specimen because they represent a specific configuration (fully fixed piers $p_1 - p_2$ and completely free piers $p_3 - p_4$), without taking into account the lateral wall along the fixed edge, as it is normal to find in real structures. However, this configuration is considered a representation of the safe side of reality, in which the specimen tends to be more deformable.

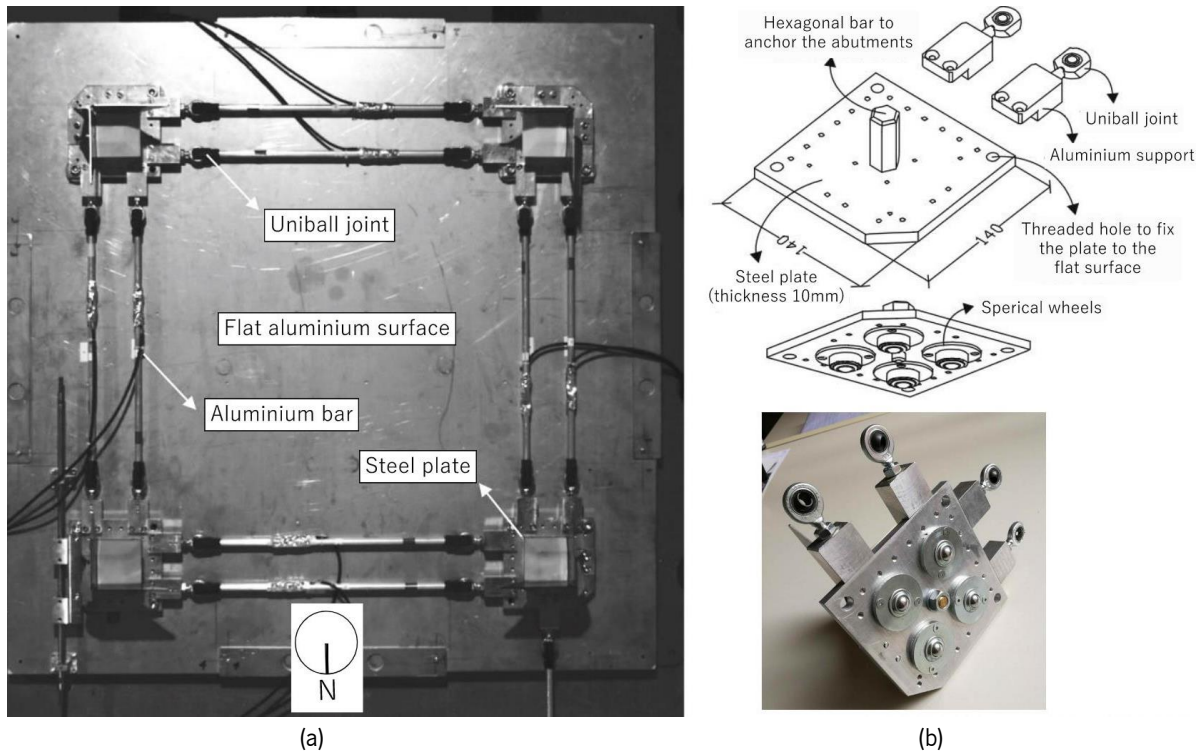


Figure 3-4. Experimental setup designed by Rossi *et al.* (2016): (a) movable frame to apply displacements, (b) details of the bottom face of the steel plates.

The instrumentation used in the shake table tests is analogous to those used for the quasi-static tests (Rossi, Calderini and Lagomarsino, 2016), though, due to the small geometrical dimensions of the specimen, specific apparatus was adopted for the shake table tests (Figure 3-5a). One linear variable displacement transducer ($LDVT_1$) is located at the NW corner, measuring the relative longitudinal displacement of the movable piers. Six piezoelectric accelerometers (Acc_{1x} , Acc_{1y} , Acc_{1z} , Acc_{2x} , Acc_{2y} , Acc_{2z} in Figure 3-4a) are placed at the bottom of the vault to measure the response of the fixed plate, while five variable capacitance unidirectional accelerometers (Acc_{3y} , Acc_{4x} , Acc_{5z} , Acc_{6x} , Acc_{7y}) are placed on the vault, since they are compatible with the dimension of the blocks in terms of dimensions and weight. Moreover, two optical cameras are used to record the response of the key of the western arch and the movable piers respectively along the plane xy ($OC_{1x,y}$) and yz ($OC_{2y,z}$). Two video cameras are placed to record the tests, one exactly at the top of the model using scaffolding pipes and one located in front of the East elevation on a tripod outside of the shaking table, for avoiding interferences and noises in the records. From those cameras, the collapse mechanism is evaluated as seen in 3.4.3 (Bianchini *et al.*, 2021). The reduced-scale specimen is placed and anchored to the North-East corner of the slab above the shaking table (Figure 3-5b). Even if this location is eccentric with respect to the barycentre of the slab, the triaxial platform of LNEC rigidly transfers the time histories of the inputs to the specimen.

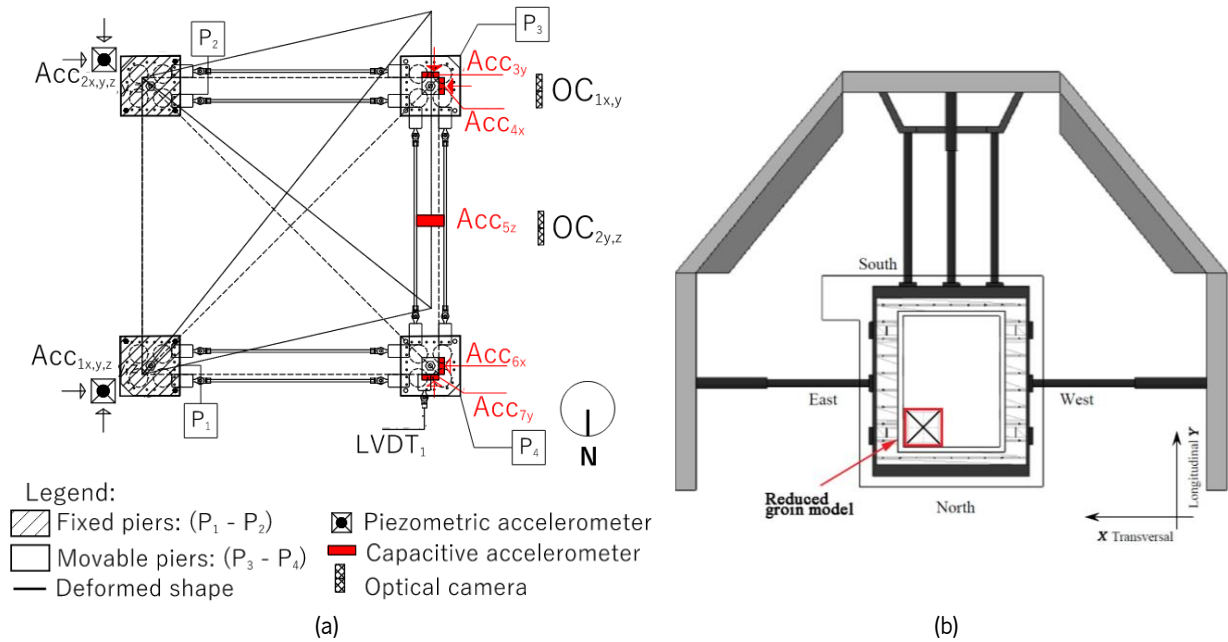


Figure 3-5. Experimental setup of the reduced-scale vault: (a) adopted instrumentation in the shake table tests (top view), (b) shake table plan with the location of the specimen (highlighted in red).

3.3 Preliminary experimental campaigns

The main results obtained from the monotonic quasi-static tests performed by Rossi *et al.* (2016) are briefly recalled in this section since they will be useful for the calibration of the numerical models (see Section 4.2). Rossi *et al.* (2016)'s tests are also summarised in order to compare analogies and differences, observed on the groin vault, due to the two types of loading: quasi-static and dynamic.

3.3.1 Monotonic quasi-static tests: in-plane shear tests

Rossi *et al.* (2016) simulate the simple shear mechanism of the masonry vault, as shown in Figure 3-6, in order to apply in-plane shear distortion. The two piers (p_1 and p_2) are fixed to the aluminium surface, while piers p_3 - p_4 are left free to move. The displacement is applied by an external actuator at the pier p_4 along the Y (longitudinal) direction. The displacement d_{s1} is monitored by means of an linear variable differential transformer (LVDT), while the related force F_{s1} are measured by a load cell close to the actuator. The development of the mechanisms up to the collapse is recorded by two high-resolution/high frame rate cameras. It is observed that, in general, all webs show a typical four-hinge asymmetric arch mechanism, opposite in sign. The diagonal shear crack in the extrados can be noted and the first collapsing web is the one connecting p_3 - p_4 where the displacement is applied. The maximum force varies approximately from 13 to 17% of the total weight of the specimen (349.2 N) while the shear distortion drift (measured by the ratio of the maximum displacement to the free span of the vault) is in the range of 3.8 - 4.8% (Figure 3-6b).

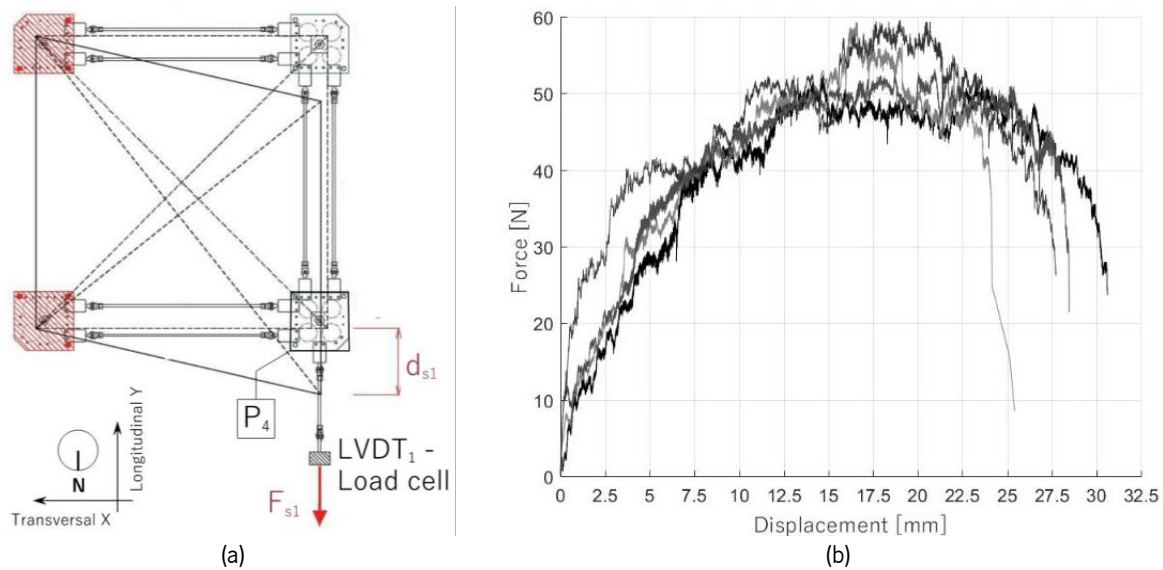


Figure 3-6. In plane-shear quasi-static tests from Rossi *et al.* (2016): (a) tests setup, (b) force-displacement curve (four tests are shown with similar conditions).

3.3.2 Monotonic quasi-static tests: tilting plane tests

Tilting plane tests were also performed under quasi-static conditions, aiming at evaluating the collapse multipliers for different directions of seismic action. Thus, the vault is subjected to horizontal forces proportional to its mass. The lateral acceleration directly acts at the mass of the vault, while all the abutments are fixed. In this static testing technique, the specimen is set on a plane that is progressively inclined at an angle β , producing horizontal inertial forces proportional to the masses. The final angle of inclination β at the collapse corresponds to the maximum horizontal multiplier of the gravity forces of the structure. At the same time, different directions of the seismic action are considered by varying the angle Φ between the axis of rotation of the tilting table and the axis of symmetry of the vault (Figure 3-7). During the tests, six values of Φ are considered, namely 0° , 9° , 18° , 27° , 36° , 45° . All the piers of the vault are fixed at the aluminium surface and the vault is on a tilting plane that can slowly rotate around one axis, being loaded by the gravity acceleration.

The resistance domain of the vault obtained from the tilting plane tests, as a function of the direction of the seismic action, is shown in Figure 3-7b. The value of the collapse angle is rather constant and always in the range of $18\text{--}19.2^\circ$, which corresponds to a $\lambda = 0.33\text{--}0.35$. The unique outlier is depicted for $\Phi = 18^\circ$. In this test, the collapse occurred at a lower value ($\alpha = 16.5^\circ$), probably due to an improper assembling of the model.

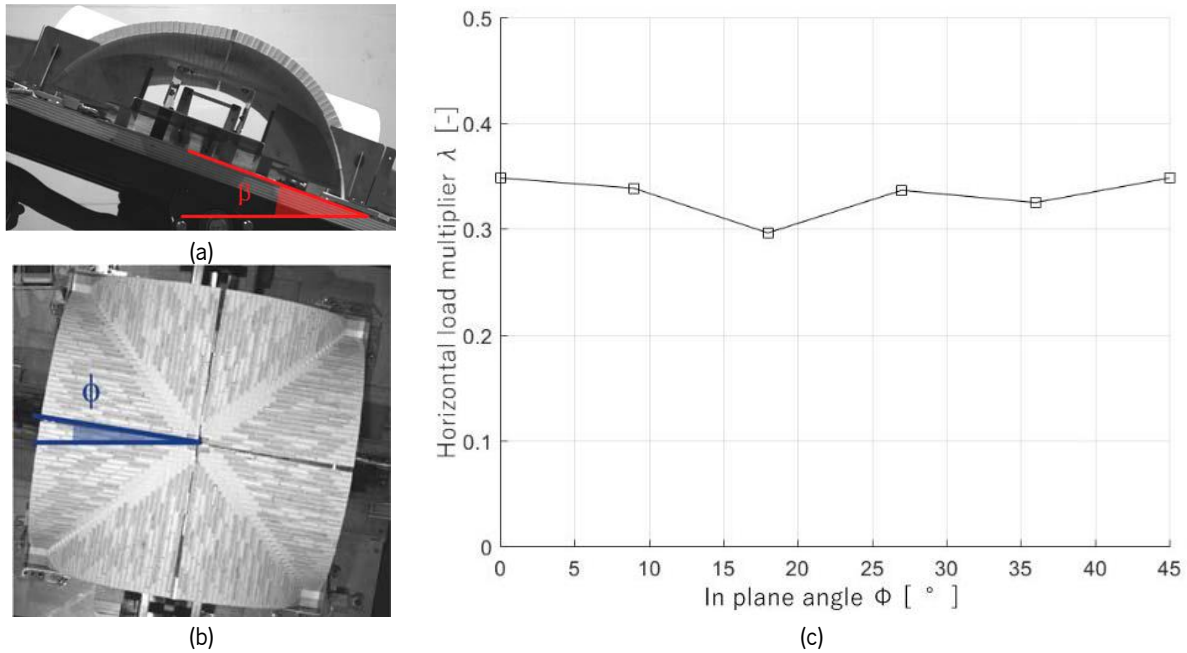


Figure 3-7. Tilting table tests from Rossi *et al.* (2016): (a) tilting angle β , (b) rotation Φ around its orthogonal axis, (c) tilting plane tests results.

3.4 Shaking table tests

The main objective of shaking table tests is to depict the modal parameters of the reduced groin vault, useful for the dynamic calibration of the numerical models, and to assess the seismic performance of the specimen when subjected to different types of earthquakes, namely the recorded Emilia earthquake, and compatible accelerogram with the design response spectrum defined by the Italian code NTC2018 (here named as “artificial”). The two objectives can be satisfied by performing dynamic identification tests and seismic tests, respectively. With both types of tests, the boundary conditions are set as described in 3.2.2 (Figure 3-5a) to induce the in-plane shear mechanism on the shell of the vault, in which the two piers of the vault are fixed to the steel base (p_1 – p_2), and the other two piers (p_3 – p_4) are free in the horizontal plane. From the dynamic tests is also possible to define a damage indicator based on the decreasing of the natural frequencies of the specimen as a function of the increasing of the seismic action amplitudes. From the seismic tests, the response of the vault is evaluated in terms of crack patterns, capacity curves and drifts for Emilia and artificial inputs.

3.4.1 Dynamic identification tests

Dynamic identification tests allow the estimation of the modal properties in the elastic regime of the specimen. In this study, forced vibration tests are performed, in which the input and the response are measured. This kind of test is, characterised by a known input, namely a “white noise” random signal

(Ramos, 2007; Mendes, Lourenço and Campos Costa, 2014), with a wide frequency range (0.1 – 40 Hz) and low amplitude, a duration of about 165 s and it is applied along all the directions by the platform (Figure 3-8). The duration of the intense phase of the signals is about 125 s and the maximum amplitudes are about 0.17 g, 0.22 g and 0.20 g in the transverse, longitudinal and vertical directions, respectively.

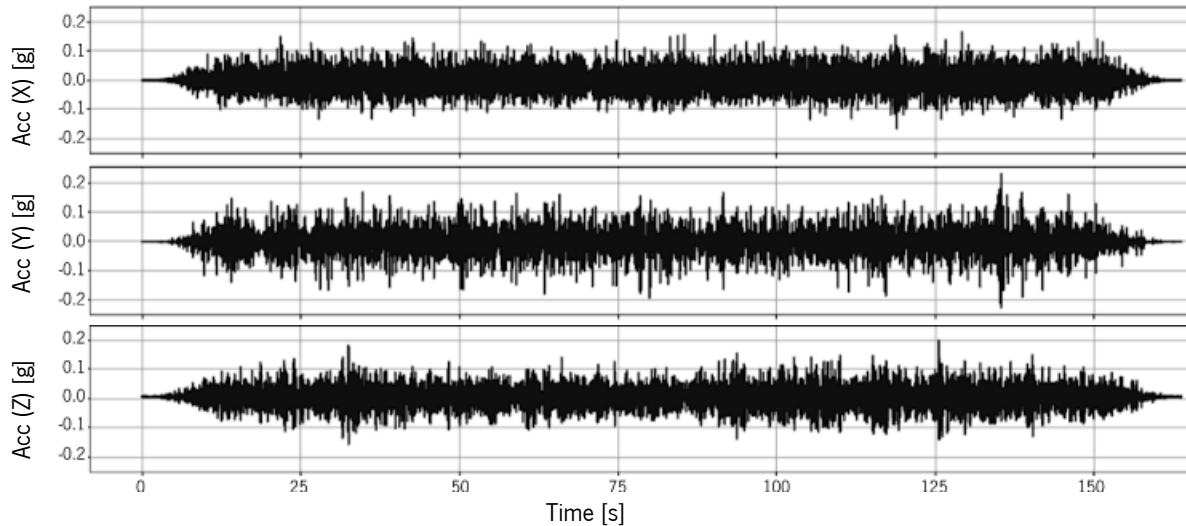


Figure 3-8. Input signals of the dynamic identification tests along X (transverse) direction, Y (longitudinal) direction and Z (vertical) direction

The dynamic identification tests aim at determining the modal parameters of the undamaged and damaged configurations making the amplitudes of the white noise input vary (displacement from 3 mm to 8 mm). This is necessary for evaluating the influence of the amplitude of this signal on the dynamic properties, and these outcomes are particularly relevant. Given the use of dry joints, their stiffness is highly dependent on normal stress and the structural vault stiffness is also dependent on the crack opening of the joints.

In fact, the frequencies range from 3.22 Hz (for 8 mm of amplitude) to 4.50 Hz (for 3 mm of amplitude), with a variation of about 0.25 Hz per 1 mm of amplitude. As expected, the increase in the signal amplitude (nominal displacement) causes a decrease in the frequency of the specimen (Figure 3-9). The reduction of the frequencies is associated with the opening of the joints (“damage” on the specimen), which is higher when the amplitude of the input is increased, corresponding to non-linear behaviour. In order to verify the sensitivity of the model to the construction process, the specimen is rebuilt four times (Construction A, B, C, D in Figure 3-9) by the same builders, following the same construction procedure. It is found that dynamic identification tests, carried out on different days, present similar frequencies for the same signal amplitude (5 mm), leading to the conclusion that the specimen exhibits a small scatter of the modal frequencies (between 3.9 and 4.2 Hz), despite the

different constructions and environmental conditions, validating the methodology adopted for these tests.

The value of 4.0 Hz (for 5 mm of amplitude) is considered the first natural frequency (initial reference value) of the specimen because it is a good compromise between the quality of the response signal and the very low non-linear behaviour (opening of the joints). The dynamic identification tests have been repeated after each seismic test, keeping constant 5 mm of amplitude, to identify small variations in the frequency of the specimen as an indicator of permanent damage due to the movement of the blocks, sometimes not easily identified by the human eye (Sharma *et al.*, 2020).

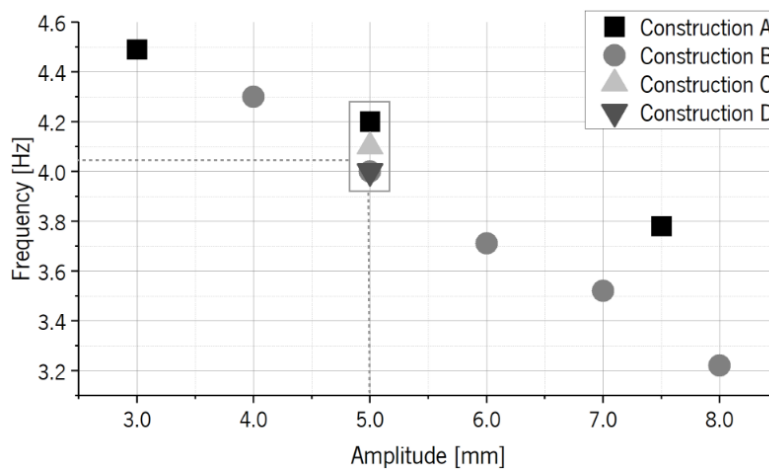


Figure 3-9. Frequencies decrease trend as a function of the increasing amplitude of the signal of the dynamic identification tests.

3.4.2 Seismic tests: inputs and damage indicators

During the seismic tests performed on the shaking table, two types of ground motions were used: Emilia earthquake and an artificial accelerogram. The first seismic input motion was recorded by the seismic station located in Mirandola (Station code: MNR) (Italy) (Moretti, Azzara, and Bono 2013), which registered the Emilia Romagna's earthquake on the 29th of May 2012 at 06:59:53 (UTC), with a Richter magnitude of 5.8. MNR is the closest station to the epicentre that belongs to the RAN network (managed by the Italian Department of Civil Protection). The second seismic input is an artificial compatible accelerogram with the elastic response spectrum defined by the Italian Code (Ministero delle Infrastrutture e Trasporti, 2018c), selecting again the municipality of Mirandola and rock type of soil.

The use of two different types of inputs (impulsive Emilia earthquake and artificial accelerogram) is determined by the significative importance of investigating the response with one dominant pulse action and one regular signal with an almost constant intense phase, expected by the Italian Code (Ministero

delle Infrastrutture e Trasporti, 2018c). Indeed, as stated in literature, *e.g.* Dejong and Ochsendorf (2010), it is expected that the primary impulse of ground motion is of crucial importance important in predicting the collapse of arches and vaults. On the other hand, artificial earthquakes have other specific characteristics, such as the multiple consecutive impulses and the higher duration of the action, that might have an amplifying effect on the rocking motion, also causing the collapse.

Figure 3-10 presents the elastic response spectrum of the Italian Code NTC 2018 (for the horizontal component) and the spectrum of the artificial accelerogram. The spectrum of the Emilia target input is also plotted in the same graph. The vertical dashed line represents the first natural frequency of the specimen equal to 4.0 Hz, corresponding to 0.25 s, in which the spectral acceleration of the Emilia target input (7.45 m/s^2) is about 3.14 m/s^2 above the spectral acceleration of the Italian Code (4.31 m/s^2). The total duration of the original recorded motions is 20 s but, before being applied in the seismic tests, it was scaled in order to follow the Cauchy-Froude's similitude, obtaining a total duration of 8.93 s. It is noted that the periods in Figure 3-10 are scaled according to the similitude relationships.

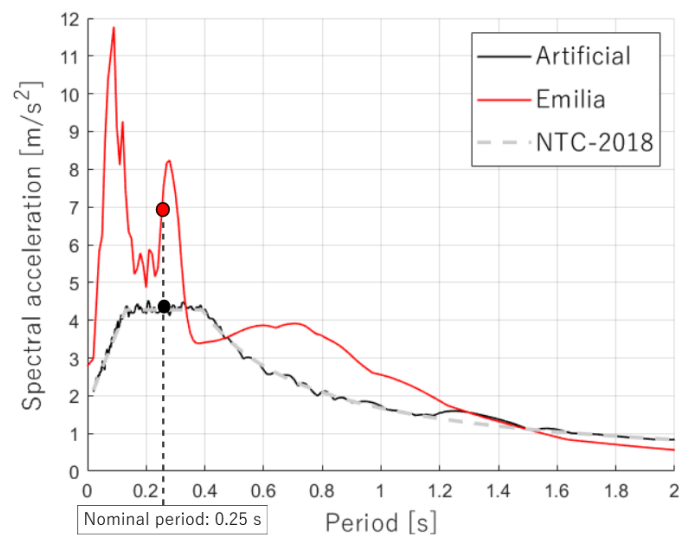


Figure 3-10. Elastic response spectrum of the selected input signals and comparison with the 475-year return period design spectrum for Emilia (Mirandola municipality) according to NTC2018.

Figure 3-11 shows the time histories of the scaled inputs, which correspond to 100% of the respective seismic action. The Emilia target input peak ground acceleration (PGA) is equal to 2.79 m/s^2 , peak ground velocity (PGV) is 0.24 m/s , and the maximum displacement (PGD) is equal to 31.00 mm . The artificial accelerogram presents a PGA equal to 3.51 m/s^2 , a PGV of 0.14 m/s and a PGD equal to 16.00 mm . The two inputs are also subjected to a signal processing based on a high pass Butterworth filter with 8 poles and a cut-off frequency equal to 1 Hz. These seismic inputs are applied to the structure during the seismic tests only longitudinally, *i.e.*, along the north-south direction, in order to excite the movable piers and induce the in-plane shear distortion on the vault (Figure 3-5).

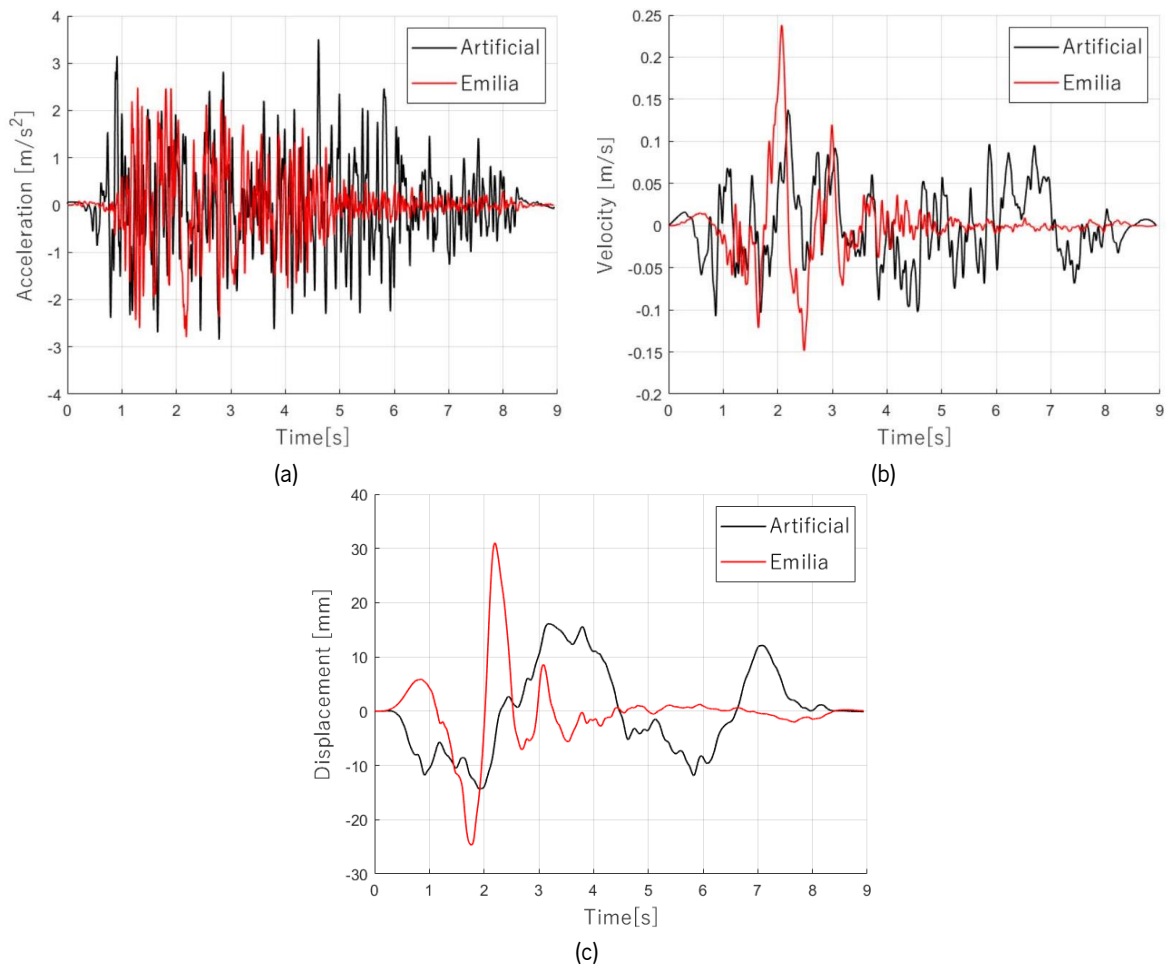


Figure 3-11. Scaled time histories of ground motions (Emilia and artificial) at the amplitude equal to 100% for the reduced specimen: (a) accelerations, (b) velocities and (c) displacements.

The testing sequence of the vault is presented in Table 3-1, in which the seismic action is applied with increasing amplitude until collapse. Before and after each seismic test, dynamic identification tests are performed, with the reference amplitude of 5 mm, in order to evaluate the decrease of frequencies as a function of the damage, which is almost equal to zero until 50% of the Emilia ground motion and until 100% of the artificial ground motion (Table 3-1). When only a few blocks fell during the test, the shell of the groin vault is repaired to keep the same starting point for the specimen (undamaged specimen). In total, the specimen has been built four times. Emilia input was applied three times to the vault (Construction 1, 2, 3 in Table 3-1), while artificial input is considered for Construction 4. Construction 2 is characterised by initial damage due to instabilities during the assembly. In fact, it presents a very low nominal frequency and only 60% of the Emilia earthquake led to a rapid collapse. The results of Construction 2 have been discarded by the post-processing analysis. In the case of the Construction 3 sequence, the damage of the specimen is not repaired, aiming at simulating a sequence of shocks and the consequent accumulation of damage.

Table 3-1. Sequence and description of the shaking table tests with the reduction of the frequencies for both types of inputs.

Tests with Emilia input			Tests with artificial input		
DIT	Seismic action	Notes	DIT	Seismic action	Notes
Frequency [Hz]	% of input		Frequency [Hz]	% of input	
Construction 1			Construction 4		
4.10		Undamaged	4.10		Undamaged
	10 %	No damage		50 %	No damage
4.10			4.00		
	25 %	No damage		75 %	No damage
4.00			4.00		
	50 %	Recovered		100 %	No damage
3.91			3.90		
	75 %	Collapse		125 %	Recovered
Construction 2 *discarded				150 %	Recovered
3.61		*initial minor damage	3.35		
	60 %	collapse		200%	Collapse
Construction 3					
4.10		Undamaged			
	55 %	unrecovered			
4.00					
	25 %	aftershock1			
3.42					
	35 %	aftershock2			
3.22					

From the sequences of dynamic identification tests and the reduction of frequencies is possible to measure the damage indicator d_n , directly linked to the variation of stiffness of the system and proportional to the ratio between the frequency $f_{i,n}$ of the n^{th} dynamic test and the first frequency f_0 equal to 4.1 Hz (close to the initial reference value). The damage indicator, defined according to Equation 3-1 (Giordano *et al.*, 2020), may range between 0, identifying the undamaged configuration, and 1, corresponding to the collapse.

$$d_n = 1 - \frac{f_{i,n}}{f_0} \quad \text{Equation 3-1}$$

Figure 3-12 presents the damage indicator as a function of the seismic amplitude, in terms of PGA, PGV and PGD, in which it is possible to observe that the slope inclination of the damaged phases, before the collapse, is the same for both kinds of inputs (Emilia and artificial) in terms of PGA, PGV and PGD.

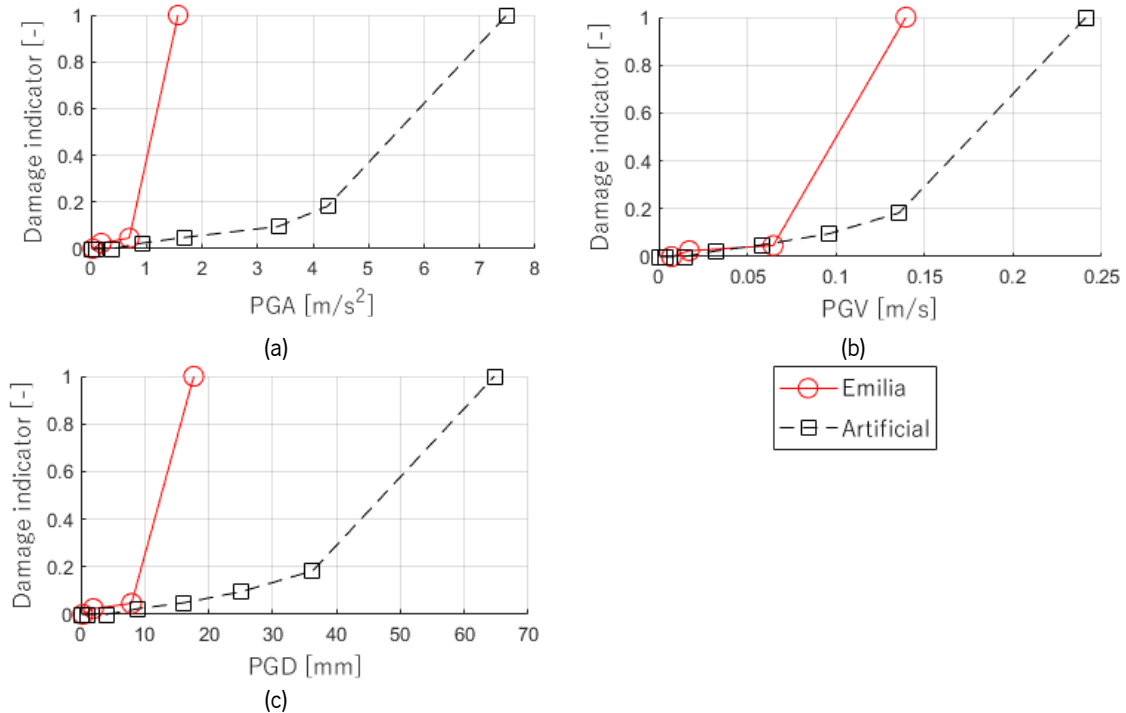


Figure 3-12. Evolution of the damage indicator as a function of the amplitude of the seismic action expressed in terms of (a) PGA, (b) PGV, (c) PGD.

3.4.3 Seismic tests: crack patterns and quantitative results

To have better insight into the possible seismic failure of historic groin vaults, an analysis of the collapse mechanisms that led to the collapse during the shaking table tests was done. The sequences of photos, extracted from videos, are useful to depict the number and locations of the hinges, the opening and closing of the joints and permanent damage (Figure 3-13). For the sake of conciseness, only the collapse mechanism and the time series of the displacements before reaching the collapse itself are compared, namely for the 75% of the Emilia input and the 200% of the artificial input (belonging to Construction 1 and 4 in Table 3-1).

A comparison with the results of the quasi-static tests carried out by Rossi *et al.* (2016) is shown. The complete set of experimental results of the reduced specimen is available in Annex 2.

Because of its impulsive nature, Emilia earthquake causes a rapid collapse of the vault, in comparison with the artificial accelerogram (Table 3-2). However, the type of collapse mechanism remains the same, in terms of the evolution of damage and the location of the hinges (Figure 3-13). Both types of seismic action are affected by in-plane shear behaviour, which occurs along the diagonals that join p_2-p_4 and p_1-p_3 , due to the positive and negative direction of the accelerations at the base. The first hinges occur at the longitudinal edges (East before and West later), while the transverse web located at the North side of the specimen keeps a simple-arch behaviour until the end of the tests. These

observations are valid for every amplitude of the shaking table tests, starting from the value of amplitudes that could cause a more relevant state of damage.

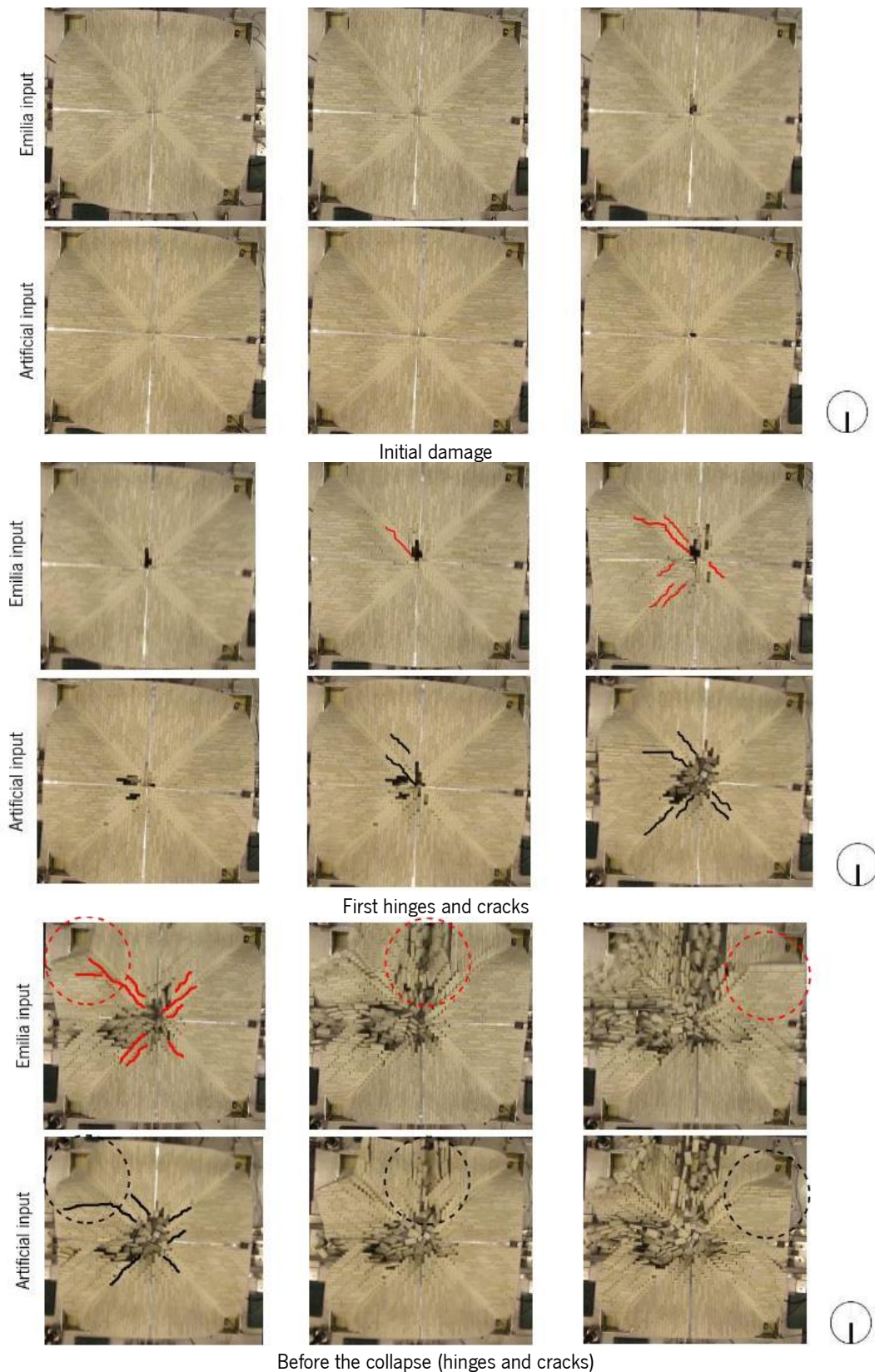


Figure 3-13. Damage progression during the intense phase of the Emilia seismic input 75% and of the artificial input (200%) (5 frames/s). (Left side: fixed supports p_1-p_2 ; right side: movable supports p_3-p_4). The main hinges are in red circles.

Looking at Figure 3-13 and Figure 3-14, the centre of the vault is the first to collapse in both kinds of tests, due to the geometrical configuration of the specimen characterised by the verticality of its joints. However, the fall of the blocks at the centre of the vault does not interfere with the shear failure, which is still recognisable. During the shaking table tests, both for the Emilia and the artificial input, the hinges started to appear from the East side of the specimen between p_1 – p_2 , the fixed piers, while during the quasi-static tests, the first hinge occurred between the movable piers (West side, p_3 and p_4) (Figure 3-14).

Analysing the shaking table tests results, the North and West webs continue to stand, even when the other webs already collapsed or are extremely compromised. The steel plates at the corners make the boundaries of the shell of the vault stiffer and, therefore, the hinges occur at the height of the curvature where the steel plates do not act anymore. This is in agreement with the prediction of Oppenheim (1992) and De Lorenzis *et al.* (2007), based on the minimum energy formulations. Considering the response obtained from the shaking table tests, the arch mechanism is clear (four hinges), and it is mainly associated with the edge side where the supports are fixed and the structure is more rigid (Figure 3-14). As widely observed for the behaviour of similar structures like arches, different loading distribution leads to different response. In the case of the vault, the three-dimensional complexity of the structure amplifies this concept - the quasi-static tests are mainly associated with the gravitational set of loads, while the shake table tests consider the inertial force acting on the structure. In this sense, the non-linear quasi-static approach may represent an approximation of the reality that does not replicate all loading scenarios. At the same time, even two different inputs in the shaking table lead to different quantitative conclusions due to the spectra contents of the seismic action itself (Figure 3-10). In fact, regarding the comparison between Emilia input and artificial input, as shown in Table 3-2, the specimen remains stable until the scaling factor of 75% and 200% for the Emilia and artificial inputs, respectively, corresponding to very different peak ground variables.

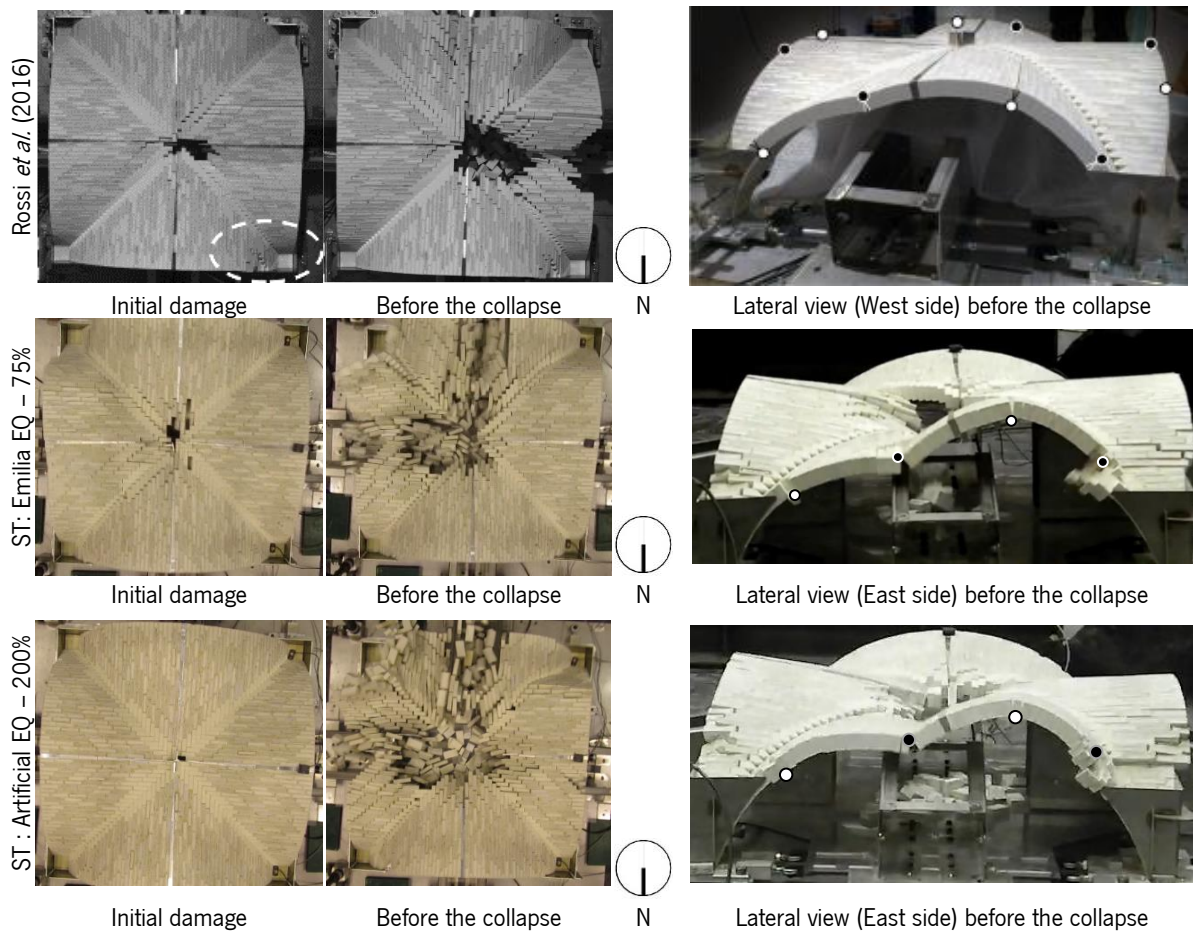


Figure 3-14. In-plane shear mechanism: pictures of the tests (white circles indicate the location of the hinges at the intrados, back circles at the extrados).

Table 3-2. Incremental dynamic testing sequence with the respective peak ground acceleration (PGA), peak ground velocity (PGV) and peak ground displacement (PGD).

Emilia input					Artificial input				
Input	PGA	PGV	PGD	Damage	Input	PGA	PGV	PGD	Damage
%	[m/s ²]	[mm/s]	[mm]		%	[m/s ²]	[mm/s]	[mm]	
10	0.03	7.23	0.31	-	10	0.01	0.53	0.16	-
25	0.19	17.22	1.96	-	25	0.09	3.75	0.99	-
35	0.33	32.67	3.87	-	50	0.39	14.52	3.99	-
50	0.69	64.58	7.94	Fall of the key blocks	75	0.92	32.47	8.99	-
55	0.83	77.80	9.53	Crack along NW / SE diagonal	100	1.69	58.15	16.10	-
75	1.57	139.47	17.67	Collapse	125	3.38	95.80	25.07	Fall of the key blocks
					150	4.27	135.72	36.27	Crack along NW / SE diagonal
					200	7.49	241.21	64.70	Collapse

At the level of the collapse, Emilia PGA (1.57 m/s²) is about 5 times less than the artificial earthquake's PGA, Emilia's PGD is about 4 times smaller than the artificial earthquake's PGD, while between the PGV of the two inputs, there is a ratio of about 1.7. The impulsive nature of the Emilia earthquake

significantly influences the response of the structure, even with lower values of spectral acceleration, inducing earlier damage to the vault (Dejong *et al.*, 2008). This aspect is also represented by the acceleration and displacement response spectra of the several time histories, which are very different in content and peaks (Figure 3-15).

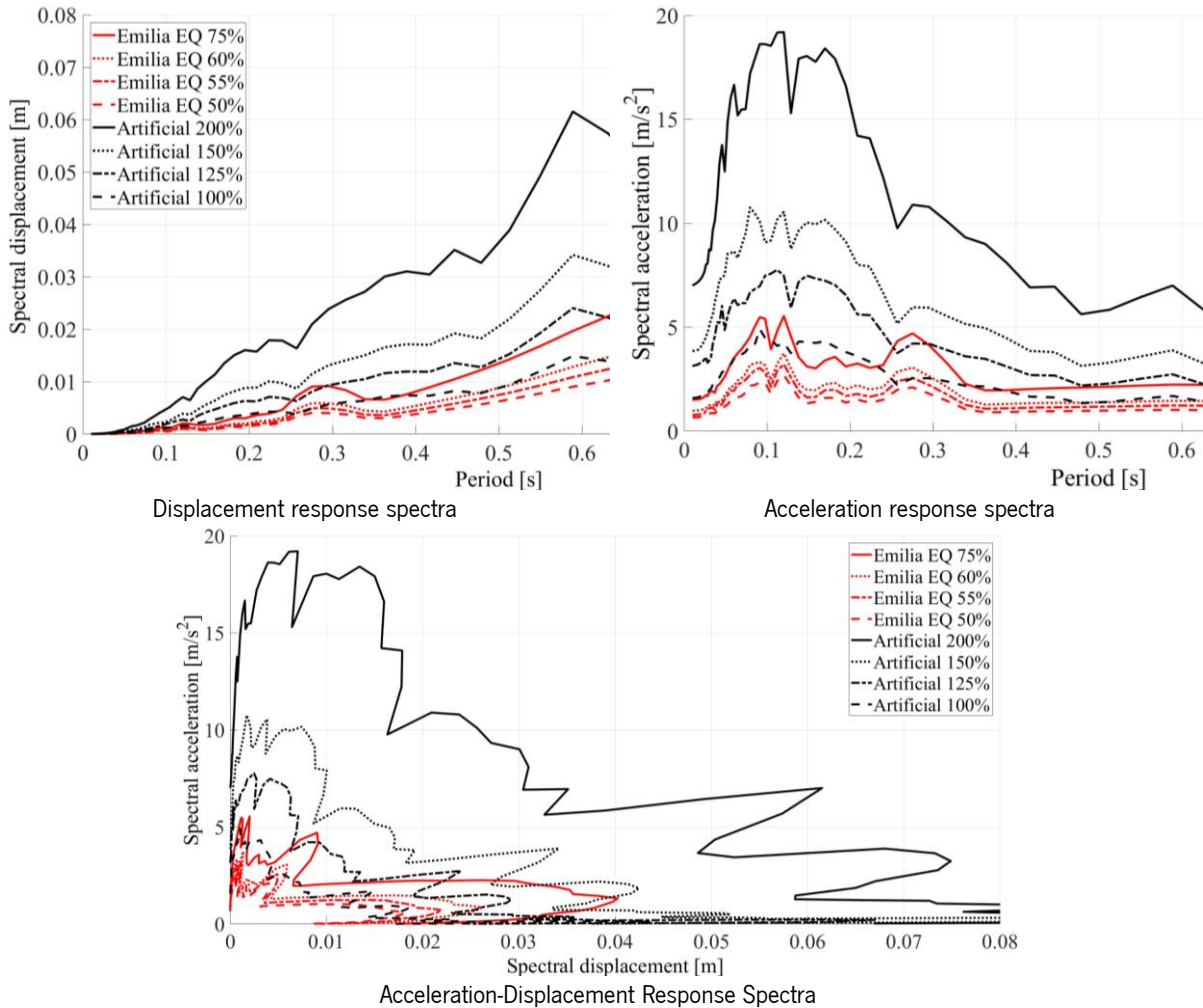


Figure 3-15. Displacement, acceleration and acceleration-displacement response spectra for the signals measured at the shaking table for the two inputs: Emilia (red) and artificial input (black).

Table 3-3 shows some relevant outputs associated with the recorded response of the structure at the level of the collapse for both earthquakes. Although the content of the two inputs is different, the displacements recorded by the movable piers show good consistency for all shaking table tests. The values of drifts, obtained by the optical camera OC_{1y} and the LVDT's measurements, placed respectively above the movable piers p_3 and p_4 , ranges from 5.1% to 7.2%, for both inputs. The drifts are calculated as the ratio between the relative absolute maximum displacement measured during the tests (about $\pm 32/45$ mm) and the span of the groin vault (0.625 m), as has been done in the quasi-static scenario.

Under the seismic motion, the maximum drift value, that led to the collapse, can be assumed on average equal to 6%, both for the Emilia and the artificial earthquake, independently of the value of PGA. In addition, the difference between the two values obtained for the different types of inputs is less than 1% when measured by the optical camera and about 0.1% by the LDVT.

Table 3-3. Test results at the collapse for Emilia and artificial input in comparison with the quasi-static tests (Rossi, Calderini, and Lagomarsino 2016).

Input	[%]	PGA	PGV	PGD	Max. absolute displacement OC_{1y}	Drift	Max. relative displacement $LVDT_1$	Drift	Drift average
		[m/s^2]	[mm/s]	[mm]	[mm]	[%]	[mm]	[%]	[%]
Emilia	75	1.6	139.5	17.8	44.8	7.2	32.0	5.1	6.2
Artificial	200	7.5	241.2	64.7	39.1	6.3	32.6	5.2	5.7
Quasi-static tests							24.7 – 31.2	3.8 – 4.8	

From this observation, it is possible to conclude that under seismic motion the limit drift value that can cause the collapse is equal to 6%. On the other hand, the ultimate drift value measured in the quasi-static tests (Rossi, Calderini, and Lagomarsino 2016) is about 4.3% of its lateral edge and it corresponds to a conservative result, in comparison with the results obtained from the shaking table tests. This confirms what has been shown in the previous works, mainly that for masonry buildings the dynamic drifts are larger than quasi-static ones (Vasconcelos, 2005; Lagomarsino, 2015; Abrams *et al.*, 2017; Gaetani, Lourenço, Monti and Moroni, 2017).

For an additional comparison between the types of input, the hysteretic behaviour of the reduced-scale vault is presented in Figure 3-16, in terms of a relation between the shear forces/horizontal inertial forces and the displacements. The shear forces developed in the structures, as well as the displacement, have been analysed based on the recorded acceleration and displacement time histories. The base shear coefficient, here named as “horizontal inertial coefficient” to avoid detrimental misunderstanding with the in-plane shear mechanism. The horizontal inertial coefficient is calculated by dividing the sum of the inertial forces associated with each web of the vault by the total self-weight of the specimen. Inertial forces associated with the webs of the vault are calculated by assuming the mass of the reference web to be lumped at the recording accelerometers. Due to the geometrical symmetry of the specimen, the mass associated with each web corresponds to $\frac{1}{4}$ of the total mass of the vault. The inertia forces are computed for each shaking table test but, for the sake of simplicity, only the most representative scenarios are presented in Figure 3-16, namely Emilia 35% vs artificial 50%, because of their similar PGA, and Emilia 75% vs artificial 200%, at the collapse. The shear coefficient is plotted versus the longitudinal displacement placed at the top of the west arch, measured by the optical

camera OC_{2y} . Figure 3-16a, which refers to stages with lower amplitudes, represents a linear elastic phase with a very low value of excitation. This behaviour is associated with the undamaged configuration of the vault, namely when the openings of the joint do not lead to the fall of blocks. The linear range is evident even for the hysteretic curves plotted at the amplitude of the collapse (Figure 3-16b), in which two vertical lines are associated with the initial phase. Then, very high non-linear behaviour, for both inputs, is observed. As noticed before in the evaluation of the drifts, the hysteretic curves also show similarities when considering the Emilia input and the artificial input. The scattered behaviour of the curve is marked by the different slopes of the curves, which represents a change in terms of stiffness and permanent deformation. Emilia input and artificial input show quite similar non-linear behaviour but are mirrored in sign. In general, when the artificial input is applied, the structure is characterised by a higher capacity in terms of shear coefficient, while with the Emilia input, the structure shows a higher deformation. Despite the different responses in terms of displacements, when compared with the quasi-static tests, the maximum strength capacity ranged between 13–17 % of the force/weight ratio, which is compatible with the value obtained by the shaking table tests (see Figure 3-16b).

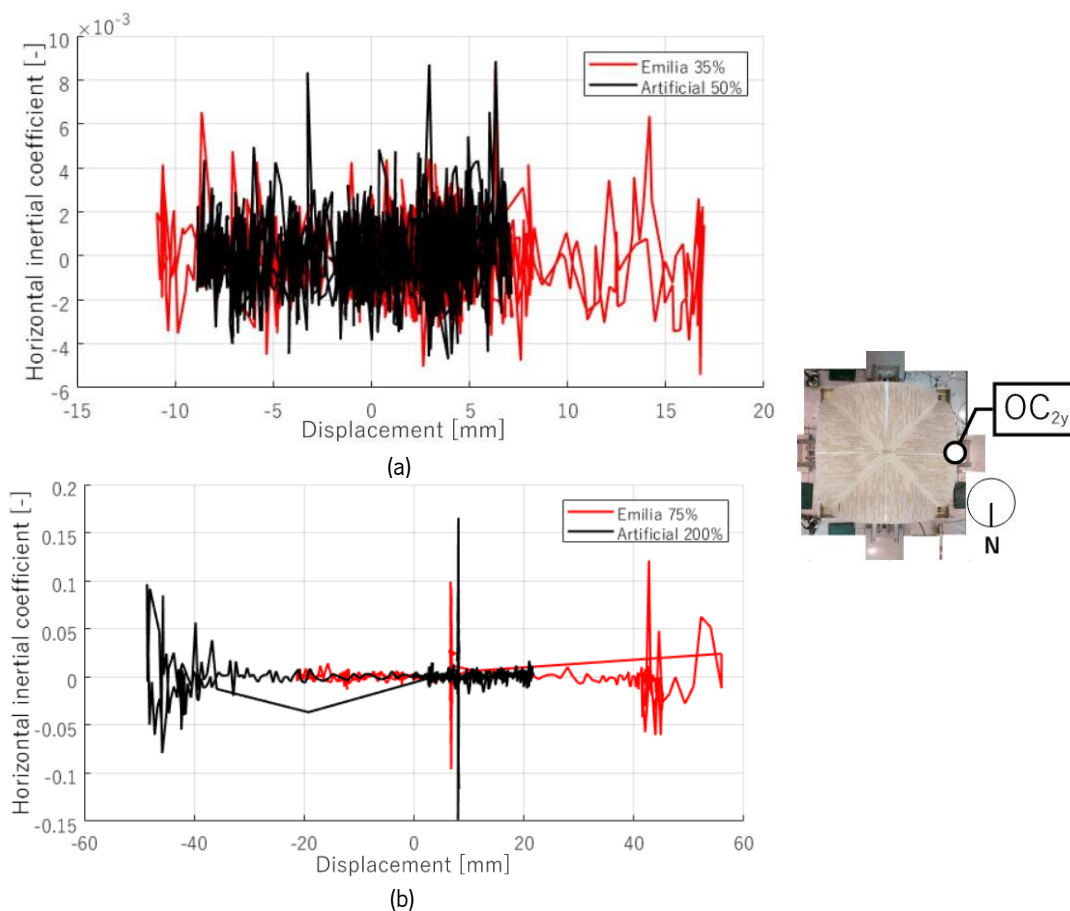


Figure 3-16. Hysteretic behaviour of the top arch control point (OC_{2y}) for different stages of testing: (a) Emilia 35% vs artificial EQ 50% and (b) Emilia EQ 75% vs artificial EQ 200% (at the collapse).

The maximum horizontal inertial coefficient at each stage of testing and the corresponding value of displacement recorded by the sensor located at the key of the west arch (OC_{2y}), occurring at the same instant of time, is reported in Figure 3-17, where the incremental dynamic response of the vault for both earthquakes is plotted. The initial parts of the two capacity curves represent the linear range of the response, whose stiffness characteristics are difficult to be read due to the low level of amplitude. During this kind of test, it is normal to get a better response for a medium value of amplitude and intensity. The two outputs, with the Emilia and the artificial inputs, show a similar capacity in terms of horizontal inertial coefficient and deformations - an outcome that is in line with what is obtained in previous research on reduced-scale specimens (Tomažević, 1999).

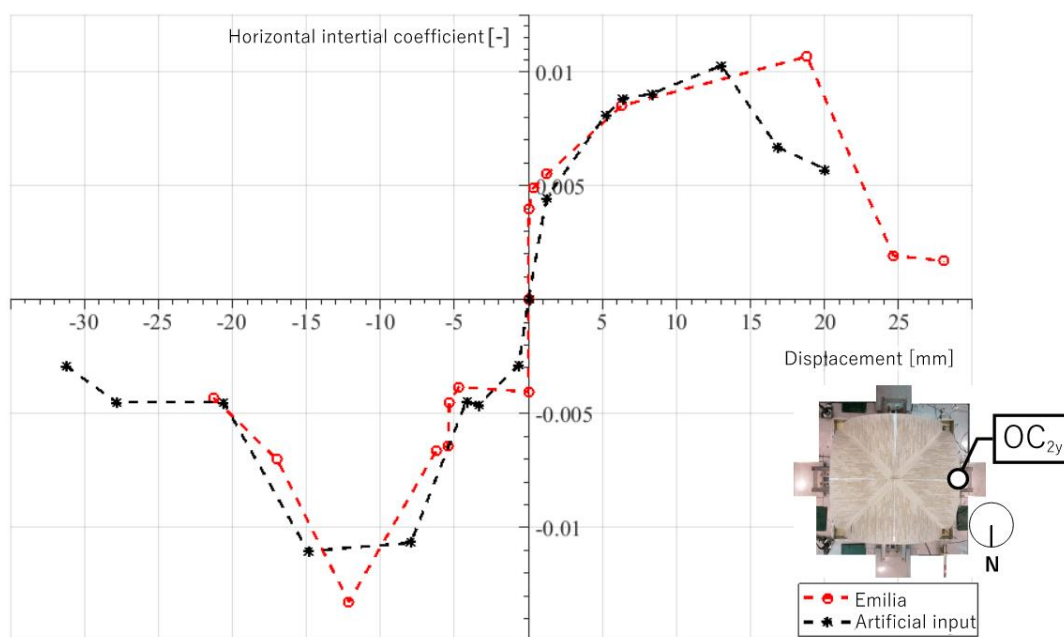


Figure 3-17. Experimental capacity curve, in terms of horizontal inertial coefficient and displacement measured by OC_{2y} .

The differences in terms of inputs and responses can be also identified in Figure 3-18. As Candeias *et al.* (2016) stressed, a straight line with a 1:1 slope means that the absolute accelerations are equal in the base and the other selected points of the specimen. This means a rigid body motion behaviour, whereas if the slope is higher means that there is dynamic amplification in the specimen. Finally, if there is an exponential increase of the plots with the increase of the input motion intensity, meaning that the specimen has reached the non-linear behaviour. Looking at Figure 3-18a, either in terms of PGA and root mean square of the accelerations (RMS_A), it is possible to observe the dynamic behaviour of the vault for the Emilia input can be defined as linear from the tests with 10% to 55%, except for the point that corresponds to the 50% of amplitude (Table 3-1). This could be associated with some relative movements during the recording state of the sensor or due to the accumulation of

damage, not fully recovered from the previous sequence. Before the collapse, it is possible to notice an exponential increase significantly evident from the accelerations recorded on the top of the movable piers (Acc_{3y} , Acc_{7y}), less remarkable for the ones placed on the fixed piers (Acc_{1y} , Acc_{2y}). On the other hand, for what concerns the artificial input (Figure 3-18b), the linear range is identified between 10% and 125% of the ground motion, while the exponential rate is mainly localised on the last two sequences of tests (150% and 200%) when effectively the severe damage occurred.

At the level of the collapse (Emilia-75% and artificial-200%), the accelerometer Acc_{7y} placed above pier p_4 , presents higher accelerations than the opposite movable pier p_3 for both types of input. One justification can be associated with the fact that the NW corner is the last to collapse and still measures accelerations while the opposite pier is already collapsed.

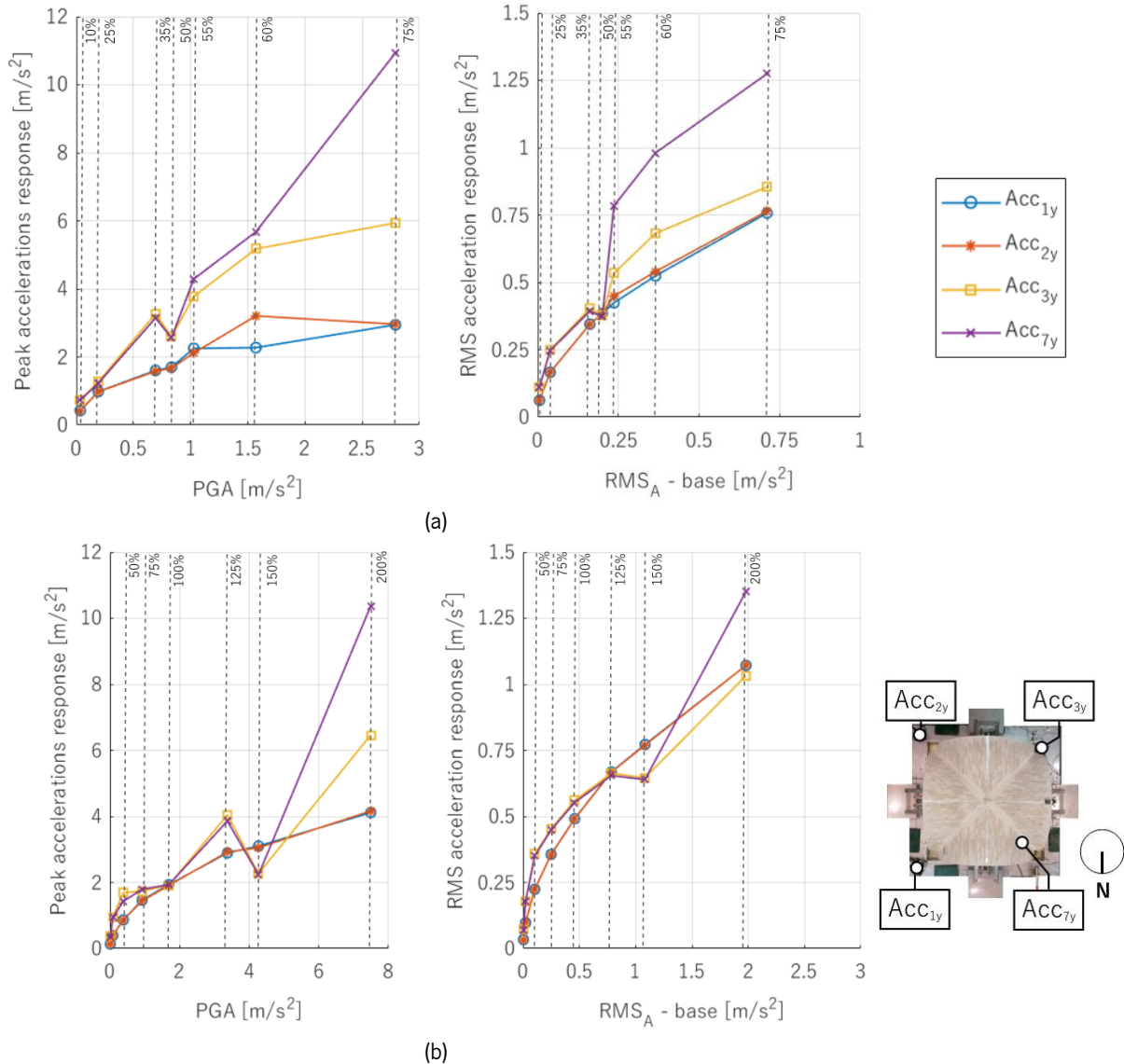


Figure 3-18. Peak and RMS acceleration of the response for the reduced-scale vault in the longitudinal direction: (a) Emilia earthquake, (b) artificial input.

3.5 Final remarks

A comprehensive experimental investigation composed of shaking table tests developed for the characterisation of the shear failure on a reduced-scale specimen (1:5) of a 3D printed groin vault is presented in this Chapter. The objective is to evaluate the variation of the response considering the two different types of loading (quasi-static and dynamic) and the two different types of seismic action applied in the shaking table tests (recorded vs artificial accelerograms). The results obtained from the dynamic identification tests, performed before and after each seismic shake table test, allow to evaluate the reduction of frequencies of the specimen, which can be used as an indicator of the damage.

The development of a four-hinge symmetric mechanism is observed between the two movable piers in the quasi-static tests. A similar mirrored mechanism is obtained for the shaking table tests, but the first location of the hinges appears between the fixed piers of the vault, associated with the stiffer behaviour of the fixed elevation. The displacement/drift levels achieved in the shaking table tests are higher (about 6% of the span) than the ultimate displacement/drift obtained from quasi-static tests (about 4% of the span), using the same boundary conditions configuration. This aspect allows concluding that, in general, the monotonic approach is more conservative than the dynamic approach. The novelty of the research is that this statement has been only studied analysing walls or simpler structures, but this work represents the first experimental contribution on groin vault structures.

Comparing the two seismic inputs (Emilia and artificial earthquake), the capacity in terms of horizontal inertial coefficient is similar in both tests. The differences in the collapse between the Emilia earthquake and the artificial seismic input are significant and influenced by the spectral acceleration of the Emilia input, which is about 3.14 m/s^2 above the spectral acceleration of the Italian Code (4.22 m/s^2), for the first period of the specimen. This stresses the fact that, as stated in some of the most recent codes, a significant number of records must be selected in order to allow a better description of the safety of the structure (Lagomarsino and Cattari, 2015).

This study, complemented by the dynamic identification tests, provides useful data for the development and calibration of numerical models, adopting different strategies, which allow to evaluate the seismic behaviour of vaults with different geometry and seismic action. Moreover, this study also provides a step for further investigations, which may contain more realistic boundary and loading conditions, such as the presence of the lateral wall, the presence of filling material, and the three components of the seismic actions.

4. Reduced-scale vault: numerical modelling

4.1 Introduction

Numerical modelling based on calibrated models can simulate the response of structures with high precision and assess the influence of multiple variables of the structure and of the modelling itself, such as stiffness, material properties and geometric non-linearity. Moreover, numerical simulations are important to save time and reduce costs, without compromising the quality of the results, especially when they are supported by experimental results. Simulations give confidence in the use of software packages and their application in the engineering practice.

Chapter 4 deals with the numerical simulations of the experimental tests performed on the 3D printed reduced-scale specimen, useful for a proper assessment of the seismic evaluation of the groin vault. The available experimental campaign and results presented in Chapter 3 and Annex 2 are used to validate the strategies adopted in the numerical modelling.

Within the context of this thesis, two different numerical strategies (finite element method (FEM) and discrete element method (DEM)) are deepened, highlighting their strengths and limitations. FEM and DEM results are compared in terms of collapse mechanism, displacement capacity and computational effort, drawing attention to the general assumptions that can be typically valid for dry joint structures. In this sense, the 3D printed dry joint reduced vault, described in Chapter 3, is particularly suitable for this kind of numerical investigation because it is rebuildable, meaning that each seismic test can be considered independent from the previous one, without accumulation of damage or without changing the initial conditions. This represents an ideal condition for comparison with numerical applications. Results from other numerical frameworks are, when possible, used to complement this study.

Additionally, this numerical study also allows investigating the role of different seismic inputs on the response of the specimen, becoming a tool that easily handles structural synthesis and refinements.

4.2 Preparation of the numerical models

Two modelling strategies are considered in parallel, namely the simplified micro-modelling technique using the FEM and DEM, with models calibrated based on the experimental results described in Chapter 3. Both modelling strategies allow the simulation of the masonry joint patterns, leading to a system of blocks or units in mechanical interaction along joints with nonelastic behaviour. The

numerical models were built in a FEM software, namely DIANA FEA BV 10.4 (2019a) and a DEM software, namely 3DEC 7.0 (Itasca Consulting Group, 2019a).

Although DeJong *et al.* (2008) adopted a numerical model with a reduced block thickness of 20%, in comparison to experimental tests. In the present study, no reduction of the thickness was done, and both models replicate the exact geometry of the experimental specimen. Differently, the experimental stiffness is calibrated from the joint stiffness.

In this Section, the main assumptions and strategies adopted in each numerical modelling approach are described, and then their calibrations are commented.

4.2.1 Discrete element model

Regarding the DEM model, the geometry of the reduced groin vault was built in Rhinoceros® (McNeel Robert, 2008), and corresponds to a model with an error smaller than 1% when comparing the real and numerical volumes. The geometry was exported in 3DEC 7.0 Environment by Itasca (2019a), using a script able to read the parametric coordinates of a geometric Rhinoceros model and able to convert them into a decipherable file, compatible with 3DEC syntax. The boundary conditions have been accommodated to the syntax of the 3DEC software using specific expedients:

- the steel plates, which surround the corners of the vault, are connected and placed at the bottom of the piers in order to keep the span of the vault fixed (Figure 4-1).
- to perform non-linear time history analysis, the software needs a rigid solid element, here called “shaking table block”, fully constrained and aligned with the axis of symmetry of the vault. The input is applied to its centroid. The “shaking table block” helps the DEM software to easily reach the equilibrium in each time step of the analysis, even in case of falls of the blocks.
- a very low shear stiffness joint is inserted below the steel plate under the movable piers, allowing movement along the longitudinal direction. On the other hand, under the fixed piers, the steel plate is perfectly fixed to the shaking table block through a rigid connection;
- two couples of aluminum cables have been placed only in the transverse direction x to avoid the opening of the vault. Inserting the cables requires the adoption of deformable blocks due to the incompatibility between the cable elements and the rigid blocks of the vault in the 3DEC 7.0 environment.

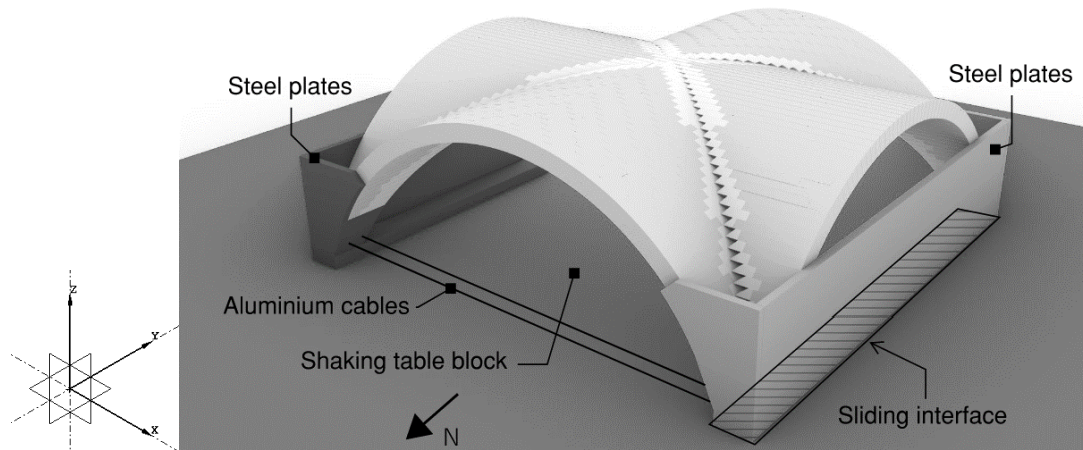


Figure 4-1. DEM model in Rhinoceros environment.

Each unit of the vault is modelled as a distinct block while the dry joints are simulated using no-tension frictional behaviour, characterised by zero-thickness interfaces. In particular, the hypothesis of rigid blocks and the Mohr-Coulomb criterion for the joints are assumed. The choice of using a specific material constitutive model is an important step of the modelling process and it may result being a compromise between the accuracy of the results and the complexity of their interpretation. Regarding the units, adopting a rigid block model means that deformations are lumped at the joints, there is no (or very small) overlap between the blocks and the displacement capacity of the structure is controlled by the contact stiffnesses and by the contact inelastic parameters (*i.e.* cohesion (c) and friction angle (θ)). A rigid block consists of a convex polyhedron shape (Figure 4-2a), being created by rigidly assembling convex sub-blocks. The motion of a rigid block, or a rigid assembly of sub-blocks, is governed by the 6 degrees-of-freedom of rigid body mechanics (Lemos, 2021a). As anticipated, some blocks in contact with the aluminium cables need to be transformed into deformable blocks (Figure 4-2b). The deformable blocks include the deformation of the block material and they are subdivided into internal finite-difference meshes of tetrahedral elements. For these blocks, the mesh size is 2.5 cm.

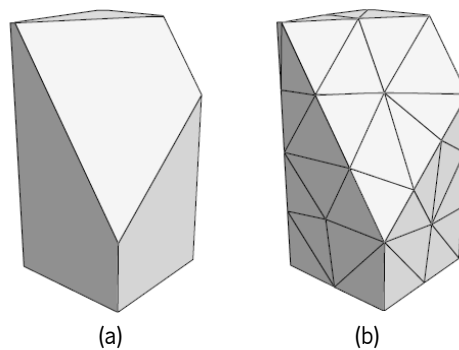


Figure 4-2. Blocks assumed in the DEM model: (a) rigid polyhedral block; (b) deformable block with tetrahedral element mesh (Lemos, 2021a).

Accounting for blocks deformability considerably increases the calculation time, compared to simulations that consider only infinitely rigid units. Thus, only the four blocks of the abutments (black blocks in Figure 3-2) are modelled as deformable. A small overlap, between the abutment blocks and the cable elements in compression, is allowed and its size is specified in terms of normal and shear contact stiffness of the bond contact, as described in Equation 4-1 (Lemos, 2007).

In particular, the Young's modulus of the aluminium cables is set at the value of $E_c = 69$ GPa and its yield strength is equal to $f_y = 241$ MPa, based on technical specifications. E_c and f_y are then used to define other input parameters, such as the bond stiffness of grout (k_{bond}) and the bond strength of grout (s_{bond}) according to Equation 4-1 and Equation 4-2 (Mehrotra, Arede and Dejong, 2015). The area of the cross-section (A) of the aluminium cables is set equal to 1.49×10^{-5} m², the density equal to 2700 kg/m³, and the embedded length (L) and the bond length are assumed equal to 1 cm.

$$k_{\text{bond}} = \frac{AE}{L} = 102.8 \frac{\text{MPa}}{\text{mm}} \quad \text{Equation 4-1}$$

$$s_{\text{bond}} = \frac{f_y \times 100}{\text{bond length}} = 2.4 \times 10^3 \frac{\text{MPa}}{\text{mm}} \quad \text{Equation 4-2}$$

Regarding the joints' contact of the DEM model, Mohr-Coulomb criterion is justified by several experimental campaigns, when a moderate level of compression is involved (Van Der Pluijm, 1999; Lourenço and Ramos, 2004; Restrepo Vélez, Magenes and Griffith, 2014). Joints' mechanical behaviour is entrusted to the contact stiffness definition, namely normal K_n and tangential K_s behaviour (Figure 4-3). In case of dry joints, the normal stiffness K_n controls the opening and closing of the joints in this direction, while in the shear direction, the stiffness K_s sets a limit to the shear force magnitude, like in Mohr-Coulomb friction model (Lemos *et al.*, 2022). When the contact normal stress σ exceeds the maximum tensile strength, the normal stress goes to zero and the joint opens. On the other hand, while working in compression a small amount of overlap may occur between the volumes of the blocks depending on K_n (Figure 4-3a). Similarly in shear, when the shear stress τ exceeds the maximum shear strength then sliding between blocks occurs (Figure 4-3b). Once sliding occurs, residual values for cohesion and friction govern the Mohr-Coulomb criterion. For sake of completeness, in case of dry joint structures, non-associate flow rule is commonly assumed (Angelillo, Lourenço and Milani, 2014), which means assuming null dilatancy angle (ψ). The dilatancy angle ψ measures the uplift of one block over the other upon shearing, which decreases to zero with increasing the vertical stress and with increasing slip.

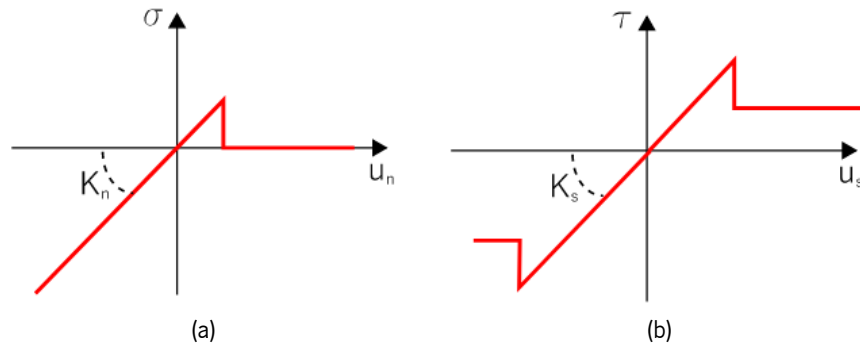


Figure 4-3. Contacts behaviour in DEM model: (a) normal direction, (b) tangential direction.

4.2.2 Finite element model

The FEM model was built in DIANA 10.4 and corresponds to a replica of the exact geometry of the model, reproduced through a 3D AutoCAD model. The representation of masonry units is done using continuum solid elements, namely four-node and three-side isoparametric solid tetrahedron elements (TE12L in Figure 4-4a), whereas 3+3 nodes plane three-dimensional interface elements are used for the representation of the mortar-unit behaviour (T18IF) (Figure 4-4c). The three couples of aluminium cables are modelled as 1D elements, namely Enhanced truss element (L6TRU in Figure 4-4b) and suitable for non-linear dynamic analysis. The mesh size is constantly equal to 6 mm.

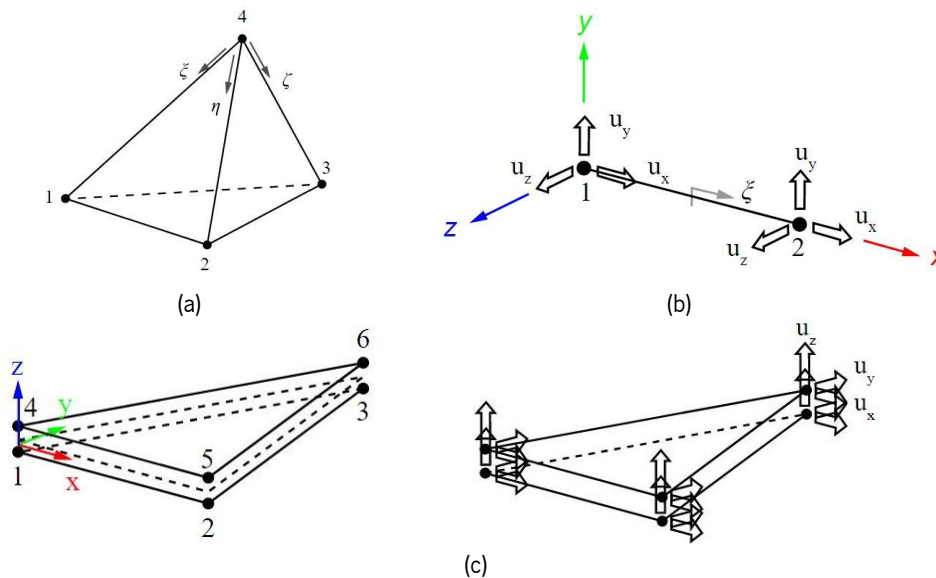


Figure 4-4. Elements adopted in the FEM model: (a) TE12L tetrahedral elements, (b) L6TRU enhanced truss element, (c) T18IF triangular interface element (topology and displacements) (DIANA 10.4, 2019b).

The masonry units are simulated assuming only linear behaviour, while a Mohr-Coulomb friction model is used for the interface elements (Figure 4-5). Mohr-Coulomb friction model can simulate frictional slip along the interface elements (DIANA 10.4, 2019b), which is expected to be the most relevant behaviour to be taken into account.

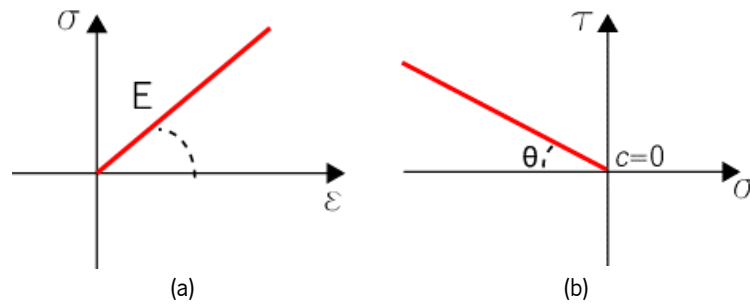


Figure 4-5. Constitutive laws used in the FEM model: (a) linear elasticity for the blocks, (b) Mohr-Coulomb criterion for the interfaces.

The FEM model is shown in Figure 4-6, and, similarly to the DEM model, some particular aspects are considered:

- the steel plates, which surround the corners of the vault, are made of solid elements to better reproduce the boundary conditions;
- the standard blocks (light grey in Figure 4-6) have been separated through another mesh set from the blocks located along the diagonals (dark grey in Figure 4-6) in order to independently change the material properties of the two sets during the calibration;
- fully fixed boundary conditions are applied below the fixed piers (East side), and partially fixed constraints, below the movable piers (West side), limited the displacements along the Z direction.

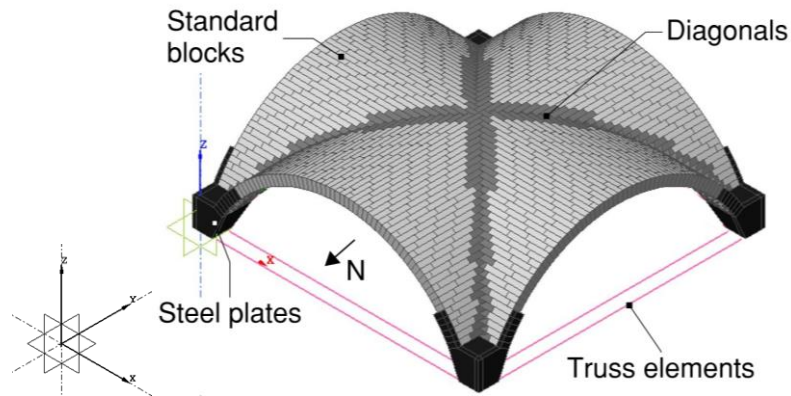


Figure 4-6. FEM model in the DIANA environment (finite element mesh not shown).

4.2.3 Material properties and calibration

During the iterative calibration process of FEM and DEM models, all the physical properties (Young's modulus of the standard blocks, friction angle and densities) are set as constant values as they were measured by Rossi *et al.* (2016), or either, in agreement with values found in the literature related to mechanical and physical properties (Gaetani, Bianchini and Lourenço, 2021) for both models. The unique exceptions correspond to the stiffnesses of the joints and Young's modulus of the blocks of the

diagonals. Those are unknown parameters, whose estimation is the subject of this and the next subsection (see 4.2.4) since indications about the ranges of stiffnesses are not available in the literature.

In the first place, the stiffnesses of the joints (normal and tangential) have been calibrated in the DEM model based on the first natural frequency of the specimen (4.1 Hz). Then, they have been set as reference values in the FEM model while Young's modulus of the blocks of the diagonals was varying, in order to match the first mode frequency.

Normal K_n and tangential K_s stiffness assumptions require additional considerations, which may help to better estimate the physical and dynamic characteristics of this specific reduced dry joints specimen. First, since the blocks are made of plastic powder, without steel filling within their thickness (see Section 3.2.1), the stiffness values are expected to be low to represent the dry joint tests without a significant pre-compression state (Bui *et al.*, 2017). Secondly, to avoid excessive block interpenetration, the limitation $K_n \geq 0.1$ MPa/mm and $K_s \geq 0.04$ MPa/mm have been assumed as lower bound (Gaetani, 2016).

The starting value of normal stiffness, before the iterative process, is defined by the relation valid for rigid block models with dry joints, introduced in Equation 4-3. The Young's modulus of the assembly E_m is equal to 123 MPa, the height of the blocks (h_b) is 240 mm and the Young's modulus of the blocks E_b is assumed equal to $10e5$ MPa (Gaetani, Bianchini and Lourenço, 2021):

$$K_n = \frac{1}{h_b \left(\frac{1}{E_m} - \frac{1}{E_b} \right)} = 0.5 \text{ MPa/mm} \quad \text{Equation 4-3}$$

The final values of normal stiffness and shear stiffness are the result of the calibration based on the dynamic properties of the specimen, which are equal to $K_n = 0.35$ MPa/mm and $K_s = 0.15$ MPa/mm, assuming $K_s = 0.4 \times K_n$ (Ptaszowska and Oliveira, 2014). With these final values, the first natural numerical frequency obtained through eigenvalue analysis, on the DEM model, is approximately equal to 4.0 Hz, with an error equal to 2.5% in comparison with the experimental results (see 3.4.1). In addition, the in-plane shear mechanism mode shape is associated with the first numerical frequency. DEM model is also validated by performing a linear static analysis applying the self-weight, in which the vertical displacement at the key of the vault is equal to 15 mm, in line with the value that was measured through a plumb line (see Section 3.1).

More extensive validation is needed for the FEM model, through the quasi-static analysis, simulating in-plane shear tests (Section 4.2.4) and tilting table tests (Section 4.2.5) to assess the correctness of the stiffnesses and the low value of Young's modulus of the diagonals (unique elastic parameter unknown

from the experimental test). Indeed, Young's modulus of the diagonals is only taken into account in the finite element formulation since the rigid blocks assumption of DEM does not consider the elasticity of the units. Also, comparisons with other FEM models replicating the same specimen available in the literature, are commented. For more information about the quasi-static experimental campaigns, here simulated, the reader can refer to Section 3.3 and Rossi *et al.* (2016).

4.2.4 Static non-linear analysis using the FEM model: in-plane shear tests

The value of 2.5 MPa, adopted for the Young's modulus of the diagonals (E_d), satisfies both the dynamic properties of the specimen (frequency and shape) and a realistic deformed shape after the application of the self-weight. This value is about 2% of the standard blocks (123 MPa) and since no indications in literature are available for the elastic properties of this specific material (vinyl polymer and carbohydrate plastic powder), to sustain that this value is consistent with the real elastic properties of the diagonals, the quasi-static tests (see Sections 3.3.1 and 3.3.2) were also numerically replicated with FEM model. The in-plane shear tests are simulated by applying in ten steps the weight of the vault and then, in further steps, by increasing displacements to its abutments, subjected to an imposed displacement of the movable piers (p_3 and p_4 in Figure 3-4b). The evaluation of the FEM model is also compared with three previous quasi-static numeric simulations (Milani *et al.*, 2016; Alforno *et al.*, 2020; Gaetani, Bianchini and Lourenço, 2021), whose characteristics have been anticipated in Section 2.2.2. Table 4-1 shows the main differences between the four contributions and a detailed comparison overview is given next to the reader.

Table 4-1. Differences and similarities related to the material properties of the numerical investigations.

	Milani <i>et al.</i> (2016)	Alforno <i>et al.</i> (2020)	Gaetani <i>et al.</i> (2021)	New model
Software	Strauss	Abaqus	DIANA 9.6	DIANA 10.4
E_m [MPa] (standard blocks)	117.0 (assumed)	80.0 (assumed)	123.0 (given)	123.0 (given)
E_d [MPa] (diagonals)	117.0 (assumed)	80.0 (assumed)	123.0 (assumed)	2.5 (calibrated)
Material behaviour interfaces	Mohr-Coulomb			
Cohesion c [MPa] (assumed)	0.02		~ 0	
Friction coefficient μ (given) [-]		0.57		
K_n [MPa/mm]	0.11 (evaluated)	5.0 (assumed)	1.0 (assumed)	0.35 (calibrated)
K_s [MPa/mm]	0.05 (evaluated)	Perfectly rigid (assumed)	0.4 (assumed)	0.15 (calibrated)
Tensile strength	Null (assumed)			
Dilatancy angle	Null (assumed)			

The frictional behaviour of the dry joint structure suggests the use of the Mohr-Coulomb criteria, with null or quasi-null cohesion, zero tensile strength and zero dilatancy angle - conditions adopted in all the studies.

Notable is the variation in the stiffness values. Alforno *et al.* (2020) and Gaetani *et al.* (2021) followed the literature values presented by Senthivel and Lourenço, (2009). Milani *et al.* (2016) calibrated the elastic stiffnesses of the interfaces (K_n , K_s) through the equivalence on energy between the discrete model and the continuous one (Kawai, 1978). Milani *et al.* (2016) assumed a hypothetic thickness of the joint equal to 1 mm, with final stiffness values close to the lower bound limit to avoid interpretation between the blocks. As already stressed, in the FEM model developed in this work, K_n and K_s are the result of a modal calibration (Bianchini *et al.*, 2023).

The FEM model also distinguishes the peculiarity of the diagonals, not only in terms of mechanical properties but also in terms of geometrical discretisation (Figure 4-7). Milani *et al.* (2016), and Alforno *et al.* (2020) simplified the connection between two adjacent webs making the interlocking completely satisfied by the link between the nodes of the mesh (Figure 4-7a-b). Gaetani *et al.* (2021) correctly modelled the cutting planes of the diagonals' blocks (Figure 4-7c) but their dimensions have been doubled, restricting their deformability. In the FEM model of this work, the interlocking is only ruled by the Mohr-Coulomb structural interfaces, by reproducing the real plane surfaces between the two blocks, as a result of the parametric-based geometrical model (Figure 4-7d).

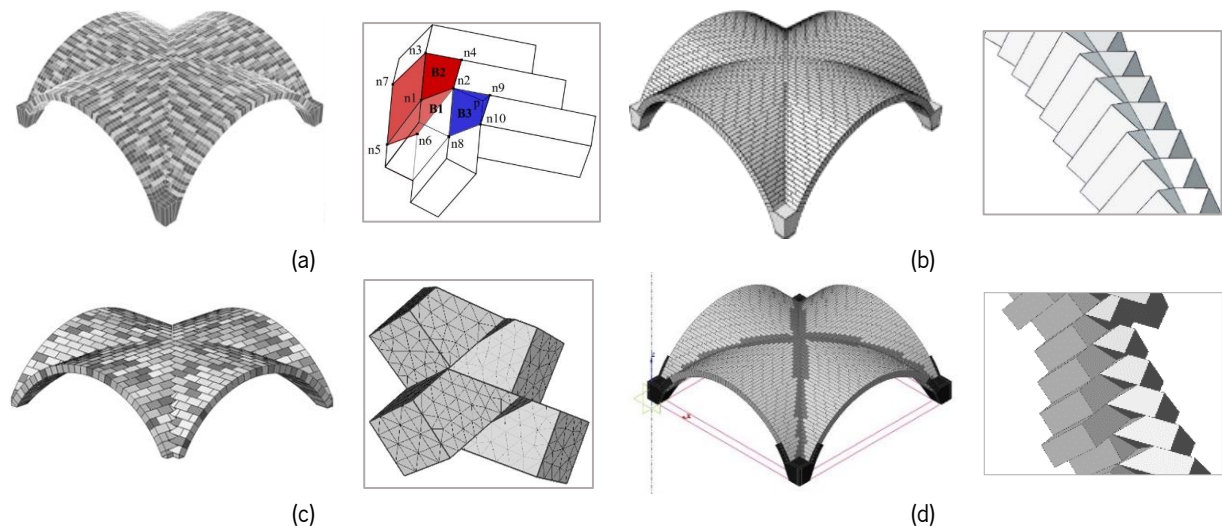


Figure 4-7. Details of the diagonals in the numerical models: (a) Milani *et al.* (2016), (b) Alforno *et al.* (2020), (c) Gaetani *et al.* (2021), (d) FEM model developed in this work.

The numerical capacity curves of the quasi-static tests are reported in Figure 4-8 in comparison to the experimental curves. Milani *et al.* (2016)'s curve has a good match with the capacity curve of the structure, and the linear range fits well with the experimental linear range. However, Milani *et al.*

(2016)'s capacity curve is not able to decrease the load-bearing capacity under large displacements, and as stressed by the same authors, one reason could be due to the role of the geometric non-linearity (not considered). Gaetani *et al.* (2021) highlight the importance of the geometric non-linearity for dry and vaulted structures, adopting the update Lagrange (UL) formulation. Since the deformation of the vault model is concentrated in the interface elements (exhibiting large displacements and strains), UL allows a more advantageous framework for the description of large inelastic deformations. Conversely, neglecting the geometrical non-linearity (dashed line curve in Figure 4-8), no matter the interface stiffness, results in an increasing monotonic trend that makes the estimation of the capacity ambiguous. Due to computational incompatibilities, Gaetani *et al.* (2021) opted for doubling the thickness of the blocks, resulting in a numerical model with half of the number of the bricks (and therefore half of the interfaces) and, at the same time, a less deformable model. As observed by Rossi *et al.* (2016), the experimental results reveal a significant ductility of the vault - the ultimate displacement recorded in the tests is larger than 4% of the span, whereas the one achieved with Gaetani's numerical model is around 3%. Regarding Alforno *et al.* (2020)'s contribution, a very good agreement between numerical and experimental results can be observed. The initial and elastic part is stiffer than the response obtained from Milani *et al.* (2016) and the FEM model developed in this work, due to the higher normal stiffness that is generally utilised for the interfaces.

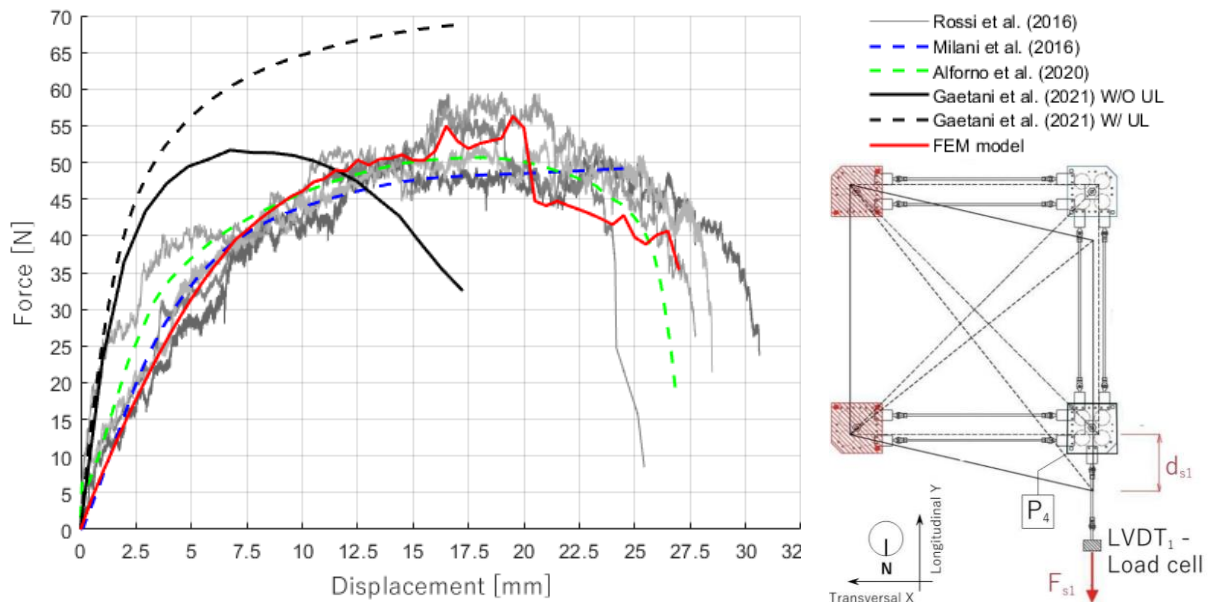


Figure 4-8. Capacity curves for the quasi-static tests: numerical results in comparison with the experimental results obtained from Rossi *et al.* 2016.

The in-plane shear test performed in the FEM model, with the updated material properties, showed good results. The curve can trace the experimental path (grey curves) with a valuable approximation, both in terms of the force and displacement capacity, also depicting the softening part. The post-elastic

phase of the tests remarks the ductility of this FEM model. The linear elastic part in the four experimental tests shows a wide scatter, which is dependent on the first initial stage of loading and on the boundary conditions. The interface stiffness plays a role of capital importance, together with the reduction of Young's modulus, along the diagonals. The numerical results are also compared with the pictures of the test in Figure 4-9, showing the deformed shapes. The position of the hinges in the perimetral arch (north elevation) and the crack formation along the diagonals, as seen in the experimental tests (Figure 4-9a), are correctly simulated by all the simulations. Alforno *et al.* (2020) catch also the fall of the blocks, due to the explicit solution implemented in Abaqus, while the other models can only replicate the deformed shape of the tests. The crack pattern of Gaetani *et al.* (2021)'s model correctly approaches the one provided by the experimental test along the diagonal, but in the FEM model developed in this work (Figure 4-9e), it is also possible to observe the concentration of deformation located on the same web. The local failure of perimetral blocks, although non-influential on the overall behaviour of the vault, is visible close to the abutments, and is more evident in Alforno and Gaetani's simulations. In this regard, the detachment of one block means an overall null stress on it, which suggests that the perimetral force flow is independent of the behaviour of the perimetral arches (*i.e.*, standard slicing technique would not be appropriate).

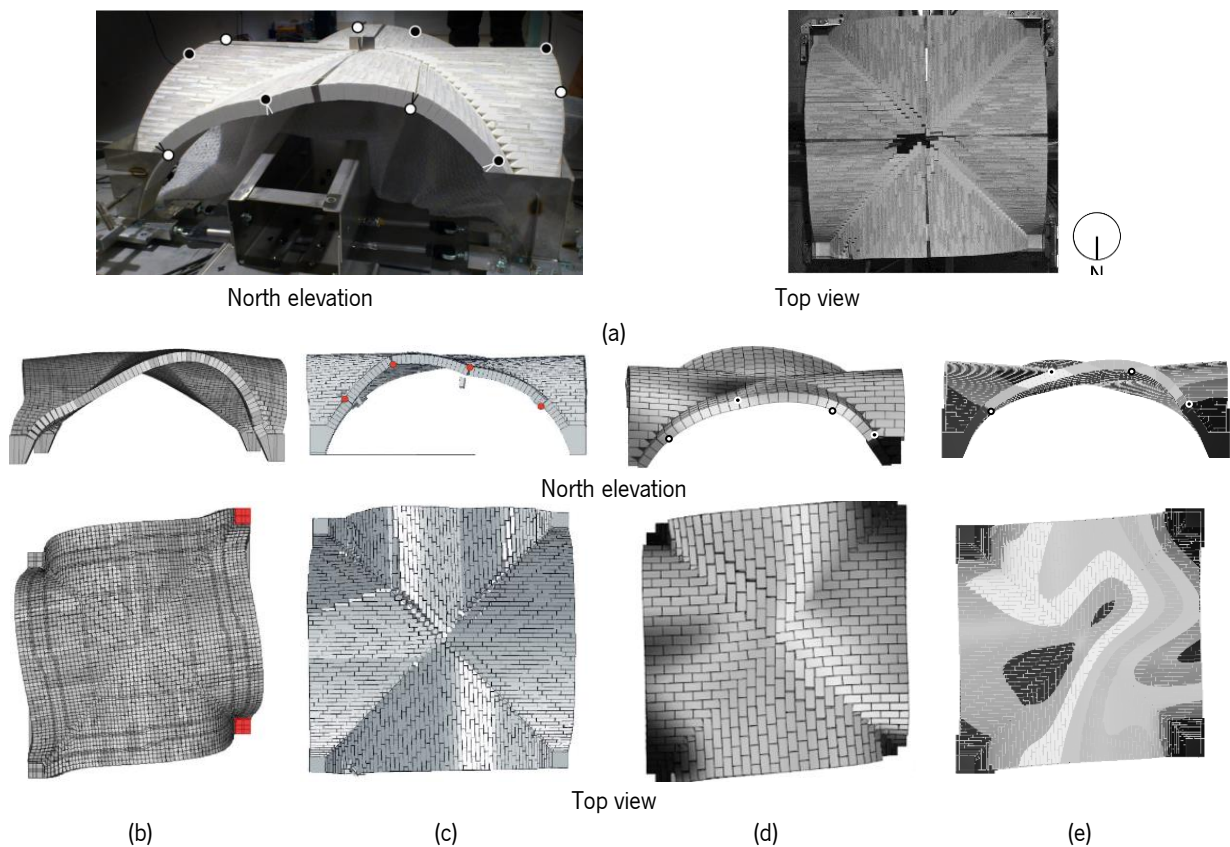


Figure 4-9. Experimental and numerical deformed shapes of the in-plane shear mechanism: (a) Rossi *et al.* (2016), (b) Milani *et al.* (2016), (c) Alforno *et al.* (2020), (d) Gaetani *et al.* (2021), (e) FEM model.

4.2.5 Static non-linear analysis using FEM model: tilting table

For the sake of completeness, also tilting plane tests (see Section 3.3.2) were numerically simulated, considering two load sets. In the first, the self-weight was applied into small load increments (10 steps). This is done because a unique single load step for self-weight application is not suitable due to problems of convergence, because the zero tensile strength of the dry joints leads to the early formation of cracks (Milani *et al.*, 2016). The second load set is the progressive inclination of the base plane, simulated up to failure, decreasing the vertical self-weight component by the multiplicative factor $\cos(\Phi)$ and increasing the horizontal load (simulating the seismic action) by the self-weight multiplied by $\sin(\Phi)$. Figure 4-10 also reports the outcomes of the analyses performed by the previous studies. In general, the numerical analyses overestimate the resultant force obtained from the tests in Rossi *et al.* (2015).

Milani *et al.* (2016)'s model have an opposite trend to the Gaetani *et al.* (2021)'s model. The FEM model shows an almost constant horizontal load multiplier λ for every angle of seismic direction, as it is seen during the experiments, a part for the value registered at 18° . If the value of $\lambda = 0.29$, obtained at 18° of the seismic direction, is considered out of trend, the average value of the error between the experimental tests and the new numerical model decreases from 6% to 3%.

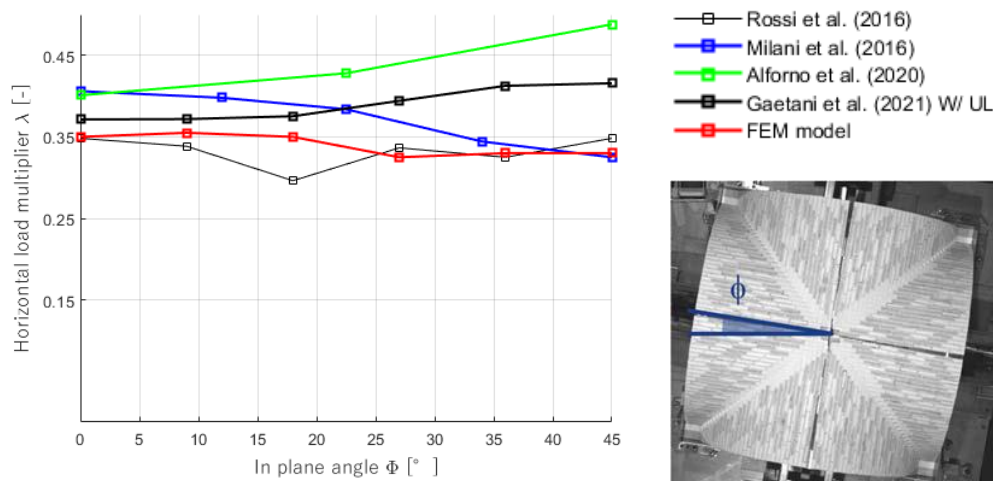


Figure 4-10. Horizontal load multiplier as a function of the direction of the seismic action.

To summarise, it is possible to conclude that the improvement between numerical models available in the state of the art and the FEM model developed in this work is mainly linked to the calibration process. For Milani *et al.* (2016), Alforno *et al.* (2020) and Gaetani *et al.* (2021), the calibration is based on the literature review and static observations, while in the new model, it is supported by the experimental results of the dynamic identification tests. Even if only the first mode shape and first mode frequency are considered in the calibration, they are sufficient to represent the global behaviour of the

structure, making this FEM model less dependent on the local imperfections. Due to this analysis and calibration, it is possible to conclude that the FEM model, is well-calibrated based on dynamic properties and quasi-static tests. The values, reported in Table 4-2, are therefore taken and considered in the next steps of this work.

Table 4-2. Linear elastic properties of the blocks and mechanical properties of the interface elements. *Estimated through eigenvalue analysis. **Estimated through quasi-static analysis.

Units	Young's modulus [MPa]		Poisson's ratio [-]		Specific mass [kg/m ³]	
	FEM	DEM	FEM	DEM	FEM	DEM
Standard blocks	123.0			0.20		2700
Diagonal blocks	2.5**	X		0.20		550
Steel elements	2.1e+05			0.30		7800
Aluminium cables	69.0e+06	69.0e+06				
	Normal stiffness K_n [MPa/mm]	Shear stiffness K_s [MPa/mm]	Cohesion c [KN/m ²]	Friction angle θ [°]	Dilatancy angle ψ [°]	
Interfaces/joints	0.35*	0.15*	~ 0	29.6	0	

4.3 Dynamic non-linear analysis using FEM and DEM models

Despite the well-known importance of performing non-linear static analyses, it is often noted that the outcomes should be interpreted with caution, especially regarding complex structures like masonry vaults. They may provide too conservative results compared to non-linear dynamic time-history analyses (Bianchini *et al.*, 2019). Hence, non-linear dynamic analyses with time integration using artificial earthquake are also carried out, based on the shaking table tests investigation (see Section 3.4), as part of the SERA project, and goal of this thesis. The objective is to validate the models by comparing the numerical results with the experimental response of the experimental specimen, including the damage and the collapse mechanism (point A in Section 1.5). Another point is the discussion of the results obtained from the two modelling strategies (FEM and DEM), considering the quality of the results, the time of analyses and the computational effort (point E in Section 1.5).

4.3.1 Analyses characteristics

The accelerograms recorded by the shaking table's actuators during the tests were filtered before being used as input for the numerical analyses. In particular, a band-pass filter with a frequency range between 0.05 and 50 Hz, using the fourth order of the polynomial trend and a cosine taper window at 10% was adopted to apply a baseline correction in the input (Faccioli and Paolucci, 2005). The filtered accelerograms were directly applied at the base of the FEM model (acting at the level of the boundary conditions). For the DEM model, the corresponding velocities were applied at the centroid of the "shaking table" block, obtained by integrating the filtered accelerogram over time. Due to the

computational effort, geometric non-linearity is not considered in the FEM model for this type of analysis.

In accordance with Section 4.2, the previous material properties were also adopted for the dynamic analysis since their validity and robustness for this specimen have been demonstrated during the static analysis. More complex anisotropic models are available for masonry in DIANA FEA BV (2019b), but these are not justified for this particular specimen characterised by dry joints.

The secant (quasi-Newton) iterative method, with a convergence criterion based on the internal energy with tolerance equal to 10^{-3} , was adopted. Another important aspect of the non-linear dynamic analysis with time integration is related to the type of integration method. The quasi-brittle behaviour of the specimen introduces numerical noise, due to the fast transition from the linear elastic behaviour to the fully cracked state involving almost zero stiffness. The quasi-instantaneous changes in the displacement field tend to originate in the propagation of high-frequency spurious vibrations (Cervera *et al.* 1995). In this sense, the adopted Hilber-Hughes-Taylor (HHT) time integration method introduces numerical dissipation without degrading the accuracy (Faria, Oliver and Cervera, 1998). The time step Δt integration can be defined as equal to the first natural period T_1 of the specimen over 20 (0.01 s), representing an error lower than 5%, and at the same time it must be much smaller than the total duration of the earthquake (about 9 s) (Mendes, 2012). For simplicity, Δt_{FEM} is set equal to 0.005 s, which is equal to the experimental time step.

The time step for the DEM model cannot be larger than a critical value to ensure numerical stability, inversely proportional to the highest natural frequency of the system (Belytschko, 1983). For this numerical model, characterised by small blocks and with 4 deformable blocks, Δt_{DEM} is automatically calculated by 3DEC 10.7 as the ratio between 2 over the highest system eigenfrequency (Lemos, 2021b). Thus, Δt_{DEM} is equal to 10^{-6} for the dry joint scaled vault numerical model and it ensures an acceptable analysis duration.

4.3.2 Damping discussion

Under high dynamic loading the damage increases during the analysis, changing the values of the frequencies and the damping ratios. Furthermore, in the non-linear dynamic analysis, an integration point totally damaged contributes to the decrease of damping forces. Thus, the update of the damping at the end of each time step would allow better simulation of the non-linear dynamic behaviour of the structures. However, this procedure is demanding and would increase the computing time (Mendes, 2012), particularly when dealing with large numerical micro-models. Thus, the viscous damping

formulation is preferred but needs further investigation. In the matter of damping formulation, the Rayleigh viscous damping C was adopted in the FEM model, as described in Chopra (2012), as a combination of mass matrix M and stiffness matrix K (Equation 4-4).

$$C = \alpha M + \beta K \quad \text{Equation 4-4}$$

The two constants α (1.55) and β (9.45e-05) were defined based on the results obtained from the eigenvalue analysis. Considering the first 25 modes, a cumulative mass participation of about 85% in each horizontal direction (x and y) is obtained. Thus, the 1st and the 25th frequencies (namely 4.10 Hz and 96.32 Hz) are adopted to determine the Rayleigh damping for the non-linear dynamic analyses, assuming the damping ratio ξ equal to 3%. A damping ratio ξ of 3% is commonly used for load-bearing masonry structures (Mendes and Lourenço, 2014; Parisse *et al.*, 2021). The constants α and β are the only two new variables added to every material of the model for this kind of analysis. All the previous material properties have been maintained as listed in Table 4-2. On the other hand, for what concerns the DEM model, Rayleigh damping is a required input parameter for non-linear time history analysis and it depends on the frequency (f_{\min}) and the respective damping ratio (ξ_{\min}) that corresponds to the minimum value of damping in the graph (grey dot in Figure 4-11). They are respectively, for the DEM model, equal to 20.00 Hz and 1.2%.

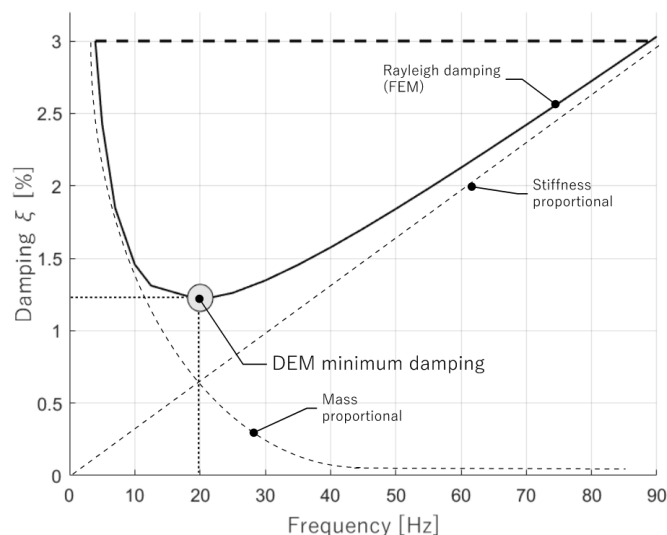


Figure 4-11. Viscous damping graph of the numerical models.

The addition of damping tends to decrease the duration of the analysis in the case of FEM models (implicit solution), while it significantly increases the duration of DEM analyses (explicit solution). The stiffness-proportional component of damping, responsible for damping the higher frequencies, is added to each contact force and the element stress of the DEM model. The reduction of the time step due to

the inclusion of the stiffness-proportional damping may be substantial, leading to prohibitive running times. In particular, with the contribution of damping, the Δt_{DEM} decreased from 10^{-6} to 10^{-9} , greatly increasing the computational effort. Without damping, the analysis takes around 12 hours to perform all the duration of the input, while with damping it takes more than 2 months. The amount of time, required for running the analysis in 3DEC 7.0, with the contribution of the damping is not sustainable (even considering only mass-proportional damping). This numerical limitation suggests the assumption of null damping, which can be in any case acceptable for dynamic simulations of seismic response of dry joint structures, as supported by state-of-the-art statements.

Stephanou *et al.* (2011), De Felice *et al.* (2011), and Malomo *et al.* (2020) applied no damping during their investigations with DEM models and seismic excitations, to keep the timestep reasonable, mainly relying entirely upon the joint friction for energy dissipation. In addition, zero damping may foresee conservative results, without underestimating the response. However, this specific choice (null damping) may change the response of the DEM model with respect to the FEM model. Thus, the damping influence needs to be validated in DIANA software. For this study, a medium damage scenario (125%) was chosen to be numerically replicated and compared between the experiments. Figure 4-12 confirms that the contribution of the damping is very low for the FEM model, underlying that, in the case of dry joint structures, the role of the joints prevails in comparison with the viscous damping dissipation.

The total duration of a single time history analysis with the FEM model, with and without damping, varies from 3 and 4 days for this amplitude. This duration is compatible with the purpose of this thesis. The maximum value of error in the time history of the displacements, comparing the numerical results with and without damping is equal to 0.18%. In terms of acceleration, there is more scatter, but still negligible for the aim of this research. Thus, supported by numerical evidence, damping contribution both for FEM and DEM models is discarded. Thus, the next analyses presented in the following Sections (see 4.3.3 and 4.4) consider null damping.

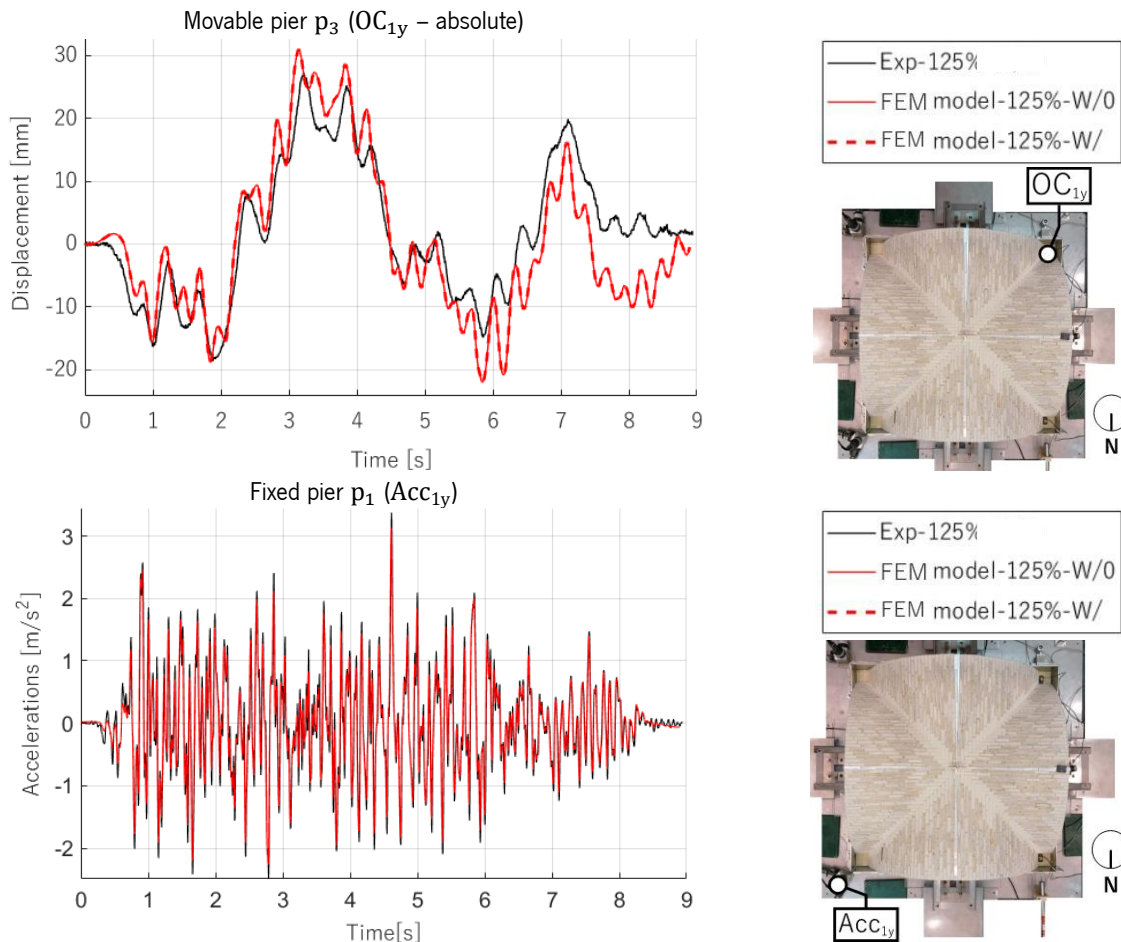


Figure 4-12. Comparison of the time histories of displacements and accelerations between the shaking table tests and the FEM model results with (W/) and without (W/O) the contribution of the Rayleigh damping.

4.3.3 Results

Several time history analyses have been carried out using incremental dynamic analysis (IDA), according to Table 3-1, with both software packages and null damping, and evaluating both qualitative (damage and failure mechanism) and quantitative results (measured variables). Three sets of amplitudes of the artificial earthquake, namely 125%, 150% and 200%, were selected to be compared in this thesis.

Regarding the deformed shapes for 125% amplitude, the centre of the vault is the most deformed part, as has been also observed in the shaking table tests (Figure 4-13). The similarity at the East side is also significant - the sliding of the blocks close to the steel plates can be seen, mainly in the FEM model, while the drop of the key of the vault is evident in the DEM model.

The main differences in terms of collapse mechanism are considerable for the 150% amplitude, where the fall of the blocks of the key of the vault is meticulously replicated by the DEM model, while the FEM model, due to its implicit nature, is limited. The evolution of the damage that occurs during the analysis

underlines the quality of the results obtained by the DEM model (Figure 4-13, Figure 4-14). For this seismic amplitude and also at the collapse (amplitude equal to 200%), the fall of the blocks matches in terms of location and time concurrence with the experiments. In the case of 150% input, the damage is mainly linked to the verticality of the joints, which is accentuated at the top of the vault. In addition, as it is observed also in the quasi-static tests, a concentration of sliding of the blocks is notable close to the steel plate corners.

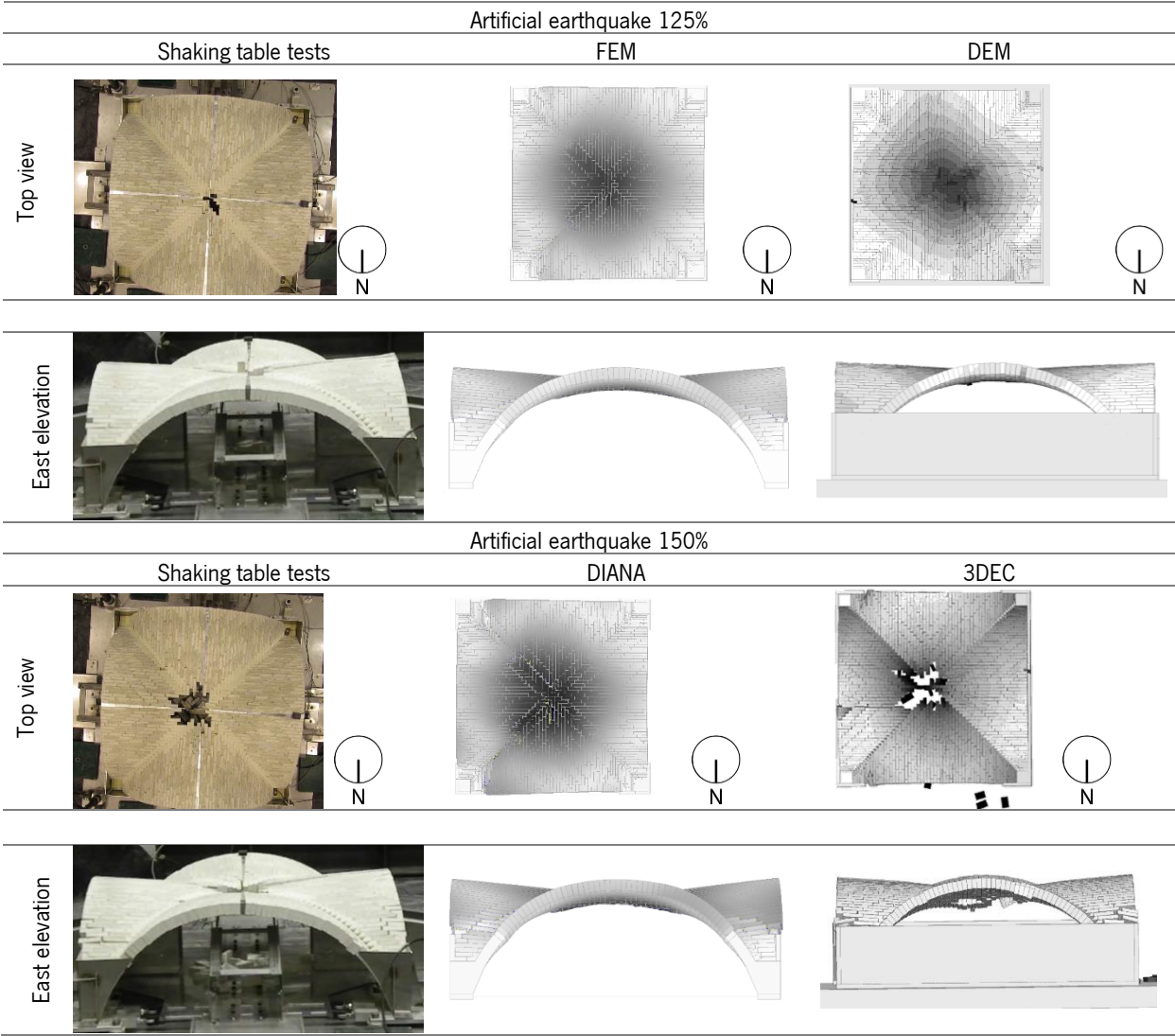


Figure 4-13. FEM and DEM deformed shapes, compared with the experimental results at the end of artificial earthquake for 125% and 150% amplitudes.

In the case of 200% input, the evolution of damage, which starts from the central blocks and ends with the complete formation of the hinges, is well replicated. Firstly, some blocks located at the eastern web start to slide down at 1.75 s. Then, around 2 s, the first hinges are identified together with the collapse of the corresponding webs, until the complete collapse of the model.

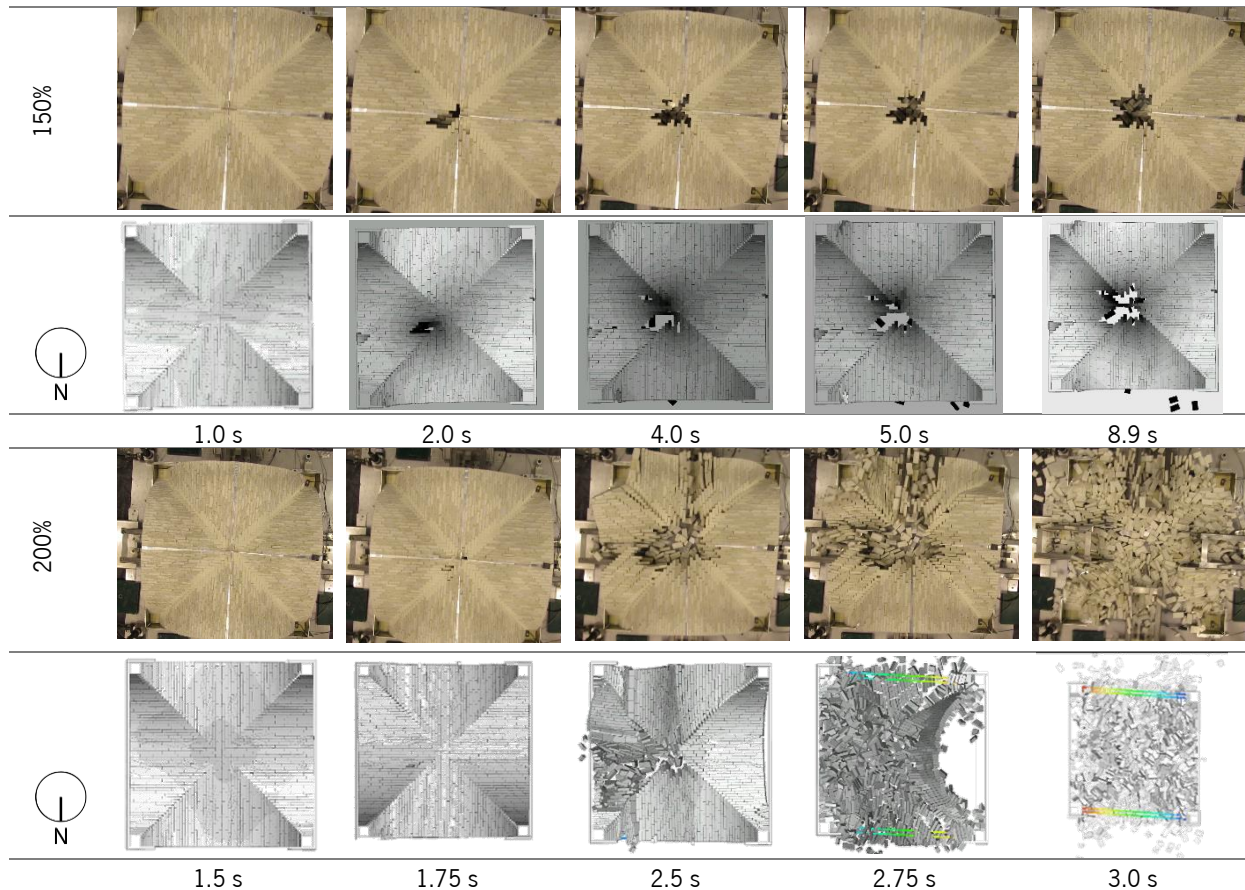


Figure 4-14. Damage propagation on the vault in comparison between shaking table tests and time history analysis for the DEM model.

This Section has shown how FEM and DEM models, besides their intrinsic differences, give reliable and important results, even considering complex 3D dry joint structures, mainly ruled by frictional laws. However, for the sake of completeness, and as suggested by Guide for the Probabilistic Assessment of the Seismic Safety of Existing Buildings by CNR (2013), while considering historic structures it is fundamental to investigate the seismic behaviour taking into consideration a wide set of inputs of different nature.

Table 4-3 presents the quantitative comparison of the results obtained from the tests and both numerical models. In terms of the accelerations, the FEM model tends to amplify the response of the movable piers p_3 and p_4 . Because of this, the Arias Intensity, defined as the integral of the squared accelerations over time - measurement of the intensity of a signal of acceleration, has higher values in the case of the FEM model. The DEM model maintains more constant values with a variation of less than 38%. On the other hand, the parameters of the displacements obtained from the FEM model are on average closer to the experiments, than the ones obtained from the DEM model.

Table 4-3. Quantitative comparison between experimental and numerical results for 125% and 150% seismic amplitudes. ★
Relative displacements determined using the LVDT₁.

Earthquake - 125%		Fixed pier - p ₁			Movable pier - p ₃			Movable pier - p ₄		
		Test	FEM	DEM	Test	FEM	DEM	Test	FEM	DEM
Maximum acceleration	Acc _{Max} [m/s ²]	3.14	3.15	3.18	1.69	4.39	2.35	1.75	4.43	2.35
Arias intensity	AI [m/s]	0.76	0.76	0.79	0.19	3.30	0.94	0.19	3.30	0.94
Root mean square of acceleration	RMS _A [m/s ²]	0.73	0.73	0.74	0.36	1.52	0.80	0.34	1.52	0.80
Maximum displacement	Displ _{Max} [mm]	27.80	27.70	27.80	27.20	31.10	34.30	6.91★	7.20★	10.55★
Root mean square of displacement	RMS _D [m]	11.80	11.75	11.75	10.80	12.10	13.10	2.48★	2.48★	4.10★
Earthquake - 150%		Fixed pier - p ₁			Movable pier - p ₃			Movable pier - p ₄		
		Test	FEM	DEM	Test	FEM	DEM	Test	FEM	DEM
Maximum acceleration	Acc _{Max} [m/s ²]	3.86	3.86	3.89	2.23	4.71	2.59	2.27	4.71	2.59
Arias intensity	AI [m/s]	1.45	1.45	1.49	0.59	3.79	0.79	0.60	3.80	0.79
Root mean square of acceleration	RMS _A [m/s ²]	1.01	1.01	1.11	0.64	1.64	0.81	0.65	1.64	0.81
Maximum displacement	Displ _{Max} [mm]	29.70	29.60	29.70	32.30	34.90	45.00	8.51★	9.79★	7.70★
Root mean square of displacement	RMS _D [m]	14.95	15.00	15.60	13.13	15.70	19.80	3.33★	3.03★	2.50★

4.4 Parametric analysis

A parametric analysis with a probabilistic basis was also performed to evaluate the influence of earthquakes with different characteristics (point B in Section 1.5) on the response of the reduced-scale vault, namely at its collapse. Thus, and since it is less time consuming, only DEM model was used.

4.4.1 Selection of ground motions

Thanks to the several databases available around the world (PEER Ground Motion Database, 2022; Dipartimento della Protezione Civile, 2022a, 2022b; Seismological Facilities for the Advancement of Geoscience (SAGE), 2022; Universidad Nacional Autónoma de México, I. d. G., 2022), several natural earthquakes were selected. They correspond to natural ground motions, registered between 1935 and 2017 with Moment Magnitude (M_w) between 6.0 and 8.2 (Richter scale). According to the Central limit theorem (CLT), when independent random variables are summed up, their normalised sum tends toward a normal distribution (called a bell curve). CLT is valid under the assumption of a data set characterised by a number of samples bigger or equal to 30. For this study, 40 earthquakes were taken into account, considering as an independent variable both two horizontal components (North-South and East-West) (Table 4-4). All 40 earthquakes have been normalised based on their PGA, in order to carry

out a study able to identify the differences between all the earthquakes for a series of ground motion parameters.

Table 4-4. List of the considered natural recorded earthquakes.

ID	Date [dd/mm/yyyy]	Station	Event name	Direction	M_w	Duration [s]	PGA [m/s^2]
1	31/10/1935	Carroll College	Helena Montana	North-South	6.0	50.92	1.58
2				East-West			
3	18/05/1940	IIA001 n° 117	El Centro	North-South	6.9	94.88	3.42
4				East-West			
5	09/02/1941	Ferndale City Hall	Northwest Calif	North-South	6.5	38.10	0.62
6				East-West			
7	21/07/1952	Pasadena CIT Athenaeum	Kern County	North-South	7.3	76.19	0.47
8				East-West			
9	28/06/1966	Cholame Shandon Array	Parkfield	North-South	6.0	44.29	0.62
10				East-West			
11	09/02/1971	2516 Via Tejon PV	San Fernando	North-South	6.5	70.19	0.25
12				East-West			
13	23/12/1972	Managua Esso	Nicaragua-01	North-South	6.3	45.69	3.65
14				East-West			
15	17/05/1976	Karakyr	Gazli, URSS	North-South	6.4	13.52	5.97
16				East-West			
17	15/09/1976	GMN	Friuli (2 nd shock)	North-South	6.5	19.42	3.18
18				East-West			
19	16/09/1978	Bajestan	Tabas, Iran	North-South	7.4	38.98	0.89
20				East-West			
21	15/04/1979	Ulcinj-Hotel Albatros	Montenegro	North-South	6.9	55.39	1.73
22				East-West			
23	19/09/1985	Zacatula	Mexico City	North-South	8.0	146.38	1.76
24				East-West			
25	17/10/1989	N° 57007	Loma Prieta	North-South	6.9	39.98	4.02
26				East-West			
27	17/01/1994	Woodland Hills 6301	Northridge	North-South	6.7	56.87	4.02
28				East-West			
29	12/09/2007	Sikuai Island	Sumatra	North-South	6.4	128.99	0.40
30				East-West			
31	06/04/2009	AQA	L'Aquila	North-South	6.3	40.00	4.35
32				East-West			
33	20/05/2012	MRN	Emilia	North-South	6.1	81.85	0.15
34				East-West			
35	24/08/2016	AMT	Central Italy	North-South	6.2	27.89	3.68
36				East-West			
37	24/08/2016	Nyaung U	Chauk	North-South	6.8	29.99	0.83
38				East-West			
39	08/09/2017	Salina Cruz	Mexico "Chiapas"	North-South	8.2	163.50	2.48
40				East-West			

This series of ground motion parameters is composed of the Arias intensity (AI), the effective duration of the earthquake ($t_{d(10-90)}$), defined as the time required to pass from 10% and 90% of the Arias Intensity, the root mean square of accelerations (RMS_A), of velocities (RMS_V) and of displacements (RMS_D), the specific input energy (IE_S), the peak ground velocity (PGV) and peak ground displacement

(PGD), the development length of a velocity ($LD_{v(10-90)}$) and the impulsivity index (IP) (Trifunac and Brady, 1975; Panella, Tornello and Frau, 2017). For all the mathematical formulations of the parameters and definitions of input characters, the reader is referred to Cosenza and Manfredi (2000) and Panella *et al.* (2017). It is noted that is important to define also integral parameters, not only peak values, because they take into account the history of amplitudes occurring in a time history signal. Then, for each parameter, a bell-shaped normalised distribution centred at their mean value was plotted and three sets of ranges were identified based on $\bar{\mu}$ (mean value), σ (standard deviation) and ε (standard error = σ / \sqrt{n} with n equal to the number of data). Those ranges are (Figure 4-15): the lower bound range A ($0; \bar{\mu} - \sigma$), the medium range B ($\bar{\mu} - \varepsilon; \bar{\mu} + \varepsilon$) and the upper range C ($\bar{\mu} + \sigma; 1$).

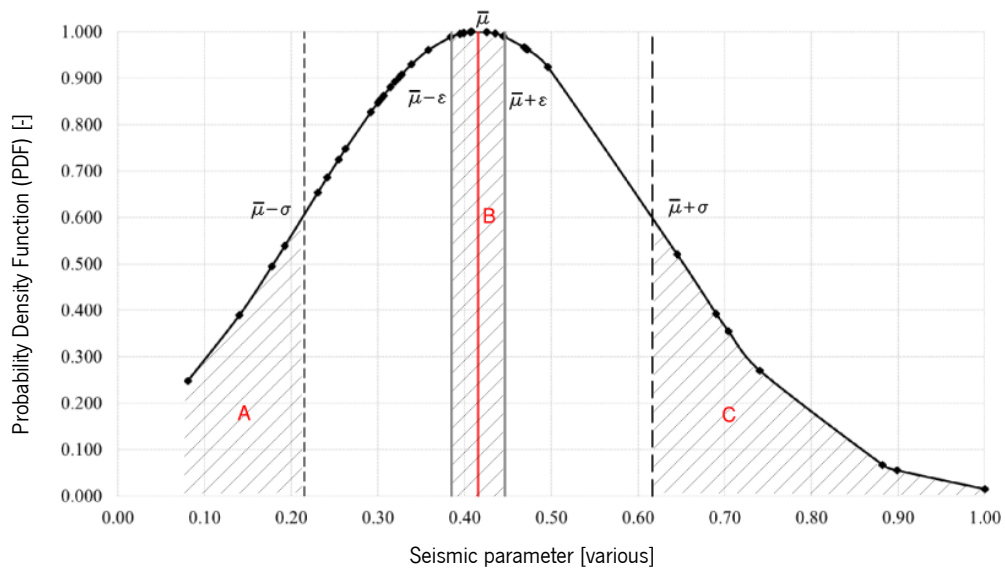


Figure 4-15. Bell distribution example with the lower, medium, and upper range limits of input.

The most recurrent ground motions, belonging to these three ranges, are chosen for performing non-linear time history analysis (Table 4-5 and Figure 4-16, Figure 4-17, Figure 4-18). In this way, the DEM model is subjected to different base excitations that correspond to three different ground motion characters: impulsive (range A), regular (range B) and oscillatory (range C).

Table 4-5. List of the recorded ground motions selected for the sensitivity study and their time histories.

ID	Date [dd/mm/yyyy]	Range	Event name	Direction	M_w	Duration [s]	PGA [m/s^2]
1	31/10/1935	A	Helena Montana	North-South	6.0	50.92	1.58
9	28/06/1966	B	Parkfield	North-South	6.0	44.29	0.62
11	09/02/1971	C	San Fernando	North-South	6.5	70.19	0.25
27	17/01/1994	C	Northridge	North-South	6.7	56.87	4.02
36	24/08/2016	A	Central Italy	East-West	6.2	27.89	8.50
40	08/09/2017	B	Mexico "Chiapas"	East-West	8.2	163.50	2.46

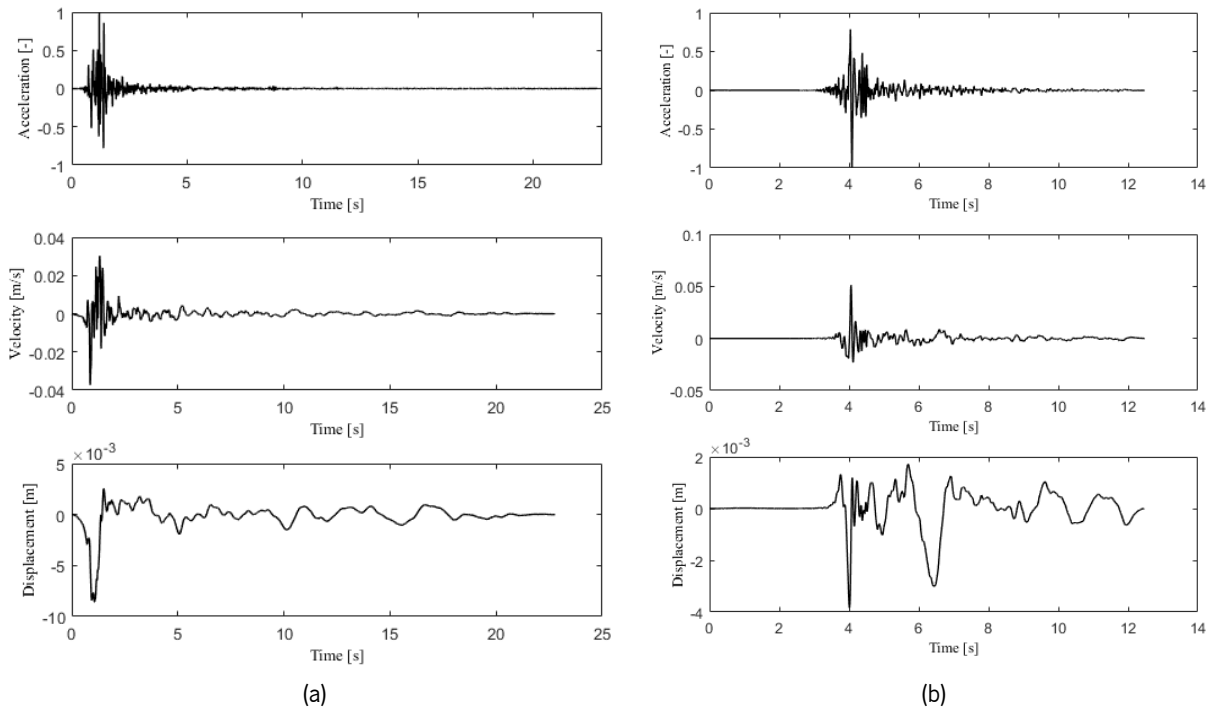


Figure 4-16. Time histories of accelerations, velocities and displacements of the impulsive earthquakes (range A): (a) Helena Montana – ID1, (b) Central Italy – ID 36

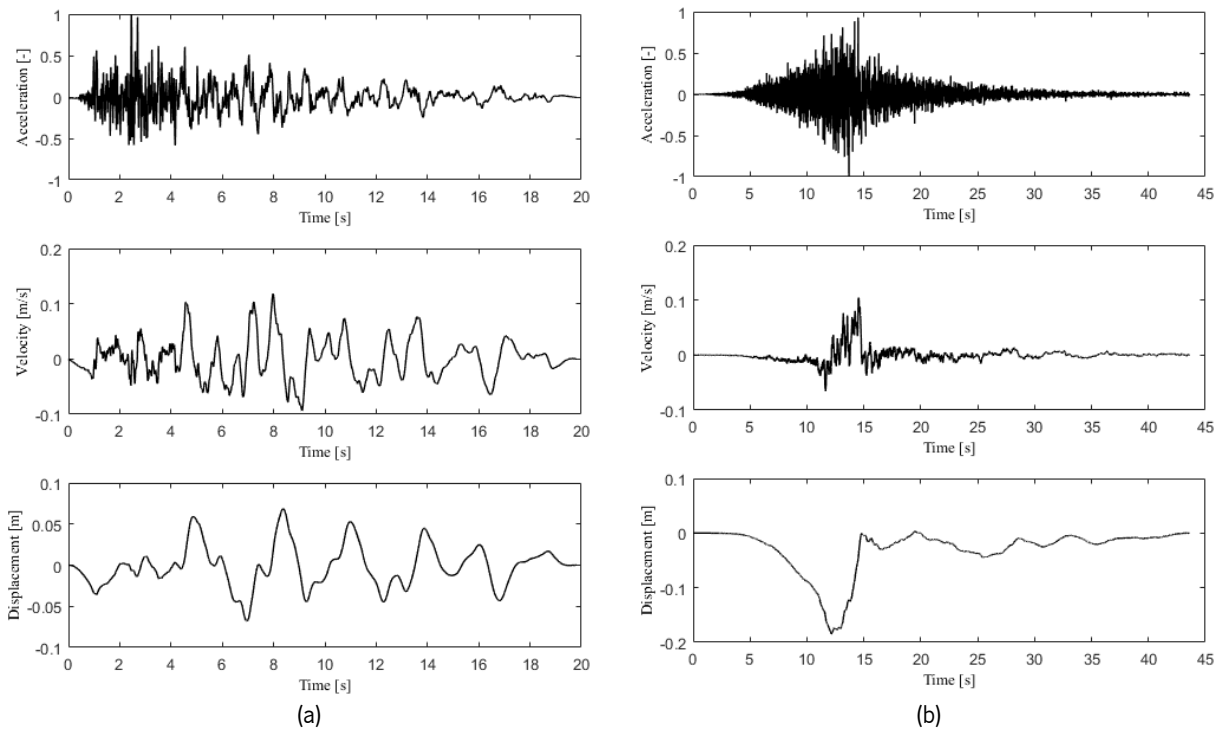


Figure 4-17. Time histories of accelerations, velocities and displacements of the regular earthquakes (range B): (a) Parkfield – ID 9, (b) Mexico Chiapas - ID 40

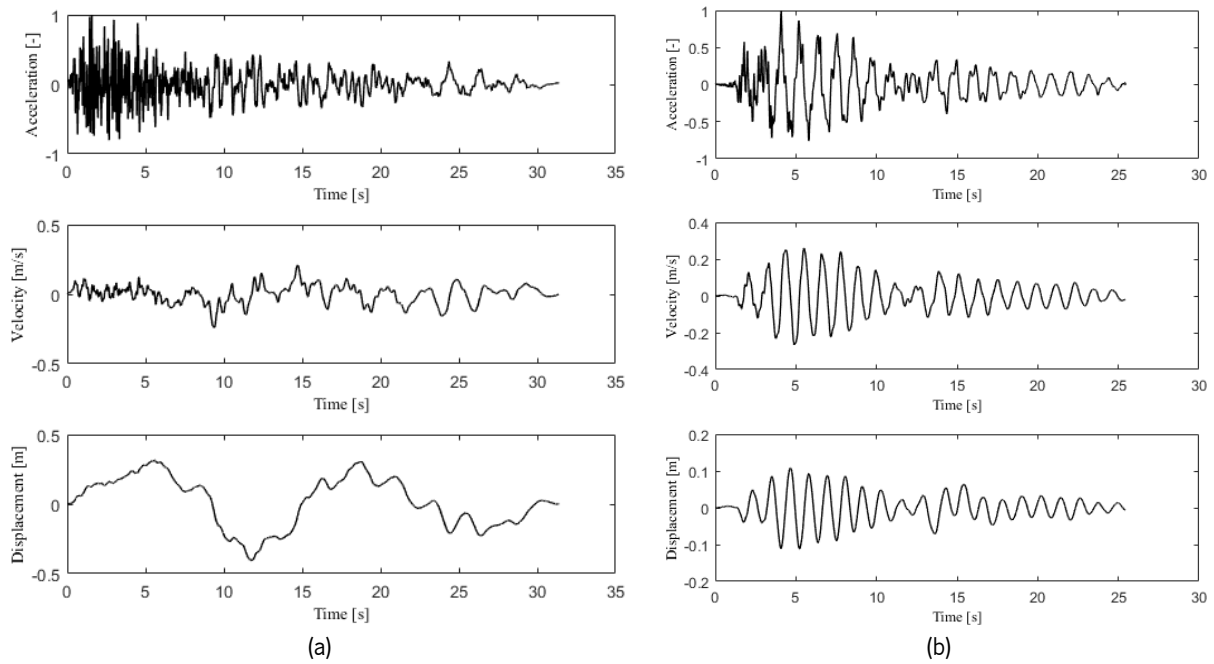


Figure 4-18. Time histories of accelerations, velocities, and displacements of the oscillatory earthquakes (range C): (a) San Fernando – ID 11, (b) Northridge – ID 27.

4.4.2 Results

The IDA was performed up to the collapse by applying an amplification factor at the time histories of the velocities in steps of 25% per each analysis. For the sake of consistency, the same scale factor is applied at the time step of the records, according to the Cauchy-Froude similitude law, as specified in Section 3.4.2. A wide scatter is detected for all the parameters presented in Table 4-6, except for the PGV, which represents a stable indicator at the collapse.

Table 4-6. Selected ground motion parameters for the non-linear time history analyses with the main results at the collapse of the DEM model.

ID Earthquake	1	36	9	40	11	27	$\bar{\mu}$	σ	ε	CoV
Range	A		B		C					
Character	Impulsive		Regular		Oscillatory					
PGA [m/s^2]	14.86	15.46	3.27	5.04	2.78	1.00	7.07	6.40	2.61	0.91
RMS _A [m/s^2]	0.93	1.19	0.50	0.56	0.53	0.24	0.66	0.34	0.14	0.52
PGV [m/s]	0.28	0.36	0.18	0.26	0.30	0.27	0.27	0.06	0.02	0.22
RMS _V [m/s]	0.02	0.03	0.05	0.03	0.08	0.09	0.05	0.03	0.01	0.56
PGD [mm]	28.81	12.01	45.96	206.48	225.98	22.27	90.25	98.40	40.17	1.09
RMS _D [m/s]	0.00	0.00	0.02	0.06	0.10	0.01	0.03	0.04	0.02	1.26
AI [m/s]	3.13	2.82	0.79	2.21	1.44	0.24	1.77	1.15	0.47	0.65
$t_{d(10-90)}$ [s]	0.64	0.50	9.21	7.34	17.55	11.69	7.82	6.59	2.69	0.84
IE _S [J]	0.30	0.27	0.31	0.52	0.79	0.36	0.42	0.20	0.08	0.48
LD _{V(10-90)}	2.73	2.24	10.79	10.84	20.44	14.07	10.19	6.93	2.83	0.68
IP ₍₁₀₋₉₀₎	9.75	6.25	60.95	41.46	68.55	53.01	40.00	26.38	10.77	0.66

On average, the PGV value at the collapse is equal to 0.27 ± 0.02 m/s. This suggests that despite very different accelerations and displacements content of the inputs, the change of velocities is more relevant at the collapse level for vaulted structures. On the other hand, the PGA, which is often taken as a reference parameter by the codes for designing and assessing structures, presents a high value of coefficient of variation (0.91), not embodying a good variable for the definition of the collapse of vaults. In addition, the impulsive character of the earthquakes (range A) does not mandatorily correspond to an earlier collapse. The time histories of velocities of the impulsive ground motion ID 1 (Helena Montana earthquake) have been amplified around fourteen times while for ID 36 (Central Italy earthquake) they have been increased only two times, in comparison with the recorded input.

Both impulsive and oscillatory motions, which have similar characteristics to sine-pulse motions, highly influence the response of the rocking type structures like the examined dry joints vault, an aspect already demonstrated in the case of dry joints arched models by De Lorenzis (2007) and Dejong (2008).

Comparing the deformed shapes for each record at collapse (Figure 4-19), the failure mechanism first involves the fixed edge of the vault, with the formation of the four hinges, leading to the collapse, similar to the experiments. However, those hinges are evident in the lower and medium ranges (A-impulsive and B-regular), while for the upper range (C-oscillatory), their occurrence is faster, resulting in a fall of the fixed web, with a complete disconnection of the diagonals. The first hinges, according to these specific boundary conditions, always occur along the same web (fixed edge), showing a detachment of the blocks along the diagonals. The unique differences are appreciable in the mechanism caused by Central Italy's input, where the transverse southern web collapses when the opposite ones are still stable.

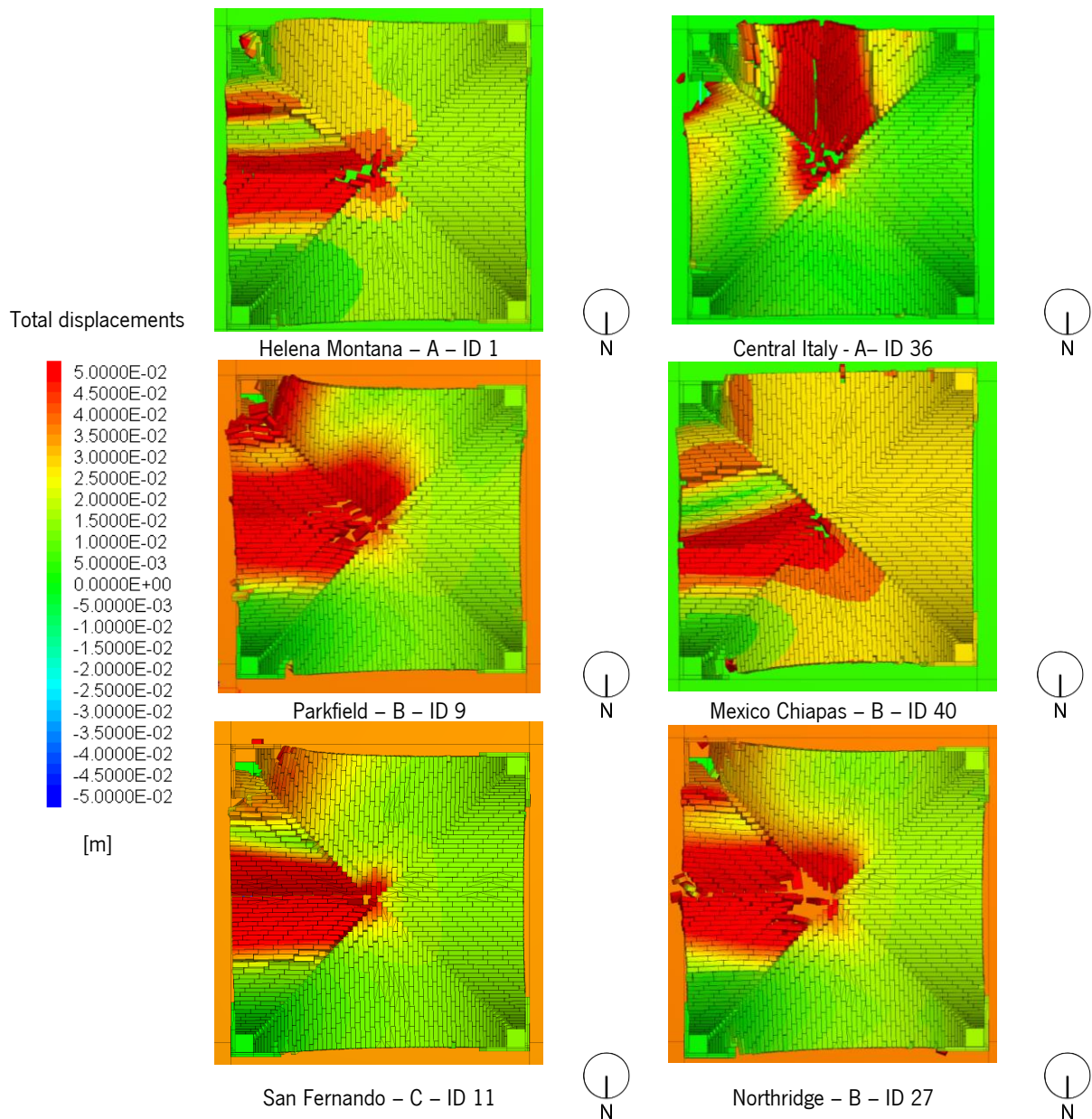


Figure 4-19. Deformed shapes of the DEM simulations before the collapse for the selected earthquakes.

4.5 Final remarks

The numerical simulations of shaking table tests of a reduced-scale vault, tested under unidirectional excitation, through FEM and DEM models are presented in this Chapter.

The calibration of the DEM model is supported by modal properties obtained from the dynamic identification tests, while FEM calibration is also based on the numerical simulation of quasi-static tests (in-plane shear tests and tilting table tests). This study allows to consciously adopt peculiar modelling strategies (*e.g.* detail of the diagonals 'geometry) and material properties of unknown parameters, such as the stiffnesses of the joints and Young's modulus of the diagonals.

Before replicating the same input sequence, as it was done in the shaking table tests, an investigation on damping is conducted on the FEM model, to justify the assumption of null damping and to be coherently comparable with the DEM model. For this kind of structure made of dry joints, the influence of the damping is not relevant, mainly because the joint's stiffness prevails in comparison with the viscous damping dissipation during the analysis. Adopting the null damping results is the most effective strategy to obtain results in a reasonable timeframe, and it has relatively little effect on the results.

Comparing FEM and DEM models with the experimental response, it is noticed that DEM is generally capable of reproducing the large displacements and replicating the collapse mechanism observed during the shaking table tests, matching in terms of cracks, falling blocks, and time occurrence of the damage sequence. DEM presents more difficulties in replicating the ultimate displacements than FEM, which is quantitatively reliable, but it lacks in terms of computational effort (six times the duration of DEM analysis).

Moreover, the implicit solution nature of FEM correctly simulates the location of the damage, but the ultimate collapse, including the falls of units, cannot be reached.

From the sensitivity analysis, which considered six different transient analyses with the DEM model, it is possible to conclude that the collapse occurs for different acceleration and displacement amplitudes, but similar peak ground velocities (PGV). Within this context, the PGV represents a stable parameter for the assessment of vaults. In addition, the collapse mechanism is pretty similar between all the analyses, showing the first hinges located at the fixed edge of the model, as observed during the shaking table tests.

The present work may be extended in the future, including imperfections (Dell'endice *et al.*, 2020) on both FEM and DEM models, and damping (*e.g.* proportional to the mass only, by using Maxwell springs, or Hunt and Crossley model) for high seismic amplitudes (close the collapse) for the DEM model to improve the numerical response and the assessment of the seismic performance of vaulted structures (Lemos and Sarhosis, 2023).

This page has been intentionally left blank

5. Full-scale vault: design, construction and test setup

5.1 Introduction

As described in the state of the art (Chapter 2), the majority of attention in the literature is given to relatively simple structures, made of composite materials, or localised structural components, whose dynamic behaviour must be widely investigated before extending their outcomes to more complex structures. Chapters 3 and 4 narrowed the scope to dynamic assessment methods for groin vaults focusing on stability, rather than strength. In practical terms, this means concentrating on the geometrical equilibrium of block structures. However, the seismic assessment of full-scale masonry groin vaults is of crucial importance, because of their prevalence in the architectural heritage and the losses (economic, cultural and casualties) that they may cause if damaged by a seismic event.

At this stage of the research development, a better understanding of the response of full-scale masonry vaults to dynamic loading is necessary, mainly to develop tools that can be used to assess the safety of these horizontal curved-shape elements. This assessment is more complex and cannot be uniquely studied from the stability point of view, especially if specific strengthening techniques have to be evaluated. Because of this, in this thesis, a full-scale mortared groin vault is tested through shaking table tests performed in the Earthquake Engineering and Structural Dynamics Division (NESDE) at the National Laboratory of Civil Engineering (LNEC), in Lisbon.

In this Chapter, the full-scale specimen is introduced and described through preliminary studies, preparatory simulations, construction phases and material characterisation tests. This level of knowledge is appropriate to undertake successful shaking table tests, which induce in-plane shear distortion in two configurations of the specimen (see Chapter 6). The first configuration is the unstrengthened groin vault specimen (UNS), while the second configuration is the same specimen repaired and strengthened at the extrados with the TRM technique (SM).

5.2 Full-scale vault: from the design to the construction of an ancient vault

In this Section, a brief description of the specimen design and setup of the boundary conditions are presented. The stages of the construction follow the instructions given by ancient treatises. Those stages are described next, together with the expedients for repairing the extrados.

5.2.1 Setup definition and boundary conditions

The specimen's geometry and boundary conditions setup are designed taking into account the dimensions and load capacity of the 3D LNEC shaking table, and the geometry, pattern and boundary conditions of the reduced-scale vault (see Chapter 3).

In order to respect the geometric scale ratio between the two specimens, some dimensions are fixed, namely the square plan ($3.50 \times 3.50 \text{ m}^2$), net span (2.90 m), the rise (1.20 m) and constant thickness (0.12 m), as shown in Figure 5-1. The total height of the specimen is equal to 1.80 m and the lengths of the three couples of steel cables (red lines in Figure 5-1) are equal to 2.40 m along the eastern edge and equal to 2.45 m along the North and South edges. The steel cables' purpose is the same as the aluminium cables in the reduced vault - avoid torsional effects of the piers and ensure in-plane shear mechanism during the dynamic action. All the final drawings are presented at the end of this document in Annex 3.

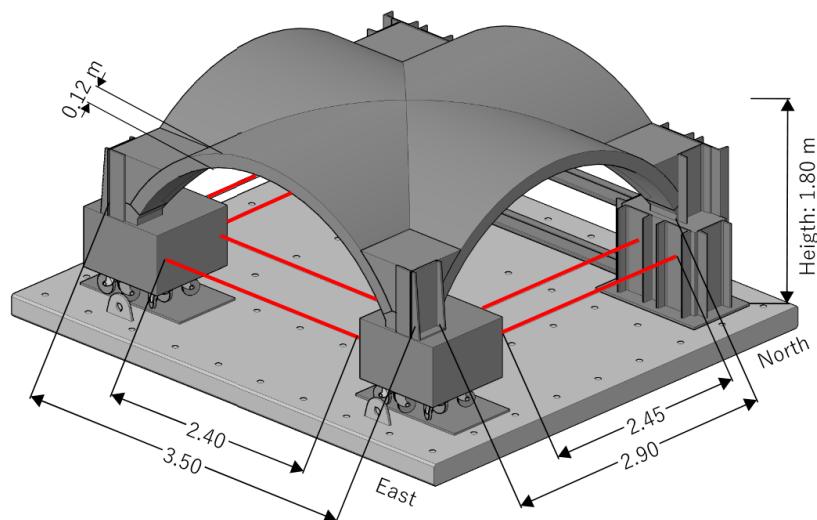


Figure 5-1. Full-scale geometrical model defined for this work in AutoCAD 3D environment. Main dimensions in m.

Figure 5-1 represents the final configuration of the full-scale vault, which is obtained as a result of several preliminary numerical analyses, done using a finite element model carried out in DIANA 10.5 (2022). Those analyses, which follow the macro-modelling approach, helped to define the most appropriate boundary conditions of the specimen to induce the desired in-plane shear mechanism (see Figure 1-9c). This numerical study aims to prevent inaccuracies that can compromise the success of the experimental campaign.

During this phase, which consists of an iterative simulation process, several boundary conditions and connections have been evaluated to identify the optimal configuration. The specimen is assumed to be placed at a specific location of a real monumental building, namely the central aisle of a lateral nave located in a generic three-nave church (Figure 5-2).

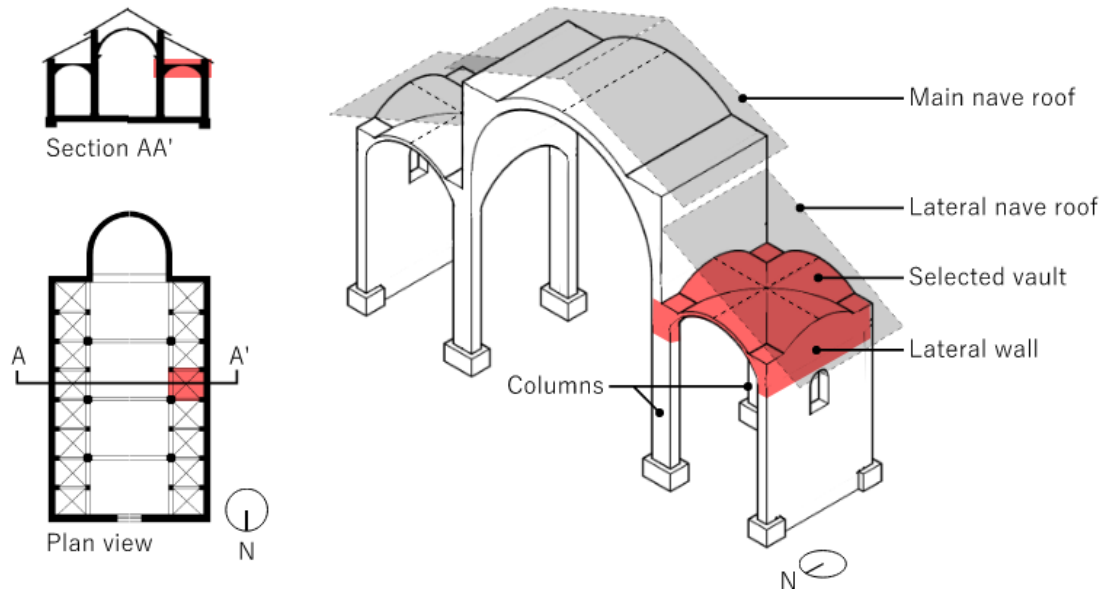


Figure 5-2. Virtual location of the specimen in an ideal three-nave church.

The optimal configuration has to respect two conditions:

- the first global mode obtained by eigenvalue analysis showcases in-plane shear behaviour;
- diagonal cracks, associated with in-plane shear behaviour, should be recognisable running transient structural analysis.

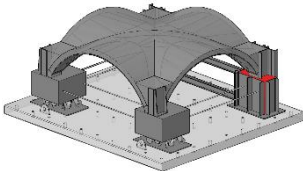
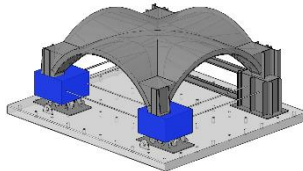
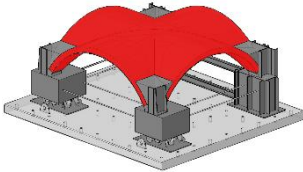
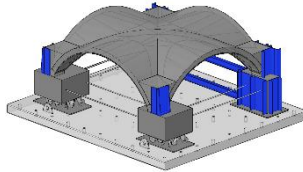
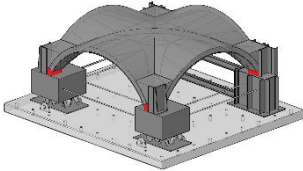
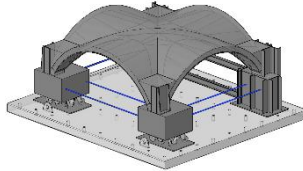
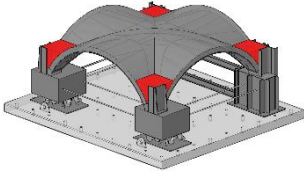
To perform this iterative numerical process, preliminary linear properties are adopted as follows: for the masonry elements of the model (piers and shell of the vault), the density is equal to 1800 kg/m^3 , Young's modulus is 1.2 GPa , the compressive strength is equal to 1.20 MPa , tensile strength is 0.12 MPa and Poisson's ratio is 0.2 . For the steel elements of the model (cables, frame and profiles), density is assumed equal to 7800 kg/m^3 , Young's modulus is equal to 210 GPa and Poisson's ratio is equal to 0.3 . Also, non-linear material properties are associated with the masonry material, namely: compressive fracture energy (1.92 KN/m) and tensile fracture energy (0.035 KN/m) (Lourenço, 2008).

Similarly to the reduced-scale specimen's boundary conditions, two movable piers, located along the eastern side of the vault, are left free to slide while the opposite two piers, along the western side, are fixed to the ground. The two movable piers stand on a system of wheels, which are numerically simulated with standard vertical constraints. In this way, movements in the longitudinal and transverse directions are allowed when horizontal static and dynamic loads are applied to the simulated vault. On the western side, simulating the external wall of the church (see Figure 1-8a,b), the two masonry piers are fixed to a reinforced concrete slab placed on the shaking table (Table 5-1). In the numerical model, this connection is simulated as fully pinned. In order to increase the piers' stiffness and to avoid relative displacements between the two piers, a steel frame made with IPE and UPN profiles was also used.

Differently from the reduced-scale model, the weight of the roof, pushing from the main nave, and the weight of the columns, which host the supports of the vault, are also taken into account through equivalent masses, using four steel masses with dimensions 0.84 m x 0.84 m x 0.27 m and 1.2 tons each placed below the movable supports (Table 5-1).

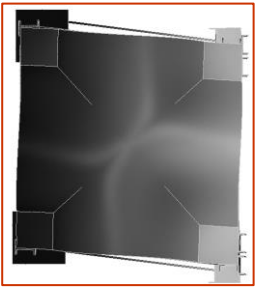
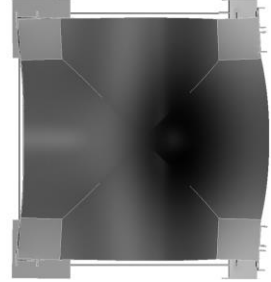
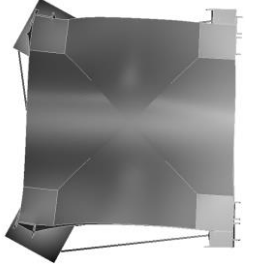
As already stated, to prevent any rotational movement of the supports, the four abutments are linked to each other by three couples of steel cables with rod ends characterised by plain spherical bearings. Their diameter ($\Phi 32$ mm) is updated through eigenvalue analysis until the first global mode associated with the in-plane shear mechanism is stable. An overlying infill is built in correspondence with the vault's four corners up to 50% of the rise of the shell of the vault (Gaetani, 2016). Steel elements (UPN and HE profiles) are added along the height of the supports and along the boundaries of the infill to avoid local failures at the corners. The steel profiles aim also at increasing the stiffness of the supports and preventing possible bending deformation. Two threaded rods, named as connectors in Table 5-1, with a diameter of $\Phi 20$ mm and length of 50 cm, are vertically inserted within the thickness of each fixed pier to avoid localised cracks close to the base of the shell of the vault, as foreseen from the preliminary analyses. Table 5-1 defines the nomenclature used in this thesis for the main components of the full-scale specimen, and their location.

Table 5-1. Nomenclature and location of the different components of the full-scale specimen. Masonry elements are highlighted in red and steel elements are highlighted in blue.

	Masonry		Steel
<p><u>Fixed piers:</u> fully pinned Mix mortar: binder Bricks bond: English</p>		<p><u>Steel masses</u> above the system of wheels, vertically constrained</p>	
<p><u>Shell of the vault:</u> Mix mortar: binder+filler Bricks bond: radial</p>		<p><u>Profiles:</u> UPN <u>Steel frame:</u> UPN and HE</p>	
<p><u>Supports of the vault</u> Mix mortar: binder Bricks bond: English</p>		<p><u>Cables with rod ends</u> diameter: $\Phi 32$ mm</p>	
<p><u>Infill</u> Mix mortar: binder+filler Bricks bond: English</p>		<p><u>Connectors</u></p>	<p>*Crossing the infill and the lateral piers (see Annex 3) 2 threaded rods: $\phi 20$mm length 50 cm</p>

At the end of the optimisation process, the numerical model comprises 752,143 elements, 165,123 nodes and about a half million degrees of freedom, with mesh size varying between 1 cm and 15 cm. This macro model satisfies the two conditions that were previously listed. From the results of the eigenvalue analysis, the mode shape of mode 1 correctly replicates the in-plane shear behaviour. Mode 2 is related to the vault's global transverse behaviour, and mode 3 involves the rotation of the steel masses (Table 5-2). The first frequency, corresponding to the shear mechanism of failure, is far from the following global frequency values, therefore mode 1 is the more likely to occur in case of seismic excitation.

Table 5-2. Principal modes of vibration of the numerical model and their frequencies.

Mode 1	Mode 2	Mode 3
		
$f_1 = 7.10$ Hz	$f_2 = 22.14$ Hz	$f_3 = 24.14$ Hz
Longitudinal	Transverse	Torsional (steel masses)

Non-linear static analysis and non-linear time history analysis are performed along the longitudinal direction (y direction of the ground motion) to study the effectiveness of the final configuration, before proceeding with the construction of the specimen. The main outcomes of the preliminary analyses are summarised below:

- the diagonal cracks, expressed in terms of tensile strains, depict in-plane shear failure since they are mainly obtained along the groins of the vault;
- the role of the infill is favourable to avoid localised damage close to the supports since it increases the effective thickness of the vault close to the corners - the infill concurs in making the model stiffer and more resistant;
- the final optimised design of the specimen allows to perform a number of shaking table tests useful to build a capacity curve and keep the in-plane shear mechanism constant for the different amplitude of ground motions. The integration of steel profiles and cables has been fundamental in achieving this outcome.

For more insight into the preliminary numerical analysis, the reader is referred to the Bianchini *et al.* (2019).

5.2.2 Construction of the specimen and application of the strengthening

The construction of the unstrengthened specimen (UNS) follows the guidelines gathered from ancient treatises and historical information (Rolla, 1869; Breyman, 1885; Ungewitter and Mohrmann, 1890; Fitchen, 1961; Heyman, 1995a; Di Pasquale, 1996). Those treatises suggest specific methodology, construction techniques and building progression, which are valid for brick-masonry groin vaults and that can be summarised by the following steps:

- realisation of the boundary conditions system;
- realization of the centring;
- construction of the shell of the vault;
- hardening.

Once the first set of shaking table tests are performed on the unstrengthened configuration, the specimen is repaired from the previous damage and strengthened (SM), following the instructions provided by Kerakoll, which are:

- closing the cracks with *Geocalce antisismico F* (2021b) and preparing the holes for the injections;
- grout injections in all the medium/severe cracks with *Geocalce antisismico FL* (2021c);
- let the liquid mortar harden for 28 days and then clean the shell;
- placing and anchoring the textile-reinforced mortar (TRM) system, namely *Geosteel grid 200* (2021d), embedded in the thin layer of compatible mortar (*Geocalce antisismico F*);
- hardening for 28 days.

All the previous steps are here described and further commented.

Boundary conditions

The full-scale vault is built on top of a reinforced concrete slab with dimensions 4.2 m × 4.9 m × 0.2 m. This slab, which is designed for rigidly moving the specimens in the laboratory, is cleaned and prepared to host this specimen. A thin layer of mortar is laid down in correspondence with the location of the steel profiles (HE and UPN along the West side) and of the steel wheels (East side). The western edge, which is the fixed edge of the specimen to replicate the lateral wall of the church, is composed of a rigid steel frame (a system of UPN300 profiles), anchored to the slab employing chemical anchors (M12 and M20).

Once the steel frame and the steel profiles are settled in their locations, the masonry lateral fixed piers (west side) are built, using solid clay bricks (provided by Cenol company), which are arranged according to the English bond stereotomy. The bricks are also used for the other masonry parts of the specimen: namely, supports, shell and infill. Within the thickness of the fixed piers, a couple of chemical anchors M20, with a total length of 50 cm, are vertically inserted to reinforce this part of the specimen (Figure 5-3a), as mentioned in the preliminary analysis (see Section 5.2.1).

The eastern side, representing the central colonnade of a main nave, hosts the movable system with the steel masses, placed above nine heavy-duty swivel caster wheels (Figure 5-3b). The wheels can rotate around their axis for 360° and rapidly change direction while the shaking table moves. The wheels lay on the top of a smooth thin steel surface to reduce friction and to ensure a pure roto-translation movement of the system. On the top of the steel surface, oil is spread before the shaking table tests.

The three couples of steel cables also belong to the system of boundary conditions, and were installed by inserting their extremes inside the rod ends fixed to the steel elements (Figure 5-3c). This took place before starting the construction of the centring, to counteract any opening of the span and taking into account the available space at the different stages of the construction sequence. Load cells with load capacity between 0 and 100 kN are embedded at 1/3 of the total length of each cable.

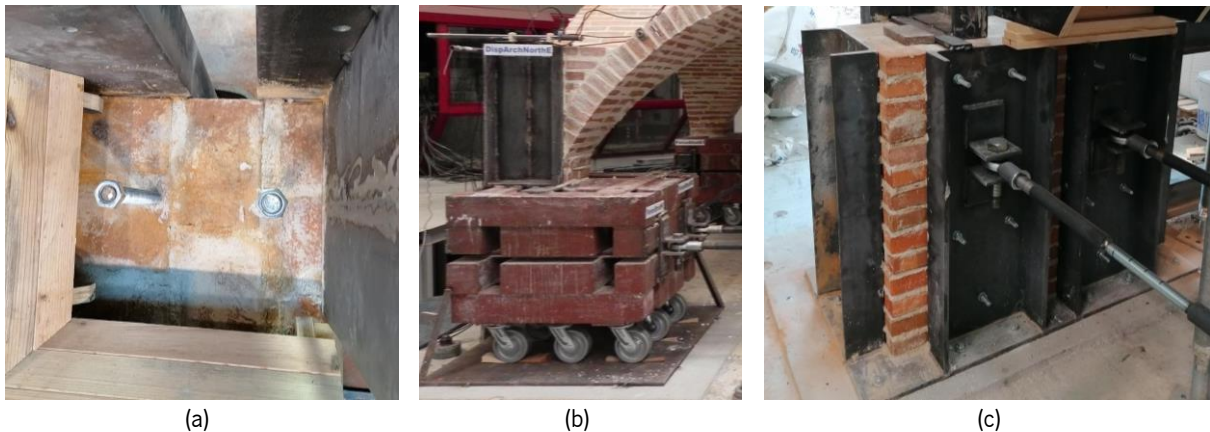


Figure 5-3. Boundary conditions details: (a) steel connectors inside the fixed piers, (b) wheels above the steel surface and anchored to the ground before the tests, (c) steel cables with rod ends and load cells in place.

Centring

The centring design is as much important as the design of the shell of the vault because each solid timber plank has to respect the final curvature of the intrados of the vault, and the centring construction is highly dependent on the ability of the carpenter (Scamozzi, 1616; Breymann, 1885; Fitchen, 1961; Cangi, 2012). Due to the peculiarity of the specimen, some expedients are needed to overcome the

physical restrictions given by the presence of the boundary conditions and by the limited space (less than 15 cm) between the upper surface of the steel masses and the impost of the vault (Figure 5-4 and Figure 5-5). Nevertheless, a historical approach is again considered for the design of the centring, as it is for the design of all parts of the specimen.

The scaffolding (centring) is composed of two parts: *centinatura* and *manto* according to Rolla's definitions (1869). *Centinatura* (Figure 5-4a) bears the weight of the vault and it is composed of a reticulated system made of strong timber beams, while *manto* reproduces the curved surfaces where the masonry of the shell is laid and left to harden (Figure 5-4b,c).

For what concerns the *centinatura*, close to the intersection of the diagonals, a timber pole bears the transverse slats. The portion of structure between the springers and the mid-stones (about 30°) is subject to a high friction coefficient so that it stays easily in equilibrium and it is self-load-bearing. At this location, the use of a very robust centring is not required, unlike the rest of the specimen, which needs considerable support and a strong *centinatura*'s system.

Following the empirical rules, *manto* is composed of two main parts: a solid timber slats system (Figure 5-4b), to sustain the first rows of bricks, and a solid timber plank (also called 'drum'), placed on top of the previous element (Figure 5-4c). The drum is 20 mm thick and it creates a uniform surface, shaped like the intrados of the vault itself. For the easiness of the construction process, the width of the slats along the *manto* is equal to the thickness of the brick plus the thickness of the following joint. In this way, while placing the bricks, the masons can follow the boundaries of the slats to ensure each layer is planar and perpendicular to the *manto*'s curvature.

The vertical timber supports of *centinatura* (four at the corners and one underneath the key) create a vertical gap along the perimeter of the plan of the vault. This gap is useful during the dismantlement operation - it allows the *manto* to slowly descends for it to be removed, making the process smooth.

Figure 5-5 shows the system of boundary conditions and the centring of the vault, before the beginning of the construction of the shell.

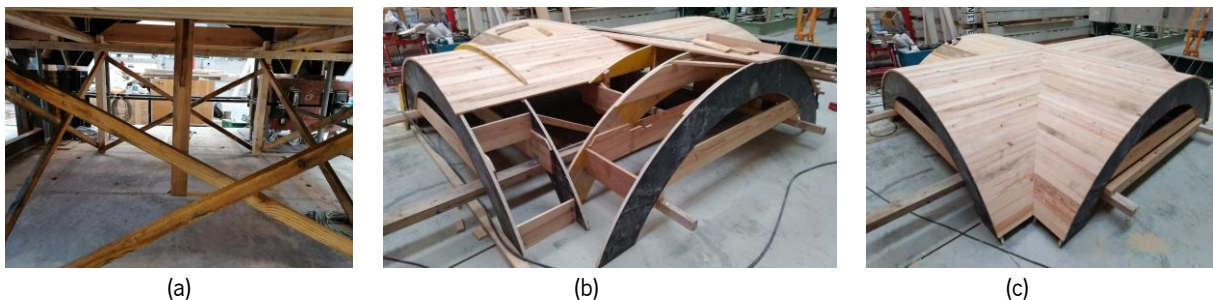


Figure 5-4. Centring of the full-scale vault: (a) *centinatura*, (b) slats system of the *manto*, (c) drum of the *manto*.

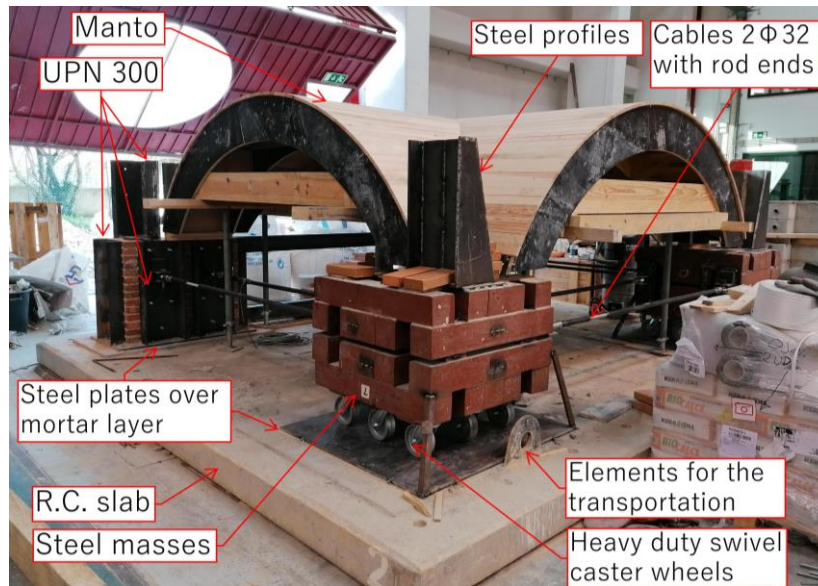


Figure 5-5. Boundary conditions of the model and its centring before the construction.

Construction of the shell

Before starting to place the bricks, preparatory precautions are needed. The cables are put in tension, fixing the value of force equal to approximately 5 kN through the load cells. This prestress force counteracts the opening of the span occurred during the construction due to the mass of the shell, which increases as the construction progresses, and due to the temporary imposed load of the masons working on top of the shell. On the other hand, higher values of prestress may induce excessive closure of the span and lead to undesired hinges on the shell, before the beginning of the tests. For the same reason, the steel masses above the system of wheels are pinned at the concrete slab through inclined steel short bars. In this way, the span of the vault is fixed during the construction and forces that may induce undesired tension actions and cracks are avoided.

Later, oil is applied above the external surface of the centring to ease the dismantlement and to avoid that mortar and bricks adhere to the timber slats.

External scaffoldings are placed around the boundaries to sustain material and masons while working at higher locations of the specimen.

After all these expedients, the bricks can start to be laid on the top of the drum of the *manto*. In regard to this phase, care and attention must be paid especially for the bricks located close to the groins, because those bricks need accurate cuts to ensure the interlocking between the two adjacent webs.

To facilitate this process, the geometry of the shell is theoretically divided into two primary webs (PW) and two secondary webs (SW) (Figure 5-6a), as indicated by treatises on ancient vaults' construction. This imaginary division helps the masons to replicate accurate and proper cuts along the diagonals, considering the typical symmetry of the groin vaults. Figure 5-6b and Figure 5-6c describe the sequence

of cuts that are required for maintaining a good construction technique and consistent methodology from the impost until the key of the shell of the vault. The first two nonplanar cuts interest the bricks to be disposed along the diagonals of the primary web. The first cut creates a surface in contact with the drum of the *manto*, while the second cut originates a surface that stably hosts the bricks of the next row, coming from the secondary web. The third cut interests the brick to be placed on the secondary web and it originates the upper surface to host the following row. The angle of the cuts varies along the diagonal of the vault, from higher values at the impost to nearly zero at the key.

This methodology belongs to the ancient construction technique, whose knowledge has nowadays been lost by the majority of masons. Because of this, preparatory timber samples are used to train the workers to cut the bricks in accordance with this method (Figure 5-6d).

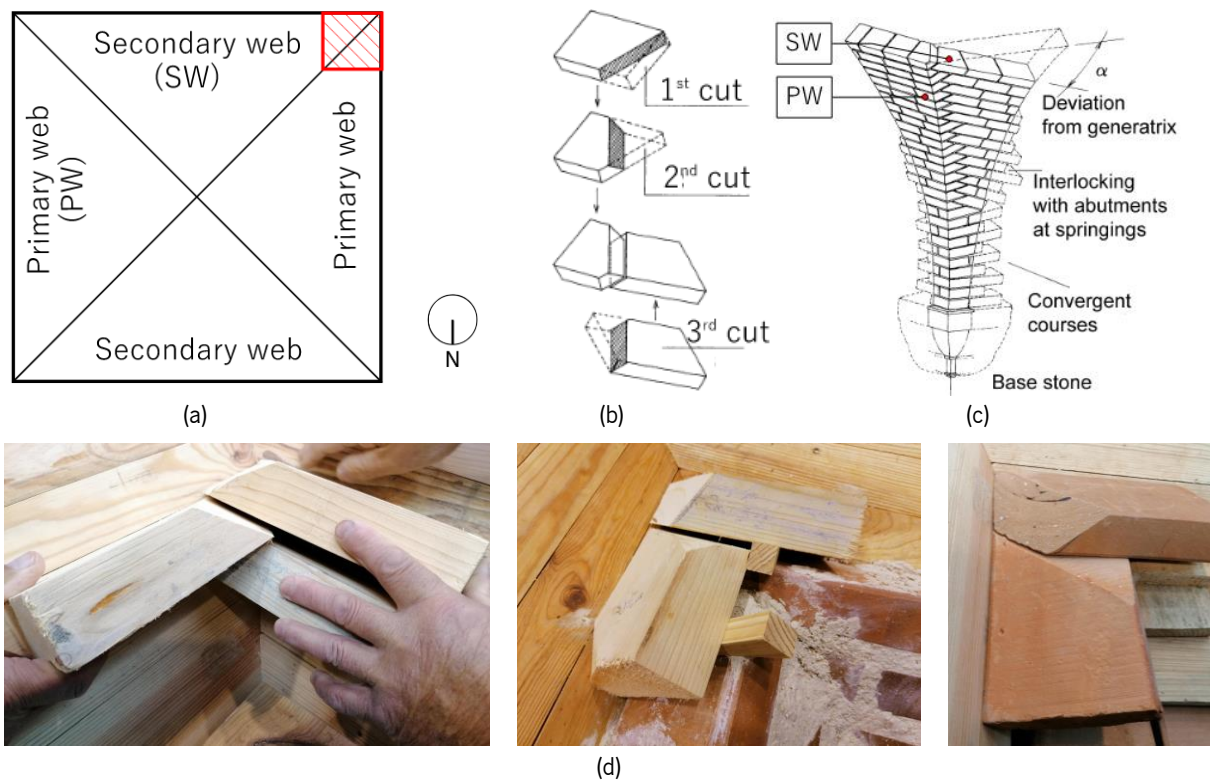


Figure 5-6. Design of the cuts of the diagonals: (a) scheme of the webs, (b) sequence of cuts (adapted from Cangì, 2016), (c) disposition along the diagonal from the intrados (adapted from Cangì, 2016), (d) explanatory timber and bricks samples.

According to the ancient rules, the construction should ideally start from the four corners and proceed simultaneously until the key of the vault, stopping at regular heights of the curvature to check the alignments of the rows (Figure 5-7). Guides, tapes, and temporary supports help the masons in this process. The interlocking of bricks along the webs and the radial pattern are guaranteed considering a misalignment of the bricks. Along the external arches, a continuous sequence made of 1 brick and $\frac{1}{2}$ brick is kept constant to ensure joints' discontinuity. This improves adhesion and avoids sliding. Each brick is wetted before being laid on the surface of the centring to increase the adhesion with the mortar.



Figure 5-7. Construction sequence of the unstrengthened specimen.

The closure of the key of the vault is a delicate phase of the construction. Depending on the accessibility to the top of the specimen in the construction site, this process may change and specific strategies need to be evaluated. In this case, the fresh mortar was intensely vibrated between the joints at the key to make it as compact as possible (Figure 5-8), using the same mix design of the other areas of the shell. Timber elements 1 cm thick are used to maintain the joints' thickness constant between the bricks. Finally, the infill above the four corners, which gives stability to the shell, is completed using an English bond pattern. Despite the infill above the shell of the historical vaults is usually made of waste material and debris, in this case, the same solid clay bricks of the webs are used. This choice is driven by the need of stability during the shaking table tests, to reduce complexity during construction and achieve homogeneous conditions at all the corners.



Figure 5-8. Closing the key of the vault: (a) disposition of the bricks with their misalignments, (b) filling the joints.

Transportation and dismantlement

As already mentioned, the construction of the specimen takes place outside of the shaking table, namely on top of a reinforced concrete slab of about 11 tons. The slab hosts four steel elements useful to lift the specimens, and holes are located at regular intervals to fix the specimens to the shaking table to achieve a perfectly fixed connection. The vault is transported onto the shaking table before removing the centring and after the curing time (Figure 5-9). Treatises propose several options for the dismantlement of the centring structure of vaults. Recent guidelines suggest waiting for at least three months before removing the centring in order to let the mortar harden and to conduct a safe dismantlement. For this specimen, the recommended curing time is exceeded, since dismantlement happened 260 days (about 9 months) after the end of the construction.

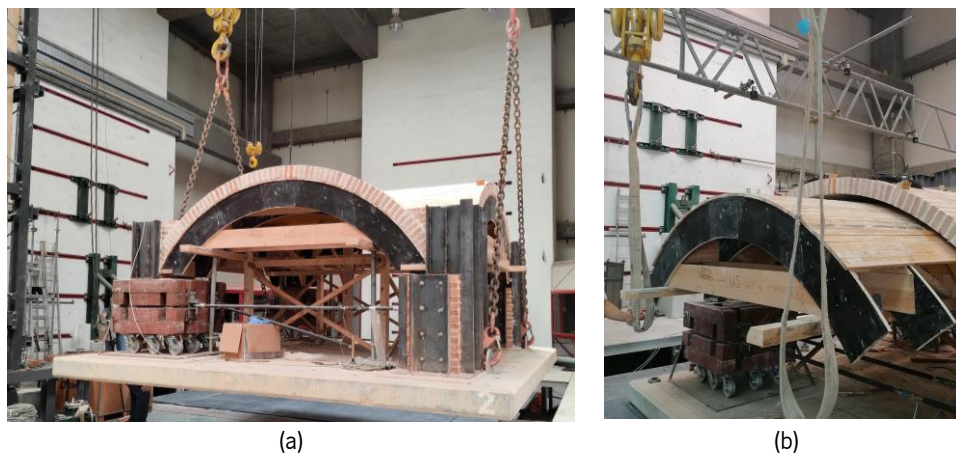


Figure 5-9. Transportation and dismantlement operations: (a) specimen before reaching the shaking table, (b) system of ropes for making the *manto* glide outside.

The dismantlement has to be undertaken slowly while measuring the displacements of selected points, in this way it is possible to monitor the occurrence of potential instabilities. In particular, the vertical displacement of the key is monitored through an optical camera during the dismantlement. A displacement of 1.40 mm was measured at the end of the operation.

Despite all the care, the transportation and dismantlement operations induced two light cracks at the key level in both longitudinal and transverse directions (North and East webs). Those initial cracks probably may be due to the deflection of the reinforced concrete slab, under the self-weight of the specimen (Figure 5-10). The cracks were repaired and injected to recover the continuity of the shell with a mortar provided by Kerakoll (*Geocalce antisismico F*) was used for sealing the external surfaces of the vault where cracks are located. Then, the more fluid mortar (*Geocalce antisismico FL*) was injected through the holes. The details of these two mortars are available in Section 5.3.

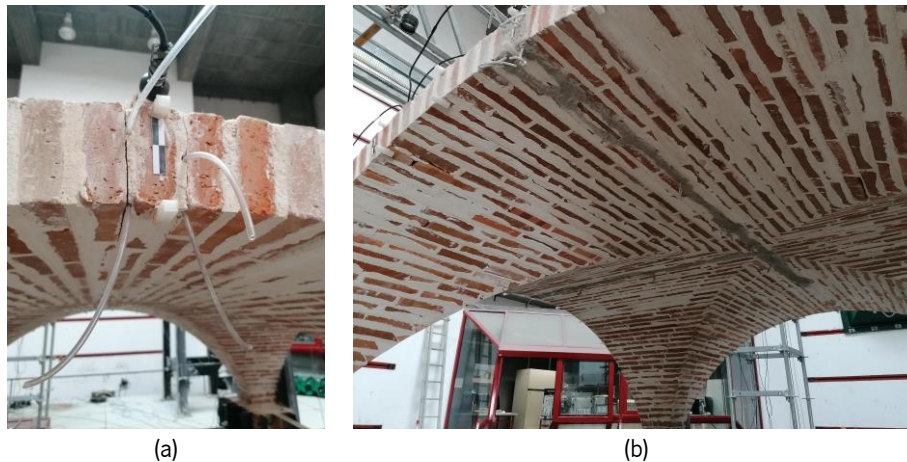


Figure 5-10. Cracks after transportation and dismantlement: (a) details of the cracks before the injection, (b) injected cracks.

In order to obtain a precise survey that represents the exact geometry and configuration of the undamaged state of the specimen, the photogrammetry technique was used. The final appearance of the specimen is shown in Figure 5-11. More than 250 photographs are taken with an exposition time of $1/500$ s, with an ISO of 100 and an aperture lens of 3.6 mm, and then processed with the software Metashape to generate a dense point cloud. Each photo portrays a frame, which is partially overlapped with the frame of the following photograph, either at the extrados or intrados to gather enough data to represent the complete geometry. Scaled markers and setup equipment are used at this stage to enhance the precision of the photogrammetry. Through the photogrammetry, a mass of 12.7 tons was obtained for the specimen.

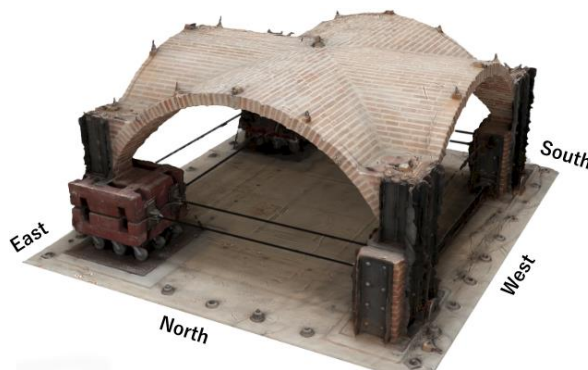


Figure 5-11. 3D photogrammetric model of the unstrengthened specimen.

Repairing and application of TRM strengthening technique

The application of the TRM at the extrados of the vault, which takes place after the first set of shaking table tests (UNS), is also here described. This operation is performed without the need of a new centring and outside of the shaking table, because of safety reasons. Once the first set of tests on the UNS specimen is completed, the cracks are sealed with *GeoCalce Antisismico F* mortar from both intrados and extrados. Then, the more fluid mortar *GeoCalce Antisismico FL* was injected (Figure 5-12a). After approximately 1 month, in line with Kerakoll's recommendations, the external surface is cleaned and the strips of steel and basalt meshes (*Geosteel grid 200*) are laid out on top of the extrados, which is previously covered by a fresh thin layer of *GeoCalce Antisismico F* mortar (Figure 5-12b).

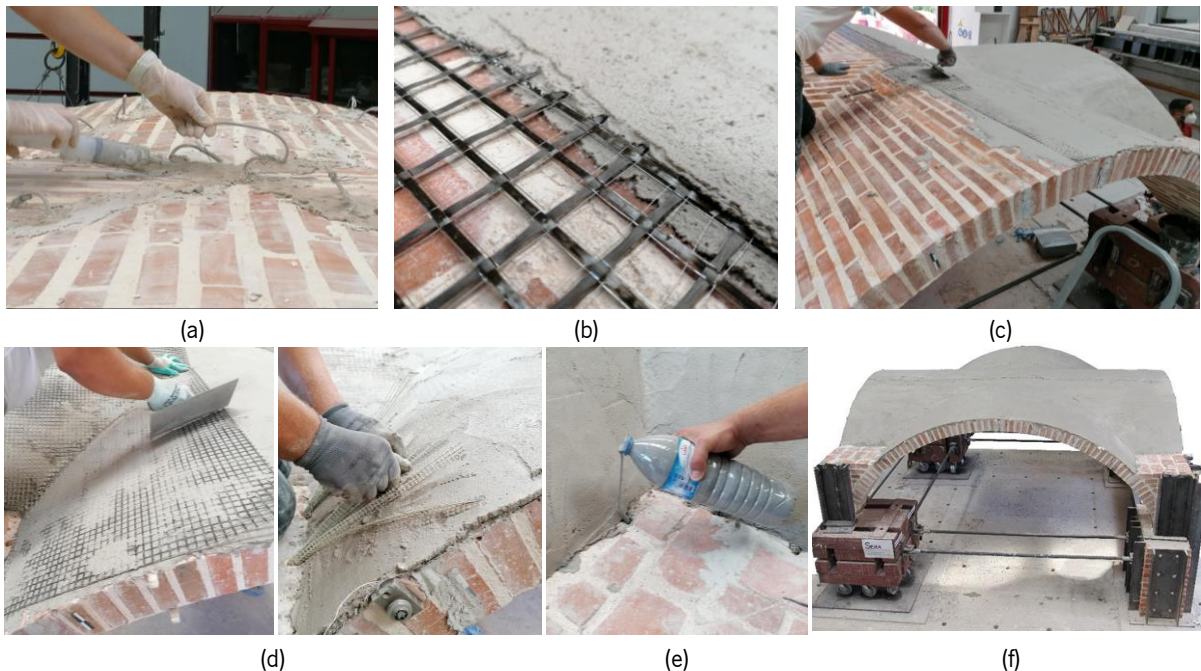


Figure 5-12. Application of the TRM strengthening system: (a) injecting fluid mortar *GeoCalce Antisismico FL* in the cracks, (b) detail of the *Geosteel grid 200* embedded in *GeoCalce Antisismico F* mortar, (c) application process, (d) detail of the corners close to the infill with *Geosteel grid 600*, (e) injecting the fluid mortar *GeoCalce Antisismico FL* mortar, (f) final appearance of the strengthened specimen (SM).

Geosteel grid 200 is spread out to cover the extrados, with approximately 20 cm of overlap between two adjacent strips of the grid. Afterwards, the system *Geosteel grid 200* is fixed to the boundaries between the infill and the beginning of the shell using another finer grid (*Geosteel grid 600*). *Geosteel grid 600* is rolled and inserted inside the thickness of the infill through holes drilled on purpose (Figure 5-12d). This enhances the adhesion of the TRM system with the shell at the corners, where the curvature of the extrados changes. The TRM system was stabilised by the liquid mortar *GeoCalce Antisismico FL* mortar,

which was used to fill the drilled holes (Figure 5-12e). The total thickness of the TRM system ranges from 8 mm to 10 mm along all the extrados.

During the construction, the repairing and strengthening phases, samples of mortars are collected to be examined in terms of construction regularity and quality. The average and final values of all the materials are presented in Section 5.3 and they will be the basis for the calibration of the numerical models (see Chapter 7).

5.3 Experimental characterization of materials

As referred in Chapter 1, the design of historic masonry vaults involves many factors, such as the geometrical parameters (units and joint dimensions), the arrangements of the units, the practical criteria on the workmanship, the centring, the curing and the mechanical properties of the materials (brick, mortar and masonry). The first factors are evident by simple visual observations and direct measurements, while the mechanical properties of the materials require a deeper level of knowledge, difficult to be achieved with limited resources. Thus, very often, in engineering practice, material properties are usually assumed by looking for similar existing examples in literature or the field.

In this work, extensive information about the materials used for the construction of the full-scale specimen was collected, to fulfil two objectives of this work, namely to replicate a historical masonry vault in the laboratory, considering its ageing process, and to provide a set of experimental data, which can be useful for other future case studies. Because of this, at each material level (bricks, mix mortars, brick-mortar bond and masonry wallets), material characterisation tests are performed and compared with literature values. All the material characterisations tests protocols and results are described in this subsection.

Units

Solid clay bricks are adopted for the construction. Their dimensions ($4.5 \times 12 \times 23$ cm) are close to or comprised within the common ranges found in literature, compatible with the Italian territorial habit (Gabrielli, 1997; Quirós Castillo, 1997). The dimensions of the full-scale bricks are based on the blocks of the reduced-scale vault, amplified five times in order to keep the same number of bricks along the webs of the vault (excluding the infill). The thickness of the joints is kept constant at the intrados and equal to 1 cm for both head and bed joints. Since clay bricks are characterised by a wide scatter in terms of strength and durability, highly dependent on the quality of the raw clay and the conditions of manufacturing (Fernandes, Lourenço and Castro, 2010), samples were tested in the laboratory to validate the technical specifications provided by the manufacturer.

According to EN 772-1 (2011), five samples of prismatic shape ($133 \times 40 \times 40 \text{ mm}^3$) were tested under compression (Prism_i with $i = 1, \dots, 5$). This test aims to obtain the Young's modulus and the compressive strength of the prisms. On the day before testing, the specimens were immersed in water with free access to all surfaces, and then removed just before the tests according to the RILEM standards.

The specimens were placed on the top of the machine platen and carefully aligned with its centre (Figure 5-13a). Afterwards, the upper platen was moved, under force control, to the top surface of the brick specimen. This platen has a hinge to prevent any unfavourable effect due to non-parallelism between the specimen faces and the platen. No interposition material between machine platens and the specimen was considered. All the prismatic specimens were tested monotonically under axial displacement control. Three axial LVDTs were placed in front of three surfaces of the prism to measure the relative displacement under two platens, while the load cells measured the force applied to the prism (see Figure 5-13a). The relative displacements were used to calculate the axial strains, evaluated at the middle third of the prism's length, while the force was used to determine the compressive stress (Figure 5-13c).

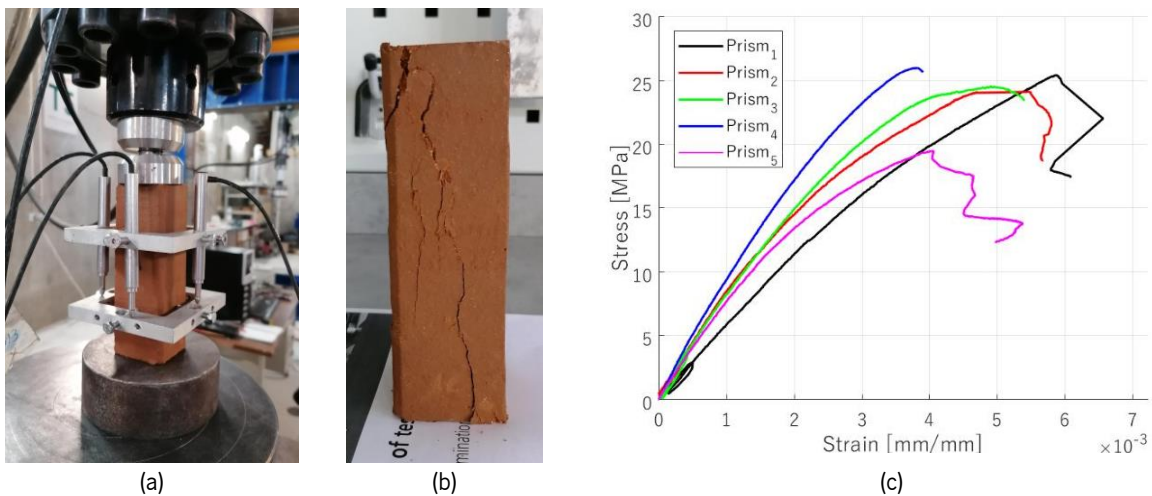


Figure 5-13. Compression tests on the bricks according to EN 772-1 (2011): (a) prism at the beginning of the test, (b) failure mode, (c) stress-strain curves.

The velocity rate was changed from $2.0 \mu\text{m/s}$, in the beginning, to a quasi-static speed of $0.5 \mu\text{m/s}$ near the peak load. The failure mode of the sample consists of the typical compression state of the units represented by vertical cracking (Figure 5-13b). From the stress-strain diagrams (Figure 5-13c), the post-peak branch is achieved after reaching a maximum peak of about compressive strength $f_c = 25 \text{ MPa}$ ($\text{CoV}=3.34\%$). The Young's modulus is calculated in the 30%–70% stress interval of the peak load because the stress-strain diagrams exhibited linear behaviour within this region, resulting in

an average value equal to $E = 6.2$ GPa. All the results from the compression tests on the bricks are summarised in Table 5-3. The obtained experimental values are compatible with the values of ranges indicated in the literature, such as the ones listed by Fernandes *et al.* (2010) and Borri *et al.* (2015).

Table 5-3. Characteristics of the bricks: mean values based on six prismatic samples (σ : standard deviation; CoV: coefficient of variation).

Tests	Dimension [mm]	Young's modulus [GPa]	Max force [kN]	Density [kg/m ³]	Compressive strength [MPa]
Compressive tests	133 × 40 × 40	6.2	46.61	2204.2	25.0
		$\sigma=1.1$	$\sigma=4.80$	$\sigma=33.7$	$\sigma=0.8$
		CoV=10.3%	CoV=11.0%	CoV=1.5%	CoV=3.3%

Mortar of the joints

In accordance with the purpose of the work, the mortar was prepared to reproduce a relatively “weak” historic mortar, in order to replicate the ageing condition of an existing vault. A wide literature review about the expected mechanical parameters of a historic mortar was carried out (see Annex 4). From this study, it was concluded that historic mortars, reproduced in laboratory conditions and made of a lime binder, show on average a bulk density of about 1680 kg/m³, a compressive strength of 2.3 MPa and a tensile strength of 0.62 MPa, after 28 days of curing. To get close to these literature values, an air lime mortar would have been ideal, being the most widely used between the 11th and 19th centuries (Vecchiattini, 2015). However, mix designs of air lime mortars are more complicated, less controllable during the construction process, and their hardening process is slower than hydraulic mortars.

For the sake of simplicity, a ready-mixed hydraulic mortar was selected, with a standardised composition, making the assembly on site easier. In fact, during the construction, only water has to be added to the mix, reducing the risk of errors in the blend. More in detail, Biocalce® MuroSano NHL-3.5 mortar, provided by Kerakoll (2021a), is the binder of this composition. According to the technical data sheet, the aggregates consist of two types of washed river silica sand (0.1 - 0.5 mm and 0.1 - 1 mm) and pure white marble powder (0 - 2.5 mm). Its compressive strength is equal to 5 MPa. Since this value is quite unrealistic for reproducing an existing historical mortar, that faced time and environmental deterioration, the influence of adding calcium carbonate filler was evaluated (Segura *et al.*, 2020). Segura *et al.* (2020) conclude that adding limestone filler can serve to adapt hydraulic lime mortars to different practical applications, like the conservation of historical masonry buildings, ensuring compatibility with the original substrates. The reference value of compressive strength achieved by Segura *et al.* (2020)'s study is equal to 1.90 MPa. For this research, the Portuguese company OMYA

provided the required filler (Betocarb - OU (2013)), collected by waste material of hydraulic cements and mortars. Table 5-4 summarises the main characteristics of the mortar and the filler that were used during this phase of the investigation.

Table 5-4. Characteristics of the mortar provided by Kerakoll and OMYA.

	Biocalce MuroSano (EN 459-1) Kerakoll	Betocarb - OU
Specific weight (bulk density)	1350 kg/m ³	900 kg/m ³
Particle size	<2.5 mm	<2.0 mm
Mixing water	≈ 4,5 ℓ / 1 bag 25 kg	
Density of hardened mortar	1700 - 1740 kg/m ³ approx.	
Compressive strength (28 days)	5 N/mm ²	
Class (EN 988-2)	M5	

Several compositions were evaluated until reaching a good workability range, by performing flow table tests (from 167 to 182 mm), and a value of about 2.0 MPa of compressive strength was obtained after 28 days of curing, as recommended by Segura *et al.* (2020). The flow table tests were conducted based on the standard EN 1015-3 (2004). The contents of four different trial mortar mixes (M_A , M_B , M_C , M_D) are expressed in terms of weight proportions of the powder materials, calculated through the respective bulk densities. Table 5-5 presents the proportions by volume and by weight with the corresponding water ratio able to get an appropriate flow value.

Table 5-5. Mortars proportioning by volume and by weight, water ratio and flow measured according to EN 1015-3.

	Powder volume [%]		Proportion by weight [kg]		Water ratio	Flow [mm]
	Hydraulic premix	Filler	Hydraulic premix	Filler		
M_A	50	50	1	0.645	19.0%	168.0
M_B	40	60	1	0.774	18.6%	170.5
M_C	60	40	1	0.516	20.0%	174.5
M_D	30	70	1	0.900	20.1%	181.5

Once the flow diameter is achieved, a set of six prismatic samples for each mix design was prepared and properly cast in metallic moulds with the standard dimensions of $160 \times 40 \times 40$ mm³. The mixing procedure and the compaction process were carried out according to the standard EN 196-1 (2016). Afterwards, the prisms are placed in a polyethene bag in order to keep the humidity constant at the range of 90%. After two days, they were removed from the bag and stored to cure in the climatic chamber at room conditions of about 15 ± 5 °C and relative humidity 65 ± 15 %.

Per each composition, the flexural strength f_b and compressive strength f_c were calculated through three-point bending tests and axial compression tests according to EN 1015-11 (2019). The prisms were tested at 7th, 14th, 28th day and 56th day, in order to observe the evolution of strengths of the different blended mixes throughout the curing time (Figure 5-14a). After 28 days, M_C presents the most

satisfactory values ($f_c = 2.45$ MPa and $f_b = 0.84$ MPa), and therefore it was adopted for the construction of the vault. Six additional prisms (with M_C mortar) were prepared and cured in lab conditions ($M_{C\text{-lab}}$), to replicate as accurately as possible the same hardening conditions of the vault (Figure 5-14b).

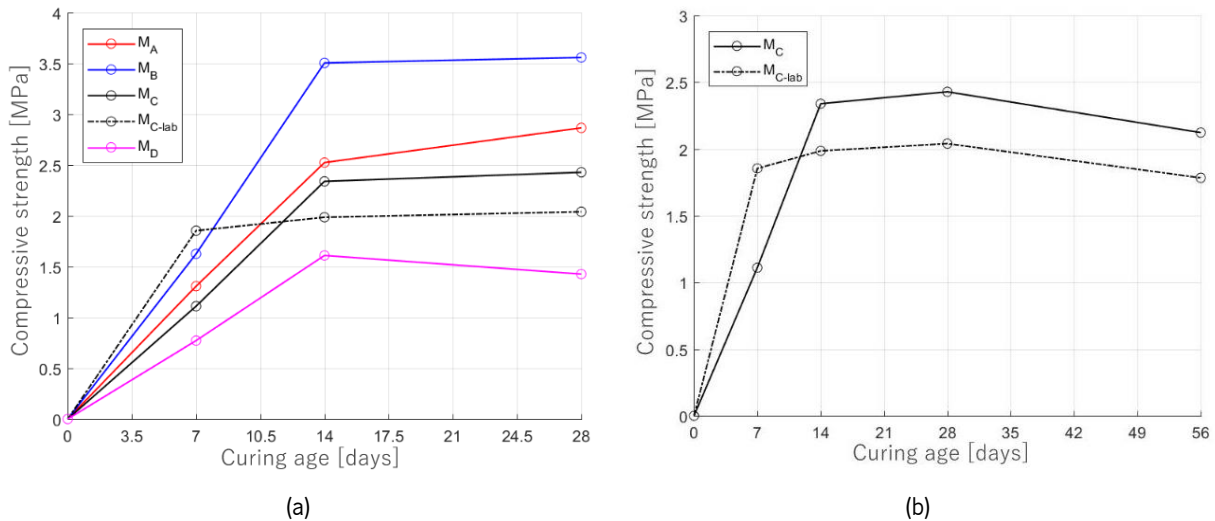


Figure 5-14. Evolution of values of compressive strengths: (a) different blended mortars, (b) M_C and $M_{C\text{-lab}}$ curves.

As expected, $M_{C\text{-lab}}$ is faster to harden than M_C because of the laboratory conditions and after 28 days its compressive strength has a value of about 2.0 MPa. Through this study, it is possible to conclude that M_C mortar is appropriate for the historic full-scale vault. During the construction of the full-scale vault in the laboratory, three prismatic samples were collected every three mixes of mortar and aged in a controlled environment to check consistency of its quality during the construction. The final bulk density of mortar joints is equal to 2029 kg/m^3 and the average flow diameter equal to 178.7 mm, which is a good value of workability.

The flexural and compression tests for all specimens were carried out on the 7th, 14th, 28th, 56th, 190th, 260th days of age (Figure 5-15). It is noted that the last test (260th day) was carried out on the same day of the shaking table tests on the full-scale vault. Each point in Figure 5-15 represents the mean value of three prisms tested for the flexural strength and the mean value of the six cubes, resulting halves, for the compressive strength. The results follow the expected path. Mortars present a higher increase between the 7th and the 14th day. Then, a plateau is visible between the 28th and 56th day. The two curves start to decrease until getting stable after about 190 days. The peaks in terms of compression and flexure are achieved at the 28th day and they are respectively $f_c = 2.50$ MPa (CoV = 6.91%) and $f_b = 0.93$ MPa (CoV = 13.56%); those strengths decrease to the values of $f_c = 1.69$ MPa (CoV = 10.11%) and $f_b = 0.64$ MPa (CoV = 16.55%) after 260 days.

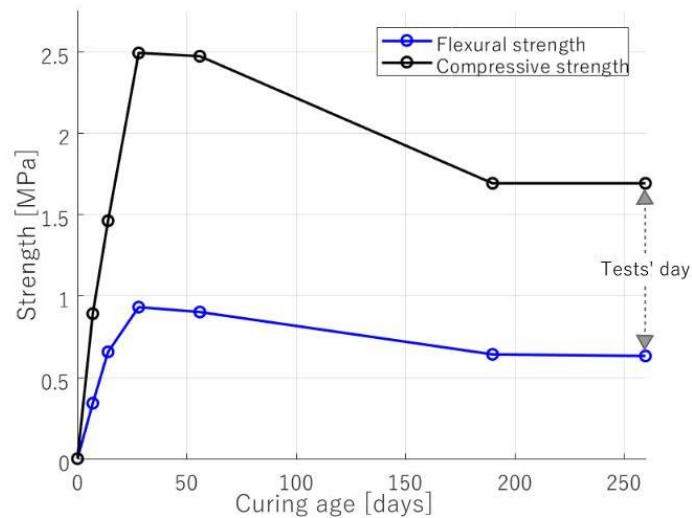


Figure 5-15. Evolution of values of flexural and compressive strength at 7th, 14th, 28th day and 56th, 190th and 260th days of age for the joints of the full-scale vault.

Also during the construction of the masonry wallets, three samples of every three mixes were collected to check the quality of the mortar. Those results are in line with the values obtained from the mortar collections of the vault (Figure 5-15). The Young's moduli of the mortar at 28th days and at the date of the tests are equal to 3978 MPa and 2801 MPa, respectively.

Mortar of the repair and strengthening technique

The modern conservation guidelines recommend the use of products that are compatible as much as possible with the historical substrates while applying a strengthening technique (Ramesh, Azenha and Lourenço, 2019; Segura *et al.*, 2020). This aspect was considered during the application of the TRM at the extrados of the vault (see Section 5.2.2). Thus, the two already cited types of mortars (*GeoCalce Antisismico F* and *GeoCalce Antisismico FL*) were examined following the same methodology described for the mortar of the joints to evaluate the strengths. The flow diameter was evaluated through the cone method, as described in EN 445 (2007). The results of these two binders, cured at the same laboratory conditions of the vault, are shown in Table 5-6.

Table 5-6. Material properties of the *GeoCalce Antisismico F* and *GeoCalce Antisismico FL* mortars, collected during the application of the strengthening technique at different ages.

GeoCalce Antisismico F					
Bulk density [kg/m ³]		Flow diameter [mm]		Density [kg/m ³]	
				28 th day	Test day
2001		166.0		1828	1812
Dynamic elastic modulus [MPa]		Flexural strength [MPa]		Compressive strength [MPa]	
28 th day	Test day	28 th day	Test day	28 th day	Test day
12480	12540	3.95	3.98	13.86	14.66

GeoCalce Antisismico FL					
Bulk density [kg/m ³]		Fluidity [mm]		Density [kg/m ³]	
				28 th day	Test day
1310.0		-		1570	1573
Dynamic elastic modulus [MPa]		Flexural strength [MPa]		Compressive strength [MPa]	
28 th day	Test day	28 th day	Test day	28 th day	Test day
7474	7810	3.92	3.35	11.98	12.53

Masonry

In order to determine Young's modulus, Poisson's ratio, and compressive, tensile and shear strengths of the masonry of the vault, eighteen wallets were prepared. Four of those wallets were earmarked for axial compression tests, two wallets for diagonal compression tests and twelve wallets for the triplet (shear) tests.

The axial compression tests were performed according to EN 1052-1 (1999), using a static hydraulic system from which the applied load, under displacement control, is directly measured. The compression testing machine has a maximum capacity of 5000 kN and it can distribute uniform compression load on the top of the wallets. The compressive force was applied at a quasi-static constant speed of 3 $\mu\text{m/s}$ until the wallet collapsed. Three LVDTs (two vertical and one horizontal) were applied on each surface to measure the elongations (Figure 5-16a,b).

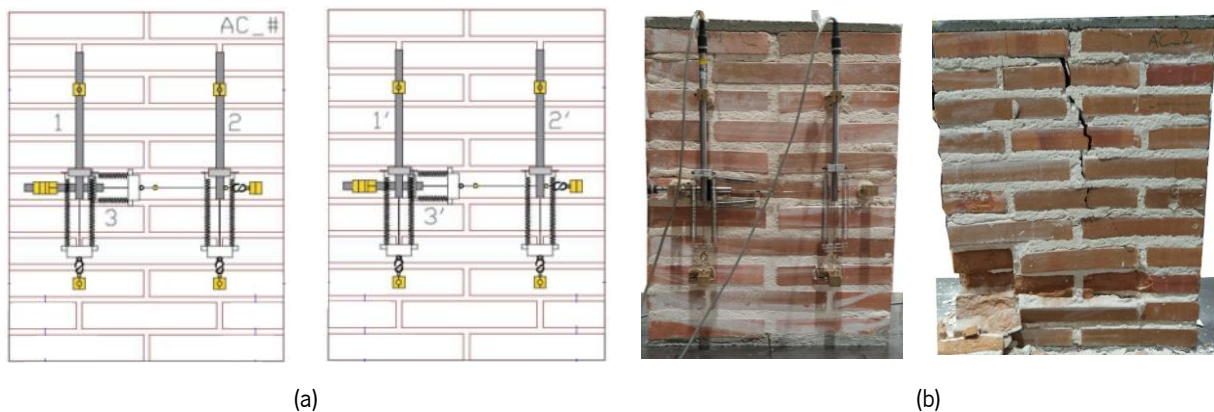


Figure 5-16. Axial compression tests: (a) setup of wallets (front and back face), (b) undamaged and damaged AC₂.

Each specimen (AC_i with i from 1 to 4) is composed of a single leaf of bricks with a height of 619 mm and a width of 468 mm (average values), with a minimum of two bricks for each course.

The Young's modulus was calculated through the average of the longitudinal stress-strain curves obtained for the four measurement positions, to a stress equal to one-third of the maximum stress. The average Young's modulus is 2.2 GPa, while the compressive strength is 9.1 MPa (Figure 5-17a). This result is in line with the well-established formulas and tables provided by national and international building codes, *e.g.* Eurocode 6 - 1996-1-1 (2001), to estimate masonry compressive strength based on mortar and unit compressive strengths, as highlighted in Figure 5-17b).

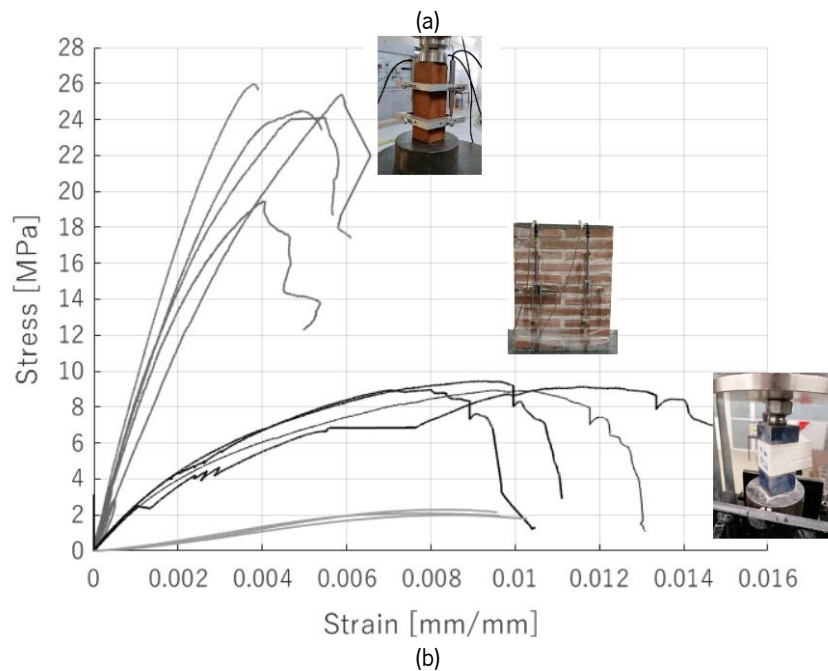
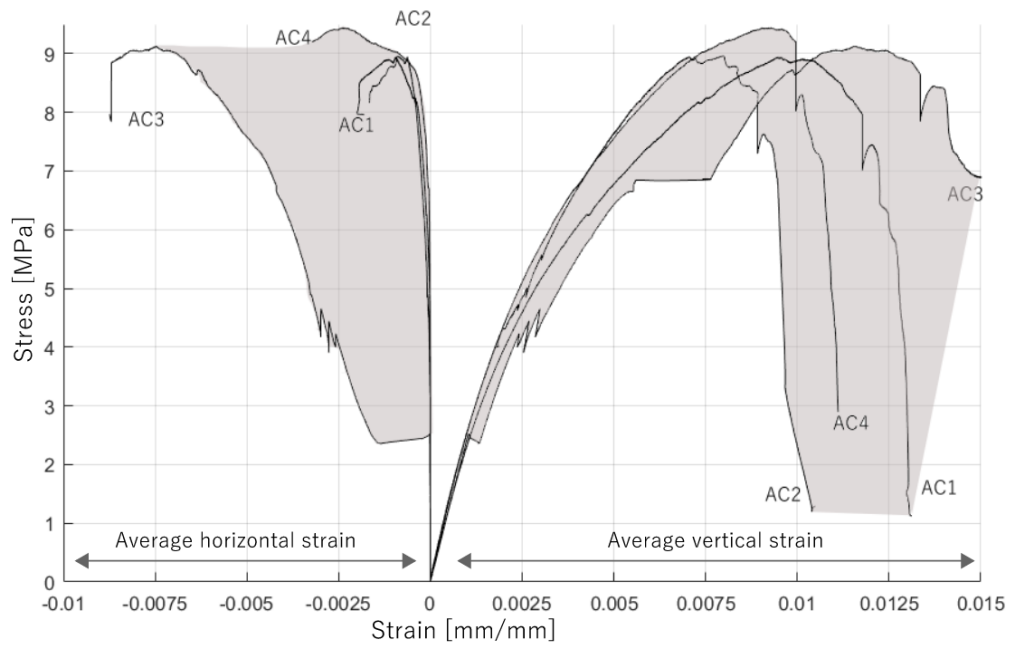


Figure 5-17. Axial compression tests: (a) Stress-strain curves of the masonry wallets (b) Stress-strain curves of the bricks, masonry wallets and mortar cubes.

The diagonal compression tests were performed according to ASTM E 519 (2002). Two wallets (DC_i with i from 1 to 2) composed of one leaf were placed in a testing machine with a maximum capacity of 5000 kN, applying a uniformly distributed load on the upper corner of the wallet rotated at 45° . The force was applied at a constant speed of $5 \mu\text{m/s}$ until the wallet collapsed. One vertical LVDT and one horizontal LVDT were used on each surface (Figure 5-18b). The obtained tensile strength and shear modulus are equal to 0.44 MPa and 762 MPa respectively.

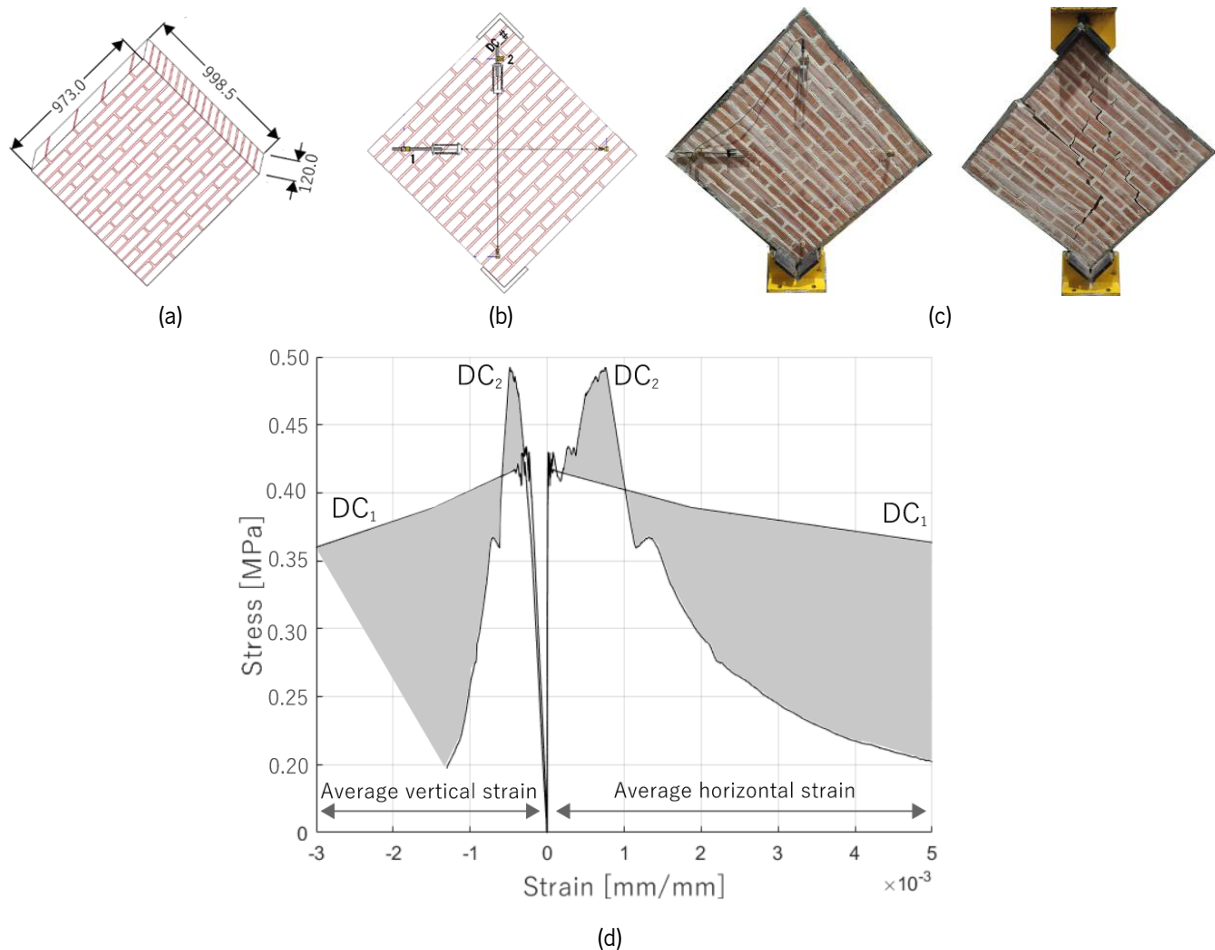


Figure 5-18. Diagonal compression tests: (a) Dimensions of DC_i in mm; (b) setup of wallets: front face; (c) undamaged and damaged wallet before and after the tests; (d) stress-strain curves.

Finally, since shear was defined as the governing mode of failure in masonry vaults subject to lateral loads, shear triplets tests (S_i with i from 1 to 12) were carried out according to EN 1052-3 (2007). The triplets are composed of three units and two joints with a constant thickness of 1 cm. The shear force is transferred by the test device with a maximum capacity of 1000 kN, applying a uniformly distributed load on the top of the triplet (Figure 5-19a), which is bottom supported on two points.

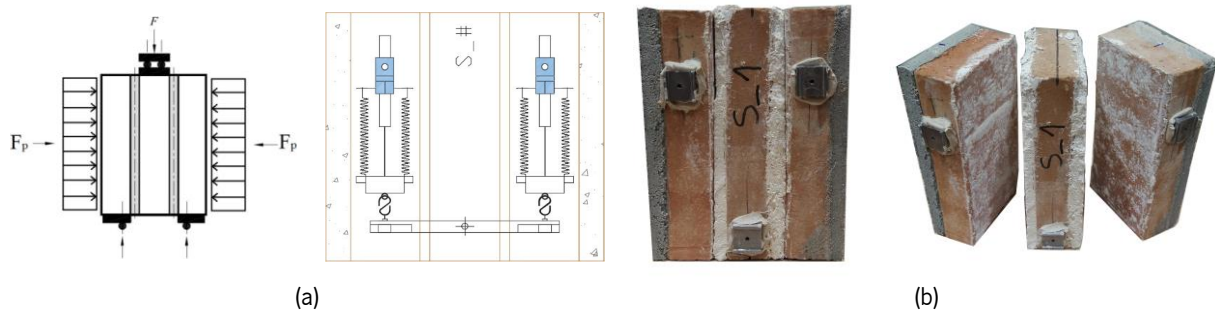


Figure 5-19. Triplet shear tests: (a) test scheme and setup of the triplets, (b) undamaged and damaged wallet before and after the tests.

The force was applied at a constant speed of $0.05 \mu\text{m/s}$ until the end of the test. The pre-compressive force was applied through a compressor circuit with two hydraulic actuators. Taking into account the limitations of the test device, three levels of pre-compressive stresses were considered, namely 0.2 MPa, 0.5 MPa and 0.8 MPa. From triplets tests, the average shear strength is equal to 0.46 MPa, while the friction coefficient is 0.785, which corresponds to a friction angle of 38° , in line with literature ranges (Van Der Pluijm, 1992; Borri, Cangi and De Maria, 2013). Table 5-7 summarises all the material characterisation test results performed on the masonry wallets.

Table 5-7. Summary of the material characterisation tests on the masonry wallets.

Axial compression						
Reference	N° of wallets	Dimension [m]	Max force [kN]	Density [kg/m^3]	Young's modulus [MPa]	Compressive strength [MPa]
EN 1052-1	4	0.47×0.62	500	2255	2223	9.1
Diagonal compression						
Reference	N° of wallets	Dimension [m]	Tensile strength [MPa]	Shear modulus [MPa]		
ASTM E 519-02	2	0.95×0.98	0.44	762.0		
Triplets tests						
Reference	N° of wallets	Dimension [mm]	Shear strength [MPa]	Cohesion [MPa]	Internal friction coefficient [-]	Friction angle [°]
EN 1052-3	12	$l_s=230$ $h_u=173$ $t_{bj}=118$	0.46	0.031	0.785	38

5.4 Testing setup

The type of devices and their locations in the testing setup of the full-scale vault were defined according to the expected behaviour, observed during the preliminary analyses (see Section 5.2.1). Displacement transducers ($LVDT_i$), optical cameras (OC_i), load cells (LC_i) and piezoelectric accelerometers (Acc_i) were used to measure the response of the specimen, both in the seismic and dynamic identification tests (see Section 6.2). Given the expected in-plane shear behaviour and the higher concentration of mass along the eastern edge of the specimen, the optical cameras were placed along this specific elevation and on the key of the vault. The four optical cameras were hung by an external scaffolding, whose basement was outside of the shaking table, to avoid noise in the recorded measurements.

Thirty-two accelerometers were directly placed on the extrados of the vault, anchored to the upper surface of a timber element fixed to the shell. The geometry of the timber elements was designed so that the bottom surface could accommodate the curvature of the shell, while the upper surface (where the accelerometers are fixed) was perfectly planar and horizontal. This allowed to consider the horizontal components of the accelerations only (independent of the angle of the curvature of the shell). The signals of the seismic action applied at the base of the specimen were measured by accelerometers and LVDTs pre-installed on the platform and the actuators. However, an accelerometer (Acc_1) was also placed on the top of the reinforced concrete slab close to the base of the fixed pier (NW corner). The sensitivity of the accelerometers is equal to 100 mV/g and their measurement range is equal to ± 50 g. The six load cells (LC_i) measured the tension forces in the cables between 0 and 100 KN. A prestress force of 5 KN was applied to the steel cables at the beginning of each shaking table test. Four couples of LVDTs measured the opening and closing of the joints along the curvatures of the external arches. They were placed both at the extrados and intrados of the same arch.

In total, 50 signals were acquired using two boards of the National Instruments connected by a trigger. The evolution of damage occurring in the specimen was recorded by five video cameras (VC_i) to draw a complete set of crack maps. Four cameras were located in front of each elevation (VC_i with i from 1 to 4), one action camera OSMO-AC001, named VC_5 , was anchored to a pipers scaffolding above the vault to record the damage at the extrados of the vault during the tests. Figure 5-20, Figure 5-21 and Figure 5-22 present the setups of all the channels, both for the unstrengthened model (UNS) and strengthened model (SM).

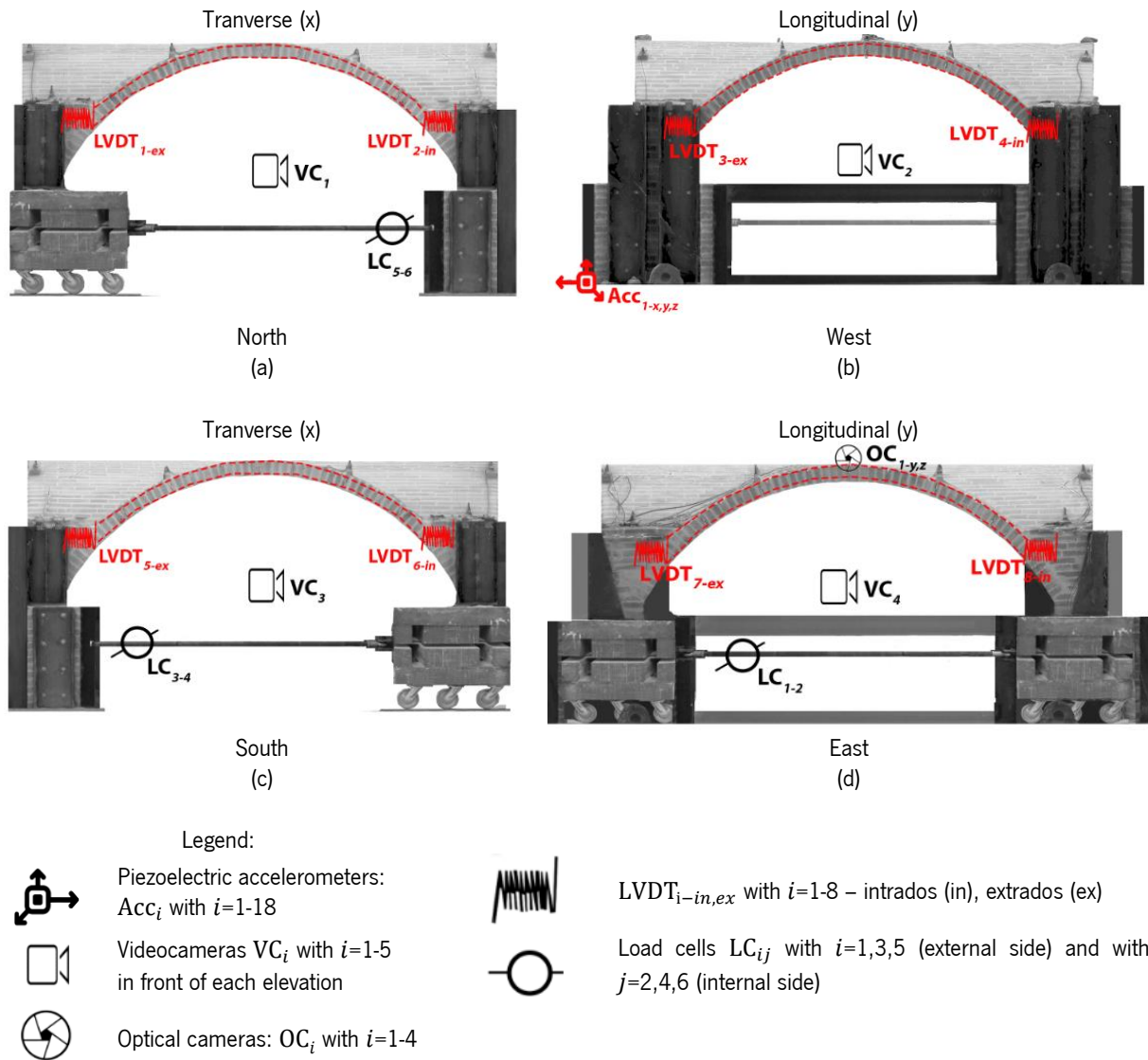


Figure 5-20. Testing setup per elevation. Valid for the unstrengthened and strengthened specimen.

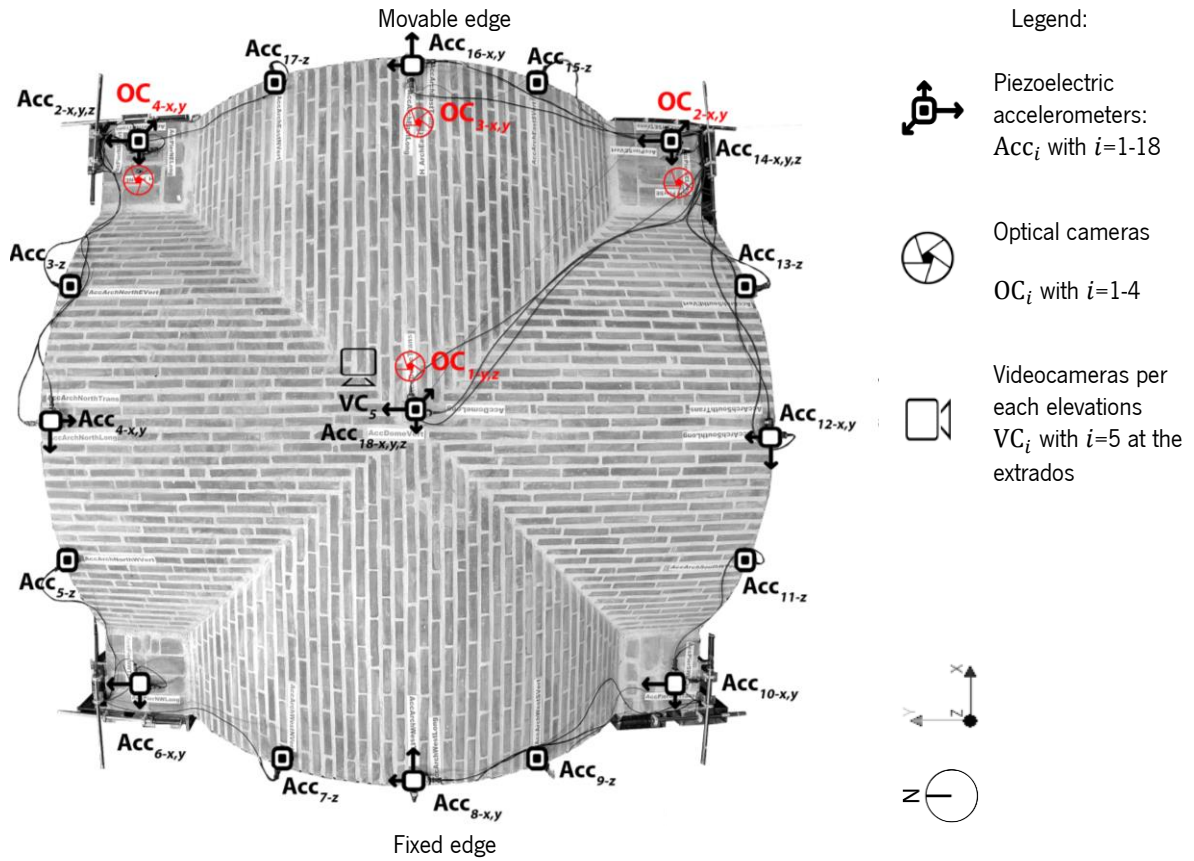


Figure 5-21. Setup of the unstrengthened model (UNS).

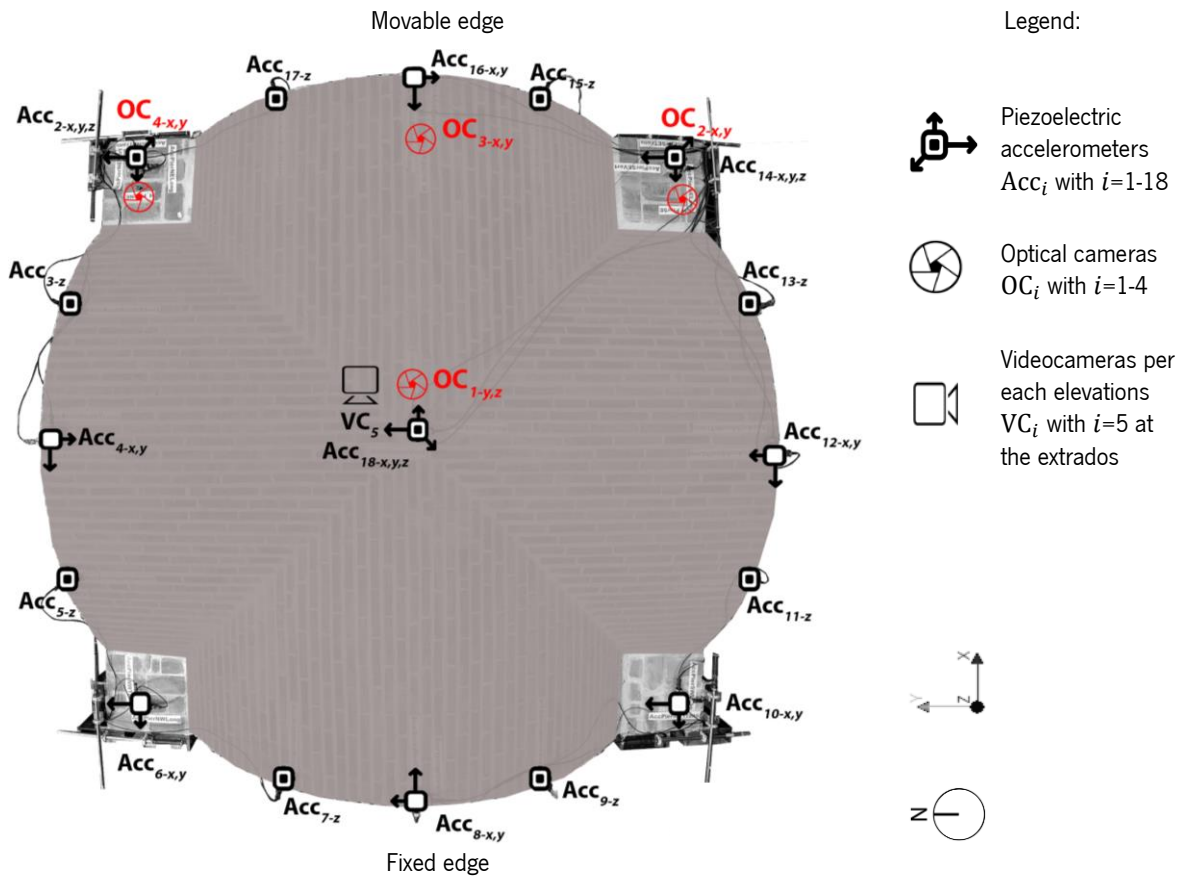


Figure 5-22. Setup of the strengthened model (SM).

5.5 Final remarks

The present chapter describes the design, construction and test setup of a full-scale mortared groin vault. The characterisation of the materials was also presented. First, the description of the design of the full-scale vault is given, keeping in mind the main objective of this thesis - to study an ancient vault subject to in-plane shear mechanism. Boundary conditions, dimensions of the elements and construction techniques were methodically studied, also through numerical simulations, to achieve the best configuration that can contribute to the success of the experimental campaign. Following ancient treatises and practical recommendations gathered from the literature, the full-scale vault was built outside the shaking table and then, carefully moved on top of it. All the critical aspects of the construction have been studied deeply: from the scaffolding system, the cuts along the diagonals, and the curing of the specimen, to the transportation, dismantlement procedure, the repair and strengthening.

Afterwards, the material characterisation tests protocols and results are described. The main outcomes at the masonry level are: average compressive strength equal to 9.1 MPa, Young's modulus equal to 2.2 GPa and friction angle at the joints equal to 38° degrees. These results are within the range of values presented in the literature for solid brick masonry assembly. Finally, the testing equipment and tools used in the shaking table tests were presented. The testing setup remains the same for both types of specimen configurations (unstrengthened and strengthened (see Chapter 6)).

6. Full-scale vault: shaking table tests

6.1 Introduction

The contents presented in Chapter 5 are preparatory to provide fundamental knowledge for the understanding of the experimental results when the vault is subjected to seismic ground motions. In this Chapter, the results of the shaking table tests on the unstrengthened (UNS) and strengthened (SM) configurations are presented. First, the inputs compatible with the shaking table capacity and with the purpose of the research are selected through numerical simulations, and then dynamic identification tests, aiming at evaluating the modal properties of the specimen, are processed. The results of the seismic tests (four in total), in which the input is applied with increasing amplitude along the longitudinal direction, are commented for the unstrengthened configuration. Later, the specimen is repaired, to re-establish the initial conditions, and strengthened with TRM application. The new set of results of the strengthened specimen (six in total) is then described and commented. In-plane shear behaviour on the shell is found to be the predominant mechanism, leading to important outcomes and conclusions in the evaluation of the structural assessment of the two configurations. The response of the specimens is evaluated in terms of damage and crack patterns, displacement fields, horizontal inertial coefficients, and capacity curves.

6.2 Input signals and tests sequences

The selection of the inputs, to be applied by the actuators, was done into account the LNEC shaking table characteristics and the objectives of this work. For the purpose of this wide experimental campaign, a sufficient number of seismic shocks is required to be able to build the capacity curve of the vault, highlighting linear and non-linear behaviour of the specimen as function of the applied amplitude at the base. Furthermore, an excessively impulsive input, such as the Emilia earthquake used in the reduced-scale vault, might lead to a rapid collapse, preventing the detailed analysis of the post-linear behaviour of the vault. Because of this, the selection of the input was also evaluated through the numerical analysis using a preliminary macro-model of the full-scale vault (see Section 5.2.1). In fact, this investigation on different inputs, through the non-linear time history analysis, helps to understand the maximum level of damage that can be reached during the experimental campaign and

to identify the most suitable input. This phase is particularly important for full-scale specimens made of masonry and expensive experimental campaigns when a unique specimen is available.

For this experimental campaign, it was decided to use again an earthquake that occurred in Italy, included in the database presented in the Table 4-4, since Italy is one of the countries where historical brick groin vaults are more spread (see Chapter 1). The selected input, adopted for both UNS and SM specimens, is a record of the North-South component of the L'Aquila earthquake, named "AQA", occurred on the 6th of April 2009 (Figure 6-1, Figure 6-2). The maximum absolute acceleration, velocity and displacement of the input are equal to 4.25 m/s^2 , 26.33 cm/s and 3.70 cm , respectively. The effective duration of the earthquake ($t_{d(10-90)}$) is equal to 5.34 s out of a total duration of 25 s .

Once AQA was selected, the input signals were prepared to be used in the shaking table. In particular, a Butterworth band pass filter between the range of $0.05 - 20 \text{ Hz}$ with sixth pole order was applied to the input signal. A bandpass filter was used to cut the higher frequencies, which are associated with the higher and less relevant modes. In general, the Butterworth filter is preferred to the Fourier filter since avoids brutal cuts in the frequency range (Figure 6-3a) and Gibbs' behaviour (Helmberg, 1994). This concurs also to solve the line base derivation, which must be removed for all the signals (Faccioli and Paolucci, 2005). From the preliminary numerical results of the non-linear dynamic analysis, it was noticed that shear failure rules the behaviour, as observed from the diagonal distribution of principal strains in Figure 6-3b and aimed in this work. Next, the AQA earthquake was scaled through increasing factors, maintaining the signal processing tools, and numerically investigated through an incremental dynamic analysis approach. Based on this study, it was proved that AQA input could be scaled up to a level of 175% of the target input, respecting the shaking table capacity. However, from the preliminary numerical simulations, the model presents severe damage from the level of 100% of AQA input.

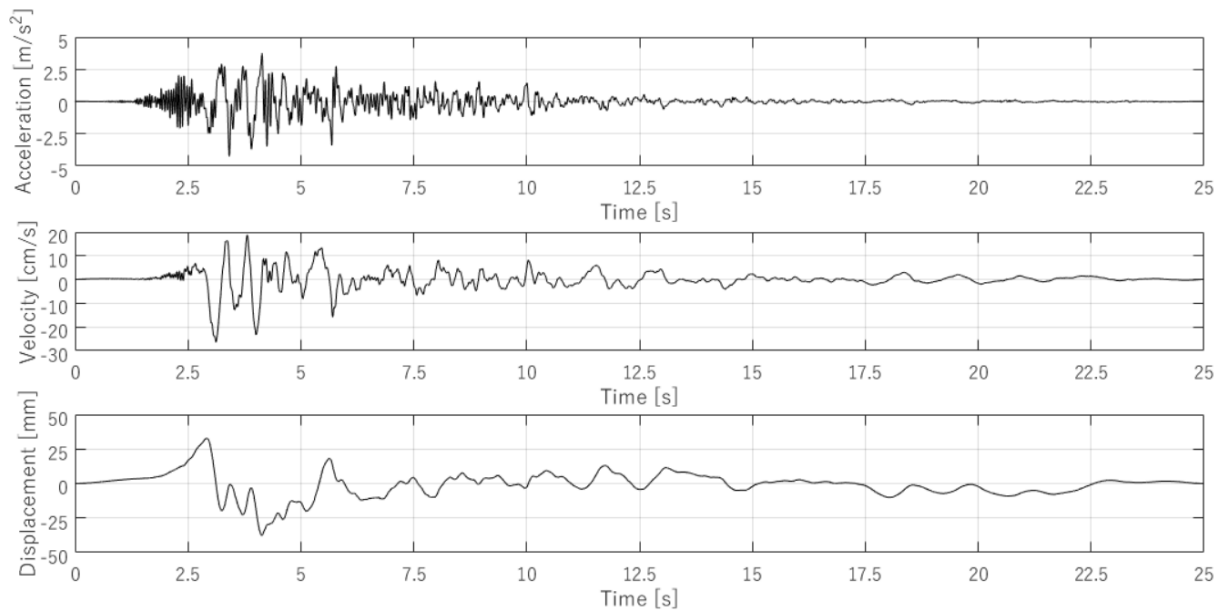


Figure 6-1. Time histories of the target input signals of recorded AQA earthquake: accelerations, velocities and displacements.

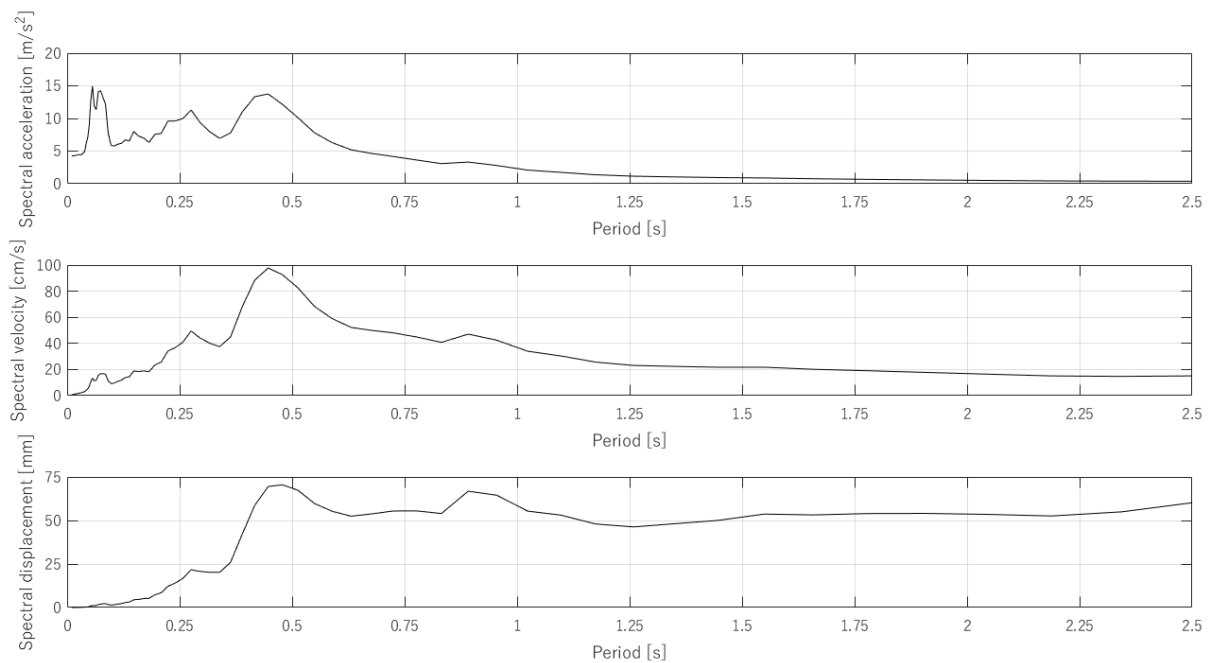


Figure 6-2. Response spectra of recorded AQA earthquake: spectral acceleration, velocity, and displacement.

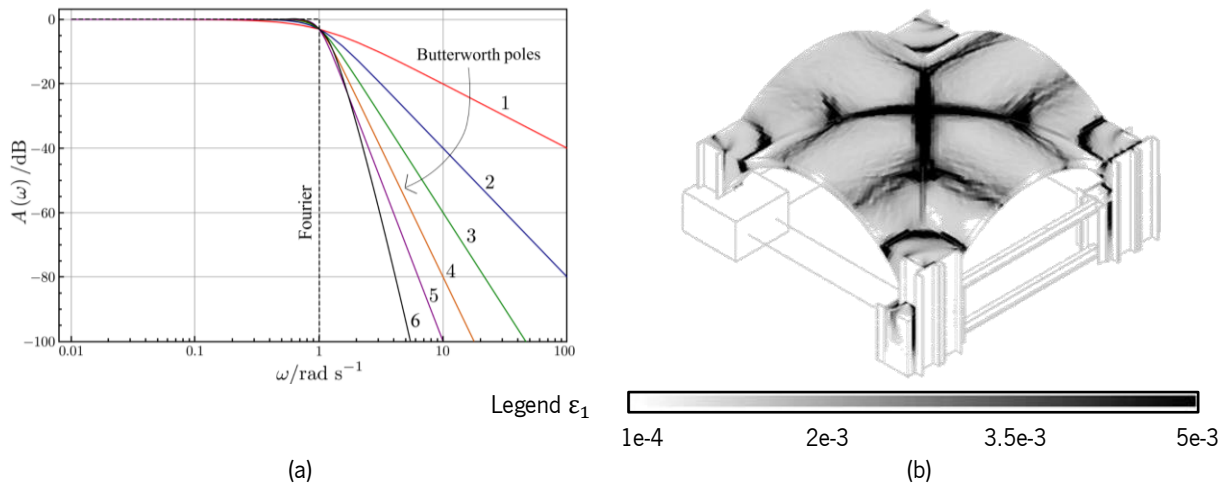


Figure 6-3. Filter effects and results: (a) gain of Butterworth low-pass filter with cut off $\omega_0 = 1$ vs Fourier filter (example for a high pass filter), (b) principal strains for the preliminary FEM model with AQA 100%.

As stressed, the seismic tests on the UNS specimen were performed until attaining a level of damage that does not compromise its structural equilibrium, so that it would be possible to be repaired. For the SM specimen, it is important to ensure the performance for several seismic amplitudes to create a proper capacity curve to be compared with the unstrengthened one and cause severe damage in the specimen. In this case, the unique upper bound limit, besides the shaking table capacity, is the integrity of the equipment above the extrados.

Before and after each sequence of shaking table tests, dynamic identification tests (DIT) were performed to estimate the reduction of frequencies with the increase of damage. The input signals used in the DIT correspond to a “white noise” of about 160 s, with a large frequency range and low amplitude (Figure 6-4). The intense phase lasts 110 s and the maximum absolute accelerations are 0.45 m/s^2 and 0.94 m/s^2 in the longitudinal and transverse directions, respectively. These amplitudes did not cause damage to the specimen. Thus, the DIT inputs were kept constant for all the dynamic identification tests, without scaling factors, in both configurations. Contrarily the reduced-scale vault, each DIT was performed unidirectionally, exciting the structure first along the North-South direction and then along the East-West direction.

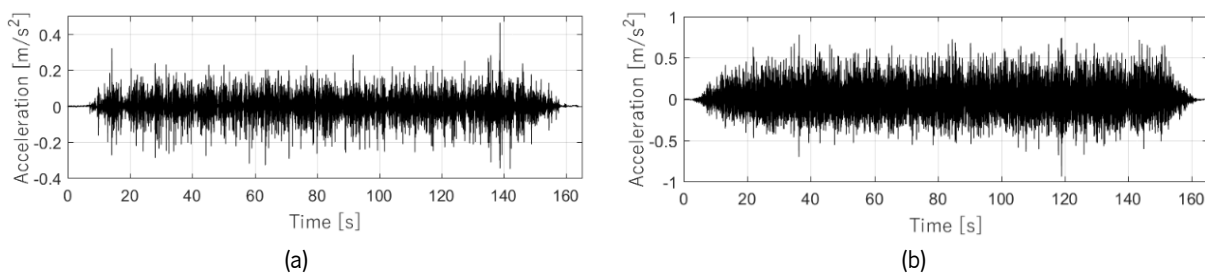


Figure 6-4. Input signals of the dynamic identification tests: (a) North-South (longitudinal) direction, (b) East-West (transverse) direction.

For what concerns the UNS specimen, nine dynamic identification tests are performed, namely five in the longitudinal direction (DIT i -UNS-Y) and four in the transverse direction (DIT i -UNS-X), with i from 0 to 3 (Table 6-1). The dynamic identification test 1B* was performed with an impact instrumented hammer to verify the effectiveness of all the devices before performing all the other dynamic identification tests. This approach is usually common to be performed on small structures with little damping (*e.g.* steel structures), while less usual for civil engineering applications because this method works at a low level of energy. However, nowadays, with the increase of the quality of the transducers and with adequate signal processing, impact instrumented hammer test is also used in civil engineering laboratories to check the consistency of the results gathered by the dynamic identification tests with “white noise” input signal (Tirelli, 2011).

The maximum level of 75% of the target input is reached during the seismic test on the UNS specimen, while, for the SM specimen, the level of 150% of the target amplitude is reached and fourteen dynamic identification tests are performed (Table 6-1, Table 6-2).

Table 6-1. List of tests carried out on the unstrengthened specimen: dynamic identification tests (DIT) and seismic tests (ST).

*Performed with the instrumented hammer.

ID	Denomination	Input direction	Description
1	DIT-0-UNS-Y	North-South	
1B*	DIT-0-UNS-Y*	North-South	Dynamic identification test of the undamaged vault
2	DIT-0-UNS-X	East-West	
3	ST-UNS-10%	North-South	Seismic test with amplitude equal to 10% of AQA eq.
4	ST-UNS-25%	North-South	Seismic test with amplitude equal to 25% of AQA eq.
5	DIT-1-UNS-Y	North-South	
6	DIT-1-UNS-X	East-West	Dynamic identification after seismic test after AQA 25%
7	ST-UNS-50%	North-South	Seismic test with amplitude equal to 50% of AQA eq.
8	DIT-2-UNS-Y	North-South	
9	DIT-2-UNS-X	East-West	Dynamic identification after seismic test after AQA 50%
10	ST-UNS-75%	North-South	Seismic test with amplitude equal to 75% of AQA eq.
11	DIT-3-UNS-Y	North-South	
12	DIT-3-UNS-X	East-West	Dynamic identification after seismic test after AQA 75%

Table 6-2. List of tests carried out on the strengthened specimen: dynamic identification tests (DIT) and seismic tests (ST).

ID	Denomination	Input direction	Description
1	DIT-0-SM-Y	North-South	Dynamic identification test of repaired and strengthened vault
2	DIT-0-SM-X	East-West	
3	ST-SM-25%	North-South	Seismic test with amplitude equal to 25% of AQA eq.
4	DIT-1-SM-Y	North-South	Dynamic identification after seismic test after AQA 25%
5	DIT-1-SM-X	East-West	
6	ST-SM-50%	North-South	Seismic test with amplitude equal to 50% of AQA eq.
7	DIT-2-SM-Y	North-South	Dynamic identification after seismic test after AQA 50%
8	DIT-2-SM-X	East-West	
9	ST-SM-75%	North-South	Seismic test with amplitude equal to 75% of AQA eq.
10	DIT-3-SM-Y	North-South	Dynamic identification after seismic test after AQA 75%
11	DIT-3-SM-X	East-West	
12	ST-SM-100%	North-South	Seismic test with amplitude equal to 100% of AQA eq.
13	DIT-4-SM-Y	North-South	Dynamic identification after seismic test after AQA 100%
14	DIT-4-SM-X	East-West	
15	ST-SM-125%	North-South	Seismic test with amplitude equal to 125% of AQA eq.
16	DIT-5-SM-Y	North-South	Dynamic identification after seismic test after AQA 125%
17	DIT-5-SM-X	East-West	
18	ST-SM-150%	North-South	Seismic test with amplitude equal to 150% of AQA eq.
19	DIT-6-SM-Y	North-South	Dynamic identification after seismic test after AQA 150%
20	DIT-6-SM-X	East-West	

6.3 Modal properties of the unstrengthened specimen

From the dynamic identification tests on the UNS specimen, three main global natural frequencies and mode shapes were depicted, based on the rational fraction polynomial method (Mendes, 2012). The analysis of DIT results is mainly focused on these three first global modes (Table 6-3 and Figure 6-5), because they are characterised by the three lowest natural frequencies and, consequently, they have the highest influence on the global dynamic behaviour of the structure (Lourenço *et al.*, 2012).

The first global mode has a frequency that ranges from 6.15 Hz (undamaged configuration: DIT-0-UNS-Y) to 5.57 Hz (most damaged configuration: DIT-3-UNS-Y). The corresponding first natural period of the specimen in the undamaged configuration is equal to $T_1 = 0.16$ s. This mode corresponds to a pure in-plane shear behaviour of the system along the North-South direction (Figure 6-5a).

The second global mode involves a global behaviour of the shell of the vault in the transverse direction, with an out-of-phase behaviour of the eastern arch (associated to Acc_{16} , see Figure 5-21), as shown in Figure 6-5b. This global mode is recognisable in both directions when performing the DIT along y and x, with differences in frequencies. Those frequencies range from 10.35 to 9.67 Hz along North-South direction (y) and from 11.62 Hz to 10.10 Hz along East-West direction (x).

The third global mode is only depicted by DIT-0,1,2-UNS-X and range from 19.39 Hz (undamaged configuration: DIT-0-UNS-X) to 19.30 Hz (after ST-UNS-50%). It corresponds to a global mode of the

shell in the vertical direction (Figure 6-5c). It is important to mention that the vertical mode is detected at the end of the shaking table tests either analysing DIT-3-UNS-Y and DIT-3-UNS-X. Higher modes involve localised behaviours of the shell where each lateral arch is individually excited (not relevant for this work).

Table 6-3. Natural vibration frequencies of the unstrengthened test specimen when excited along the longitudinal and transverse directions. *Performed with the instrumented hammer.

ID DIT	Input direction	1 st global mode		2 nd global mode		3 rd global mode	
		Frequency [Hz]	Shape	Frequency [Hz]	Shape	Frequency [Hz]	Shape
DIT-0-UNS-Y	North-South	6.15	Shear	10.35	Transverse	-	
DIT-0-UNS-Y*	North-South	6.18		10.35		-	
DIT-0-UNS-X	East-West	-		11.62	Transverse	19.39	Vertical
DIT-1-UNS-Y	North-South	6.15	Shear	10.15	Transverse	-	
DIT-1-UNS-X	East-West	-		11.38	Transverse	19.38	Vertical
DIT-2-UNS-Y	North-South	5.86	Shear	10.15	Transverse	-	
DIT-2-UNS-X	East-West	-		10.79	Transverse	19.30	Vertical
DIT-3-UNS-Y	North-South	5.57	Shear	9.67	Transverse	-	
DIT-3-UNS-X	East-West	-		10.10	Transverse	-	

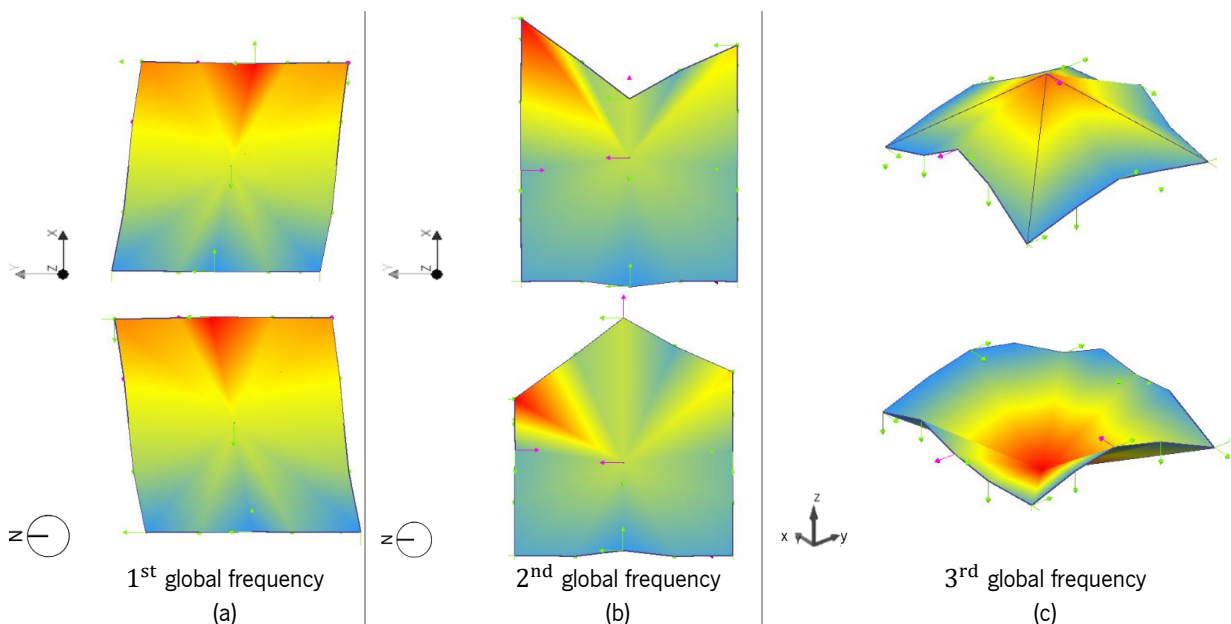


Figure 6-5. Mode shapes of the unstrengthened specimen: (a) first global longitudinal mode obtained from the DIT-0-UNS-Y test, (b) second global transverse mode obtained from the DIT-0-UNS-X, (c) third global vertical mode obtained from the DIT-0-UNS-X.

In order to verify that the detected mode shapes are consistent between the several shocks while the damage increases, the modal assurance criterion (MAC) was computed for all DITi-UNS-Y, X (Ewins,

2000). MAC value consists in a statistical indicator that is sensitive to large differences and relatively insensitive to small differences in the mode shapes and it is described by Equation 6-1.

$$MAC_{u,d} = \frac{|\sum_{i=1}^n \varphi_i^u \varphi_i^d|}{\sum_{i=1}^n (\varphi_i^u)^2 (\varphi_i^d)^2} \quad \text{Equation 6-1}$$

φ_i^u and φ_i^d are the mode shape vectors for two different modal conditions (DITi) and n is the number of degrees of freedom, hence, the positions of the accelerometers and the corresponding nodes in the discretised geometry in ArteMIS (2018). MAC values vary between 0 and 1, in which a value close to 0 indicates that the modes are inconsistent while MAC equal to 1 indicates fully consistent mode shapes (Pastor, Binda and Harčarik, 2012). MAC yields a good statistic indicator and a degree of consistency between mode shapes, either experimentally or numerically estimated. In the first case, the mode stability is checked between the first dynamic identification test and the following ones, when the specimen is increasingly damaged after each test. In the second case, in general, MAC values are used for the calibration of the numerical models, mainly for undamaged states.

For the UNS specimen, MAC values are evaluated for the three global modes to understand if, after the accumulation of damage due to the seismic tests, their mode shapes are still consistent and recognisable (Table 6-4). Based on that, the coherence linked to the first global mode, associated with the shear behaviour, remains very high also after ST-UNS-75%. In fact, analysing the difference between DIT-0-UNS-Y and DIT-3-UNS-Y, the maximum MAC variation is equal to 0.012. On the other hand, mode 2 and mode 3 showcase a more significant change in the shape, which is reflected by higher MAC variations of 0.051 for mode 2 and a variation of 0.070 for mode 3.

Table 6-4. Decrease of frequencies and modal assurance criterion (MAC) for the first three global modes obtained from the DITi-UNS-Y and DITi-UNS-X tests.

1 st global mode			2 nd global mode			3 rd global mode		
ID DIT	f_1	MAC_{exp}	ID DIT	f_2	MAC_{exp}	ID DIT	f_3	MAC_{exp}
DIT-0-UNS-Y	6.15	-	DIT-0-UNS-X	11.62	1.000	DIT-0-UNS-X	19.39	-
DIT-1-UNS-Y	6.15	0.999	DIT-1-UNS-X	11.38	0.995	DIT-1-UNS-X	19.38	0.965
DIT-2-UNS-Y	5.89	0.996	DIT-2-UNS-X	10.79	0.981	DIT-2-UNS-X	19.30	0.930
DIT-3-UNS-Y	5.57	0.988	DIT-3-UNS-X	10.10	0.949	DIT-3-UNS-X	-	-

6.4 Seismic results of the unstrengthened test specimen

The results of the shaking table tests on the UNS specimen are discussed in terms of qualitative and quantitative parameters, such as crack pattern, displacement profiles and horizontal inertial coefficients. Within this context, the link between the results of the dynamic identification tests with the propagation of the damage and quantitative results gives reliability to the conclusions.

It is remarked that in the shaking table tests, the total accelerations are obtained directly from the 32 accelerometers placed on the specimen. The total displacements of the four measured points are directly evaluated through the optical cameras' records, without resorting to the double integration of the accelerations in the frequency domain. In total, for the UNS specimen, 200 time history responses were processed using Matlab (2022) codes, taking into account also the LVDT and load cells' measurements. However, considering the high number of measured points and that the objective of this study is the in-plane shear mechanism, this Section focuses on the longitudinal response, which is the direction of the input and the direction of interest. Nevertheless, in Annex 5, all the results of each shaking table test sequence are plotted.

6.4.1 Crack pattern

The evolution of damage is indispensable for the assessment of the seismic performance of the specimen. The distribution of the cracks along the vault and their widths allow to identify and describe the mechanism that prevails during the seismic action. The crack pattern is correlated with the reduction of frequency obtained from the dynamic identification tests and linked to the failure mechanism of the vault. Visual inspections were conducted after each seismic test to identify the opening, closing and development of cracks. The inspections were undertaken using manual tools (*e.g.*, tapes, levels, and metal rods) to monitor the increase in severity of the cracks between one shock and the following ones. Moreover, through the videos recorded in front of each elevation, it was possible to check frame by frame, the crack propagation during the shocks, even if, at the end of the tests, the damage has been recovered by the self-weight of the vault. To be consistent and objective during all the surveys, four limits of crack width (*cw*) have been adopted:

- light cracks have $cw \leq 0.20$ mm;
- medium cracks have $0.2\text{mm} < cw \leq 1.0$ mm;
- moderate cracks have $1.0 \text{ mm} < cw \leq 2.0$ mm;
- severe cracks are characterized by $cw > 2.0$ mm.

As anticipated in Section 5.2.2 and in Figure 5-10, due to bending effects caused by the transportation of the specimen to the shaking table, two longitudinal light cracks occurred on the Northern and Eastern webs before the beginning of the seismic tests. Being immediately closed, those cracks has not compromised or influenced the subsequent behaviour of the vault. Those locations did not face in any damage also at the end of all the seismic sequences.

After the first two seismic tests (ST-UNS-10%, ST-UNS-25%), no significant damage was notable, and only light cracks close to the NW and NE corners were recognisable (Figure 6-6). From the videos recorded by VC_5 , it was possible to observe that diagonal cracks, associated with the in-plane shear behaviour, at the key of the vault appeared during ST-UNS-50%. However, those cracks closed under the self-weight of the vault at the end of the shock. Conversely, after ST-UNS-75% significant damage linked to the in-plane shear mechanism occurred, as severe cracks remained open at the end of the tests, as shown in Figure 6-6 and Figure 6-7a,b.

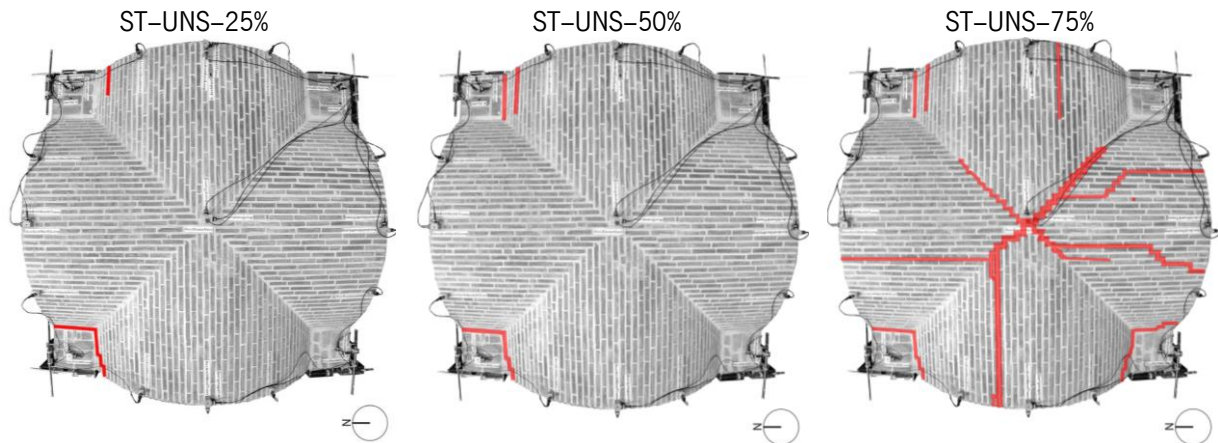


Figure 6-6. Crack patterns of the extrados for the unstrengthened specimen at the end of ST-UNS-25%, 50%, 75%.

All four webs presented damage caused by the in-plane shear mechanism. The two major diagonal cracks crossed both the extrados and intrados of the shell with a crack width higher than 1 cm (Figure 6-7a,b). The formation of hinges was notable in correspondence between the Northern and Western arches (Figure 6-7d,e). After the last sequence (ST-UNS-75%), further minor longitudinal cracks were observed, suggesting a diagonal symmetry of the mechanism, as shown in Figure 6-6. The interface between masonry elements and steel elements (piers and frame, infill and profiles) was not affected by any damage.

This was in agreement with the fact that higher vertical compressive stresses are favourable to the behaviour of the masonry structures under horizontal loads. In fact, where the thickness of the specimen was bigger (close to the corners between masonry and steel elements), less damage has been observed.



Figure 6-7. Details of the damage for the unstrengthened specimen after ST-UNS-75%, for (a) to (e) views.

Due to the oscillatory nature of the earthquake, the action camera VC₅ placed at the top of the extrados, recorded the opening and closing of the cracks in the shell of the vault (Figure 6-8). On average, 450 frames have been exported from the videos with a total duration of 25 s, meaning that each frame has been extrapolated with a time difference of 0.055 s from the previous one.

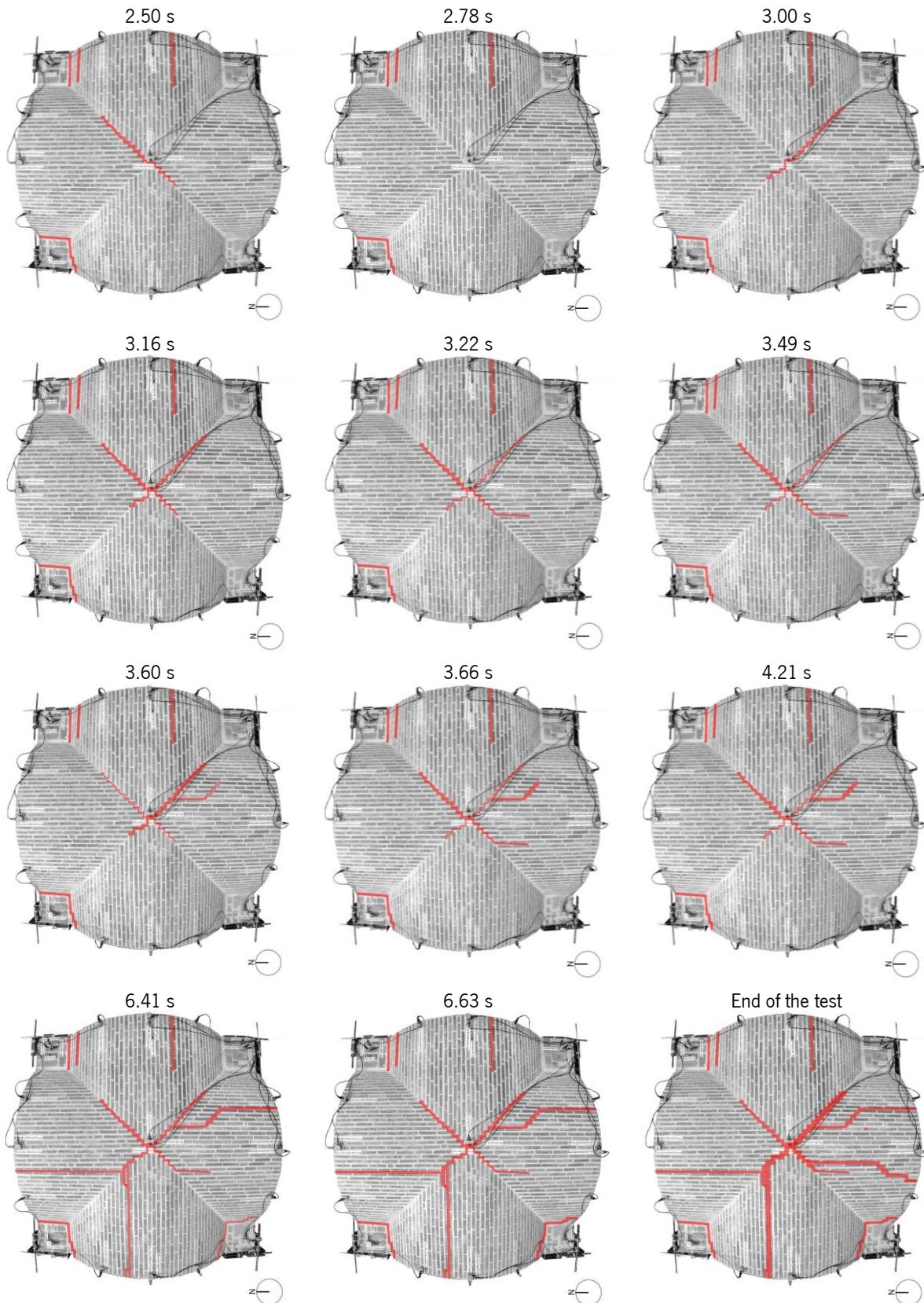


Figure 6-8. Evolution of cracks at the extrados appreciated by VC_5 during ST-UNS-75 with estimated time occurrence.

In the case of the ST-UNS-75% (Figure 6-8), the first diagonal crack along the NE/SW diagonal occurred at $t \approx 2.50$ s and it closed at around $t \approx 2.78$ s. At $t \approx 3.00$ s the opposite crack that

interested the SE/NW diagonal appeared, increasing its width during the intense phase of the ground motion, and it never closed. In general, the crack pattern was almost symmetric along the diagonals, showing a higher level of damage close to the NW and SW corners. The fixed piers were not involved by the mechanism, and only the boundaries between the curvature of the shell and the infill present medium cracks (Figure 6-7c). As shown in Figure 6-7 and Figure 6-8, the level of damage was severe, but the complete collapse has been avoided.

Even if it would have been interesting to investigate the UNS configuration at the collapse, this final level of damage was compatible with the purpose of the project, which foresaw the repairing and strengthening of the specimen. The level of damage on the UNS specimen can be considered “extremely severe”. In a realistic scenario, the space below the vault should not be accessible to people and the ceiling should be repaired to maintain the integrity of the structure.

6.4.2 Deformation profiles and displacement field

As described in the previous Sections, the shell of the vault presented a predominant in-plane shear behaviour with respect to the fixed edge, and this effect has been evaluated by analysing the deformation of the vault. To characterise the deformation of the vault, the displacements measured by the optical cameras are processed. The analysis of the in-plane deformation of the vault is undertaken for each testing sequence, taking advantage of the locations of the optical cameras (along the movable East edge and at the key of the shell). Due to the characteristics of the optical cameras, only absolute values are analysed for the assessment of the seismic performance of the vault, and, for the sake of graphical visualisation, each measured displacement of each optical camera has been amplified 10 times. Per each sequence, the first measured value of each optical camera represents a small residual displacement that derived from the previous dynamic identification tests. This value has been subtracted from each time history before analysing the displacement performance. In addition, since the optical cameras were not located above the fixed edge, no information about the displacements of the fixed piers is available. Because of this, the double integration of the accelerations (in both directions) for this elevation has been done and it has been found that those displacements were negligible in comparison with the ones along the eastern locations and above the key, as expected. Hence, the Western edge is assumed as perfectly fixed in the displacement profile; and they have been plotted for the instant when the $OC_{1,2,3,4}$ measurements presented their maximum absolute displacements (Figure 6-9 and, Figure 6-10).

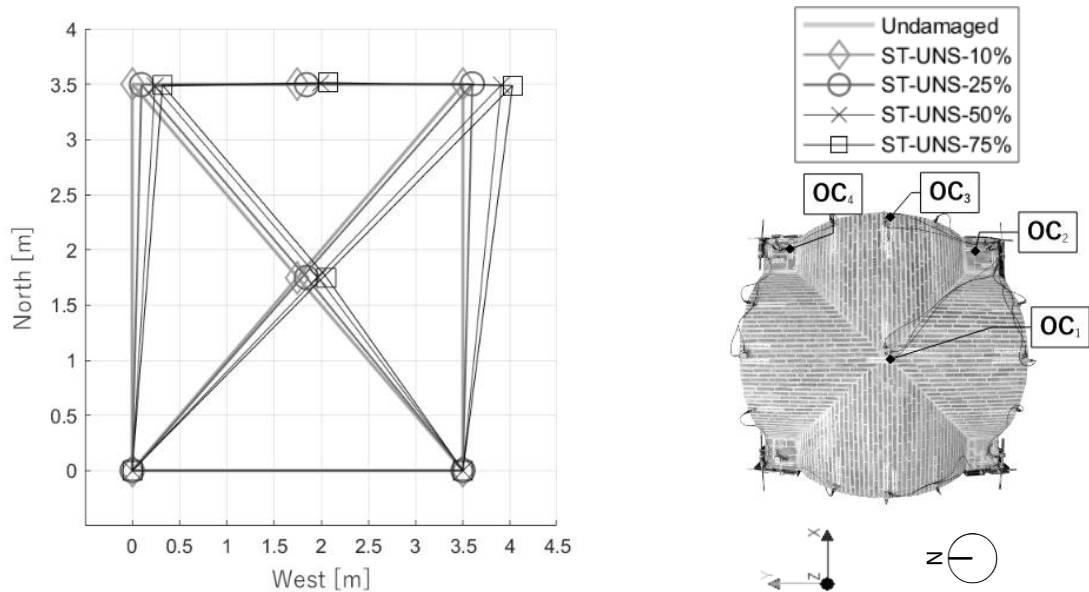


Figure 6-9. In-plane deformation profiles per each seismic test carried on the unstrengthened specimen when $OC_{2,4}$ measure their maximum displacements at $t \approx 4.31$ s. Deformation factor:10.

The main outcomes highlight some important aspects that concord with the observed damage (see Section 6.4.1). In particular, the shell of the vault moved mainly along the North-South direction, developing a simple in-plane shear mechanism, without generating transverse components of the displacements (Figure 6-9 and Figure 6-10). In particular, the longitudinal displacements were up to 40 times higher than transverse displacements (refer to Annex 5). During ST-UNS-50% and ST-UNS-75%, the displacement profiles non-linearly increased, as reflected by the higher level of damage (Figure 6-7, Figure 6-6), which mainly involved the movable SE corner, associated with the biggest crack that opened along the NW/SE diagonal. Because of the oscillatory nature of the motion, similar behaviour was observed also in the opposite direction (South-North), as stressed by the symmetric crack pattern (Figure 6-8). For example, for ST-UNS-75%, the vault presented two main displacement profiles for two different time occurrences. The first occurs at a time equal to 2.93 s when the vault moves in the positive direction, from South to North (red profile in Figure 6-10) and when $OC_{1,3}$ measured their absolute maximum displacements. The opposite scenario, more severe, occurred at a time equal to 4.31 s, when $OC_{2,4}$ measured their absolute maximum displacements. This is represented by the black line in Figure 6-10.

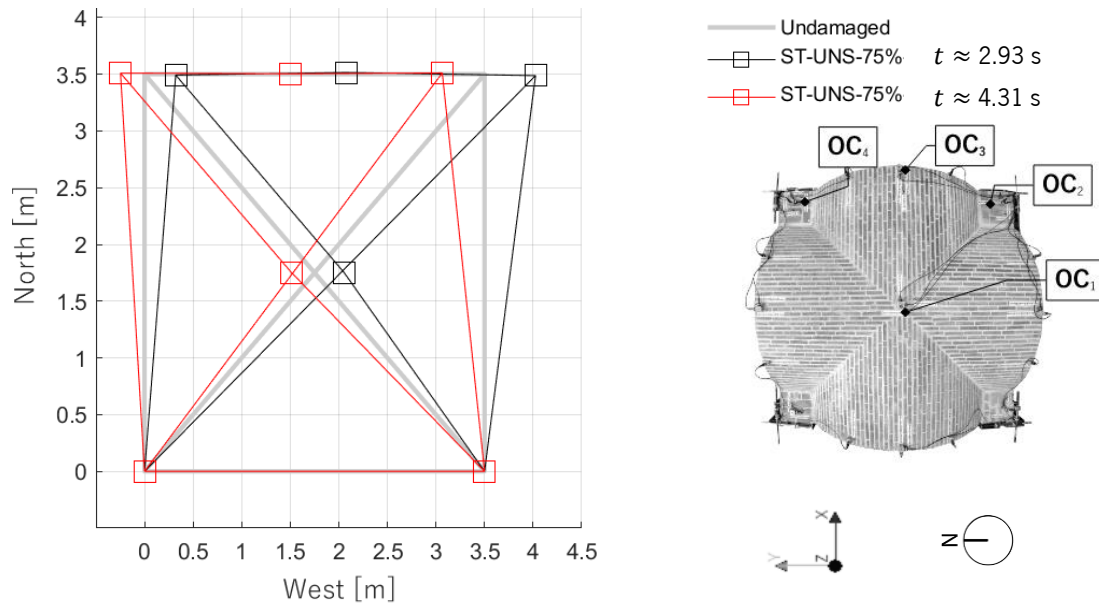


Figure 6-10. In-plane deformation profiles of the ST-UNS-75% for $OC_{1,2,3,4}$ at two instants. Deformation factor: 10.

The red displacement profile corresponds to the formation of the diagonal crack (NE/SW), which was noticed at $t \approx 2.93$ s. On the other hand, the black displacement profile corresponds to the more spread damage, which also interested the opposite diagonal after at $t \approx 4.31$ s. From the absolute maximum displacement values measured by the optical cameras (Table 6-5), it is possible to calculate the value of the shear distortion drift of the full-scale vault (ratio between the maximum displacement and the free span). When considering OC_2 , that reached unexpectedly a maximum displacement of 52.51 mm for the last sequence ST-UNS-75%, the value of drift resulted to be about 2.2%, while when considering the other optical cameras like OC_3 , the value of drift is about 1.4%.

Analysing the vertical deformation at the key of the vault, measured by OC_1 , the maximum drop was equal to 10.64 mm, while the maximum raising was only 0.48 mm. All the negative vertical displacements have been completely recovered by the end of the seismic tests.

Table 6-5. Summary of the absolute maximum displacements measured by $OC_{1,2,3,4}$ for each test of the unstrengthened specimen.

Test sequence	PGA [m/s^2]	OC_1 [mm]		OC_2 [mm]		OC_3 [mm]		OC_4 [mm]	
		NS	Vertical	WE	NS	WE	NS	WE	NS
ST-UNS-10%	0.57	4.49	-1.45	1.46	4.70	1.12	4.21	1.16	4.34
ST-UNS-25%	1.37	9.46	-0.66	0.56	9.92	0.72	9.83	1.27	9.80
ST-UNS-50%	2.57	21.73	-6.38	1.05	40.54	2.29	24.80	0.29	24.08
ST-UNS-75%	3.62	30.74	-10.64	4.4	52.51	5.08	32.80	1.25	32.05

Even if it would be desirable to measure the entity of the openings of the single joints throughout the test, LVDTs only provided the measurement of the cumulative relative displacements of the opening and

closing of all the joints along all the linear lengths of the arches, either at the extrados or intrados. LVDT₁ registered a maximum displacement of 7 mm, as the cumulative opening of all the joints along the Northern arch. Looking at the video recorded by VC₁, in front of this elevation, the formation of a hinge is notable (Figure 6-11), in agreement with the damage pattern from the extrados that presented a longitudinal crack on the Northern web (Figure 6-8 at $t \approx 6.41$ s). This result agrees with the vertical accelerations registered along the shell of the vault during the tests. In fact, it was expected that the points located at about 1/3 of each elevation ($Acc_{3,5,7,9,11,13,15,17}$) presented higher vertical accelerations than the points at the corners. Nevertheless, the key of the vault, measured by Acc_{18} , was the most excited during all the shocks reaching a value of 8.5 m/s^2 during ST-UNS-75%, which is more than the double of the maximum applied PGA.

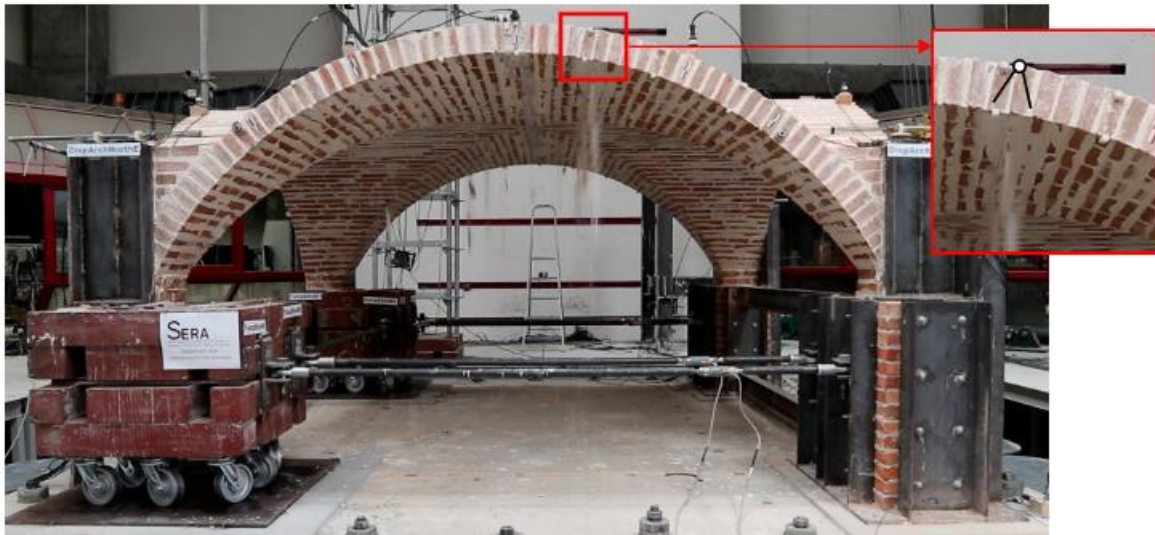


Figure 6-11. The visible hinge on the North arch during ST-UNS-75% at $t \approx 6.41$ s.

6.4.3 Hysteretic response

The acceleration time history response is fundamental in providing a better understanding of the inertial forces distributed on the specimen during the seismic inputs. For this purpose, only the longitudinal accelerometers placed at the level of the shell are considered, being the ones mainly excited by the first mode associated with in-plane shear behaviour. The transverse accelerometers and Acc_1 are not taken into account in this Section. At the time equal to 2.45 s of the total duration of the ST-UNS-75%, when the highest accelerations on the shell were measured along the North-South direction, it is possible to notice few outcomes (Figure 6-12). By performing a linear interpolation of the recorded accelerations, the NE corner was the one that was more dynamically excited, even if its displacements were limited in comparison with the SE corner (Figure 6-10). The fixed Western edge, which was expected to have a symmetric behaviour, showed a discrepancy between its two corners. The SW corner experienced

higher accelerations, suggesting an amplification effect of the upper part of the vault. The distribution of accelerations, shown in Figure 6-12, was asymmetric also along the diagonals, due to the not complete symmetry during the construction and the effect of the cumulative damage as a result of the seismic test sequences.

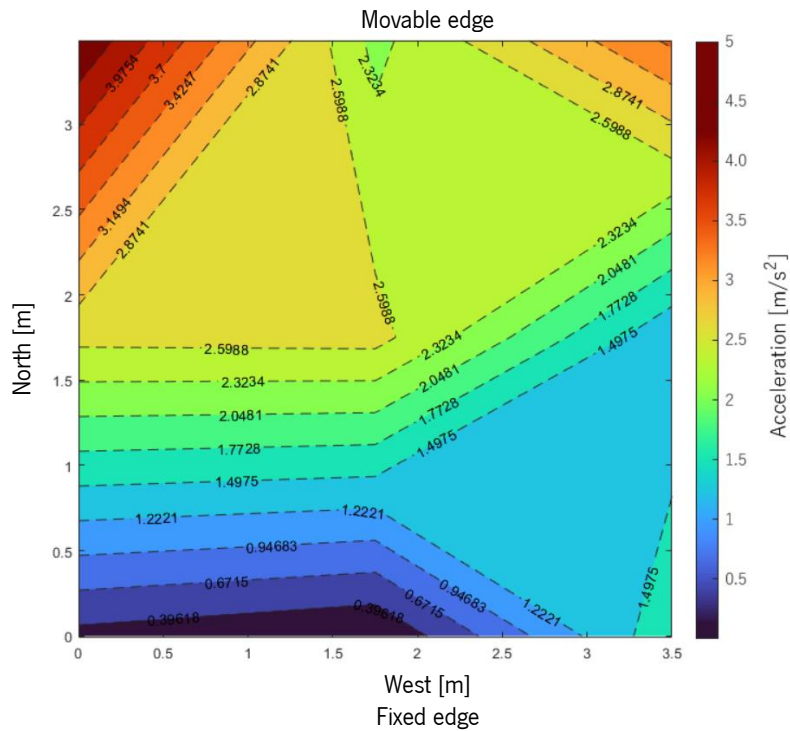


Figure 6-12. Colourmap of accelerations of each measured point along North-South direction when Acc_2 reaches its peak for $t = 2.45$ s during ST-UNS-75%.

The acceleration time history of each measured point allows the evaluation of the horizontal inertial coefficient, commonly known in the literature as the “shear coefficient”, summing the horizontal forces applied to the structure. In the shaking table tests, only the inertial forces are considered, which implies considering a different influential area per each accelerometer and a different distribution of densities and materials according to the specimen. This aspect requires a discretisation process that sometimes lacks in uniqueness (Beyer, Tondelli and Petry, 2014; Romanazzi *et al.*, 2022). In this case, it has been decided to adopt a pure geometrical subdivision of the influential areas, as described in Figure 6-13, similar to the geometrical subdivision carried out for the reduced-scale specimen (see Section 3.4.3). Those inertial forces are evaluated for each sequence, considering all the nine accelerometers that measure the longitudinal accelerations.

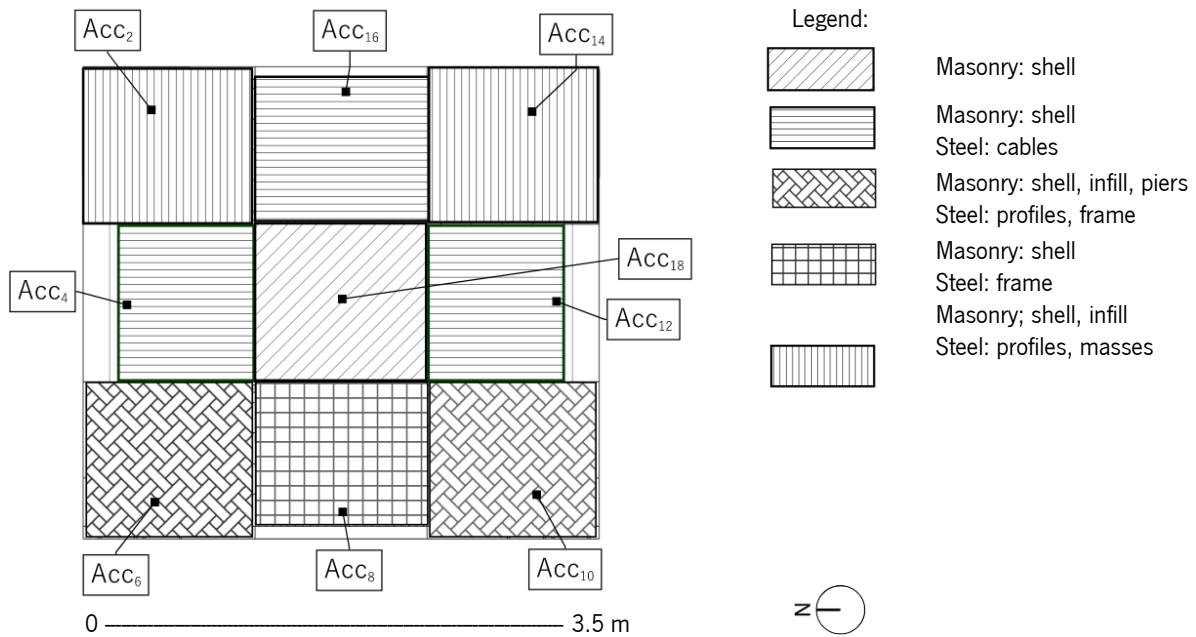


Figure 6-13. Influence area for each considered accelerometer.

The dynamic equilibrium is based on the equilibrium between the inertial forces, damping forces, restoring forces and external load. Damping and restoring forces are difficult to be measured in the shaking table tests. For more insights, the reader is referred to Candeias *et al.* (2008), Mendes (Mendes, 2012) and Romanazzi *et al.* (2022) and to the next Chapter 7. The inertial forces are then calculated through the extension of a multi-degree of freedom system, in which their equivalent discrete lumped system of mass is associated with the time histories of the accelerations, measured at specific locations. In addition, the hypothesis that the mass of the specimen is constant during the shaking table tests is assumed (12.7 tons). Thus, the sum of all the inertial forces, measured along the shell, represents the total horizontal shear force, which can be normalised by dividing by the total weight of the specimen per each instant t . Figure 6-14 shows the normalised horizontal shear force, here called “horizontal inertial coefficient”, versus the total displacements measured by the optical cameras for the UNS vault.

For the ST-UNS-10% and ST-UNS-25%, the stiffness of the response is higher than the stiffness for the following sequences (ST-UNS-50% and ST-UNS-75%), due to the severe level of damage at the final loading stages. The horizontal inertial coefficient ranges between -0.28 (ST-UNS-75%) and 0.3 (ST-UNS-50%). At the highest levels of damage, therefore comparing ST-UNS-50% with ST-UNS-75%, it is noted that the minimum horizontal inertial coefficient remains almost constant (-0.28), while the maximum horizontal inertial coefficient decreases from 0.3 , for ST-UNS-50%, to 0.27 for ST-UNS-75%. The responses are similar for OC_1 , OC_3 and OC_4 , while OC_2 shows higher displacements, mainly at the last two shocks.

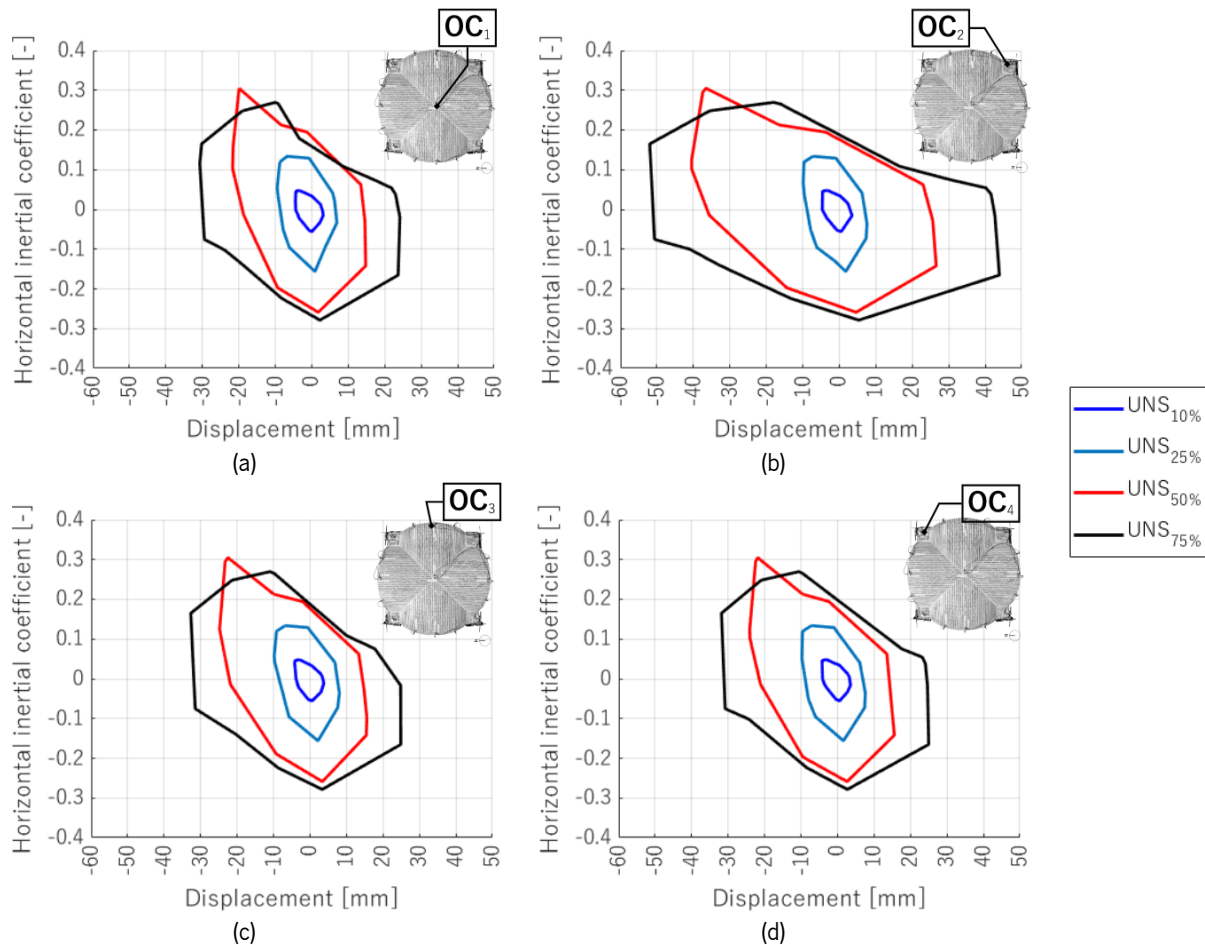


Figure 6-14. Envelope response curves of the unstrengthened specimen considering four optical cameras for each seismic test in the North-South direction: (a) OC₁, (b) OC₂, (c) OC₃, (d) OC₄.

To conclude, the analysis of the seismic performance of the UNS by use of quantitative parameters, obtained from the seismic tests, is according to the expected behaviour of this type of cross vault, showing an in-plane shear mechanism along the diagonal as a consequence of the different stiffness between the fixed edge and the movable edge. The parameters of the response of the specimen, mainly the maximum longitudinal displacements present a non-linear increase along the testing, with respect to the West edge, which is due to the concentration of damage at the groins.

6.5 Modal properties of the strengthened specimen

After the shaking table tests on the UNS, the shell of the vault has been repaired and reinforced with TRM application, as described in Section 5.2.2. This procedure is commonly used because of the high costs that the shaking table tests involve (Mendes, 2012; Avila, 2014), in particular, when the objective is to assess the seismic response of a specimen together with its strengthening solution. In fact, the objective of the experimental campaign on the strengthened vault is to evaluate the potential enhancement of the vault after the TRM application (see point C Chapter 1). The strengthened

specimen (SM) must be as similar as possible to the undamaged configuration in terms of modal properties. The dynamic identification tests allow establishing how much the reparation and reinforcement application have been able to recover the previous damage by comparing the first natural frequencies of the UNS and SM, before starting the new set of seismic tests. In particular, the first natural frequency at the end of ST-UNS-75%, which is equal to 5.57 Hz, has been increased to 6.15 Hz, after the repair and TRM application (DIT-0-SM-Y). This value is equal to the first natural frequency of the undamaged UNS, obtained through DIT-0-UNS-Y. Within this condition, it is possible to affirm that the two specimens are comparable. It is also noted that the additional mass of the retrofitting system (*Geocalce* F layer, Geosteel grid 200 and *Geocalce* FL injections) is negligible in comparison with the total mass of the specimen.

For the SM, fourteen dynamic identification tests are performed, namely seven in the longitudinal direction (DIT-*i*-SM-Y) and seven in the transverse direction (DIT-*i*-SM-X), with *i* from 0 to 6. Two main global natural frequencies and mode shapes (Figure 6-5) were estimated using the rational fraction polynomial method (Mendes, 2012). The first global mode has a frequency that ranges from 6.15 Hz (undamaged configuration: DIT-0-SM-Y) to 4.5 Hz (most damaged configuration: DIT-6-SM-Y) after the 150% of the seismic tests (Table 6-6). This mode corresponds to a pure shear behaviour of the system along the North-South direction (Figure 6-5a). Even if the in-plane shear is maintained in the strengthened configuration, the main difference between DIT-0-UNS-Y and DIT-0-SM-Y is represented by the fact that the central accelerometers ($Acc_{4,12,18}$) have limited longitudinal modal components in the strengthened configuration, in comparison with the unstrengthened specimen. The second global mode presents a combined global behaviour of the shell of the specimen with in-plane translational and rotation movements (Figure 6-5b). No other global modes have been found.

The experimental MAC value associated with the first global mode, remains very high also after AQA-150%, in which the maximum MAC variation for the DIT-6-SM-Y is 0.006. On the other hand, mode 2 presents a more unstable MAC when the damage increases, with a MAC variation of 0.145.

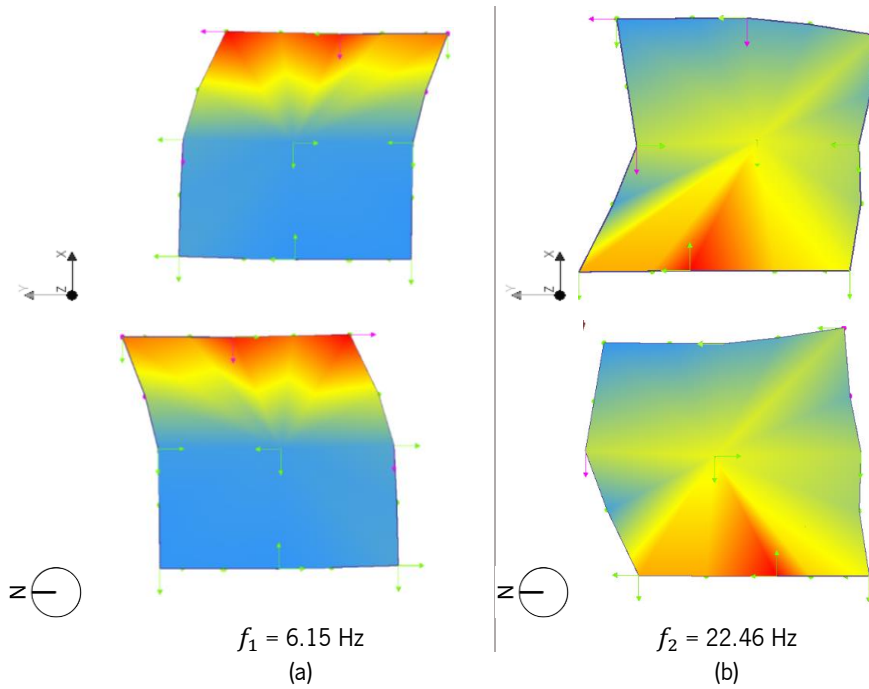


Figure 6-15. Natural vibration modes of the strengthened test specimen obtained from the DIT-0-SM-Y: (a) first global longitudinal mode, (b) second global transverse mode.

Table 6-6. First two natural vibration frequencies and MAC values of the strengthened specimen when excited in the longitudinal and transverse directions.

ID DIT	Input direction	1 st global mode			2 nd global mode		
		Frequency [Hz]	Shape type	MAC _{exp}	Frequency [Hz]	Shape type	MAC _{exp}
DIT-0-SM-Y	North-South	6.15	Shear	-	-	-	-
DIT-0-SM-X	East-West	-	-	-	22.46	Combined	-
DIT-1-SM-Y	North-South	5.86	Shear	0.999	-	-	-
DIT-1-SM-X	East-West	-	-	-	22.66	Combined	0.875
DIT-2-SM-Y	North-South	5.86	Shear	0.998	-	-	-
DIT-2-SM-X	East-West	-	-	-	22.56	Combined	0.901
DIT-3-SM-Y	North-South	5.66	Shear	0.997	-	-	-
DIT-3-SM-X	East-West	-	-	-	21.58	Combined	0.972
DIT-4-SM-Y	North-South	5.27	Shear	0.997	-	-	-
DIT-4-SM-X	East-West	-	-	-	20.996	Combined	0.930
DIT-5-SM-Y	North-South	4.59	Shear	0.996	-	-	-
DIT-5-SM-X	East-West	-	-	-	19.82	Combined	0.867
DIT-6-SM-Y	North-South	4.49	Shear	0.994	-	-	-
DIT-6-SM-X	East-West	-	-	-	17.29	Combined	0.855

6.6 Seismic results of the strengthened test specimen

The results of the shaking table tests on the strengthened specimen are here discussed in terms of qualitative and quantitative parameters, such as crack pattern, displacements profiles and horizontal inertial coefficient, similar to Section 6.4. In total, 300 time history responses of the SM are processed. This Section covers the most remarkable results of the seismic test. The results of all shaking table tests are available in Annex 5.

6.6.1 Crack pattern

The evolution of damage in the strengthened specimen has been conducted by using the same tools and procedure, as per the UNS. Figure 6-16 presents the damage crack pattern at the extrados for each sequence, evaluated from the videos recorded by VC₅. After ST-SM-25% and after ST-SM-50%, a light crack close to the NE corner appeared and increased in width (reaching $cw < 0.20$ mm). Likely, it consisted of a recurrent crack since it was also visible after ST-UNS-10%. After ST-SM-25% and after ST-SM-50%, the SM specimen did not exhibit any other significant damage, in line with the results of the dynamic identification tests. Following ST-SM-50%, light diagonal cracks developed at the base of the groins (NE-NW-SW corners), likely linked to the detachment of the TRM system in those locations where the curvature of the changes. Those diagonal cracks (visible in Figure 6-16) occurred at the shell extrados with an average crack width of less than 0.5 mm, while intrados remained almost undamaged until the end of the seismic tests. The in-plane shear mechanism remained predominant for the first seismic sequences up to ST-SM-75% (included). From ST-SM-100% a complex mechanism was observed, which was characterised by uplifts and torsions involving the steel masses, the impost of the vault and the fixed piers. This complex mechanism caused damage to the TRM system in correspondence with the Northern and Western webs (Figure 6-17d). At other locations, the TRM system remained tightly fixed to the masonry extrados until the end of the seismic tests.

During the last two seismic tests (ST-SM-125%, ST-SM-150%), severe cracks occurred at the SW corner, damaging the fixed pier and the Southern arch (Figure 6-17b). In this location, detachments of some bricks were also distinguishable (Figure 6-17a, b). Those cracks developed at the boundaries of the strengthened surface. A part of this location, the crack patterns of ST-SM-125% and ST-SM-150% were mainly an evolution of the damage observed in the previous seismic test. Although the damage increased, the strengthened specimen presented severe damage only at the end of the final seismic test. The movable edge at the opposite side presented a complete separation of the bed joints between the supports and the shell of the vault, where the impost of the vault begins (Figure 6-17c,e).

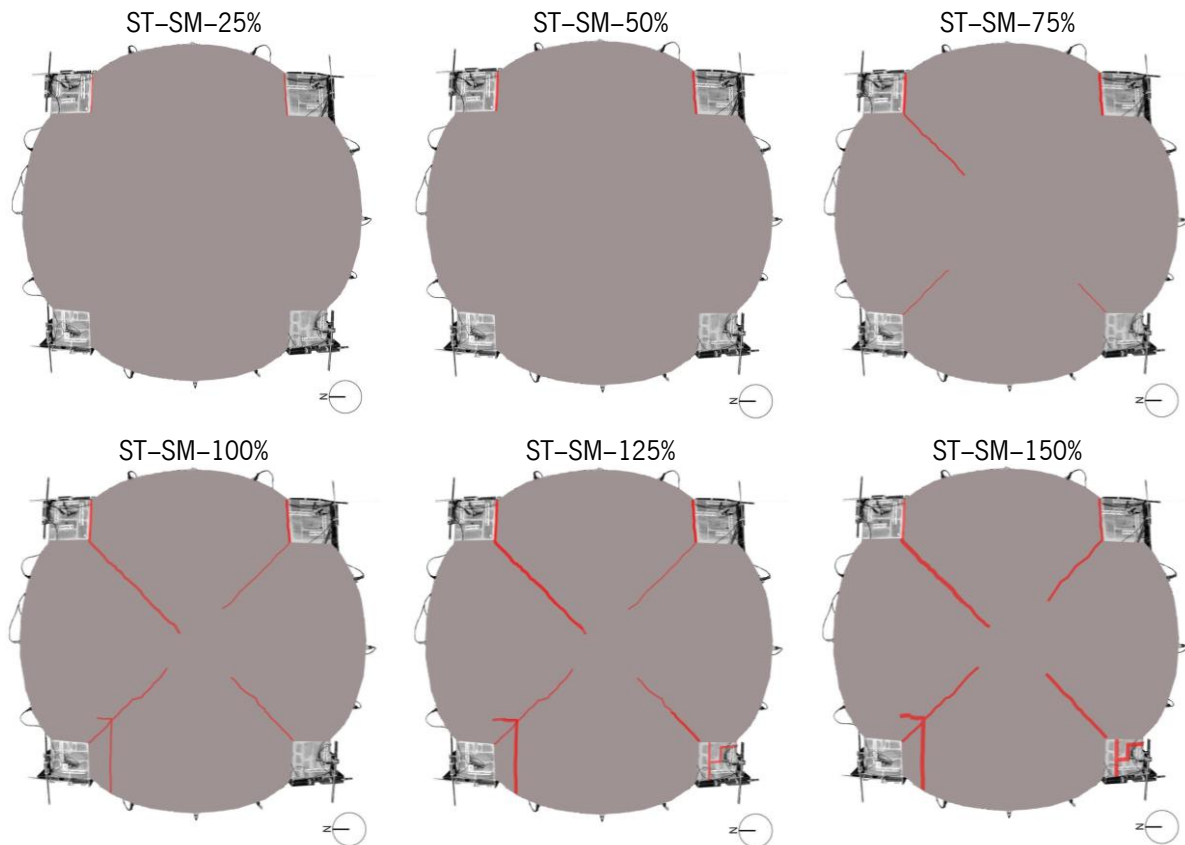


Figure 6-16. Crack patterns at the shell extrados at the end of each shaking table test for the strengthened specimen.

Horizontal cracks between the steel masses and the supports of the vault were also visible in the videos taken by VC_4 , in front of the Eastern elevation. However, those cracks close at the end of the seismic shock, due to the self-weight of the shell. The intrados presented light diagonal cracks (Figure 6-17c), close to the groins. It is also important to mention that repaired and injected cracks from the unstrengthened configuration were adequately repaired. In fact, they did not open during this second set of tests.

Rocking effects at the base of the fixed piers are also visible in the videos recorded by $VC_{1,3,4}$, without causing damage to the vault, but influencing the mechanism. This aspect is really important, and it has to be considered while performing the numerical simulations (see Chapter 7). Additional sequences after ST-SM-150% were avoided, even if the collapse was not reached, because further seismic tests would have compromised the integrity of the equipment. Moreover, the decrease in the first frequency and the damage were already consistent.

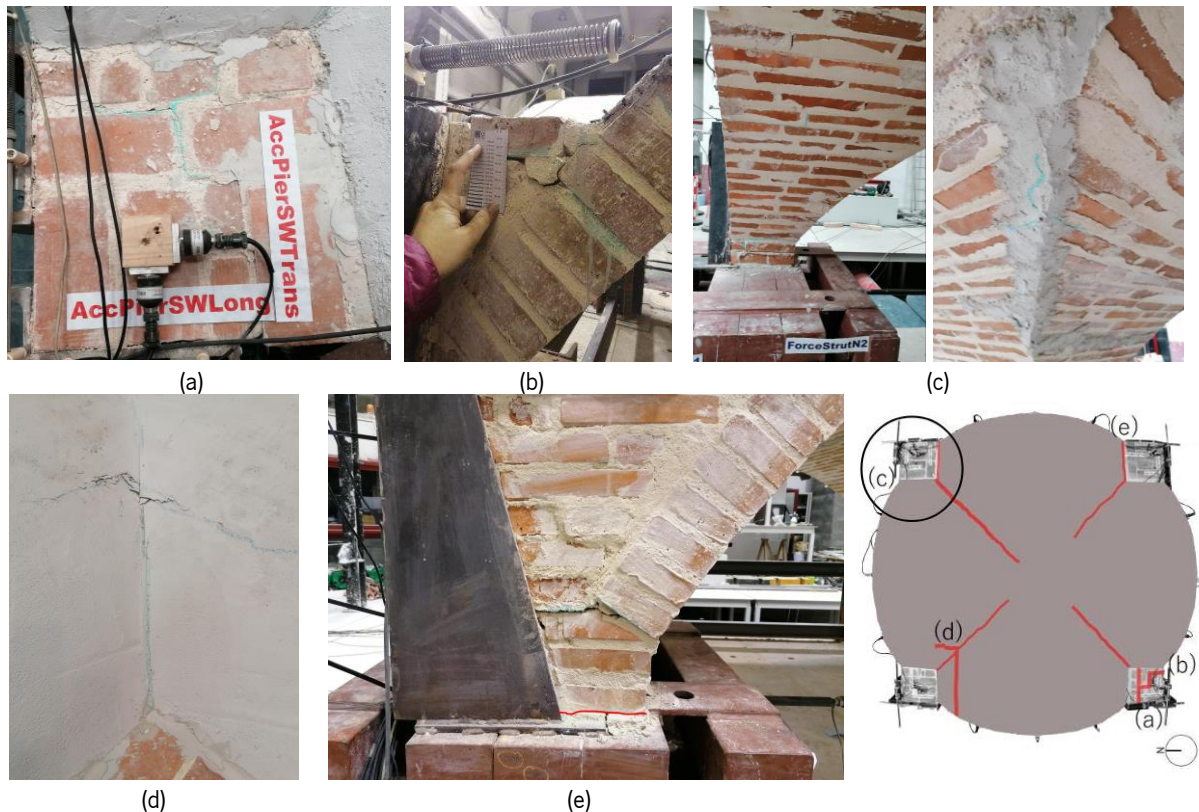


Figure 6-17. Details of the damage for the strengthened specimen after ST-SM-150%, for (a) to (e) views.

The level of damage on the strengthened specimen can be considered “extremely severe” and in a realistic scenario, the space below the vault should not be accessible to people. However, this level was achieved for double the maximum PGA applied on the UNS and it is distributed among all the structure and not localised only along the diagonals.

6.6.2 Deformation profiles and displacement field

The analysis of the in-plane deformation of the vault with the TRM application is undertaken for each testing sequence, amplifying 10 times the measured displacement time history for each optical camera (Figure 6-18). The deformation profiles along the shell vault are plotted when the optical cameras $OC_{1,2,3,4}$ measure their absolute maximum displacements. The maximum displacements are measured at the same time step from each sensor and in the same direction. The North-East corner (measured by OC_4) moved predominantly along the North-South direction, as expected by a simple in-plane shear mechanism, until the end of the shaking table tests. On the other hand, the South-East corner (measured by OC_2) showcased higher transverse displacements which developed marginal rotational effects. In fact, in OC_2 , the transverse displacement achieved a value which is 3.6 times higher than in the other locations ($OC_{1,3,4}$).

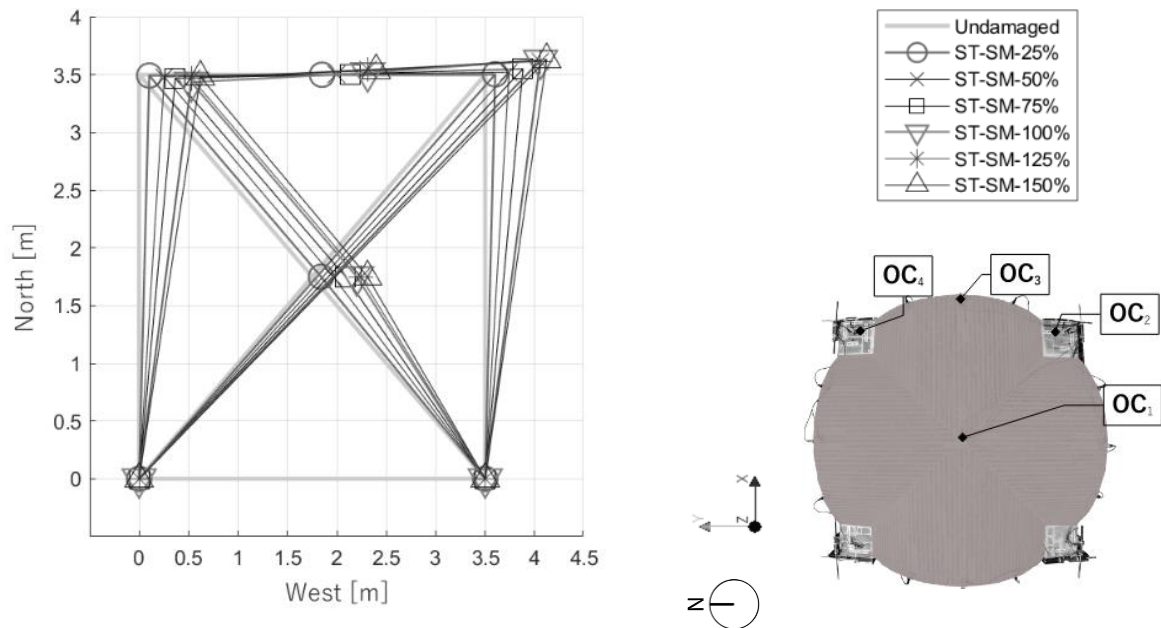


Figure 6-18. In-plane deformation profiles of the strengthened configuration per each sequence when all the optical cameras measure the maximum displacements. Deformation factor:10.

The absolute maximum longitudinal displacement was achieved by the S-E corner, measured by OC_3 at time 4.31 s and it was equal to 64.68 mm for the last sequence ST-SM-150%, which corresponds to 2.7% of drift, as presented in Table 6-7 (almost double of the unstrengthened specimen). The vertical displacement remained positive until ST-SM-50%. Then, it started to be negative, reaching a maximum drop of 12.51 mm.

Table 6-7. Summary of the absolute maximum displacements measured by $OC_{1,2,3,4}$ for each test and the strengthened specimen.

Test sequence	PGA [m/s^2]	OC_1 [mm]		OC_2 [mm]		OC_3 [mm]		OC_4 [mm]	
		NS	Vertical	WE	NS	WE	NS	WE	NS
ST-SM-25%	1.39	8.98	1.20	1.61	10.11	1.38	10.00	5.19	11.62
ST-SM-50%	2.48	21.50	1.49	4.18	24.11	1.08	24.35	5.49	25.46
ST-SM-75%	3.56	33.57	-2.33	5.64	38.19	1.63	38.24	6.41	36.60
ST-SM-100%	4.47	46.26	-7.20	14.04	55.89	2.91	56.13	8.34	53.04
ST-SM-125%	5.54	49.22	-12.42	25.59	55.21	7.17	56.45	8.54	53.11
ST-SM-150%	7.27	56.03	-12.51	42.81	63.48	15.79	64.68	12.77	62.17

Processing the LVDT records, the maximum cumulative relative displacement of all the joints can be appreciated along the Southern arch, where $LVDT_6$ measured 16 mm of opening during the last shock (ST-SM-150%), in agreement with the damage pattern. The highest opening was observed along the South edge (Figure 6-17b and Figure 6-19). All the other elevations presented an average cumulative opening of joints ranging from 1 mm to 7 mm.

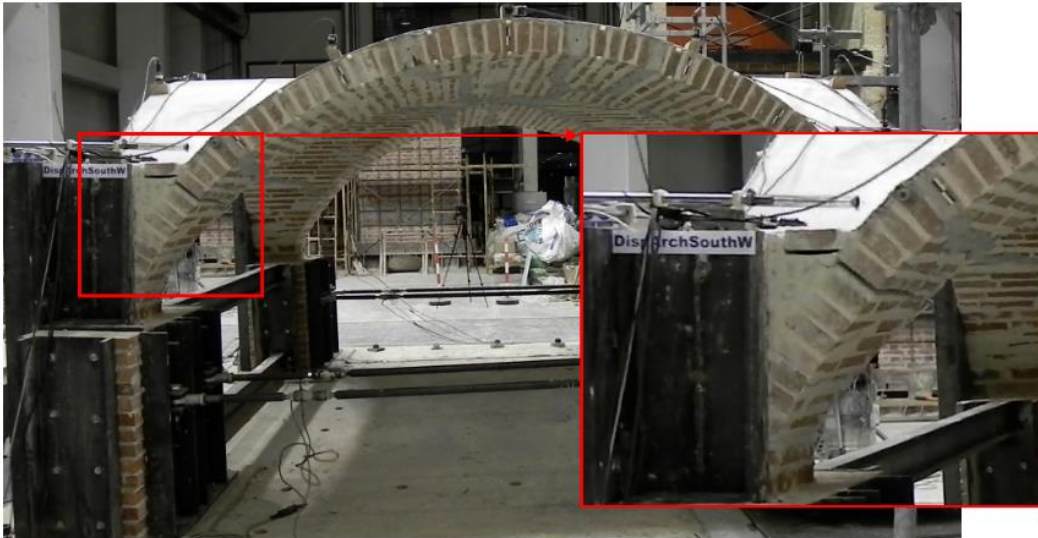


Figure 6-19. Detail of the opening of the joints at the South-West corner during ST-SM-150%.

6.6.3 Hysteretic response

The inertial forces are calculated following the same procedure explained in Section 6.4, through the extension of multi-degree of freedom system, in which for each acceleration, measured at specific locations, an equivalent discrete lumped system of mass is associated. These horizontal inertial coefficients versus the total displacements, measured by the optical cameras, are plotted in Figure 6-20 for all the seismic tests. Until sequence ST-SM-100% (included), the stiffness of the response follows the same trend, and the horizontal inertial coefficients continuously increase. From ST-SM-125%, stiffness and horizontal inertial coefficients drop due to the higher level of damage at the final loading stages. In particular, the horizontal inertial coefficient ranges between -0.45 [-] and 0.45 [-], at the highest level of damage (ST-SM-150%) while for ST-SM-100% it ranges between -0.65 and 0.8 , minimum and maximum values, respectively. This is valid for each optical camera, showing a similar response also in terms of maximum deformations. The hysteretic curves are asymmetric in terms of displacements, which is potentially related to the characteristics of the input, the accumulation of damage and the imperfections of the specimen.

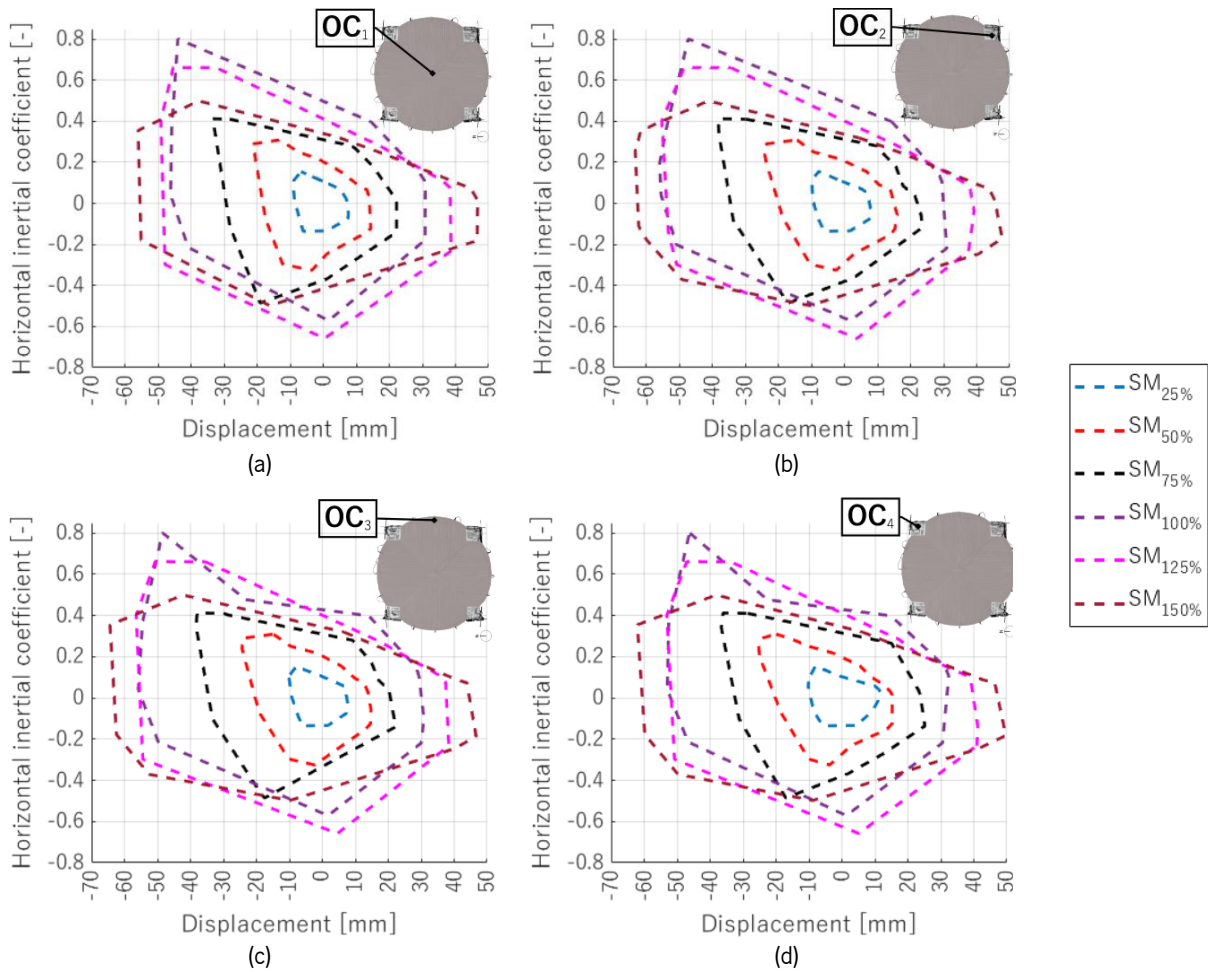


Figure 6-20. Envelope response curves of the strengthened specimen considering four control points for each seismic test in the North-South direction: (a) OC_1 , (b) OC_2 , (c) OC_3 , (d) OC_4 .

The analysis of the seismic performance of the strengthened specimen through quantitative parameters highlights how TRM applications may influence the mechanisms of the groin vaults under seismic actions. Even if the in-plane shear mechanism along the diagonal is still predominant, other mechanisms play an important role in leading to a complex distribution of damage, which requires attention while designing a strengthening intervention. This is valid, in any case, for the double PGA and drift value in comparison with the unstrengthened configurations. The outcomes of the strengthened configuration are generally divergent from the unstrengthened ones. The comparison between the two configurations is commented on in the next Section, highlighting the most representative outcomes.

6.7 Comparisons of the results: unstrengthened vs strengthened specimen

As anticipated in Section 1.5, the assessment of the effectiveness of an innovative strengthening technique for masonry cross vaults is one of the complementary objectives of this thesis. In order to fulfil it, a deeper comparison between UNS and SM is needed. In the first comparison, the seismic

vulnerability curves for the first mode are used, since the reduction of modal characteristics reflects the loss of structural integrity and damage (Mendes, 2012; Avila, 2014). Both two configurations present a reduction of frequencies, but to be able to compare it is important to assume that the mass of the specimen is kept almost constant during all the seismic tests, in both configurations (UNS and SM). This assumption is deemed to be acceptable as the very thin layer of mortar and the TRM grid represent a mass increase equal to less than 1.5% of the total mass of the vault. Assuming a constant mass of the specimen, the progress of the damage is only related to the stiffness degradation, which is associated with the frequency reduction. A simple way to estimate the effectiveness of the strengthening technique is through the damage indicator d_n , already adopted for the reduced-scale vault (see Section 3.4.2), and calculated as described in Equation 3-1, (Di Pasquale and Cakmak, 1987; Giordano *et al.*, 2020).

For both scenarios (UNS and SM), the damage indicator has been evaluated considering mode 1 in relation to the increase of peak ground acceleration (PGA) (Figure 6-21a), peak ground velocity (PGV) (Figure 6-21b) and peak ground displacement (PGD) (Figure 6-21c) for each shaking table tests.

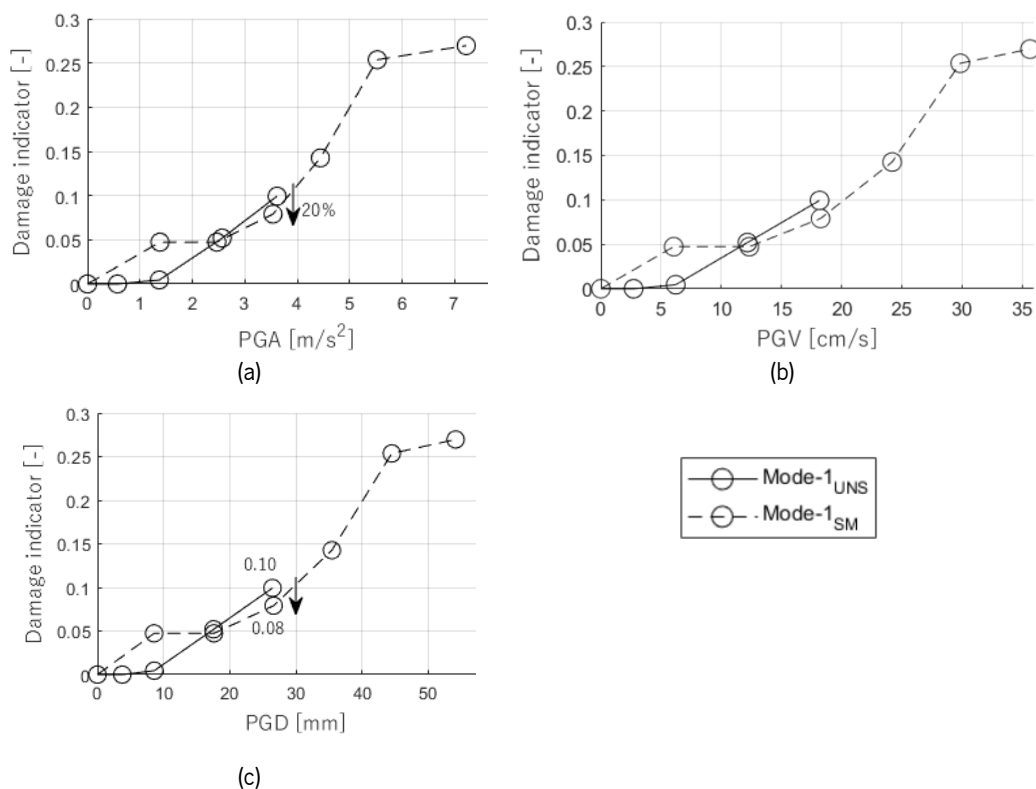


Figure 6-21. Damage indicator using mode 1 versus: (a) peak ground accelerations, (b) peak ground velocity and (c) peak ground displacements for both UNS and SM configurations.

The maximum value of the damage indicator for the UNS vault is equal to 0.1 (first mode) at the level of ST-UNS-75%, while for the SM vault is equal to 0.27 at the level of ST-SM-150%. Comparing the two

responses for the same seismic amplitude (ST-UNS,SM-75%), there is almost no damage on the strengthened vault at this stage. The variation of damage indicator at this level (ST-UNS,SM-75%) is equal to 20%. The trend of the UNS curves remains above the strengthened one, because the unstrengthened specimen develops micro-cracks, which are not visible but are able to influence the dynamic identification test results, decreasing the frequencies. Conversely, in the strengthened specimen, the TRM application avoids the opening of the cracks, reducing the variation of frequencies. At the beginning of the seismic tests in the strengthened condition, at the level of ST-SM-25%, the vault presents a higher damage indicator, which is not expected. This value remains constant also for the following shock, ST-SM-50%, considered out of the trend. The slope of the unstrengthened vault's curve is steeper, rapidly leading to severe damage conditions. At the level of ST-UNS-50% and ST-SM-50%, there is a coincident damage indicator for both curves (UNS and SM).

To summarise, the damage indicator increases along the testing and agrees with the evolution of the damage observed in the crack patterns. This assessment confirms that the strengthening technique enhances the response of the vault to dynamic actions and improves its seismic performance. Comparing the damage patterns of the last two seismic tests for both configurations, further discussions arise. Contrary to what has been observed in the unstrengthened specimen, after ST-SM-50% and ST-SM-75%, the extrados of the strengthened specimen present low damage and few diagonal cracks. Looking at the extrados in Figure 6-22, the in-plane shear mechanism is represented by the diagonal cracks, clearly evident for the UNS. Such crack patterns put in evidence the lower tensile strength of the key of the vault of the UNS specimen, contrary to the SM, because the TRM increases the tensile strength of the vault shell. The strengthening system can counteract the evolution of damage, transferring the deformation from the shell to the supports (either movable or fixed).

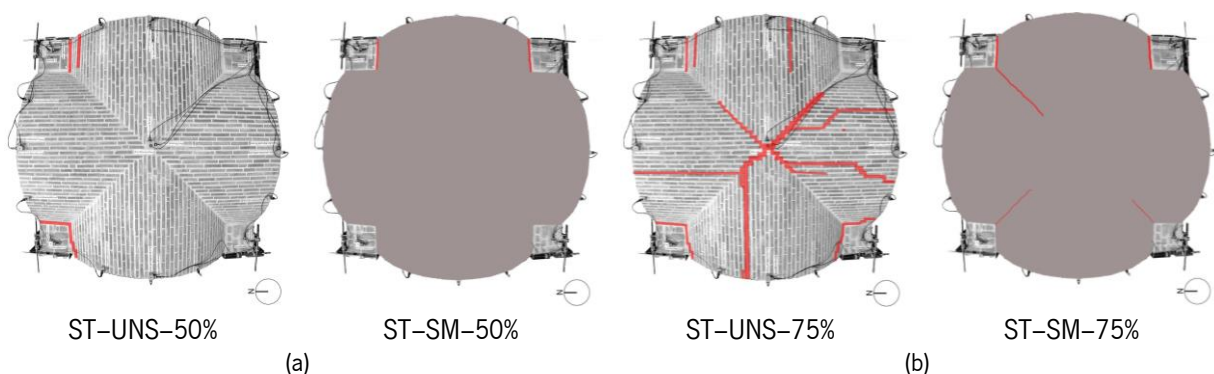


Figure 6-22. Comparison of crack pattern of extrados for UNS and SM configurations: (a) ST-50%, (b) ST-75%.

The intrados of the SM presents cracks close to the fixed support, while the repaired cracks maintain their integrity without transferring the damage to the closest joints. Most of the differences are notable

by observing the damage maps of the elevations of the last two seismic tests of each configuration (Figure 6-23). Most of the damage of the UNS vault occurs at the shell and the extrados, while in the SM, the supports suffer damage due to uplift and detachment from their base (East), but also due to rocking (visible at the base of the fixed pier in the North elevation).

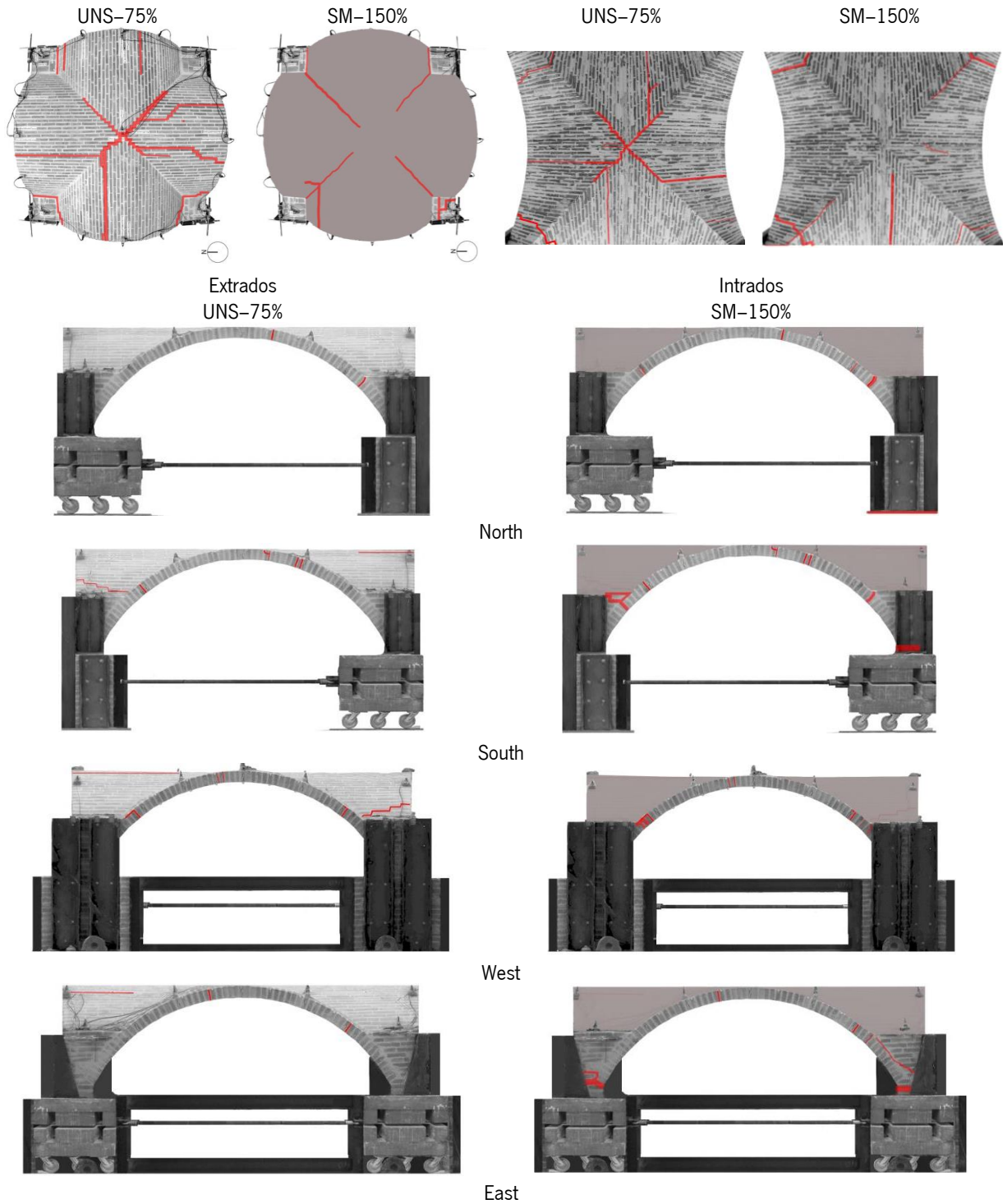


Figure 6-23. Comparison of crack patterns for the last seismic tests performed on the unstrengthened and strengthened configurations: UNS-75% vs SM-150%.

Concerning the deformation of the shell during the shaking table tests in the unstrengthened and strengthened configurations, the displacement profiles are shown in Figure 6-24. The absolute total displacements are limited and contained by the effect of the TRM at the extrados in the SM. Even if the in-plane shear mechanism is predominant until the end of the tests, the torsional effects of the extrados are also notable. The maximum total displacement in the longitudinal direction is comparable between the last shocks (ST-UNS-75% and ST-SM-150%) with only 10 mm of difference in the negative and 4 mm of difference in the positive direction (Figure 6-24a). While comparing the same level of amplitude in both scenarios (Figure 6-24b), the deformation is similar for all the optical cameras, except for OC₂, which shows a decrease in maximum displacements of about 40% in the longitudinal direction (SM specimen). Again, this underlines the effectiveness of the strengthening technique in counteracting the opening of the cracks during the dynamic action. The vertical displacement measured by OC₁ remains almost the same for both configurations, and it is fully recovered at the end of the tests.

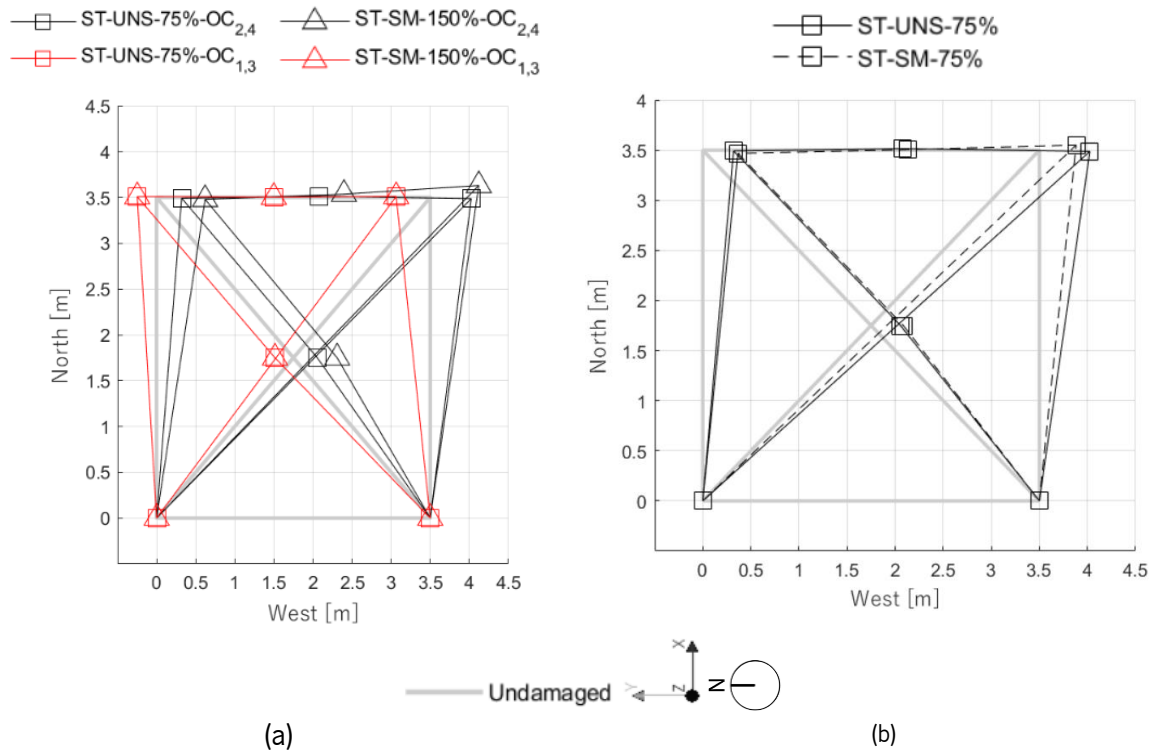


Figure 6-24. In-plane deformation profiles for the last seismic tests: (a) ST-UNS-75% vs ST-SM-150%, (b) ST-UNS-75% vs ST-SM-75%. Deformation factor: 10.

In terms of hysteretic response, only the seismic sequences in common between the two configurations are plotted in Figure 6-25. From three optical cameras OC₁, OC₃ and OC₄, it is possible to observe that the behaviour of the vault remains linear and comparable up to the level of ST-50%, with similar displacements and horizontal inertial coefficients. In addition, for all the curves of the SM, up to the level of 75%, there is a linear increase in the horizontal inertial coefficient. The maximum horizontal

inertial coefficient for ST-SM-75% is about 30% higher than the maximum horizontal inertial coefficient for ST-UNS-75%. On the other hand, in terms of displacement deformation, both configurations present comparable responses. As an exception, as observed in the crack pattern, non-linear effects are already recognisable at the level of ST-UNS-50% from OC₂, located at the S-E corner, making differ the two hysteretic curves.

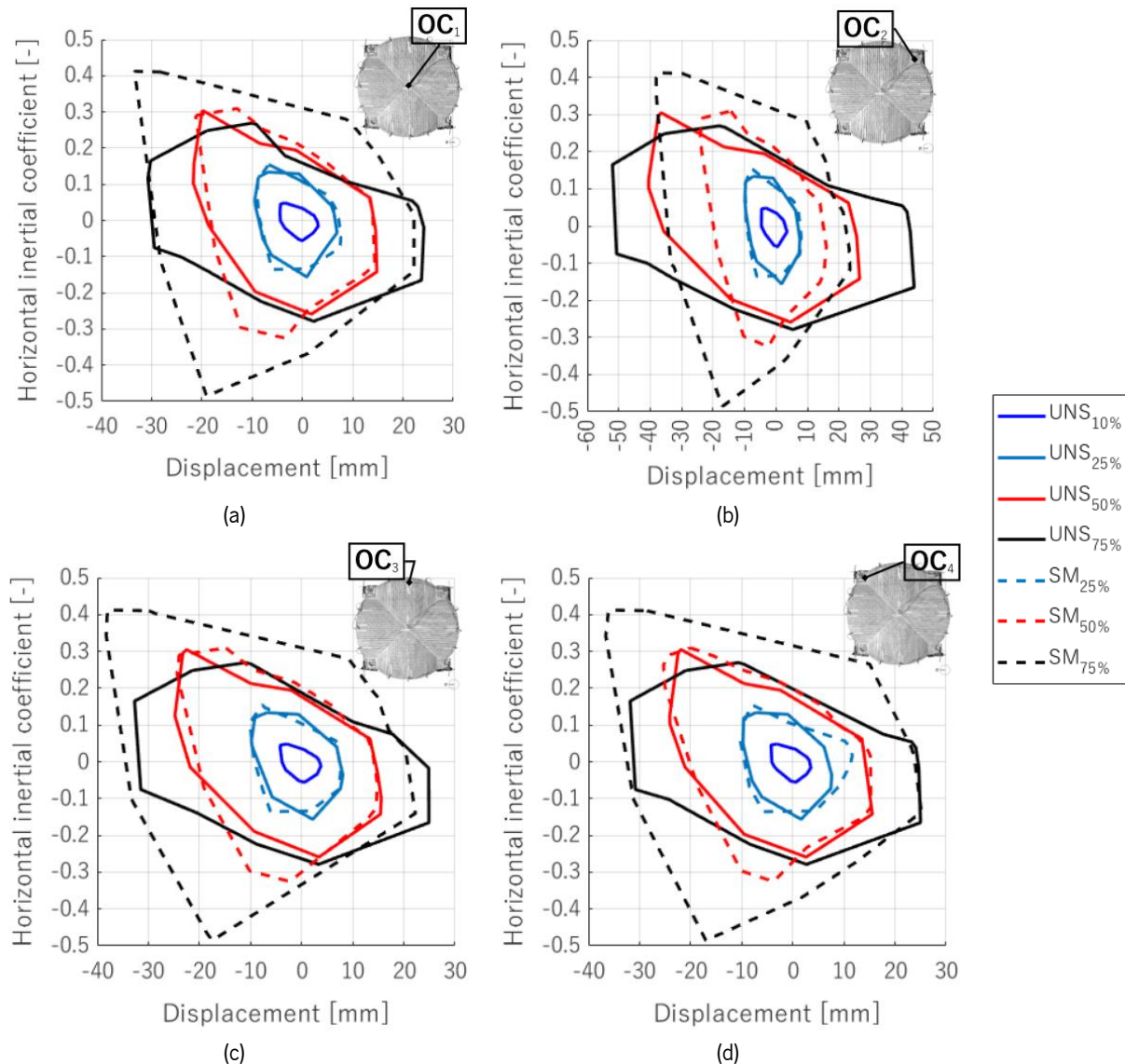


Figure 6-25. Envelope response curves in comparison of the UNS and SM considering four control points: (a) OC₁, (b) OC₂, (c) OC₃, (d) OC₄.

As a final comparison, the capacity curves for the unstrengthened and strengthened specimens are shown in Figure 6-26. The capacity curves are defined for each optical camera, based on their maximum deformation, but only the one associated to OC₁ is plotted. The points associated with ST-SM-100% have been discarded as being out of the trend (record issues in some accelerometers). The two curves in the positive and negative direction are different due to the not completely symmetric

deformation response of the vault. Larger displacements are recorded when the vault is moving along the North-South direction in concordance with the first peak of the ground motion. Both capacity curves have a marked non-linear behaviour in the positive direction. The linear limit (onset of cracking) occurs up to a deformation equal to 15 mm and 40 mm for the unstrengthened and strengthened configuration, respectively. In the opposite direction, the unstrengthened capacity curve does not show a post-peak behaviour, such as observed in the strengthened configuration. It is possible also to conclude that the strengthened specimen can stand almost double horizontal inertial coefficients and deformation in both directions.

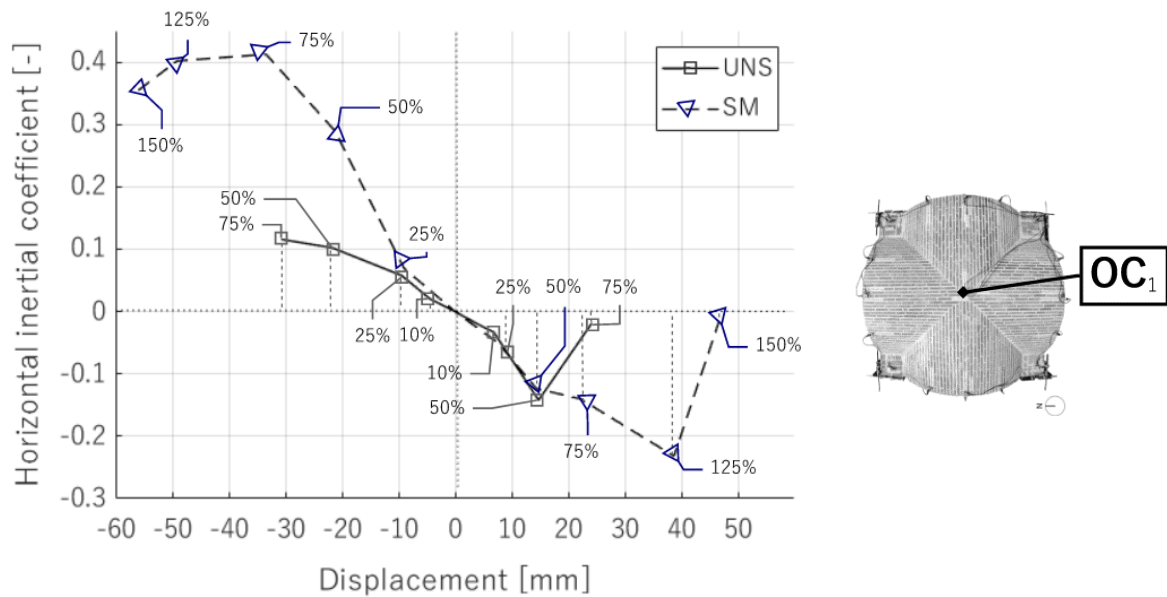


Figure 6-26. Experimental capacity curve, in terms of horizontal inertial coefficient and displacement at the key of the vault (OC_1).

For what concerns the loads registered by the load cells on the steel cables, no significant difference has been noted between the two configurations. The maximum force reached during ST-UNS-75% and ST-SM-75% is about 9.0 kN, while for the strengthened specimen the maximum force is measured during ST-SM-150% and it is about 17 kN. Both forces have been registered by LC_3 on the Southern side.

6.8 Final remarks

This Chapter reports the results of the shaking table tests performed on the full-scale unstrengthened and strengthened vault, subjected to incremental ground motion amplitudes. The experimental campaign aims to define the seismic capacity of the vault when in-plane shear distortions are induced to the shell, and, then, to assess the effectiveness of the TRM strengthening solution. For both

configurations (unstrengthened and strengthened) the results of the dynamic identification tests and the seismic tests are described and compared. The main outcomes are here summarised.

- The results of the dynamic identification are used to obtain the modal properties of the vault and the experimental seismic vulnerability curves of the specimens. In particular, the first mode corresponds to the in-plane shear distortion of the shell and the first frequency decreases while damage increases on the vault. The evolution of the modal properties was studied in terms of MAC value, frequency reduction and damage index. The last has been used to plot the experimental seismic vulnerability curves, which correlate the damage indicator, defined based on the decrease of the frequencies of the modes along the testing, with the seismic level of amplitude, expressed in terms of PGA, PGV and PGD. After the 75% amplitude of the shaking table tests, in both scenarios, the strengthened specimen presents a reduction of the damage indicator for the first mode of about 20% with respect to the unstrengthened vault. This leads to the conclusion that the strengthening technique is efficient in the reduction of the seismic vulnerability of the specimen.
- Regarding the crack patterns, the unstrengthened specimen presents a higher concentration of damage along all the diagonals of the vault, with severe cracks located at the key. Light cracks involve the boundaries of the specimen. This crack pattern agrees with the in-plane shear distortion (the main mechanism involved during the shaking table tests) and with the preliminary analysis used to define the design of the specimen and its setup. Although the collapse of the unstrengthened is not achieved, it is expected that with the increase of the seismic amplitude, the existing damage may increase in severity, leading to the partial or global collapse of the webs, which is common in churches and palaces under seismic excitation.
- After 75% of seismic amplitude, the unstrengthened vault has been repaired, aiming at re-establishing the initial conditions and then the application of a strengthening technique (TRM) is undertaken. TRM is used at the extrados to increase the strength of the vault. Comparing the two configurations at the same level of amplitude (75%), it is possible to notice that the strengthened vault presents only light cracks, indicating that the inertial forces of the shell have been absorbed by the TRM strengthening technique, improving the seismic performance of the vault.
- At the last seismic sequence (ST-SM-150%), the strengthened vault presents a higher concentration of damage along the piers and the supports of the specimen, not only along the groins. This damage is represented by detachments and horizontal cracks, meaning that it is related to both in-plane distortions but also rocking and torsions of the fixed piers. This outcome is important for the research because, based on these results, engineers may consider a design that

involves the complete strengthening of the vault, also including the reinforcement of the piers, when possible.

- In general, the main conclusion is that the crack patterns of the two specimens are much different, even if the in-plane shear mechanism is the predominant one of both configurations. The repair and the strengthening technique concur to double the horizontal inertial coefficient, drift value and displacements (ST-UNS-75% vs ST-SM-150%). In conclusion, TRM-strengthening enhances the performance of the vault, providing further capacity to the vault under dynamic loads and it is an effective solution for reducing the seismic vulnerability of masonry groin vaults.

This page has been intentionally left blank

7. Full-scale vault: numerical modelling

7.1 Introduction

This chapter addresses the application of the two numerical modelling approaches for the analysis of masonry cross vaults, based on the shaking table test results described in Chapter 6. This is undertaken to fulfil one of the objectives of this research, namely the assessment of the reliability of numerical models to forecast the seismic behaviour of full-scale masonry cross vaults (see point E in Section 1.5). The numerical approaches, used in the simulations reported herein, are based on the finite element method (FEM) and discrete element method (DEM). FEM and DEM are accurate numerical approaches for seismic assessment through non-linear dynamic analysis, as observed in Chapter 4 for studying the reduced-scale vault. DEM approach allows to build discontinuous models and to evaluate the response for large displacements, which is particularly relevant for studying the behaviour of masonry vaults taking into account the arrangement of the units. Nevertheless, FEM continuum macro-models attract wide scientific interest, since they offer a certain degree of simplification and allow to upscale the meso-mechanical characteristics of the components to the macro-scale. In particular, macro-models represent a computationally efficient way to model large structures, which can hardly be modelled with discrete approaches. Moreover, FEM macro-modelling approach allows the meticulous implementation of the strengthening technique (TRM) and its simulation within the complex dynamic of the vault.

Two different approaches are proposed for the calibration of the numerical models, considering the experimental dynamic properties of the specimen: (i) simulating the dynamic identification tests on the DEM model; (ii) model updating calibration based on the eigenvalue analysis for the FEM model.

The seismic sequences described in Chapter 6 during the experimental campaign have been numerically simulated through non-linear time history analysis and compared highlighting the pros and cons of each approach. The numerical results are presented in terms of damage parameters, displacement profiles, failure mechanisms and horizontal seismic coefficient. A direct comparison between the experiments without and with the strengthening technique and the numerical models is undertaken.

7.2 Preparation of the numerical models

The two modelling strategies, FEM macro-modelling and DEM approaches, are considered in parallel. The numerical models are built through the FEM software, namely DIANA 10.5 (2022) and a DEM software, namely 3DEC 7.0 (Itasca Consulting Group, 2019a), both replicating the exact geometry of the full-scale specimen. A similar procedure to the one adopted for the reduced-scale vault (see Section 4.2) has been followed to build the numerical models, with some specific modifications required for the full-scale specimen. The numerical models represent the replica of the specimen in terms of geometry and materials. In total, three numerical models have been calibrated and studied:

- DEM–UNS: discrete element model to replicate the unstrengthened configuration.
- FEM–UNS: continuous macro-model to replicate the unstrengthened configuration.
- FEM–SM: continuous macro-model to replicate the repaired and strengthened configuration.

7.2.1 Finite element models: FEM–UNS and FEM–SM

The geometry of the FEM models of the full-scale masonry vault is built in AutoCAD 3D, transforming the shell of the vault and the infill into a solid continuous element (Figure 4-6). It is similar to the preliminary numerical model used for the designing of the specimen (Chapters 5 and Chapter 6), but it considers modifications, that occurred during the construction, and more realistic boundary conditions. The geometry has been exported in different *iges* files and a specific geometry group is associated with each portion of the model, according to the distribution of the materials. The FEM model characteristics are here described and summarised in Table 7-1:

- the geometry of steel profiles and steel frame is simplified to avoid complex elements, which counteract the regularity of the mesh.
- the system of wheels is discarded in the FEM model, being numerically irreplicable. It is substituted by vertical constraints, directly applied below the steel masses.
- between the steel masses and the vertical constraints, a very low shear stiffness boundary interface (CQ48I) has been inserted. CQ48I is an interface element between two planes in a three-dimensional configuration. It allows movement along the longitudinal direction with low friction. On the other hand, the elements along the Western edge are perfectly fixed to the shaking table block through a rigid connection. This choice is driven to improve the calibration of FEM–UNS and FEM–SM.

- three couples of steel cables have been placed as in the real specimen and modelled using truss elements. Their cross-section (A) and density are equal to $8.04 \times 10^{-4} \text{ m}^2$ and 7800 kg/m^3 , respectively.
- two couples of steel bars with $3.10 \times 10^{-4} \text{ m}^2$ of cross-section and density of 7800 kg/m^3 , named “connectors”, are inserted inside the thickness of the fixed piers as embedded elements.

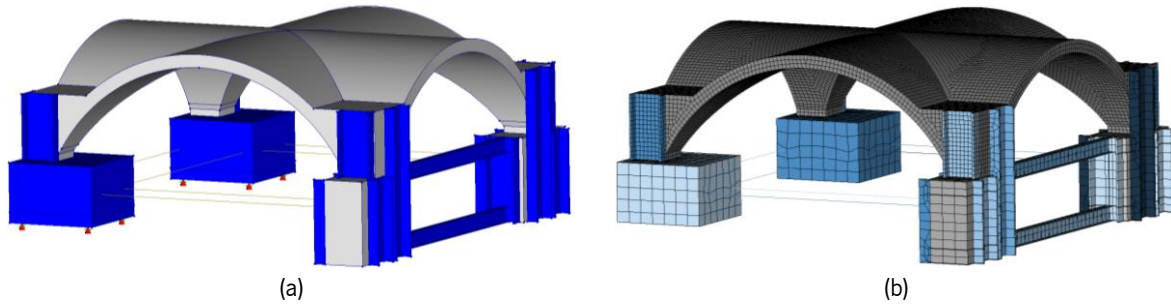


Figure 7-1. FEM-UNS macro-model of the full-scale vault in DIANA environment: (a) geometry, (b) mesh of the model.

Table 7-1. Element types of the numerical FEM-UNS and FEM-SM models built in DIANA 10.5 (2022).

Material	Type of element	Denomination
Masonry	Tetrahedron solid element (CHX60)	Fixed piers
		Shell and filling
		Supports
Steel		Steel masses
		Steel profiles
		Steel frame
Steel	Enhanced truss element, straight (L6TRU)	Three couples of steel cables
Steel	Embedded bar in solid element	Steel connectors inside the fixed piers
	Interface element (CQ48I)	Boundary interface below the steel masses

The representation of masonry elements is conducted using continuum solid elements with a quadratic twenty-node isoparametric solid brick element (CHX60 in Table 7-1). The mesh size is constant and equal to 4 cm along the shell to guarantee the presence of 3 elements within the thickness of the vault (6 integration points). Mesh size ranges from 1 cm to 12 cm for the steel elements as function of their smaller thickness dimension. The three couples of steel cables, meshed per division, are modelled as 1D elements, namely enhanced truss element (L6TRU) - a two-node directly integrated truss element, suitable for non-linear dynamic analysis.

The non-linear behaviour of the masonry is ruled by the Total Strain Based Crack Model (TSCR) implemented in DIANA (Selby and Vecchio, 1997). This model describes the tensile and compressive behaviour of a material with one stress-strain relation. In particular, a rotating crack model is assumed. Within this approach, the stress-strain relationship is evaluated in the principal directions of the strain vector, which, at the same time, defines the direction of the cracks (DIANA 10.5, 2022). TSCR represents the physical non-linear compressive and tensile behaviour of masonry, with inelastic mechanisms developing from a diffused pattern of micro-cracks to localized macro-cracks (DIANA 10.5, 2022). In this work, the stress-strain relationship of the TSCR is characterised by a hysteretic diagram with exponential tension–softening for the tensile behaviour and linear for the compressive behaviour (Figure 4-5a). Tensile strength f_t is set at the value of 0.1 MPa, considered as lower bound. The compressive behaviour has been assumed as linear. It is noted that the maximum principal stress in compression was checked at the end of the dynamic analyses, concluding that cracking is the unique type of damage and no crushing occurs. The shear behaviour is linear, in which the shear stiffness is reduced after cracking according to the shear retention factor (set at the value of 0.1). All the steel elements present linear elastic behaviour (Figure 4-5b).

The sliding interface follows Mohr–Coulomb friction behaviour to simulate frictional slip along the interface elements below the steel masses (Figure 4-5c). To allow the in-plane shear mechanism the values of stiffnesses are the following: $K_n = 20.0 \times 10^6 \text{ KN/m}^3$, almost infinite to avoid any separation and interpenetration, $K_s = 2.0 \text{ KN/m}^3$ to allow almost pure sliding. The friction angle θ is set at the very low value of 2° , while cohesion c and dilatancy ψ angle are null.

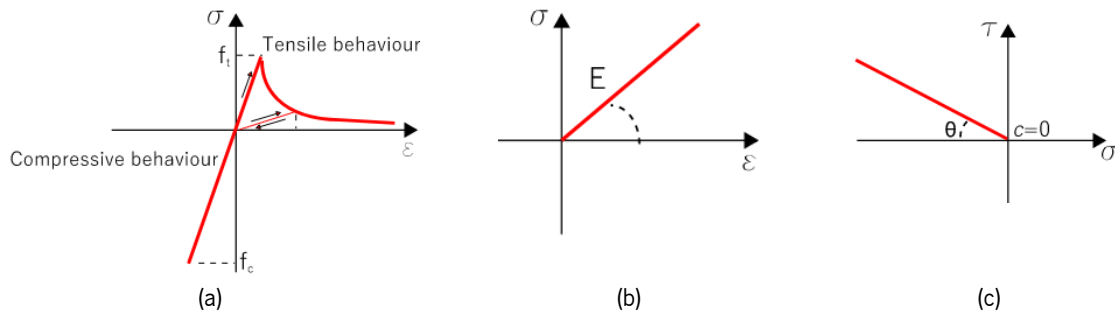


Figure 7-2. Constitutive laws used in the FEM-UNS and FEM-SM models: (a) non-linear hysteretic behaviour of masonry elements, (b) linear elasticity diagram for steel elements, (c) Mohr-Coulomb criterion for sliding interface.

For what concerns the FEM-SM model, the TRM technique is modelled as reinforcement sheets, namely a reinforcement grid embedded in the curved shell layer elements (CQ40S), both placed above the extrados of the shell. CQ40S is a six-node triangular isoparametric curved shell element, which simulates the mortar *Geocalce F* (Figure 7-3a). The reinforcement grid requires specification of the diameters and spacings of the grid, which is given by KeraKoll technical specifications to be equal to 17×17 mm (Figure 7-3b). DIANA 10.5 (2022) automatically calculates and applies the equivalent thickness parameter for the reinforcement grids based on the given spacings. The location of the grid in the curved shell element must be within the thickness domain of the element, meaning that the eccentricity along z axis of the grid should be smaller than half the thickness of the curved element. For simplicity, the thickness of the *Geocalce F* has been kept constant along the extrados and is equal to 10 mm. The material behaviour of mortar *Geocalce F* and the reinforcement grid is linear elastic (Figure 4-5b) and the maximum stresses were verified at the end of the analysis.

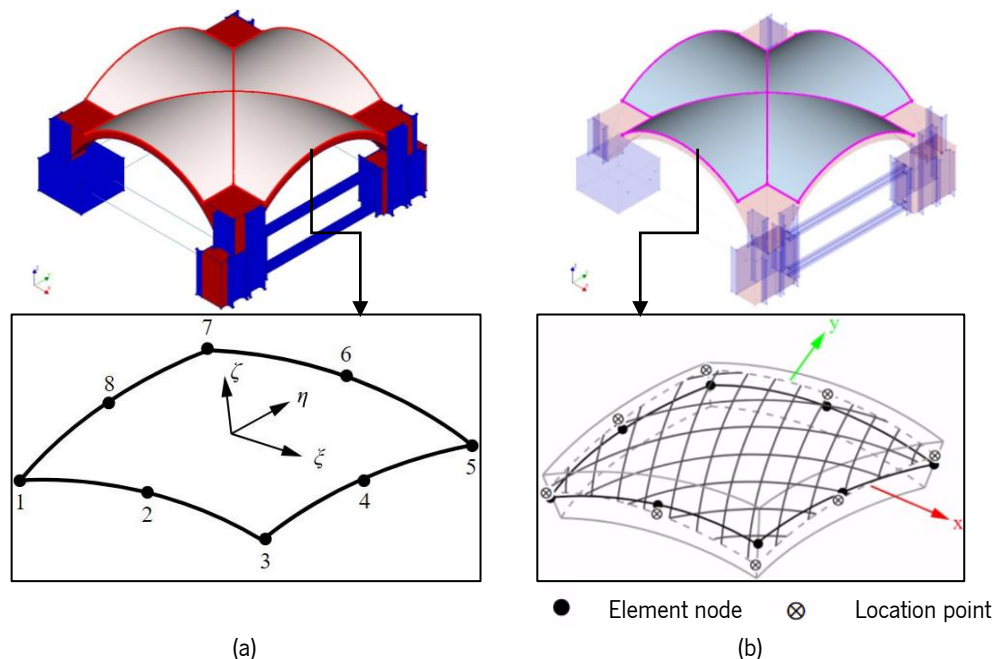


Figure 7-3. Strengthened FEM-SM macro model of the full-scale vault in DIANA 10.5 (2022) environment: (a) shell element for the GEOCALCE F through CQ40S, (b) embedded grid to simulate Geosteel grid 200.

Based on some preliminary results, here discarded for the sake of succinctness, the role of the grout injections, used to repair the UNS, is crucial to avoid a high level of damage at the intrados, which was not observed in the experiments (see Section 6.6.1). As stated by Lourenço and Gaetani (2022), grout injection affects the strengths and elastic modulus. In fact, without the higher properties of *Geocalce FL* along the diagonals at the intrados, high strains concentration along the groins caused preliminary cracking and inconsistent results. Very few examples of modelling of grout injections are available in the literature (Van Rickstal, 2000; Doran *et al.*, 2020), mainly using the micro-modelling approach, which is in this case computationally unsustainable, due to the size of the model. Thus, for considering the grout injections in the FEM–SM model, where the higher characteristics of Mortar *Geocalce FL* were applied, five solid curved shapes have been inserted from the intrados within the thickness of the vault for a height of 8 cm (Figure 7-4). For these elements, the non-linear behaviour Total Strain Based Crack Model (TSCR) is assumed, like the masonry shell. However, the injections have different linear elastic values which have been gathered from the material characterisation tests for Mortar *Geocalce FL* (Table 7-2).

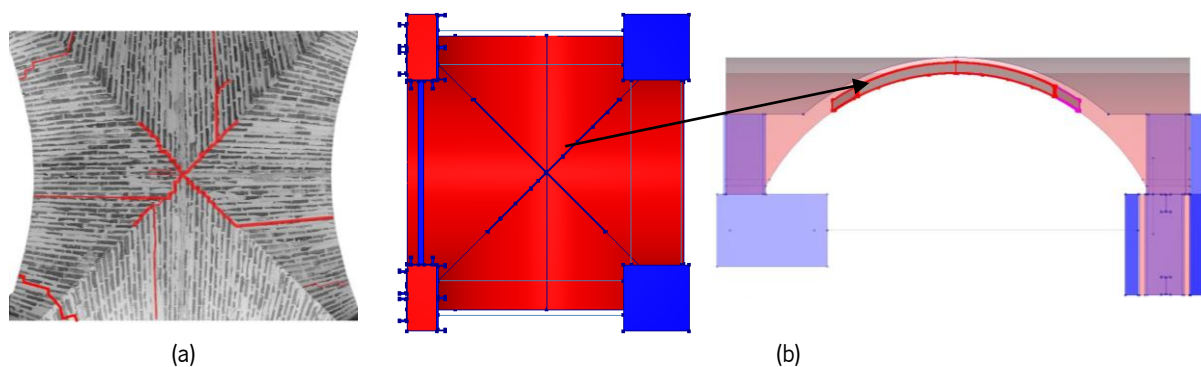


Figure 7-4. Grout injections modelled in the strengthened FEM–SM model in DIANA 10.5 (2022): (a) damaged intrados at the end of the ST–UNS–75%, (b) solid elements to simulate injections (intrados and North elevation).

Table 7-2. Mechanical properties for the TRM system adopted in the numerical FEM–SM (DIANA 10.5, 2022).

Material	Young's modulus [GPa]	Density [kg/m ³]	Total mass [g/m ²]	Thickness [mm]
Grid Geosteel 200	62.0		200	10 mm
Mortar Geocalce F	12.5	1800		
Mortar Geocalce FL	7.81	1600	X	X

Before reaching this final configuration of FEM–SM, several options have been investigated to improve the numerical response of the strengthened model. For example, boundary interface elements at the base of the fixed piers and/or between the steel masses and the supports of the vault have been included, trying to simulate the uplift behaviour of the shell. The boundary interfaces below the fixed piers concur in bringing only smaller improvements to the detriment of higher computational

complications. Another option considered higher Young's modulus for the shell of the vault to replicate the improvement of the injections. However, this decreases the quality of the calibration and leads to underestimated strains' distribution.

Since the objective is to perform non-linear time history analysis, the non-linear parameters of the masonry elements of the FEM models also include the exponential softening under tension through mode-I fracture energy, G_f^I . In this regard, it is possible to refer to Lourenço (2018; 2022), who also proposed the following relation for the estimation of fracture energy in tension $G_f^I = 0.02$ [N/mm].

7.2.2 Discrete element model: DEM–UNS

The geometry of the DEM model of the full-scale masonry vault is built in Rhinoceros® (McNeel Robert, 2008), and it corresponds to a model formed by 1399 blocks with an error smaller than 2% when comparing the real and numerical volume. The geometry is exported layer by layer from Rhinoceros and a specific geometry group is associated with each portion, according to the distribution of the materials along the model. Changes in the default tolerance ranges (from 1e-05 to 1e-03) are studied for each group to better improve the creation of sub-contacts in 3DEC 7.0, due to the complexity of the vault.

The boundary conditions have been slightly discretised to fulfil the syntax of 3DEC 7.0 (2019a) satisfying some requirements, in particular:

- the geometry of the steel profiles and the steel frame has been simplified to avoid concave elements.
- a rigid solid element "*shaking table block*", fully constrained and aligned with the axis of symmetry of the vault is introduced to apply the input to its centroid. Since the system of wheels is discarded in the DEM model, being numerically irreplacable, the shaking table block has an irregular stepped cross-section which allows to take into account the height of the system of wheels (see Figure 4-1).
- similarly to the reduced-scale specimen, between the steel masses and the shaking table block, a very low shear stiffness joint K_{s-base} is inserted. It allows movement along the horizontal directions with very low frictional effects below the system of wheels. The contact stiffness value of the sliding interface is a result of the calibration process (see Section 7.3.2).
- the elements along the Western edge are perfectly fixed to the shaking table block through a rigid connection.
- three couples of steel cables have been placed as in the real specimen. The cross-section (A) and density of the steel cables are equal to $8.04e-04$ m² and 7800 kg/m³ respectively. The embedded length (L) and the bond length are assumed equal to 2.5 cm. The four blocks in contact with them

are made deformable, namely the two steel masses and two UPN profiles, which are subdivided into finite-difference meshes of tetrahedral elements characterized by a mesh size of 10 cm.

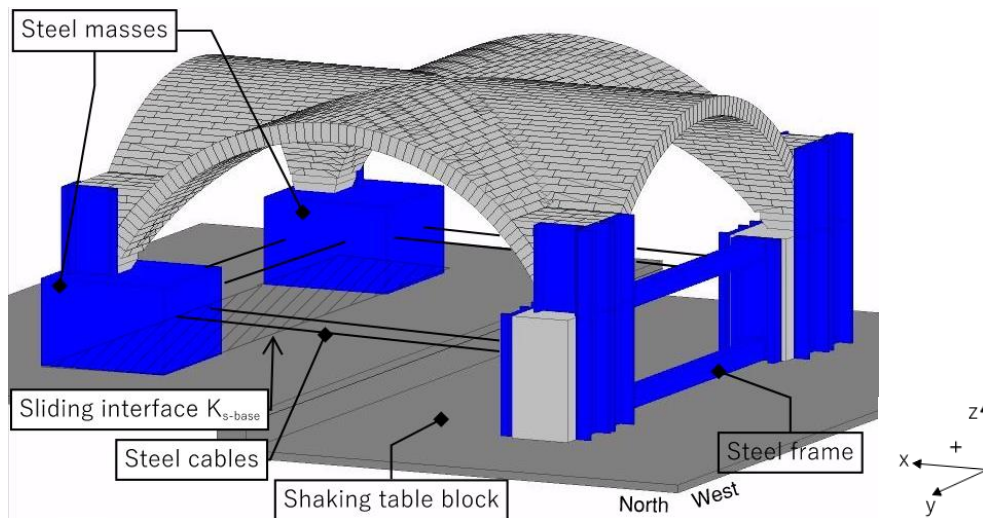


Figure 7-5. Geometry of the DEM model in 3DEC 7.0 environment.

As explained in Chapter 4, the deformable blocks in contact with the cable elements may allow a small overlap in compression. The overlap size is specified in terms of normal and shear contact stiffness of the bond contact, as described in Equation 4-1 (Lemos, 2007). In this case, Young's modulus of the steel cables is $E_c = 210$ GPa and the yield strength is equal to $f_y = 350$ MPa. The bond stiffness of grout (k_{bond}) and the bond strength of grout (s_{bond}) are defined according to Equation 4-3 and Equation 4-4 (Mehrotra, Arede and Dejong, 2015) and they are equal to 6753.6 MPa/mm and 1400 MPa/mm, respectively. All the other blocks follow a rigid block model, which is appropriate for problems involving units of strong material, like the brick masonry of the vault.

All the contacts that do not consider the shell of the vault (bricks to steel elements, steel elements to steel elements, shaking table to bricks, shaking table to steel elements) are described according to the elastic joint model, represented by the blue cross symbol in Figure 7-6.

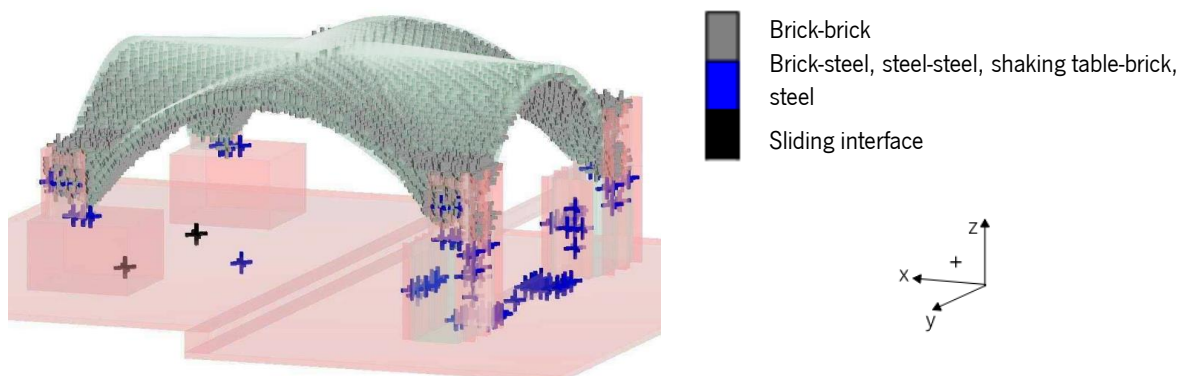


Figure 7-6. List of joints contact of the DEM model in 3DEC 7.0 environment.

The elastic joint model (Figure 4-3a) is used to simulate construction joints that are required to build model geometries. They do not correspond to real slipping joints or faults. Their behaviour is governed by normal and shear joint stiffness, and no yielding can occur, creating elastic joints (Itasca Consulting Group, 2019b).

On the other hand, the joints along the shell of the vault (grey brick-brick contacts in Figure 7-6) are modelled considering the classic Mohr–Coulomb criterion, with zero-thickness and the assumptions adopted for the reduced vault (for the first analysis). Mohr–Coulomb is characterised by frictional behaviour. It is the most common non-linear contact model standard choice used in the literature for simulating blocks' interaction. Within Mohr–Coulomb criterion, cohesion and friction angle simulate the shear behaviour, whereas the uniaxial behaviour is controlled by the tensile strength. Upon exceeding the tensile strength, the normal stress is set to zero, and the shear strength is lost, showing a relatively brittle material behaviour (Pulatsu *et al.*, 2023). Since the Mohr–Coulomb criterion for the brick-to-brick contacts is assumed, the joint stiffness is simulated as a combination of unit and mortar stiffness, according to Equation 7-1 and Equation 7-2.

$K_n = \left(\frac{h_b}{E_b} + \frac{h_m}{E_m} \right)^{-1} = 67.2 \text{ MPa/mm}$	Reference (Senthivel and Lourenço, 2009)	Equation 7-1
$K_s = 0.4 K_n = 26.9 \text{ MPa/mm}$	(Pulatsu, Erdogmus, Lourenço, Lemos and Tuncay, 2020) (Senthivel and Lourenço, 2009)	Equation 7-2

E_m is Young's modulus of the mortar (2800 MPa), E_b of the blocks is equal to 6200 MPa, h_b is the height of the masonry bricks (120 mm), and h_m is the mortar joints' thickness (10 mm). For this study, these values of stiffnesses, K_n and K_s are the initial values for the calibration of the DEM model (see Section 7.3).

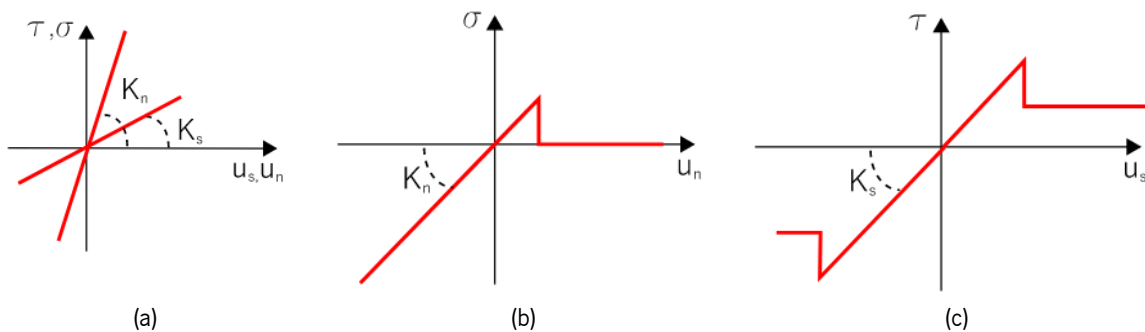


Figure 7-7. Contacts behaviour in the DEM model: (a) elastic joint model between brick-steel, shaking table-brick, shaking table-steel and steel-steel, (b) Mohr–Coulomb criterion between brick-brick in the normal direction, (c) Mohr–Coulomb criterion between brick-brick in the tangential direction.

Additionally to the classic Mohr–Coulomb (MC), with the same assumptions adopted for the reduced-vault, a combined material behaviour of Mohr–Coulomb criterion with shear, crushing and cracking,

implemented in 3DEC by Pulatsu *et al.* (2020) - here named as MC-CM - is also used with DEM-UNS model. Both contact constitutive laws share the same tension-shear coupling formulation, while they differ in the compression-shear regime as represented in Figure 7-8. MC-CM varies the shear strength once the compression stress exceeds a specific limit. The yield function for cap mode implemented for MC-CM is ruled by the non-dimensional constant C_s , which controls the shape of the function. A value of C_s close to zero makes the cap mode tending the compression cut-off curve (MC); C_s equal to 9 has been recommended by Lourenço and Gaetani (2022).

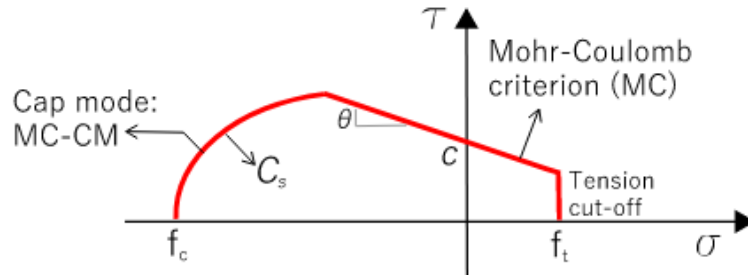


Figure 7-8. Failure surface implemented for Mohr-Coulomb (MC) and combined material behaviour of Mohr-Coulomb (MC-CM). Adapted by Pulatsu (2023).

As adopted in FEM model and since the objective is to perform non-linear time history analysis, the non-linear parameters are also defined for DEM with MC-CM model. In particular, the tensile strength ($f_t=0.1$ MPa) fracture energy in tension ($G_f^I=0.02$ KN/m), shear ($G_f^{II}=0.15$ KN/m) and compression ($G_c=0.8$ KN/M) regimes are assumed according to Lourenço and Gaetani (2022).

7.3 Model updating

The model updating process is part of the validation of the numerical models and it contributes to the calibrated numerical model behaves according to the experimental specimen, at least in the linear range. The calibration of the numerical models (DEM-UNS and FEM-UNS, FEM-SM) is performed by comparing the frequencies and mode shapes of the numerical models with the experimental modal parameters obtained from the dynamic identification tests. The elastic stiffness properties of the joints (DEM model) and of the homogenised values of the masonry and interfaces (FEM model) are the parameters set for modal updating in this Section. However, the two approaches follow two different methods. The calibration of the FEM-UNS model is carried out through an eigenvalue analysis, while, for the DEM-UNS model, a time domain analysis is performed. It is important to mention that, for simplicity, justified by the predominant in-plane shear behaviour, the numerical models are uniquely calibrated based on the first mode.

7.3.1 Finite element model: FEM–UNS and FEM–SM

The model updating is based on the results of the dynamic identification tests, minimising the differences between the experimental modal properties and the numerical ones. This calibration consists of tuning and optimising the Young's modulus of the masonry of the shell and the infill, to obtain a good matching of experimental data and simulation of the model, starting from the preliminary material properties, obtained from the material characterisation tests (see Chapter 5 and Table 5-7). The calibration only involves the linear elastic properties of the masonry shell, while the linear elastic parameters of the masonry fixed piers and steel elements are constant.

Using the original Young's modulus of the masonry (2.22 GPa), the first global frequency of FEM–UNS has a value of 7.99 Hz, which is 30% higher than the experimental one. Because of that, it is necessary to decrease the Young's modulus, remaining close to realistic values expected from literature and National Codes for masonry with solid bricks (Fernandes, Lourenço and Castro, 2010; *Ministero delle Infrastrutture e Trasporti*, 2019). In particular, it has been reduced to about half of the original value estimated through the material characterisation tests (0.96 GPa) to match the first frequency. This highlights that the stiffness of the vault is significantly lower than what is expected and measured quasi-statically during the axial compression tests.

As anticipated, the assessment of the correspondence between the experimental and the numerical modes can be achieved by calculating the MAC (Modal Assurance Criterion) value of each modal configuration, which makes it possible to directly obtain a quantitative notion of the correlation between the various mode shapes. The modal configurations are usually rather complex, and, hence, the use of the matrix of coefficients MAC is recommended for performing a quantitative evaluation of the level of correlation between the vibration mode, numerically calculated, and the vibration mode that is experimentally identified. Matrix MAC is calculated by expression described in Equation 6-1 where, in this case, φ_i^u and φ_i^d are the mode shape vectors for the two different modal conditions DIT*i* and *n* is the number of degrees of freedom, hence, the positions of the accelerometers and the corresponding nodes in the numerical model.

With the calibrated value of Young's modulus (0.96 GPa), the MAC value is equal to 0.92 for the FEM–UNS model, by performing eigenvalue analysis, representing a good matching with the in-plane shear mechanism of the UNS specimen (Figure 7-9a, b).

The same calibration approach has been adopted for the FEM–SM model. The material properties of the Grid Geosteel 200, Mortar Geocalce F and Mortar Geocalce FL are kept constant and equal to the values obtained from the material characterisation tests (Table 7-2). However, since the strengthening

application can slightly increase the stiffness of the model, the Young's modulus of the masonry of the shell and infill has been also slightly corrected with a lower value, namely 0.93 GPa, to respect the coherence in terms of frequency and mode shapes (Figure 7-9c, d). This assumption is realistic, given the fact that the masonry shell suffered severe damage because of the previous shocks, and micro-cracks can remain after repair the specimen. The MAC value of the first frequency between the DIT-SM-0-Y and the FEM-SM model is again 0.92.

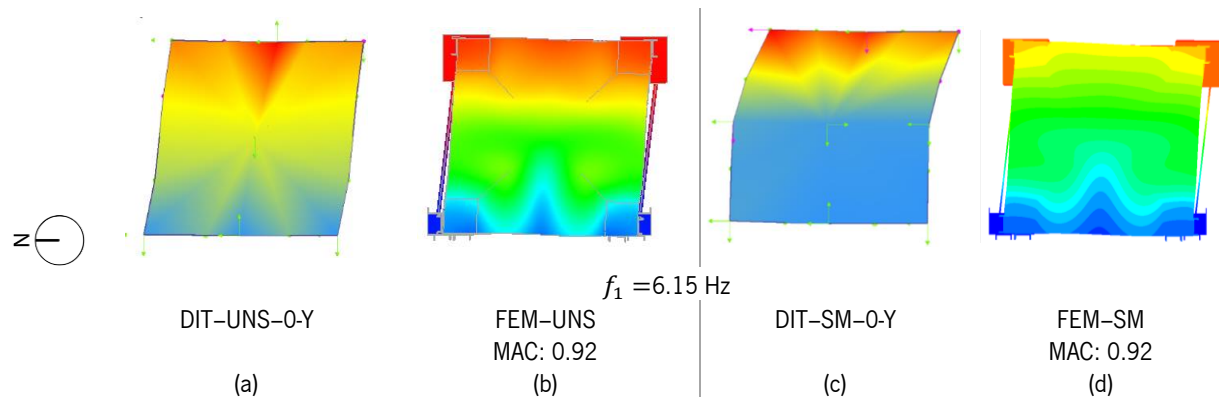


Figure 7-9. Mode shapes of the first modes of the specimens (UNS and SM) and numerical models: (a) DIT-0-UNS-Y test; (b) first mode obtained from eigenvalue analysis for FEM-UNS model; (c) DIT-0-SM-Y test; (d) first mode obtained from eigenvalue analysis for FEM-SM model.

The final non-linear material properties of the masonry, Geocalce F and Geocalce FL in tension are listed and recalled in Table 7-3.

Table 7-3. Final properties after the calibration for FEM-UNS and FEM-SM models. *Calibrated properties.

	Linear properties				
	Masonry (shell and infill)	Masonry (fixed piers)	Geocalce F	Geocalce FL	Steel elements
Young's modulus [GPa]	0.96 (FEM-UNS)* 0.93 (FEM-SM)*	2.22	12.54	7.81	210.00
Mass density [kg/m ³]	2260.0	2260.0	1800	1600	7800
Poisson's ratio	0.2	0.2	0.14	0.2	0.3
Non-linear properties: TSCR material behaviour					
	Masonry (shell and infill)	Masonry (fixed piers)	Geocalce F	Geocalce FL	X
	Exponential				
Tensile strength [MPa]	0.1	0.30	1.3	0.8	

FEM-UNS and FEM-SM models have also been evaluated under self-weight. Both models present a maximum vertical displacement approximately equal to 1 mm, located at the key of the vault. After the application of the self-weight in the numerical models, no cracks appear along the shell of the vault, highlighting the fact that the initial cracks, which have been immediately repaired after the transportation of the specimen on the shaking table (see Figure 5-10), are associated with the vertical

loading of the self-weight. Thus, those cracks were effectively linked with the bending effects due to transportation.

7.3.2 Discrete element model: DEM–UNS

3DEC software has difficulties in calculating the stiffness matrix. Thus, eigenvalue analysis cannot be easily performed, and a specific calibration process is needed (Gomes and Lemos, 2020). The calibration of DEM–UNS model is composed of two main stages. In the first stage, a time history of velocities of about 150 s (Figure 7-10) is applied along the NS direction at the centroid of the shaking table block, which corresponds to the integration of the time history of the accelerations used during the dynamic identification tests. Secondly, when the analysis has finished, the acceleration time histories, numerically recorded under this noise-vibration state, are exported at the same locations of the accelerometers of the specimen.

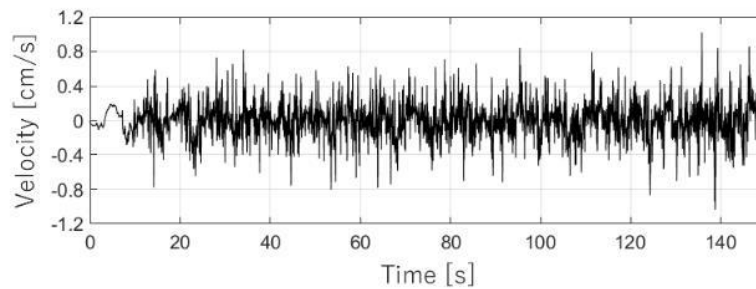


Figure 7-10. Velocity time history adopted in the dynamic identification for the calibration of DEM–UNS model.

In this way, the response at the measurement locations is compared with the experimental results in terms of frequency peaks and mode shapes. The time series of the response is processed using the Frequency Response Functions (FRF) to determine the natural frequencies, as seen in Figure 7-11.

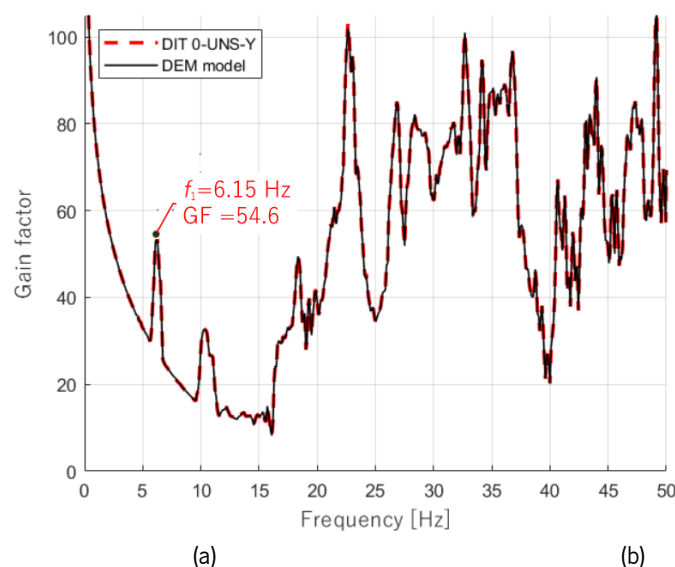


Figure 7-11. Comparison of Frequency Response Functions obtained from the numerical modelling and the dynamic identification tests. (DIT–0–UNS–Y, red dashed line) and the numerical model (DEM–UNS, black solid line).

The match of the first frequency and mode shape has been obtained by adopting an iterative process, where K_n and K_s of the joints and the K_{s-base} below the steel masses have been changed, to fulfil a good agreement with the tests. In particular, K_n and K_s have been reduced by about 75% of their initial values, until the values of 16.3 MPa/mm and 6.5 MPa/mm respectively. The value of K_n is realistically connected with the calibrated Yong's modulus of masonry of the FEM-UNS model (0.96 GPa) by the relation $E=K_n \cdot w_b$, given the width of the units w_b in 3DEC block equal to 60 mm.

For the K_{s-base} a very low value (almost equal to zero) was obtained, while the normal stiffness K_{n-base} has been defined to avoid separation and interpenetration between the steel masses and the shaking table block. In this case, its value is set at 20 MPa/mm, when the first frequency is stabilised. Table 7-4 summarised the final material properties of the joints after the calibration of the DEM-UNS model.

Table 7-4. Final properties of joints after the calibration for classic Mohr-Coulomb criterion in DEM-UNS model. *Calibrated properties.

Joints	Normal stiffness K_n [MPa/mm]	Shear stiffness K_s [MPa/mm]	Friction angle θ [°]	Dilatancy angle ψ [rad]
Steel masses – shaking table (base)	20.0*	≈ 0 *	2	null
Bricks – bricks	16.3*	6.5*	38	

It can be observed that, with these values, the first frequency of the in-plane shear mode obtained by the numerical dynamic identification is well-matched with the experimental results (FRF). For modes 2 to 3, a quite good agreement of numerical and experimental frequencies is also found, but it is discarded by the numerical calibration of the DEM model in terms of mode shapes, presenting lower MAC values (Figure 7-12a).

Figure 7-12a presents the matrix of the coefficients for the first mode. The orange-coloured values correspond to high MAC values, which indicate a good correspondence between experimental and numerical results, close to the unit for the first mode (MAC=0.99). The graphical representation of the first mode shapes is presented in Figure 7-12b.

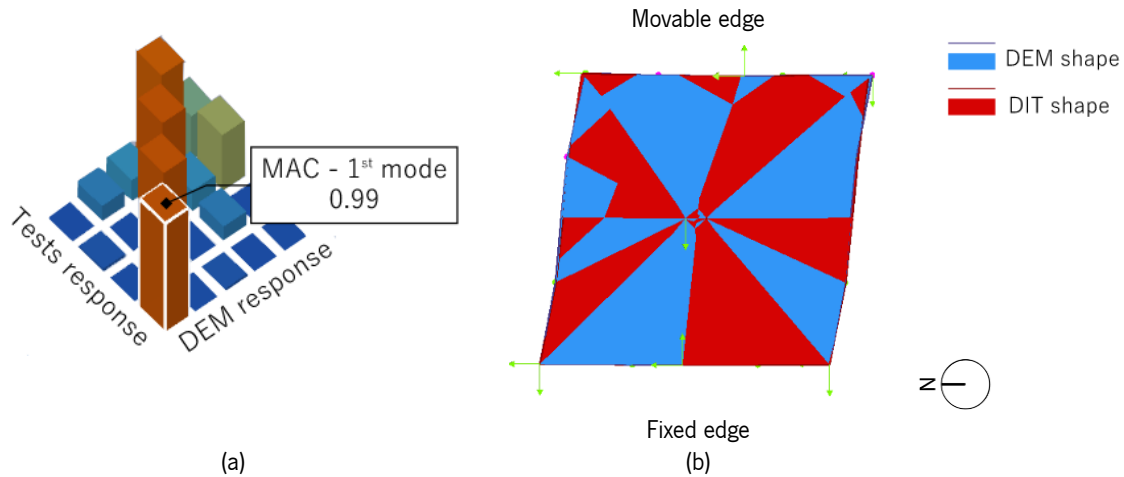


Figure 7-12. DEM calibration: (a) MAC matrix, (b) first mode shape between DIT and DEM–UNS model performing vibration analysis.

7.4 Non-linear dynamic analysis

In agreement with the objective of this thesis (see Section 1.5), dynamic analyses with time integration are performed with DEM–UNS and FEM–UNS and FEM–SM models, combining the non-linear behaviour of the materials and the seismic actions. The goal is to validate the models by comparing the numerical results with the experimental response of the full-scale vault, including the damage and the collapse mechanism (point A in Section 1.5). Another point is the discussion of the results obtained by the two strategies (FEM and DEM), considering the quality of the results, the time of analyses and the computational efforts (point E in Section 1.5), overcoming the limitations due to the reduced-scale (see Chapter 4).

According to the experimental testing protocol, the following analyses have been performed as listed in Table 7-5. Incremental non-linear dynamic analyses are carried out, when possible, considering the seismic input applied in series (all the inputs applied as a continuous ground motion in the same analysis). In this way, the accumulation of damage is considered and the real incremental input loading, implemented on the shaking table tests, has been simulated (Table 6-1 in Section 6.2). This procedure would be computationally demanding for FEM models. Thus, this approach has been only considered in DEM–UNS, while for FEM–UNS model, each test has been applied at the undamaged state. Only the last seismic shock of the strengthened configuration (ST–SM–150%) has been simulated through FEM–SM model.

Table 7-5. List of analyses carried out on the unstrengthened and strengthened numerical models.

Unstrengthened						
Denomination	PGA [m/s ²]	PGV [cm/s]	PGD [mm]	Shaking table tests	DEM-UNS	FEM-UNS
ST-UNS-25%	1.37	6.22	3.76			✓
ST-UNS-50%	2.58	12.17	8.57	✓	✓ (In series)	✓
ST-UNS-75%	3.62	18.17	17.57			✓
ST-UNS-100%	4.47	24.20	24.47	✗	✓	✗
Strengthened						
Denomination	PGA [m/s ²]	PGV [cm/s]	PGD [mm]	Shaking table tests	DEM	FEM-SM
ST-SM-150%	7.27	35.65	54.60	✓	✗	✓

7.4.1 Analysis characteristics

The accelerograms recorded by the shaking table's actuators during the tests are filtered before being used as input for the numerical analyses. A double filtering process is undertaken through LNEC-SPA (2007) software implementing two sample offset removals. The first offset is based on the time history of the displacements measured by the shaking table control system between 0 and 10 s, while the second offset is based on the time history of the accelerations recorded from 10 s to 25. Both offset removals have a low-pass Fourier filter with a frequency range between 0.05 and 40 Hz, which can correct the baseline derive of the inputs (Faccioli and Paolucci, 2005). The filtered accelerogram is directly applied at the base of the FEM models (acting at the level of the boundary conditions). For DEM-UNS model, the corresponding velocities are applied at the centroid of the "shaking table" block, obtained by integrating the filtered signals over time.

For what concerns FEM-UNS and FEM-SM models, the secant (Quasi-Newton) iterative method, with a convergence criterion based on the internal energy and tolerance equal to 10^{-3} , and the line search algorithm are considered. Hilber-Hughes-Taylor (HHT) time integration method, with $\alpha = -0.1$, is adopted, which introduces numerical dissipation without degrading the accuracy (Faria, 1994), while the Parallel direct sparse solver is taken adopted to solve the system of equations.

The integration time step Δt_{FEM} is defined to be smaller than the first natural period of the specimen (T_1) with interest for the behaviour of the structure over 20. The obtained ratio (0.01 s) allows to take into account the contribution of the period T_1 with an error less than 5%. Moreover, the time step should be much smaller than the total duration of the earthquake (25 s) (Mendes, 2012). For simplicity, Δt_{FEM} is set at the value of 0.005 s, which is equal to time step of the signals of the experimental tests. With these characteristics, one analysis with a total duration of 25 s takes around 14 days to run. The two damping constants, valid for FEM-UNS and FEM-SM, are α (2.165) and β (1e-05), defined based on the eigenvalue analysis results, for which the first 28 modes with a

cumulative mass participation of about 86% in each horizontal direction (x and y) are considered. The assumed damping ratio ξ is equal to 3% (Figure 7-13), as suggested by other studies on masonry structures (Mendes and Lourenço, 2014; Parisse *et al.*, 2021). The central finite-difference procedure is used as time integration method in DEM–UNS. The time step of the DEM analysis Δt_{DEM} must be lower than a critical value to ensure numerical stability. In this case, Δt_{DEM} is equal to $4 \cdot 10^{-6}$, which allows to obtain an acceptable analysis duration. This Δt_{DEM} is associated with the criterion adopted for the damping, for which, only the mass proportional formulation was adopted (Figure 7-13). In conclusion, being Δt_{DEM} sufficiently big, Rayleigh damping's contribution (mass proportional only) can be contemplated, conversely to the reduced-scale model. From DEM–UNS, the minimum value of damping in the graph, are reached for a frequency equal to 23.00 Hz and a damping ratio equal to 1.49%. One analysis with a total duration of 25 s takes around 1 day to run.

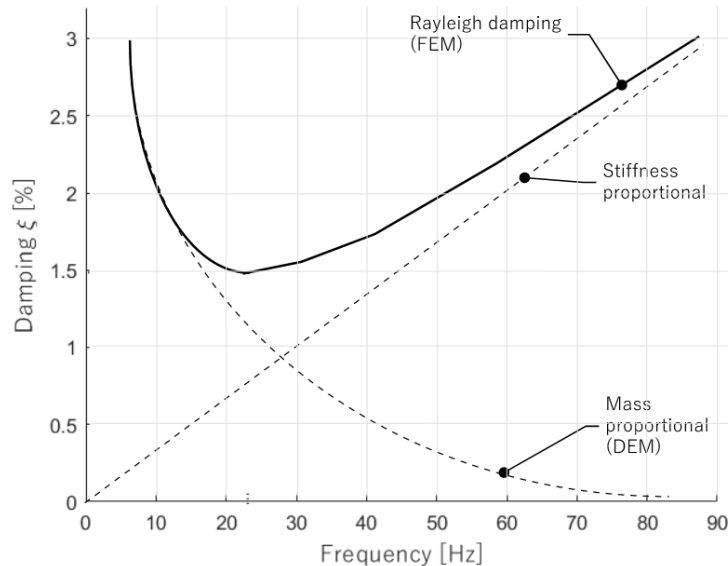


Figure 7-13. Viscous damping graph of the numerical models.

7.4.2 Non-linear dynamic analysis of the unstrengthened models: DEM–UNS and FEM–UNS

The responses of DEM–UNS and FEM–UNS are compared with the results obtained in the shaking table tests, using the same parameters as in the analysis of the experimental behaviour of the specimen, namely the deformed shapes and principal strains used as cracks indicators, displacements profiles and maximum absolute displacements along the movable edge and at the key of the vault, horizontal seismic coefficients, accelerations response, and drifts.

Figure 6-8 presents the comparison between the damage maps between the shaking table tests during ST–UNS–75% and numerical simulation results for the same seismic sequence. In DEM–UNS, the crack pattern is represented by the deformed shapes, which are plotted with a deformation factor of 100 to better visualise the opening of the joints. In FEM–UNS, the damage is represented by the

distribution of principal tensile strains along the numerical model - an indicator of the cracking. DIANA considers a 'scan' output command to plot the cumulative strain distribution. This command searches and keeps the maximum at each time step over all the analysis. At the beginning of the analysis, the same crack along the NW/SE diagonal appears in both numerical models at $t \approx 3.00$ s, and, similarly at $t \approx 3.16$ s, the opposite diagonal crack is observed. When the direction of the input changes, the deformed shape of DEM-UNS model also changes and the numerical model can close diagonal cracks, previously opened. For this time instant, $t \approx 3.16$ s, the crack that surrounds the NW corner above the boundaries of the infill is visible in DEM-UNS, while in FEM-UNS is still not present. Since $t \approx 3.60$ s, both diagonal cracks remain open until the end of the analysis, as it is in the experimental tests. It is only at $t \approx 6.41$ s that the hinges are recognisable in the numerical simulations. The first hinge appears on the Western and Southern webs in DEM-UNS, while for FEM-UNS are diametrically opposite to the diagonals. Their severity and length are underestimated in comparison with the experimental tests and their locations are shifted of some rows. Both models present the cracks at the boundaries of the infill of the Western edge at $t \approx 6.41$ s. At the end of the analysis ($t \approx 25$ s), both DEM-UNS and FEM-UNS show a very similar distribution of cracks, coherent with the experimental evidence, mainly while comparing the NW corner and the fixed edge. The main difference is represented by the hinge located along the Eastern web, represented by a transverse crack, which is visible in DEM-UNS, while in FEM-UNS, it is only partially developed. It is interesting the fact that, due to the characteristic of the DEM-UNS, the same shifting of the webs, that has been observed at the end of ST-UNS-75% (see Figure 6-7d), is detected.

For what concerns the previous seismic numerical analysis (ST-UNS-25%, ST-UNS-50%), no relevant damage has been observed in the numerical models, in which the behaviour remains mainly linear. The damage has been plotted uniquely from the extrados, being the most representative view for the description of the damage distribution of the unstrengthened configuration.

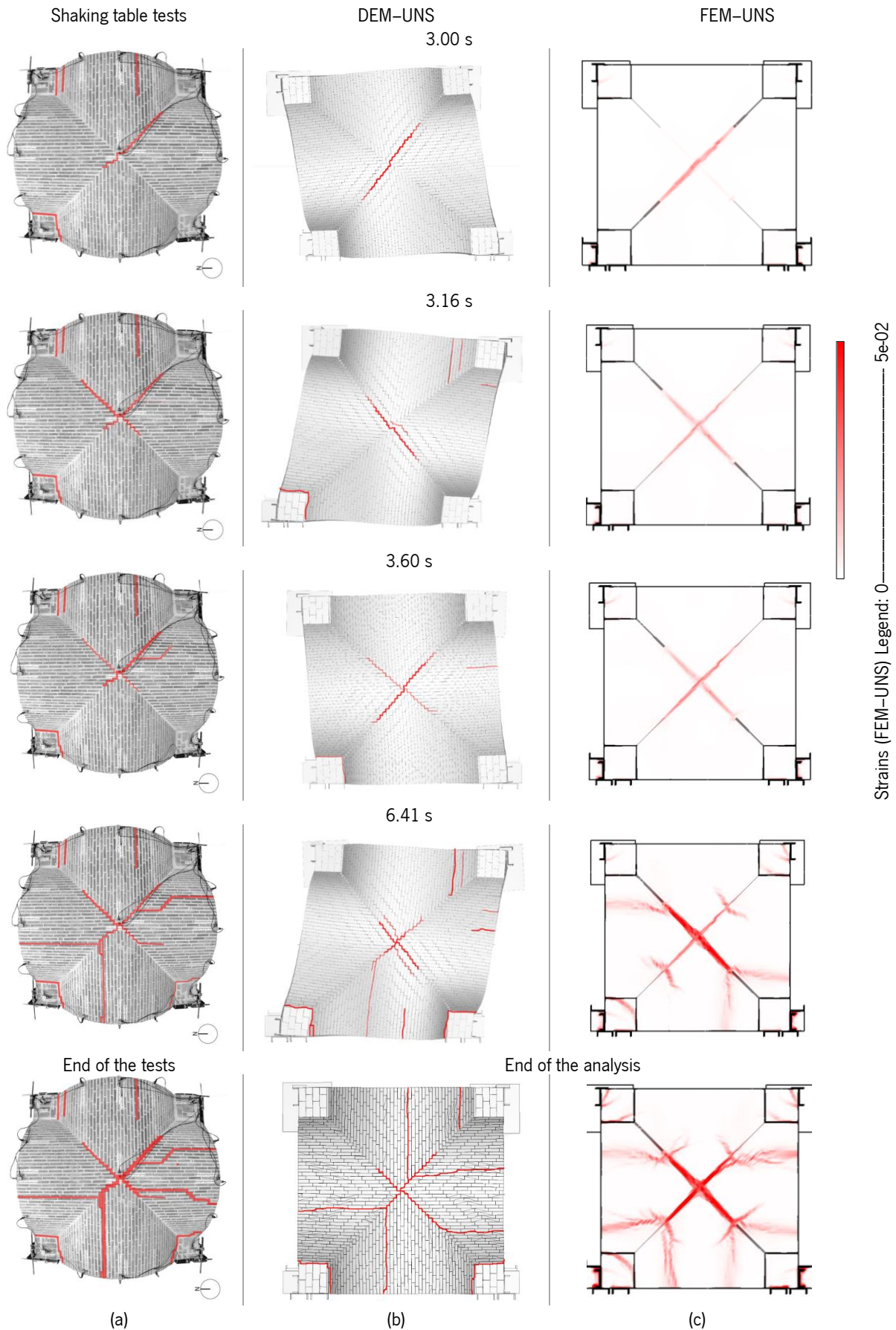


Figure 7-14. Evolution of cracks at the extrados: (a) ST-UNS-75, (b) deformed shapes of DEM-UNS model (deformation factor: 100), (c) strains distribution in FEM-UNS model.

Figure 7-15 presents the comparison between the displacements of the experimental specimen and the numerical models for two instants, for 75% of the earthquake. The displacement fields in the numerical models are coherently showing in-plane shear deformation in both cases and, in general, quite symmetric between the positive and negative directions. On average their absolute values are lower than the experimental. The response in the positive direction (from South to North) is very similar, comparing the two numerical models, while in the negative direction, at $t \approx 4.31$ s, FEM-UNS presents more deformability than DEM-UNS.

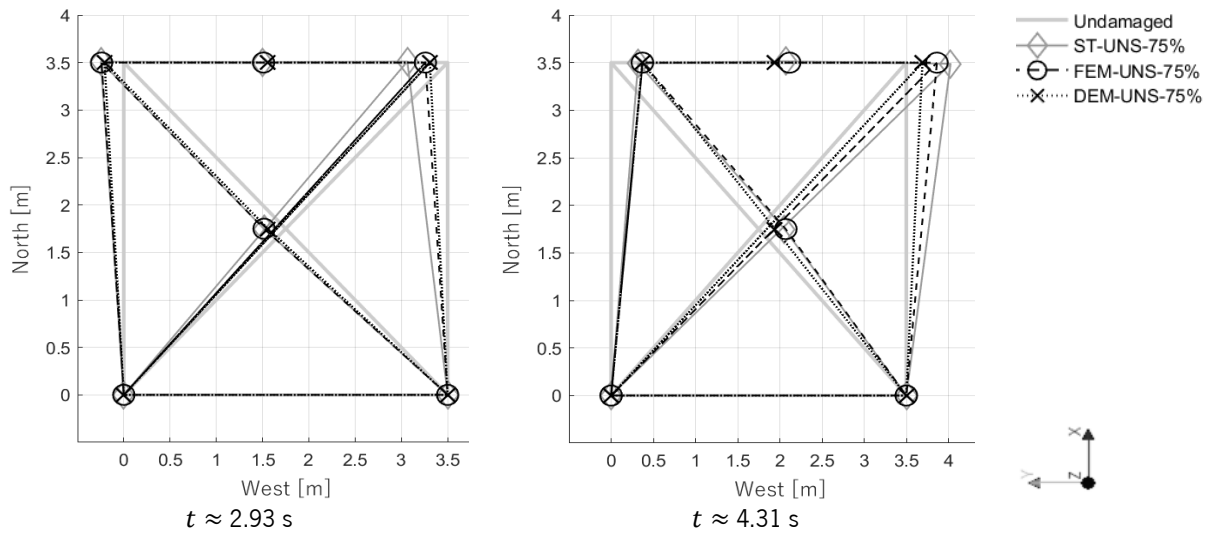
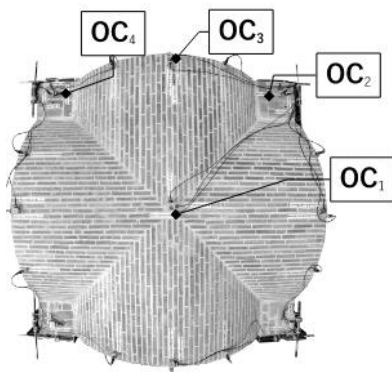


Figure 7-15. Comparison of the displacement profiles between experiments and numerical responses.

The average errors of the maximum displacement peaks $\bar{\epsilon}$ between numerical and experimental displacements are very different for DEM-UNS ($\sim 42\%$) and the FEM-UNS ($\sim 15\%$), considering the experimental results in the longitudinal direction as reference (see Table 7-6). When looking at the average value of the root mean square of displacement (RMSD) in the longitudinal direction (NS), it is possible to notice that the average error $\bar{\epsilon}$ of DEM-UNS and FEM-UNS models are equal to $\sim 24\%$ and $\sim 17\%$, respectively. This highlights the fact, that despite the numerical computational effort, FEM-UNS better depicts the deformability of the specimen. As anticipated in Section 7.2.2, the combined material behaviour of Mohr-Coulomb criterion (MC-CM) is also considered to simulate cut-off tensile strength and compressive strength with DEM-UNS model. The distribution of damage and cracks occurrence for MC-CM is similar to the one shown in Figure 6-8 for MC, while in terms of peaks of displacements and RMSD, MC-CM brings improvements to the results (Table 7-6). Still, while comparing the transverse response at the last seismic test, it is highlighted that the displacements are on average underestimated.

Table 7-6. Peak values and root mean square of displacements (RMSD) and average errors between the results measured by $OC_{1,2,3,4}$ for each seismic test of the unstrengthened specimen and obtained by DEM-UNS and FEM-UNS models.

Sequence	OC_1 [mm]		OC_2 [mm]		OC_3 [mm]		OC_4 [mm]	
	NS	Vertical	WE	NS	WE	NS	WE	NS
ST-UNS-25%	9.46	-0.66	0.56	9.92	0.72	9.83	1.55	9.8
FEM-UNS-25%	8.89	-0.94	0.17	9.19	0.04	9.20	0.14	9.21
DEM-UNS-25% with MC	7.20	-1.10	2.38	6.72	0.41	6.74	1.00	6.72
DEM-UNS-25% with MC-CM	8.38	-0.59	0.09	8.39	0.37	8.39	0.13	8.45
ST-UNS-50%	21.73	-6.38	1.05	40.54	2.29	24.8	4.70	24.08
FEM-UNS-50%	18.30	-1.25	0.28	18.76	0.16	18.79	0.35	18.84
DEM-UNS-50% with MC	14.60	-2.69	5.76	13.23	1.02	13.28	2.95	13.21
DEM-UNS-50% with MC-CM	16.39	-4.39	0.34	14.68	1.32	16.40	0.38	17.6
ST-UNS-75%	30.72	-10.64	4.40	52.51	5.08	32.80	7.77	32.05
FEM-UNS-75%	32.09	-8.51	1.13	36.3	1.08	36.56	0.98	37.09
DEM-UNS-75% with MC	22.23	-4.19	9.10	19.78	1.64	19.88	5.04	19.69
DEM-UNS-75% with MC-CM	23.70	-3.45	0.74	22.61	2.51	23.50	0.63	26.60

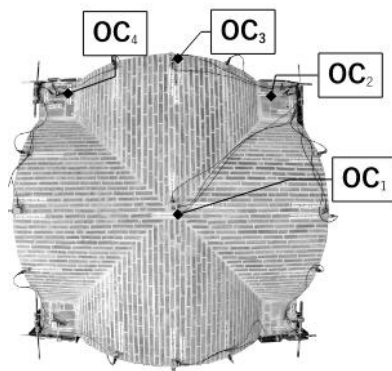


Average error $\bar{\epsilon}$ [%]
(All the analyses: 25%, 50%, 75%), all OC_i , NS direction)

	FEM-UNS	DEM-UNS with MC	DEM-UNS with MC-CM
Peak values	14.45	41.95	30.06
RMSD	16.57	24.12	18.92

Average error $\bar{\epsilon}$ [%]
(All the analyses: 25%, 50%, 75%), OC_2 discarded, NS direction)

	FEM-UNS	DEM-UNS with MC	DEM-UNS with MC-CM
Peak values	12.53	35.37	21.57
RMSD	7.60	15.55	10.00



Average error $\bar{\epsilon}$ [%]
(only 75%, all OC_i , NS direction)

	FEM-UNS	DEM-UNS with MC	DEM-UNS with MC-CM
Peak values	4.10	46.10	34.80
RMSD	29.06	42.45	35.04

Average error $\bar{\epsilon}$ [%]
(only 75%, OC_2 discarded, NS direction)

	FEM-UNS	DEM-UNS with MC	DEM-UNS with MC-CM
Peak values	10.64	36.60	22.78
RMSD	16.70	31.95	22.7

Those considerations are more visible by looking at Figure 7-16, where the RMSDs are plotted in function of the seismic input. Until ST-UNS-50% experimental and numerical values follow the same trend for optical cameras OC_1 , OC_3 , OC_4 . The highest difference (0.2 mm) is very low and occurs in DEM with MC. However, the numerical models follow the experimental results with less accuracy for the last seismic input a more remarkable scatter appears for ST-UNS-75% when higher damage occurs. The numerical response of OC_2 (Figure 7-16b) differs more from the tests because of the unexpected amplification and damage localised on the S-E diagonal. Thus, OC_2 is no longer considered for further discussions in this thesis.

In general, and comparing the two DEM models, DEM with MC-CM achieves better results in terms of displacements, while DEM with MC underestimates the displacement capacity.

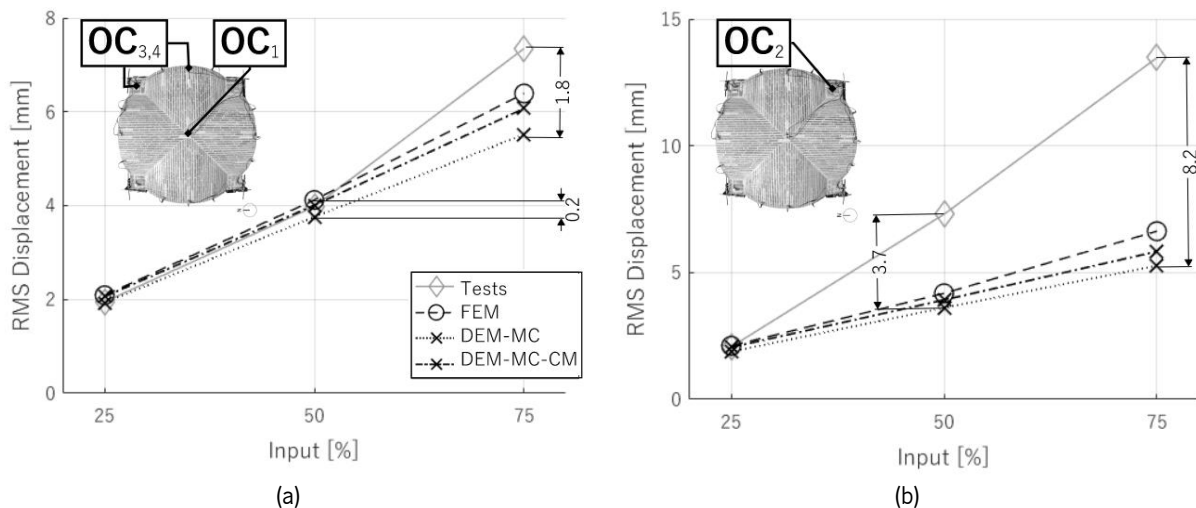


Figure 7-16. RMSDs in the longitudinal direction: (a) OC_1 , OC_3 , OC_4 , (b) OC_2 .

For the sake of completeness, also the acceleration response has to be checked before concluding that the FEM model and DEM with MC-CM are better representing the response of the vault in comparison with the classic Mohr-Coulomb (DEM with MC). In particular, the response of the vault is evaluated through the numerical envelope curves for ST-UNS-75% (Figure 7-17) plotting the value of the horizontal coefficient versus the displacement at a control point (measured by the optical camera OC_1). Two methods have been used to plot the hysteretic behaviour of the structure. The first evaluates the ratio between the corresponding base shear force (BSF) and the self-weight of the model. The second method considers only the inertial forces of lumped masses of the structure, discarding restoring and damping forces, similar to the experimental hysteretic curve. For what concerns DEM models (with MC and with MC-CM), the inertial forces have been obtained by integrating over time the time histories of the velocities of the blocks, where the longitudinal accelerometers are located according to Figure 6-13's distribution, while for FEM the accelerations have been directly processed.

As expected, the curves obtained from the BSF time history present maximum horizontal coefficients higher than the experimental one (inertial force only). The (absolute) maximum horizontal inertial coefficient is equal to 0.32 for FEM_{BSF} , 0.31 for DEM with MC_{BSF} , and again 0.28 for DEM with $MC-CM_{BSF}$, while the experimental maximum horizontal inertial coefficient is equal to 0.28. On the other hand, the inertial curves, which are represented by the solid lines and * symbol in Figure 7-17, underestimate the response in the case of DEM models. The (absolute) maximum horizontal inertial coefficient is equal to 0.15 for DEM with MC^* and DEM with $MC-CM^*$ (obtained indirectly from the integration of the velocities). The maximum horizontal inertial coefficient for FEM^* is equal to 0.32, which is equal to one obtained from FEM_{BSF} .

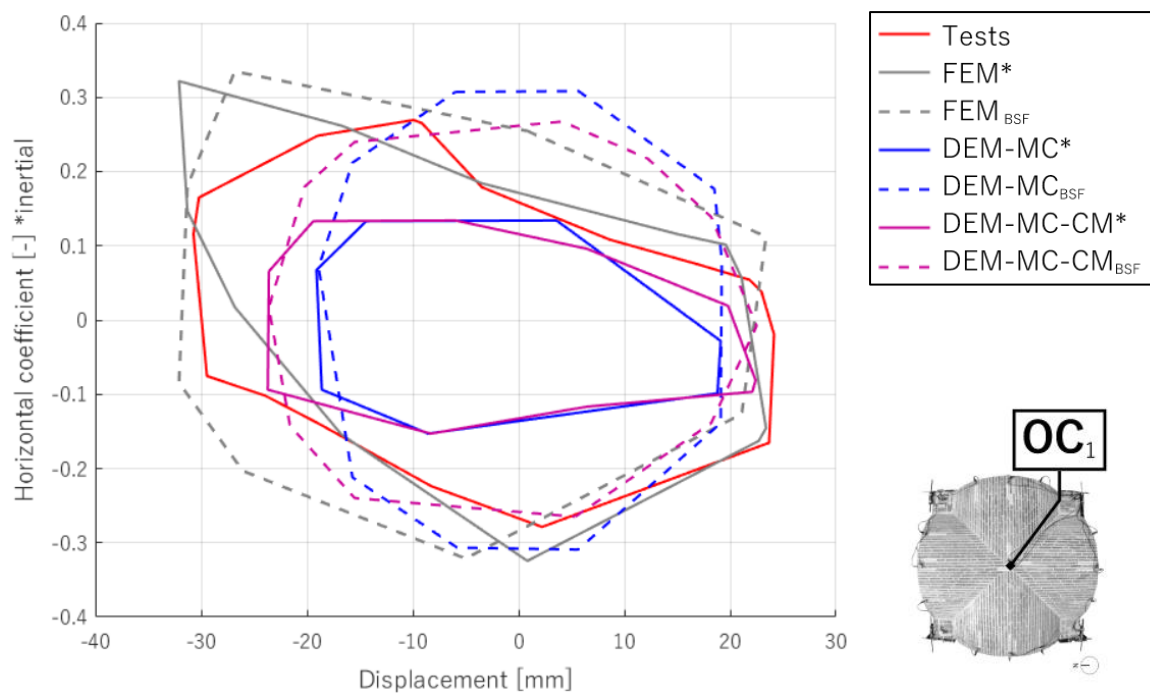


Figure 7-17. Experimental and numerical envelope response curves (FEM, DEM-MC and DEM-MC-CM) of the unstrengthened specimen considering OC_1 for ST-UNS-75%.

The curves presented in Figure 7-16 and Figure 7-17 arise some important conclusions:

- all the optical cameras' response is well described by the numerical models, apart for OC_2 which is considered an outlier.
- FEM model and DEM (with MC and with MC-CM) models present similar horizontal inertial coefficients, but, on average, FEM has also similar stiffness to the experimental one.
- for ST-UNS-75%, when higher non-linearities occurs and start being predominant, FEM depicts the response of the vault in a satisfying way, even if the analysis discards the accumulation of damage.

Between the two material behaviours implemented in DEM model, DEM with MC–CM is closer to the experimental displacements.

- FEM and DEM with MC–CM models provide a more accurate prediction of the force–displacement response. However, FEM model requires high computational effort.
- the maximum drift of the vault (evaluated as the ratio between the maximum absolute displacement and the span of the vault) for the last seismic test is evaluated by comparing the response of OC₃. The maximum drift of DEM with MC is 1%, 1.2% for DEM with MC–CM, while for FEM it is equal to 1.5%. The maximum experimental drift is set at the value of 1.4% for the same optical camera.

It is noted that the influence of no damping and lower friction angle (30°) has been also evaluated in the response of the DEM–UNS model. However, no significant betterment of the results was achieved. Thus, those results were discarded.

It is important to mention that the input of 75% is not causing the full collapse, but it induces a severe damage state that allowed the repair and the application of the strengthening. For research purposes, it is interesting to investigate the numerical simulation of the unstrengthened specimen at the level of the collapse. Hence, another non-linear dynamic analysis with increasing input is carried out only using DEM with MC–CM model. The non-linear dynamic analyses with FEM–UNS would require rather large computational efforts. Thus, the further incremental FEM dynamic analysis is discarded in this study. From the DEM simulation, it is found that the collapse is reached for 100% of the input, which corresponds to the original level of input of the 2009 L'Aquila earthquake.

At the beginning of this new analysis, the numerical model presents similar damage to the one observed during the shaking table tests. However, the collapse for this input is the result of two contributions: (1) the in-plane shear mechanism that causes severe cracking along the NE-SW diagonal, (2) the detachment of the shell from the fixed edge in the NW corner (Figure 7-18a). The detachment also influences the roto-translational response in the EW direction since the transverse stiffness of the Northern arch drastically decreases causing the rotation of the steel mass at the NW corner. This type of collapse is expected to be very peculiar for this isolated specimen, for which the vaults of other bays, the stabilising weights from the upper levels, the lateral external wall, the role of the main nave and the counteracting elements are partially omitted. It is realistic to assume that the detachment of the shell from the fixed edge is rare to occur in existing scenarios. However, in some post-earthquake surveys, this kind of damage has been recognised (Figure 7-18b,c).

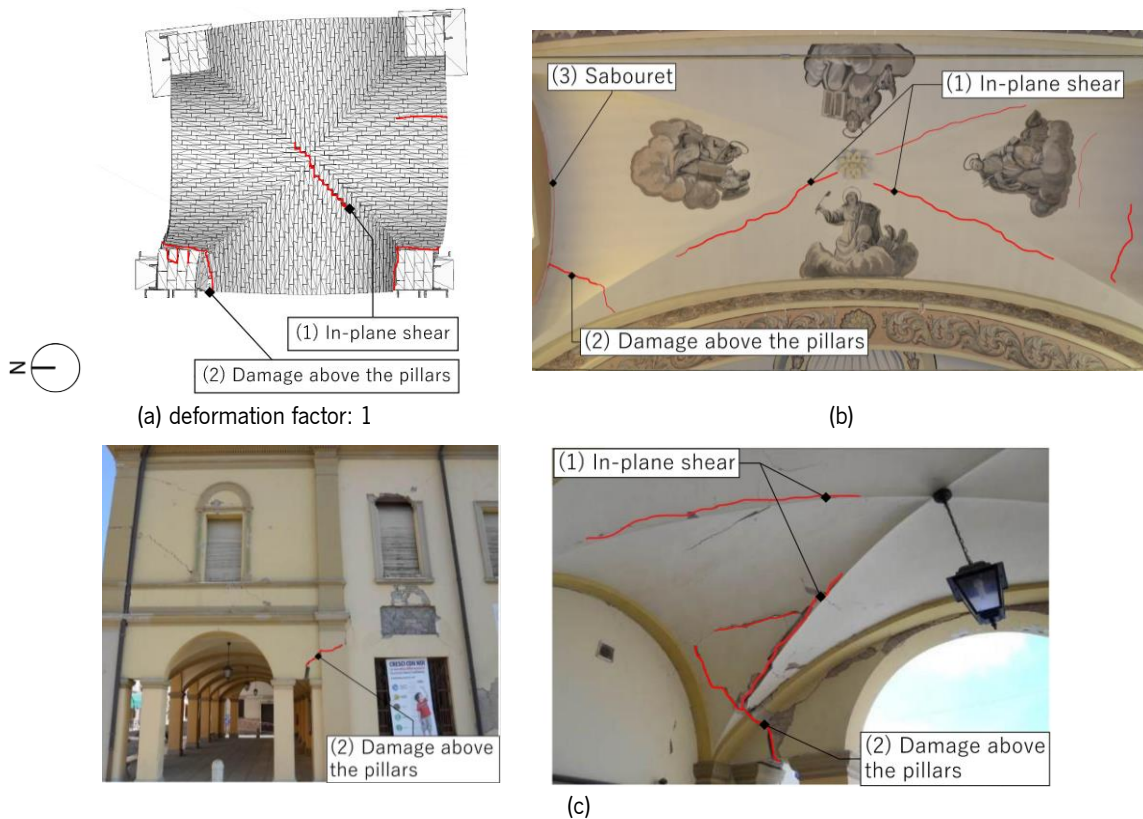


Figure 7-18. Failure at the level of the collapse on groin vaults: (a) deformed shapes of DEM model for 100% of the input, (b) seismic damage at the intrados of the groin vault in Sant'Andrea church (Sigillo) after Central-Italy earthquake 2016, (c) seismic damage on the vault of Town Hall of Novi di Modena after Emilia earthquake 2012.

7.4.3 Non-linear dynamic analysis for the strengthened model: FEM–SM

The TRM strengthening technique, used in the experimental campaign, is an innovative and powerful reinforcement solution that is rarely implemented in the FEM models for walls and even less while dealing with vaulted structures (Allahvirdizadeh, Oliveira and Silva, 2019; Milani *et al.*, 2019), and never implemented in three-dimensional DEM models. 3DEC software considers only steel bars, partially embedded in masonry elements (Smoljanović, Nikolić and Živaljić, 2015; Mehrotra, 2018) or externally bonded reinforcement modelled through few truss elements connected to the vault through non-linear contacts, considering equivalent spacings and properties to be able to represent the real grid distribution of the TRM (Gobbin, de Felice and Lemos, 2020; Lemos *et al.*, 2022).

In light of the results of the unstrengthened models and to decrease the computational effort, as anticipated in the previous Sections, only the calibrated FEM–SM has been prepared (Sections 7.2.1 7.3.1) and considered for the non-linear time history analysis. FEM–SM only investigates the response of the vault for the last shaking table test (ST–SM–150%).

The same analysis characteristics, described in Section 7.4.1, are still valid and the response of FEM–SM is compared to the results obtained in the shaking table tests, using the same parameters as

in the analysis of the experimental behaviour of the specimen, namely: deformed shapes and principal strains used as cracks indicators, displacements profiles and maximum absolute displacements along the movable edge and at the key of the vault, horizontal inertial coefficient, accelerations response, and drifts.

In general, the numerical results are rigorous in depicting the experimental damage, mainly while comparing the final distribution at the end of the analysis (Figure 7-19). Figure 7-19 presents the comparison between the numerical damage, represented by the distribution of tensile strains for different elevations in comparison with the experimental damage observed at the end of ST-SM-150%. In general, observing the extrados, the numerical diagonal cracks are characterised by a lower severity in comparison with the experimental one, maybe due to the perfect connection of the TRM system in the numerical model. The damage at the fixed pier, mainly the one located at the SW corner is coincident. The hinges are recognisable in the numerical simulations from both lateral views, with particular attention to the SW angle, which is correctly the most damaged. The severity of damage at the intrados is overestimated in FEM-SM, but the strains coherently develop at the boundaries of the locations where the injections have been simulated and where better material properties are applied. Moreover, at the intrados, the four corners are present also damage, in the same location where the thickness of the vault decreases at the boundaries of the infill. The main difference corresponds to the lack of an uplifting movement, which occurs between the steel masses and the impost of the vault along the Eastern edge. This mechanism can be simulated through additional interface elements, whose calibration would require further investigations and experimental considerations.



Figure 7-19. Damage map for: (a) ST-SM-150%, (b) principal strains distribution in FEM-SM model.

Figure 6-18 presents the comparison between the experimental displacement profiles and the numerical ones at $t = 4.31$ s, for the 150% earthquake. The displacement fields in the numerical models present an in-plane shear deformation and, on average, their absolute values are remarkably similar to the experimental ones for all the optical cameras. In the strengthened case, OC₂ behaves more homogeneously together with the other corner points. At this instant, both the experimental

specimen and FEM–SM model registered more limited transverse displacement at the key point of the eastern arch (OC_3).

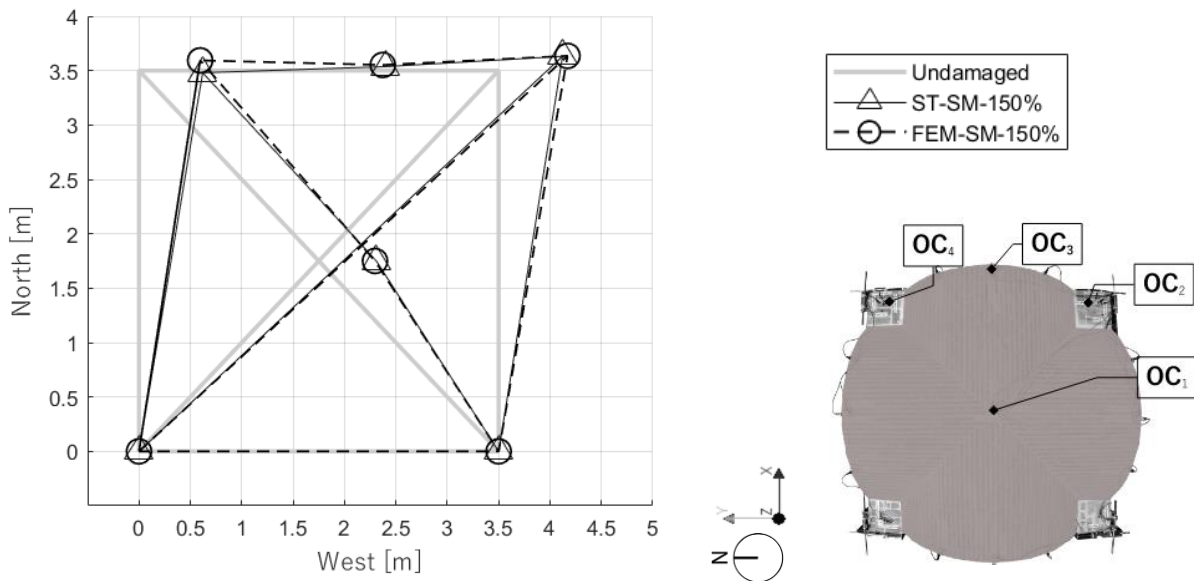


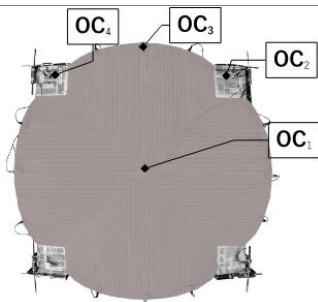
Figure 7-20. In-plane deformation profiles of the strengthened configuration for the ST-SM-150% when all the optical cameras measure the maximum displacements. Deformation factor: 10.

Looking at the absolute displacements in the longitudinal direction (NS) (Table 7-7), it is possible to notice that the average error $\bar{\epsilon}$ of FEM–SM model is equal to 1.2% and 6.4% when comparing the peaks values and the RMSD, respectively. These outputs highlight the quality of the strengthened FEM model results and validate the methodology used for modelling the strengthening technique.

However, similarly to the FEM–UNS model, FEM–SM underestimate the transverse capacity of the shell of the vault, suggesting the need of further investigation increasing the deformability in x direction, in order to better replicate the uplifting of the shell.

Table 7-7. Peak values and root mean square (RMSD) of displacements and average errors obtained from $OC_{1,2,3,4}$ of the ST-SM-150% and the FEM–SM model.

Sequence	OC_1 [mm]		OC_2 [mm]		OC_3 [mm]		OC_4 [mm]	
	NS	Vertical	WE	NS	WE	NS	WE	NS
ST-SM-150%	56.03	12.80	42.81	63.48	15.80	64.68	12.77	62.17
FEM-SM-150%	54.70	11.43	13.51	67.02	5.19	62.26	9.35	59.51
Average error (all OC_i in NS direction) $\bar{\epsilon}$ [%]								
FEM-SM								
Peak values						1.2%		
RMSD						6.4%		



The response of the vault is again evaluated through the envelope curves for ST-SM-150% (Figure 7-21), plotting the value of the horizontal inertial coefficient versus the displacement at a control point (measured by the optical camera OC_1). In the strengthened configuration, the responses of all the optical cameras are comparable. The (absolute) maximum horizontal inertial coefficient is equal to 0.33 for FEM-SM*, underestimating the response with respect to the experimental horizontal inertial coefficient of about 32%. On the other hand, the (absolute) maximum horizontal seismic coefficient obtained by the BSF is equal to 0.44 for FEM-SM_{BSF}, which matches the experimental horizontal inertial coefficient. In general, the decrease in the inertial coefficient corresponds to a lower bound domain, which can be considered a safer indicator in the evaluation of the seismic capacity of the vault.

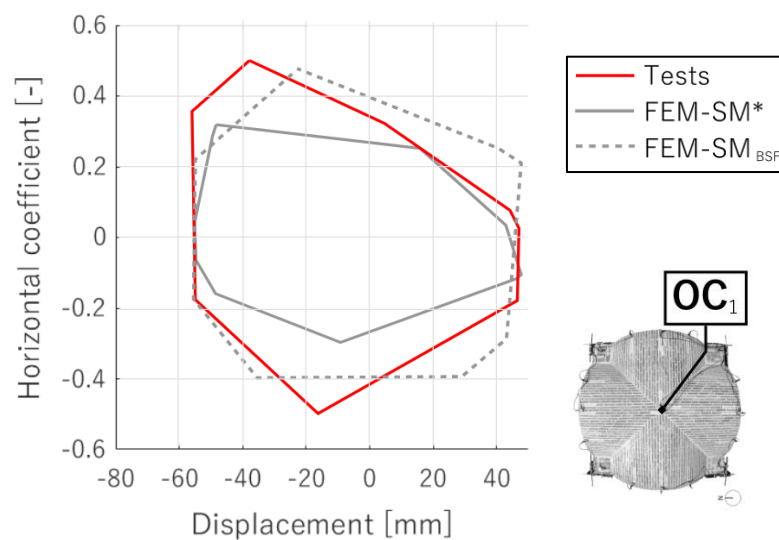


Figure 7-21. Experimental and numerical envelope response curves of the strengthened specimen for ST-SM-150% considering the optical camera OC_1 .

The last outcomes presented for FEM-SM model allow to arise important conclusion:

- the tensile principal strains distribution well replicates the experimental distribution of damage, highlighting the most vulnerable part of the structure when it is strengthened at the extrados, namely the fixed piers and the supports of the vault. In a generic church, those parts are stronger due to the presence of massive lateral walls, transverse arches and pillars.
- taking into account the grout injections concurred in achieving realistic damage without causing high principal strains distribution at the intrados, which would have also caused convergency problems.
- the displacement response is well described by the numerical model. They have an acceptable error in comparison with the experiments (less than 10%), while in terms of horizontal seismic

coefficient the scatter corresponds to an error of 32% while only considering the inertial contribution, and to an error of 9.5% while taking into account the base shear forces.

- if the maximum drift of the vault for the last seismic test is evaluated by comparing the response of OC₃, for FEM–SM, the maximum drift is 2.6%. The maximum experimental drift is set at the value of 2.7% for the same optical camera OC₃.

7.5 Final remarks

The numerical models of the unstrengthened and strengthened full-scale specimen is prepared, calibrated, and validated. The elaboration of reliable numerical models based on experimental data constitutes one of the solid bases for further structural studies and designs on masonry vaults. Three numerical models are considered: FEM–UNS (unstrengthened numerical finite element model), DEM–UNS (unstrengthened numerical discrete element model), and FEM–SM (strengthened numerical finite element model). Those numerical models are calibrated using the model updating, namely taking into account the first mode, which is associated with the in-plane shear mechanism, excited by the direction of the input. The calibration process of numerical models plays an important role in the subsequent non-linear analysis, as the non-linear simulation depends also on the linear mechanical properties considered for masonry material. The main changes are applied to Young's modulus of the masonry for FEM–UNS and FEM–SM, and the stiffness of the joints in DEM–UNS.

In what concerns the mode shapes, the MAC values show that the correlation between the experimental and numerical modal displacements is good in the longitudinal direction for all the models (FEM–UNS, DEM–UNS and FEM–SM models). With this respect, it is important also to notice that the evaluation of the experimental modal parameters before any seismic input test reveals to be an important tool for the calibration of the numerical model. The calibration should be taken as part of the whole validation process and considered one of the most fundamental parts of the numerical analysis.

The quality of the numerical results of the non-linear dynamic analyses agrees with the conclusions of the model updating. In fact, non-linear dynamic analyses with time integration are carried out following the same experimental sequence for the unstrengthened models (FEM–UNS and DEM–UNS), namely ST–UNS–25%, ST–UNS–50% and ST–UNS–75%.

This Chapter also discusses the effect of different contact constitutive laws within the DEM framework, namely two contact models: Mohr–Coulomb (MC) and combined material behaviour of Mohr–Coulomb with shear, crushing and cracking (MC–CM).

Only ST–SM–150% is numerically replicated with FEM–SM and compared with the strengthened experimental response.

For all these analyses, the response of the numerical models is compared with the experimental results in terms of damage patterns, displacement profiles, and envelope curves. From the results obtained from non-linear time history analyses, it is possible to conclude that:

- The correct simulation of the experimental boundary conditions in the most realistic way has been demonstrated to play an important role in the numerical analysis of the structure. In this study, it was observed through the boundary interface below the steel masses influenced the response.
- The FEM–UNS implemented in this work, with the rotating total strain crack constitutive model adopted for masonry, demonstrated to be accurate enough for the study and general understanding of the non-linear dynamic behaviour of unreinforced masonry vaults. It simulates the displacement and hysteretic response with an acceptable approximation. However, it requires a relevant computational effort.
- In the numerical simulations of the unstrengthened vault, the last seismic input (ST–UNS–75%) lacks in the accuracy of the simulations in comparison with the first two shocks (ST–UNS–25%, ST–UNS–50%) for both FEM and DEM model, but, on average, the value of drift obtained in the 75% earthquake by the numerical models is on the safe side.
- Comparing FEM and DEM models with the experimental response, it is noticed that both models are generally capable of replicating the collapse mechanism observed during the shaking table tests, matching in terms of cracks, the opening of the joints and time occurrence of the experimental damage. DEM–MC presents more difficulties in replicating the ultimate displacements and the hysteretic behaviour than FEM. Those difficulties are recovered by MC–CM behaviour assigned to the joints, which improves the results either in terms of displacement and resistance capacity. FEM lacks in terms of computational effort (fourteen times the duration of DEM analysis).
- FEM–SM demonstrated to be accurate for the study and the general understanding of the non-linear dynamic behaviour of strengthened masonry vaults when both grout injections and TRM applications are simulated. Both the displacement and hysteretic response are replicated with a small error in comparison with the ST. However, similar to FEM–UNS, requires a relevant computational effort.
- As a future work, accounting the damage caused by the previous earthquake may be a useful tool for the description of the incremental dynamic behaviour of the unreinforced masonry building tested in the shaking table for increasing seismic inputs.

This page has been intentionally left blank

8. Conclusions

This final chapter summarises the main results and conclusions of this work. A brief summary of the research outline is provided. Then, the main outcomes of the experimental and numerical investigations are recalled for both specimens: reduced-scale and full-scale vault. The main findings suggest new research possibilities and works in the field of strengthening and numerical analysis of masonry cross vaults subjected to seismic actions. Chapter 8 also succinctly discusses the original contributions of this research to the state of the art, being the existing literature mostly limited to quasi-static (experimental and numerical) investigations of unstrengthened specimens/models. Thus, future works suggestions are provided at the end of the Chapter.

8.1 Research outline

The work presented in this thesis addresses the evaluation of the seismic assessment of groin vaults subjected to dynamic actions that cause in-plane shear mechanism on the shell of the vault. The research was organized into different tasks, which can be subdivided into two main groups. The first group (Chapters 3 and 4) includes the experimental and numerical investigations at the reduced-scale level using a 1:5 3D printed groin vault, characterised by dry joints. The second group (Chapters 5,6 and 7) includes the experimental and numerical investigations at the full-scale level using a masonry groin vault specimen, characterised by mortared joints that reproduces a historic vault located in a central bay of a lateral nave in a generic three-nave church.

The tasks involved two experimental campaigns on the shaking table, as well as numerical simulations on both specimens with finite and discrete element models.

Due to the peculiar features of the reduced-scale vault, it was also possible to repeat several shaking table tests, always starting from the undamaged configuration and with two ground motions applied in percentage of increasing amplitude (recorded Emilia earthquake 2012 vs artificial accelerogram). From the numerical point of view, a comparison between FEM and DEM micro-models was done, taking also into account the experimental results.

A damping investigation was conducted on the FEM model, in order to justify the assumption of null damping, such as in the discrete model. Moreover, the influence of several ground motions, characterised by different input nature was evaluated through the discrete element model, which included a parametric and statistical study.

Regarding the full-scale vault, extensive historic research about the traditional construction techniques and a wide experimental campaign were conducted with the 1:1 groin vault made of masonry. The experimental program on the full-scale vault included dynamic identification tests and shaking table tests without and with the strengthening technique (TRM).

The simulation results performed with FEM (macro-modelling) and DEM models were compared against the experimental results, and the corresponding material parameters were calibrated based on the modal properties, in order to improve the prediction of damage distribution, displacements field and hysteretic behaviour. Classic Mohr-Coulomb (DEM-MC) and combined material of Mohr-Coulomb with shear, crushing and cracking (DEM-MC-CM) have been implemented to describe the shear-compression state of the joints in the DEM model and their outcomes were discussed. The FEM model was also employed to simulate the repairing with grout injections and the TRM application to the shell of the vault and again compared with the experimental evidence. Likewise, the numerical prediction of damage distribution, displacements field and hysteretic behaviour was assessed.

8.2 Conclusions from the study on the reduced-scale vault

The results obtained from the shaking table tests on the 1:5 reduced-scale vault are compared with quasi-static tests on the same specimen, already available in the literature. In particular, the development of a four-hinge symmetric mechanism was observed in two webs during the quasi-static tests. A similar mechanism was obtained for the shaking table tests, but the first location of the hinges appears between the fixed piers of the vault, associated with the stiffer behaviour of the fixed edge. The displacement/drift levels achieved in the shaking table tests were higher (about 6% of the span) than the ultimate displacement/drift obtained from quasi-static tests (about 4% of the span), concluding that the monotonic approach is more conservative than the dynamic approach. The novelty of the work is that it was for the first time experimentally observed on a 3D curved structure.

One of the main objectives, related to the investigations on the reduced-scale vault, was to better understand and characterise the in-plane shear behaviour of groin vaults, by means of shaking table tests, in which two different types of seismic action are considered (recorded Emilia earthquake and artificial accelerogram). Within this framework, when applying the Emilia earthquake and the artificial seismic input, the failure mechanism and inertial coefficient were similar, but the collapse occurred for different levels of seismic amplitude. This difference was influenced by the spectral acceleration of the Emilia input that is about 0.17 g above the spectral acceleration of the Italian Code (0.43 g), while intersecting the first period of the specimen, as well as the different nature of the two input signals. This

stresses the fact that a significant number of records is necessary to allow a better description of the safety of the structure, as already suggested by the most recent codes (Baraschino, Baltzopoulos and Iervolino, 2019; Ministero delle Infrastrutture e Trasporti, 2019).

The experimental results have contributed to extend the available database on the dynamic response of vaults under seismic actions, representing a consistent reference that might be used as input for numerical models, as well as for validation of simulation results.

Assessing the capability of different modelling approaches to predict the seismic response of masonry cross vaults confirmed that, for dry joint structures, the influence of the damping is not predominant, mainly because the joint's stiffness prevails in comparison with the damping dissipation during the analysis. Comparing FEM and DEM models with the experimental response, it was found that DEM is generally capable of reproducing the large displacements and replicate the collapse mechanism observed during the shaking table tests, matching in damage and time occurrence. DEM faced more difficulties in correctly replicating the ultimate displacements. FEM model is quantitatively reliable, as displacements and accelerations are comparable with the experimental data, but computational effort is high.

From the study related to the influence of different ground motions, which considered six different transient analyses with DEM, it is possible to conclude that the collapse occurs for different acceleration and displacement amplitudes, but similar peak ground velocities (PGV). Thus, the PGV represents a stabler parameter for the assessment of vaults. In addition, the collapse mechanism was pretty similar between all the analyses, showing the first hinges located at the fixed edge of the model, as observed during the shaking table tests.

8.3 Conclusions from the study on the full-scale vault

The main objectives of the study related to the full-scale vault were to better understand and characterise the in-plane shear behaviour of masonry groin cross vaults, by means of shaking table tests on both full-scale without (UNS) and with the TRM strengthening technique (SM) assess the capability of different modelling approaches to predict the seismic response of masonry cross vaults, based on the experimental results.

Likewise the reduced-scale vault, the experimental results have contributed to extend the limited database on the dynamic response of full-scale vaults under seismic actions - a consistent reference that might be used as input for quantifying the improvement brought from the TRM application and for the validation of simulation results.

In-plane shear behaviour on the shell is found to be the predominant mechanism, leading to important outcomes and conclusions in the evaluation of the structural assessment of the two configurations (UNS and SM). The dynamic identification tests showed that the first modes correspond to the in-plane shear distortion of the shell for both UNS and SM, and the first frequency decreased while damage increased on the vault. However, after the 75% amplitude of the shaking table tests, the strengthened specimen presented a reduction of the damage indicator for the first mode of about 20% with respect to the UNS. This leads to the conclusion that the strengthening technique is efficient in the reduction of the seismic vulnerability of the specimen.

To quantify this improvement, it is important to first highlight that the UNS presented a higher level of damage for 75% of the seismic amplitude. To reach a similar level of damage, the double of the seismic amplitude (150%) had to be applied on the SM. TRM application has increased the strength of the vault. In fact, comparing the two configurations at the same level of amplitude (75%), it is possible to notice that the strengthened vault presents only light cracks, indicating that the inertial forces of the shell have been absorbed by the TRM strengthening technique, improving the seismic performance of the vault.

At the last seismic sequence (ST-SM-150%), the strengthened vault presents a higher concentration of damage along the piers and the supports of the specimen, not only along the groins as it was for the UNS. This damage is related to both in-plane distortions but also rocking and torsions of the fixed piers. This aspect may suggest considering a design that includes also the strengthening of the piers in practice, when possible. The effectiveness of the TRM strengthening presents also higher strength capacity. Indeed, grout injections and TRM strengthening enhanced the performance of the vault, providing further capacity to the vault under dynamic loads (horizontal inertial coefficient, drift value and displacements) and it is an effective solution for reducing the seismic vulnerability of masonry groin vaults.

From the numerical point of view, the correct simulation of the experimental boundary conditions in the most realistic way played an important role in the betterment of the numerical simulations. The FEM-UNS implemented in this work, with the rotating total strain crack constitutive model adopted for masonry, demonstrated to be accurate enough for the study and general understanding of the non-linear dynamic behaviour of unstrengthened masonry vaults. FEM-UNS simulated the displacement and hysteretic response with a satisfying approximation but required a relevant computational effort.

Both FEM and DEM models were capable of replicating the collapse mechanism, observed during the shaking table tests on the UNS, matching the crack patterns, the opening of the joints and the time occurrence of the experimental damage. On average, the value of drift obtained at the 75% of the

amplitude for both FEM and DEM numerical models is conservative and on the safe side, while for the first two shocks (ST-UNS-25%, ST-UNS-50%), when the specimen and the models are still in the linear range, a good matching between tests and numerical results was obtained.

DEM with MC presents more difficulties in replicating the ultimate displacements and the hysteretic behaviour than FEM, which is more reliable. FEM underperforms in terms of computational effort (fourteen times the duration of DEM analysis), representing a strong limit for its adoption in practice. Remarkable improvements are observed while adopting DEM with MC-CM behaviour, assigned to the joints, which enhances the results either in terms of displacement and capacity.

FEM-SM model demonstrated to be accurate for the assessment of strengthened masonry vaults when both grout injections and TRM applications are simulated. Both damage, displacement and hysteretic response are replicated with a good approximation in comparison with the seismic tests. However, it requires an high computational effort.

8.4 Future works

The experimental and numerical program presented in the thesis provided a better understanding of the behaviour of groin vaults at reduced and full-scale levels. The present thesis aim was to contribute to the preservation of the masonry groin vault and the cultural heritage, by improving the knowledge of their seismic behaviour and assessing the effectiveness of possible strengthening techniques that can be easily implemented. A further step is to render the findings in recommendations for further investigations and practitioners.

The work on the reduced-scale vault may be extended in the future, including the following topics for a fruitful continuation of this work:

- new studies on damping formulation (*e.g.* proportional to the mass only, Maxwell springs, or Hunt and Crossley model).
- assess the sensitivity of the seismic capacity to variation in the geometry, interlocking, materials properties and bricks dimensions, contemplating a more ambitious overview of the diversity of realistic scenarios.

The work on the full-scale vault, based on the fulfilled objectives and the gathered experience, may be extended through the following future works:

- consider the imperfections of construction and already damaged structure analysis in both FEM and DEM models to better assess existing groin vaults.

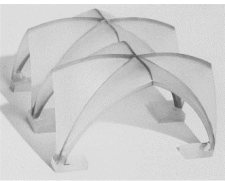


- carry out further numerical investigations varying the type of bricks, arrangement and dimensions.
- sensitivity analysis of the numerical models varying the modelling approach and material properties, and investigating the role of the lateral walls and the transverse arch as in real scenarios.
- consider the amplification of the seismic amplitude along the height of the columns, taking into account the location of vaults in real structures.
- evaluate the role of different TRM-strengthening characteristics (*e.g.* geometry, inelastic properties, Young's modulus).



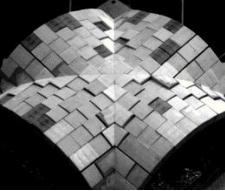


Annexes

This page has been intentionally left blank

1. Annex – Works carried out on masonry cross vaults

Table A1-1. Experimental works carried out in masonry vaults, from the 1970s until the most recent works

Reference	Picture	Scale	Dimensions	Type of		Material	Comments
				action	tests		
Mark <i>et al.</i> (1973)		1:50	$0.1 \times 0.2 \text{ m}^2$	Static	Dead load (Photoelastic technique)	Epoxy resin	FEM models (SAP)
Faccio <i>et al.</i> (1999)		1:1	$7.36 \times 7.36 \text{ m}^2$	Quasi-static	Monotonic point load at the key of the vault	Bricks	FEM models: Creazza <i>et al.</i> (2002), Milani <i>et al.</i> (2012) DMEM model: Calio (2010) and Cannizzaro (2011)
Briccoli Bati <i>et al.</i> (2002)		1:3	$2.3 \times 2.3 \text{ m}^2$	Quasi-static	Monotonic point load at the key of the vault	Bricks, 0.5cm lime joints	Strengthened: ties and GFRP
Theodossopoulos <i>et al.</i> (2002,2003)		1:4	$1.5 \times 1.84 \text{ m}^2$	Quasi-static	Horizontal displacement	Wood	Replica of Abbey of Holyrood (UK) FEM model: ABAQUS
Miltiadou-Fezans (2008)		-	$1.275 \times 0.945 \text{ m}^2$	Dynamic	Shaking table tests (Athens earthquake)	Bricks	Strengthened: grout injections Replica of Dafni's monastery FEM model ACORD

Reference	Picture	Scale	Dimensions	Type of		Material	Comments
				action	tests		
Williams <i>et al.</i> (2012)		1:25	0.89 × 0.896 m ²	Dynamic	Shaking table tests (sinusoidal pulse)	Plaster and sand	Replica of Maxentius basilica
De Matteis and Mazzolani (2012)		1:5.5	~2.0 × 1.1 m ²	Dynamic	Shaking table tests (Calitri earthquake)	Bricks	Replica of Fossanova church
							Strengthened: ties, buttresses, expansive aluminium-cement mortar
							FEM model: ABAQUS
Shapiro (2012)		~1:10	278 × 278 mm ²	Quasi-static	Monotonic point load/Spreading supports/Tilting tests	Plaster and powder material	
Rossi <i>et al.</i> (2016) Milani <i>et al.</i> (2016)		1:5	0.65 × 0.65 m ²	Quasi-static	Horizontal shear displacement/Tilting plane tests	Plastic powder sintering/Steel	FEM micromodels: Milani <i>et al.</i> (2016), Alforno <i>et al.</i> (2020, 2021, 2022), Gaetani <i>et al.</i> (2021)
Fagone <i>et al.</i> (2016)		1:5	1.63 × 1.58 m ²	Quasi cyclic tests	Constant vertical load and cyclic horizontal load	Sandstone/Cement lime mortar	Replica of St. John Hospital Jerusalem
							Strengthened: CFRP Strips
							FEM model vs NURBS-KLA: Milani <i>et al.</i> (2019)

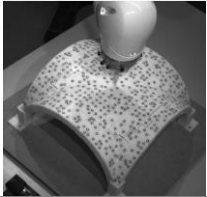





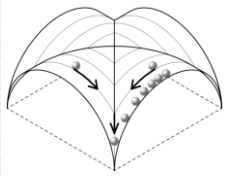

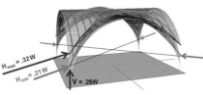

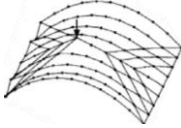
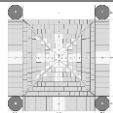
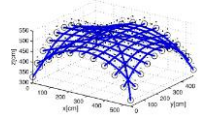
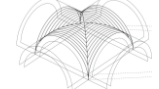
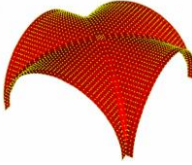
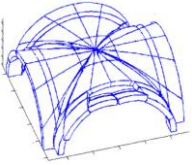

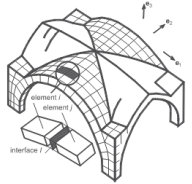
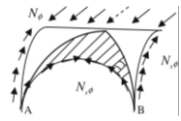
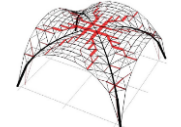
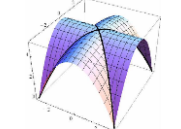

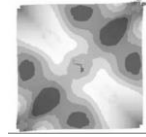
Reference	Picture	Scale	Dimensions	Type of		Material	Comments
				action	tests		
Rossi <i>et al.</i> (2017b)			343 × 343 mm ²	Quasi static	Monotonic pointed loads/Vertical displacements of the abutments	Plaster and powder material	DEM model: Dell'endice <i>et al.</i> (2020)
Carfagnini <i>et al.</i> (2018) Baraccani <i>et al.</i> (2020)		1:4	0.88 × 1.1 m ²	Quasi static	Horizontal shear displacements	Timber bricks/lime mortar	Replica of Abbey of Holyrood (UK) FEM model: ABAQUS
Foti <i>et al.</i> (2015; 2018)		1:5	1 × 1 m ²	Quasi static	Vertical and horizontal displacements at one support	Polystyrene	DEM model: 3DEC
Torres <i>et al.</i> (2019; 2019)		1:1	4 × 4 m ²	Quasi static	Vertical displacements at one support	(timbrel) Bricks	Replica of Church of San Lorenzo de Castell de Cabres (Spain) FEM model: LUSAS
Rossi <i>et al.</i> (2020)		1:1	3.50 × 3.60 m ²	Dynamic	Shaking table tests (Keddara earthquake)	Bricks	Replica of Mosque of Dey, Algiers Strengthened: ties FEM model: ANSYS
Silvestri <i>et al.</i> (2021)			2 × 2 m ² plan 0.7 m height	Dynamic	Shaking table tests (sinusoidal inputs)	Plastic-mortar blocks	-

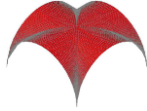
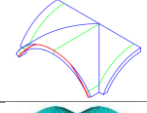

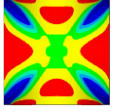
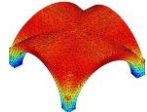
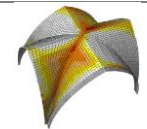
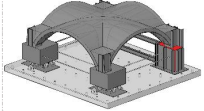
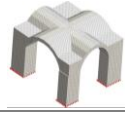
Table A1-2. Numerical works carried out in masonry vaults


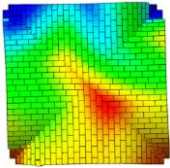
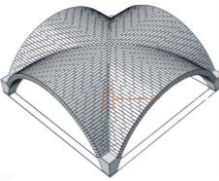
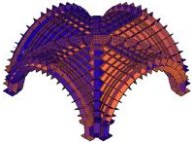
Methods	References	Pictures	Solution and analysis	Strain and stress	Failure mechanism	Ultimate strength	3D behaviour	Horizontal loads	Main contributions comments
Historical methods	Catenary	-	Equilibrium analyses (only) Lower bound approach	X	X	X	X	X	Applicable to arches. Thrust line within the middle third of the section (Méry, 1840)
				X	X	X	X	X	Applicable to arches and barrel vault.
	Slicing technique Graphical		Equilibrium analysis Lower bound approach	X	X	X	X	X	Applicable to compound vaults.
				X	X	X	X	X	Reduction from three-dimensional into in-plane analysis.
Limit analysis	Standard formulation		Equilibrium analysis and compatibility Lower/ upper bound approach	X	Dual problems (limit analysis theorems)	✓	X	X	Applicable to general masonry structure.
				X			-	-	Applicable to general masonry structure. 3D behaviour and horizontal loads handled only with FEM.

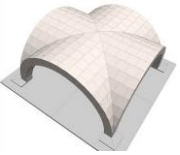
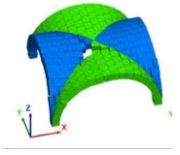

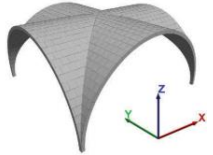


Methods	References	Pictures	Solution and analysis	Strain and stress	Failure mechanism	Ultimate strength	3D behaviour	Horizontal loads	Main contributions comments	
Limit analysis	TNM	Block <i>et al.</i> (2002, 2007; 2005, 2009; 2006; 2014; 2020; 2020; 2021)		Equilibrium analyses (only) Lower bound approach Net of 3D complex structures			✓	3D compression only net	Minimum and maximum thrust state solutions (within the thickness) Very suitable for DEM comparisons	
		O'Dwyer (1999)		Funicular method through a discrete network of forces.			-	X	Allow the estimation of the max load factor. Good for barrel vault. Iterative process with min. eccentricity	
		Andreu <i>et al.</i> (2007)		Equilibrium analyses (only) Iterative procedure Lower bound approach			-	3D compression only net	Net of 3D complex structures Output: geometry safety factor Applicable to any kind of vault.	
		D'Ayala <i>et al.</i> (2008)	-	Equilibrium analysis Lower bound approach Coulomb friction law	X	X	X	3D compression only surface	X	Output: geometric safety factor Iterative procedure with minimum eccentricity Tangential stress admissibility constrains
		Galassi <i>et al.</i> (2012)								-
		Marmo and Rosati (2017)		Lower bound approach Equilibrium analysis			✓	X	Applicable to any kind of vault.	
		Intrigila <i>et al.</i> (2019)								Suitable for gravity loads and abutments spread.

	Methods	References	Pictures	Solution and analysis	Strain and stress	Failure mechanism	Ultimate strength	3D behaviour	Horizontal loads	Main contributions comments
Limit analysis	FEM limit analysis upper bound	Milani <i>et al.</i> (2008; 2012; 2014)		Upper bound approach Compatibility and yield function						3D failure mechanism. Rigid-infinitely resistant elements with plastic dissipation at the interfaces Homogenization technique. Validation on Faccio <i>et al.</i> (1999)
	Non-standard limit analysis	Orduna <i>et al.</i> (2005b, 2005a)	-	Equilibrium Compatibility Yield function						Applicable to any kind of vault.
		Gilbert <i>et al.</i> (2006)	-	Flow rule						
	NURBS adaptive limit analysis	Chiozzi <i>et al.</i> (2017a)		Upper bound approach Kinematic analysis Parametric surfaces and mesh	X	✓	✓	✓	X	Applicable to barrel and groin vault. Searching the minimum collapse load multiplier. Validation on Faccio <i>et al.</i> (1999)
		Grillanda <i>et al.</i> (2020)								Rigid-infinitely resistant elements allowing plastic dissipation at the interfaces.
FEM limit analysis lower bound	Milani (2022)		Lower bound approach							A classic no-tension material and with an orthotropic behaviour with small but non-zero strength in tension

Methods	References	Pictures	Solution and analysis	Strain and stress	Failure mechanism	Ultimate strength	3D behaviour	Horizontal loads	Main contributions comments	
Membrane theory	Tomasoni (2008)	-	Only static equilibrium Linear elastic analysis						Applicable to thin vaults. No out of plane stresses. Tensile stresses within the structure	
	Como (2017)		Equilibrium Linear elastic. Closed form solution						No tension and membrane forces within the thickness	
	Fraternali (2010)		Equilibrium (only)	✓	X	X	✓	X	Description of the structure as graph of functions. It contemplates only surfaces.	
	Contestabile (2016)		Equilibrium Linear elastic						Allow to understand the stability of the structure Applicable to thin vaults.	
Finite element method	Macro	Theodossopoulos <i>et al.</i> (2002-2003)	-	Equilibrium Incremental loading analysis non-linear					Partly irreversible deformations. Stiffness variability with respect the load history.	
		Creazza <i>et al.</i> (2002)		It describes the failure mechanism in every point and step of the load history Non-linear analysis	✓	✓	✓	✓	✓	Validation on Faccio <i>et al.</i> (1999) Post-peak resistance degradation stiffness and strength progressive degradation after cyclic loads. Applicable to any kind of vault.
		Cattari <i>et al.</i> (2008)		Elastic FEM simulations – shell elements						It works as an equivalent membrane

Methods	References	Pictures	Solution and analysis	Strain and stress	Failure mechanism	Ultimate strength	3D behaviour	Horizontal loads	Main contributions comments		
Finite element method	Macro		Elastic FEM simulations	✓		✓			It gives the ultimate load and failure mechanisms.		
			Shell elements								
			Homogenized limit analysis approach								
		Holzer (2013)		Simplified FEM. Incremental loading analysis.		Only strains			✗	Fast method for three-dimensional situations.	
		Giresini (2014)		Equivalent trusses (Simplified FEM)						Suitable for the comparison with global FEM.	
		Lengyel, Bagi (2015)		Elastic FEM simulations – shell elements						Suitable for the comparison with global DEM.	
		Bruggi- Talercio (2015)		Non-incremental analysis under given loads topology optimization.		✓			✓	✓	Applicable to any 3D masonry vaults.
		Carfagnini <i>et al.</i> (2018)		Non-linear static analysis							Suitable for the comparison with experimental data in Carfagnini <i>et al.</i> (2018) and Baraccani <i>et al.</i> (2020)
Bianchini <i>et al.</i> (2019)		Non-linear static and dynamic analysis				Study of a large structure. Suitable for the comparison between static and dynamic analysis.					
Santini <i>et al.</i> (2022)		Non-linear static analysis				Supported by means of UAV inspection, NDT measures, and AVT monitoring					

Methods	References	Pictures	Solution and analysis	Strain and stress	Failure mechanism	Ultimate strength	3D behaviour	Horizontal loads	Main contributions comments
Finite element method	Discrete	Scacco <i>et al.</i> (2020)	-	Pseudo-static analysis					Applicable to any 3D masonry vaults.
	Micro	Milani <i>et al.</i> (2016)		Non-linear static analysis	✓	✓	✓	✓	It studies irreversible deformations and the stiffness variability with respect the load history after cyclic loads.
		Gaetani <i>et al.</i> (2018; 2021)							Validation on Rossi <i>et al.</i> (2016)
		Alforno <i>et al.</i> (2020, 2021, 2022)							It studies the stiffness, friction angle variability and geometric non-linearities.
								Validation on Rossi <i>et al.</i> (2016)	
DMEM	Cannizzaro Calìò (2011; 2012)		Non-linear dynamic/cyclic analysis Definition of the macro-element	Only at the springs	✓	✓	✓	✓	Time history analysis under development. Applicable to any kind of vault.

Methods	References	Pictures	Solution and analysis	Strain and stress	Failure mechanism	Ultimate strength	3D behaviour	Horizontal loads	Main contributions comments
Discrete element method	Van Mele <i>et al.</i> (2012)		Non-linear static analysis	X	✓	✓	✓	✓	Suitable for the comparison with experimental data.
									No modal analysis.
	Foti (2015)		Gravitational loads						It analyses the spread of the abutments.
									No modal analysis
	McInerney – Dejong (2015)		Displacement capacity						Suitable for the comparison with Thrust line analysis.
									No modal analysis
Lengyel, <i>et al.</i> (2017; 2018)		Non-linear dynamic analysis	First 3D time-history analysis.						
			Suitable for the comparison with FEM approach.						
			No modal analysis						
Fang-Napolitano (2018)		Gravitational loads	Suitable for the comparison with Trust line analysis.						
			No modal analysis						
Masi (2020)		Non-linear dynamic analysis (blast)	First loading history and collapse under blast analysis.						
			No modal analysis						

This page has been intentionally left blank

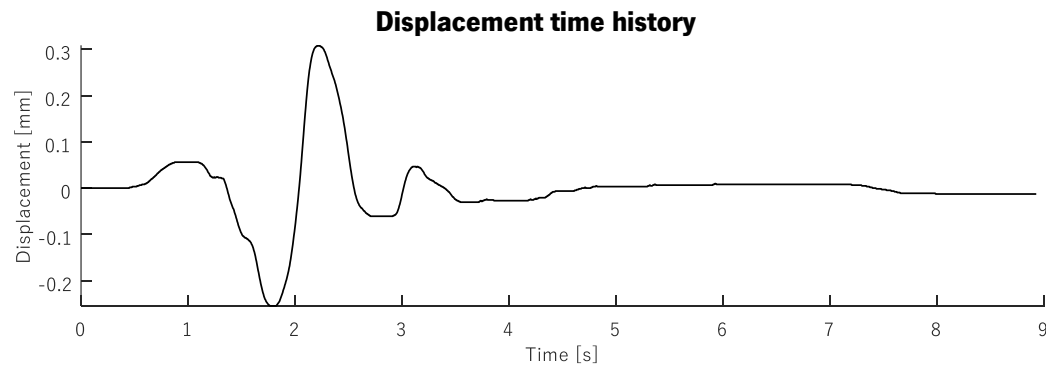
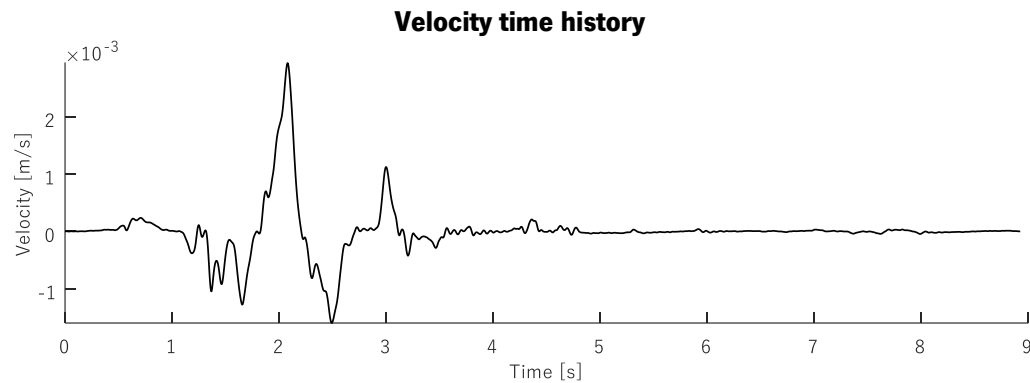
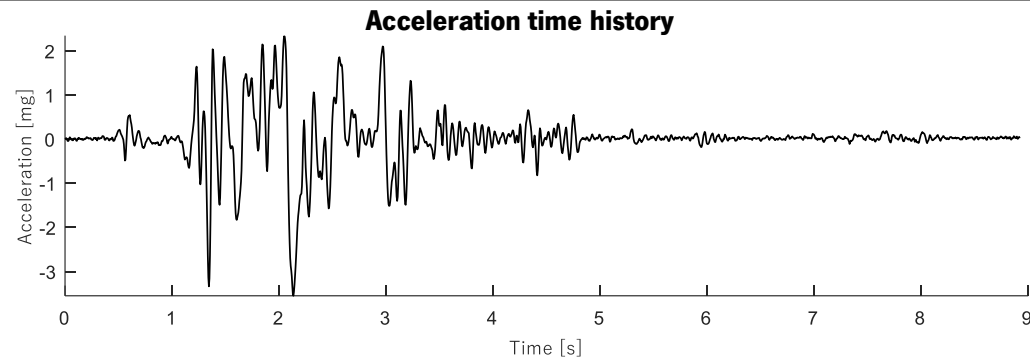
2. Annex – Reduced-scale vault: shaking table tests results

Table A2-1. List of shaking table tests on the reduced-scale vault.

Tests with Emilia input		
DIT	Seismic action	Notes
Frequency [Hz]	% of action	
Construction 1		
4.10		Undamaged configuration
	10 %	No damage
4.10		
	25 %	No damage
4.00		
	50 %	Recovered
3.91		
	75 %	Collapse
Construction 2 *discarded		
3.61		*initial minor damage
	60 %	collapse
Construction 3		
4.10		Undamaged configuration
	55 %	unrecovered
4.00		
	25 %	aftershock1
3.42		
	35 %	aftershock2
3.22		

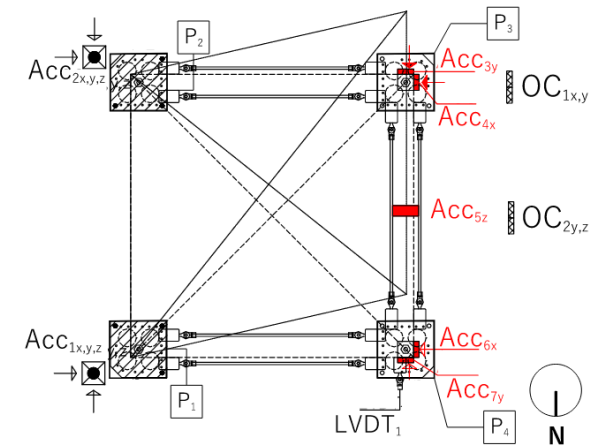
Tests with Artificial input		
DIT	Seismic action	
Frequency [Hz]	% of action	
Construction 4		
4.10		Undamaged configuration
	50 %	No damage
4.00		
	75 %	No damage
4.00		
	100 %	No damage
3.90		
	125 %	Recovered
3.71		
	150 %	Recovered
3.35		
	200%	Collapse

Table A2-2. Emilia earthquake 10%: input data and time histories



Peak ground variable		Root mean square variable	
PGA [mg]	3.55	RMS _A [mg]	0.60
PGV [mm/s]	7.23	RMS _V [mm/s]	0.12
PGD [mm]	0.31	RMS _D [mm]	0.07

Setup plan



- Legend:
- Fixed piers: (P₁ - P₂)
 - Movable piers: (P₃ - P₄)
 - Piezometric accelerometer
 - Capacitive accelerometer
 - Deformed shape
 - Optical camera

Accelerometer shake table: Acc_{STx} - Acc_{STy} - Acc_{STz}

Displacement shake table: D_{STx} - D_{STy} - D_{STz}

Table A2-3. Emilia earthquake 10%: response time histories

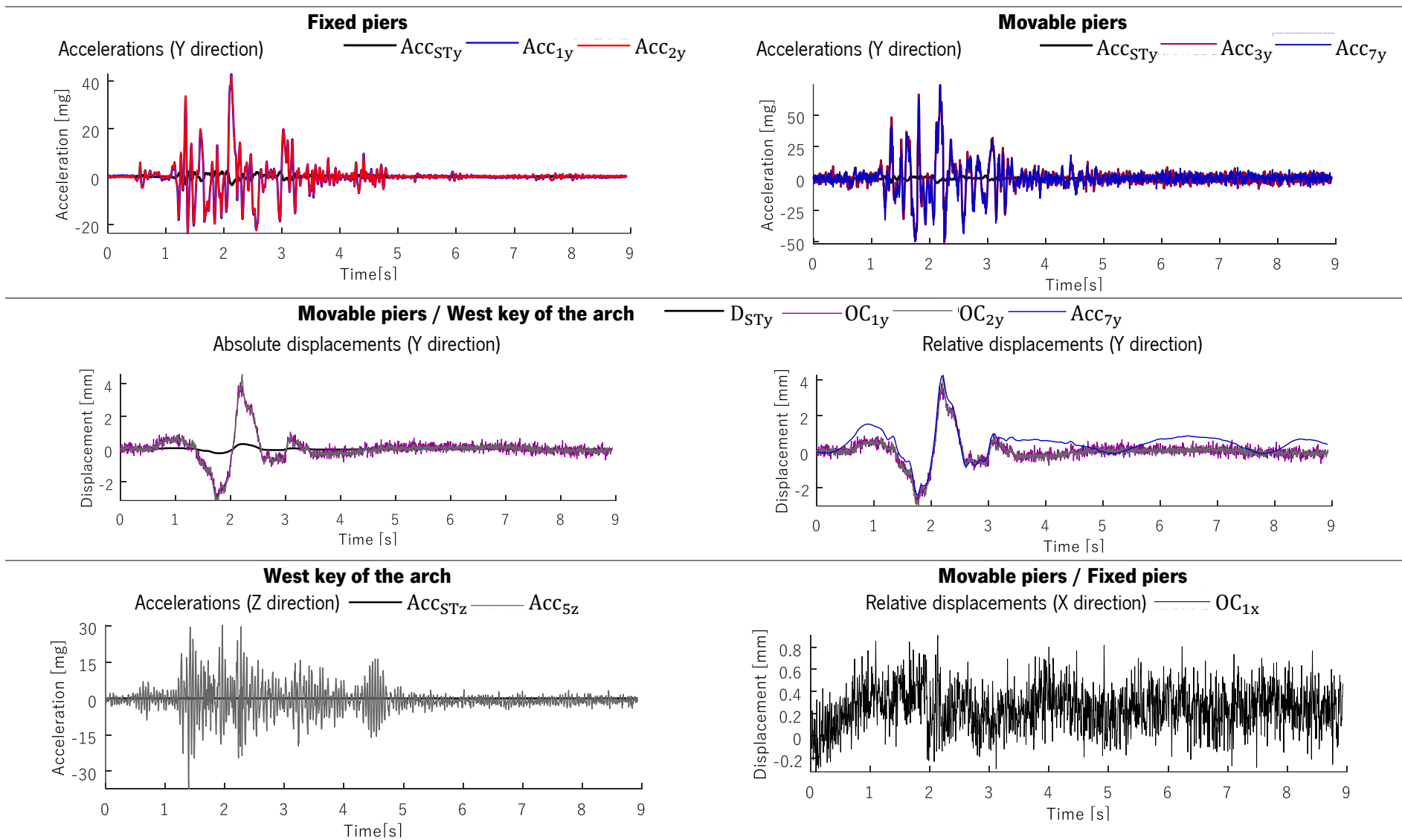
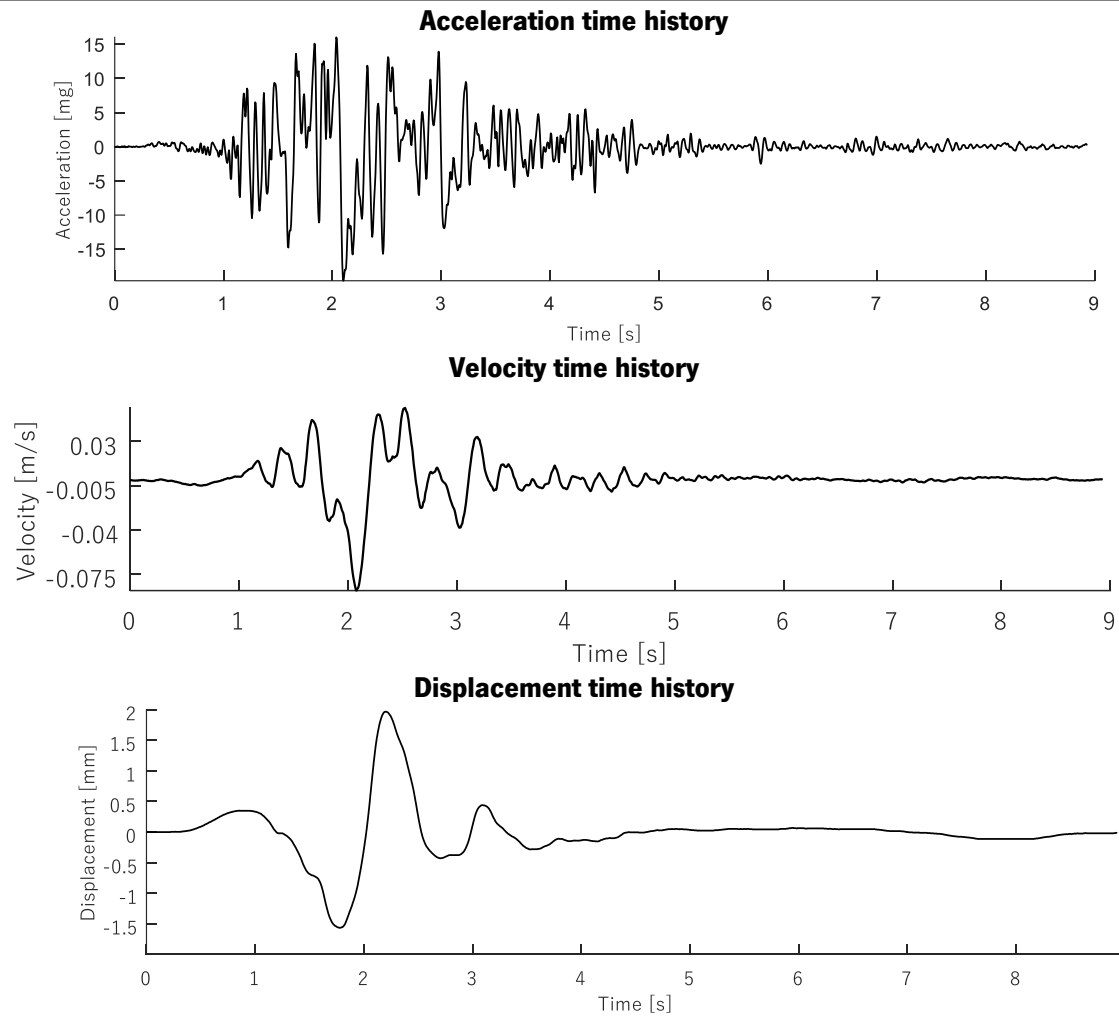
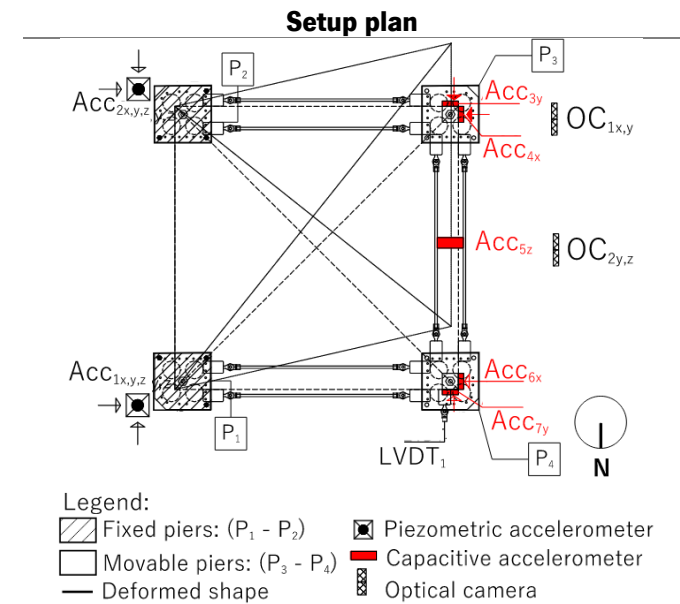


Table A2-4. Emilia earthquake 25%: input data and time histories



	Peak ground variable		Root mean square variable
PGA [mg]	19.17	RMS _A [mg]	3.98
PGV [mm/s]	17.22	RMS _V [mm/s]	15.48
PGD [mm]	1.96	RMS _D [mm]	0.45



Accelerometer shake table: ACC_{STx} - ACC_{STy} - ACC_{STz}

Displacement shake table: D_{STx} - D_{STy} - D_{STz}

Table A2-5. Emilia earthquake 25%: response time histories

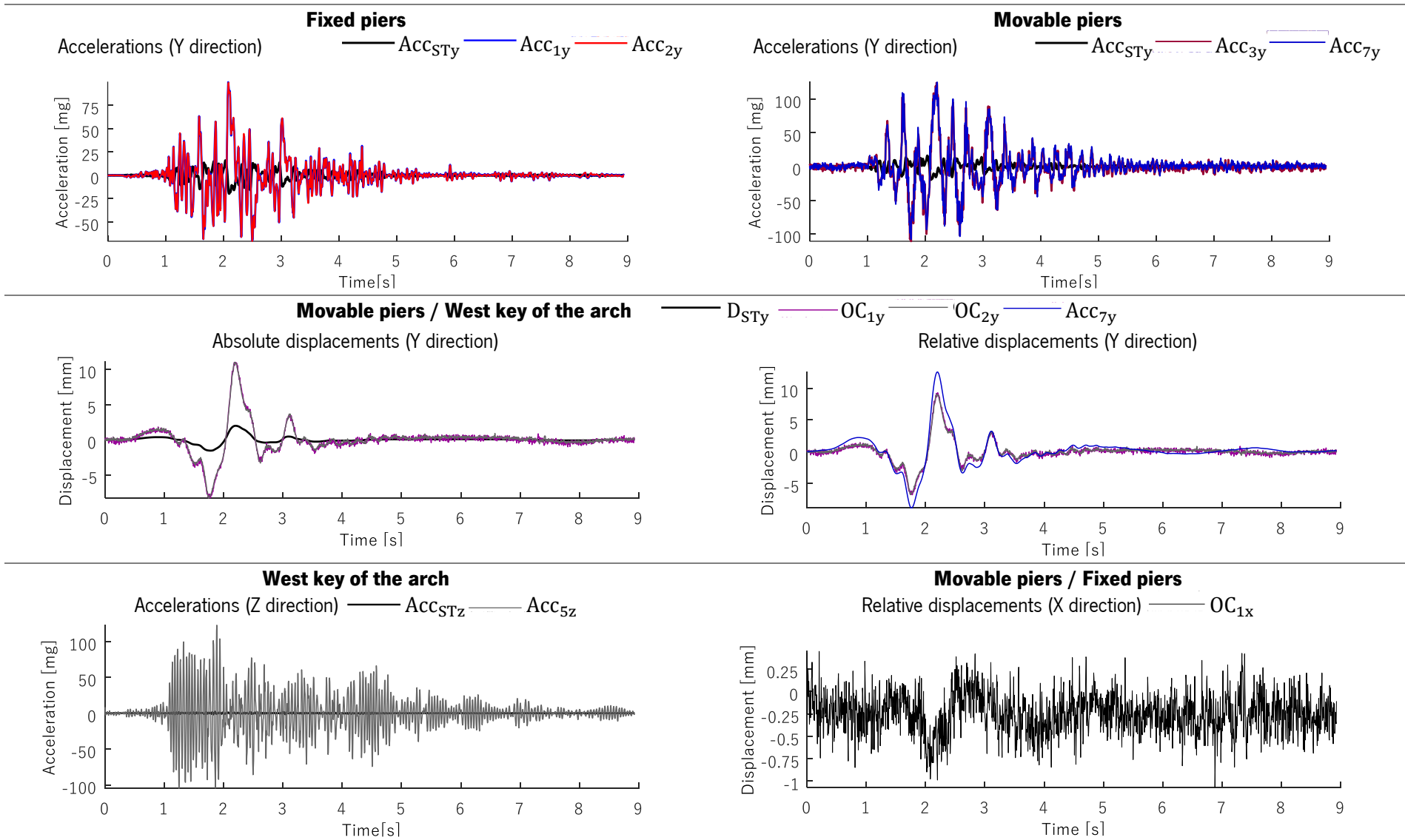
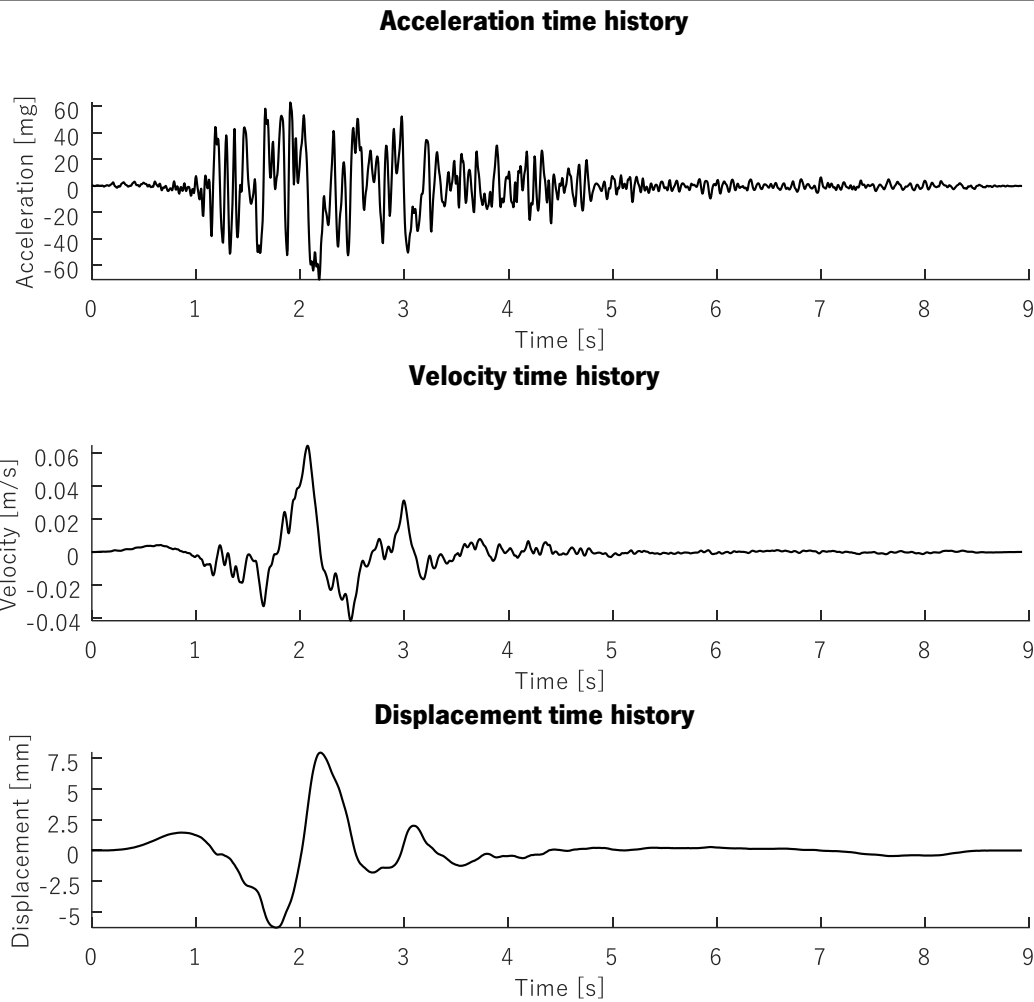


Table A2-6. Emilia earthquake 50%: input data and time histories



Peak ground variable		Root mean square variable	
PGA [mg]	70.65	RMS _A [mg]	16.51
PGV [mm/s]	64.58	RMS _V [mm/s]	10.64
PGD [mm]	7.94	RMS _D [mm]	1.82

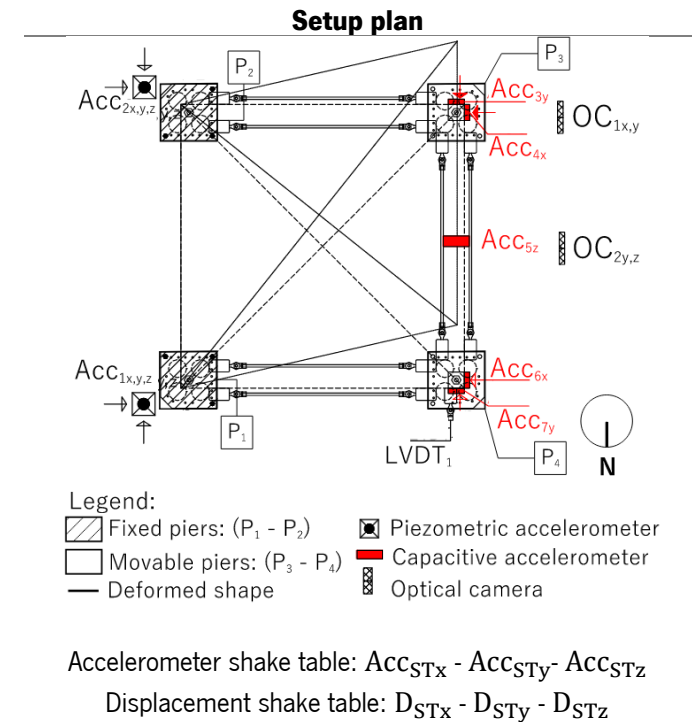


Table A2-7. Emilia earthquake 50%: response time histories

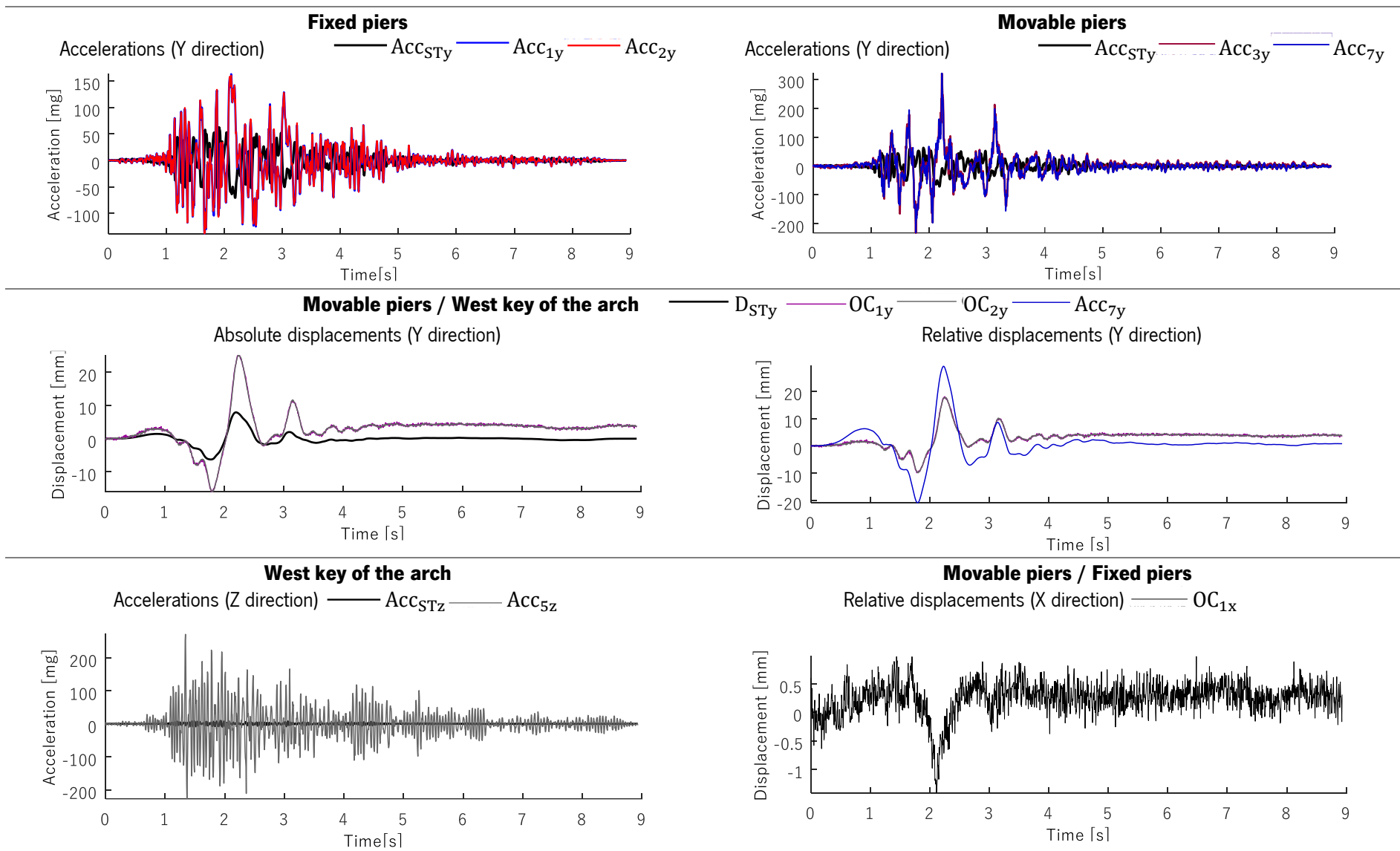


Table A2-8. Emilia earthquake 50%: collapse mechanism

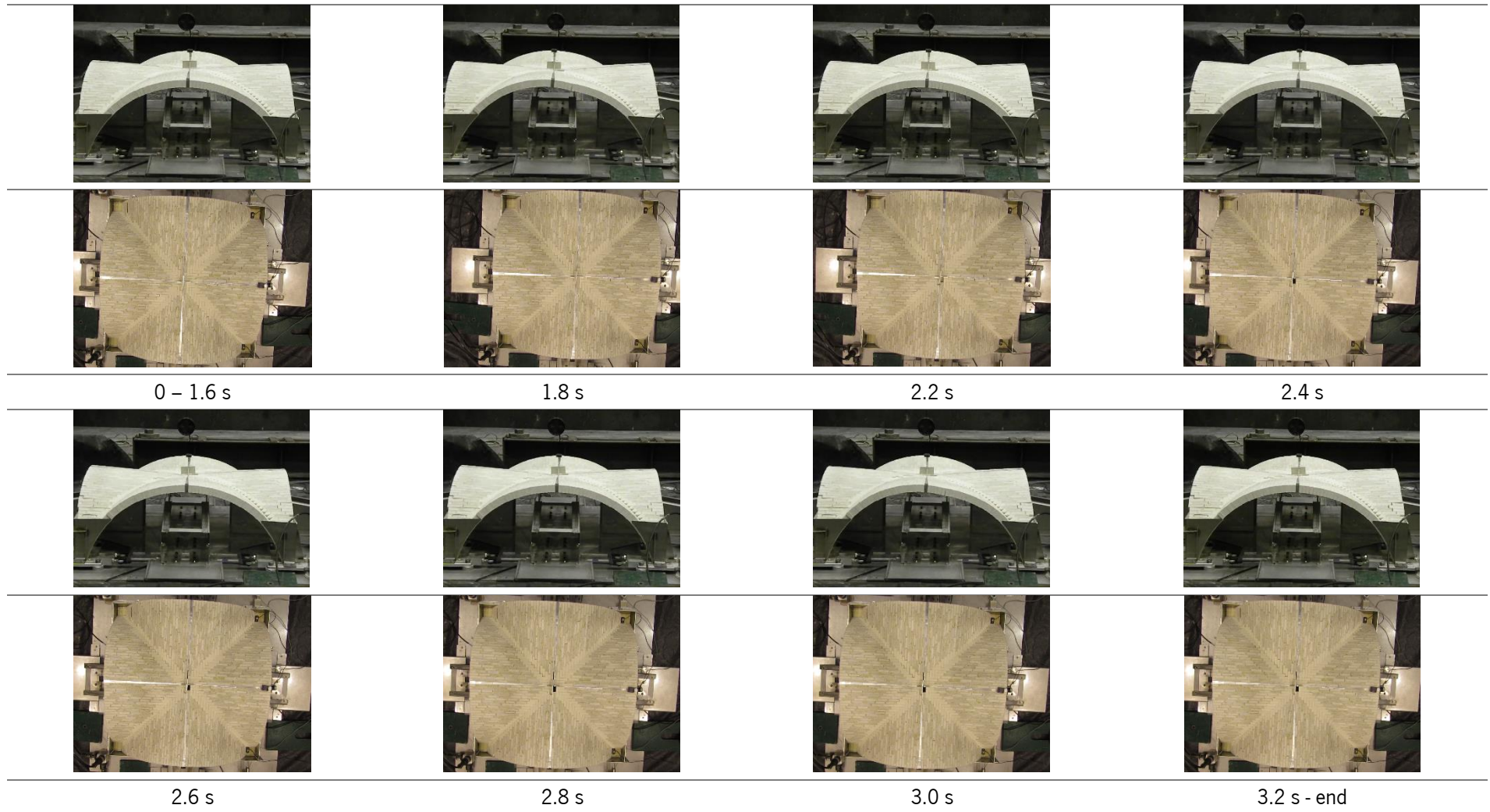
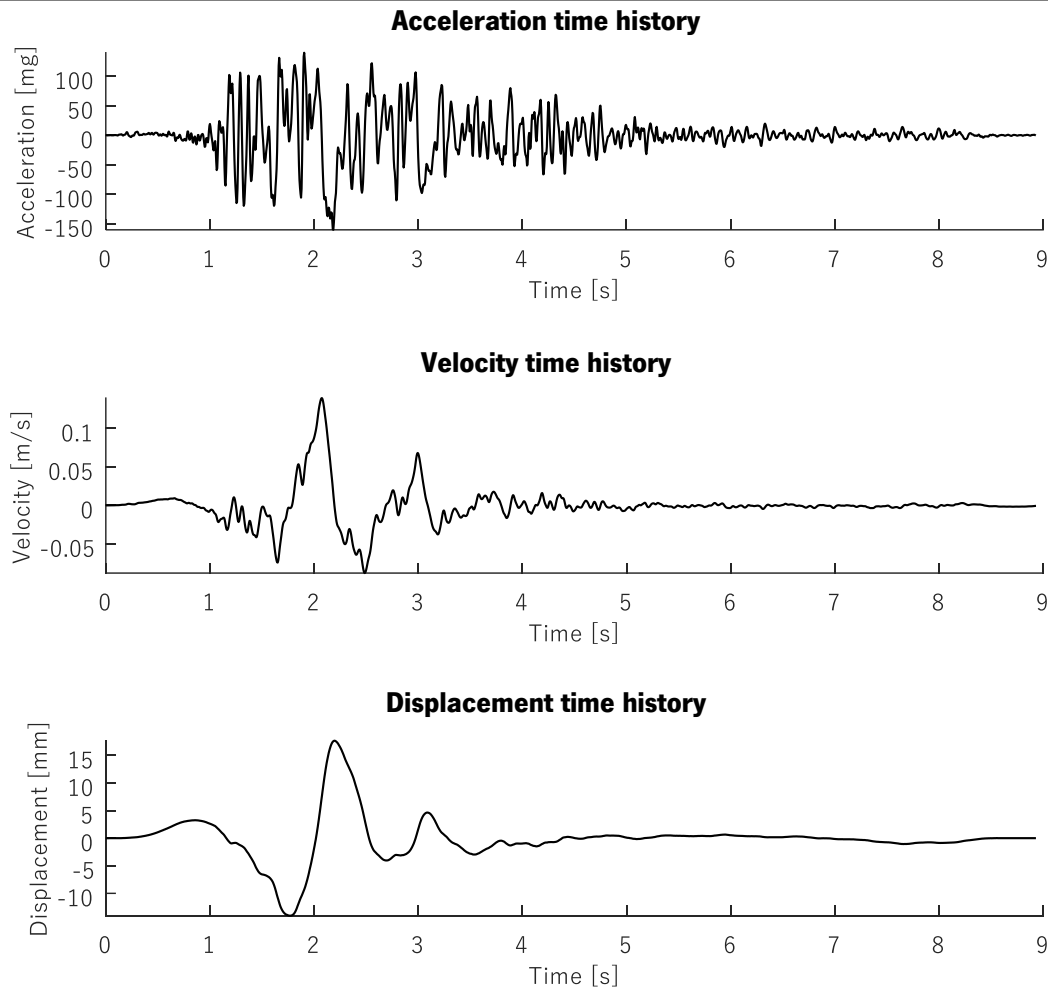


Table A2-9. Emilia earthquake 75%: input data and time histories



Peak ground variable	Root mean square variable
PGA [mg]	160.10
PGV [mm/s]	139.47
PGD [mm]	17.67

Root mean square variable	Peak ground variable
RMS _A [mg]	37.25
RMS _V [mm/s]	23.64
RMS _D [mm]	4.04

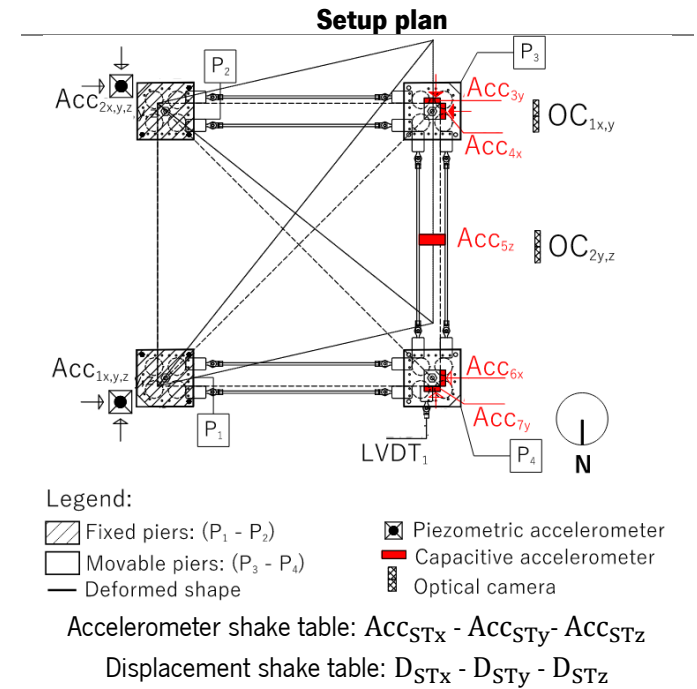


Table A2-10. Emilia earthquake 75%: response time histories

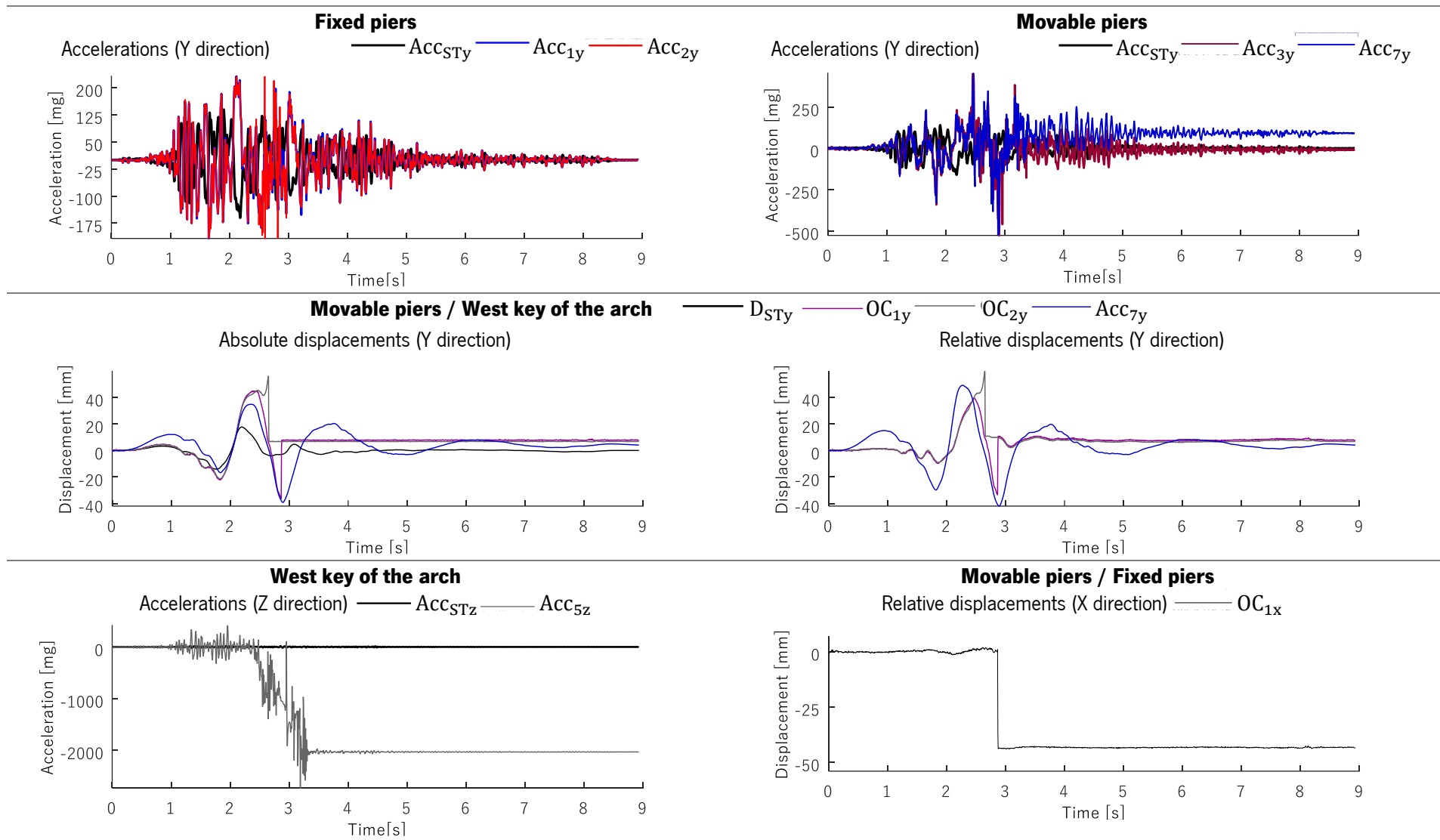


Table A2-11. Emilia earthquake 75%: collapse mechanism

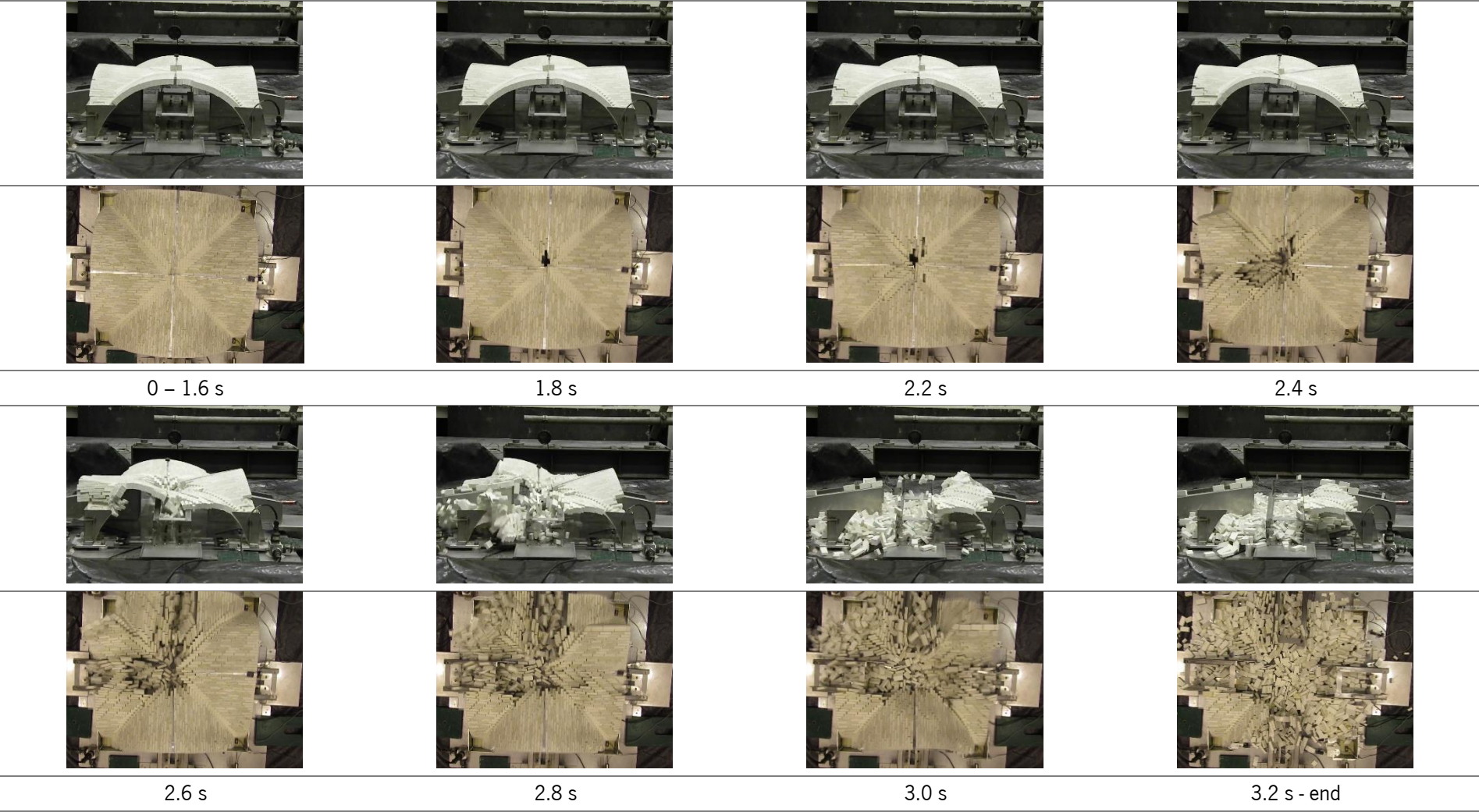
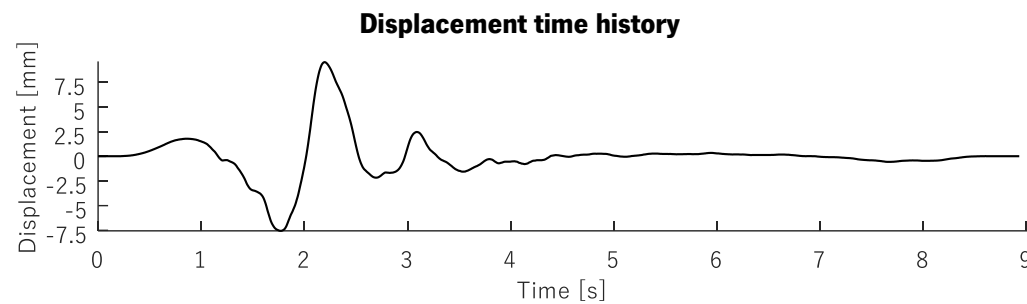
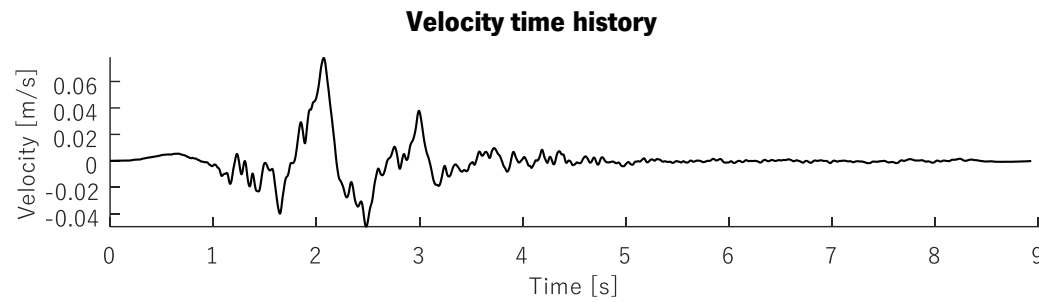
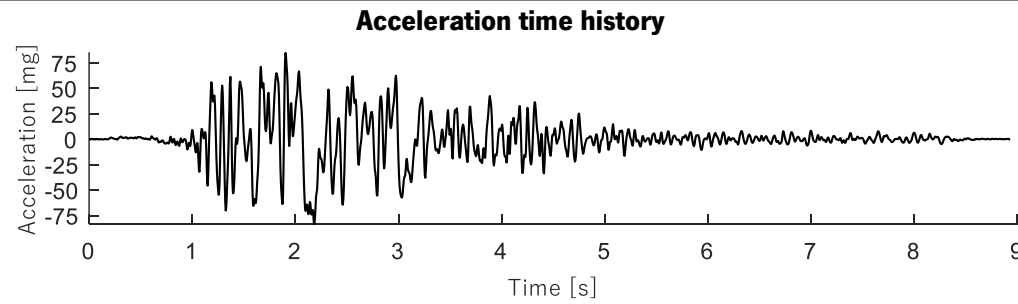
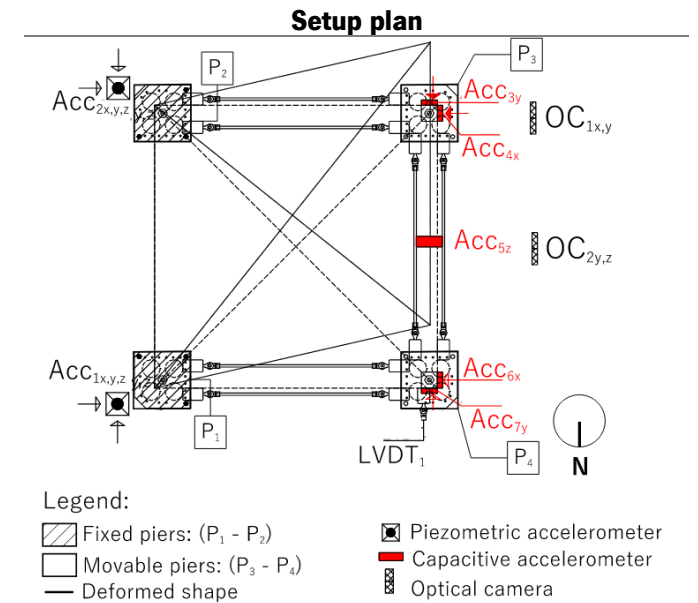


Table A2-12. Emilia earthquake 55%: input data and time histories



Peak ground variable		Root mean square variable	
PGA [mg]	84.85	RMS _A [mg]	20.44
PGV [mm/s]	77.80	RMS _V [mm/s]	12.86
PGD [mm]	9.53	RMS _D [mm]	2.18



Accelerometer shake table: Acc_{STx} - Acc_{STy} - Acc_{STz}

Displacement shake table: D_{STx} - D_{STy} - D_{STz}

Table A2-13. Emilia earthquake 55%: response time histories

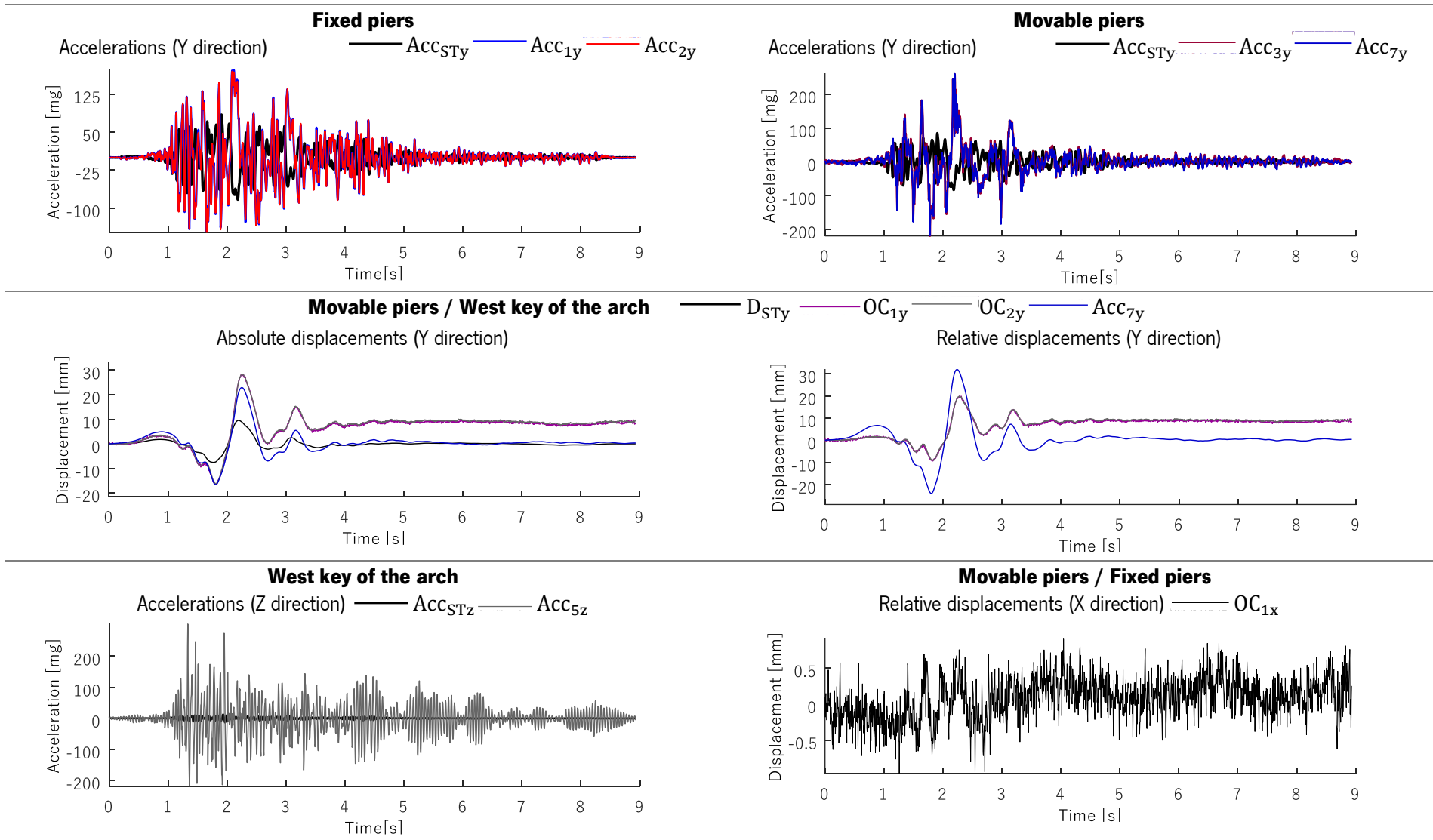


Table A2-14. Emilia earthquake 55%: collapse mechanism

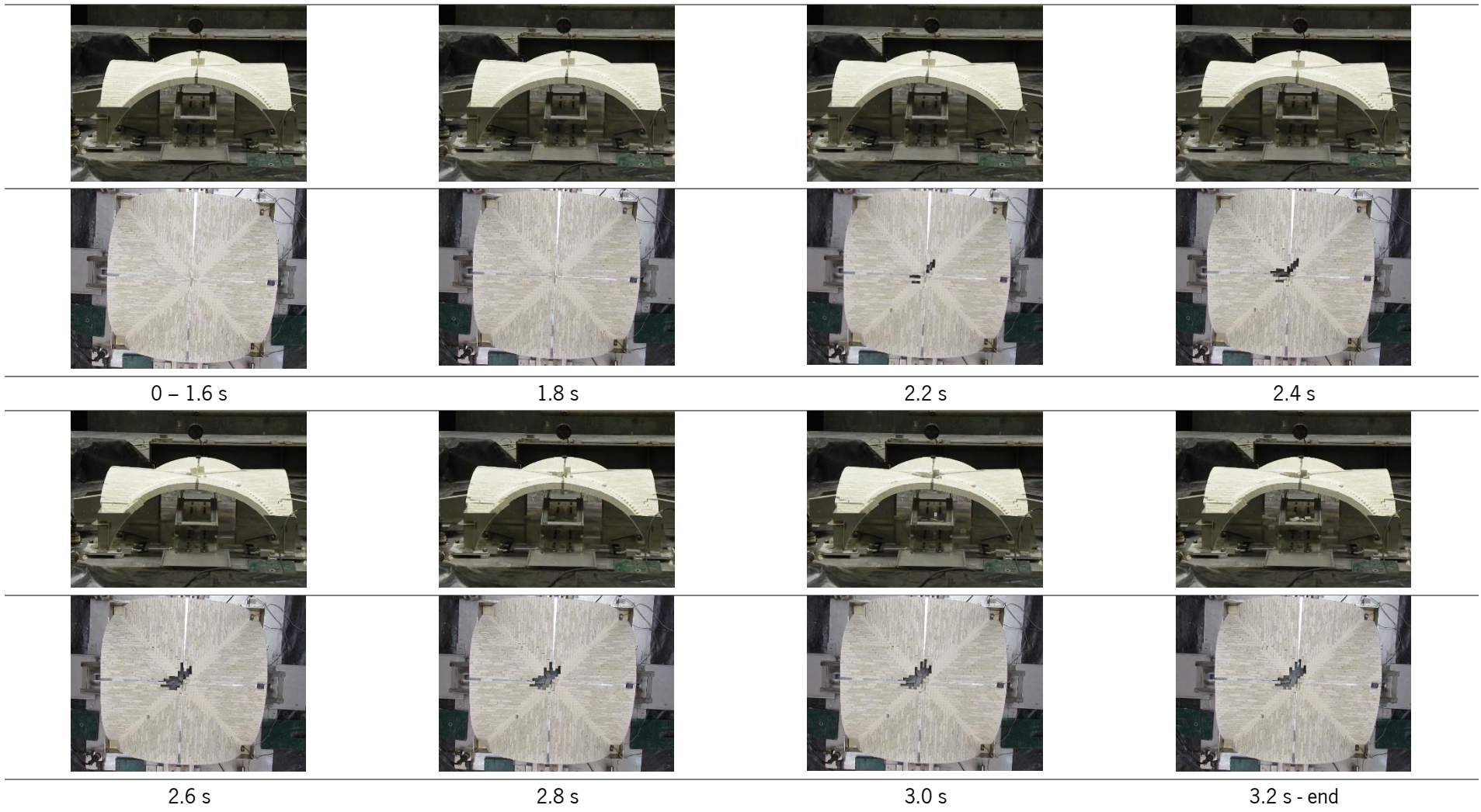
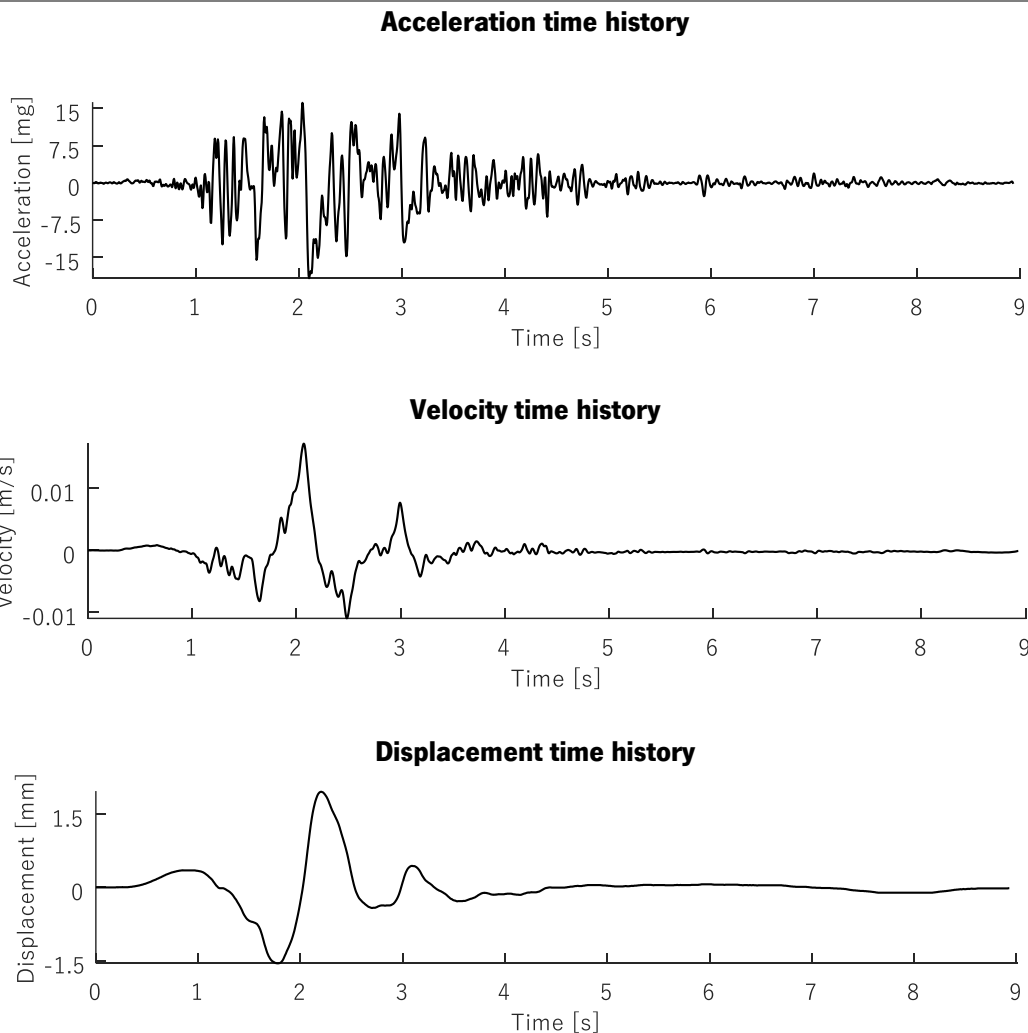


Table A2-15. Emilia earthquake after shock-25%: input data and time histories



	Peak ground variable		Root mean square variable
PGA [mg]	19.17	RMS _A [mg]	3.97
PGV [mm/s]	17.22	RMS _V [mm/s]	2.60
PGD [mm]	1.96	RMS _D [mm]	0.45

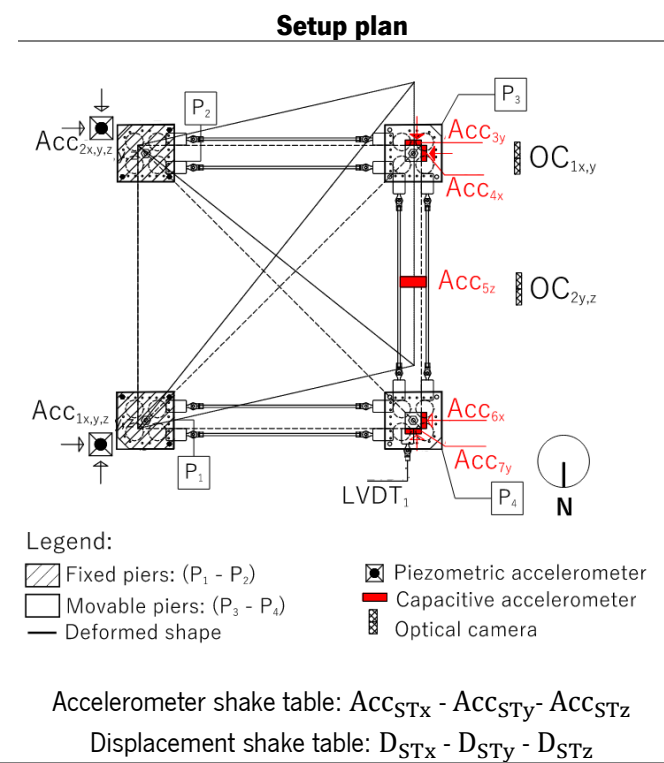


Table A2-16. Emilia earthquake after shock-25%: response time histories

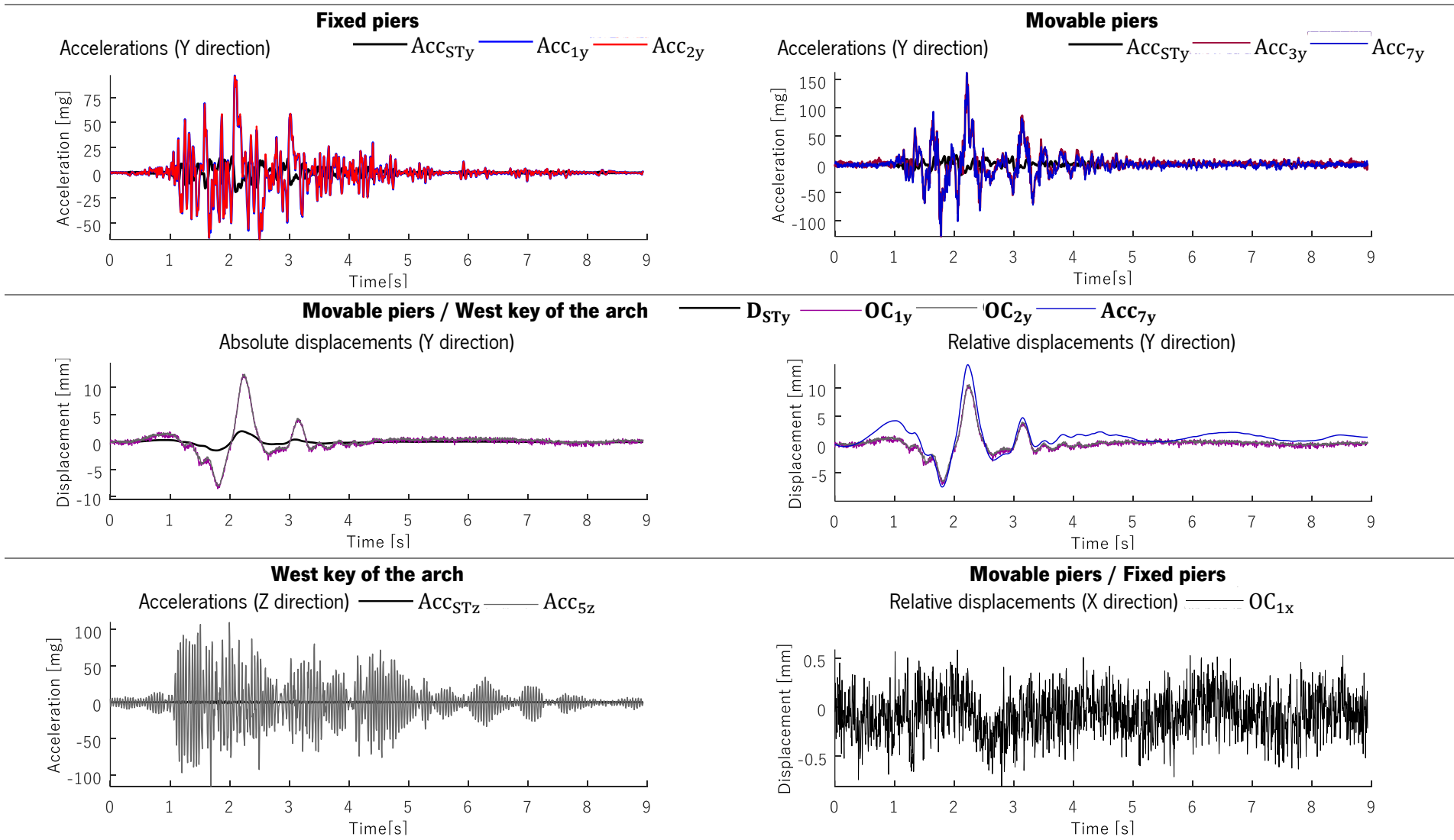


Table A2-17. Emilia earthquake after shock-25%: collapse mechanism

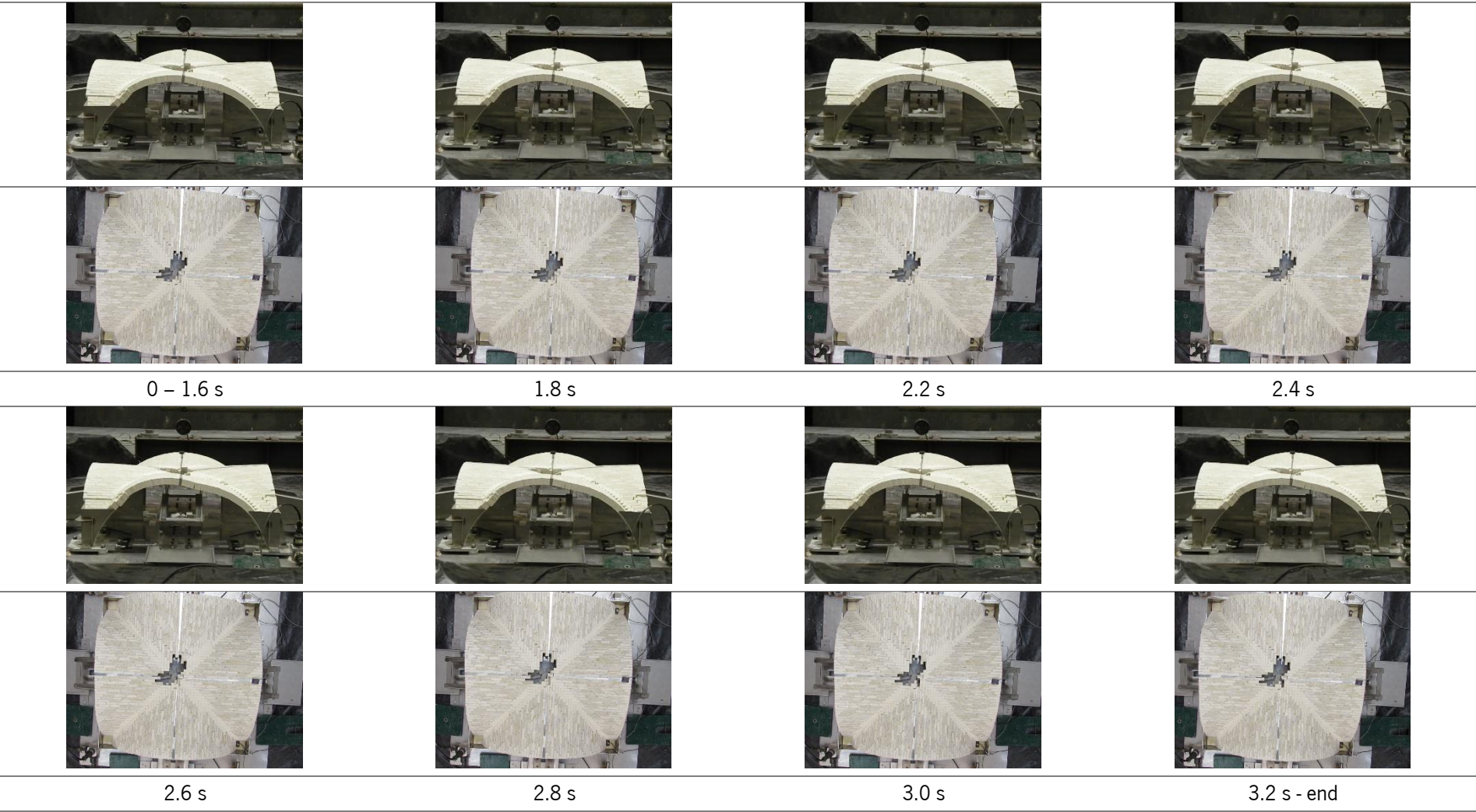
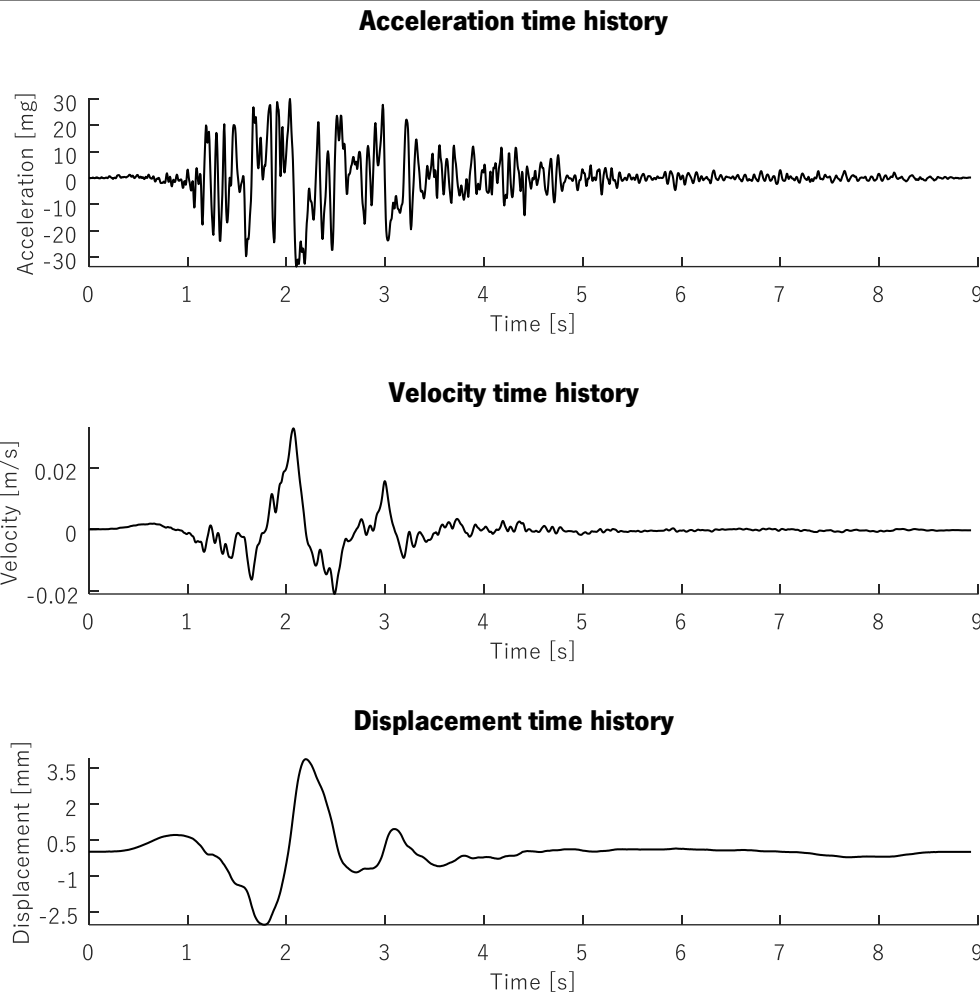


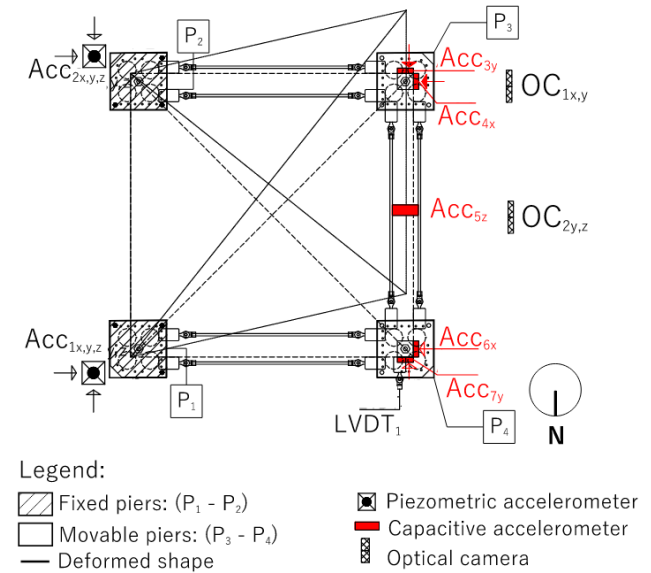
Table A2-18. Emilia earthquake after shock-35%: input data and time histories



Peak ground variable Root mean square variable

PGA [mg]	33.70	RMS _A [mg]	8.10
PGV [mm/s]	32.67	RMS _V [mm/s]	5.25
PGD [mm]	3.87	RMS _D [mm]	0.89

Setup plan



Accelerometer shake table: Acc_{STx} - Acc_{STy} - Acc_{STz}

Displacement shake table: D_{STx} - D_{STy} - D_{STz}

Table A2-19. Emilia earthquake after shock-35%: response time histories

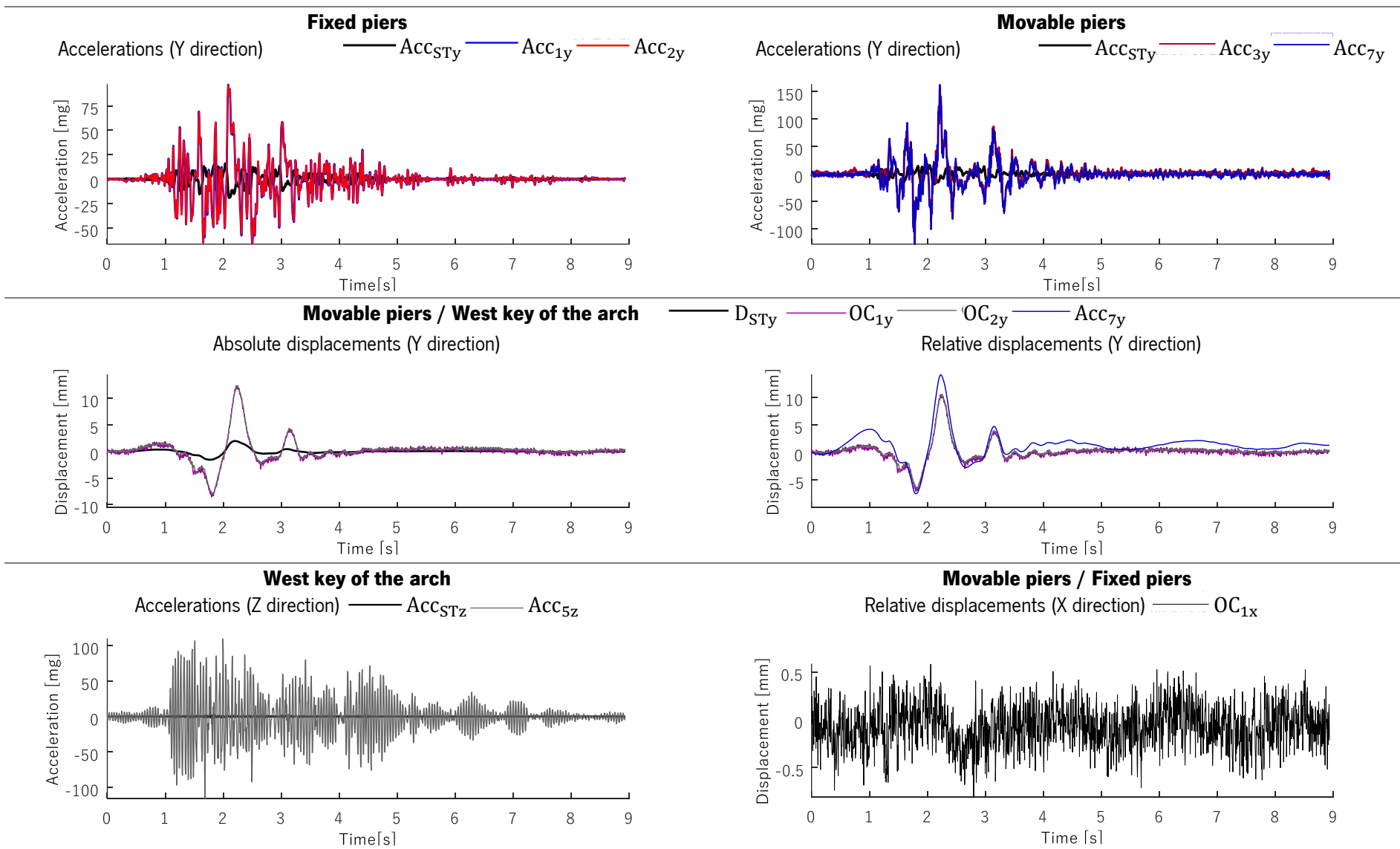


Table A2-20. Emilia earthquake after shock-35%: collapse mechanism

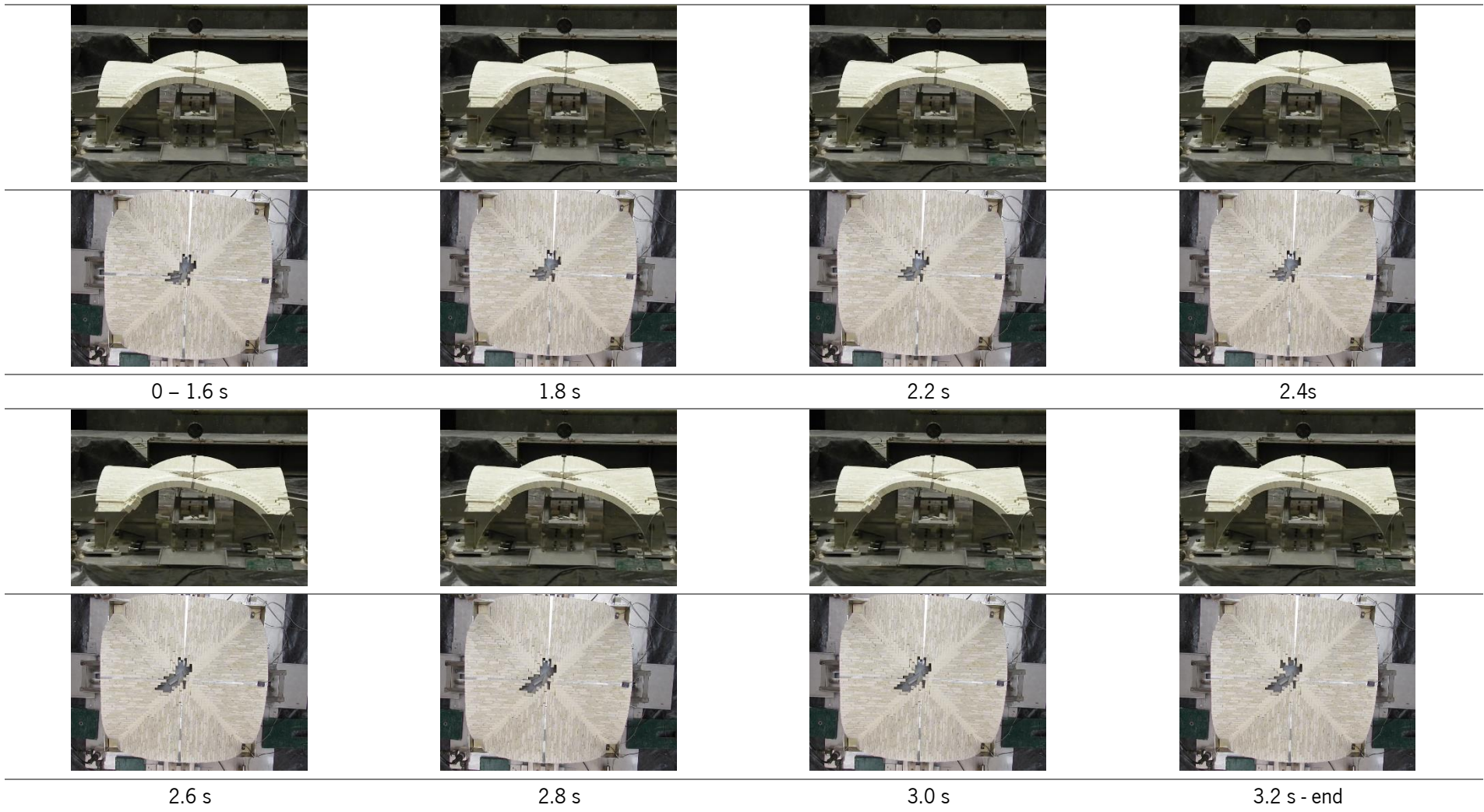
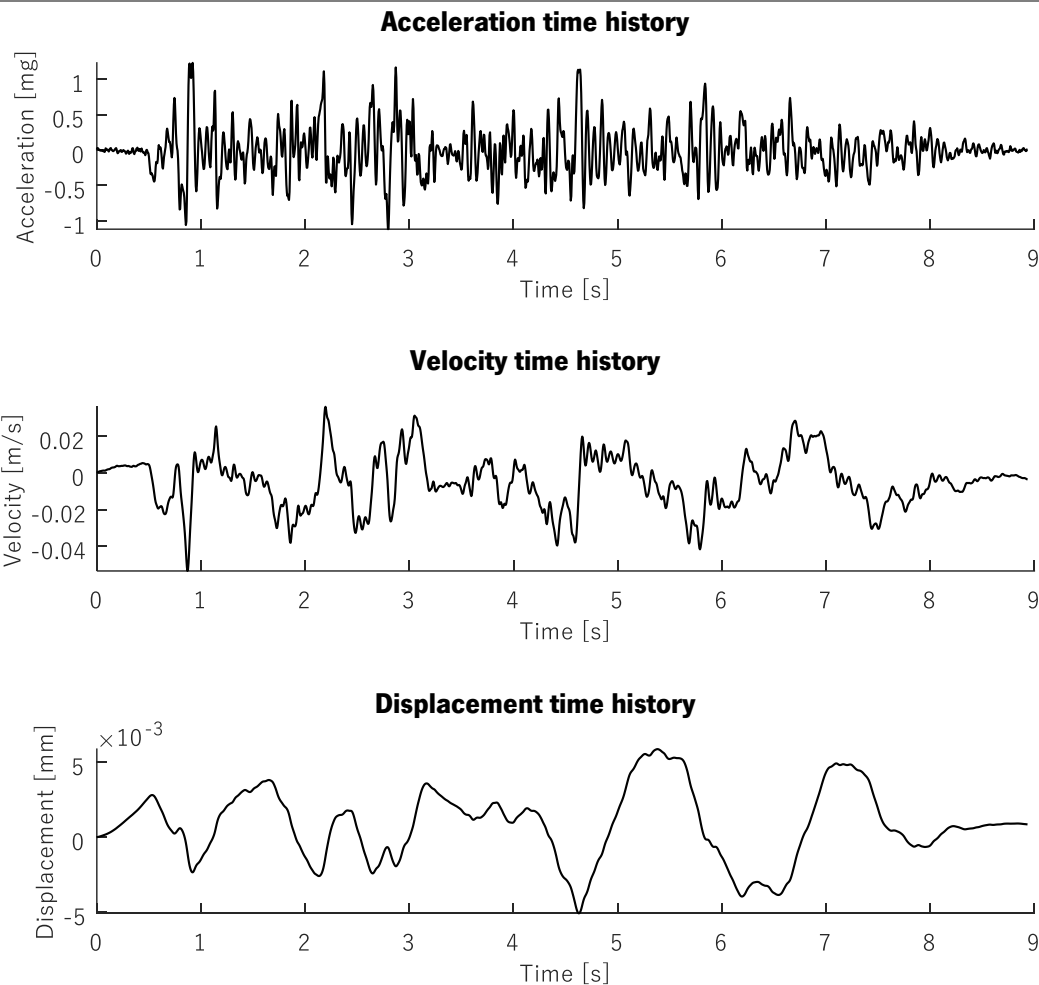
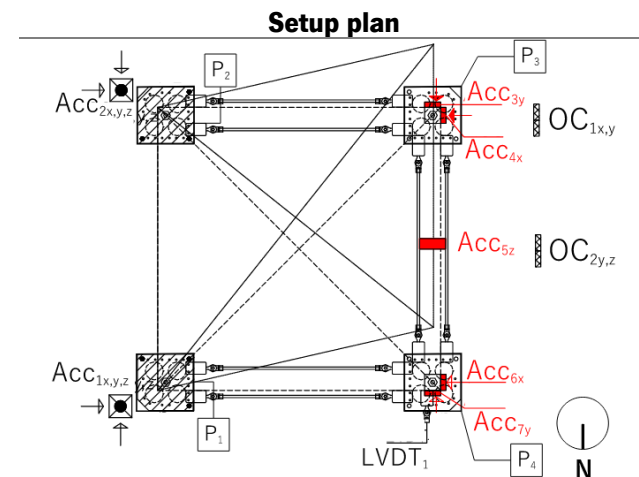


Table A2-21. Artificial earthquake 10%: input data and time histories



Peak ground variable Root mean square variable

PGA [mg]	1.23	RMS _A [mg]	0.32
PGV [mm/s]	0.53	RMS _V [mm/s]	0.14
PGD [mm]	0.16	RMS _D [mm]	0.08



Legend:

- Fixed piers: (P₁ - P₂)
- Movable piers: (P₃ - P₄)
- Deformed shape

Accelerometer shake table: Acc_{STx} - Acc_{STy} - Acc_{STz}

Displacement shake table: D_{STx} - D_{STy} - D_{STz}

Table A2-22. Artificial earthquake 10%: response time histories

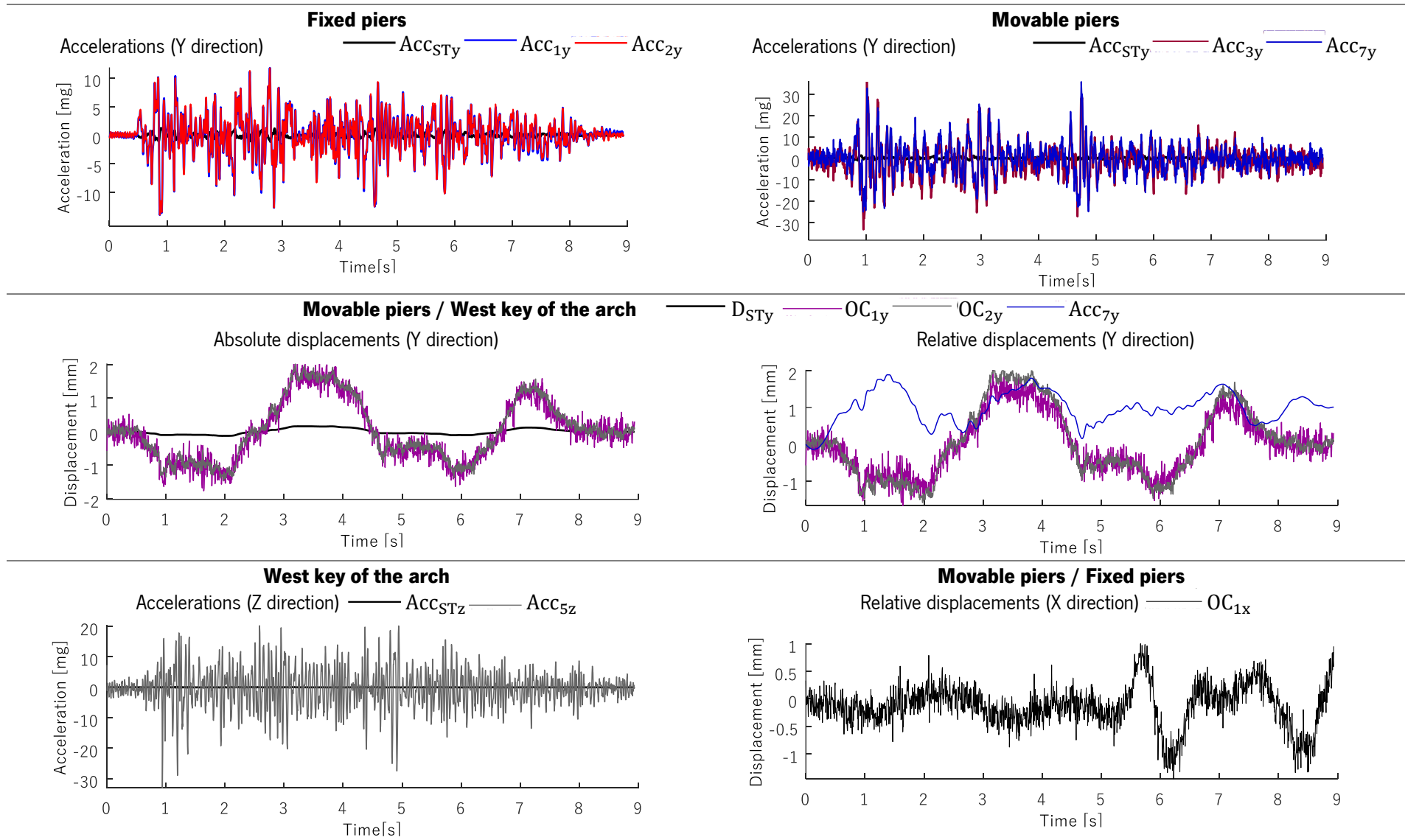
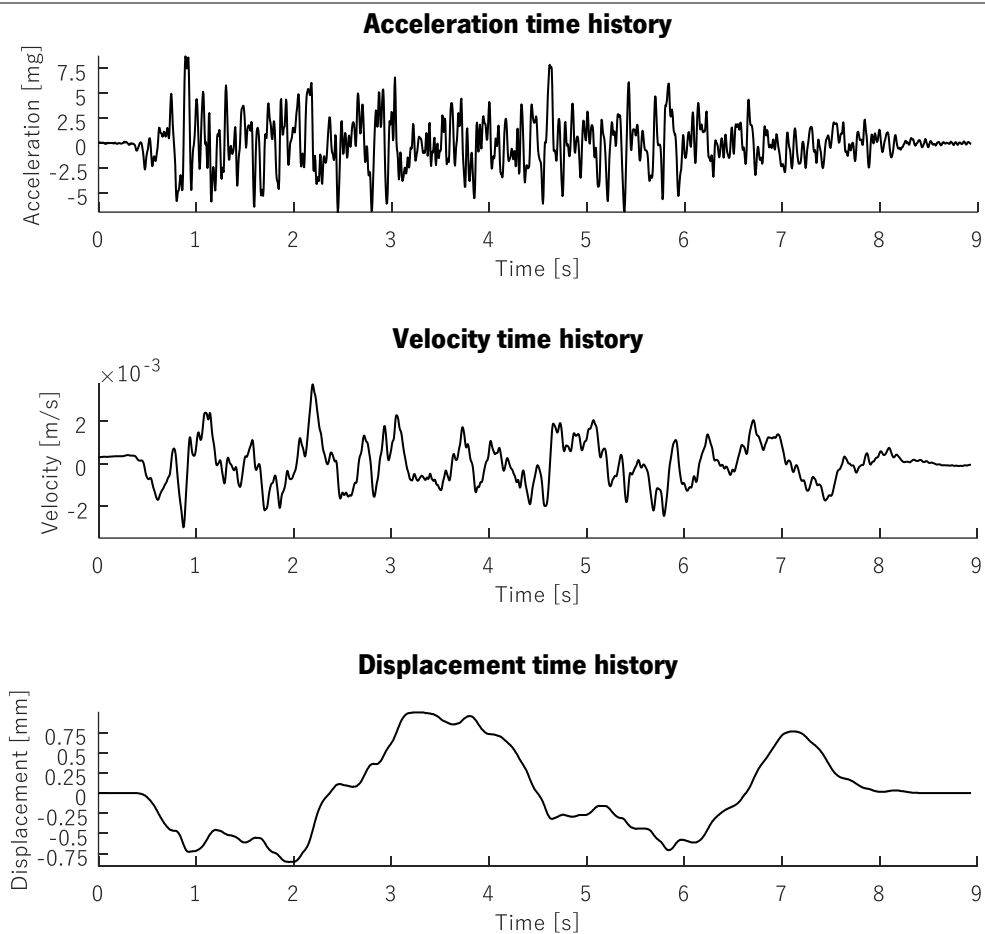
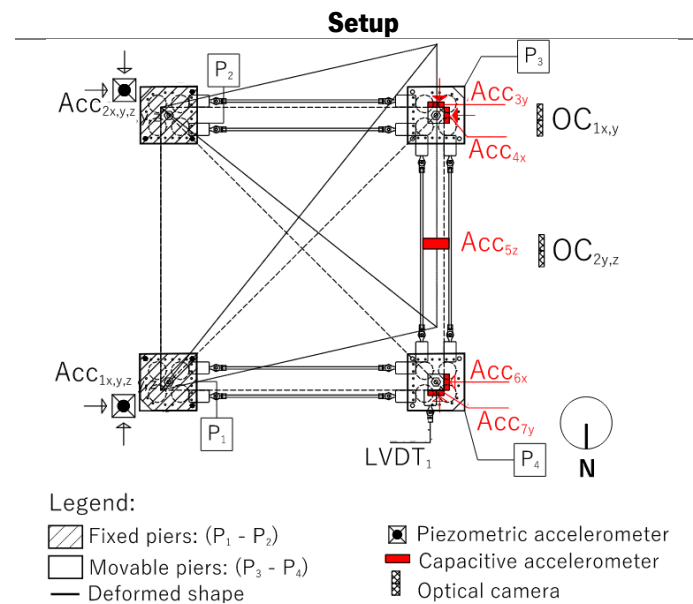


Table A2-23. Artificial earthquake 25%: input data and time histories



Peak ground variable	Root mean square variable
PGA [mg]	8.72
PGV [mm/s]	3.75
PGD [mm]	0.99

Root mean square variable	Peak ground variable
RMS _A [mg]	2.29
RMS _V [mm/s]	1.19
RMS _D [mm]	0.50



Accelerometer shake table: Acc_{STx} - Acc_{STy} - Acc_{STz}
 Displacement shake table: D_{STx} - D_{STy} - D_{STz}

Table A2-24. Artificial earthquake 25%: response time histories

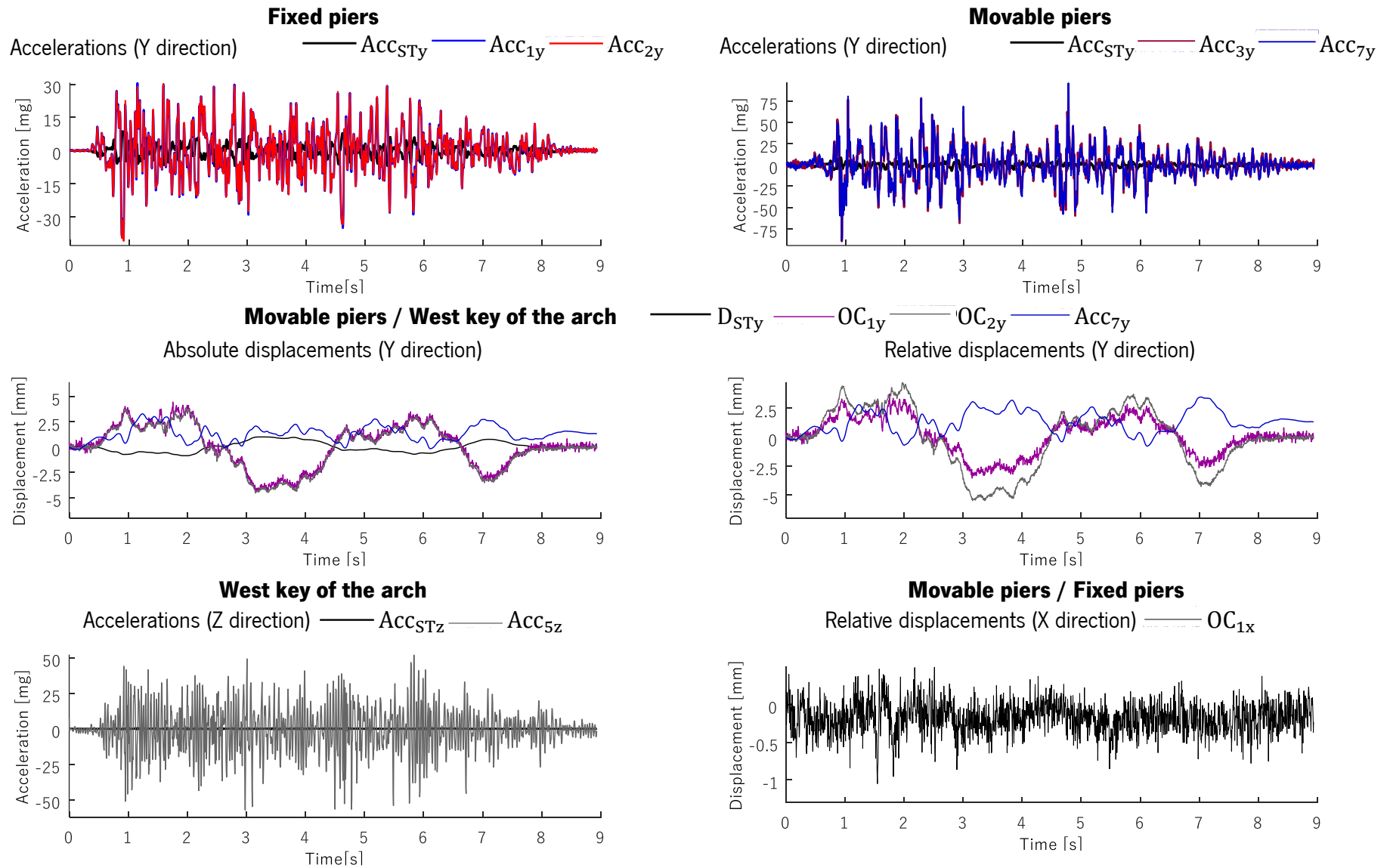
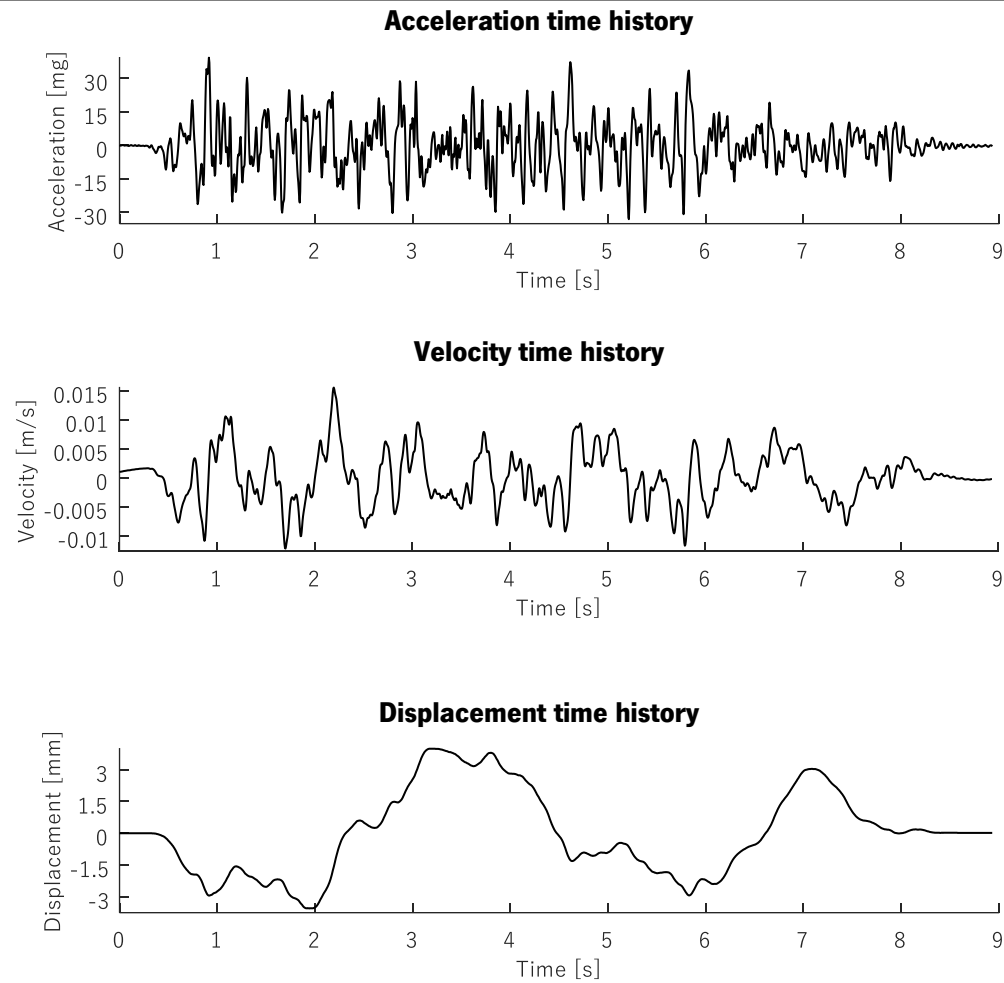
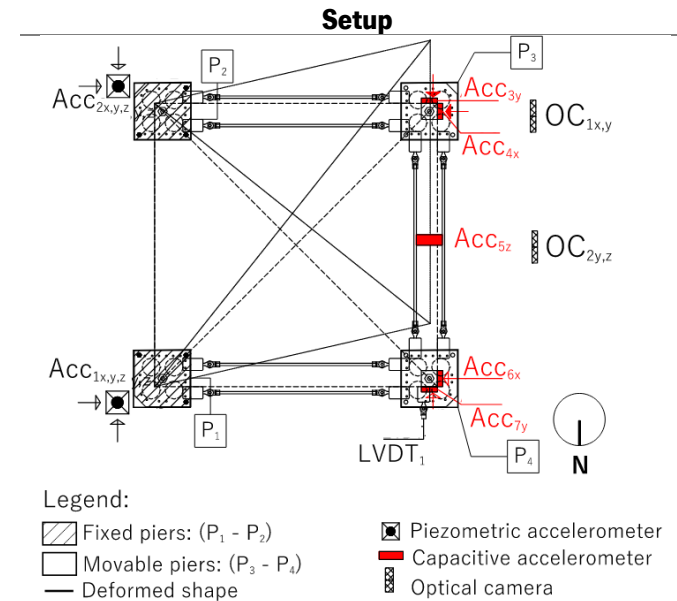


Table A2-25. Artificial earthquake 50%: input data and time histories



Peak ground variable Root mean square variable

PGA [mg]	39.30	RMS _A [mg]	10.60
PGV [mm/s]	14.52	RMS _V [mm/s]	4.86
PGD [mm]	3.99	RMS _D [mm]	1.99



Accelerometer shake table: Acc_{STx} - Acc_{STy} - Acc_{STz}

Displacement shake table: D_{STx} - D_{STy} - D_{STz}

Table A2-26. Artificial earthquake 50%: response time histories

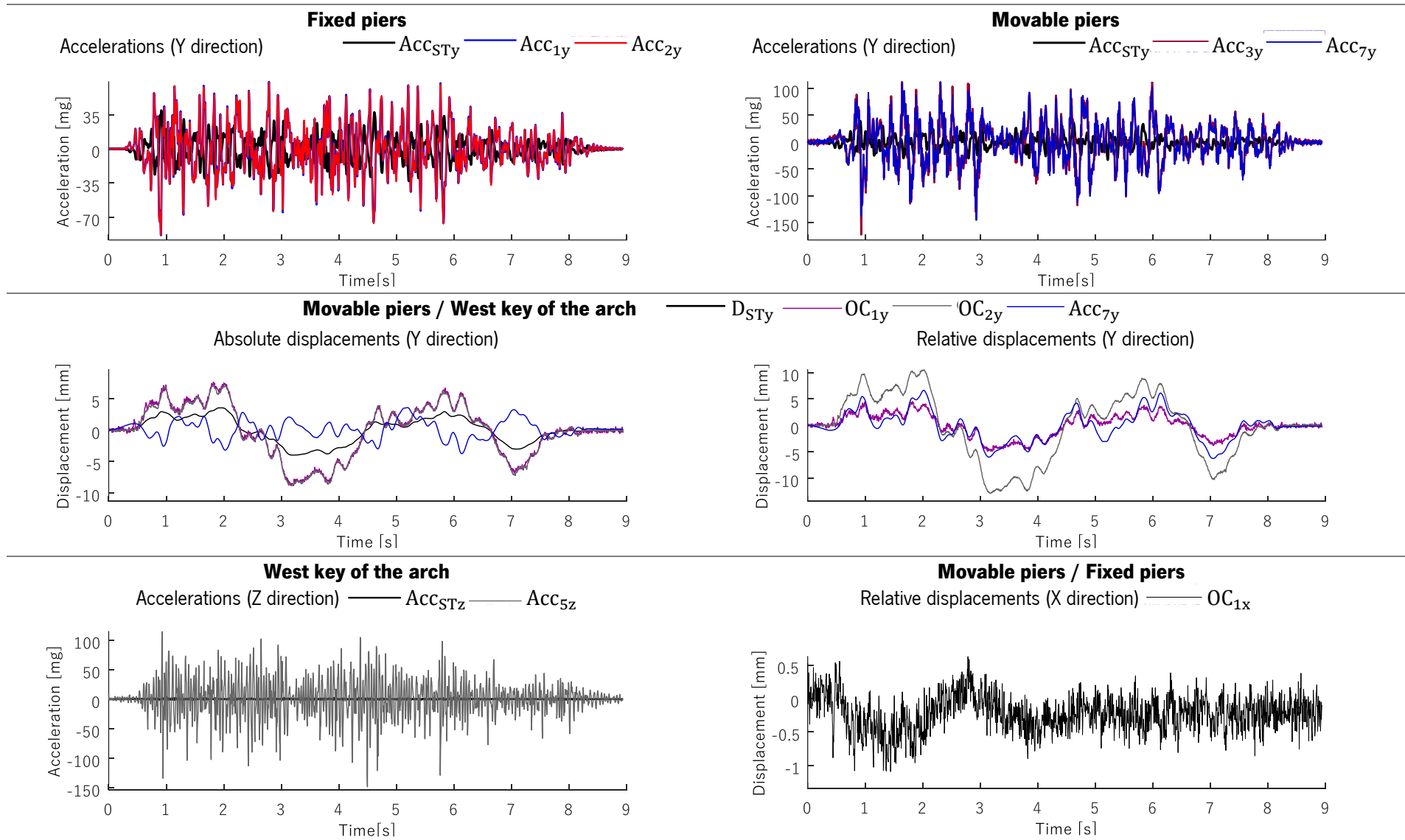
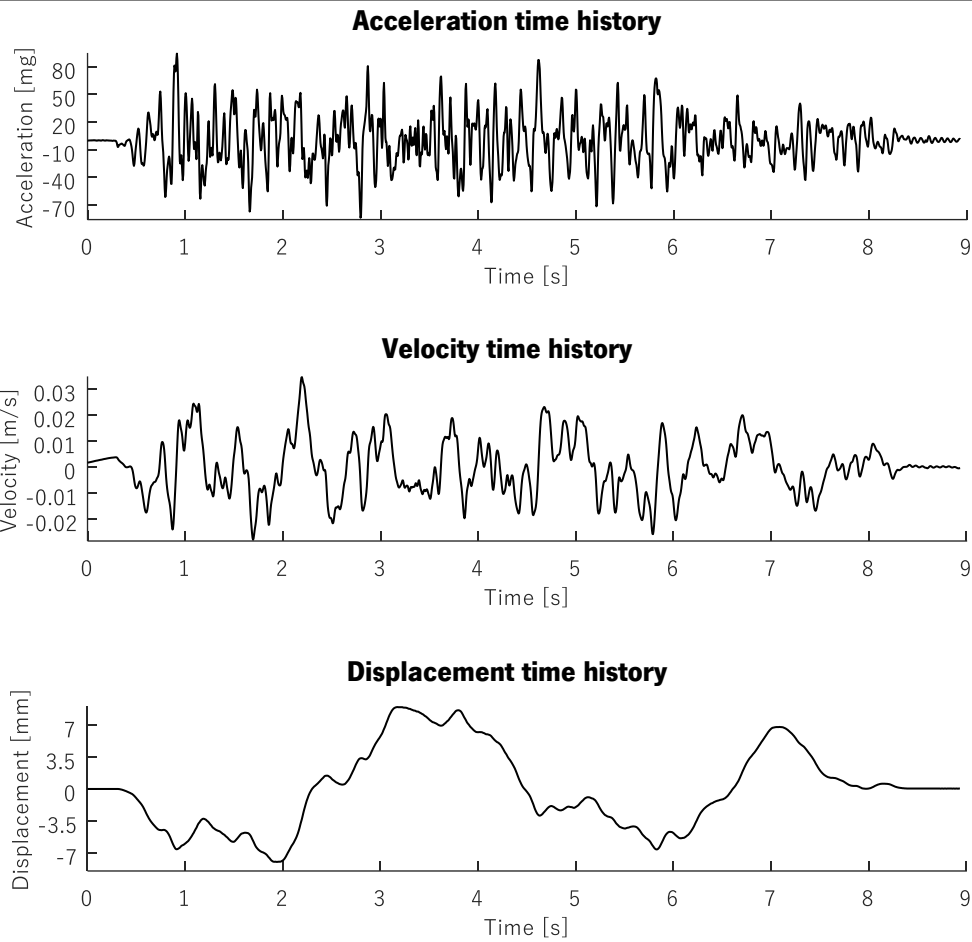


Table A2-27. Artificial earthquake 75%: input data and time histories



Peak ground variable Root mean square variable

PGA [mg]	94.27	RMS _A [mg]	25.37
PGV [mm/s]	32.47	RMS _V [mm/s]	10.99
PGD [mm]	8.99	RMS _D [mm]	4.44

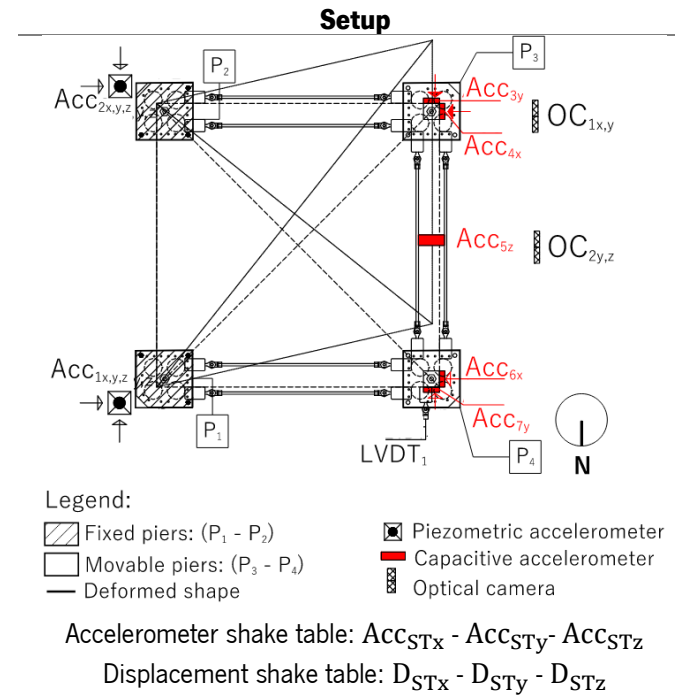


Table A2-28. Artificial earthquake 75%: response time histories

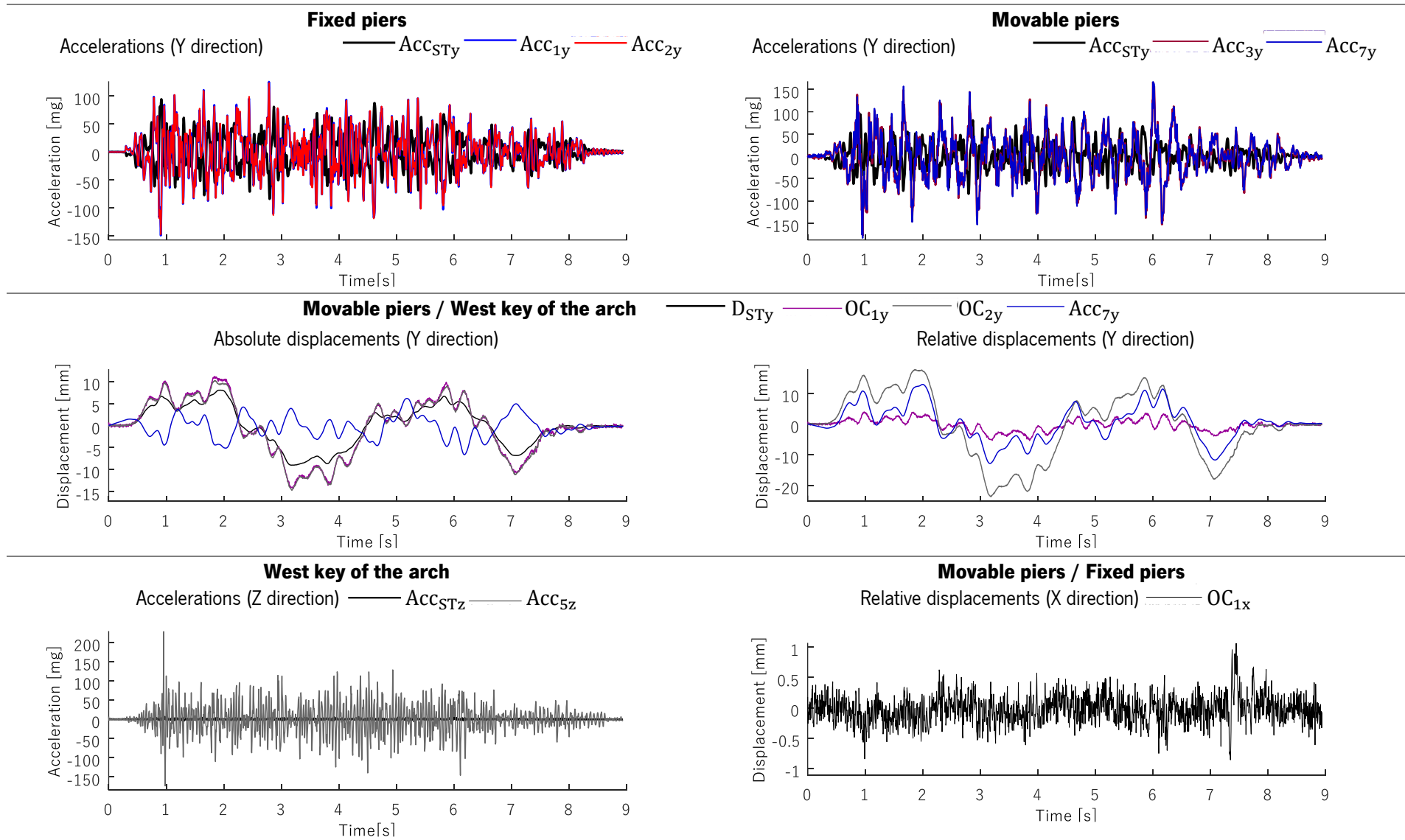
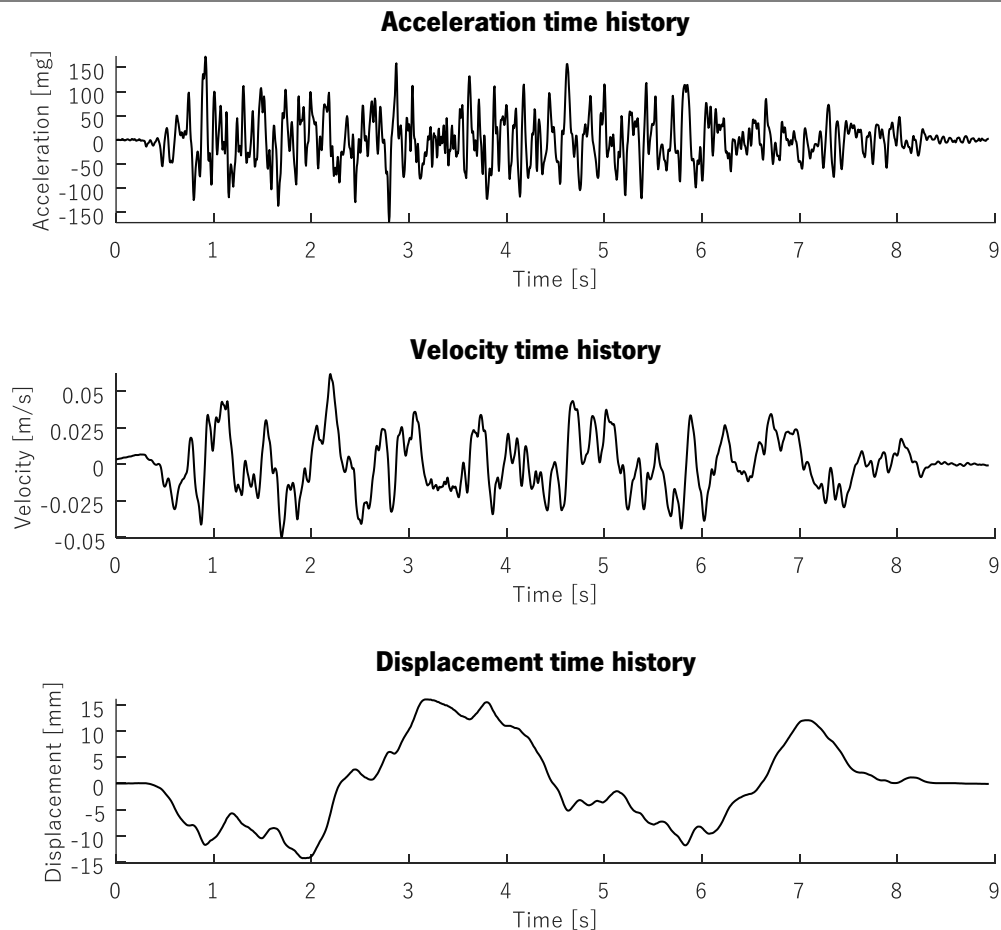


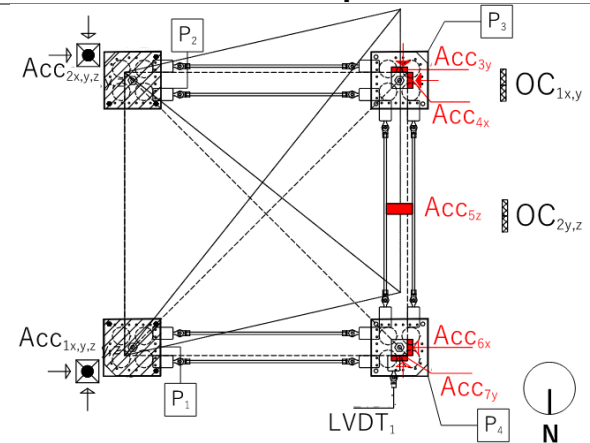
Table A2-29. Artificial earthquake 100%: input data and time histories



Peak ground variable Root mean square variable

PGA [mg]	172.30	RMS _A [mg]	46.75
PGV [mm/s]	58.15	RMS _V [mm/s]	19.85
PGD [mm]	16.10	RMS _D [mm]	7.87

Setup



Legend:

- Fixed piers: (P₁ - P₂)
- Movable piers: (P₃ - P₄)
- Deformed shape
- Piezometric accelerometer
- Capacitive accelerometer
- Optical camera

Accelerometer shake table: ACC_{STx} - ACC_{STy} - ACC_{STz}

Displacement shake table: D_{STx} - D_{STy} - D_{STz}

Table A2-30. Artificial earthquake 100%: response time histories

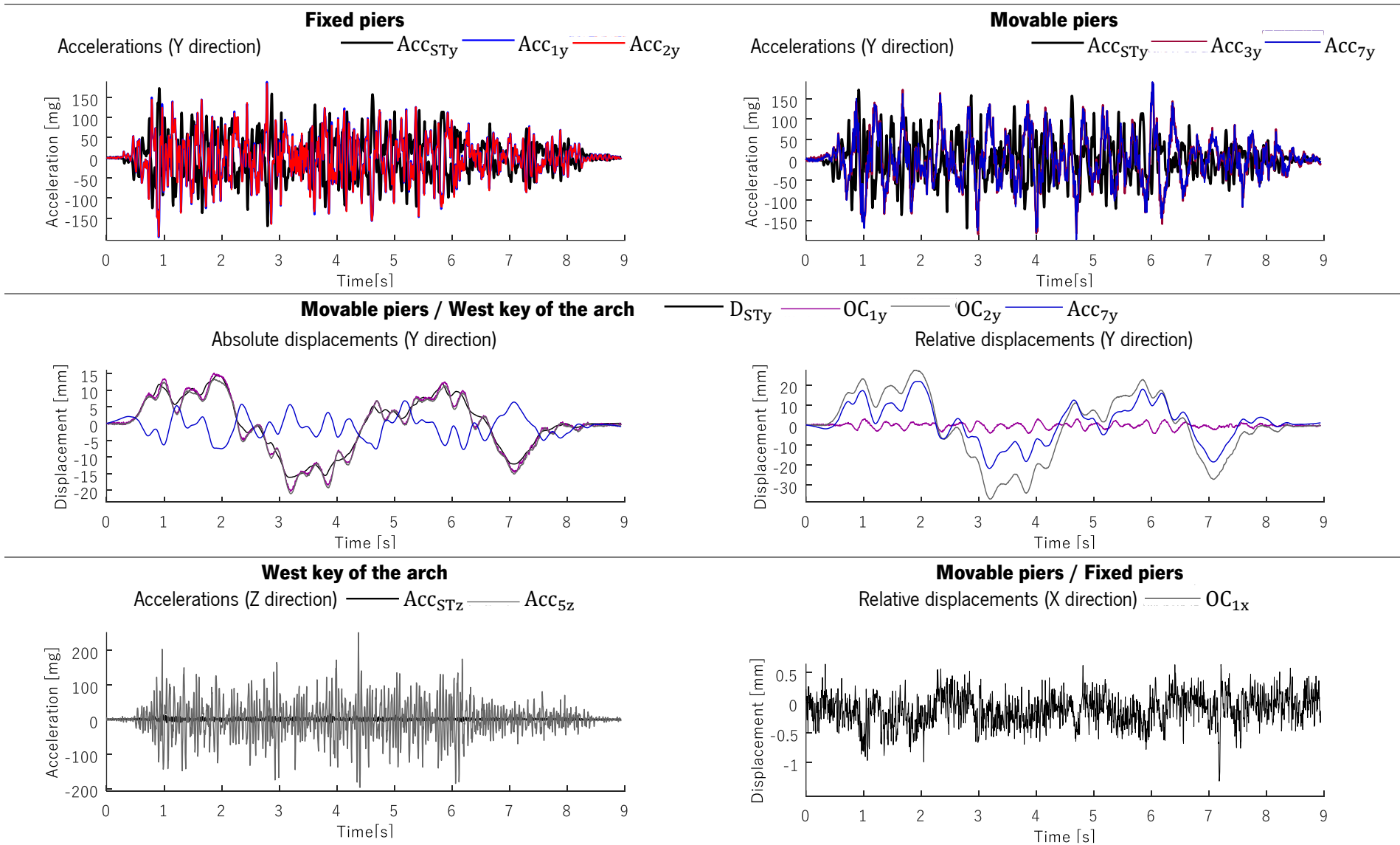
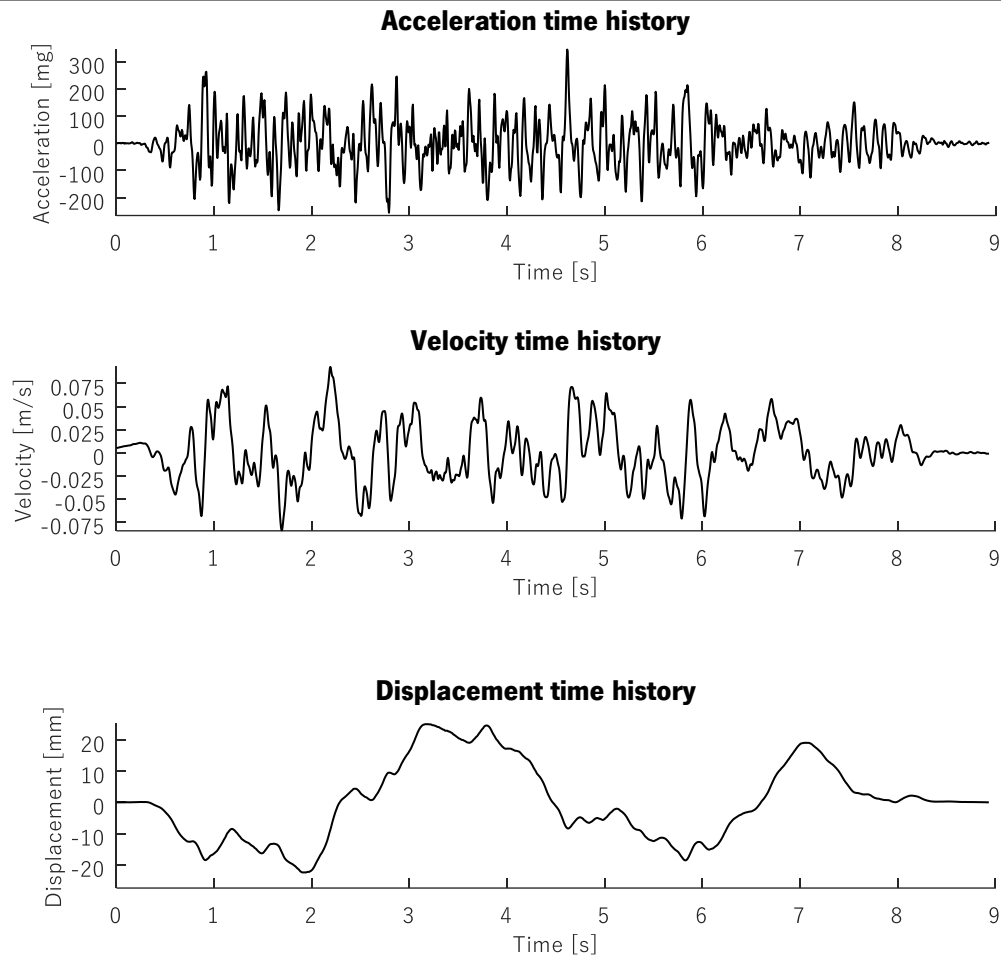


Table A2-31. Artificial earthquake 125%: input data and time histories



Peak ground variable Root mean square variable

PGA [mg]	344.19	RMS _A [mg]	79.97
PGV [mm/s]	95.80	RMS _V [mm/s]	31.82
PGD [mm]	25.07	RMS _D [mm]	12.28

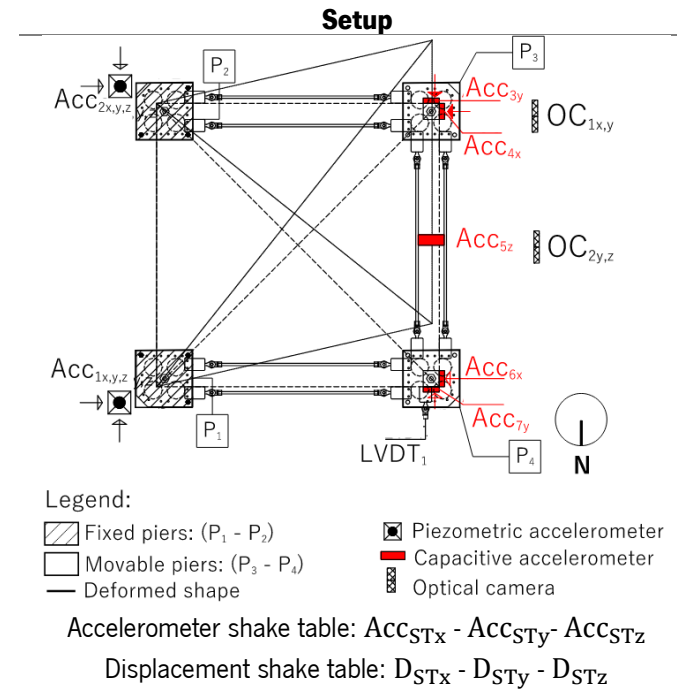


Table A2-32. Artificial earthquake 125%: response time histories

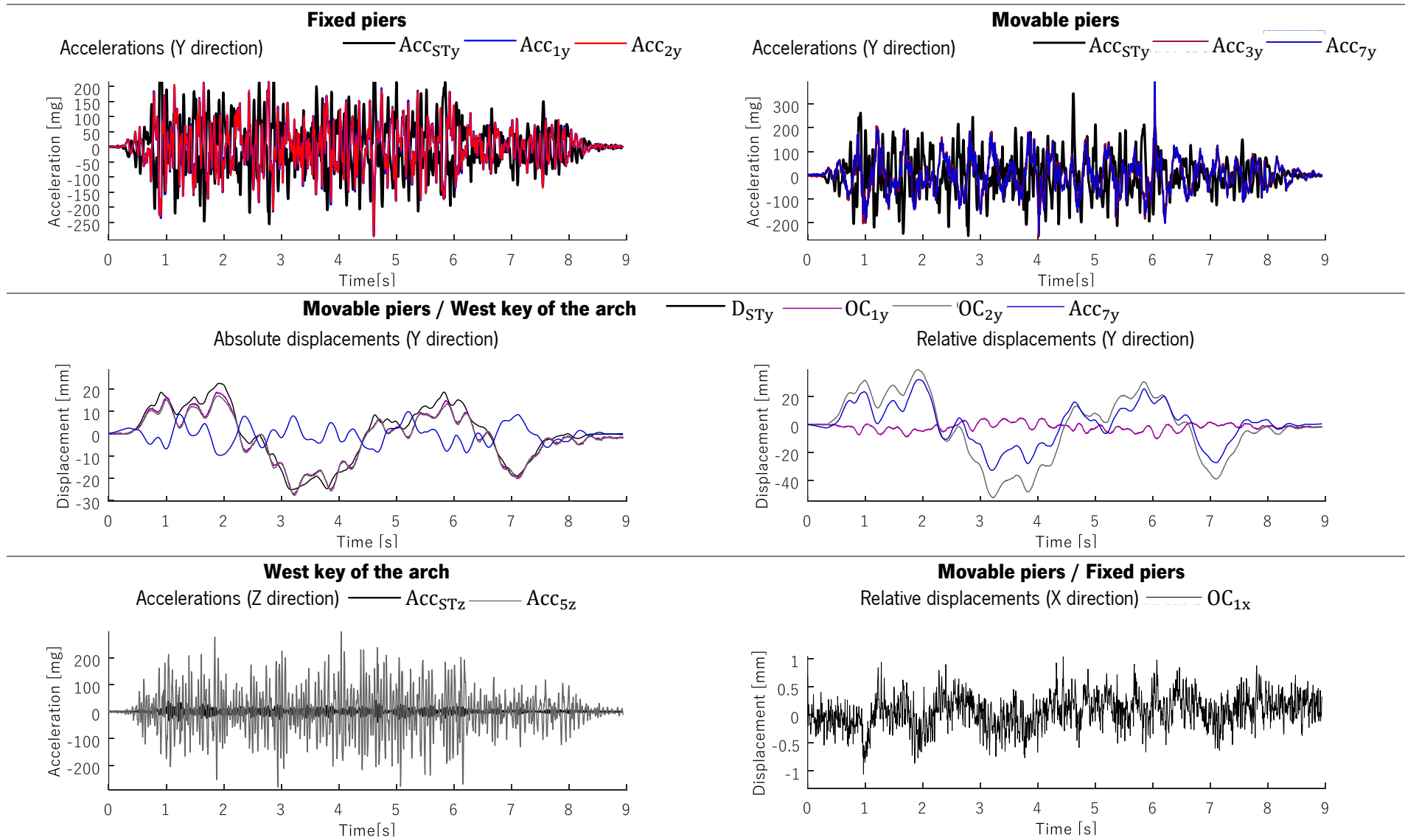


Table A2-33. Artificial earthquake 125%: collapse mechanism

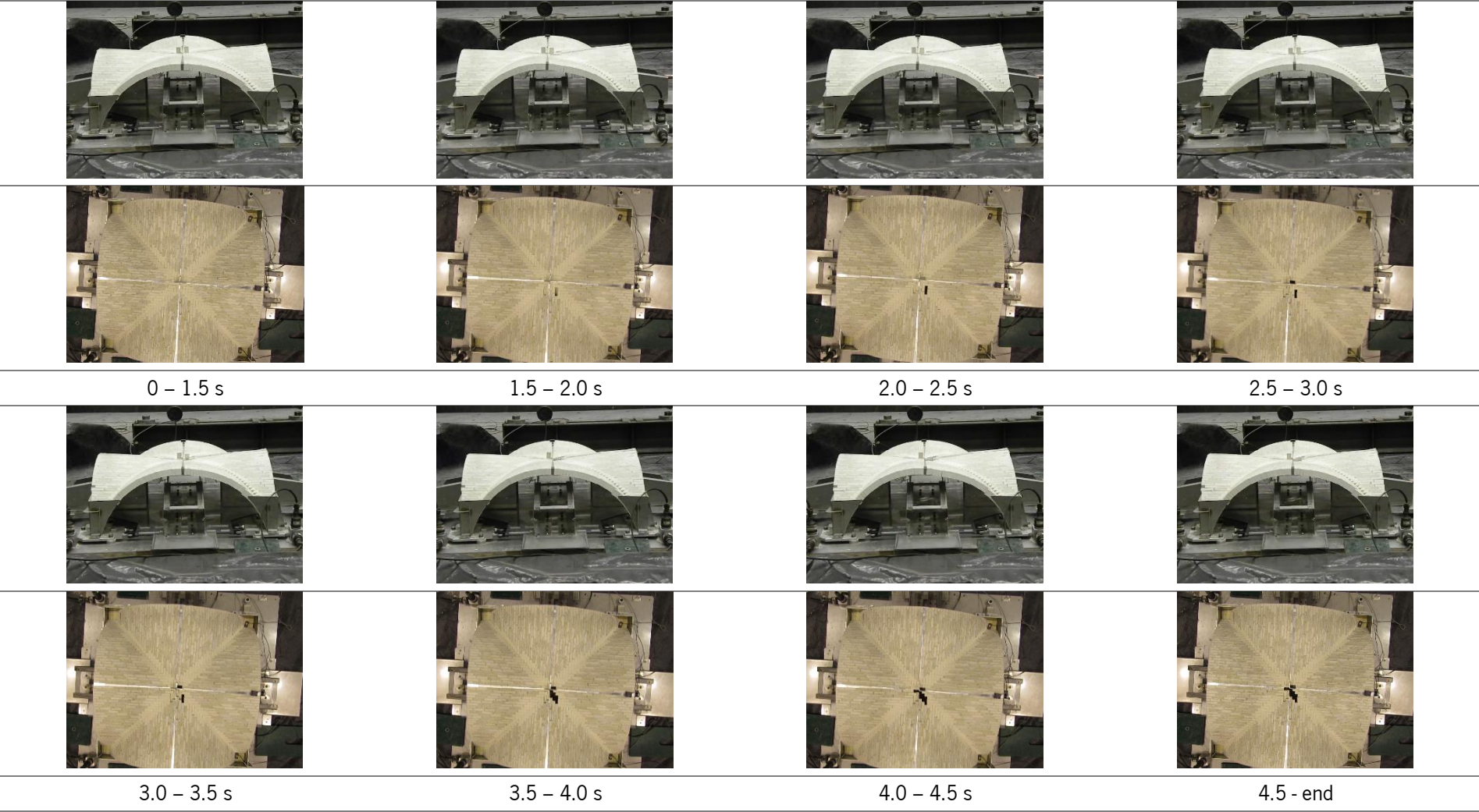
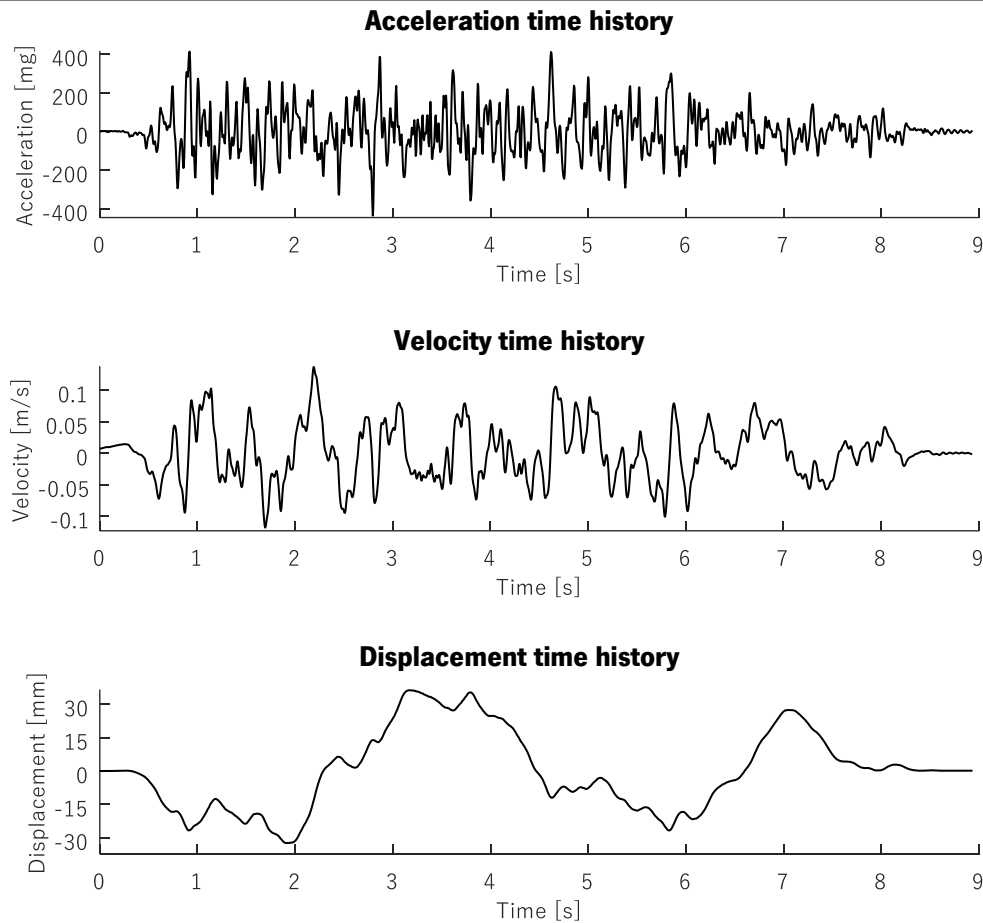


Table A2-34. Artificial earthquake 150%: input data and time histories



Peak ground variable		Root mean square variable	
PGA [mg]	435.12	RMS _A [mg]	110.46
PGV [mm/s]	135.72	RMS _V [mm/s]	45.57
PGD [mm]	36.27	RMS _D [mm]	17.69

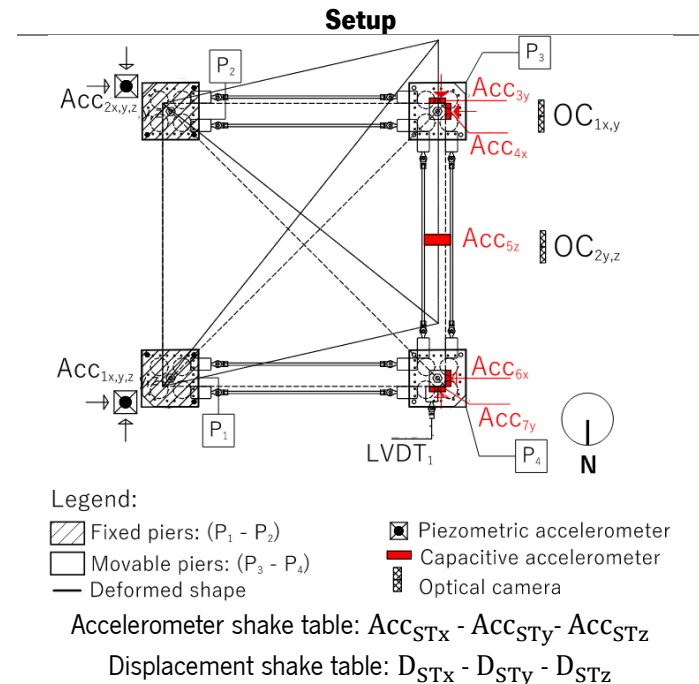


Table A2-35. Artificial earthquake 150%: response time histories

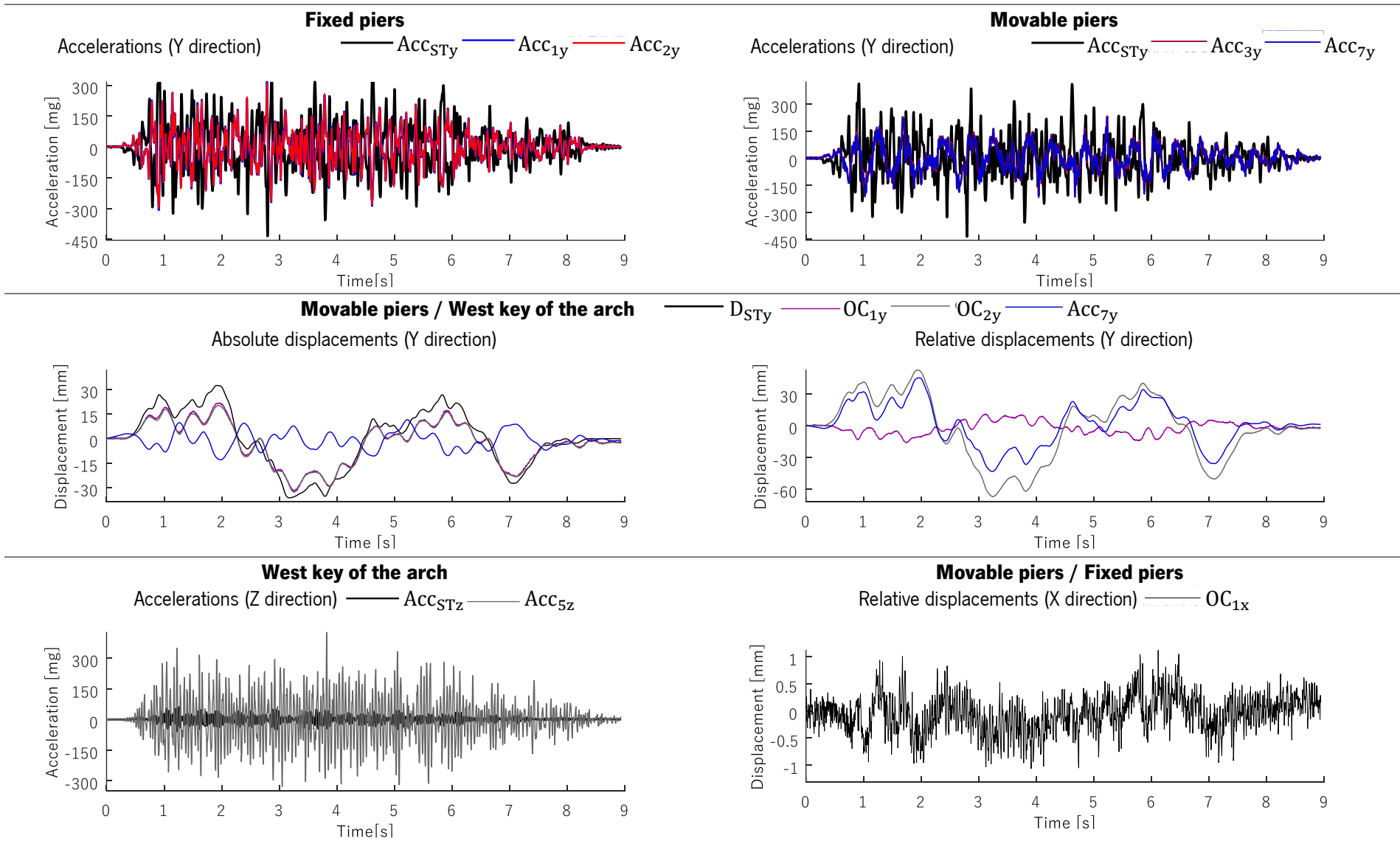


Table A2-36. Artificial earthquake 150%: collapse mechanism

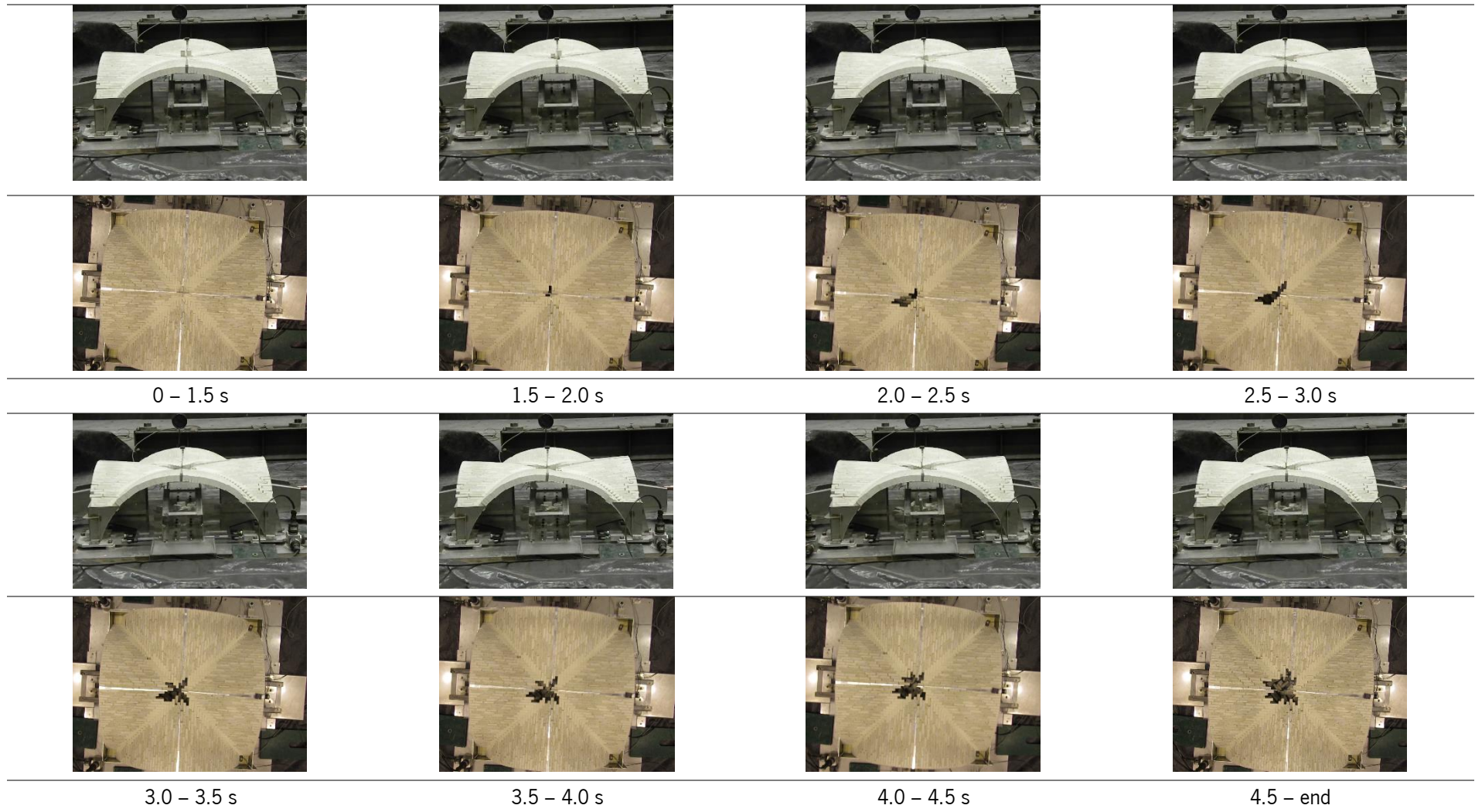
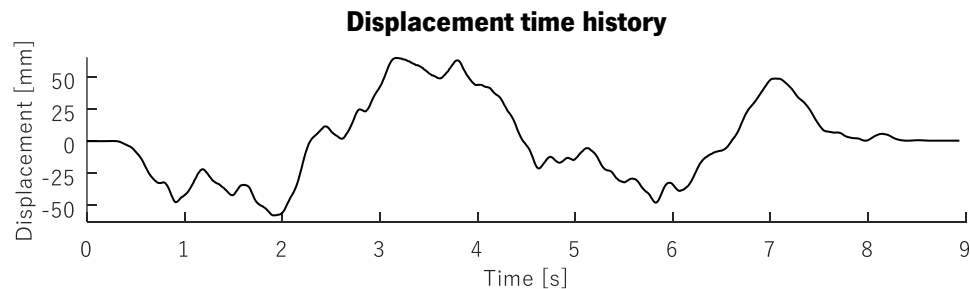
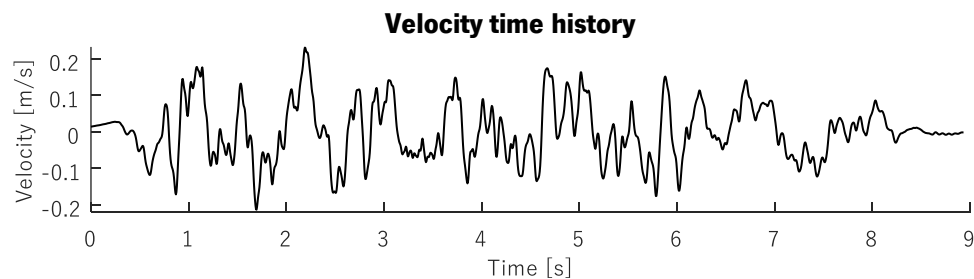
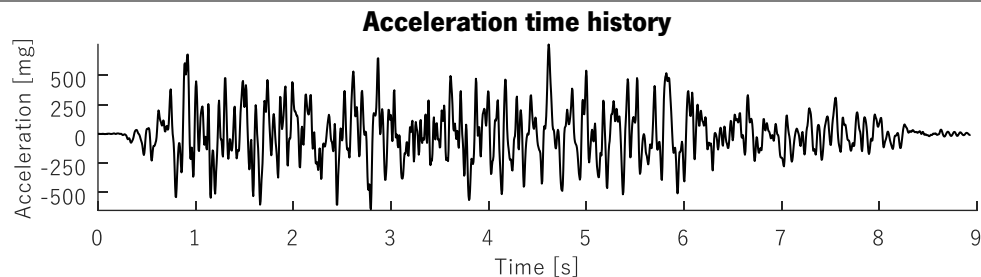


Table A2-37. Artificial earthquake 200%: input data and time histories



Peak ground variable		Root mean square variable	
PGA [mg]	763.66	RMS _A [mg]	201.90
PGV [mm/s]	241.21	RMS _V [mm/s]	80.56
PGD [mm]	64.70	RMS _D [mm]	31.45

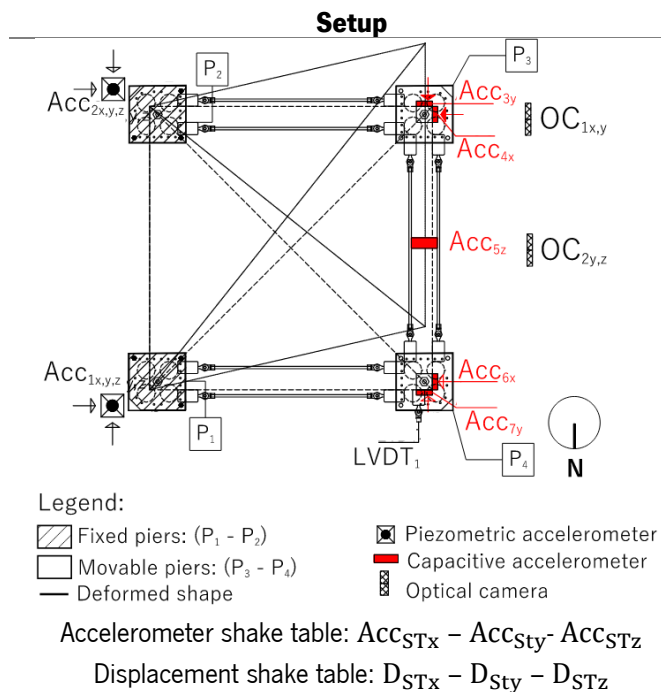


Table A2-38. Artificial earthquake 200%: response time histories

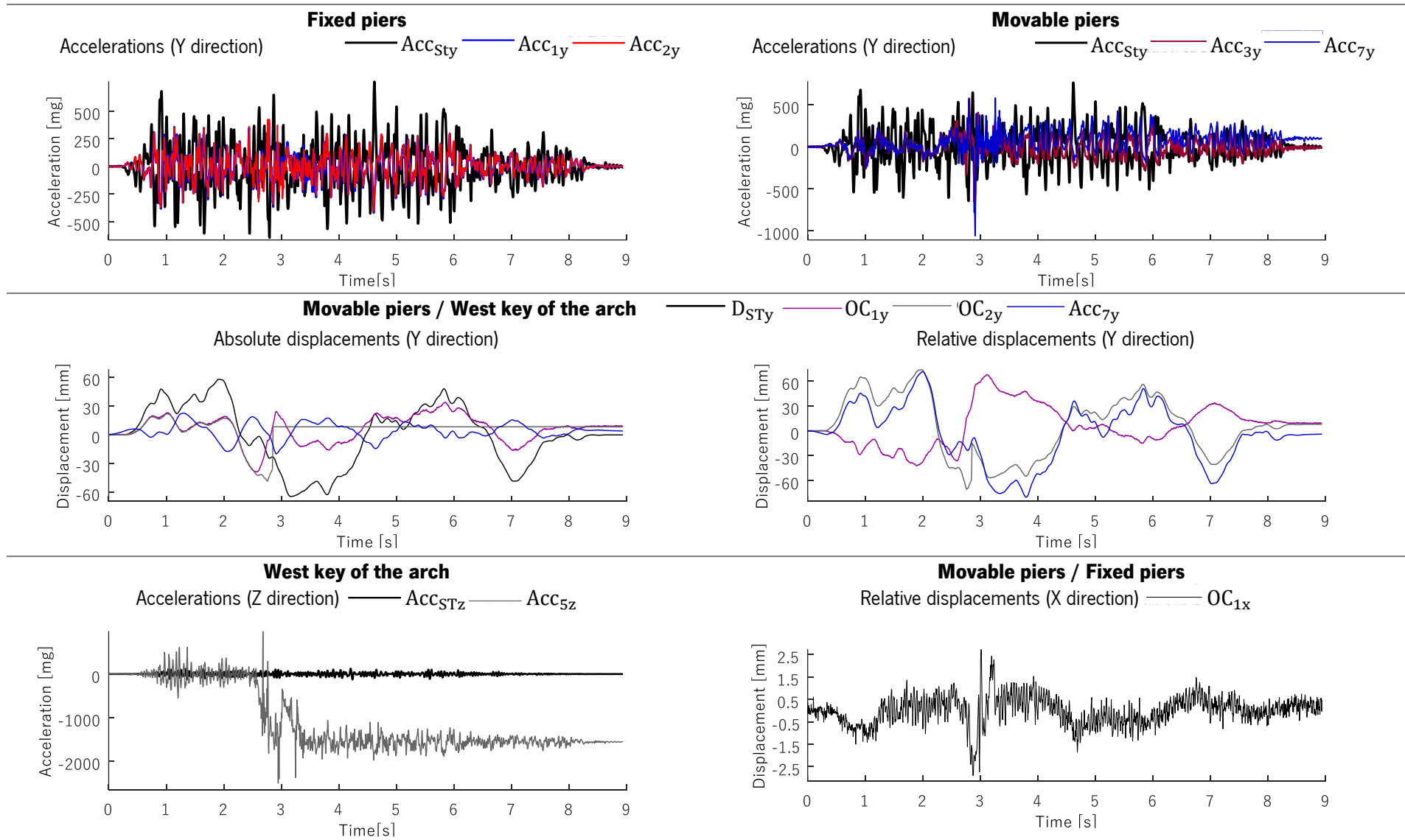
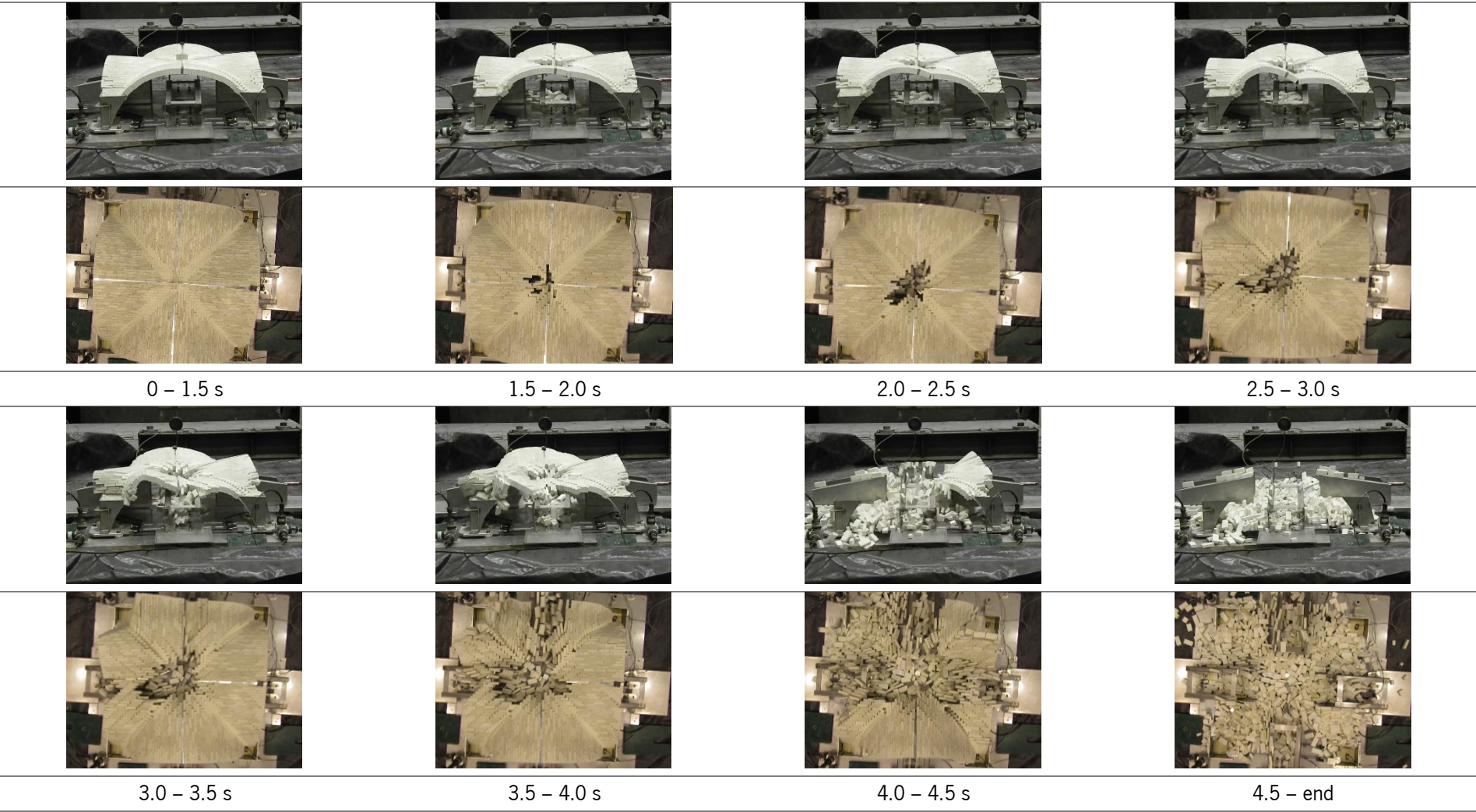
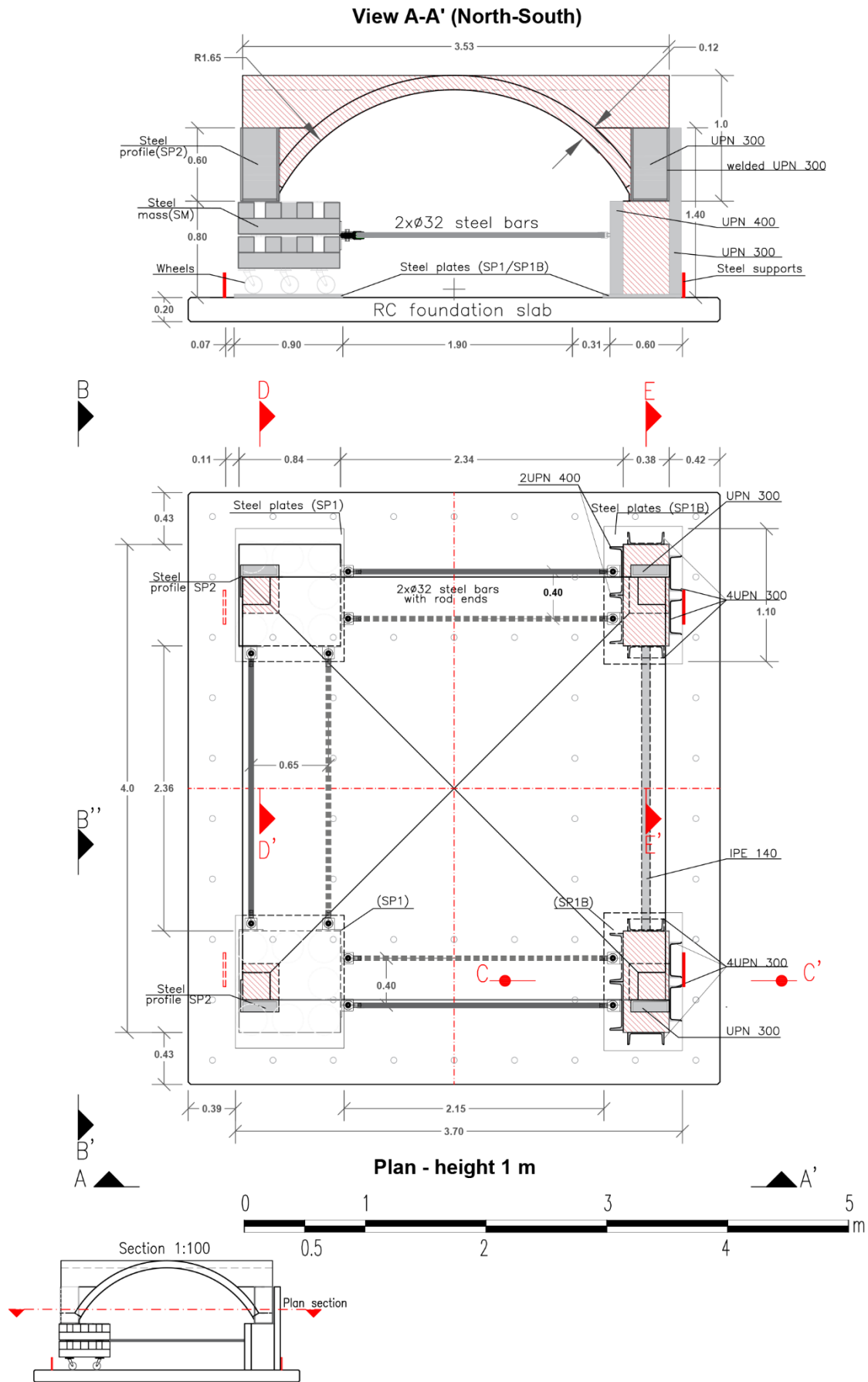
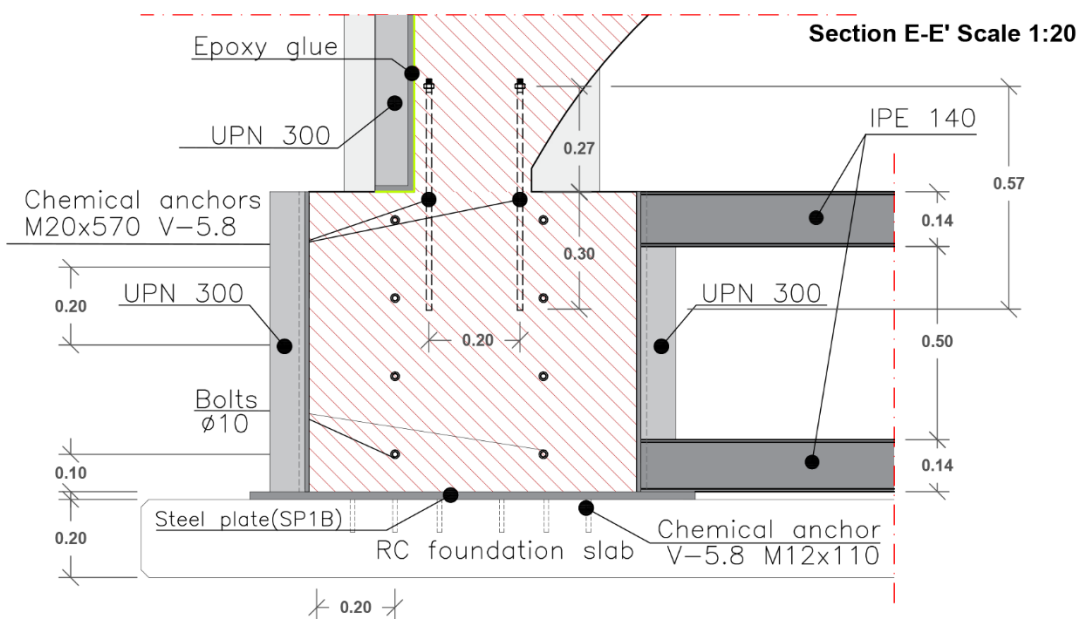
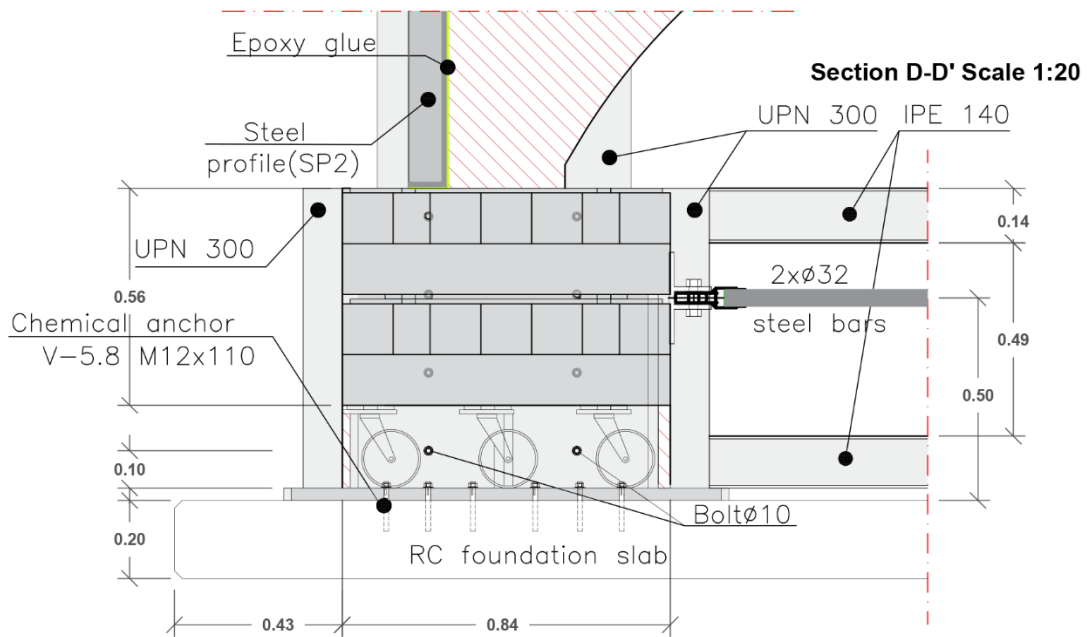
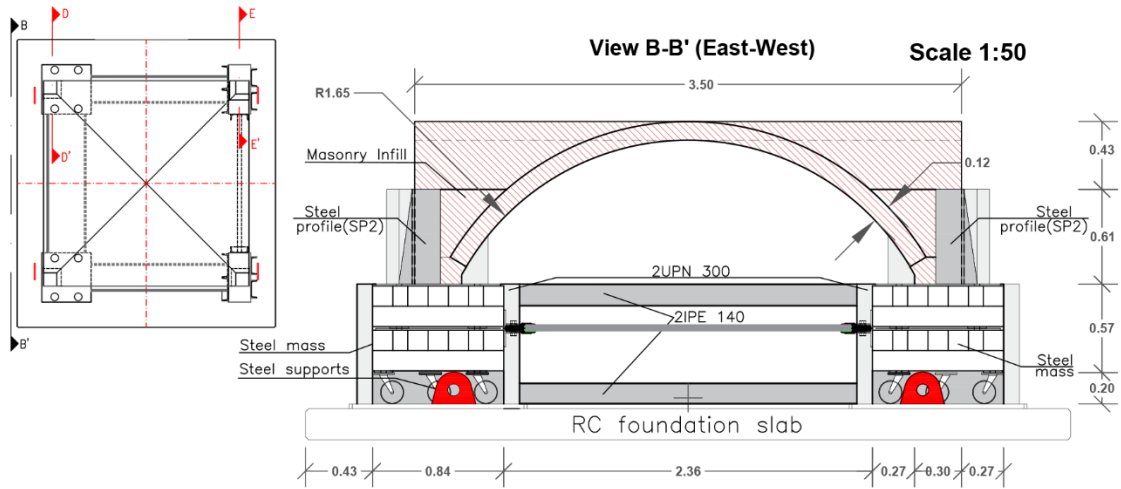


Table A2-39. Artificial earthquake 200%: collapse mechanism



3. Annex – Full-scale vault: technical drawings



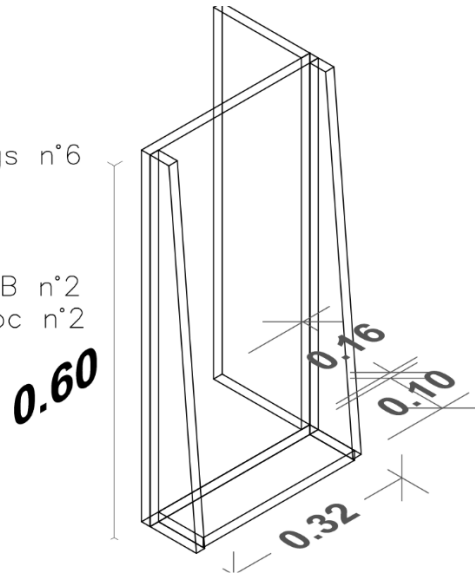


Dimensions in m

List of elements

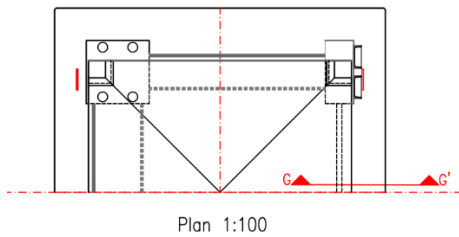
Steel elements

- Steel masses: LNEC n° 2
- Steel rods: Type SKF SI(30) ES Bearings n°6
- Steel profiles: Type S275
 - UPN 300 n°10
 - UPN 400 n°4
 - Steel plates SP1n°2/SP1B n°2
 - Steel profiles SP2 ad hoc n°2
- Chemical anchors:
 - M12x110, M20x570 V-5.8
- Steel Bolts: $\varnothing 10$ n°16

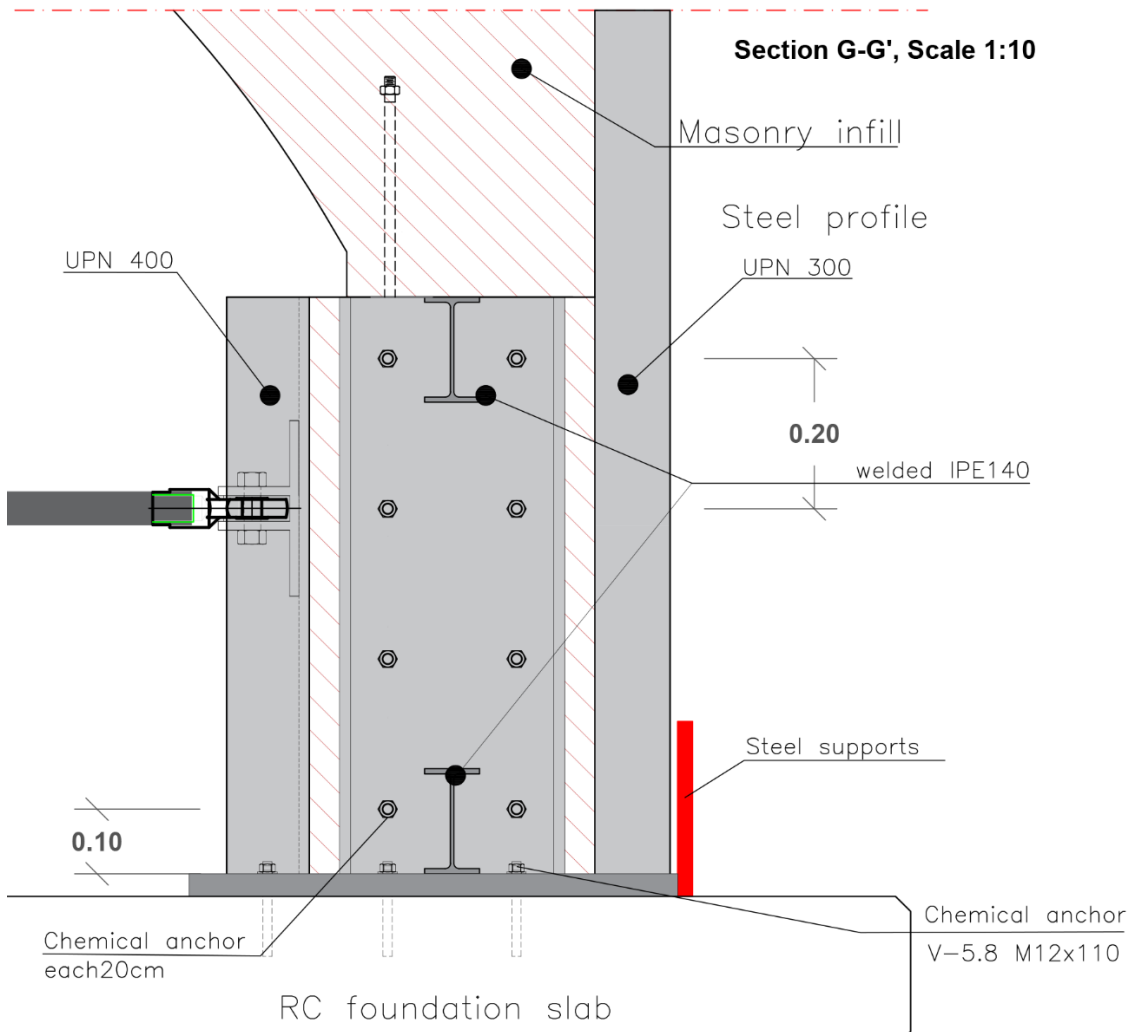


Steel profiles SP2 3D view Scale 1:10

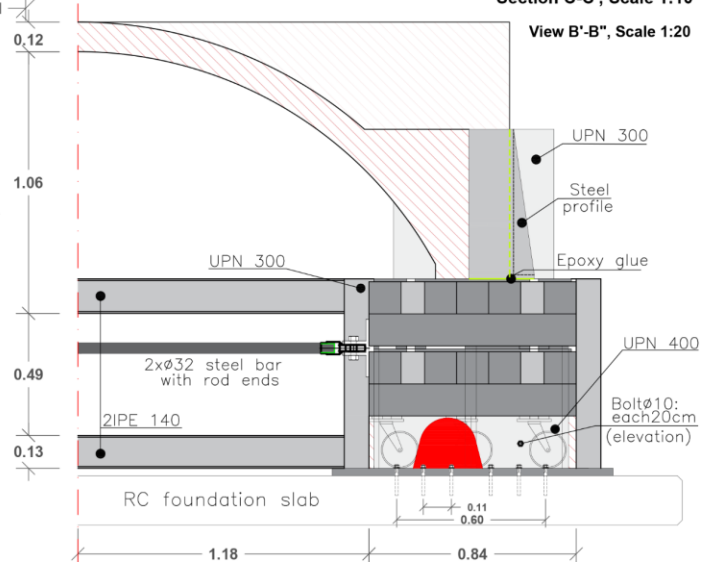
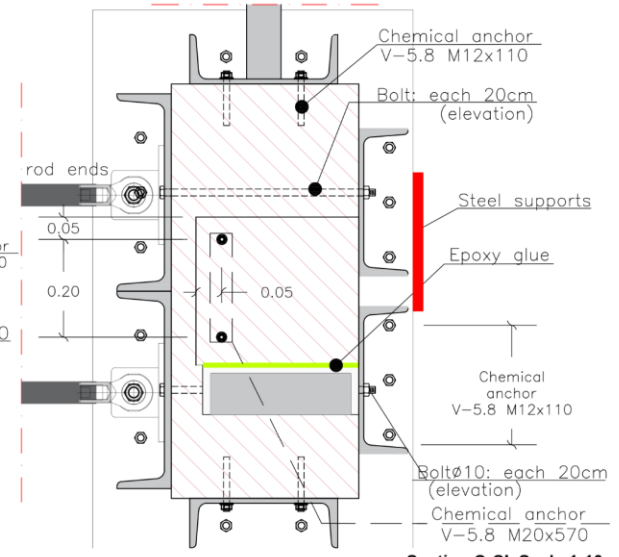
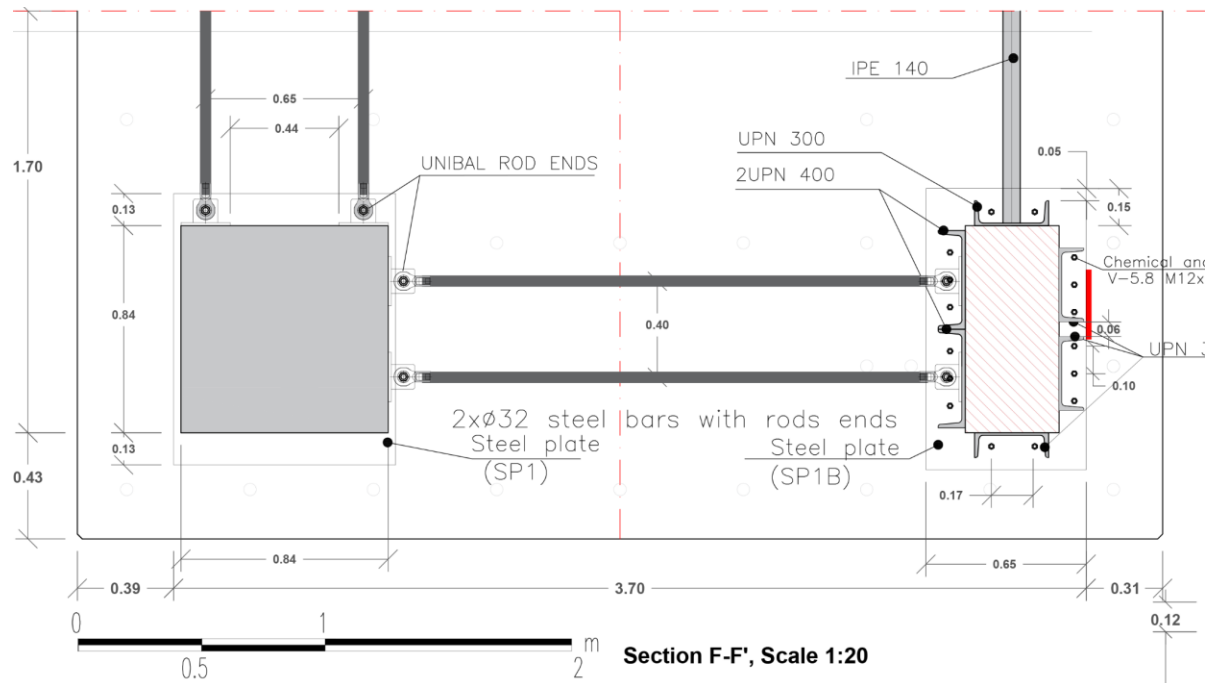
Steel profiles ad hoc n°2 fixed with Epoxy mortar to the masonry



Plan 1:100



Dimensions in m

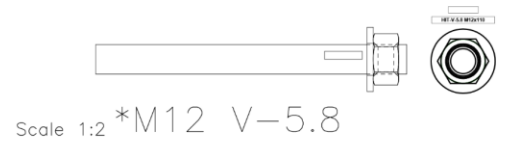
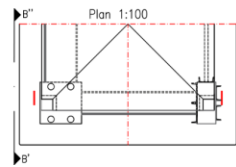
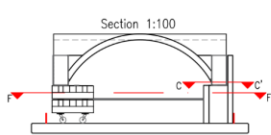


Legend materials

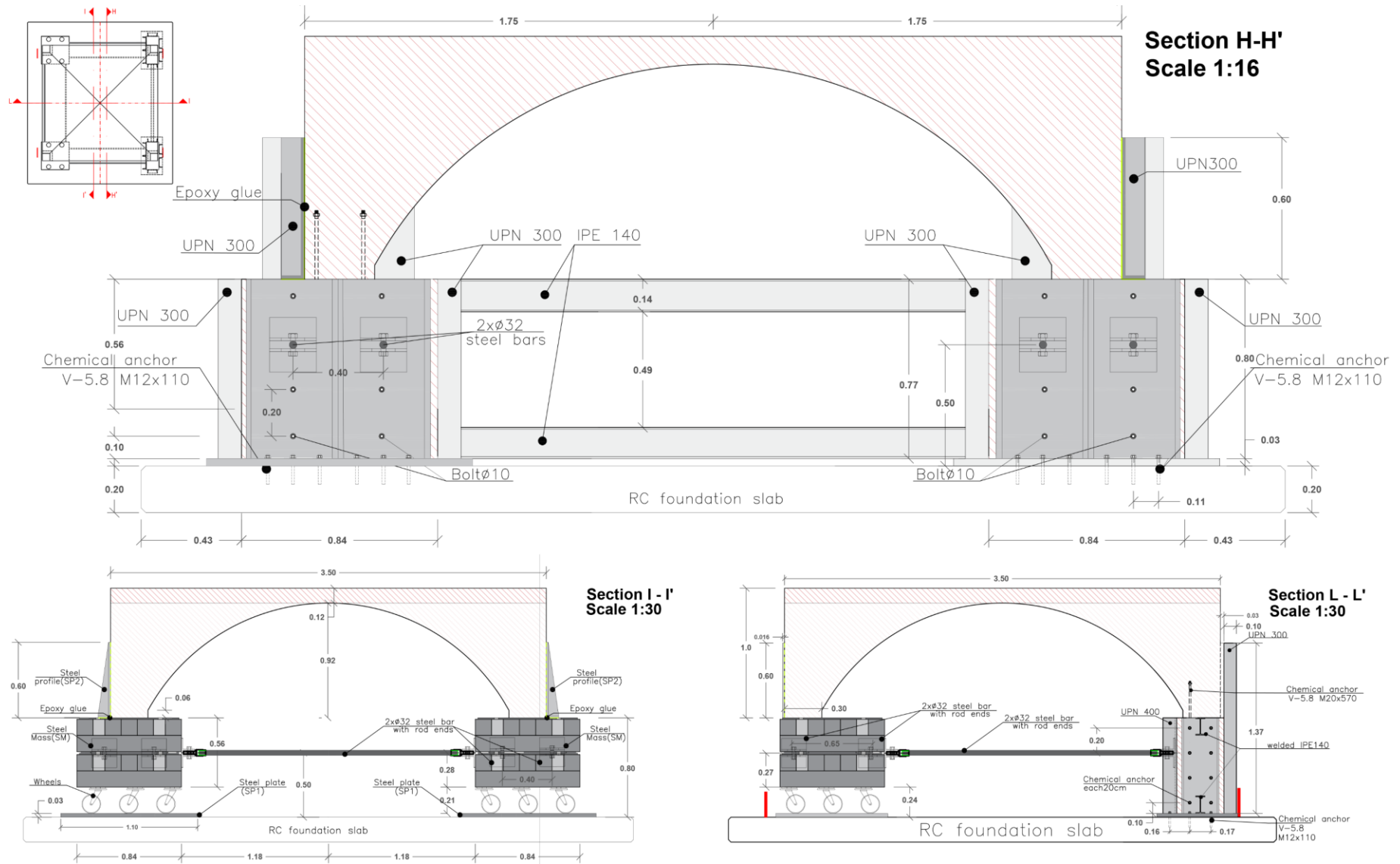
Steel elements

Masonry

- Steel masses: LNEC
- Steel rods: Type SKF SI(30) ES
- Steel profiles: Type S275
- Chemical anchors: M12 V-5.8 & M20 V-5.8 injected with hybrid mortar
- Bolt diameter 10mm n°16
- Mortar: Biomortar – Type "Biocalce MuroSano" Kerakoll + Filler
- Fired bricks: Dimensions 4.5x12x23 (cm) – Type Cenol
- Epoxy mineral adhesive for the steel elements: thickness 3mm – Type "GeoLiteGel" Kerakoll



Dimensions in m



4. Annex – Literature review on historic mortars

Table A4-1. Historic mortars characteristics from the late XIX century until the most recent works, in situ and in laboratory tested

Reference	Curing	Mortar	Filler	W/B ratio	Environmental conditions	Bulk density [kg/m ³]	f_c [Mpa]	f_t [Mpa]	Comments
Curioni (1868)	>>365 days	Lime	Sand		In situ	1630	2.94	0.78	
					1700		1.37		
	540 days		Pozzolana			1460	3.63		
Campanella (1928)	>14 years	Hydraulic lime	Sand			1850–2000	2.94 – 4.9	0.19 – 0.49	
Italian Infrastructure and Transportation Ministry (1987)	28 days	Hydraulic lime	Sand		Lab		>2.5		M4 class
Binda <i>et al.</i> (1988)	28 days	Lime	Pozzolana sand (1:4:9,28)	0.54	Lab	1752			Sample cube: 500×250×600 mm
Baronio and Binda (1991)	>>365 days	Lime putty	Siliceous 1:3 - 1:5		In situ	1899	6.24		Pavia tower (XI century) cubes of side 27 to 36 mm 30x30x30mm in average
Binda et al (1994)	28 days	Lime					2.61		
	>14 years			1.1	Lab		1.78		Sample cube: 40×40×40 mm ³
	>>365 days						1.07		

Reference	Curing	Mortar	Filler	W/B ratio	Environmental conditions	Bulk density [kg/m ³]	f_c [MPa]	f_t [MPa]	Comments
Binda <i>et al.</i> (1996)	28 days	Hydraulic lime		1	Lab		3.63	1.08	Similar to Pavia Tower
Middendorf (2002)	>7days	Lime		1			4.0		German standards
Baroni <i>et al.</i> (2003)	>>365 days	Hydraulic lime	Sand, calcareous aggregates		Lab		0.72	0.23	Material from Noto Cathedral Sample cubes: 40×40×40 mm ³
Veiga, Magalhaes and Bokan-borosilikov (2004)	>>365 days	Light brown lime mortar	White lime grains, siliceous sand, and clay		In situ		1.61		Joints from a Castle in South Portugal, XII c.
	>>365 days	White lime mortar (1:3) made from traditionally produced lime putty	Siliceous sand		In situ		2.10		Rendered clay brick wall for field studies (Ljubljana) dated XX century.
	>28 days	Hydraulic lime	Sand from Lisbon region 1:3		Lab	1890	3.10		Replica of old mortar samples
	28 days	Lime	Cement and sand from Lisbon region 1:1:6		Lab	1760	2.9		-
Lanas <i>et al.</i> (2004)	28 days	NHL	1:4		Lab		2.0		-
Giavarini (2010)	>>365 days	Lime	Tufa, travertine, basalt, or pumice	0.5	In situ	1340			From Maxentius basilica terrace floor in Rome

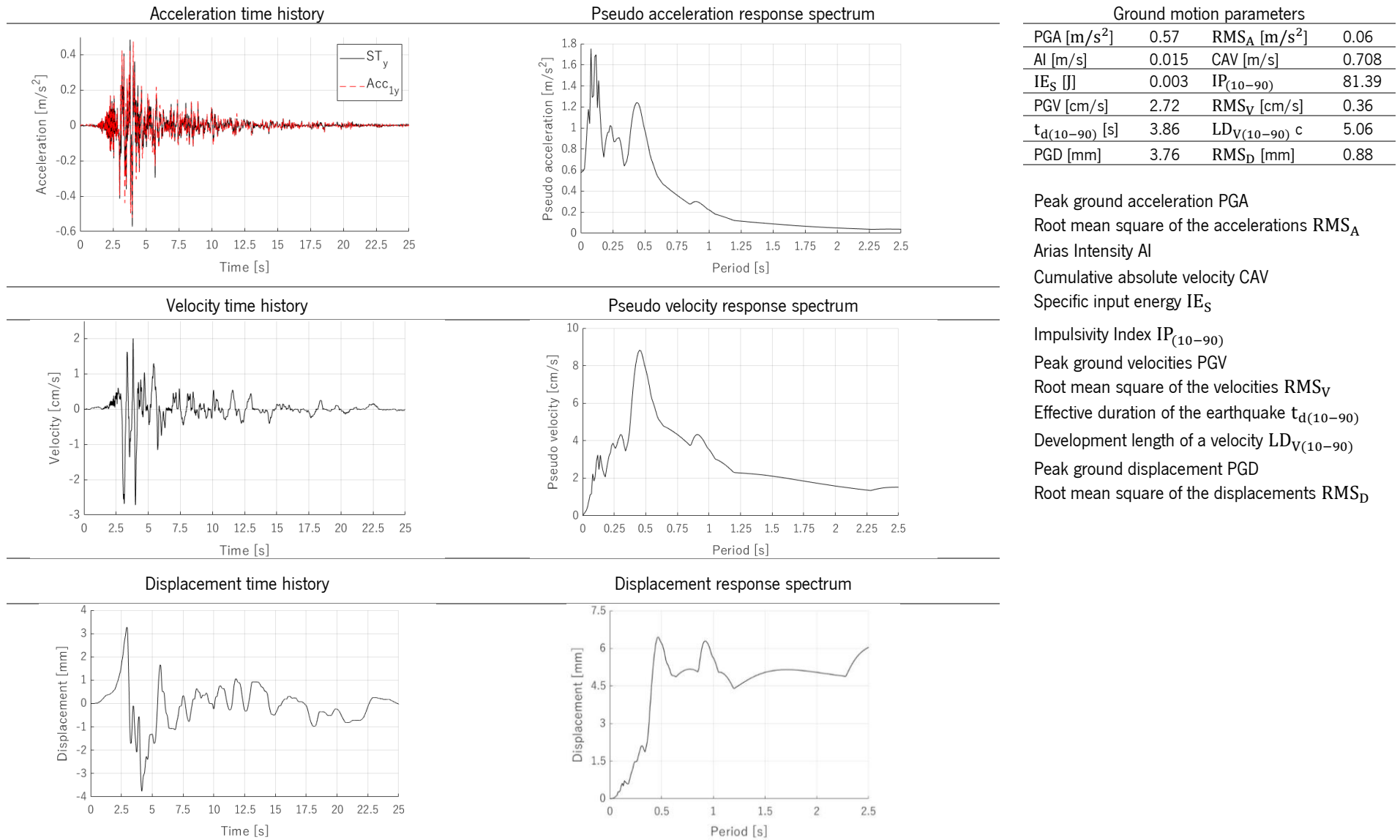
Reference	Curing	Mortar	Filler	W/B ratio	Environmental conditions	Bulk density [kg/m ³]	f_c [MPa]	f_t [MPa]	Comments
Costigan and Pavia (2012)	28 days	NHL 3.5	Siliceous aggregate				4.0	0.65	Sample cube: 40×40×40 mm ³
Silva, Ferreira Pinto and Gomes (2015)	28 days	Hydraulic lime	Aggregate cement clay (1:3)	1.35	Lab		1.65 – 3.95	0.3 – 1.2	-
Papayianni and Pachta (2015)	>>365 days	Lime	Pozzolana, brick dust and clay		In situ		2.82		Typology: panagia acheiropoitos byzantine
Garijo <i>et al.</i> (2019)	7 days	NHL		0.8			1.35	0.49	Sample cube: 40×40×40 mm ³
Segura <i>et al.</i> (2020)	28 days	NHL 3.5	Limestone filler				1.91	0.68	Sample cube: 40×40×40 mm ³
Autiero <i>et al.</i> (2020)	>>365 days	Lime	Pozzolana (1:3)		Lab	1105	2.87 (5%)	0.56 (13%)	Sample cube: 40×40×40 mm ³ UNI EN 1015-11:2007
		Lime	Sand and crushed ceramic particles				3.04		Conimbra archaeological site Portugal (I - IV c.)
(Velosa <i>et al.</i> , 2007)	>>365 days	Lime	Volcanic tuff basalt, trachyte natural pozzolan and black volcanic sand.		In situ		1.0 – 2.0		Azores

5. Annex – Full-scale vault: shaking table tests results

Table A5-1. List of shaking table tests on the full-scale vault.

Shaking table tests: UNSTRENGTHENED (UNS)				Shaking table tests: STRENGTHENED (SM)			
ID	Denomination	Direction	Description	ID	Denomination	Direction	Description
1	DIT-0-UNS-Y	N - S	Dynamic identification test of undamaged vault *with hammer	13	DIT-0-SM-Y	N - S	Dynamic identification test of repaired and strengthened vault
1B*	DIT-0-UNS-Y	N - S		14	DIT-0-SM-X	E - W	
2	DIT-0-UNS-X	E - W		15	ST-SM-25%	N - S	Seismic test with amplitude equal to 25% of AQA eq.
3	ST-UNS-10%	N - S	Seismic test with amplitude equal to 10% of AQA	16	DIT-1-SM-Y	N - S	Dynamic identification after 25% seismic test
4	ST-UNS-25%	N - S	Seismic test with amplitude equal to 25% of AQA	17	DIT-1-SM-X	E - W	
5	DIT-1-UNS-Y	N - S	Dynamic identification after 25% seismic test	18	ST-SM-50%	N - S	Seismic test with amplitude equal to 50% of AQA eq.
6	DIT-1-UNS-X	E - W		19	DIT-2-SM-Y	N - S	Dynamic identification after 50% seismic test
7	ST-UNS-50%	N - S	Seismic test with amplitude equal to 50% of AQA	20	DIT-2-SM-X	E - W	
8	DIT-2-UNS-Y	N - S	Dynamic identification after 50% seismic test	21	ST-SM-75%	N - S	Seismic test with amplitude equal to 75% of AQA eq.
9	DIT-2-UNS-X	E - W		22	DIT-3-SM-Y	N - S	Dynamic identification after 75% seismic test
10	ST-UNS-75%	N - S	Seismic test with amplitude equal to 75% of AQA	23	DIT-3-SM-X	E - W	
11	DIT-3-UNS-Y	N - S	Dynamic identification after 75% seismic test	24	ST-SM-100%	N - S	Seismic test with amplitude equal to 100% of AQA eq.
12	DIT-3-UNS-X	E - W		25	DIT-4-SM-Y	N - S	Dynamic identification after 100% seismic test
				26	DIT-4-SM-X	E - W	
				27	ST-SM-125%	N - S	Seismic test with amplitude equal to 125% of AQA eq.
				28	DIT-5-SM-Y	N - S	Dynamic identification after 125% seismic test
				29	DIT-5-SM-X	E - W	
				30	ST-SM-150%	N - S	Seismic test with amplitude equal to 150% of AQA eq.
				31	DIT-6-SM-Y	N - S	Dynamic identification after 150% seismic test
				32	DIT-6-SM-X	E - W	

Table A5-2. ST-UNS-10%: input data and time histories



Peak ground acceleration PGA
 Root mean square of the accelerations RMS_A
 Arias Intensity AI
 Cumulative absolute velocity CAV
 Specific input energy IE_S
 Impulsivity Index IP₍₁₀₋₉₀₎
 Peak ground velocities PGV
 Root mean square of the velocities RMS_V
 Effective duration of the earthquake $t_{d(10-90)}$
 Development length of a velocity LD_{V(10-90)}
 Peak ground displacement PGD
 Root mean square of the displacements RMS_D

Table A5-3. ST-UNS-10%: acceleration response

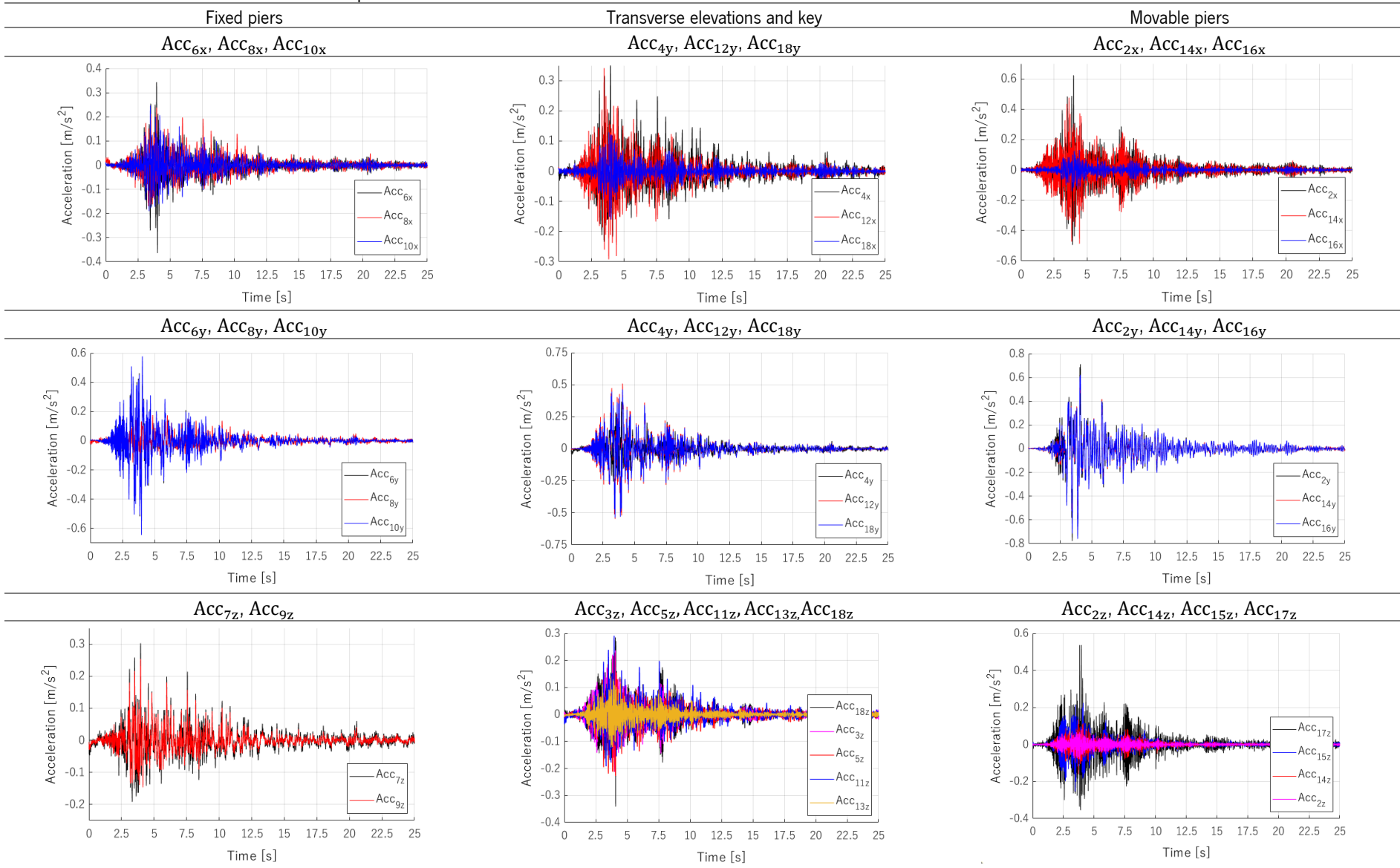


Table A5-4. ST-UNS-10%: displacements and force response

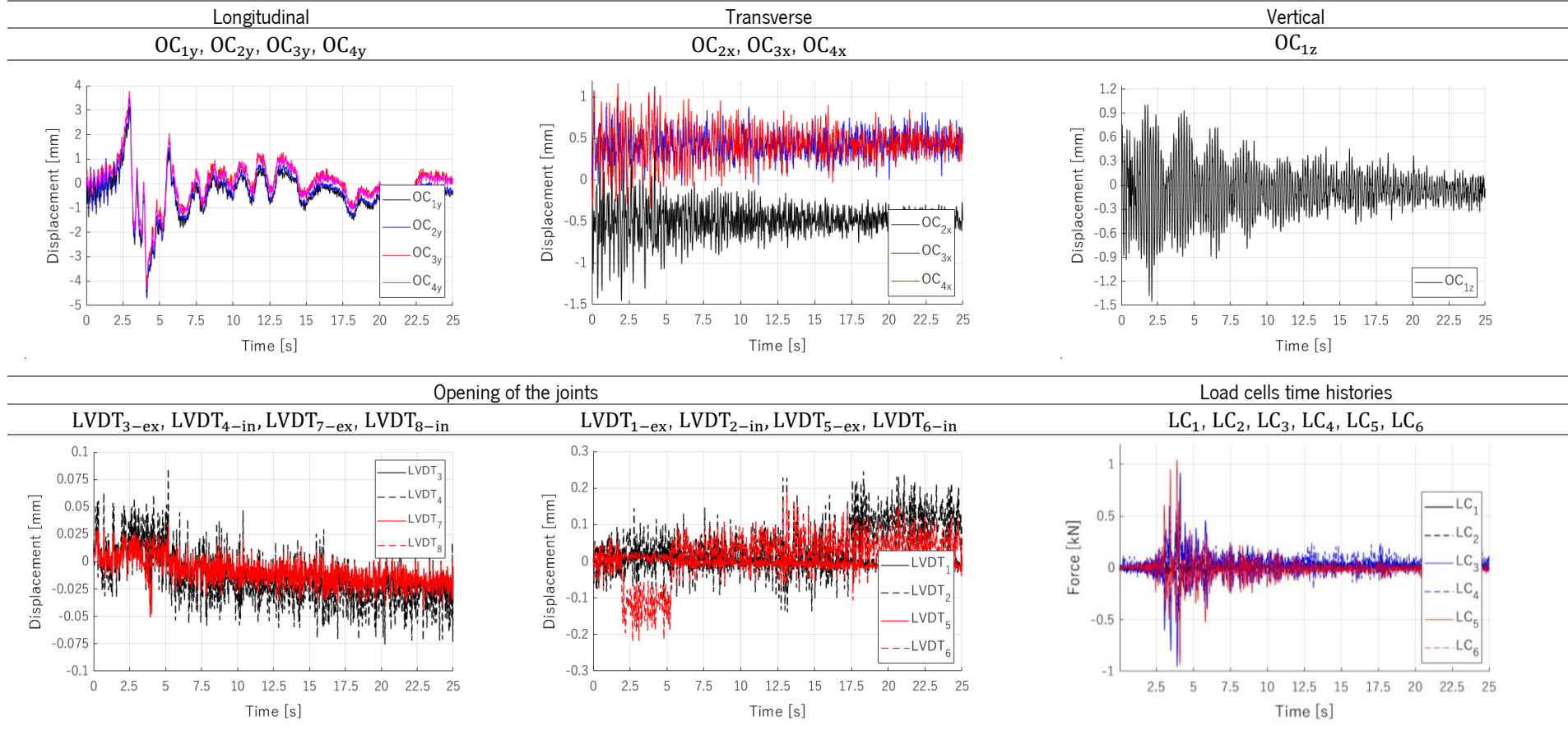
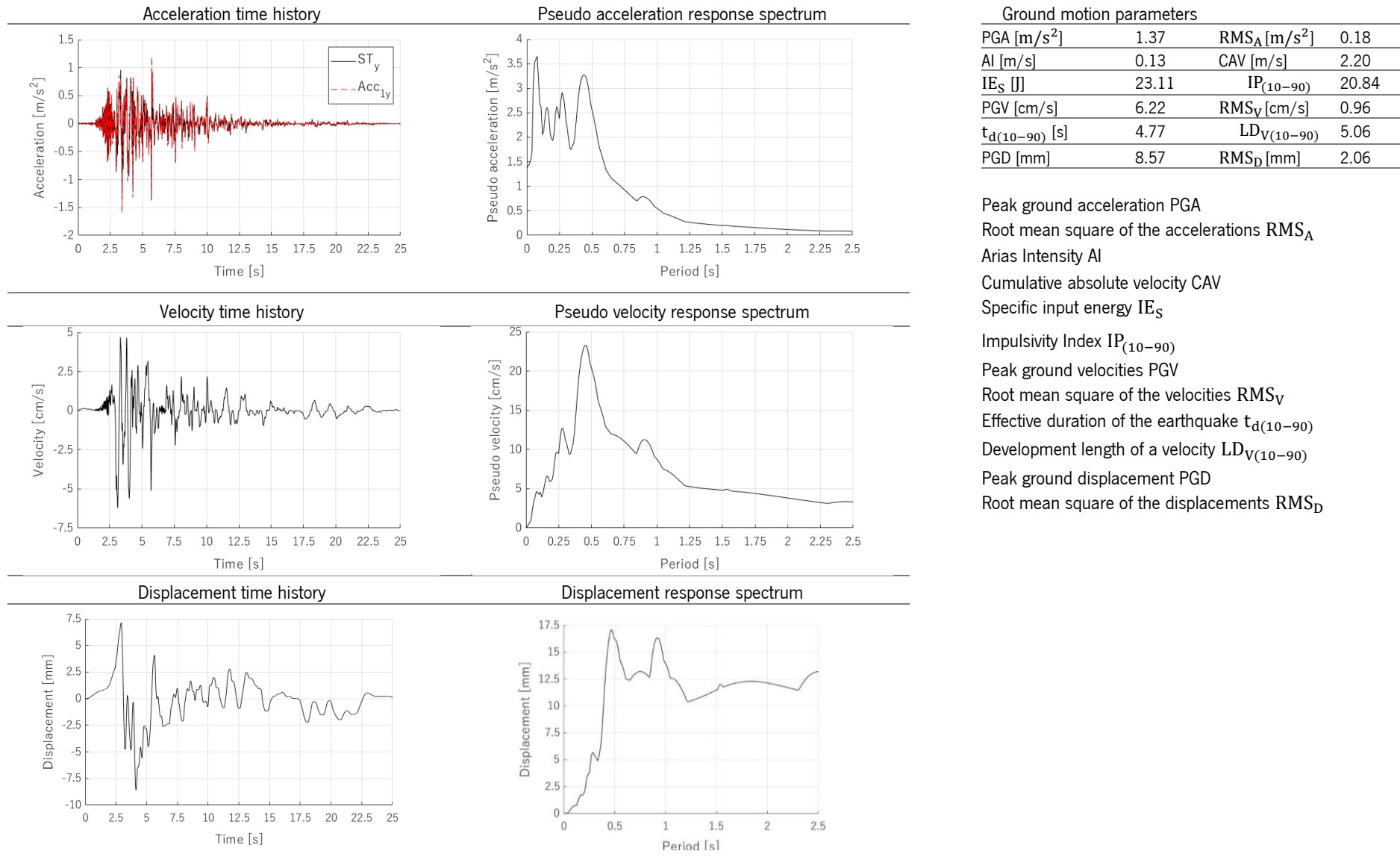


Table A5-5. ST-UNS-25%: input data and time histories



Peak ground acceleration PGA
 Root mean square of the accelerations RMS_A
 Arias Intensity AI
 Cumulative absolute velocity CAV
 Specific input energy IE_S
 Impulsivity Index IP₍₁₀₋₉₀₎
 Peak ground velocities PGV
 Root mean square of the velocities RMS_V
 Effective duration of the earthquake t_{d(10-90)}
 Development length of a velocity LD_{V(10-90)}
 Peak ground displacement PGD
 Root mean square of the displacements RMS_D

Table A5-6. ST-UNS-25%: acceleration response

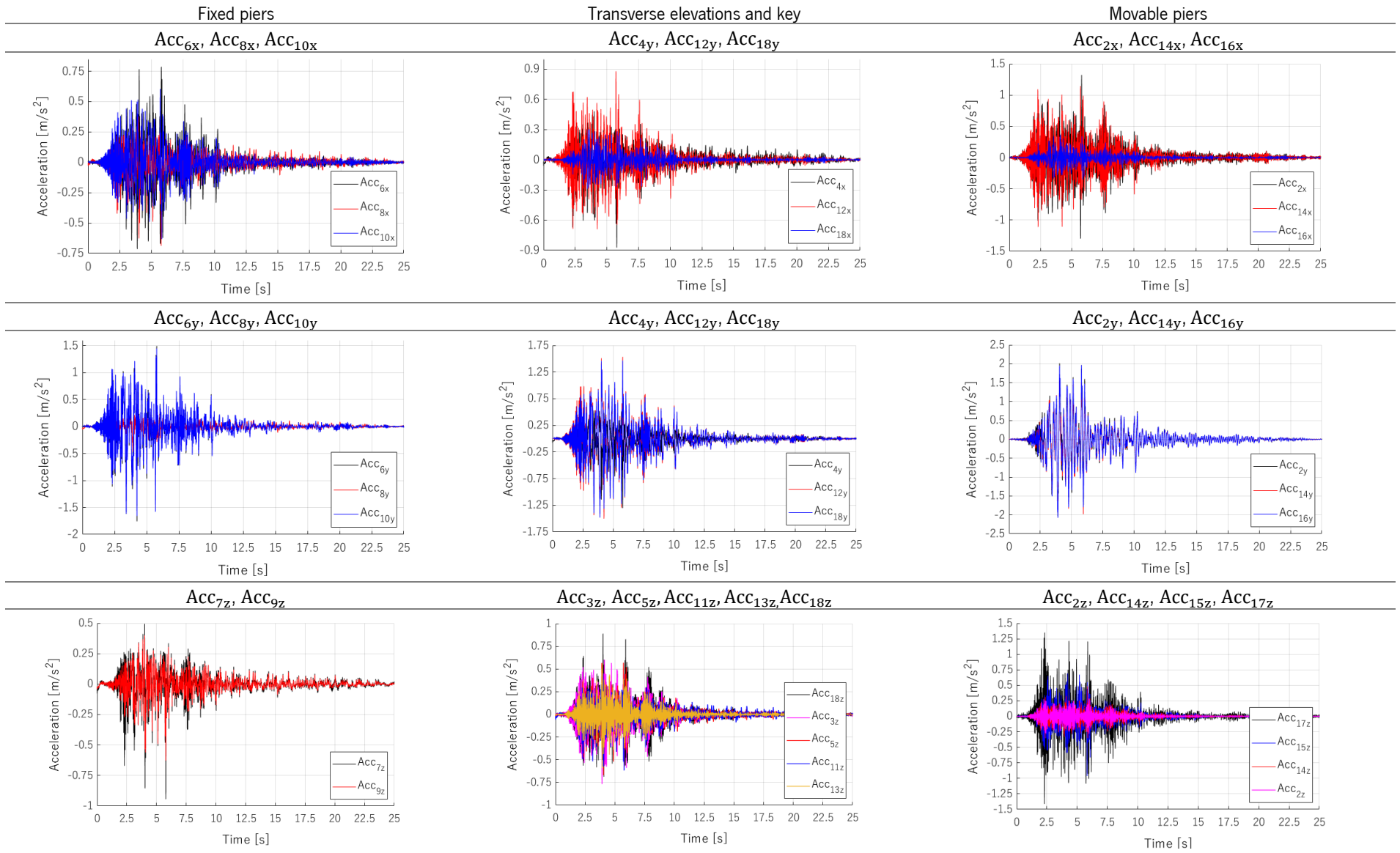


Table A5-7. ST-UNS-25%: displacements and force response

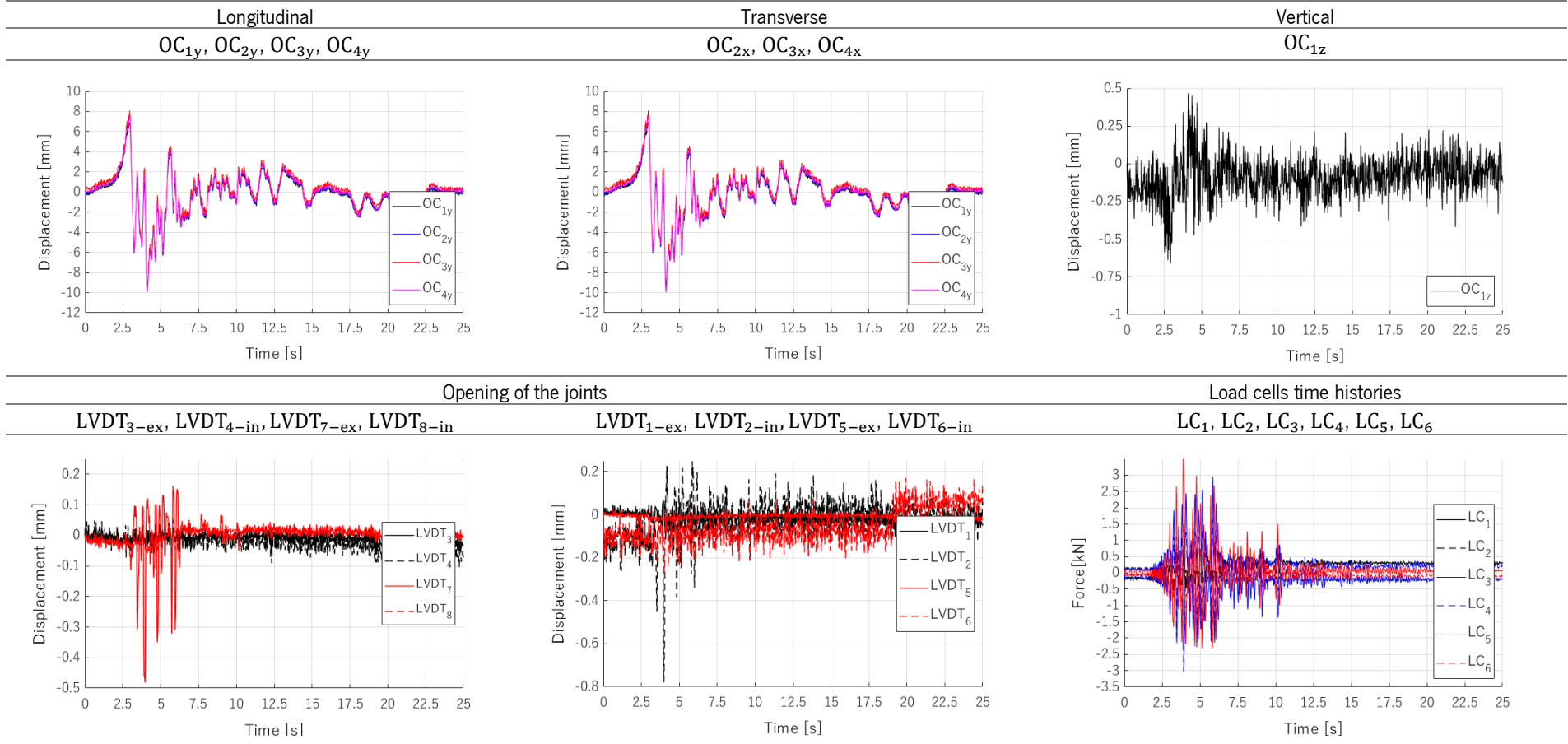


Table A5-8. ST-UNS-50%: input data and time histories

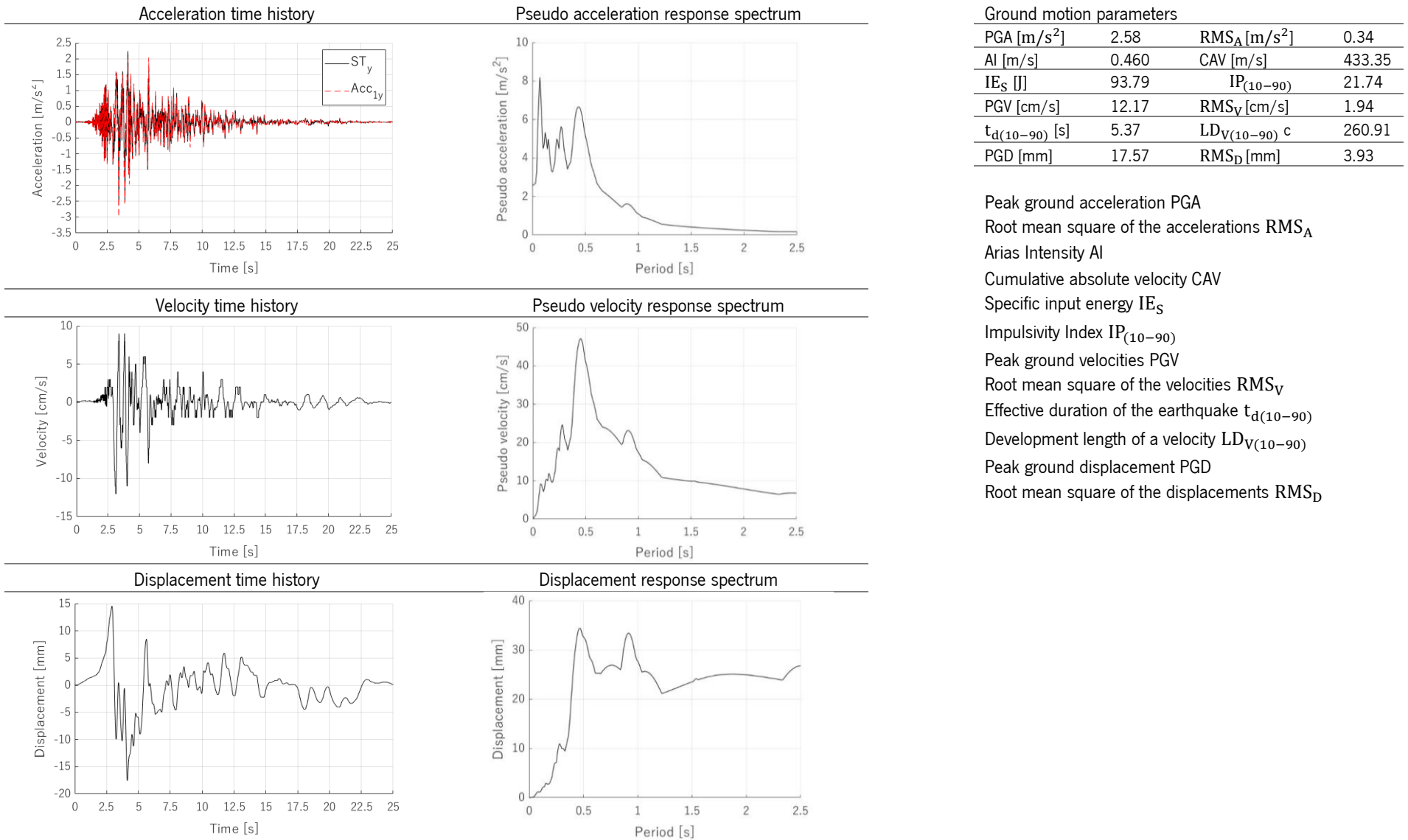


Table A5-9. ST-UNS-50%: acceleration response

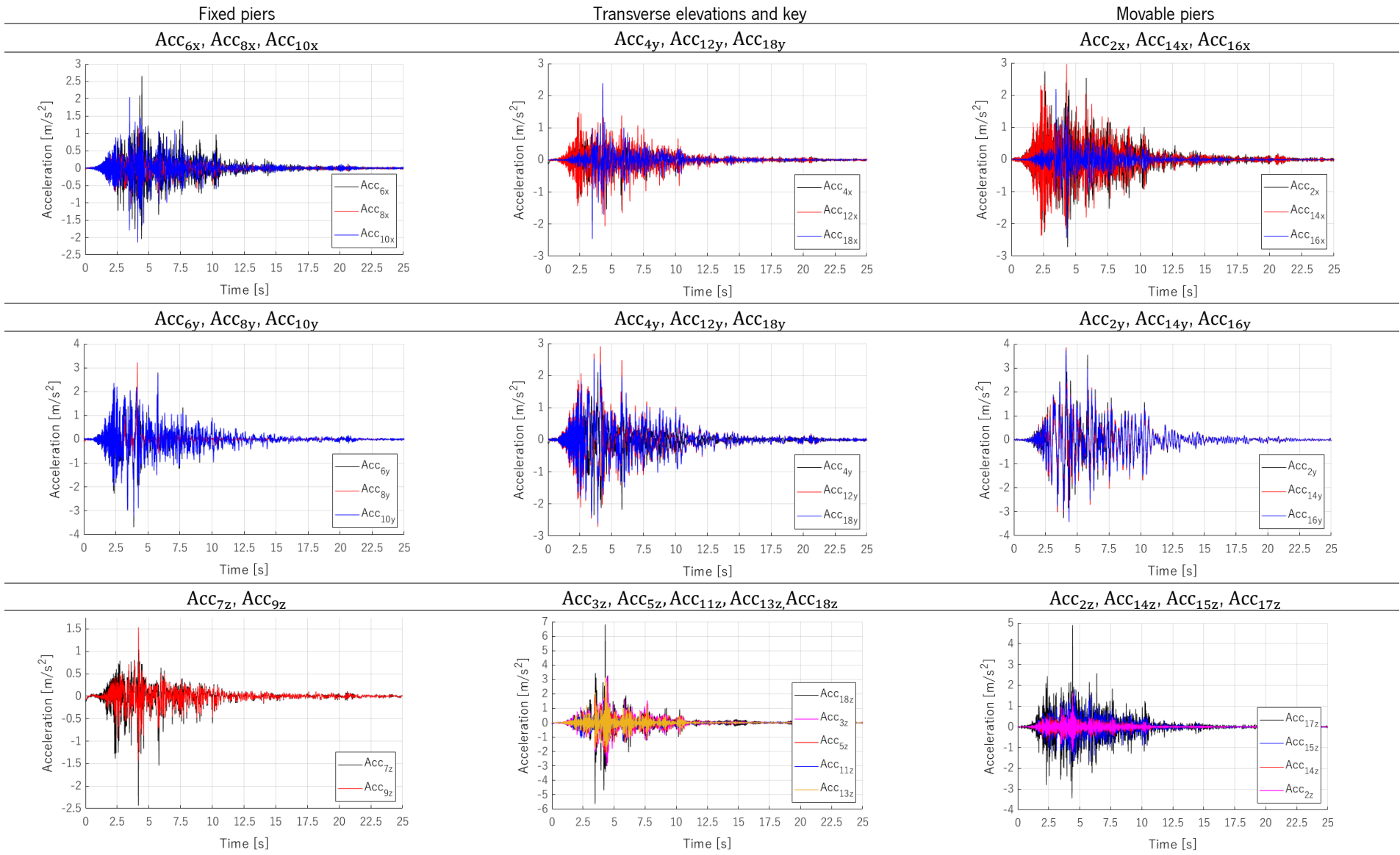


Table A5-10. ST-UNS-50%: displacements and force response

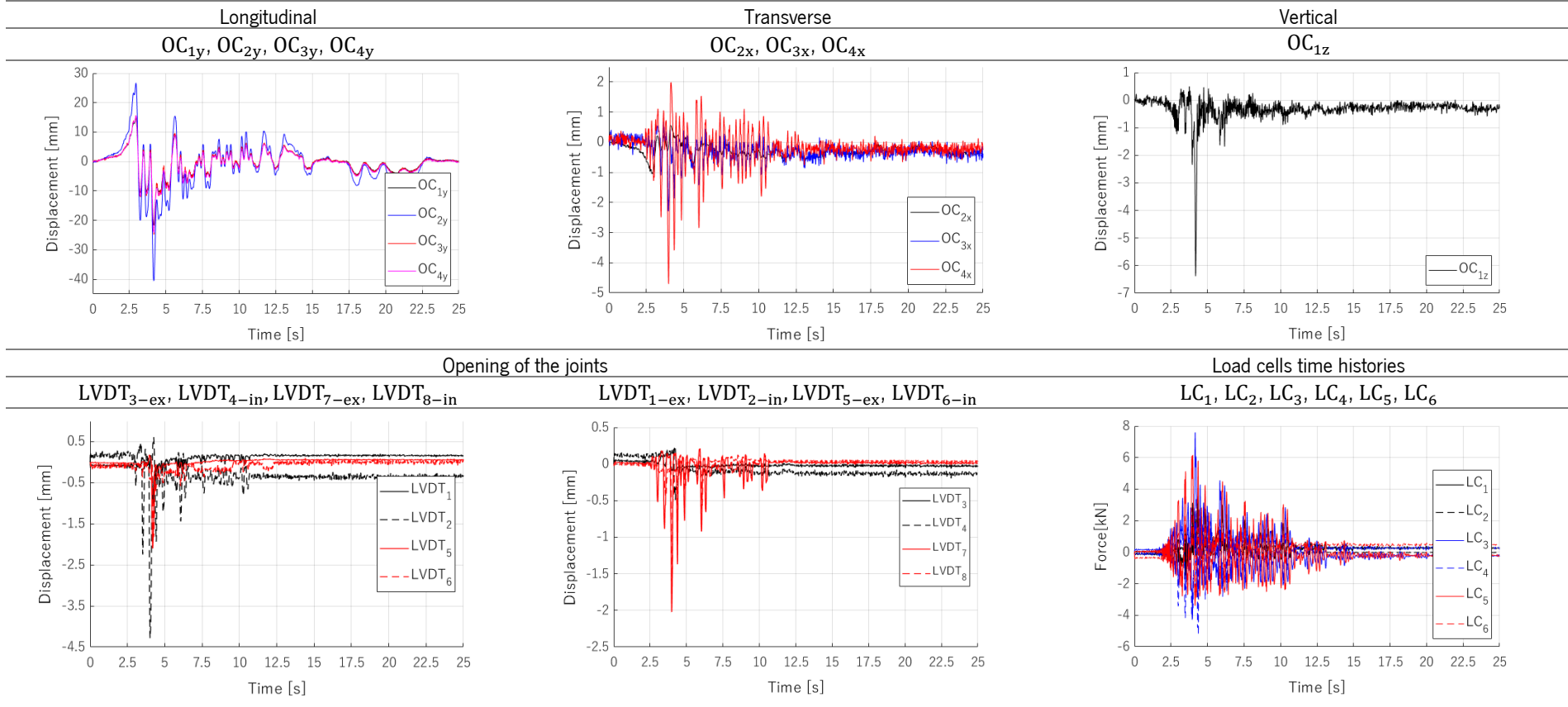
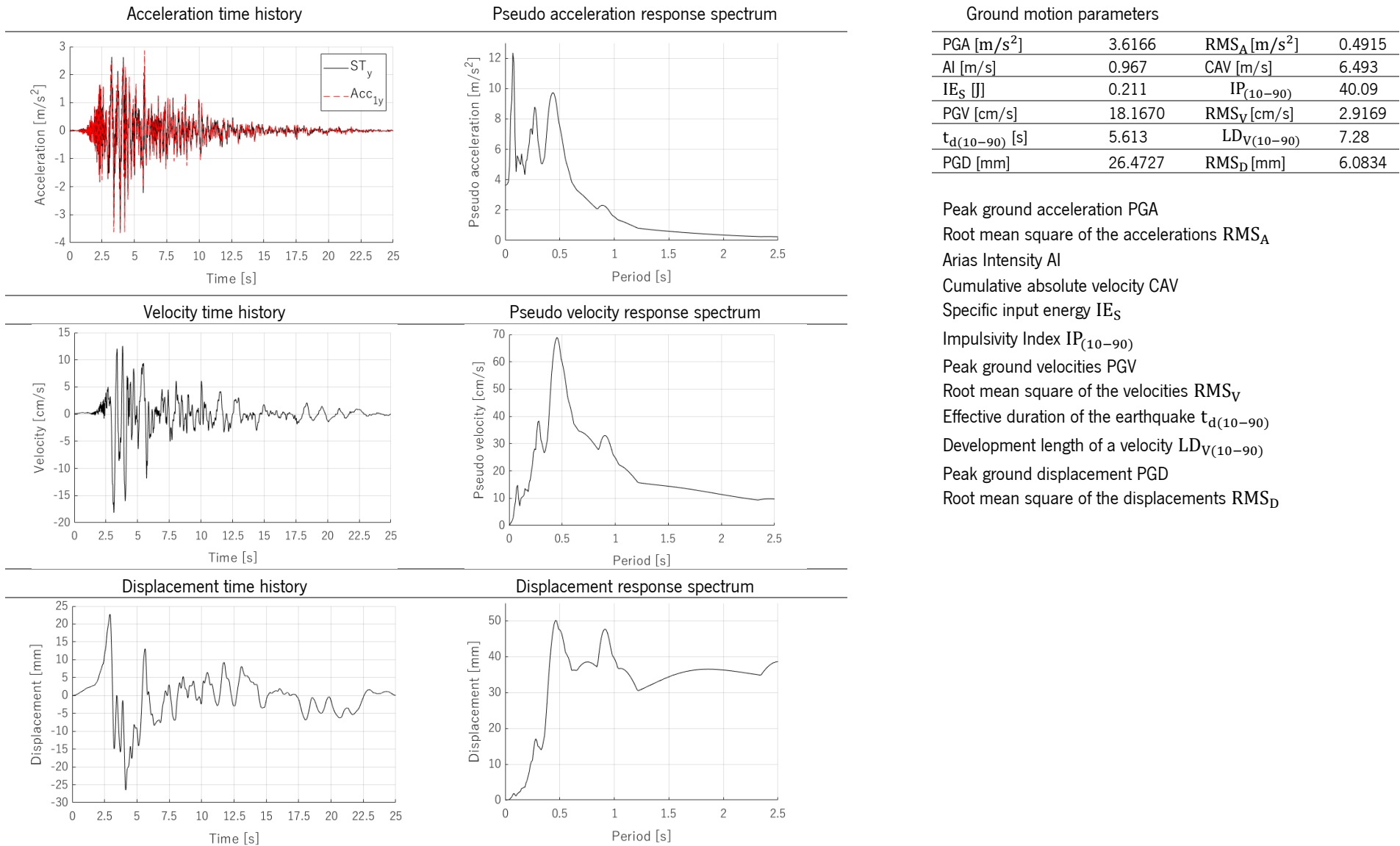


Table A5-11. ST-UNS-75%: input data and time histories



Peak ground acceleration PGA
 Root mean square of the accelerations RMS_A
 Arias Intensity AI
 Cumulative absolute velocity CAV
 Specific input energy IE_S
 Impulsivity Index IP₍₁₀₋₉₀₎
 Peak ground velocities PGV
 Root mean square of the velocities RMS_V
 Effective duration of the earthquake t_{d(10-90)}
 Development length of a velocity LD_{V(10-90)}
 Peak ground displacement PGD
 Root mean square of the displacements RMS_D

Table A5-12. ST-UNS-75%: acceleration response

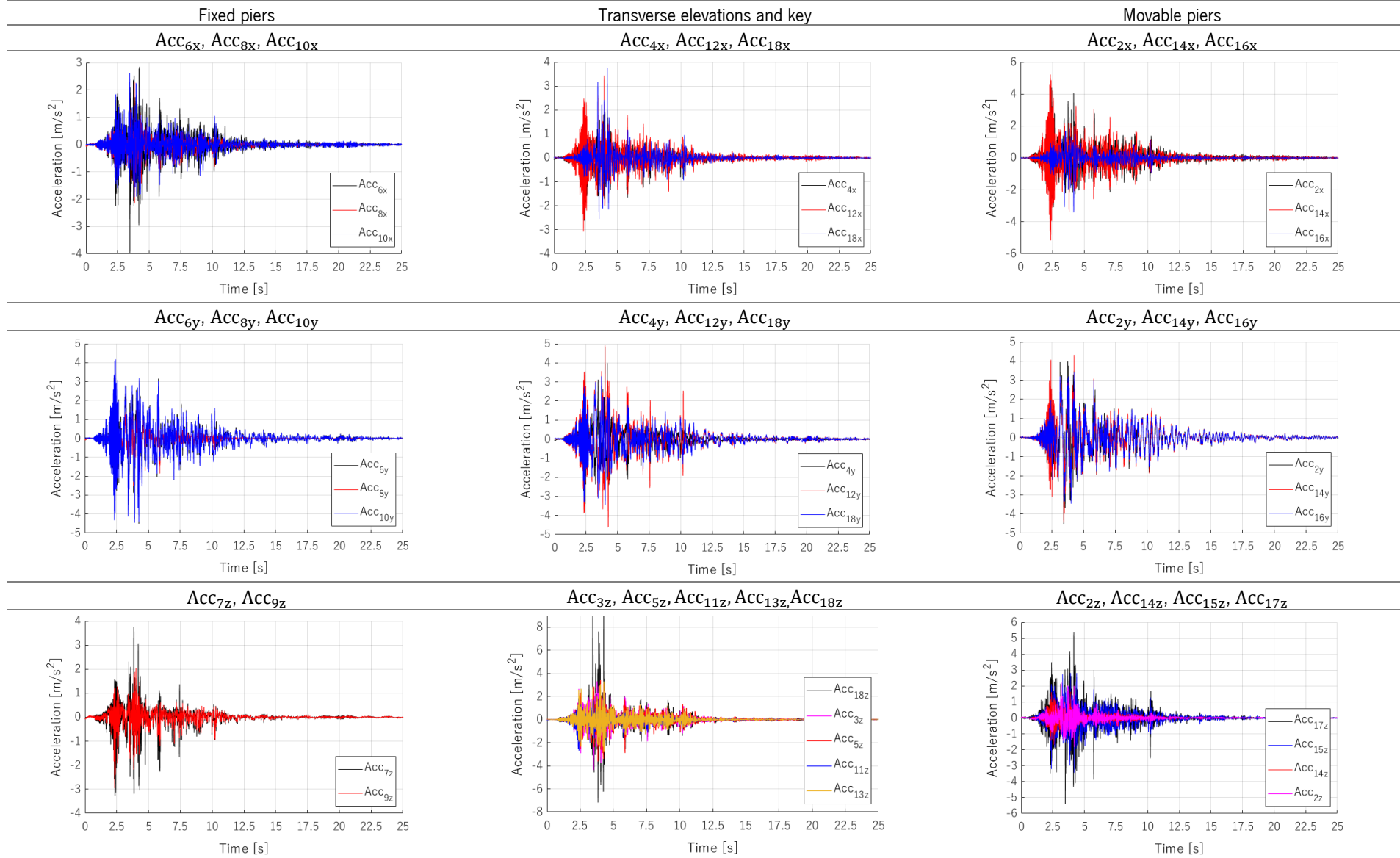


Table A5-13. ST-UNS-75%: displacements and force response

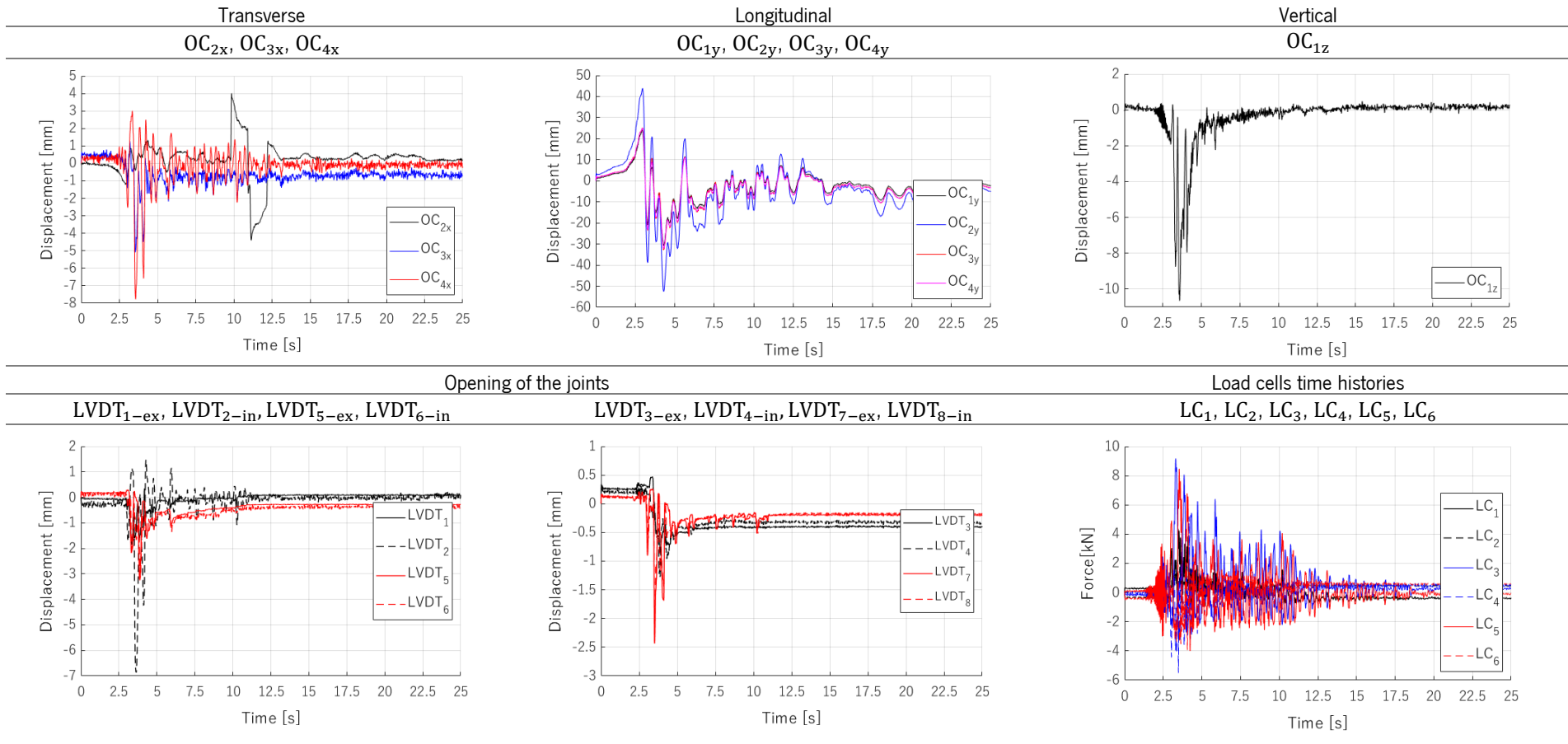
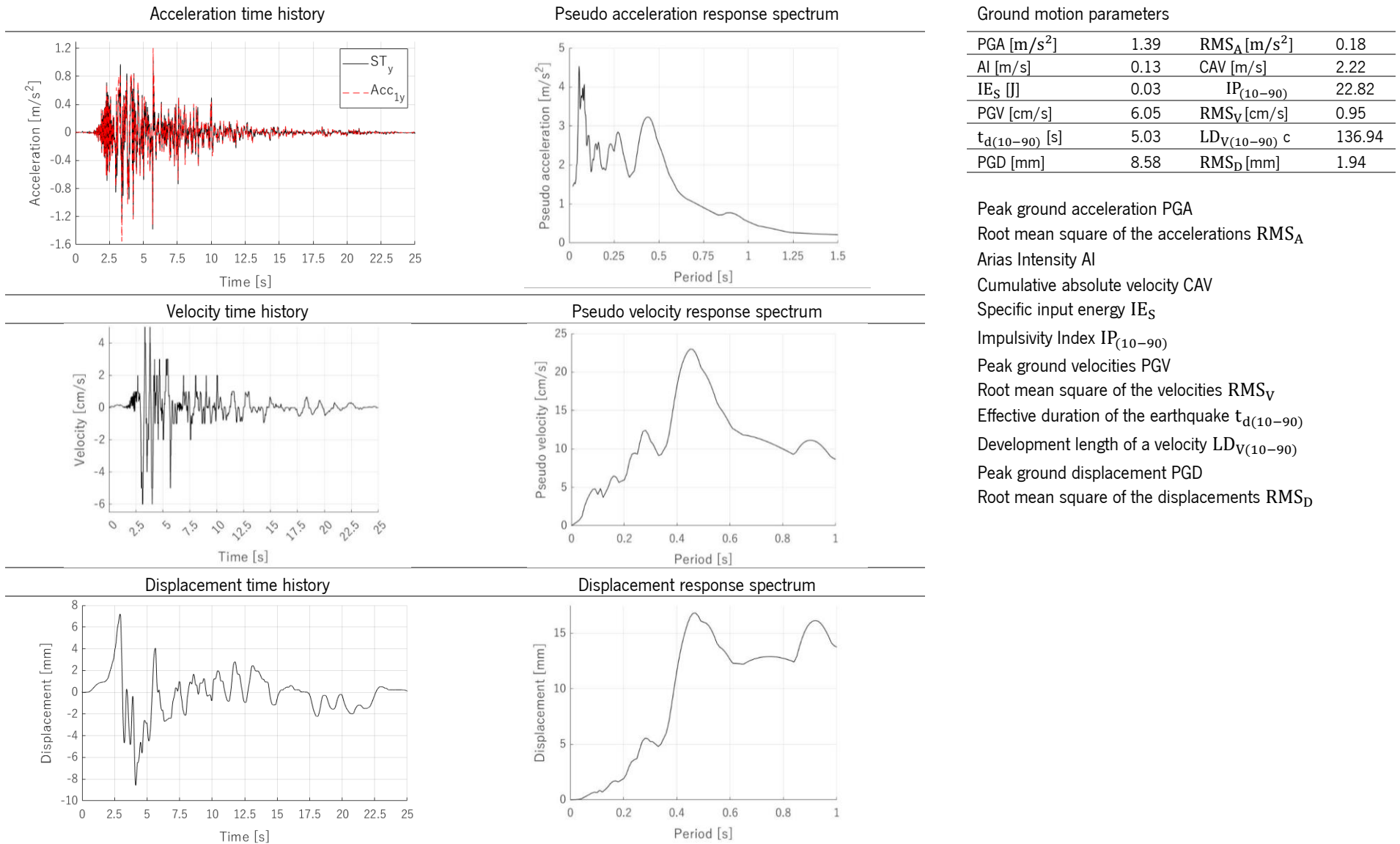


Table A5-14. ST-SM-25%: input data and time histories



- Peak ground acceleration PGA
- Root mean square of the accelerations RMS_A
- Arias Intensity AI
- Cumulative absolute velocity CAV
- Specific input energy IE_S
- Impulsivity Index IP₍₁₀₋₉₀₎
- Peak ground velocities PGV
- Root mean square of the velocities RMS_V
- Effective duration of the earthquake t_{d(10-90)}
- Development length of a velocity LD_{V(10-90)}
- Peak ground displacement PGD
- Root mean square of the displacements RMS_D

Table A5-15. ST-SM-25%: acceleration response

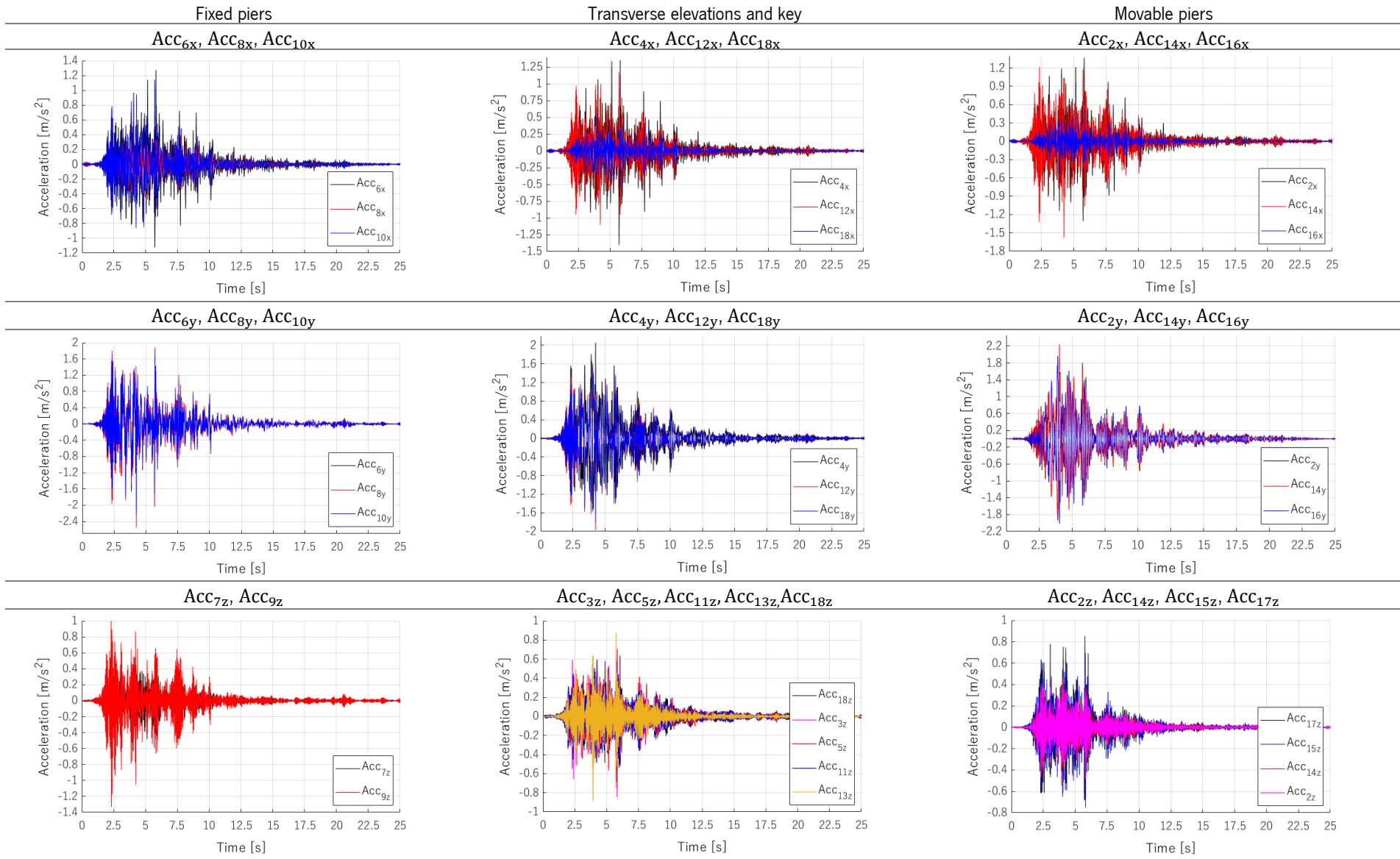


Table A5-16. ST-SM-25%: displacements and force response

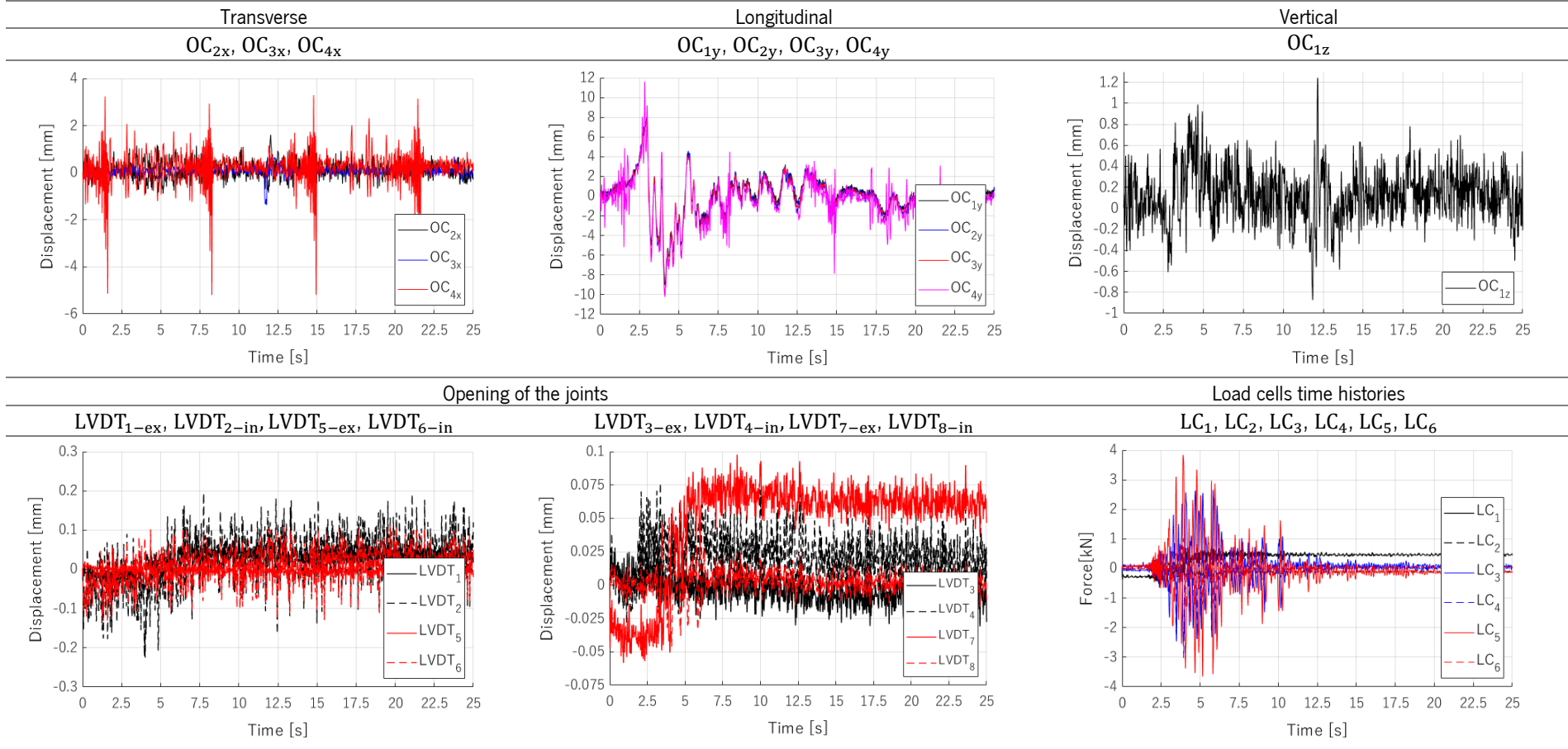
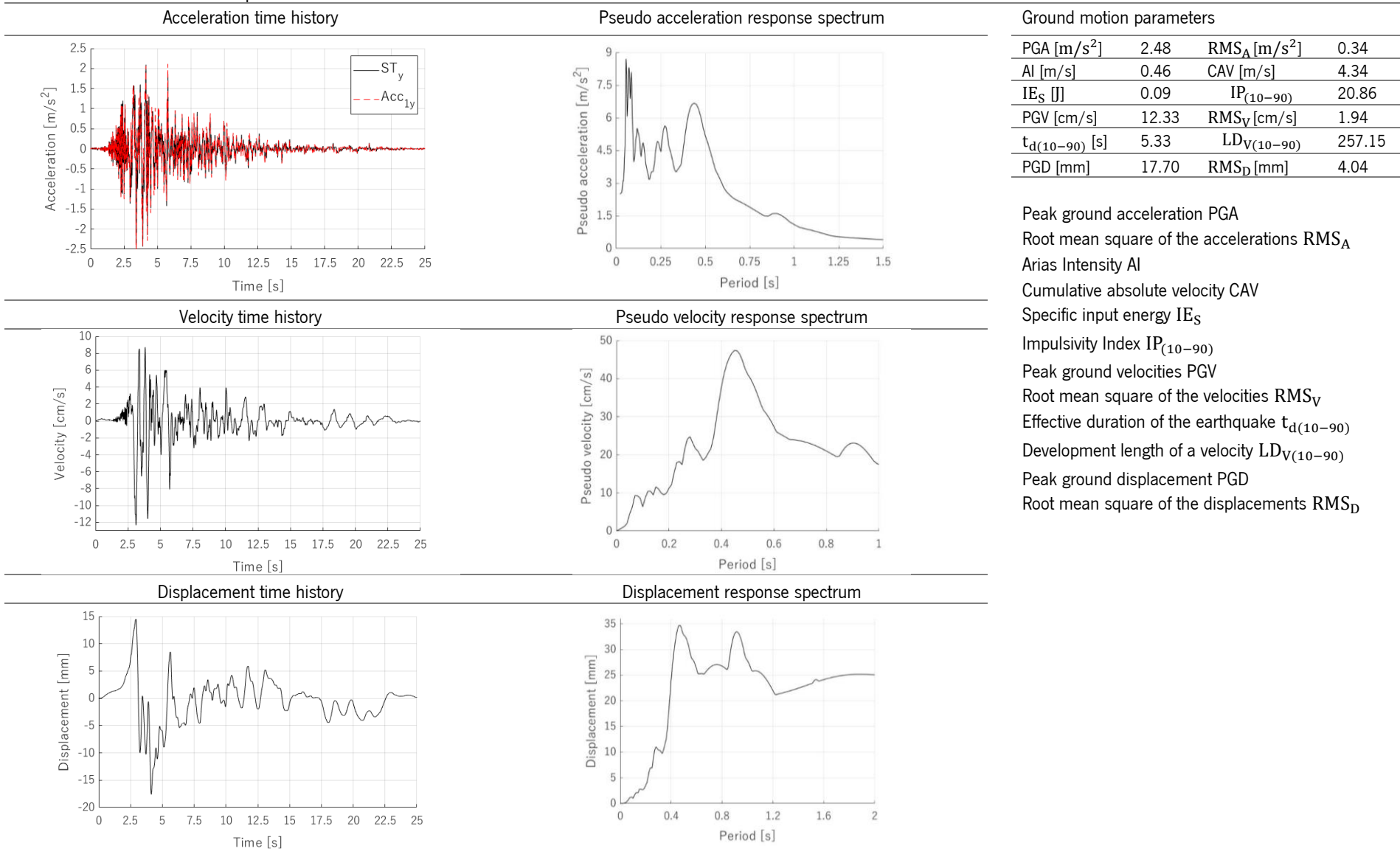


Table A5-17. ST-SM-50%: input data and time histories



Peak ground acceleration PGA
 Root mean square of the accelerations RMS_A
 Arias Intensity AI
 Cumulative absolute velocity CAV
 Specific input energy IE_S
 Impulsivity Index IP₍₁₀₋₉₀₎
 Peak ground velocities PGV
 Root mean square of the velocities RMS_V
 Effective duration of the earthquake t_{d(10-90)}
 Development length of a velocity LD_{V(10-90)}
 Peak ground displacement PGD
 Root mean square of the displacements RMS_D

Table A5-18. ST-SM-50%: acceleration response

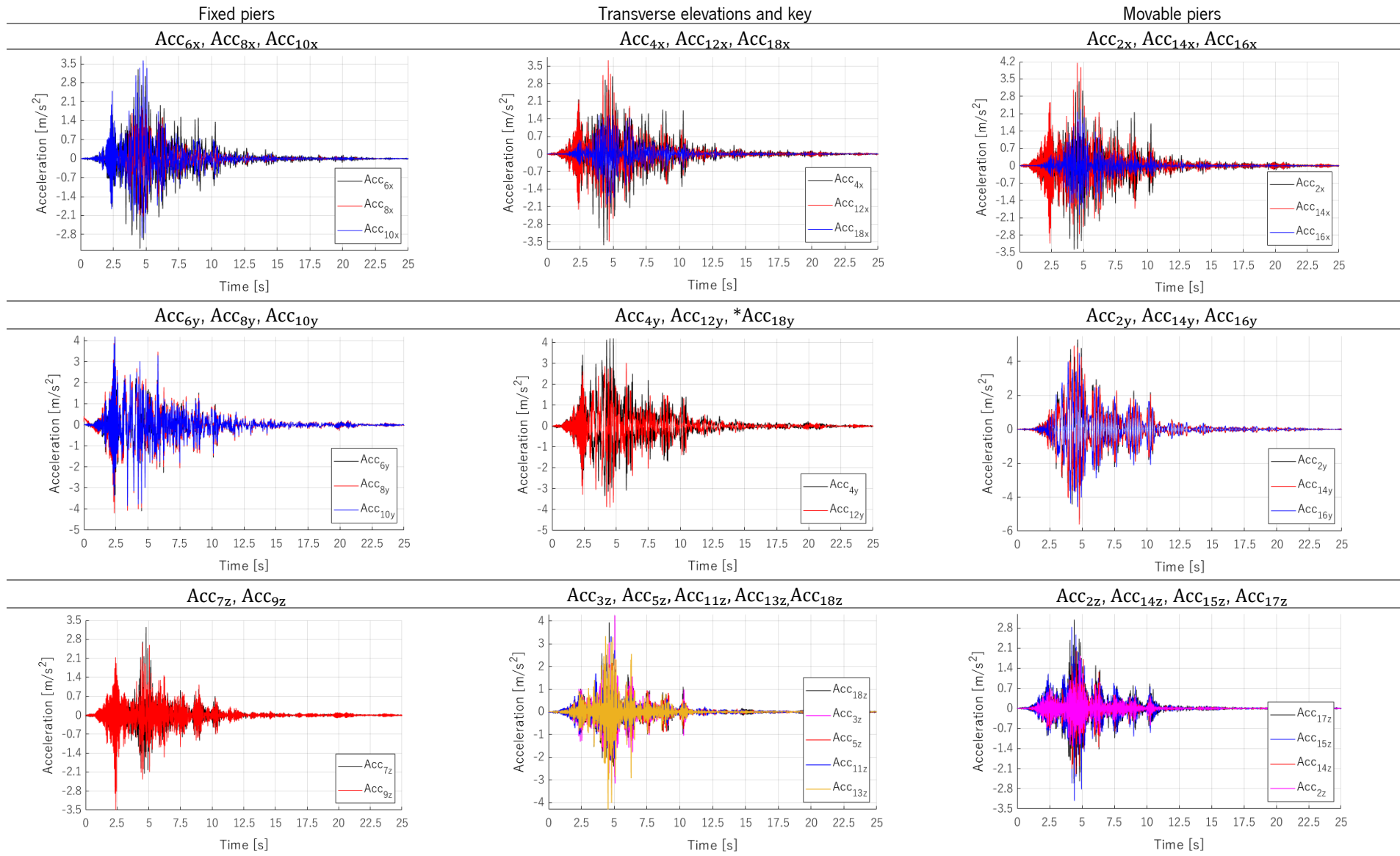


Table A5-19. ST-SM-50%: displacements and force response

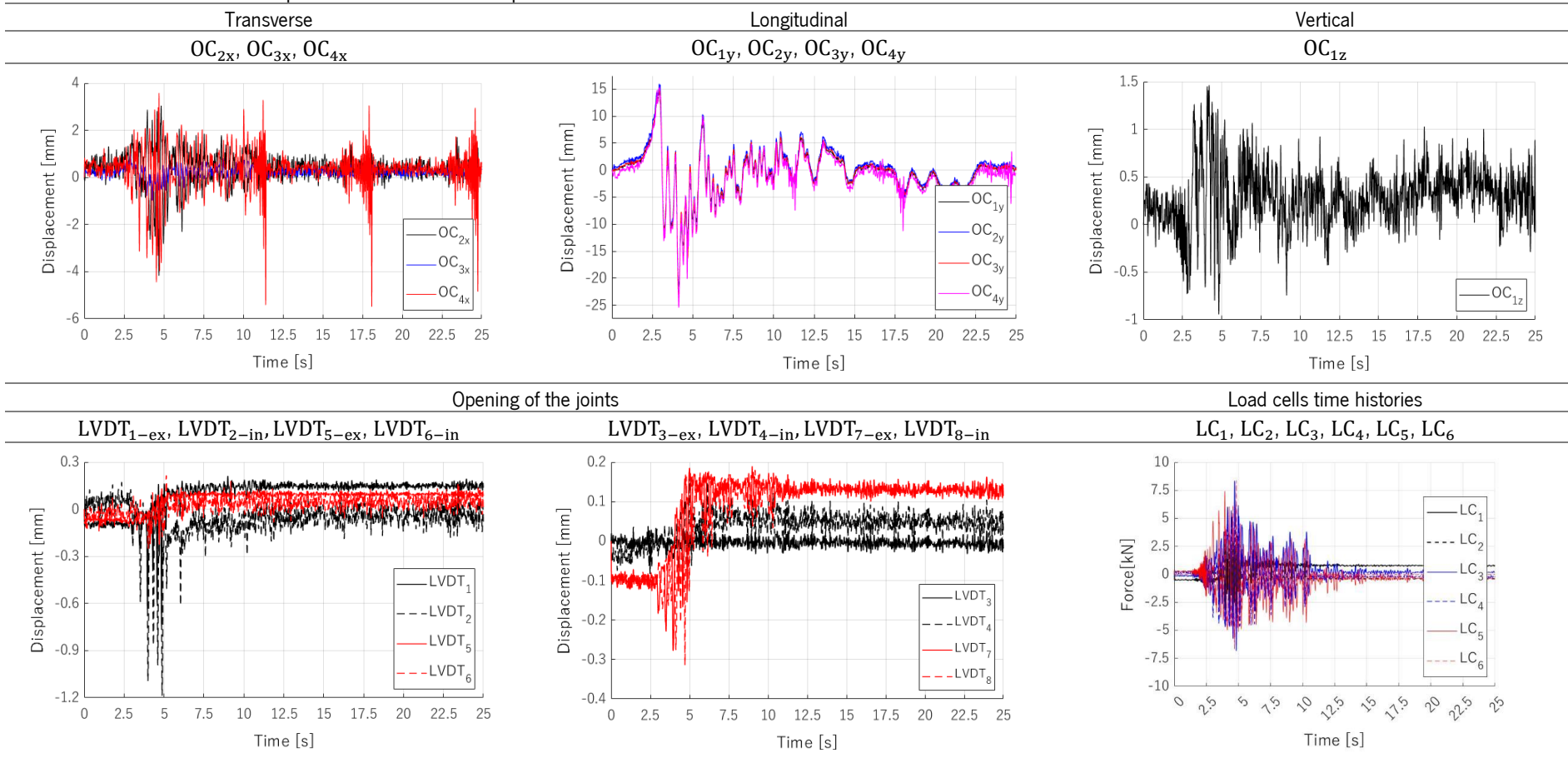
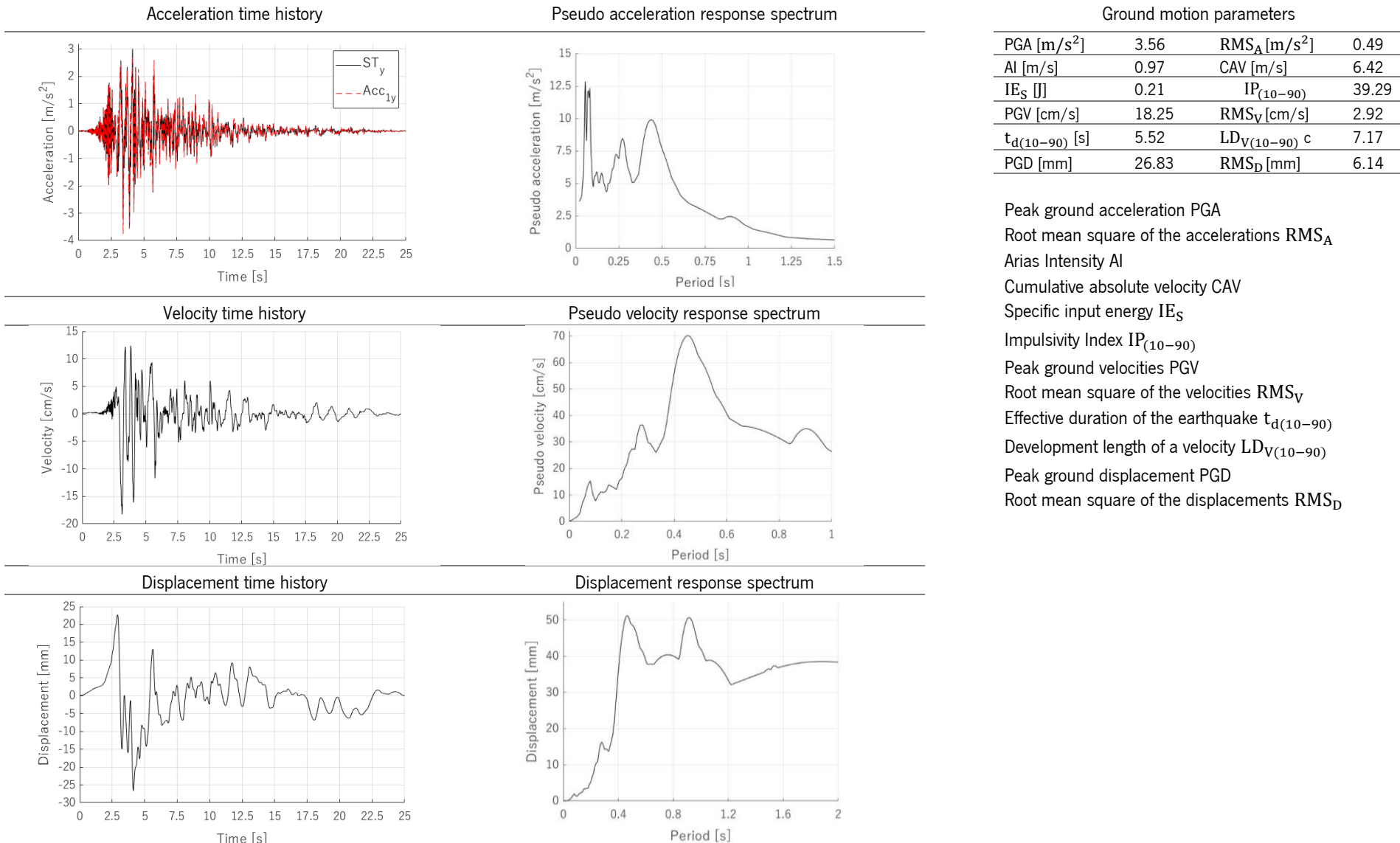


Table A5-20. ST-SM-75%: input data and time histories



- Peak ground acceleration PGA
- Root mean square of the accelerations RMS_A
- Arias Intensity AI
- Cumulative absolute velocity CAV
- Specific input energy IE_S
- Impulsivity Index IP₍₁₀₋₉₀₎
- Peak ground velocities PGV
- Root mean square of the velocities RMS_V
- Effective duration of the earthquake t_{d(10-90)}
- Development length of a velocity LD_{V(10-90)}
- Peak ground displacement PGD
- Root mean square of the displacements RMS_D

Table A5-21. ST-SM-75%: acceleration response

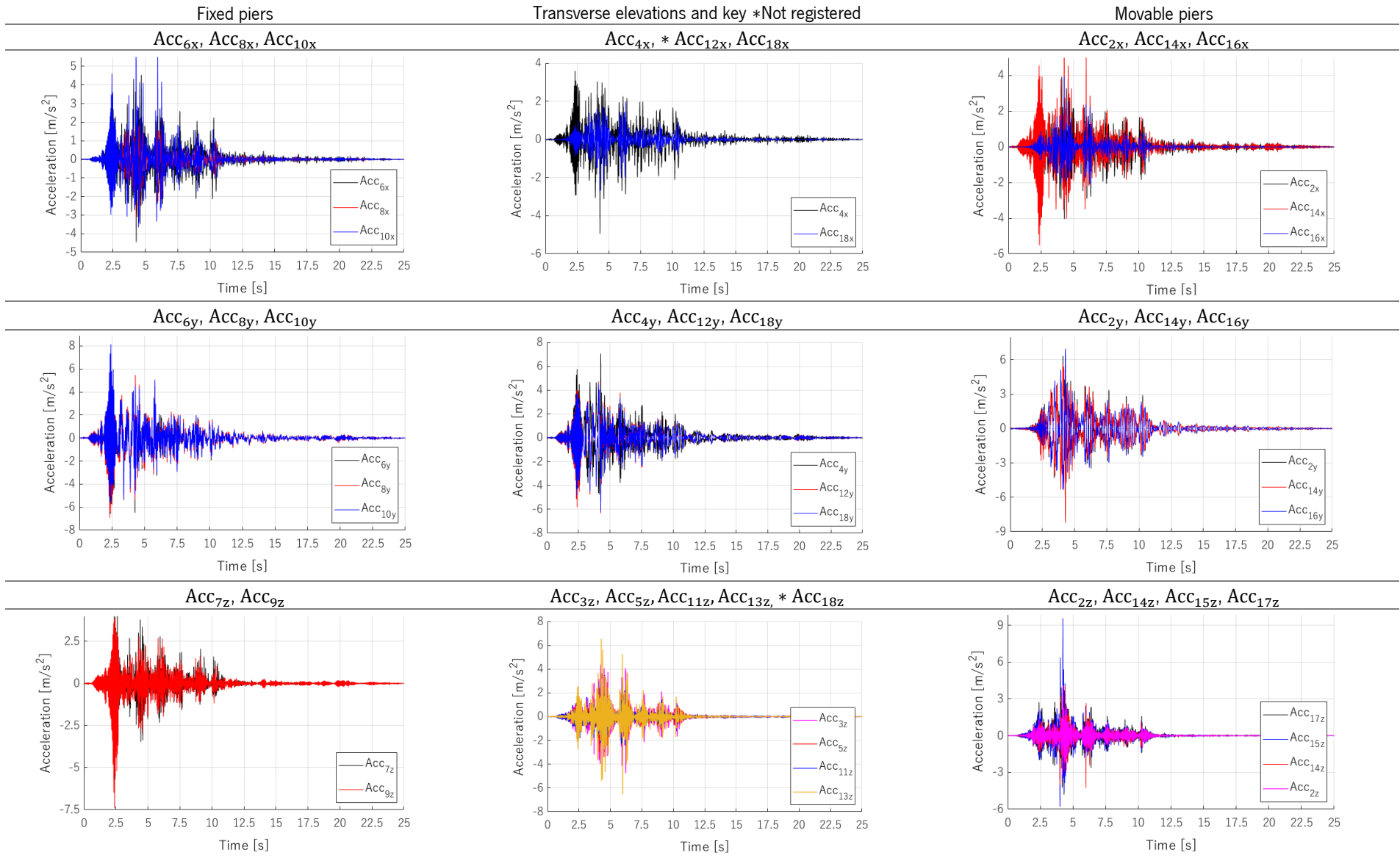


Table A5-22. ST-SM-75%: displacements and force response

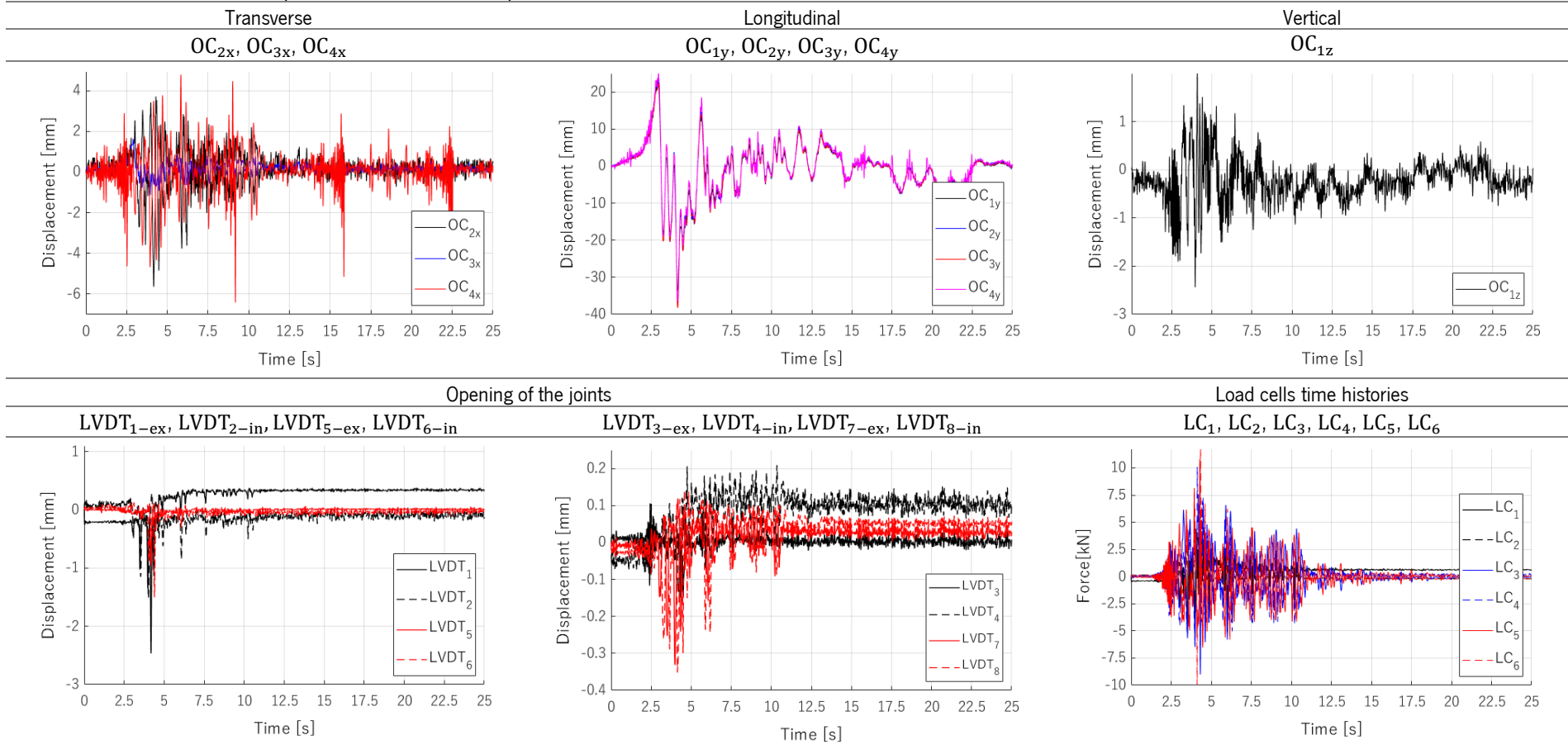


Table A5-23. ST-SM-100%: input data and time histories

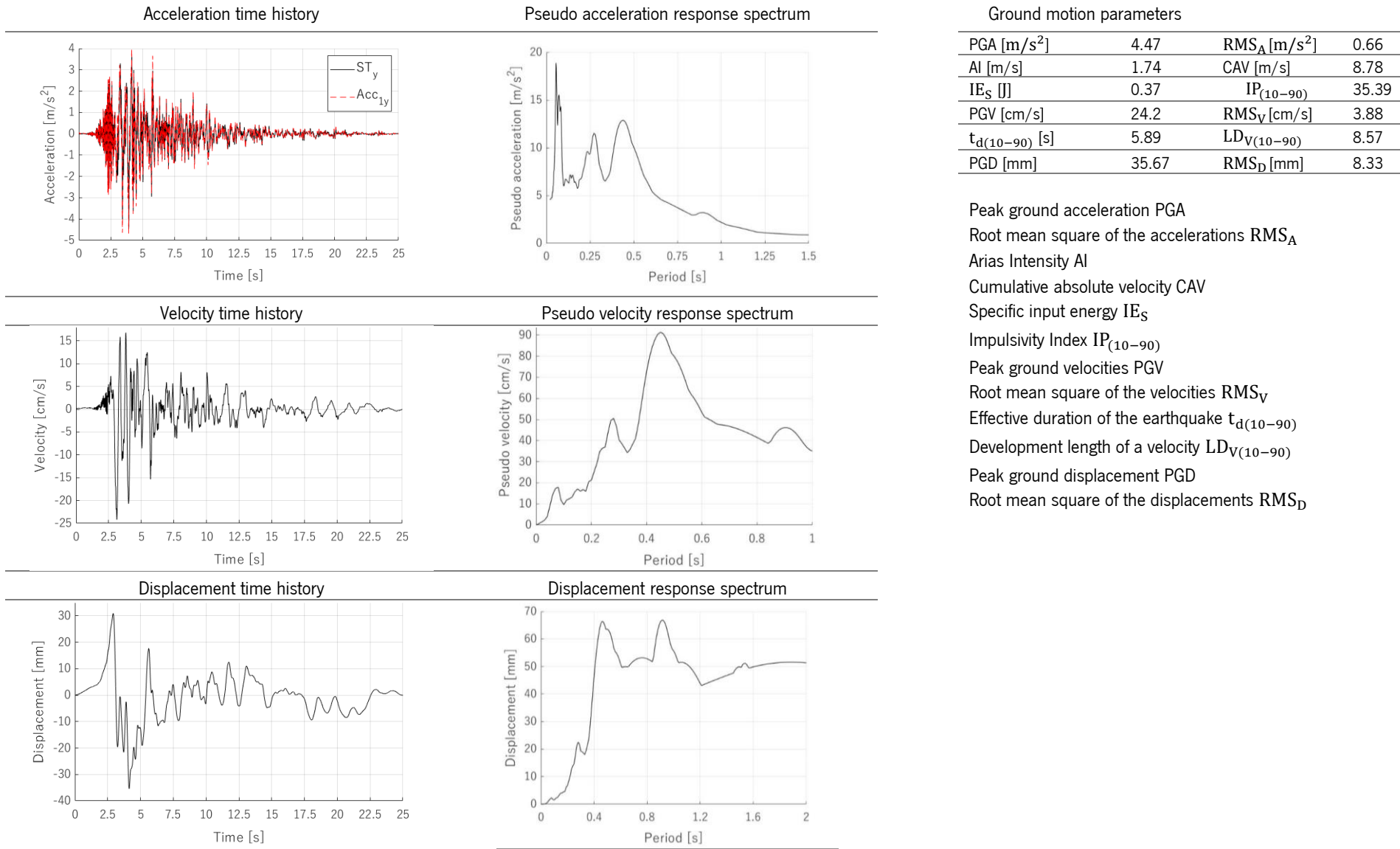


Table A5-24. ST-SM-100%: acceleration response

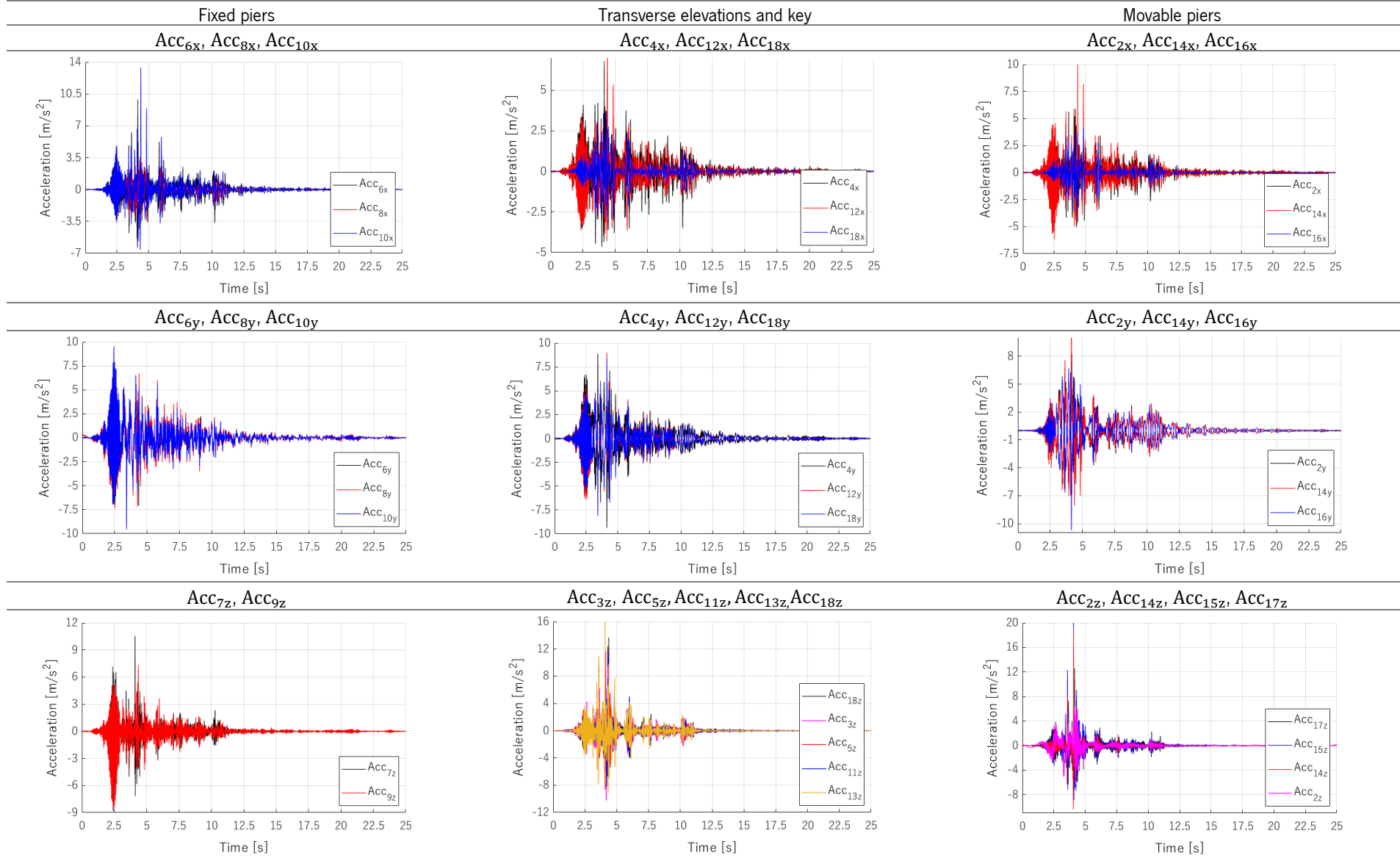


Table A5-25. ST-SM-100%: displacements and force response

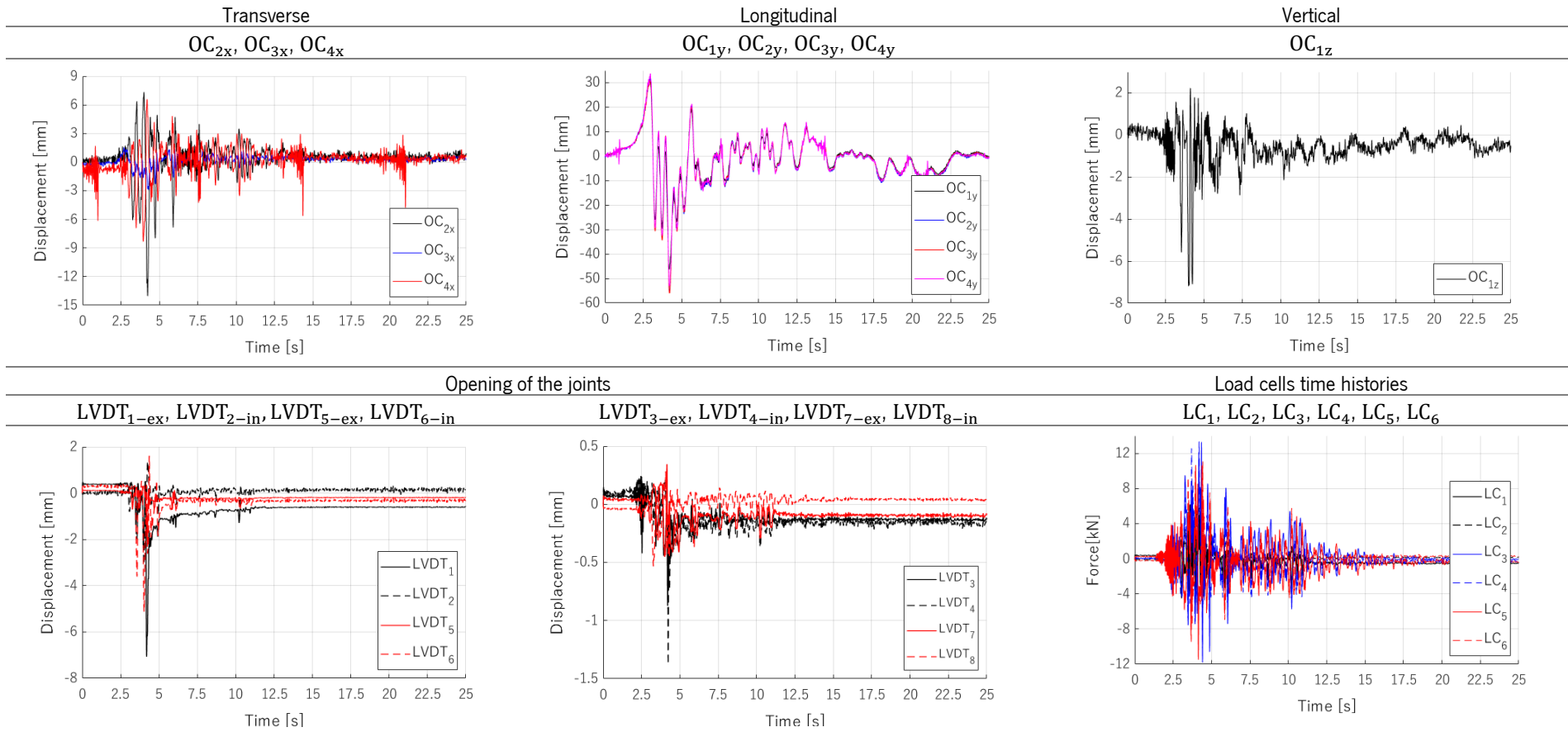
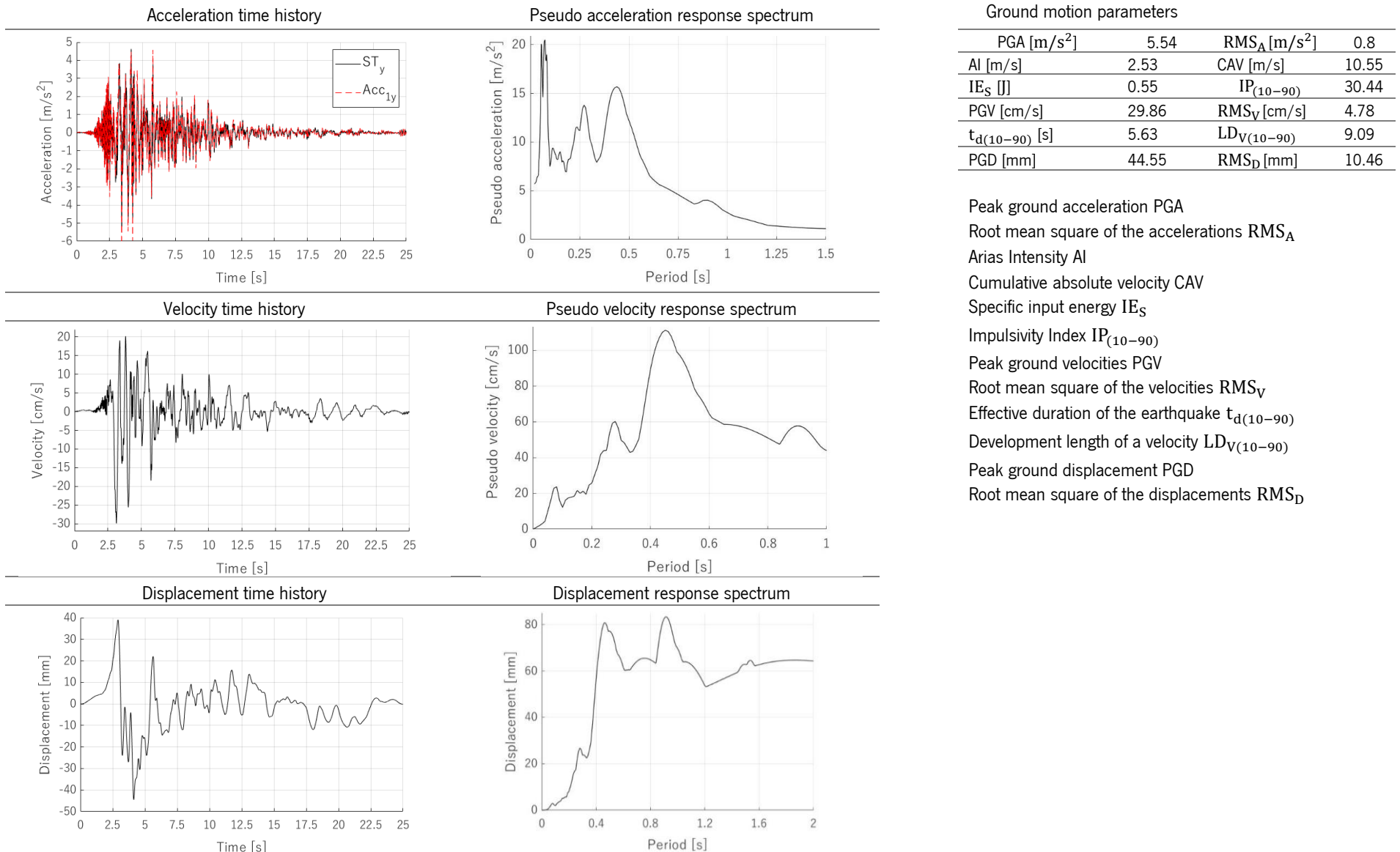


Table A5-26. ST–SM–125%: input data and time histories



Peak ground acceleration PGA
 Root mean square of the accelerations RMS_A
 Arias Intensity AI
 Cumulative absolute velocity CAV
 Specific input energy IE_S
 Impulsivity Index IP₍₁₀₋₉₀₎
 Peak ground velocities PGV
 Root mean square of the velocities RMS_V
 Effective duration of the earthquake t_{d(10-90)}
 Development length of a velocity LD_{V(10-90)}
 Peak ground displacement PGD
 Root mean square of the displacements RMS_D

Table A5-27. ST-SM-125%: acceleration response

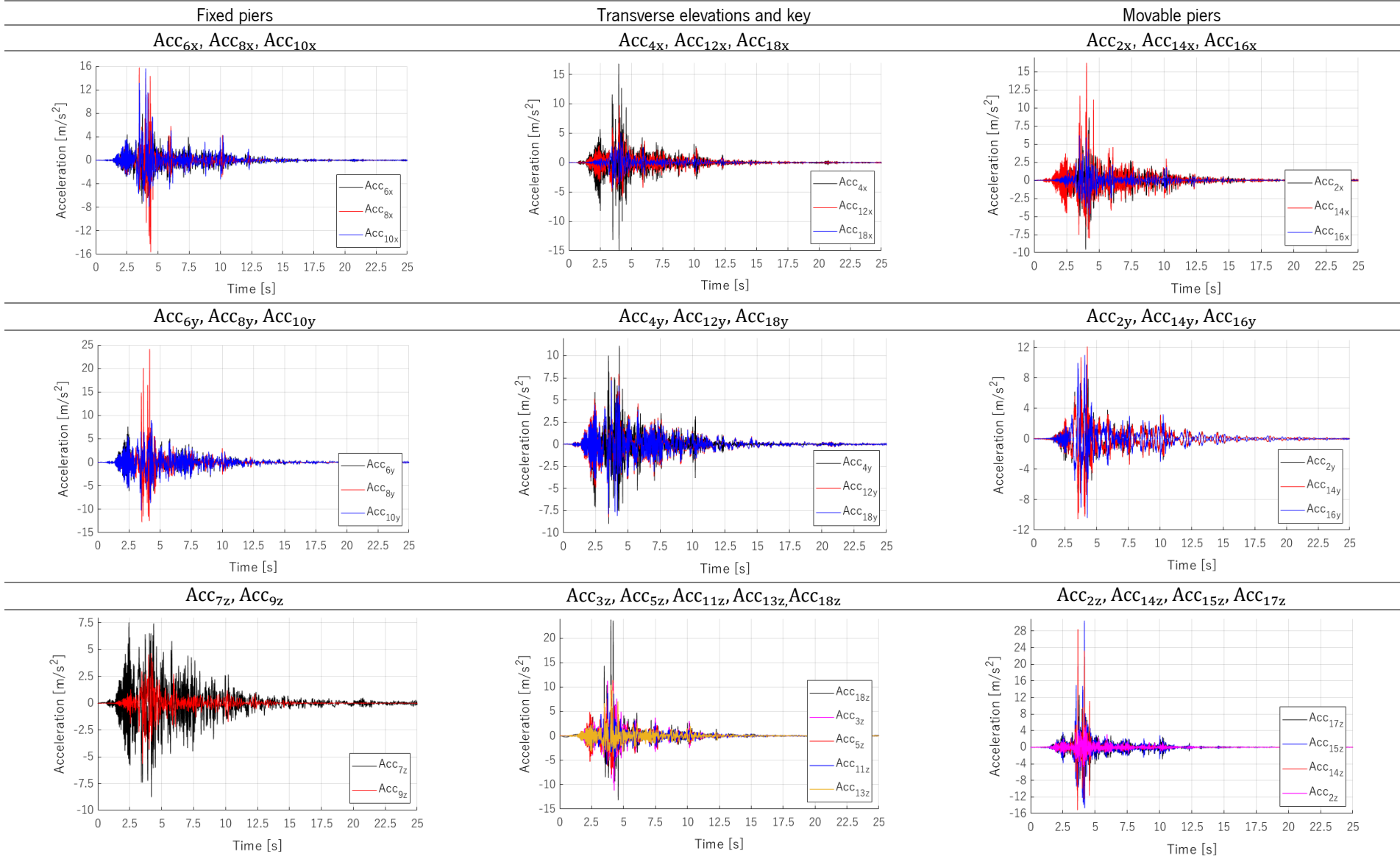


Table A5-28. ST-SM-125%: displacements and force response

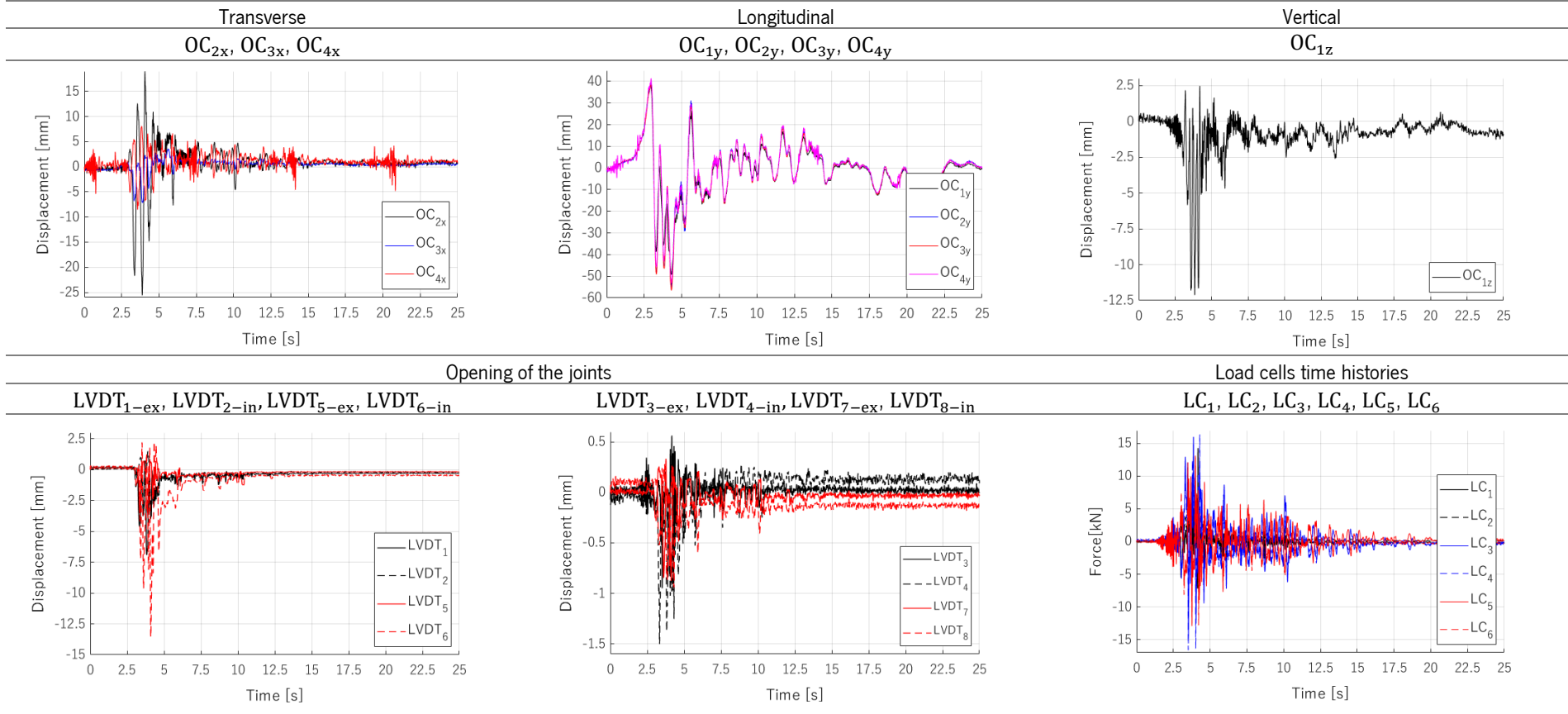


Table A5-29. ST-SM-150%: input data and time histories

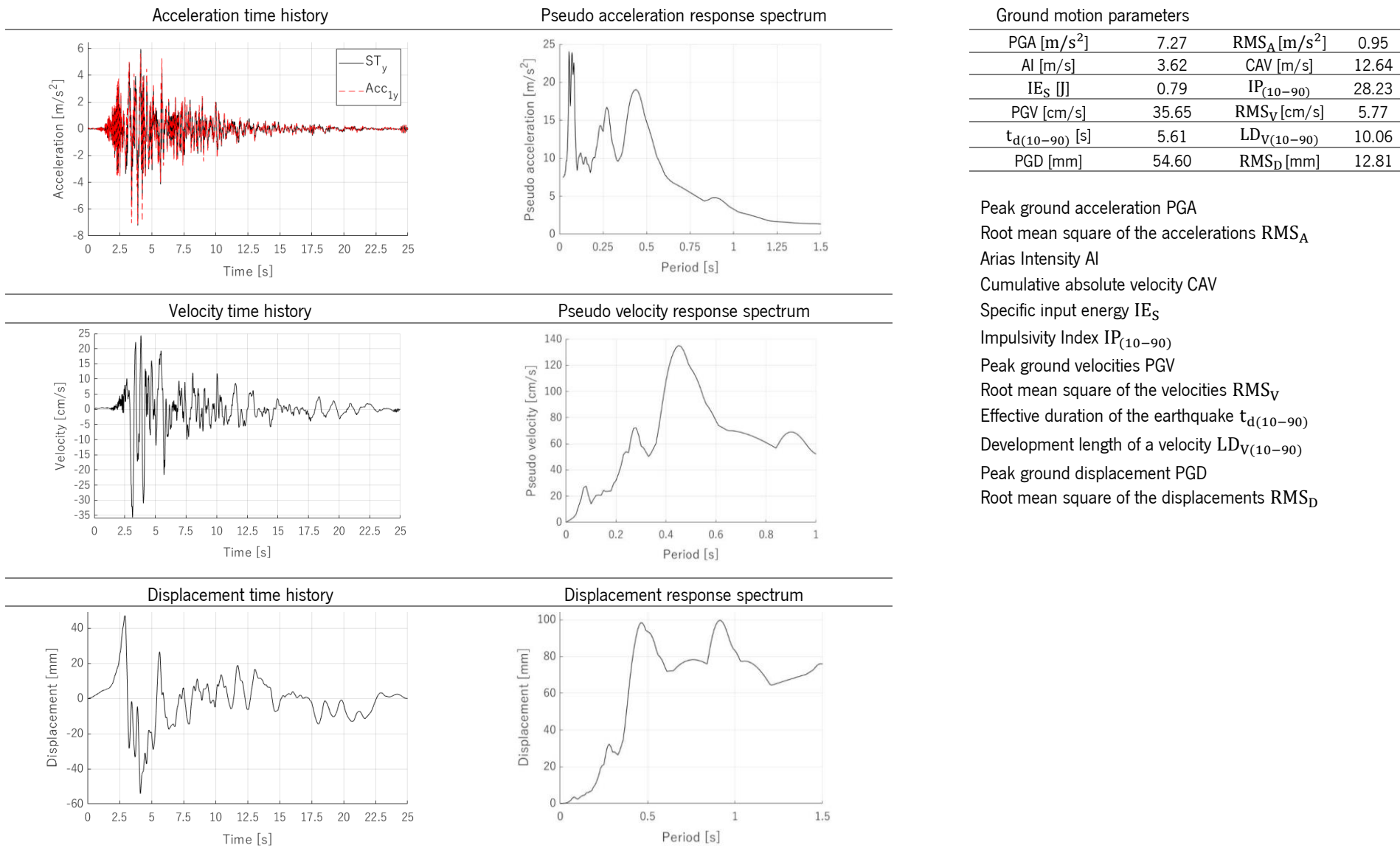


Table A5-30. ST-SM-150%: acceleration response

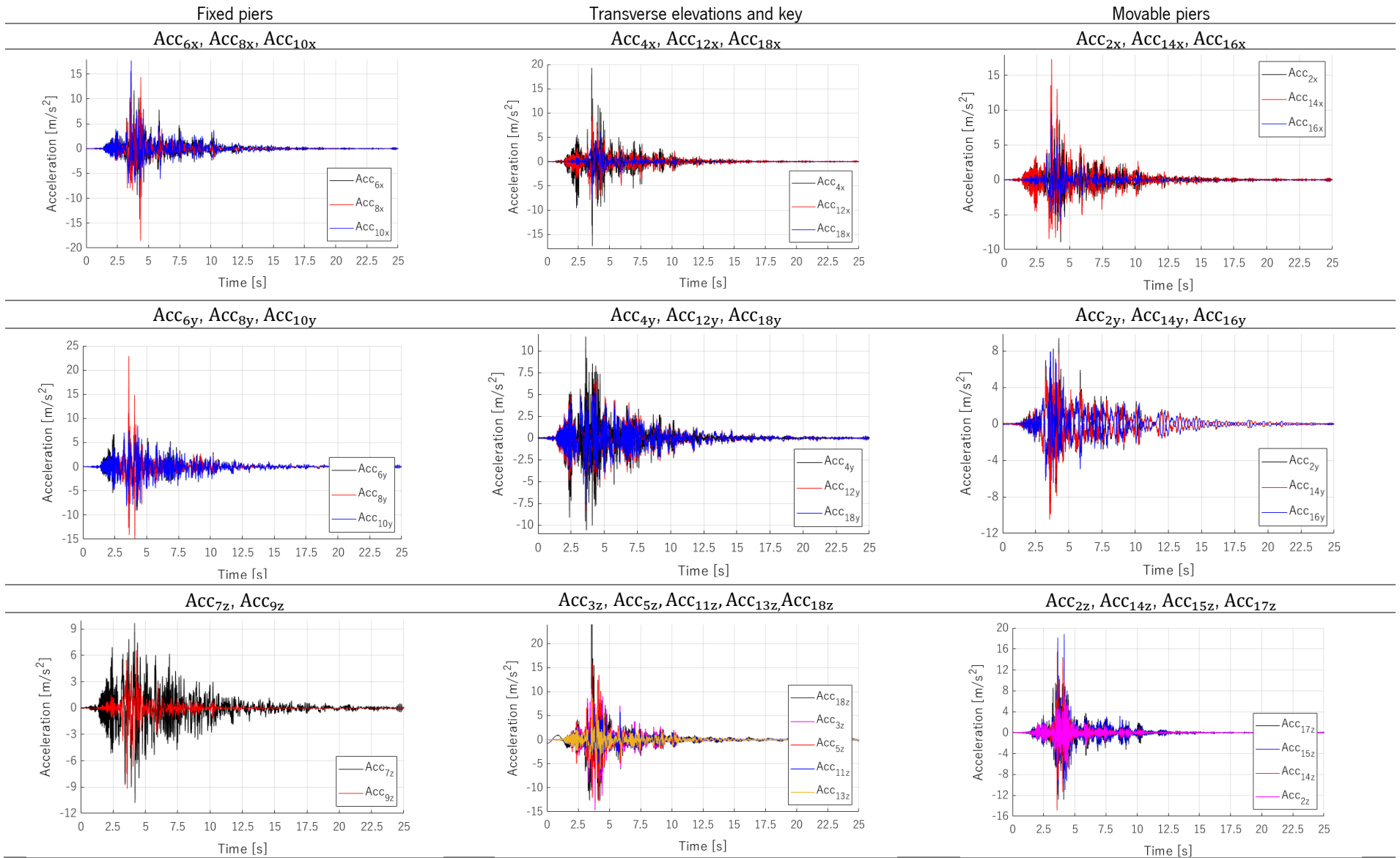
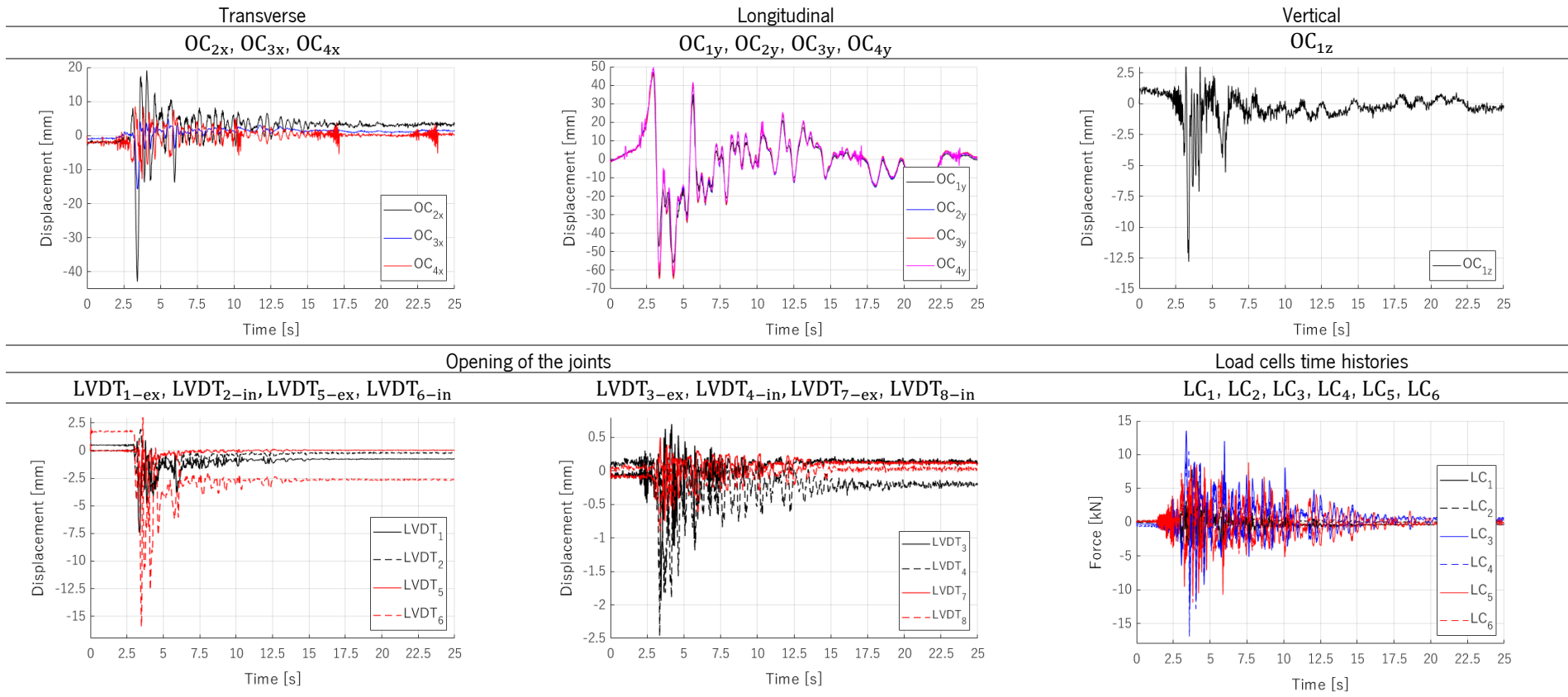


Table A5-31. ST-SM-150%: displacements and force response



References

- Abraham, D. (1934) *Viollet-le-Duc et le rationalisme médiéval, Bulletin Monumental. (in French)*. Paris: Vicent, Fréal et Cie. doi:10.3406/bulmo.1934.10100.
- Abrams, D. *et al.* (2017) 'Out-of-Plane Seismic Response of Unreinforced Masonry Walls: Conceptual Discussion, Research Needs, and Modeling Issues', *International Journal of Architectural Heritage*, 11(1), pp. 22–30. doi:10.1080/15583058.2016.1238977.
- Alberti, L.B. (1485) *De re aedificatoria (I dieci libri dell'Architettura)*. Edited by G. Zempel. Translated in Italian by Cosimo Bartoli: Nicolai Laurentii Alamani.
- Albuerne, A. and Williams, M.S. (2017) 'Structural appraisal of a Roman concrete vaulted monument: The Basilica of Maxentius', *International Journal of Architectural Heritage*, pp. 1–35. doi:10.1080/15583058.2017.1309086.
- Alforno, M. *et al.* (2020) 'Validation of Simplified Micro-models for the Static Analysis of Masonry Arches and Vaults', *International Journal of Architectural Heritage*, pp. 1–17. doi:10.1080/15583058.2020.1808911.
- Alforno, M. *et al.* (2021) 'Numerical investigation of the influence of constructive aspects on the structural behaviour of masonry cross vaults', *International Journal of Architectural Heritage* [Preprint].
- Alforno, M. *et al.* (2022) 'Seismic behaviour of cross vaults with different brick pattern', *Bulletin of Earthquake Engineering* [Preprint], (0123456789). doi:10.1007/s10518-022-01347-6.
- Allahvirdizadeh, R., Oliveira, D.V. de C. and Silva, R.A. (2019) 'Numerical modeling of the seismic out-of-plane response of a plain and TRM-strengthened rammed earth subassembly', *Engineering Structures*, 193(May), pp. 43–56. doi:10.1016/j.engstruct.2019.05.022.
- Andreu, A., Gil, L. and Roca, P. (2007) 'Computational analysis of masonry structures with a funicular model', *Journal of Engineering Mechanics*, 133(4), pp. 473–480. doi:10.1061/(ASCE)0733-9399(2007)133:4(473).
- Angelillo, M., Lourenço, P.B. and Milani, G. (2014) 'Masonry behaviour and modelling', *CISM International Centre for Mechanical Sciences, Courses and Lectures*, 551, pp. 1–26. doi:10.1007/978-3-7091-1774-3_1.
- ArteMis (2018) 'Ambient Response Testing and Modal Identification Software.'
- ASTM-E519 (2002) 'Standard Test Method for Diagonal Tension (Shear) in Masonry Assemblages'. United States.

- Autiero, F. *et al.* (2020) 'Mechanical performance of full-scale Pompeii-like masonry panels', *Construction and Building Materials*, 251, p. 118964. doi:10.1016/j.conbuildmat.2020.118964.
- Avelino, R.M. *et al.* (2021) 'Parametric Stability Analysis of Groin Vaults'.
- Avila, L. (2014) *Seismic behavior of concrete block masonry buildings*.
- Baraccani, S. *et al.* (2020) 'Experimental test on a fibre-reinforced scaled cross vault subjected to in-plane shear displacements at the springings', *Construction and Building Materials*, 265, p. 120305. doi:10.1016/j.conbuildmat.2020.120305.
- Baraschino, R., Baltzopoulos, G. and Iervolino, I. (2019) 'A note on the selection of accelerograms according to the circular on the application of the NTC18', *Progettazione Sismica*, 12(2), pp. 25–34. doi:10.7414/PS.11.2.25-34.
- Baronio, G. *et al.* (2003) 'Characterisation of the materials used in the construction of the Noto Cathedral', *Construction and Building Materials*, 17(8), pp. 557–571. doi:10.1016/j.conbuildmat.2003.08.007.
- Baronio, G. and Binda, L.A. (1991) 'Experiment Approach To a Procedure for the Investigation of Historic Mortars', *9th Int. Brick-Block Masonry Conference*, 3, pp. 1397–1405. Available at: <http://www.hms.civil.uminho.pt/ibmac/1991/1397.pdf>.
- Belytschko, T. (1983) 'An Overview of Semidiscretization and Time Integration Procedures', in T. Belytschko and T.J.R. Hughes (ed.) *Computational Methods for Transient Analysis*. New York: Elsevier Science Publishers, B.V, pp. 1–65.
- Bertolesi, E. *et al.* (2019) 'Research and practice on masonry cross vaults – A review', *Engineering Structures*, 180, pp. 67–88. doi:10.1016/j.engstruct.2018.10.085.
- Beyer, K., Tondelli, M. and Petry, S. (2014) 'Seismic response of a 4 storey building with reinforced concrete and unreinforced masonry walls', *International Masonry Conference 2014*, pp. 1–11.
- Bianchini, N. *et al.* (2019) 'Seismic assessment of masonry cross vaults through numerical nonlinear static and dynamic analysis', in Papadrakakis, M. and Fragiadakis, M. (eds) *COMPADYN 2019 7th ECCOMAS Thematic Conference on Computational Methods in Structural Dynamics and Earthquake Engineering*. Crete, Greece, pp. 600–612. Available at: <https://doi.org/10.7712/120119.6942.18709>.
- Bianchini, N. *et al.* (2020) *Seismic Response of Masonry Cross Vaults: Shaking table tests and numerical validations*. Available at: <https://sera-crossvault.wixsite.com/blindprediction>.

- Bianchini, N. *et al.* (2021) 'Seismic performance of masonry cross vaults through shaking table testing on a scaled model', in Roca, P., Pelà, L., and Molins, C. (eds) *12th International Conference on Structural Analysis of Historical Constructions*. Barcelona.
- Bianchini, N. *et al.* (2023) 'Modelling of the dynamic response of a reduced scale dry joints groin vault', *Journal of Building Engineering*, 66. Available at: <https://doi.org/10.1016/j.jobbe.2023.105826>.
- Binda, L.A., Fontana, A. and Mirabella, G. (1994) 'Mechanical behaviour and stress distribution in multiple-leaf stone walls', in *10th Int. Brick/Block Masonry Conference*. Calgary, pp. 51–59.
- Binda, L.A., Mirabella Roberti, G. and Tiraboschi, C. (1996) 'Problemi di misura dei parametri meccanici della muratura e dei suoi componenti (in Italian)', *La Meccanica delle Murature tra Teoria e Progetto*, pp. 45–54.
- Block, P. (2005) 'Equilibrium systems', *Architectural Engineering*, pp. 1–42.
- Block, P. (2009) *Thrust Network Analysis: exploring three-dimensional equilibrium*. PhD thesis, Massachusetts Institute of Technology. Available at: <http://hdl.handle.net/1721.1/49539>.
- Block, P., Ciblac, T. and Ochsendorf, J.A. (2006) 'Real-time limit analysis of vaulted masonry buildings', *Computers and Structures*, 84(29–30), pp. 1841–1852. doi:10.1016/j.compstruc.2006.08.002.
- Block, P. and Lachauer, L. (2014) 'Three-Dimensional (3D) Equilibrium Analysis of Gothic Masonry Vaults', *International Journal of Architectural Heritage*, 8(3), pp. 312–335. doi:10.1080/15583058.2013.826301.
- Block, P. and Ochsendorf, J.A. (2002) 'Lower-bound Analysis of Masonry Vaults', (1892).
- Block, P. and Ochsendorf, J.A. (2007) 'Thrust network analysis: a new methodology for three-dimensional equilibrium', *Journal of the International Association for Shell and Spatial Structures (J. IASS)*, 48(3), pp. 1–8. Available at: http://18.89.2.136/sites/all/files/attachments/project/block_ochs_IASS_2007.pdf.
- Boni, C., Ferretti, D. and Lenticchia, E. (2021) 'Effects of Brick Pattern on the Static Behavior of Masonry Vaults', *International Journal of Architectural Heritage*, 00(00), pp. 1–21. doi:10.1080/15583058.2021.1874565.
- Borri, A. *et al.* (2015) 'A method for the analysis and classification of historic masonry', *Bulletin of Earthquake Engineering*, 13(9), pp. 2647–2665. doi:10.1007/s10518-015-9731-4.
- Borri, A. and Bussi, L. (2011) *Archi e volte in zona sismica. Meccanica delle strutture voltate. (in Italian)*. Edited by Doppiovoce.

- Borri, A., Cangi, G. and De Maria, A. (2013) 'Caratterizzazione meccanica delle murature (anche alla luce del recente sisma in Emilia) e interpretazione delle prove sperimentali a taglio (in Italian)', in Braga, F., Galeota, D., and Occhiuzzi, A. (eds) *ANIDIS XV _ 15° convegno Associazione Nazionale Italiana di Ingegneria Sismica*. L'Aquila (in Italian).
- Borri, A., Corradi, M. and Vignoli, A. (2001) 'Seismic upgrading of masonry structures with FRP', in *7th International Conference on Inspection Appraisal Repairs and Maintenance of buildings and structures*. Nottingham Trent - UK.
- Brandonisio, G. *et al.* (2013) 'Damage and performance evaluation of masonry churches in the 2009 L'Aquila earthquake', *Engineering Failure Analysis*, 34, pp. 693–714. doi:10.1016/j.engfailanal.2013.01.021.
- Breymann, G.A. (1885) 'Costruzioni in pietra e strutture murali', in *Costruzione dei coperti in pietra naturale ed in mattoni. (in Italian)*. Biblioteca Internazionale dell'Ingegnere.
- Briccoli Bati, S. *et al.* (2002) 'Costruzioni voltate in muratura prototipo volta a crociera', in *Italian*. Firenze.
- Bruggi, M. and Taliercio, A. (2015) 'Analysis of masonry vaults as a topology optimization problem', in *Third International Conference on Mechanical Models in Structural Engineering*. Seville, pp. 91–100.
- Bui, T.T. *et al.* (2017) 'Discrete element modelling of the in-plane and out-of-plane behaviour of dry-joint masonry wall constructions', *Engineering Structures*, 136(January), pp. 277–294. doi:10.1016/j.engstruct.2017.01.020.
- Bussi, L. (2011) 'Le strutture resistenti per forma', in Borri, A. and Bussi, L. (eds) *Archi e volte in zona sismica (in Italian)*. Doppiovoce. Napoli, pp. 1–306.
- Caliò, I., Cannizzaro, F. and Marletta, M. (2010) 'A discrete element for modeling masonry vaults', *Advanced Materials Research*, 133–144, pp. 447–452. doi:10.4028/www.scientific.net/AMR.133-134.447.
- Caliò, I., Cannizzaro, F. and Pantò, B. (2012) 'A macro-element approach for modeling the nonlinear behaviour of monumental buildings under static and seismic loadings', in *World Conference in Earthquake Engineering*.
- Campanella, G. (1928) *Trattato generale teorico pratico dell'arte dell'ingegnere civile, industriale ed architetto, in Italian*. Edited by Vallardi. Milano.
- Candeias, P.X. (2008) *Seismic vulnerability assessment of masonry buildings*. PhD thesis, University of Minho and Laboratório Nacional de Engenharia Civil.

- Candeias, P.X. *et al.* (2016) 'Experimental Assessment of the Out-of-Plane Performance of Masonry Buildings Through Shaking Table Tests', *International Journal of Architectural Heritage*, pp. 31–58. doi:10.1080/15583058.2016.1238975.
- Cangi, G. (2009) 'Tipologie costruttive e tipologie di intervento', in *Ruolo delle volte e tecniche di consolidamento*, pp. 1–14.
- Cangi, G. (2011) 'Geometrie, comportamento meccanico e tecniche costruttive.', in Borri, A. and Bussi, L. (eds) *Archi e volte in zona sismica. Meccanica delle strutture voltate. (in Italian)*. Napoli: Doppiovoce.
- Cangi, G. (2012) *Manuale del recupero strutturale e antisismico*. 2nd edn. Rome: DEI.
- Cangi, G. (2016) *VOLTE Geometrie , comportamento meccanico e tecniche costruttive (in Italian)*.
- Cannizzaro, F. (2011) *Un nuovo approccio di modellazione della risposta sismica degli edifici storici*. PhD thesis, Università degli studi di Catania. doi:10.13140/RG.2.1.3094.3125.
- Carfagnini, C. *et al.* (2018) 'The effects of in-plane shear displacements at the springings of Gothic cross vaults', *Construction and Building Materials*, 186, pp. 219–232. doi:10.1016/j.conbuildmat.2018.07.055.
- Carozzi, F.G. *et al.* (2018) 'Ancient masonry arches and vaults strengthened with TRM , SRG and FRP composites: Experimental evaluation', *Composite Structures*, 187, pp. 466–480. doi:10.1016/j.compstruct.2017.12.075.
- Carvalho, E. (1998) 'Seismic testing structures', in *11th European conference on Earthquake Engineering*.
- Cattari, S., Resemini, S. and Lagomarsino, S. (2008) 'Modelling of vaults as equivalent diaphragms in 3D seismic analysis of masonry buildings', in D'Ayala, D.F. and Fodde (eds) *Structural Analysis of Historical Constructions*. London: Taylor & Francis Group, pp. 517–524.
- Cescatti, E., Da Porto, F. and Modena, C. (2018) 'In-Situ Destructive Testing of Ancient Strengthened Masonry Vaults', *International Journal of Architectural Heritage*, 12(3), pp. 350–361. doi:10.1080/15583058.2017.1323243.
- Chiozzi, A., Milani, G. and Tralli, A. (2017a) 'A Genetic Algorithm NURBS-based new approach for fast kinematic limit analysis of masonry vaults', *Computers and Structures*, 182, pp. 187–204. doi:10.1016/j.compstruc.2016.11.003.
- Chiozzi, A., Milani, G. and Tralli, A. (2017b) 'Fast kinematic limit analysis of FRP-reinforced masonry vaults. II: Numerical simulations', *Journal of Engineering Mechanics*, 143(9), pp. 1–19. doi:10.1061/(ASCE)EM.1943-7889.0001268.

- Chopra, A.K. (2012) *Numerical Evaluation of Dynamic Response, Dynamics of Structures, Theory and Applications to Earthquake Loading*.
- Civerra, C., Lemme, A. and Cifani, G. (2007) 'Strumenti per il rilievo del danno e della vulnerabilità sismica dei beni culturali', *Ministero per i Beni e le Attività Culturali Soprintendenza per i Beni Architettonici, per il Paesaggio e per il Patrimonio Storico, Artistico e Etnoantropologico del Molise*, (Sisma Molise 2002), pp. 1–248. Available at: http://www.art-conservation.fr/programmes/strumenti_sismica.pdf.
- CNR-DT 200 R1 (2013) 'Guide for the Design and Construction of Externally Bonded FRP Systems for Strengthening Existing Structures'. Italy. Available at: <https://www.cnr.it/en/node/2636>.
- CNR-DT 212 (2013) 'Guide for the Probabilistic Assessment of the Seismic Safety of Existing Buildings'. Italy.
- Como, M. (2017) *Statics of Historic Masonry Constructions*. Third. Edited by M. Frémond and F. Maceri. Rome: Springer (Series in Solid and Structural Mechanics). doi:10.1007/978-3-642-30132-2.
- Contestabile, M. *et al.* (2016) 'Static Analysis of Cross Vaults: The Case of the Cathedral of Casertavecchia', pp. 329–345. doi:10.2174/1874836801610010329.
- Cosenza, E. and Manfredi, G. (2000) 'Damage indices and damage measures', *Progress in Structural Engineering and Materials*, 2, pp. 50–59. doi:[https://doi.org/10.1002/\(SICI\)1528-2716\(200001/03\)2:1<50::AID-PSE7>3.0.CO;2-S](https://doi.org/10.1002/(SICI)1528-2716(200001/03)2:1<50::AID-PSE7>3.0.CO;2-S).
- Couplet, P. (1730) 'Seconde partie de l'examen de la poussée des voûtes', *Mémoires de l'Académie Royale des Sciences de Paris (in French)*, pp. 117–141.
- Creazza, G. *et al.* (2002) 'Analyses of Masonry Vaults: A Macro Approach based on Three-Dimensional Damage Model', *Journal of Structural Engineering*, 128(5), p. 646. doi:10.1061/(ASCE)0733-9445(2002)128:5(646).
- Creazza, G., Meroi, E. and Saetta, A. (2002) 'Analisi delle strutture voltate in muratura soggette a degrado', in Di Pasquale, S. (ed.) *Costruzioni voltate in muratura. (in Italian)*. Firenze: Lib. Alfani, pp. 109–140.
- Croci, G. (1997) 'Strengthening the Basilica of St Francisco of Assisi after the September 1997 Earthquake', *Structural Engineering International*, 3, pp. 1–4.
- Cundall, P.A. and Hart, R.D. (1992) 'Numerical Modelling of Discontinua', *Engineering Computations*, 9(2), pp. 101–113. doi:10.1108/eb023851.
- Cundall, P.A. and Strack, O.D.L. (1979) 'A discrete numerical model for granular assemblies',

- Géotechnique*, 29(1), pp. 47–65. doi:10.1680/geot.1979.29.1.47.
- Cundall, P.A. and Strack, O.D.L. (1980) 'Discussion: A discrete numerical model for granular assemblies', *Géotechnique*, 30(3), pp. 331–336. doi:10.1680/geot.1980.30.3.331.
- Curioni, G. (1868) *L'arte di fabbricare - Materiali da costruzione (in Italian)*. Available at: <https://ejournal.poltektegal.ac.id/index.php/siklus/article/view/298%0Ahttp://repositorio.unan.edu.ni/2986/1/5624.pdf%0Ahttp://dx.doi.org/10.1016/j.jana.2015.10.005%0Ahttp://www.biomedcentral.com/1471-2458/12/58%0Ahttp://ovidsp.ovid.com/ovidweb.cgi?T=JS&P>.
- D'Ayala, D.F. and Tomasoni, E. (2008) 'The structural behaviour of masonry vaults: limit state analysis with finite friction', in D'Ayala, D.F. and Fodde (eds) *Structural Analysis of Historical Constructions*. London: Taylor & Francis Group, pp. 47–61.
- Dejong, M.J. *et al.* (2008) 'Rocking stability of masonry arches in seismic regions', *Earthquake Spectra*, 24(4), pp. 847–865. doi:10.1193/1.2985763.
- Dejong, M.J. and Ochsendorf, J.A. (2010) 'Dynamics of in-plane arch rocking: an energy approach', *Proceedings of the Institution of Civil Engineers - Engineering and Computational Mechanics*, 163(3), pp. 179–186. doi:10.1680/eacm.2010.163.3.179.
- Dell'endice, A. *et al.* (2020) 'Role of imperfections in unreinforced masonry structures: comparison between Discrete Element Modelling and experiments on a 3D-printed scale model of a pavilion vault', *Engineering Structures*, p. 111499. doi:10.1016/j.engstruct.2020.111499.
- DIANA 10.4 (2019a) 'Documentation'. Edited by F. Denise and M. Jonna. Delft, The Netherlands: DIANA FEA BV.
- DIANA 10.4 (2019b) 'Finite element modelling software'. Edited by F. Denise and M. Jonna. Delft, The Netherlands: DIANA FEA BV.
- DIANA 10.5 (2022) 'Finite element modelling software'. Delft, Netherlands.
- Dipartimento della Protezione Civile (2022a) *ITACA 3.1, Italian ACcelerometric Archive*. Available at: http://itaca.mi.ingv.it/ItacaNet_31/#/home.
- Dipartimento della Protezione Civile (2022b) *Rete Accelerometrica Nazionale - RAN*. Available at: <http://ran.protezionecivile.it/IT/>.
- Doran, B. *et al.* (2020) 'Numerical Modeling of Traditional Masonry Walls Strengthened with Grout Injection', *International Journal of Architectural Heritage*, 14(10), pp. 1517–1532. doi:10.1080/15583058.2019.1618970.
- EN 1015-11 (2019) 'Standards Publication Methods of test for mortar for masonry'.
- EN 1015-3 (2004) 'Methods of test for mortar for masonry — Part 3 : Determination of consistence of

- fresh mortar (by flow table)'.
EN 1052-1 (1999) 'Methods of test for masonry - Part 1: Determination of compressive strength', *European Committee for standardization*.
EN 1052-3 (2007) 'Methods of test for masonry – Part 3: Determination of initial shear strength'.
EN 196-1 (2016) 'Methods of testing cement Part 1: Determination of strength'.
EN 445 (2007) 'Grout for prestressing tendons - Test methods'.
EN 772-11 (2011) 'Methods of test for masonry units Part 11 : Determination of water absorption of aggregate concrete , manufactured stone and natural action and the initial rate of water', *BSI Standards Publication*.
EUCENTRE (2017) 'SERA 1st call weight proposals', pp. 1–5.
Eurocode 6 (2001) 'EN 1996-1-1 -Design of Masonry Structures', *Design Studies*.
Ewins, D.J. (2000) *Modal testing: theory, practice and application*. 2nd Editio. Baldock, Hertfordshire, England: Research Studies Press LTD.
Faccio, P., Foraboschi, P. and Siviero, E. (1999) 'Volte in muratura con rinforzi in FRP (in Italian)', *L'Edilizia*, 7/8, pp. 44–50.
Faccioli, E. and Paolucci, R. (2005) *Elementi di sismologia applicata all'ingegneria, (in Italian)*. Edited by Pitagora.
Fagone, M., Rotunno, T. and Briccoli Bati, S. (2016) 'The Groin Vaults of St. John Hospital in Jerusalem: An Experimental Analysis on a Scale Model', *International Journal of Architectural Heritage*, 10, pp. 903–918. doi:10.1080/15583058.2016.1158331.
Fang, D.L. *et al.* (2018) 'Assessing the stability of unreinforced masonry arches and vaults : a comparison of analytical and numerical strategies', *International Journal of Architectural Heritage*, pp. 1–15. doi:10.1080/15583058.2018.1463413.
Faria, R. (1994) *Evaluation of the seismic behaviour of concrete dams via continuum damage model*. University of Porto, Portugal.
Faria, R., Oliver, J. and Cervera, M. (1998) 'A strain-based plastic viscous-damage model for massive concrete structures', *International Journal of Solids and Structures* [Preprint]. doi:10.1016/S0020-7683(97)00119-4.
Fernandes, F.M., Lourenço, P.B. and Castro, F. (2010) 'Ancient Clay Bricks : Manufacture and Properties', in M. Bostenaru Dan et al. (ed.) *Materials, Technologies and Practice in Historic Heritage Structures*. 1st edn. Springer. doi:10.1007/978-90-481-2684-2.
Fitchen, J. (1961) *The Construction of Gothic Cathedrals*. Phoenix Ed. Chicago: The University of

- Chicago Press.
- Foraboschi, P. (2016) 'The central role played by structural design in enabling the construction of buildings that advanced and revolutionized architecture', *Construction and Building Materials*, 114, pp. 956–976. doi:10.1016/j.conbuildmat.2016.03.092.
- Formenti, C. (1893) *La pratica del fabbricare per l'ingegnere, (in Italian)*. Milano: Ulrico Hoepli.
- Foster, P. *et al.* (2006) 'Strengthening masonry buildings with FRP composites', in *International Conference Structural Faults and Repair*.
- Foti, D. (2015) 'Structural Behaviour of Historical Stone Arches and Vaults : Experimental Tests and Numerical Analyses', *Key Engineering Materials*, 2, pp. 43–48. doi:10.4028/www.scientific.net/KEM.628.43.
- Foti, D., Vacca, V. and Facchini, I. (2018) 'DEM modeling and experimental analysis of the static behavior of a dry-joints masonry cross vaults', *Construction and Building Materials*, 170, pp. 111–120. doi:10.1016/j.conbuildmat.2018.02.202.
- Fraternali, F. (2010) 'A thrust network approach to the equilibrium problem of unreinforced masonry vaults via polyhedral stress functions', *Mechanics Research Communications*, 37(2), pp. 198–204. doi:10.1016/j.mechrescom.2009.12.010.
- Frézier, A.F. (1737) *La théorie et la pratique de la coupe de pierres et des bois pour la construction des voûtes et autres parties des bâtiments civils et militaires, ou traité de stéréotomie à l'usage de l'architecture (in French)*. Strasbourg/Paris: Charles-Antoine Jombert.
- Gabrielli, R. (1997) *Prime Analisi Mensiocronologiche dei laterizi della città di Bologna*. Available at: <https://www.yumpu.com/it/document/read/16229935/prime-analisi-mensiocronologiche-dei-laterizi-della-citta-di-bologna>.
- Gaetani, A. *et al.* (2016) 'Design and Analysis of Cross Vaults Along History', *International Journal of Architectural Heritage*, 10, pp. 841–856. doi:10.1080/15583058.2015.1132020.
- Gaetani, A. (2016) *Seismic Performance of Masonry Cross Vaults: Learning from Historical Developments and Experimental Testing*. PhD Thesis, University of Minho.
- Gaetani, A., Lourenço, P.B., Monti, G. and Milani, G. (2017) 'A parametric investigation on the seismic capacity of masonry cross vaults', *Engineering Structures* [Preprint]. doi:10.1016/j.engstruct.2017.07.013.
- Gaetani, A., Lourenço, P.B., Monti, G. and Moroni, M. (2017) 'Shaking Table Tests and Numerical Analyses on a Scaled Dry-Joint Arch Undergoing Windowed Sine Pulses', *Bulletin of Earthquake Engineering*, 15, pp. 4939–4961. doi:10.1007/s10518-017-0156-0.

- Gaetani, A., Bianchini, N. and Lourenço, P.B. (2021) 'Simplified micro-modelling of masonry cross vaults: Stereotomy and interface issues', *International Journal of Masonry Research and Innovation*, 6, pp. 97–125. doi:10.1504/IJMRI.2021.112076.
- Gaetani, A. and Lourenço, P.B. (2018) 'Finite element modelling of masonry cross vaults: considerations on block interlocking and interface properties', in Milani, G., Taliercio, A., and Garrity, S.W. (eds) *10th International Masonry Conference*. Milan.
- Galassi, S. (2008) *Analisi numerica di sistemi voltati in muratura rinforzati con materiali compositi (FRP)*. PhD Thesis, University of Florence.
- Galassi, S., Paradiso, M. and Tempesta, G. (2012) "' X - Vaults ": a Software for the Analysis of the Stability of Masonry Cross- Cross - Vaults', *International Journal of Computer Science*, 9(2), pp. 133–142.
- Garijo, L. *et al.* (2019) 'Stiffness evolution of natural hydraulic lime mortars at early ages measured through EMM-ARM', *Construction and Building Materials*, 216, pp. 405–415. doi:10.1016/j.conbuildmat.2019.04.258.
- Garmendia, L. *et al.* (2011) 'Rehabilitation of masonry arches with compatible advanced composite material', *Construction and Building Materials*, 25(12), pp. 4374–4385. doi:10.1016/j.conbuildmat.2011.03.065.
- Giamundo, V. *et al.* (2014) 'Evaluation of different computational modelling strategies for the analysis of low strength masonry structures', *Engineering Structures*, 73, pp. 160–169. doi:10.1016/j.engstruct.2014.05.007.
- Gilbert, M., Casapulla, C. and Ahmed, H.M. (2006) 'Limit analysis of masonry block structures with non-associative frictional joints using linear programming', *Computers and Structures*, 84(13–14), pp. 873–887. doi:10.1016/j.compstruc.2006.02.005.
- Giordano, E. *et al.* (2020) 'Expeditious damage index for arched structures based on dynamic identification testing', *Construction and Building Materials*, 265, p. 120236. doi:10.1016/j.conbuildmat.2020.120236.
- Giovanetti, F. (2000) *Manuale del recupero del Comune di Città di Castello, in Italian*. Rome: DEI.
- Giresini, L. *et al.* (2014) 'Numerical calibration of macro-element for vaulted systems in historic churches', in Peña, F. and Chávez, M. (eds) *9th International Conference on Structural Analysis of Historical Constructions*. Mexico City, Mexico, pp. 14–17.
- Gobbin, F., de Felice, G. and Lemos, J. V (2020) 'A Discrete Element Model for Masonry Vaults Strengthened with Externally Bonded Reinforcement', *International Journal of Architectural*

- Heritage*, 15, pp. 1959–1972. doi:10.1080/15583058.2020.1743792.
- Gomes, J.P. and Lemos, J. V (2020) ‘Characterization of the dynamic behavior of a concrete arch dam by means of forced vibration tests and numerical models’, *Earthquake Engineering and Structural Dynamics*, 49, pp. 679–694. doi:10.1002/eqe.3259.
- Grillanda, N. *et al.* (2019) ‘Collapse behavior of masonry domes under seismic loads: an adaptive NURBS kinematic limit analysis approach’, *Engineering Structures*, accepted, p. 109517. doi:10.1016/j.engstruct.2019.109517.
- Grillanda, N. *et al.* (2020) ‘Efficient meta-heuristic mesh adaptation strategies for NURBS upper-bound limit analysis of curved three-dimensional masonry structures’, *Computers and Structures*, 236, p. 106271. doi:10.1016/j.compstruc.2020.106271.
- Helmberg, G. (1994) ‘The Gibbs Phenomenon for Fourier Interpolation’, *Journal of approximation theory*, 7, pp. 41–63.
- Heyman, J. (1982) *The masonry arch*. Edited by Horwood. Chichester: Ellis Horwood Limited.
- Heyman, J. (1993) ‘The collapse of stone vaulting’, *Transactions on the Built Environment*, 4.
- Heyman, J. (1995a) *The stone skeleton: structural engineering of masonry architecture*. 2nd edn. Edited by Cambridge University Press. Cambridge: Cambridge University Press. doi:10.1016/0020-7683(66)90018-7.
- Heyman, J. (1995b) *The stone skeleton*. 2nd edn. Edited by Cambridge University Press. Cambridge: Cambridge University Press. doi:10.1016/0020-7683(66)90018-7.
- Holzer, S. (2011) ‘Vault analysis: continuum mechanics and rigid body approaches’, in *Construction History Europe- an Summer School: Two Millennia of Vaults, Domes and Shells*. Cambridge.
- Holzer, S. (2013) ‘Numerical arch and vault analysis’, *Journal of Heritage Conservation*, 1, pp. 7–17.
- Hooke, R. (1676) *A description of helioscopes and some other instruments*. London. doi:10.3931/e-rara-2171.
- Huerta, S. (2001) ‘Mechanics of masonry vaults: The equilibrium approach’, in Lourenço, P.B. and Roca, P. (eds) *Historical Constructions*. Guimarães, Portugal: University of Minho, pp. 47–69.
- Huerta, S. (2004) *Arcos, bóvedas y cúpulas: geometría y equilibrio en el cálculo tradicional de estructuras de fábrica*. Madrid, España: Instituto Juan de Herrera.
- Iannuzzo, A. *et al.* (2020) ‘Numerical Limit Analysis-based modelling of masonry structures subjected to large displacements’, *Computers and Structures*, 242, p. 106372. doi:https://doi.org/10.1016/j.compstruc.2020.106372.
- ICOMOS-ISCS. (2003) ‘Recommendations for the analysis, conservation and structural restoration of

- architectural heritage', in *14th General Assembly*. Victoria Falls, Zimbabwe, pp. 3–6.
- Intrigila, C., Nodargi, N.A. and Bisegna, P. (2019) *Square Cross Vaults on Spreading Supports*. Edited by R. 2019. Springer International Publishing. doi:10.1007/978-3-319-99441-3.
- ISO 13822 (2009) 'Bases for design of structures – Assessment of existing structures', *International Organization*. doi:10.1021/es0620181.
- Itasca Consulting Group, I. (2019a) '3DEC 7.0—Three-dimensional distinct element code.' Minneapolis, MN.
- Itasca Consulting Group, I. (2019b) '3DEC Online Manual', *3DEC Manual*, pp. 1–6.
- Kawai, T. (1978) 'New discrete models and their application to seismic response analysis of structures', *Nuclear Engineering and Design*, 48(1), pp. 207–229. doi:10.1016/0029-5493(78)90217-0.
- Kerakoll Spa (2021a) *Biocalce MuroSano*. Available at: [https://products.kerakoll.com/yep-repository/kerakoll/media/Biocalce_MuroSano_2021_\(pt\).pdf](https://products.kerakoll.com/yep-repository/kerakoll/media/Biocalce_MuroSano_2021_(pt).pdf).
- Kerakoll Spa (2021b) *GeoCalce F Antisismico*. Available at: <https://products.kerakoll.com/sr-SRB/p/geocalce-f-antisismico>.
- Kerakoll Spa (2021c) *GeoCalce FL Antisismico*. Available at: <https://products.kerakoll.com/it-IT/p/geocalce-fl-antisismico>.
- Kerakoll Spa (2021d) *GeoSteel Grid G200*. Available at: http://products.kerakoll.com/catalogo_dett.asp?idp=8454.
- Kooharian, A. (1953) 'Limit analysis of voussoir (segmental) and concrete arches', *Proceedings of the American Concrete Institute*, (4), pp. 317–328.
- Krstevska, L. *et al.* (2017) 'Shaking Table Testing of Models of Historic Buildings and Monuments-IZIIS ' Experience', (December). doi:10.1007/978-94-007-1977-4.
- Kurrer, K.-E. (2008) *The history of the theory of structures: from arch analysis to computational mechanics*. Berlin: Ernst & Sohn.
- Lagomarsino, S. (2015) 'Seismic assessment of rocking masonry structures', *Bulletin of Earthquake Engineering*, 13(1), pp. 97–128. doi:10.1007/s10518-014-9609-x.
- Lagomarsino, S. and Cattari, S. (2015) 'PERPETUATE guidelines for seismic performance-based assessment of cultural heritage masonry structures', *Bulletin of Earthquake Engineering*, 13(1), pp. 13–47. doi:10.1007/s10518-014-9674-1.
- Lanas, J. *et al.* (2004) 'Mechanical properties of natural hydraulic lime-based mortars', *Cement and Concrete Research*, 34(12), pp. 2191–2201. doi:10.1016/j.cemconres.2004.02.005.
- Lemos, J. V (2007) 'Discrete element modeling of masonry structures', *International Journal of*

- Architectural Heritage*, 1, pp. 190–213. doi:10.1080/15583050601176868.
- Lemos, J. V (2021a) 'Discrete Element Models for the Static and Dynamic Analysis of Masonry Structures', in Bagi, K. and Angelillo, M. (eds) *CISM International Centre for Mechanical Sciences, Courses and Lectures*. Udine, pp. 1–40.
- Lemos, J. V (2021b) 'Discrete Element Models for the Static and Dynamic Analysis of Masonry Structures', in Bagi, K. and Angelillo, M. (eds) *CISM International Centre for Mechanical Sciences, Courses and Lectures*. Udine.
- Lemos, J. V *et al.* (2022) 'Discrete Element Modelling of Masonry Arch Bridges, Arches and Vaults', in Milani, G. and Sarhosis, V. (eds) *From Corbel Arches to Double Curvature Vaults: Analysis, Conservation and Restoration of Architectural Heritage Masonry Structures*. Cham: Springer International Publishing, pp. 233–256. doi:10.1007/978-3-031-12873-8_5.
- Lemos, J. V and Campos Costa, A. (2017) 'Simulation of Shake Table Tests on Out-of-Plane Masonry Buildings. Part (V): Discrete Element Approach', *International Journal of Architectural Heritage*, 11(1), pp. 117–124. doi:10.1080/15583058.2016.1237587.
- Lemos, J. V and Sarhosis, V. (2023) 'Dynamic analysis of masonry arches using Maxwell damping', 49, pp. 583–592. doi:10.1016/j.istruc.2023.01.139.
- Lengyel, G. (2017) 'Discrete element analysis of gothic masonry vaults for self-weight and horizontal support displacement', *Engineering Structures*, 148, pp. 195–209. doi:10.1016/j.engstruct.2017.06.014.
- Lengyel, G. and Bagi, K. (2015) 'Numerical analysis of the mechanical role of the ribs in groin vaults', *Computers and Structures*, 158, pp. 42–60. doi:10.1016/j.compstruc.2015.05.032.
- Lengyel, G. and Németh, R.K. (2018) 'The Mechanical Behavior of Ribs in Masonry Groin Vaults Subjected to Seismic Load', *International Journal of Architectural Heritage*, pp. 1–15. doi:10.1080/15583058.2018.1491652.
- Lescher, F. (1911) *Sources of influence on Gothic Architecture*. University of illinois.
- De Lorenzis, L. *et al.* (2007) 'Failure of masonry arches under impulse base motion', *Earthquake Engineering & Structural Dynamics*, 36(14), pp. 2119–2136. doi:10.1002/eqe.719.
- Lourenço, P.B. (1996) *Computational strategies for masonry structures*. PhD thesis, Delft University of Technology. doi:90-407-1221-2.
- Lourenço, P.B. (2002) 'Computations on historic masonry structures', *Progress in Structural Engineering and Materials*, 4(3), pp. 301–319. doi:10.1002/pse.120.
- Lourenço, P.B. (2008) *Structural Masonry Analysis: Recent Developments and Prospects*, *Journal of*

- Chemical Information and Modeling*. doi:10.1017/CB09781107415324.004.
- Lourenço, P.B. *et al.* (2012) 'Seismic performance of the St. George of the Latins church: Lessons learned from studying masonry ruins', *Engineering Structures*, 40, pp. 501–518. doi:<https://doi.org/10.1016/j.engstruct.2012.03.003>.
- Lourenço, P.B. *et al.* (2016) 'Shaking Table Testing for Masonry Infill walls: Unreinforced vs. Reinforced solutions', *Earthquake Engineering & Structural Dynamics*, 45(14), pp. 1–22. doi:10.1002/eqe.2756.
- Lourenço, P.B. and Gaetani, A. (2022) *Finite Element Analysis for Building Assessment: Advanced Use and Practical Recommendations*. Taylor & Francis Group.
- Lourenço, P.B. and Pereira, J.M. (2018) *Recommendations for Advanced Modeling of Historic Earthen Sites: Seismic Retrofitting Project Research Report*. Los Angeles, CA: Getty Conservation Institute.
- Lourenço, P.B. and Ramos, L.F. (2004) 'Characterization of cyclic behavior of dry masonry joints', *Journal of Structural Engineering*, 130(5), pp. 779–786. doi:10.1061/(ASCE)0733-9445(2004)130:5(779).
- Máca, J. and Oliveira, D.V. (2017) 'Seismic behaviour and structural dynamics', in *Advanced Master in Structural Analysis of Monuments and Historical Constructions*. Czech Technical University in Prague, Universidade do Minho, University of Padova, Technical University of Catalonia.
- Malomo, D., Pinho, R. and Penna, A. (2020) 'Simulating the shake table response of unreinforced masonry cavity wall structures tested to collapse or near-collapse conditions', *Earthquake Spectra*, 36(2), pp. 554–578. doi:10.1177/8755293019891715.
- Mark, R., Abel, J.F. and O'Neill, K. (1973) 'Photoelastic and finite-element analysis of a quadripartite vault', *Experimental Mechanics*, 13(8), pp. 322–329. doi:10.1007/BF02322391.
- Marmo, F. and Rosati, L. (2017) 'Reformulation and extension of the thrust network analysis', *Computers and Structures*, 182, pp. 104–118. doi:10.1016/j.compstruc.2016.11.016.
- Masi, F. (2020) *Fast-dynamic response and failure of masonry structures of non-standard geometry subjected to blast loads*. PhD thesis, L'école centrale de Nantes.
- Matlab (2022) 'MATLAB: The language of technical computing'. USA: The MathWorks.
- De Matteis, G., Cacace, D. and Rouhi, J. (2019) 'Masonry Vaults: Architectural Evolution, Structural Behaviour and Collapse Mechanisms', in *7th Structural Engineers World Congress*. Istanbul.
- De Matteis, G. and Mazzolani, F.M. (2010) 'The Fossanova Church: seismic vulnerability assessment by numeric and physical testing', *International Journal of Architectural Heritage: Conservation*,

- Analysis, and Restoration*, 4(December), pp. 222–245. doi:10.1080/15583050903078903.
- De Matteis, G. and Mazzolani, F.M. (2012) 'The Fossanova Church : Seismic Vulnerability Assessment by Numeric and Physical Testing', *International Journal of Architectural Heritage: Conservation, Analysis, and Restoration* [Preprint], (December). doi:10.1080/15583050903078903.
- McInerney, J. and Dejong, M.J. (2015) 'Discrete Element Modeling of Groin Vault Displacement Capacity', *International Journal of Architectural Heritage*, 9(8), pp. 1037–1049. doi:10.1080/15583058.2014.923953.
- McNeel Robert, A. (2008) 'Rhinoceros NURBS modeling for Windows'.
- Mehrotra, A. (2018) 'A Computational Tool for Seismic Collapse Assessment of Masonry Structures', (December).
- Mehrotra, A., Arede, A. and Dejong, M.J. (2015) 'Discrete element modeling of a post-tensioned masonry arch', *Civil-Comp Proceedings*, pp. 1–16. doi:10.4203/ccp.108.49.
- Melaragno, M. (1991) *Introduction to Shell Structures*.
- Van Mele, T. *et al.* (2012) 'Physical and computational discrete modelling of masonry vault collapse', in Jasieńko, J. (ed.) *Structural Analysis of Historical Constructions*. Wrocław: Jerzy Jasieńko (Ed.), pp. 2552–2560.
- Mendes, L.A.M. and Campos Costa, A. (2007) 'LNEC-SPA, Signal Processing and Analysis Tools for Civil Engineers – Version 1.0 - Build 12', *LNEC Report n°29/2007-NESDE* [Preprint].
- Mendes, N. (2012) *Seismic assessment of ancient masonry buildings: Shaking table tests and numerical analysis*. PhD thesis, University of Minho.
- Mendes, N. (2015) *Masonry Macro-block Analysis*. Edited by M. Beer et al. Encyclopedia of Earthquake Engineering. Available at: https://link.springer.com/referenceworkentry/10.1007/978-3-642-35344-4_154.
- Mendes, N. and Lourenço, P.B. (2014) 'Sensitivity analysis of the seismic performance of existing masonry buildings', *Engineering Structures*, 80, pp. 137–146. doi:10.1016/j.engstruct.2014.09.005.
- Mendes, N., Lourenço, P.B. and Campos Costa, A. (2014) 'Shaking table testing of an existing masonry building : assessment and improvement of the seismic performance', *Earthquake engineering & structural dynamics*, 43(August 2013), pp. 247–266. doi:10.1002/eqe.
- Michiels, T.L. (2018) *Form finding of arches and shell structures subjected to seismic loading*.
- Middendorf, B. (2002) 'Physico-mechanical and microstructural characteristics of historic and

- restoration mortars based on gypsum: Current knowledge and perspective', *Geological Society Special Publication*, 205, pp. 165–176. doi:10.1144/GSL.SP.2002.205.01.13.
- Milani, E., Milani, G. and Tralli, A. (2008) 'Limit analysis of masonry vaults by means of curved shell finite elements and homogenization', *International Journal of Solids and Structures*, 45(20), pp. 5258–5288. doi:10.1016/j.ijsolstr.2008.05.019.
- Milani, G. *et al.* (2016) 'Tilting plane tests on a small-scale masonry cross vault: Experimental results and numerical simulations through a heterogeneous approach', *Engineering Structures*, 123, pp. 300–312. doi:10.1016/j.engstruct.2016.05.017.
- Milani, G. *et al.* (2019) 'Advanced non-linear numerical modeling of masonry groin vaults of major historical importance: St John Hospital case study in Jerusalem', *Engineering Structures*, 194(May), pp. 458–476. doi:10.1016/j.engstruct.2019.05.021.
- Milani, G. (2022) 'Simple lower bound limit analysis model for masonry double curvature structures', *Computers and Structures*, 269, p. 106831. doi:10.1016/j.compstruc.2022.106831.
- Milani, G., Milani, E. and Tralli, A. (2009) 'Upper bound limit analysis model for FRP–reinforced masonry curved structures. Part II: Structural analyses', *Computers and Structures*, 87(23–24), pp. 1534–1558. doi:10.1016/j.compstruc.2009.07.010.
- Milani, G., Simoni, M. and Tralli, A. (2014) 'Advanced numerical models for the analysis of masonry cross vaults: A case-study in Italy', *Engineering Structures*, 76, pp. 339–358. doi:10.1016/j.engstruct.2014.07.018.
- Milani, G. and Tralli, A. (2012) 'A simple meso-macro model based on SQP for the non-linear analysis of masonry double curvature structures', *International Journal of Solids and Structures*, 49(5), pp. 808–834. doi:10.1016/j.ijsolstr.2011.12.001.
- Millais, M. (2005) *Building structures from concepts to design*. 2nd edn. Edited by Taylor & Francis Group. Spon Press.
- Miltiadou-Fezans, A. (2008) 'A multidisciplinary approach for the structural restoration of the Katholikon of Dafni Monastery in Attica Greece', in D'Ayala, D.F. and Fodde (eds) *Structural Analysis of Historical Constructions*. London: Taylor & Francis Group, pp. 71–87.
- Ministero delle Infrastrutture e Trasporti (1906) 'GU n.225 del 27-9-1906'.
- Ministero delle Infrastrutture e Trasporti (1909) 'GU n.95 del 22-4-1909'.
- Ministero delle Infrastrutture e Trasporti (1981) 'DM 2 Luglio 1981 Normativa per le riparazioni ed il rafforzamento degli edifici danneggiati dal sisma nelle regioni Basilicata, Campania e Puglia'.
- Ministero delle Infrastrutture e Trasporti (1987) 'Norme tecniche per la progettazione, esecuzione e

- collaudo degli edifici in muratura e per il loro consolidamento’.
- Ministero delle Infrastrutture e Trasporti (2006) ‘Scheda per il rilievo del danno ai beni culturali - chiese. Modello A-DC. (in Italian)’.
- Ministero delle Infrastrutture e Trasporti (2018a) ‘Bozza circolare esplicativa Norme Tecniche per le Costruzioni’. Italy.
- Ministero delle Infrastrutture e Trasporti (2018b) ‘Norme tecniche per le costruzioni’.
- Ministero delle Infrastrutture e Trasporti (2018c) ‘NTC 2018 - Capitolo 3 - Azioni sulle costruzioni’.
- Ministero delle Infrastrutture e Trasporti (2019) ‘Circolare esplicativa delle norme tecniche per le costruzioni’.
- Musso, S.F. (2002) ‘Volte in muratura. Parole, definizioni e forme. (In italian).’, in *Costruzioni voltate in muratura*. Firenze: Libreria Alfani editrice, pp. 235–269.
- Navascués Palacio, P. (1974) *El libro de arquitectura de Hernán Ruiz, el Joven, in Spanish*. Madrid: Escuela Tecnica Superior de Arquitectura de Madrid, ETSAM.
- O’Dwyer, D. (1999) ‘Funicular analysis of masonry vaults’, *Computers and Structures*, 73(1–5), pp. 187–197. doi:10.1016/S0045-7949(98)00279-X.
- Occhiuzzi, A. et al. (2012) *Terremoto dell’emilia. Report preliminare sui danni registrati nel comune di Novi di Modena (MO) in seguito agli eventi sismici del 20 maggio, del 29 maggio e del 3 giugno 2012*.
- OMYA (2013) *Betocarb - OU*. Available at: <https://concrete.omya.com/>.
- Oppenheim, I.J. (1992) ‘The masonry arch as a four-link mechanism under base motion’, *Earthquake Engineering & Structural Dynamics*, 21(11), pp. 1005–1017. doi:10.1002/eqe.4290211105.
- Orduña, A. and Lourenço, P.B. (2005a) ‘Three-dimensional limit analysis of rigid blocks assemblages. Part I: Torsion failure on frictional interfaces and limit analysis formulation’, *International Journal of Solids and Structures*, 42(18–19), pp. 5140–5160. doi:10.1016/j.ijsolstr.2005.02.010.
- Orduña, A. and Lourenço, P.B. (2005b) ‘Three-dimensional limit analysis of rigid blocks assemblages. Part II: Load-path following solution procedure and validation’, *International Journal of Solids and Structures*, 42(18–19), pp. 5161–5180. doi:10.1016/j.ijsolstr.2005.02.011.
- Panella, D.S., Tornello, M.E. and Frau, C.D. (2017) ‘A simple and intuitive procedure to identify pulse-like ground motions’, *Soil Dynamics and Earthquake Engineering*, 94(January), pp. 234–243. doi:10.1016/j.soildyn.2017.01.020.
- Pantò, B. et al. (2016) ‘3D macro-element modelling approach for seismic assessment of historical

- masonry churches', *Advances in Engineering Software*, 97, pp. 40–59. doi:10.1016/j.advengsoft.2016.02.009.
- Papayianni, I. and Pachta, V. (2015) 'Experimental study on the performance of lime-based grouts used in consolidating historic masonries', *Materials and Structures/Materiaux et Constructions*, 48(7), pp. 2111–2121. doi:10.1617/s11527-014-0296-5.
- Parisse, F. *et al.* (2021) 'Benchmarking the seismic assessment of unreinforced masonry buildings from a blind prediction test', *Structures*, 31, pp. 982–1005. doi:10.1016/j.istruc.2021.01.096.
- Di Pasquale, E. and Cakmak, A. (1987) *DETECTION AND ASSESSMENT OF SEISMIC STRUCTURAL DAMAGE*. Princeton, NJ.
- Di Pasquale, S. (1996) *L'arte del costruire. Tra conoscenza e scienza*. Venezia: Marsilio.
- Pastor, M., Binda, M. and Harčarik, T. (2012) 'Modal assurance criterion', *Procedia Engineering*, 48, pp. 543–548. doi:10.1016/j.proeng.2012.09.551.
- PEER Ground Motion Database* (2022). Berkely. Available at: <https://ngawest2.berkeley.edu/site>.
- Pittaluga, D. (2002) 'Il contributo dell'archeologia dell'architettura per la conoscenza delle strutture voltate: il caso di Genova', in *Italian* [Preprint].
- Van Der Pluijm, R. (1992) 'Material properties of masonry and its components under tension and shear', *Proc. 6th Canadian Masonry Symposium*, pp. 675–686.
- Van Der Pluijm, R. (1999) *Out-of-Plane Bending of Masonry Behaviour and Strength*. doi:10.6100/IR528212.
- Ptaszkowska, J. and Oliveira, D.V. de C. (2014) 'Numerical modeling of masonry vaults strengthened with transversal diaphragms', in F. Peña and M. Chávez (ed.) *SAHC2014 - 9th International Conference on Structural Analysis of Historical Constructions*. Mexico City, Mexico.
- Pulatsu, B. (2015) *Simulation of the failure of masonry walls subjected to out-of-plane loading using the discrete element method*. Master Thesis, University of Minho.
- Pulatsu, B. *et al.* (2019) 'In-plane static response of dry-joint masonry arch-pier structures', *AEI 2019: Integrated Building Solutions - The National Agenda - Proceedings of the Architectural Engineering National Conference 2019*, (April), pp. 240–248. doi:10.1061/9780784482261.028.
- Pulatsu, B., Erdogmus, E., Lourenço, P.B., Lemos, J. V and Hazzard, J. (2020) 'Discontinuum analysis of the fracture mechanism in masonry prisms and wallettes via discrete element method', *Meccanica*, 55, pp. 505–523. doi:10.1007/s11012-020-01133-1.

-
- Pulatsu, B., Erdogmus, E., Lourenço, P.B., Lemos, J. V and Tuncay, K. (2020) 'Simulation of the in-plane structural behavior of unreinforced masonry walls and buildings using DEM', *Structures*, 27, pp. 2274–2287. doi:10.1016/j.istruc.2020.08.026.
- Pulatsu, B. *et al.* (2023) 'Computational investigations on the combined shear–torsion–bending behavior of dry-joint masonry using DEM', *Computational Particle Mechanics*, 10, pp. 249–260. doi:10.1007/s40571-022-00493-7.
- Pulatsu, B. (2023) 'Coupled elasto-softening contact models in DEM to predict the in-plane response of masonry walls', *Computational Particle Mechanics* [Preprint]. doi:10.1007/s40571-023-00586-x.
- Quirós Castillo, J.A. (1997) 'La mensiocronologia dei laterizi della toscana: problematiche e prospettive di ricerca', in *Archeologia dell'architettura: II, 1997. in Italian*. Firenze, pp. 159–165. doi:https://doi.org/10.1400/236192.
- Raimondi, A. (2013) *La chiesa di Santa Maria in Scaria. Gestire la complessità: dal rilievo al BHIM (in Italian)*. Master thesis, Politecnico di Milano.
- Ramaglia, G. *et al.* (2017) 'Seismic Strengthening of Masonry Vaults with Abutments Using Textile-Reinforced Mortar', *Journal of Composites for Construction*, 21(2), p. 04016079. doi:10.1061/(asce)cc.1943-5614.0000733.
- Ramesh, M., Azenha, M. and Lourenço, P.B. (2019) 'Mechanical properties of lime–cement masonry mortars in their early ages', *Materials and Structures/Materiaux et Constructions*, 52(1). doi:10.1617/s11527-019-1319-z.
- Ramos, L.F. (2007) *Damage Identification on Masonry Structures Based on Vibration Signatures*. PhD thesis, Universidade do Minho.
- Restrepo Vélez, L.F., Magenes, G. and Griffith, M.C. (2014) 'Dry stone masonry walls in bending-Part I: Static tests', *International Journal of Architectural Heritage*, 8(1), pp. 1–28. doi:10.1080/15583058.2012.663059.
- Van Rickstal, F. (2000) *Grout injection of masonry, scientific approach and modeling*.
- Roca, P. *et al.* (2010) 'Structural analysis of masonry historical constructions. Classical and advanced approaches', *Archives of Computational Methods in Engineering*, 17(3), pp. 299–325. doi:10.1007/s11831-010-9046-1.
- Roca, P., Lourenço, P.B. and Gaetani, A. (2019) *Historic Construction and Conservation. Materials, Systems and Damage*. Lisbon: Taylor & Francis Group.
- Rolla, E. (1869) *Cenni sulle volte (in Italian)*. Master thesis, Università di Torino.
-

- Romanazzi, A. *et al.* (2022) *Out-of-plane shake table test of a rammed earth sub-assembly*, *Bulletin of Earthquake Engineering*. Springer Netherlands. doi:10.1007/s10518-022-01525-6.
- Rondelet, J. (1802) *Traité théorique et pratique de l'art de bâtir*. 7th ed. Pa, in French. 7th ed. Pa. Paris: Chez l'auteur.
- Rossi, M. (2015) *Evaluation of the Seismic Response of Masonry Cross Vaults*. PhD thesis, Università degli Studi di Genova.
- Rossi, M. *et al.* (2017a) 'Collapse Analysis of Unreinforced Masonry Vaults Using 3D-printed Scale-model Testing', in *7th International Conference on Advances in Experimental Structural Engineering Collapse*.
- Rossi, M. *et al.* (2017b) 'Experimental study on the behaviour of masonry pavilion vaults on spreading supports', *Structures*, 11(May), pp. 110–120. doi:10.1016/j.istruc.2017.04.008.
- Rossi, M. *et al.* (2020) 'Seismic analysis of a masonry cross vault through shaking table tests: The case study of the Dey Mosque in Algiers', *Earthquake and Structures*, 18(1), pp. 57–72. doi:10.12989/eas.2020.18.1.057.
- Rossi, M., Calderini, C. and Lagomarsino, S. (2016) 'Experimental testing of the seismic in-plane displacement capacity of masonry cross vaults through a scale model', *Bulletin of Earthquake Engineering*, 14(1), pp. 261–281. doi:10.1007/s10518-015-9815-1.
- Ruggieri, N. (2016) 'The Borbone " Istruzioni per Gli Ingegneri ": A Historical Code for Earthquake-Resistant Constructions', *International Journal of Architectural Heritage*, pp. 1–13. doi:10.1080/15583058.2016.1212128.
- Sanabria, S.L.S.L. (1982) 'The mechanization of design in the 16th century: the structural formulae of Rodrigo Gil de Hontañón', *Journal of the Society of Architectural Historians*, 41(4), pp. 281–293. doi:10.2307/989800.
- Santini, S., Baggio, C. and Sabbatini, V. (2022) 'Seismic Assessment of Roman Concrete Groin Vaults through UAV, NDT and 3D Analyses', *Heritage*, 5(1), pp. 311–331. doi:10.3390/heritage5010017.
- De Santis, S., De Felice, G. and Roscini, F. (2019) 'Retrofitting of Masonry Vaults by Basalt Textile-Reinforced Mortar Overlays', *International Journal of Architectural Heritage*, 13(7), pp. 1061–1077. doi:10.1080/15583058.2019.1597947.
- Sarhosis, V., Garrity, S.W. and Sheng, Y. (2015) 'Influence of brick–mortar interface on the mechanical behaviour of low bond strength masonry brickwork lintels', *Engineering Structures*, 88, pp. 1–11. doi:10.1016/j.engstruct.2014.12.014.

-
- Scacco, J., Milani, G. and Lourenço, P.B. (2020) 'Automatic mesh generator for the non-linear homogenized analysis of double curvature masonry structures', *Advances in Engineering Software*, 150(September), p. 102919. doi:10.1016/j.advengsoft.2020.102919.
- Scamozzi, V. (1616) *L'idea dell'architettura universale, in Italian*. Edited by T. Stefano. Milano: Coi tipi di Borroni e Scotti (edition of 1838).
- Segura, J. *et al.* (2020) 'Influence of recycled limestone filler additions on the mechanical behaviour of commercial premixed hydraulic lime based mortars', *Construction and Building Materials*, 238, p. 117722. doi:10.1016/j.conbuildmat.2019.117722.
- Seismological Facilities for the Advancement of Geoscience (SAGE) (2022) *IRIS Data Services*. Available at: <https://ds.iris.edu/ds/nodes/dmc/data/#requests>.
- Selby, R.G. and Vecchio, F.J. (1997) 'A constitutive model for analysis of reinforced concrete solids', pp. 460–470.
- Senthivel, R. and Lourenço, P.B. (2009) 'Finite element modelling of deformation characteristics of historical stone masonry shear walls', *Engineering Structures*, 31(9), pp. 1930–1943. doi:10.1016/j.engstruct.2009.02.046.
- Shapiro, E.E. (2012) *Collapse mechanisms of small-scale unreinforced masonry vaults*. Master thesis, Massachusetts Institute of Technology. Available at: <http://hdl.handle.net/1721.1/72648>.
- Sharma, S. *et al.* (2020) 'Two-way bending experimental response of URM walls subjected to combined horizontal and vertical seismic excitation', *Engineering Structures*, 219(July), p. 110537. doi:10.1016/j.engstruct.2020.110537.
- Silva, B.A., Ferreira Pinto, A.P. and Gomes, A. (2015) 'Natural hydraulic lime versus cement for blended lime mortars for restoration works', *Construction and Building Materials*, 94, pp. 346–360. doi:10.1016/j.conbuildmat.2015.06.058.
- Silvestri, S. *et al.* (2021) 'Shaking table testing of groin vaults made by 3D printers', *Soil Dynamics and Earthquake Engineering*, 150(April), p. 106880. doi:10.1016/j.soildyn.2021.106880.
- Smoljanović, H., Nikolić, Ž. and Živaljić, N. (2015) 'A finite-discrete element model for dry stone masonry structures strengthened with steel clamps and bolts', *Engineering Structures*, 90, pp. 117–129. doi:10.1016/j.engstruct.2015.02.004.
- Stefanou, I., Psycharis, I.N. and Georgopoulos, I.O. (2011) 'Dynamic response of reinforced masonry columns in classical monuments', *Construction and Building Materials*, 25(12), pp. 4325–4337. doi:10.1016/j.conbuildmat.2010.12.042.
- Szołomicki, J.P. (2009) 'Structural behaviour of masonry vaults', (July), pp. 7–9.

- Szołomicki, J.P., Berkowski, P. and Barański, J. (2014) 'Computer modelling of masonry cross vaults strengthened with fiber reinforced polymer strips', *Archives of Civil and Mechanical Engineering*, 5, pp. 1–16. doi:10.1016/j.acme.2014.05.006.
- Theodossopoulos, D. *et al.* (2002) 'Assessment of the structural response of masonry cross vaults', *Strain*, 38(3), pp. 119–127. doi:10.1046/j.0039-2103.2002.00021.x.
- Tirelli, D. (2011) *Modal Analysis of Small & Medium Structures by Fast Impact Hammer Testing Method*. doi:10.2788/80576.
- Tomasoni, E. (2008) *Le volte in muratura negli edifici storici: tecniche costruttive e comportamento strutturale (in Italian)*. PhD thesis, Università degli Studi di Trento. doi:10.1007/bf00141161.
- Tomažević, M. (1999) *Earthquake-Resistant Design of Masonry Buildings*. London: Imperial College Press.
- Torres, B., Bertolesi, E., Calderón, P.A., *et al.* (2019) 'A full-scale timber cross vault subjected to vertical cyclical displacements in one of its supports', *Engineering Structures*, 183(July 2018), pp. 791–804. doi:10.1016/j.engstruct.2019.01.054.
- Torres, B., Bertolesi, E., Moragues, J.J., *et al.* (2019) 'Experimental investigation of a full-scale timber masonry cross vault subjected to vertical settlement', *Construction and Building Materials*, 221, pp. 421–432. doi:10.1016/j.conbuildmat.2019.06.015.
- Tralli, A., Alessandri, C. and Milani, G. (2014) 'Computational methods for masonry vaults: A review of recent results', *Open Civil Engineering Journal*, 8(1), pp. 272–287. doi:10.2174/1874149501408010272.
- Trifunac, M.D. and Brady, A.G. (1975) 'A study on the duration of strong earthquake ground motion. 14F, 1T, Refs.', *Bulletin of the Seismological Society of America*, 65(3), pp. 581–626. doi:10.1016/0148-9062(76)90487-3.
- Ungewitter, G.G. and Mohrmann, K. (1890) *Lehrbuch der gotischen Konstruktionen*. 3rd ed. Leipzig: Weigel.
- Universidad Nacional Autónoma de México, I. d. G., S.S.N. (2022) *National Seismological Service of Mexico*. Available at: <http://www2.ssn.unam.mx:8080/catalogo/%0A%0A>.
- Vasconcelos, G. (2005) *Experimental investigations on the mechanics of stone masonry: Characterization of granites and behavior of ancient masonry shear walls*. PhD thesis, Universidade do Minho.
- Vecchiattini, R. (2015) *Mensiochronology of bricks and chronotipology of mortars*. Genoa.
- Veiga, R., Magalhaes, A.C. and Bokan-bosilikov, V. (2004) 'Capillarity tests on historic mortar samples

extracted from site. Methodology and compared results', in *13th International Brick and Block Masonry Conference Amsterdam, July 4-7, 2004*, pp. 1–10.

Velosa, A.L. *et al.* (2007) 'Characterisation of roman mortars from Conímbriga with respect to their repair', *Materials Characterization*, 58(11-12 SPEC. ISS.), pp. 1208–1216. doi:10.1016/j.matchar.2007.06.017.

Williams, M.S. *et al.* (2012) 'Model Scale Shaking Table Tests on Masonry Barrel and Cross Vaults', in *15 WCEE, Lisbon*.

Zampieri, P. *et al.* (2018) 'A review of methods for strengthening of masonry arches with composite materials', *Engineering Structures*, 171, pp. 154–169. doi:10.1016/j.engstruct.2018.05.070.